

THE LOW FREQUENCY MAGNETIC PROPERTIES OF NICKEL-IRON  
FILMS AND THEIR INVESTIGATION BY BH CURVE PLOTTER  
TECHNIQUES

Thesis submitted for the Degree of

Doctor of Philosophy

by

R. Vaughan, B.Sc., B.E.



School of Electrical Engineering

University of Sydney.

April, 1964.

THE LOW FREQUENCY MAGNETIC PROPERTIES OF NICKEL-  
IRON FILMS AND THEIR INVESTIGATION BY BH CURVE  
PLOTTER TECHNIQUES

SUMMARY

The present thesis deals with the low frequency or quasistatic properties of thin vacuum evaporated nickel-iron films, in particular with extending the range and accuracy with which these properties can be measured by audio-frequency BH plotter techniques.

An integral part of this work has consequently been the design and construction of a suitable BH plotter, together with a critical examination of the theoretical and practical factors limiting the performance of an instrument of this type. Considered in detail are the optimum integration transfer functions for low noise, and the best geometrical shape of the sense coil for the maximum coupling with the film sample. Circuits are given for the transistorized, high accuracy, phase compensated pre-amplifier and feedback integrator used in the BH plotter.

Theoretical and experimental results are given in the use of the BH plotter for the measurement of such



quantities as anisotropy torque curves to 0.1 per cent accuracy, which have previously required more complex and delicate instruments. Easy axis hysteresis loops are examined and the switching processes, and consequently the coercive force, shown to be dependent on the time rate of change of the measuring field. The effects of anisotropy dispersion is considered throughout, and a rigorous analysis is given of the wavelength and amplitude of the resulting magnetizational ripple.

The properties of thin films are critically dependent on the conditions during deposition. This thesis also describes a self-supporting electron bombardment source with instrumentation for the control of film thickness and the stabilization of the deposition rate.

## TABLE OF CONTENTS

2.3	STATEMENT OF ORIGINALITY AND SCOPE OF THESIS	14
CHAPTER 1		
INTRODUCTION		
1.1	A Brief Historical Background	21
1.2	Current Interests	22
1.3	List of References	27
1.4	List of principal symbols (removable)	Back Cover Pocket
CHAPTER 2		
BASIC MAGNETIC PROPERTIES OF THIN NICKEL-IRON FILMS AT LOW FREQUENCIES		
2.1	Introduction	29
2.2	The Coherent Rotational and Independent Region Models	30
2.3	Quasistatic Switching Based on the Coherent Rot- ational Model	36
2.4	Anisotropy Dispersion and Magnetisation Ripple	44
2.41	A Statistical Representation of Anisotropy Dispersion	45
2.42	Magnetisation Ripple	50

	<u>Page</u>
2.43 Switching Thresholds and the Unstable Growth of Magnetisation Ripple	59
2.5 Switching by Wall Motion for Fields Near the Easy Axis	59
2.6 Switching by Partial Rotation for Fields Inclined to the Easy Axis at Greater than the Critical Angle $\gamma_c$	64
2.61 Deficiencies of the Simple Theory	67
2.7 Switching by Labyrinth Propagation for Fields Inclined to the Easy Axis at Greater than the Critical Angle $\gamma_c$	69
2.71 $\beta=0$ : Shape Anisotropy and $\chi$ for Thick Films	74
2.72 $\beta=\infty$ : Propagation Effects and $\chi$ for Thin Films	75
2.73 Reconciliation of Partial Rotation and Labyrinth Switching Processes	78
2.8 Torque Measurements and Rotational Hysteresis	78
2.81 Theoretical Torque Curves Based on the Coherent Rotational Model	80
2.82 Departures from the Coherent Rotational Model	82
2.83 Anisotropy Measurements	86

2.9 List of References 87

CHAPTER 3

THE ORIGIN OF MAGNETIC ANISOTROPY IN THIN EVAPORATED NICKEL-IRON FILMS

3.1 Introduction 94

3.2 Crystal Orientation and Microstructure 97

3.21 Crystallite Size, Shape and Orientation 97

3.22 Oxide and Other Impurities 99

3.23 Structural Defects 101

3.24 Chemical Inhomogeneity 101

3.3 Mechanical Stress 102

3.31 Causes of Stress 102

3.32 Methods of Measuring Stress. 105

Reported Experimental Data

3.4 Some Properties of Ni and Fe Films. 109

Pseudo-rotatable and Rotatable Anisotropies

3.5 Directional Ordering 112

3.51 Ordering in Bulk Materials 120

3.52 The Origin of the Ordering Interaction 121

Energy

3.6	Anisotropy in Normally Incident Films.	123
	Preferred Crystalline Alignment and Isotropic Stress	
3.61	Calculation of the Anisotropy Produced by a Crystalline Texture Axis	124
3.62	Anisotropies in Fe and Ni. Contradictions of the Texture Axis Theory with Experiment	126
3.7	Anisotropy in Normally Incident Permalloy Films. Directional Ordering	133
3.71	Fixed Anisotropies and Anisotropies Rotatable by Low Temperature Magnetic Anneal	133
3.72	The Variation of Anisotropy with Substrate Temperature	137
3.8	The Dependence of the Non-rotatable Anisotropy $K_u$ of Normally Incident Films on Composition. Directional Ordering and Anisotropic Stress	140
3.81	An Interpretation of Anisotropic Stress in Terms of Directional Ordering of Imperfections	144
3.82	The Effects of Oxygen	145
3.9	Pseudo-rotatable Anisotropy in Normally Incident Films. Random Anisotropy Centres	146

3.10 Anisotropy in Oblique Incident Films	151
3.(10)1 Crystalline Texture	152
3.(10)2 The Formation of an Anisotropic Crystallite Chain Structure and Anisotropic Stress	152
3.11 List of References	158

#### CHAPTER 4

#### BH PLOTTER HYSTERESIS LOOPS AND LOW FREQUENCY SWITCHING PROPERTIES OF FILMS

4.1 Introduction	170
4.2 Typical Switching Waveforms and Hysteresis Curves	171
4.3 Instrumentational Errors	171
4.4 Departures from the Coherent Rotational Model	182
4.5 Switching Voltage Waveforms and the Occurrence of Multiple Reversal Processes	189
4.6 The Time Dependence of Certain Reversal Processes and the Associated Dependence of Coercive Force on the Frequency and Amplitude of the Applied AF Field	195
4.7 List of References	208



## CHAPTER 5

MEASUREMENT OF TORQUE CURVES AND OF THE ANISOTROPY  
ENERGY FUNCTION OF THIN FILMS

5.1	Introduction	209
5.2	Basic Methods of Measurement of Torque Curves	211
5.21	Direct Measurement of the Mechanical Torque	214
5.22	Measurement of the Component of the Magnetisation Normal to the Applied Field	214
5.23	Measurement of the Angular Position of the Magnetisation	216
5.3	Measurement of Torque Curves by Determining the Angular Position of the Magnetisation. The Method of Rossing and Stolen	217
5.31	A Description of the Method	217
5.32	The Theoretical Accuracy	219
5.4	Measurement of High Field Torque Curves by Determining the Angular Position of the Magnetisation	223
5.41	Introduction	223
5.42	A Description of the Method	224
5.43	The Theoretical Accuracy	231
5.44	A Discussion of the Null Condition for Real Films	237

5.45	Some Practical Details of the Method and Experimental Errors	253
5.46	Experimental Torque Curves for a Number of Films	255
5.47	A Variation of the Method for the Measure- ment of the Saturated Magnetisation of a Film	261
5.5	Methods of Measuring Film Anisotropy. Initial and Saturated Measurements	263
5.51	Initial Measurements	263
5.52	High Field Measurements	266
5.6	Measurement of the Anisotropy by the Hard Axis Initial Susceptibility Method Using an MH Plotter	266
5.61	The Effects of Anisotropy Dispersion	266
5.62	Practical Details and Experimental Errors for the Present MH Plotter	274
5.7	List of References	280

## CHAPTER 6

### THE DESIGN OF AN MH PLOTTER FOR THE ACCURATE MEASUREMENT OF THIN FILMS

6.1	Introduction	282
6.2	Principles of Operation	286

6.21	A Description of the System	286
6.22	The Limiting Sensitivity	291
6.23	A Comparison with the Vibrating Sample Magnetometer and the Mechanical Torque Balance	292
6.3	The Mechanical Construction	299
6.31	A General Description	299
6.32	The Sense Coil Assembly	302
6.33	The Film Holder	303
6.4	The Field Coils $D_1$ and $D_2$	304
6.41	The Diameter of the Coils	307
6.42	AF Power Requirements	308
6.43	The Impedance Level and Tuning	308
6.44	The Production of Simultaneous AF and DC Fields	309
6.45	The Orthogonality of the Field Coils and Induced AF Currents	310
6.46	Possible Modification	312
6.5	The Orientation of a Film and Cancellation of the Earth's Magnetic Field	313
6.51	Determining the Easy and Hard Axis Directions	313
6.52	Cancellation of the Earth's Magnetic Field	316

6.6	Factors in the Stable Cancellation of the Air Flux Voltage	318
6.61	Introduction	318
6.62	Conditions for Stable and Frequency Independent Cancellation	322
6.63	Cancellation Stability. First Order Amplitude Unbalance	325
6.64	Cancellation Frequency Dependence. First Order Phase Unbalance, Higher Order Terms and other Extraneous Voltages	333
6.65	The Cancellation Bridge	338
6.66	Some Additional Considerations	346
6.7	Frequency Response Errors in Hysteresis Loop Displays	348
6.71	Introduction	348
6.72	Errors due to Limited Frequency Response of the Flux Detection System	350
6.73	Phase Errors in the Field Display	357
6.8	List of References	363
7.15	Uncompensated Transfer Functions	411
7.16	Phase Compensated Transfer Functions	423
7.17	Transfer Functions of Higher Complexity	424
7.18	Realization of the Transfer Function	425

## CHAPTERS 7

FACTORS IN OBTAINING THE MAXIMUM SENSITIVITY  
OR SIGNAL TO NOISE RATIO IN THE DETECTION OF  
THE FILM FLUX

7.1	Introduction.	366
	An Expression for the Signal to Noise Ratio	
7.2	The Choice of the Repetition Frequency $\omega_0$ .	370
	The Amplifier Noise Figure $F$ and the Optimum Impedance Level of the Sense Coil	
7.21	Introduction	370
7.22	Transistor Amplifiers	372
7.23	Value Amplifiers	389
7.24	A Comparison Between Transistor and Value Amplifiers	401
7.3	The Choice of the Transfer Function $A(s)$	403
7.31	Introduction	403
7.32	The Form of $A(s)$ for Physical Realisability	405
7.33	The Fractional Integration Error	406
7.34	The Effective Noise Bandwidth	410
7.35	Uncompensated Transfer Functions	411
7.36	Phase Compensated Transfer Functions	413
7.37	Transfer Functions of Higher Complexity	424
7.38	Realization of the Transfer Function	425

7.4	The Design of the Sense Coil	430
7.41	Introduction	430
7.42	Basic Types of Sense Coils and General Considerations	432
7.43	The Optimum Shape of the Sense Coil for Minimum Noise	434
7.44	An Analytic Solution for a Uniformly Magnetised Rectangular Film Sheet and an Idealised "Rectangular" Shaped Sense Coil	436
7.45	The Optimum Shape for a Sense Coil Enclosing the Film	445
7.46	The Optimum Shape for a Sense Coil Lying on One Side Only of the Film	448
7.47	The Special Case of a Rectangular Film Sheet and an Indefinitely Long Sense Coil	449
7.48	Properties of the Sense Coil of the Present Instrument	455
7.5	List of References	457

## CHAPTER 8

CIRCUITS FOR THE AMPLIFICATION AND INTEGRATION  
OF THE SENSE COIL VOLTAGE

8.1	Introduction	459
8.2	General Considerations	461
8.3	The Preamplifier	467
8.4	The Integrator	470
8.41	The Integrator Transfer Function and Low Frequency Stability	470
8.42	High Frequency Stability	475
8.5	Test and Adjustment of the Amplifier and Integration System	482
8.6	Low Impedance Input Circuits	486
8.61	The Reaction Field due to the Voltage Induced by the Air Flux	487
8.62	The Reaction Field due to the Voltage Induced by the Film Itself	488
8.63	A Low Input Impedance Preamplifier	490
8.64	A Low Input Impedance Feedback Integrator	492
8.7	Reduction of Noise by Synchronous DC Restoration	494
8.71	Introduction	494
8.72	A Circuit for a Transistorised Synchronous DC Restorer	498
8.8	List of References	508

## STATEMENT OF ORIGINAL CONTRIBUTION CHAPTER 9 SCOPE OF THESIS

## THE VACUUM EVAPORATION OF THE FILM SAMPLES

9.1	Introduction	509
9.2	The Experimental Setup	509
9.21	The Substrate	513
9.22	The Electron Bombardment Evaporation Source	516
9.23	The Operating Procedure	522
9.3	A Feedback Film Thickness and Deposition Rate Control	523
9.4	List of References	529

## APPENDIX A

534

Statistical Results Pertaining to the Effect of Dispersion on Anisotropy Field Measurements

## APPENDIX B

537

## A General Purpose Precision Magnet Supply

## ACKNOWLEDGEMENTS

542



## STATEMENT OF ORIGINALITY AND SCOPE OF THESIS

The present thesis deals with the low frequency or quasistatic properties of thin vacuum evaporated nickel-iron films.

### A General Outline

In thin films, a need exists for increased accuracy in experimental measurements, coupled with a clear definition of the film parameters actually determined. This thesis is largely concerned with these questions, and in particular with extending the range and accuracy with which film properties can be studied by audio-frequency BH plotter techniques. An integral part of this thesis has consequently been the design and construction of a suitable BH plotter, together with a critical examination of the theoretical and practical factors limiting the performance of an instrument of this type. Theoretical and experimental results are given in the use of a BH plotter in the measurement of such quantities as anisotropy torque curves, which have previously required more complex and delicate instruments.

The properties of thin films are critically dependent on the conditions during deposition. Hence this thesis also

describes a self-supporting electron bombardment source with instrumentation for the control of film thickness and the stabilization of the deposition rate.

### The Scope of the Thesis

In greater detail, Chapters 1 to 5 consider film properties, Chapters 6 to 8 describe the BH plotter and Chapter 9 the vacuum evaporation equipment.

Chapter 1 is a brief introductory outline of the early history of ferromagnetic films, with a reference to their current importance in fundamental research and digital computer applications.

Chapter 2 is basically a review of standard results on low frequency switching behaviour needed in understanding the experimental measurements of Chapters 4 and 5. Worthy of note is Section 2.4, which introduces the original and useful concept of a vector anisotropy function and gives a rigorous derivation of magnetization ripple, leading to an expression for the mean squared ripple amplitude which has not been previously presented in the literature.

Chapter 3 is a critical evaluation of published experimental results relating to the causes of the uniaxial anisotropy in films. This work is a necessary preliminary to a full understanding of film behaviour.

Chapter 4 is concerned with experimental measurements on films using the BH plotter described in Chapter 6. The main emphasis is on the voltage switching waveforms. These show multiple peaks indicating the presence of more than one reversal process. The threshold fields for these processes vary with the transverse field and the time rate of change of the applied audio-frequency field. This approach could usefully supplement Bitter pattern techniques and does not appear to have been explored in detail by other workers.

Chapter 5 deals with experimental measurements of the anisotropy energy function. Section 5.4 describes a useful and original method whereby high field torque curves can be measured to 0.1 per cent accuracy using the BH plotter of Chapter 6. Experimental torque curves for some films show small departures from the true uniaxial  $K\sin^2\phi$  form, suggesting dispersion centres of other than uniaxial anisotropy. These effects are resolved only because of the high accuracy of the method used and have not been reported previously. In the course of these measurements an irreversible "ripple jump" hysteresis has been observed, occurring for small oscillations of the magnetization well above the coherent rotational threshold. An expression is derived for the magnitude of this effect in terms of anisotropy dispersion. An estimate of anisotropy dispersion may be obtained

either by the Crowther technique, or from easy axis remanence values. The present effect appears to correlate more closely with the remanence values. Finally, in Section 5.6, experimental measurements of the anisotropy field  $H_K$  by extrapolation of the initial hard axis hysteresis loops are compared with the previous torque curves results. Small differences exist which may be explained in terms of anisotropy dispersion, but again show no convincing correlation with Crowther dispersion values, reflecting the inadequacy of the models so far available to describe the details of film behaviour.

Chapter 6 is concerned with those practical details in the design of the BH plotter, which contribute to the absence of critical adjustment and the accuracy and overall convenience of the instrument. Previously, imperfect cancellation of the air flux voltage, in particular of its harmonic distortion components, has imposed one of the principal limitations on the useful sensitivity. Section 6.6 contains an original analysis of the uncanceled voltage which allows the various error terms to be experimentally distinguished and separately cancelled to give a complete elimination of harmonic components.

In Chapter 7, a general theoretical treatment is developed of the conditions necessary for the maximum sensitivity

of the BH plotter. An optimum operating frequency and an upper limit to the sensitivity is established in terms of certain fixed parameters, including the inductance and the self-capacitance of the sense coil. Section 7.3 contains an original analysis of the approximation problem to the integrator transfer function having minimum low frequency noise. The method is based on the successive compensation of phase, amplitude and higher order error terms and extends to transfer functions of arbitrary complexity. Pole and zero positions in the complex plane are considered directly, giving a simple understanding of the effects of extraneous poles and an immediate relation to experimental adjustment procedures. It is felt that this material, coupled with its practical application to the transistorized integrator of Chapter 8, represents a useful contribution to the theory of electronic integrators. Section 7.4 presents general design curves for the best geometrical shape of the sense coil. While the analysis is conceptually straightforward, previous treatments have considered only a sense coil surrounding the film. They contain serious approximations which prevent their extension to the present case, where for mechanical reasons the sense coil is located on one side of the film only.

Chapter 8 gives detailed circuits for the transistorized preamplifier, feedback integrator and synchronous DC

automatic control of the film thickness and deposition rate. restorer used with the BH plotter and discusses aspects of the overall circuit design peculiar to this application. Emphasis is placed on the test and adjustment of the system to be reliably free from phase error, essential if hysteresis loop displays are not to show serious errors in coercive force. The preamplifier and synchronous restorer are basically conventional. The integrator is based on the development of Section 7.3 and has significant advantages over previous designs, including the elimination of DC output drift problems and the avoidance of the high frequency instabilities normally troublesome with multi-stage transistor feedback integrators. Finally, low input impedance preamplifiers are shown to be possible for thin film application, in contrast to the situation for bulk samples. These offer improved high frequency response and other advantages over present conventional circuits.

Chapter 9 describes the vacuum evaporation system constructed for the preparation of the film samples used in this thesis. A self-supporting electron bombardment source is used with feedback stabilization of the deposition rate. The present system, although relatively new at its inception, no longer represents any significant contribution in this field. Useful circuitry is however described for a four-terminal resistivity measuring device necessary for the

automatic control of the film thickness and deposition rate.

Appendix A contains certain simple statistical results required in the analysis given in Section 5.61 of the effect of dispersion on anisotropy field measurements.

Appendix B is a published article describing a precision electromagnet power supply containing a number of novel features. Outlined in this article is a transistorized chopper amplifier developed for DC measurements, such as thermocouple voltages, in connection with the vacuum evaporation system of Chapter 9. The author is solely responsible for the chopper design and jointly with P.H. Cole for its application to the magnet supply.

All the above theoretical, experimental and design work, including the construction of the electronic equipment used and the fabrication of the vacuum evaporation unit of Chapter 9 has been carried out solely by the author, apart from some assistance from the workshop staff of the School of Electrical Engineering, and excluding the magnet power supply of Appendix B. This work has not been submitted elsewhere for a higher degree.

## CHAPTER 1

### INTRODUCTION

#### 1.1 A BRIEF HISTORICAL BACKGROUND

The study of the structure and physical properties of thin films is not of recent origin, but has occupied many workers over a period of almost one hundred years, since sputtered films were first observed on the walls of glow discharge tubes. A tremendous impetus has been given during the last twenty-five years by the many industrial applications which have developed. Evaporated films have been used for metallizing coatings of all kinds. In optics, reflecting surfaces, anti-reflecting coatings for lenses and more complex multiple layer interference filters have been made. In the electronics field, nickel-chromium films have been used for resistance elements, and a wide range of metal and dielectric films have been employed for evaporated micro-circuits<sup>B5</sup>. A formidable volume of experiment and theoretical literature has consequently accumulated.

The main emphasis has thus, until recently, been clearly on the mechanical structure and the optical, chemical and electrical properties. A number of comprehensive works have appeared in these fields including the volume on general



deposition techniques by Holland<sup>H1</sup>; noteworthy theoretical thesis on optical properties by Mayer<sup>M2</sup>, Heavens<sup>H2</sup> and others<sup>V1</sup>, and numerous literature surveys<sup>A1,C1</sup>. Now, largely of historical interest, isolated investigations of ferromagnetic films made in very early years has included work by Beetz<sup>B1</sup> (1860), Maurain<sup>M1</sup> (1901) and Kaufman and Meyer<sup>K1</sup> (1911). However, the present intense activity in magnetic properties dates from the preparation by Blois<sup>B2</sup> (1955) of permalloy alloy films having square loop behaviour and low anisotropy. The application of these films to digital computer storage is clear.

## 1.2 CURRENT INTERESTS

Current interest in ferromagnetic films may be broadly classified into two levels. Firstly, thin films provide a unique opportunity for the study of certain fundamental physical problems, in particular loss mechanism and exchange in spin waves, and theories of the ferromagnetism of a two-dimensional array of atoms with the related problem of the thickness dependence of the saturation magnetization<sup>T1,B3,G1</sup>. Secondly, as discussed, permalloy films have technical application as bi-stable switching devices in digital computer storage.

In toroidal ferrite cores, two stable states of zero demagnetizing energy exists. Transition between these by

coherent rotation of the magnetization is prohibited by intermediate states of high demagnetizing energy. Reversal instead proceeds by the time consuming process of domain wall motion. The switching time  $\Delta t$  is given by the relation  $\Delta t(H-H')=S_w$ , where  $H$  is the applied field,  $H'$  a threshold field for irreversible switching and  $S_w$  lies in the range near  $0.5$  oe  $\mu\text{sec}$ . For thin films, bi-stable operation results from a permanently induced uniaxial magnetic anisotropy. Under suitable conditions, reversal proceeds by a coherent rotation of the magnetization in the plane of the film. No demagnetizing fields or high energy intermediate states are produced. The reversal time approaches the intrinsic spin lattice relaxation time of the material. Values of  $S_w$  lie in the range near  $0.01$  sec.

We may remark on three important aspects of film behaviour not yet fully understood:

- it is increasingly clear that the properties of thin films are extremely dependent on anisotropy dispersion. The range of anomalous films and their progressively increasing anomalous behaviour must be considered in terms of the nature, magnitude, extent and density of irregularities or dispersion centres in the film. The transition between various reversal mechanisms is determined by this dispersion. Understanding

of these problems is qualitative rather than quantitative at the present time. A detailed theoretical analysis can come only by the explicit consideration of dispersion fluctuations with exchange and magnetostatic couplings. Possibly, the micro-magnetics approach developed by Brown<sup>B4</sup> may ultimately provide a satisfactory description of these matters.

The present thesis is principally concerned with increasing the range and accuracy with which film properties can be studied by audio-frequency BH plotter techniques. In view of the preceding remarks, attention is paid throughout to providing clear definitions of the film parameters actually determined by such experimental measurements, with a close consideration of the effects on these measurements of dispersion and other departures of real films from ideal coherent rotation. Likewise, dispersion and magnetization ripple is discussed in some detail in Section 2.4.

- The high speed switching of films has been investigated by numerous workers. The multiple peaks and long tail of the switching voltage waveform, with the lack of conservation of the traverse component of the magnetization, indicate the existence of other reversal mechanisms in addition to the expected coherent rotation. Smith<sup>S1</sup> has given a comprehensive analysis of coherent rotation. At the present

time, however, there exists no quantitative description of the degeneration of this coherent mode into the various non-coherent processes, nor of the increased value of the intrinsic damping parameter over that observed in small signal ferromagnetic resonance experiments. It is likely that both are related to the exponential growth of spin waves coupled to the uniform mode by inhomogeneities in the film material.

- the origin of the uniaxial anisotropy is still uncertain. Clear differentiation must be made between the various rotatable and non-rotatable anisotropy components. An important means of effecting this separation lies in determining the time constants associated with various magnetic anneal processes. From these considerations, it appears that pseudo-rotatable and rotatable anisotropies must be explained on a micro-domain model considering anisotropy dispersion. Past work has been hampered by the variability of the film samples. Films are critically affected by impurities. Impurities may arise from the residual atmosphere during evaporation, from the substrate, from the source or crucible used and from the initial starting material. Substrate temperature, deposition rate and thickness are all important variables. Future work must involve ultra-high vacuum evap-

oration from self-supporting sources with control of the relevant evaporation parameters.

To provide some clarification of the above situation, the present thesis contains in Chapter 3 an evaluation of published results on the causes of anisotropy. Chapter 9 describes a contamination free electron bombardment source, together with instrumentation for the control of film thickness and rate of deposition. This system is intended as a preliminary step to a suitable ultra-high vacuum set-up which would allow serious investigation of anisotropy causes.

- Proc. International Conference on the Structure and Properties of Thin Films, Lake George, p.371, (1969).
- 34 Brown, W.F., Jr.,  
"Micromagnetism, Domains and Resonance".  
J. Appl. Phys. (Suppl.), 30, 628, (1959).
- 35 Bohrer, J.V.,  
"Thin Film Circuit Techniques".  
Trans. Inst. Radio Engrs., P.C.C.P., 7, 37, (1960).
- 61 Cotton, F., Richard, P.,  
"Proprietés Optiques des Couches Minces Solides".  
J. de Physique et de Radium, 11, 477, (1939).
- 61 Goodenough, J.B., Smith, D.G.,  
"Magnetic Properties of Films".  
"Magnetic Properties of Metals and Alloys".  
American Soc. of Metals, Cleveland, p. 112, (1964).
- 81 Holland, L.,  
"Vacuum Deposition of Thin Films".  
Chapman and Hall Ltd., London, (1956).
- 82 Heavens, O.S.,  
"Optical Properties of Thin Solid Films".  
Butterworths Scientific Publications, London, (1965).

## 1.3 LIST OF REFERENCES

- A1 Aron, A.,  
"Thin Metallic Films".  
Ann.Phys., Paris, 1, 361, (1946).
- B1 Beetz, W.,  
Ueber die Inneren Vorgänge, welche die Magnetisierung bedingen.  
Poggendorf's Annalen der Physik, 111, 107, (1860).
- B2 Blois, M.S., Jr.,  
"Preparation of Thin Magnetic Films and Their Properties".  
J.Appl.Phys., 26, 975, (1955).
- B3 Bean, C.P.,  
"Aspects of the Ferromagnetism of Thin Films".  
Proc.International Conference on the Structure and Properties of Thin Films, Lake George, p.331, (1959).
- B4 Brown, W.F., Jr.,  
"Micromagnetics, Domains and Resonance".  
J.Appl.Phys. (Suppl.), 30, 62S, (1959).
- B5 Bohrer, J.J.,  
"Thin Film Circuit Techniques".  
Trans.Inst.Radio Engrs., P.G.C.P., 7, 37, (1960).
- C1 Cotton, P., Rouard, P.,  
"Proprietés Optiques des Lames Minces Solides".  
J. de Physique et le Radium, 11, 477, (1950).
- G1 Goodenough, J.B., Smith, D.O.,  
"Magnetic Properties of Films",  
"Magnetic Properties of Metals and Alloys".  
American Soc. of Metals, Cleveland, p. 112, (1958).
- H1 Holland, L.,  
"Vacuum Deposition of Thin Films".  
Chapman and Hall Ltd., London, (1956).
- H2 Heavens, O.S.,  
"Optical Properties of Thin Solid Films".  
Butterworths Scientific Publications, London, (1955).

- K1 Kaufman, W., Meyer, W.,  
 "Magnetic Properties of Electrolytic Iron".  
 Physik Z., 12, 513, (1911).
- M1 Maurain, C.,  
 "Propriétés des Dépôts Électrolytiques de Fer obtenus  
 dans un Champ Magnétique".  
 J.de Physique (et le Radium), 10, 123, (1901).  
 "Magnetic Properties of Very Thin Sheets of Iron and  
 Nickel".  
 J.de Physique (et le Radium), 11, 151, (1902).
- M2 Mayer, H.,  
 "Physik Dünner Schichten".  
 Wissenschaftliche Verlagsgesellschaft m.b.H., Stuttgart,  
 I (1950), II (1955).
- S1 Smith, D.O.,  
 "Static and Dynamic Behaviour of Thin Permalloy Films".  
 J.Appl.Phys., 29, 264, (1958).
- T1 Tannewald, P.E.,  
 "Spin Waves in Magnetic Films".  
 Proc.International Conference on the Structure and  
 Properties of Thin Films, Lake George, p.387, (1959).
- V1 Vašiček, A.,  
 "Optics of Thin Films".  
 North-Holland Publishing Co., Amsterdam, (1960).

## CHAPTER 2

## BASIC MAGNETIC PROPERTIES OF THIN NICKEL-IRON

## AT LOW FREQUENCIES

## 2.1 INTRODUCTION

The following chapter is basically a review of standard results on the low frequency behaviour of thin films needed for an understanding of Chapter 3 and of the experimental measurements of Chapters 4 and 5. Section 2.4 contains, however, an extended and more rigorous treatment of magnetization ripple than given in the literature.

Section 2.2 discusses the assumptions and validity of the Coherent Rotational (CR) and the Independent Region (IR) models commonly used to describe film behaviour. For completeness, an analysis of low frequency or quasistatic hysteresis curves based on the CR or Stoner and Wolfarth model is included in Section 2.3. Section 2.4, as stated, contains a treatment of anisotropy dispersion and the resulting magnetization ripple. An arbitrary uniaxial anisotropy may be represented in terms of component uniaxial anisotropies along two fixed axes. In this form the anisotropy has the properties of a vector. Linear vector superposition holds, and it is possible to develop a statistical representation of a random anisotropy in terms of plane waves. In particular this



model predicts the fractional magnitude dispersion of the anisotropy to be twice the angular dispersion. A derivation of magnetizational ripple is given based on a first order micromagnetics approach and includes exchange and magneto-static coupling forces. Expressions are derived for the mean ripple amplitude and wavelength based on the previous statistical analysis. Sections 2.5, 2.6 and 2.7 discuss aspects of the departure of quasistatic switching from the CR model, including partial switching and labyrinth propagation processes. Section 2.8 includes a description of rotational torque curves. Usage of the IR model and of the magnetization ripple concept is clearly defined.

## 2.2 THE COHERENT ROTATIONAL AND INDEPENDENT REGION MODELS

Thin ferromagnetic nickel-iron films, deposited for example by vacuum evaporation on a glass substrate, commonly display a preferential direction of alignment of the magnetization, or magnetic anisotropy, in the plane of the film. While the physical mechanism for this anisotropy in films is complicated and in some cases still obscure, an anisotropy can be established by almost any means which defines a particular direction in space during the deposition of the film, for example, a magnetic field, evaporation at oblique incid-

ence, or structure in the underlying substrate.

The domain structure of thin (of the order of a few thousand Å) films consists of domains extending through the complete film thickness, the latter being only of the order of the width of a domain wall in the material. The domain pattern in the film plane represents in the normal way an overall minimum in the total energy arising from

- domain wall energy,
- external applied fields and demagnetizing fields due to free poles at the edges of the film,
- anisotropy energy, including local anisotropy centres caused by inhomogeneities and imperfections in the film such as crystallite structure, stresses, voids and inclusions which orientate the magnetization in the direction of minimum energy at that point.

If demagnetizing fields and random inhomogeneities are sufficiently small, then the film can exist in a single domain state where, in the first instance, the anisotropy and the magnetization can be considered as everywhere uniform over the area of the film. Further, under certain conditions, a film initially single domain can maintain approximately a single domain state during a magnetization reversal (switch-

ing) or other change. For these processes the magnetization may be described by a single vector  $\underline{M}$  whose magnitude is conserved and which moves by a "coherent rotation" according to a suitable dynamical equation of motion such as that due to Landau and Lipshitz<sup>L1</sup>. These assumptions may be termed the "Coherent Rotational" (CR) model of film behaviour.

Theoretical predictions of a single domain structure for thin films by Kittel<sup>K2</sup> were first substantiated by the investigations of Crittenden, Hudimac and Strough<sup>C1</sup> and Crittenden and Hoffman<sup>C2</sup> on Ni films. Direct observation of the domains has been made by a number of techniques including

- the Bitter pattern method<sup>K3</sup> used by Sherwood and Williams<sup>S5</sup> and more recently by a great number of workers<sup>H2,M3</sup>. Refinements of the process have been discussed by Moon<sup>M1</sup> and Garrod<sup>G2</sup>.

- the Kerr magneto-optical effect used by Fowler, Fryer and Stevens<sup>F1,F2,F3</sup> and others<sup>P1</sup>. The limitations of the method have been considered by Treves<sup>T3</sup>.

- the Faraday magneto-optical effect described by Roberts and Bean<sup>R1</sup> and others<sup>H4</sup>.

- electron microscopy techniques described by Fuller, Hale and Rubinstein<sup>H3,F4</sup> and numerous others<sup>B3,F5,M5,W1</sup>.

Under the CR model the switching of a film is analogous to the switching of any single domain particle having uniaxial anisotropy. At low frequencies, the dynamic equation of motion of  $\underline{M}$  reduces to an equation of equilibrium of the total torque acting on  $\underline{M}$ . Hysteresis curves for this case are readily obtained and were first described in a comprehensive paper by Stoner and Wolfarth<sup>S2</sup>. At high frequencies the full dynamic equation of motion with appropriate damping terms must be used. An analysis of high speed switching has been given by Smith<sup>S6</sup>. While straightforward in principle, an analytic solution is possible only over an intermediate range of switching speeds by using a "viscous-flow" approximation in which the angular rotational velocity of  $\underline{M}$  in the plane of the film is always proportional to the instantaneous torque. At higher speeds, rotation out of the plane of the film must be considered and only a numerical solution is possible.

The Coherent Rotational model provides a valid description of film switching only in those processes throughout which the film maintains a uniform single domain state. In quasistatic switching only in special cases is this true.\*

---

\* A number of experimental hysteresis curves with traverse bias fields applied to ensure a single domain state have been given by Oguey<sup>03</sup>.

---

For switching along the easy axis, while a square hysteresis loop is obtained, reversal occurs at a field usually less than the anisotropy field. The magnetization measured in the traverse direction shows no rotating component. For switching along the hard axis, a closed hysteresis loop is not obtained for fields greater than a reversibility limit  $H_r$  typically about  $0.5 H_K$ . Again, the magnetization measured in the traverse direction shows no rotating component. High speed switching has been investigated by numerous workers<sup>C3,C4,S6,O2,H1,D1</sup>. The multiple peaks and long tail of the switching voltage waveform, with the lack of conservation of the traverse component of  $\underline{M}$  indicate the existence of other reversal mechanisms in addition to the fast coherent rotation.

It is found that domain wall processes, incoherent or partial rotational processes, and coherent rotation all occur under various conditions. No theory exists at present which is satisfactory for all cases. Basically, real films are far from uniform, but have considerable variation or dispersion of their properties. Certain features of film behaviour have been explained by supposing the film to consist of many small regions in which the anisotropy has small variations in magnitude and direction from the mean value averaged over the entire film. Each region is considered to

have no exchange or magnetostatic coupling between them, these being, if necessary, introduced later as small perturbations. Each region is assumed to obey the coherent rotational equation for the particular anisotropy of that region. The Independent Region (IR) model has been used in the explanation of certain aspects of quasistatic hysteresis curves, in "labyrinth" switching (an incoherent rotational process discussed by Smith<sup>S10</sup>) and elsewhere. It is an underlying assumption in the methods of measuring magnitude and angular dispersion<sup>C8</sup>.

An alternative approach is to consider explicitly the effects of exchange and magnetostatic coupling. It may be shown that only sinusoidal variations or "longitudinal ripple" of the magnetization with wavelengths greater than about  $2\mu$  are permitted. To date, this analysis has been performed only by assuming small magnetization variation and has not been extended to the large magnetization changes occurring during switching. The principal use has thus been in predicting the initial course of a change such as in the "partial rotation" process described by Methfessel et al<sup>M6</sup>. Further, a useful indication is provided of the minimum size and orientation one to the other of those regions which can be considered as independent under the IR model. Clearly, the two approaches are complementary, and either or both should be used as best suited.

### 2.3 QUASISTATIC SWITCHING BASED ON THE COHERENT ROTATIONAL MODEL

This section describes the switching of a film for those cases, where the film remains a single domain in accordance with the CR model. Quasistatic switching is by definition switching taking place under fields changing so slowly that the instantaneous position of  $\underline{M}$  is simply the equilibrium position of  $\underline{M}$  under the instantaneous values of the applied fields at that time. Any dynamical equation of motion of  $\underline{M}$  reduces to an equation of equilibrium in the total torque  $\underline{T}$  acting on  $\underline{M}$

$$\underline{T} = 0 \quad (2.31)$$

The quasistatic hysteresis loops of  $\underline{M}$  against an applied field  $\underline{H}$  are readily found from equation (2.31).

Referring to Fig. 2.31,  $H_L$  and  $H_T$  are external fields applied in the plane (xy) of a film. The position of the magnetization vector  $\underline{M}$  is specified by the angular co-ordinates  $(\phi, \psi)$ .  $(\underline{i}_r, \underline{i}_\phi, \underline{i}_\psi)$  are an orthogonal right-handed set of unit vectors in a moving frame of reference attached to  $\underline{M}$ . The anisotropy of the film is uniaxial, with the preferred direction or easy axis taken along the x-axis. The free potential energy of the film is given by

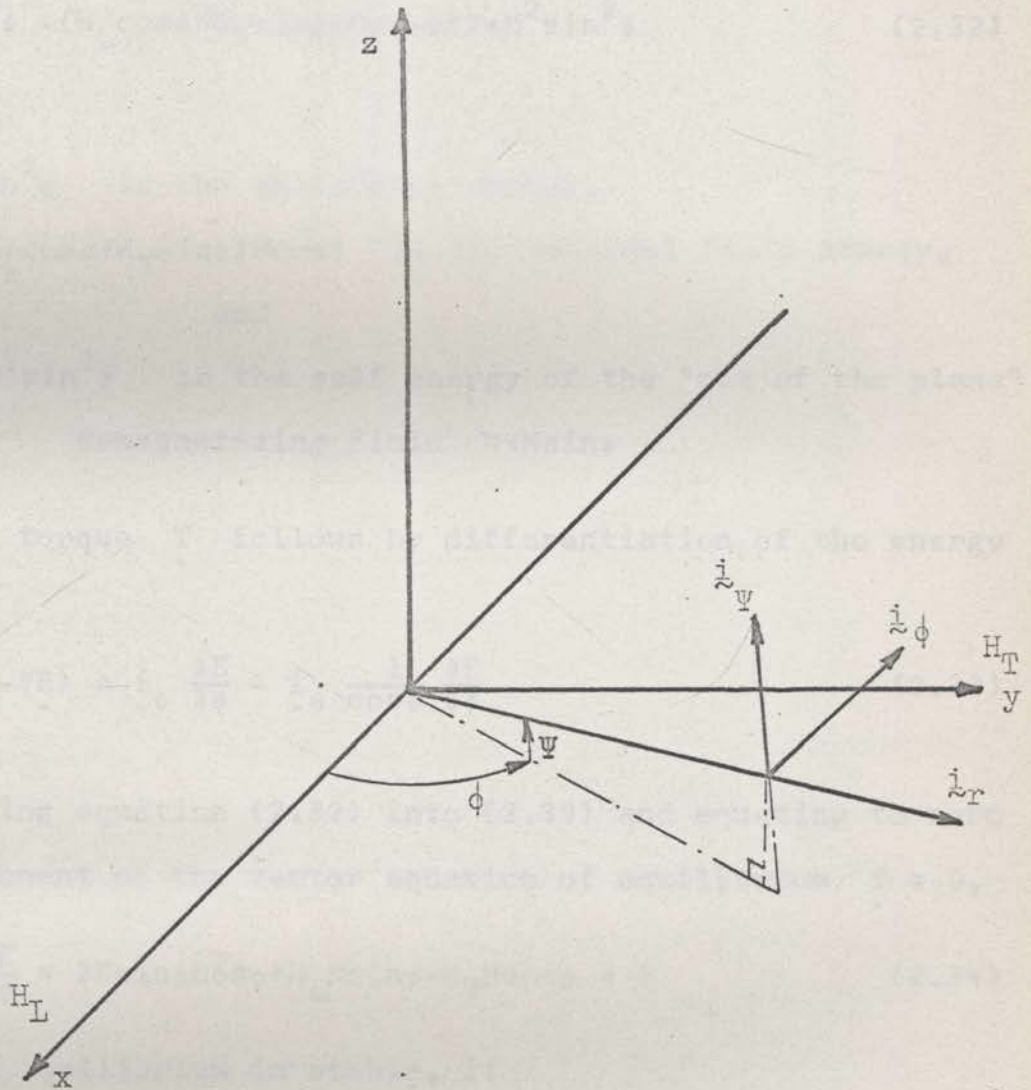


Fig..2.31 Co-ordinate System Defining the Position of the Magnetization During Coherent Rotational Switching.



$$E = K \sin^2 \phi - (H_L \cos \phi + H_T \sin \phi) M \cos \psi + 2\pi M^2 \sin^2 \psi \quad (2.32)$$

where

$K \sin^2 \phi$  is the anisotropy energy,

$-(H_L \cos \phi + H_T \sin \phi) M \cos \psi$  is the external field energy,

and

$2\pi M^2 \sin^2 \psi$  is the self energy of the "out of the plane" demagnetizing field  $4\pi M \sin \psi$ .

The total torque  $\vec{T}$  follows by differentiation of the energy  $E$ ,

$$\vec{T} = \vec{i}_r \times (-\nabla E) = \vec{i}_\phi \frac{\partial E}{\partial \phi} - \vec{i}_\psi \frac{1}{\cos \psi} \frac{\partial E}{\partial \psi} \quad (2.33)$$

Substituting equation (2.32) into (2.33) and equating to zero each component of the vector equation of equilibrium  $\vec{T} = 0$ ,

$$-T_{i_\psi} = \frac{\partial E}{\partial \psi} = 2K \sin \phi \cos \phi + H_L M \sin \phi - H_T M \cos \phi = 0 \quad (2.34)$$

while the equilibrium is stable, if

$$\frac{\partial^2 E}{\partial \phi^2} = 2K \cos 2\phi + H_L M \cos \phi + H_T M \sin \phi > 0 \quad (2.35)$$

Equations (2.34) and (2.35) can be normalized in terms of an anisotropy field  $H_K = \frac{2K}{M}$  derived from the anisotropy constant  $K$  as

$$- \frac{\partial T'_1}{\partial \phi} = \frac{\partial E'}{\partial \phi} = \sin\phi \cos\phi + h_L \sin\phi - h_T \cos\phi = 0 \quad (2.36)$$

$$\frac{\partial^2 E'}{\partial \phi^2} = \cos 2\phi + h_L \cos\phi + h_T \sin\phi > 0 \quad (2.37)$$

where

$$T' = T/2K,$$

$$E' = E/2K, \text{ and}$$

$$h_L, h_T = H_L/H_K, H_T/H_K, \text{ respectively.}$$

The primed notation for the normalized quantities  $T'$  and  $E'$  will be disregarded in later sections of this thesis, where no ambiguity is caused.

Equation (2.36) is most easily solved by assuming a given  $\phi$  and solving for corresponding  $h_L$  and  $h_T$ . This forms the basis of Diagram 2.32 which provides a convenient graphical method of solution. The lines are lines of zero torque in the  $(h_L, h_T)$  plane with  $\phi$  as parameter obtained by writing equation (2.36) as

$$h_T = h_L \tan\phi + \sin\phi$$

The fields at the switching threshold  $h_{cr} = H_{cr}/H_K$  can be found by simultaneously solving

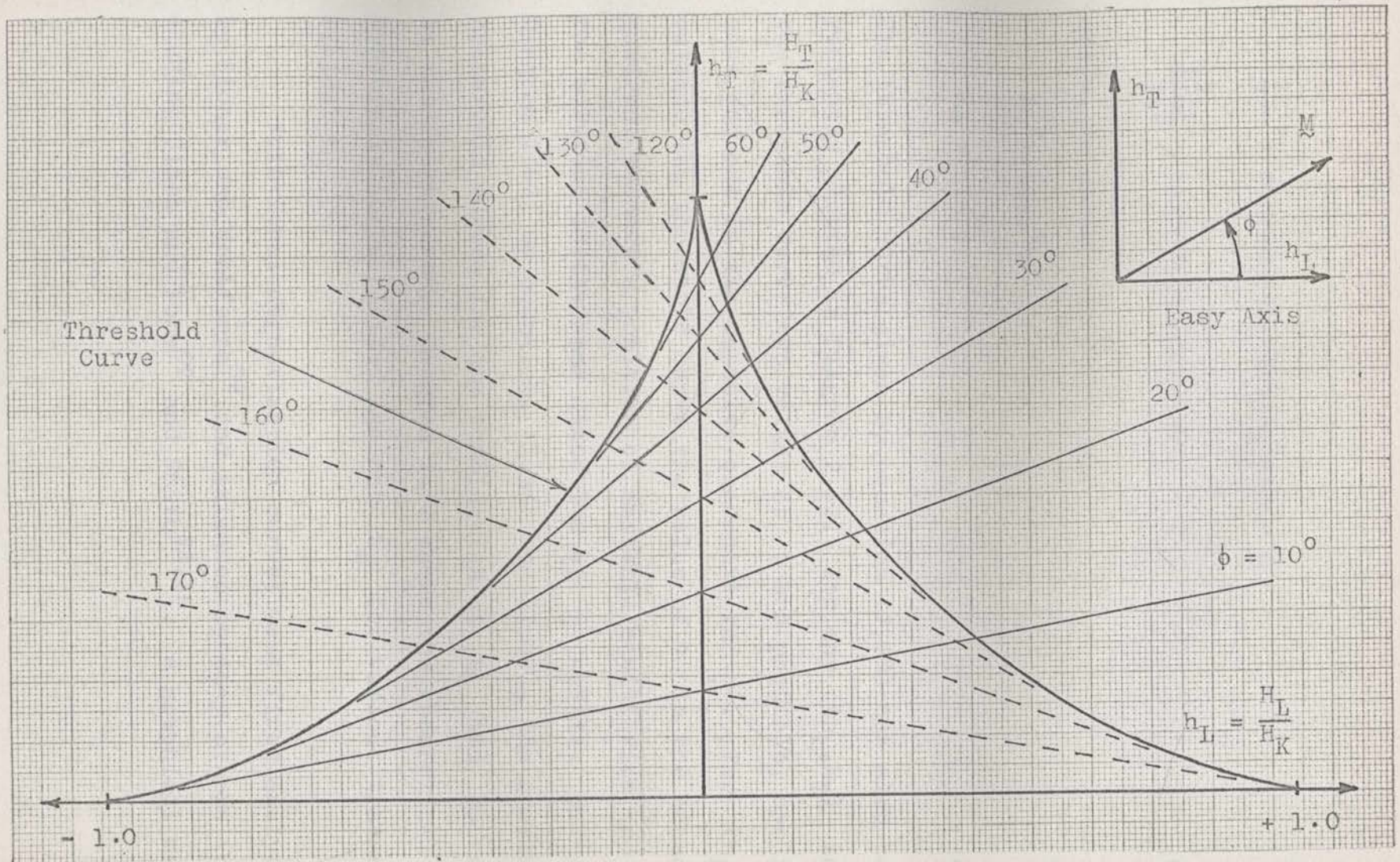


Fig. 2.32 Diagram Showing the Magnetization Direction  $\phi$  and the Coherent Rotational Threshold Curve as a Function of the Applied Fields  $h_L$  and  $h_T$  .

$$\frac{\partial E'}{\partial \phi} = \sin\phi \cos\phi + h_L \sin\phi - h_T \cos\phi = 0$$

$$\frac{\partial^2 E'}{\partial \phi^2} = \cos 2\phi + h_L \cos\phi + h_T \sin\phi = 0 \quad (2.38)$$

which, in parametric form, are

$$\begin{aligned} h_L &= -\cos^3 \phi \\ h_T &= \sin^3 \phi \end{aligned} \quad (2.39)$$

The threshold curve given by equation (2.39) can also be conveniently plotted in Diagram 2.32. For any  $(h_L, h_T)$  inside the threshold curve two values of  $\phi$  are possible, one in the same and one in the opposite quadrants to  $\underline{h}$ . For  $(h_L, h_T)$  outside the threshold curve the value of  $\phi$  in the opposite quadrant becomes a position of unstable equilibrium and only the solution in the same direction as  $\underline{h}$  exists. Using Diagram 2.32, or equations (2.36) and (2.39), the quasistatic hysteresis curves for any combination of  $h_L$  and  $h_T$  can be easily obtained. Diagram 2.33 shows the theoretical hysteresis loops plotted against  $h_L$  for various traverse fields  $h_T$ .

Rotational magnetization curves were first analysed by Stoner and Wohlfarth<sup>S2</sup> and extended by many others including Olsen and Pohn<sup>02</sup> and Smith<sup>S3, S6</sup>. A graphical method

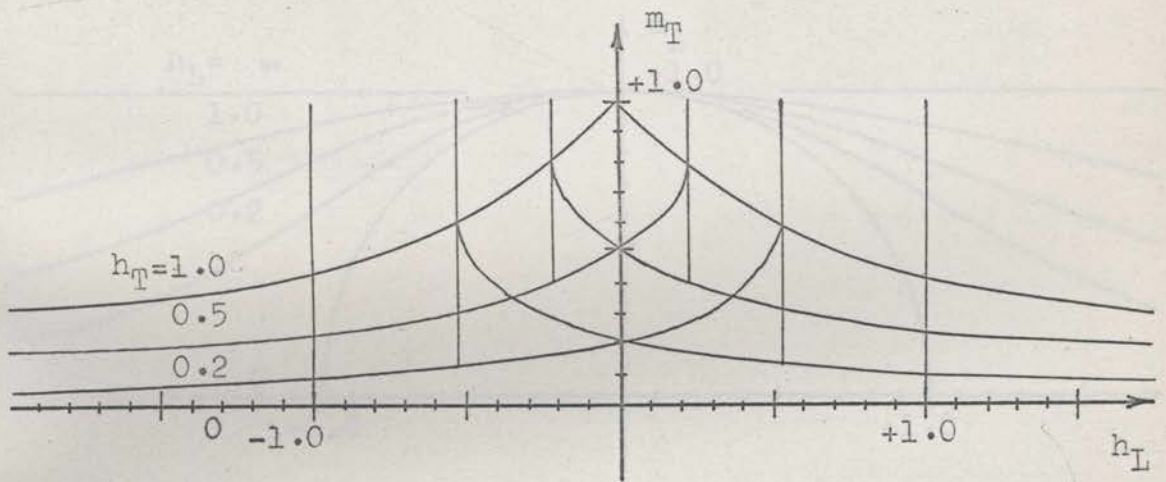
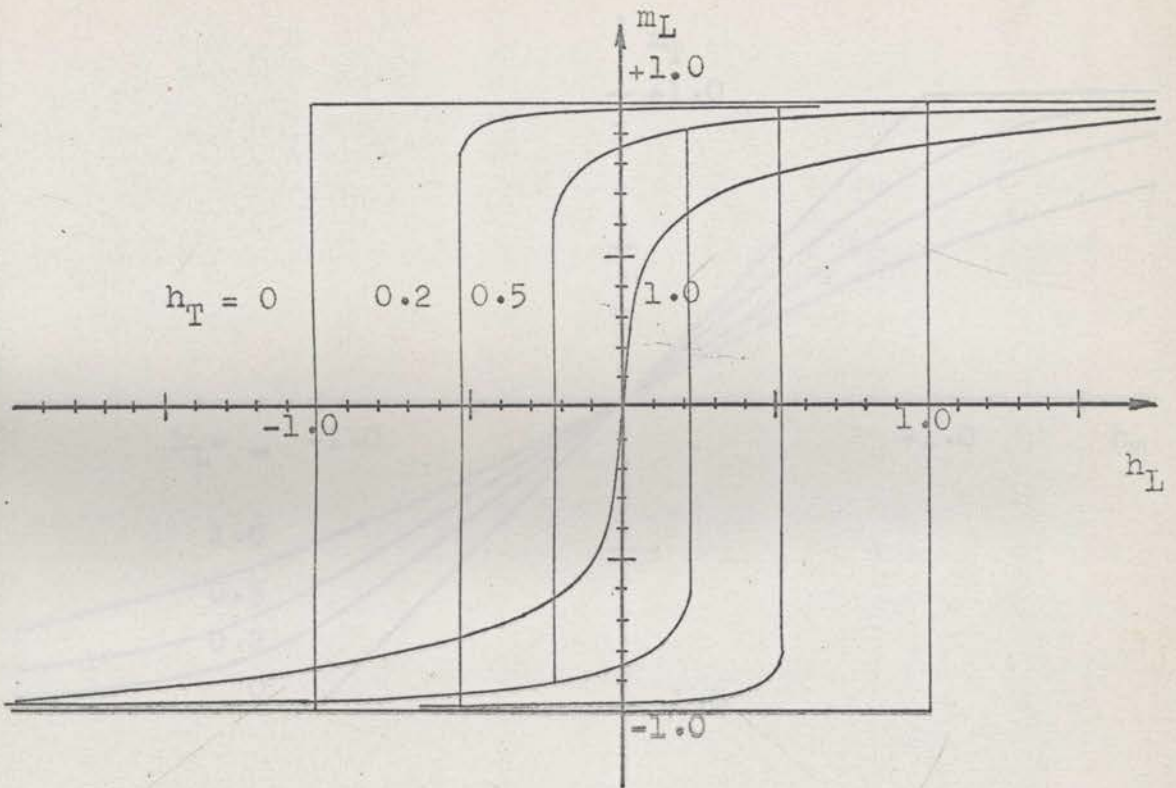


Fig. 2.33a Coherent Rotational Hysteresis Curves as a Function of the Easy Axis Field  $h_L$  with the Hard Axis Field  $h_T$  as Parameter.

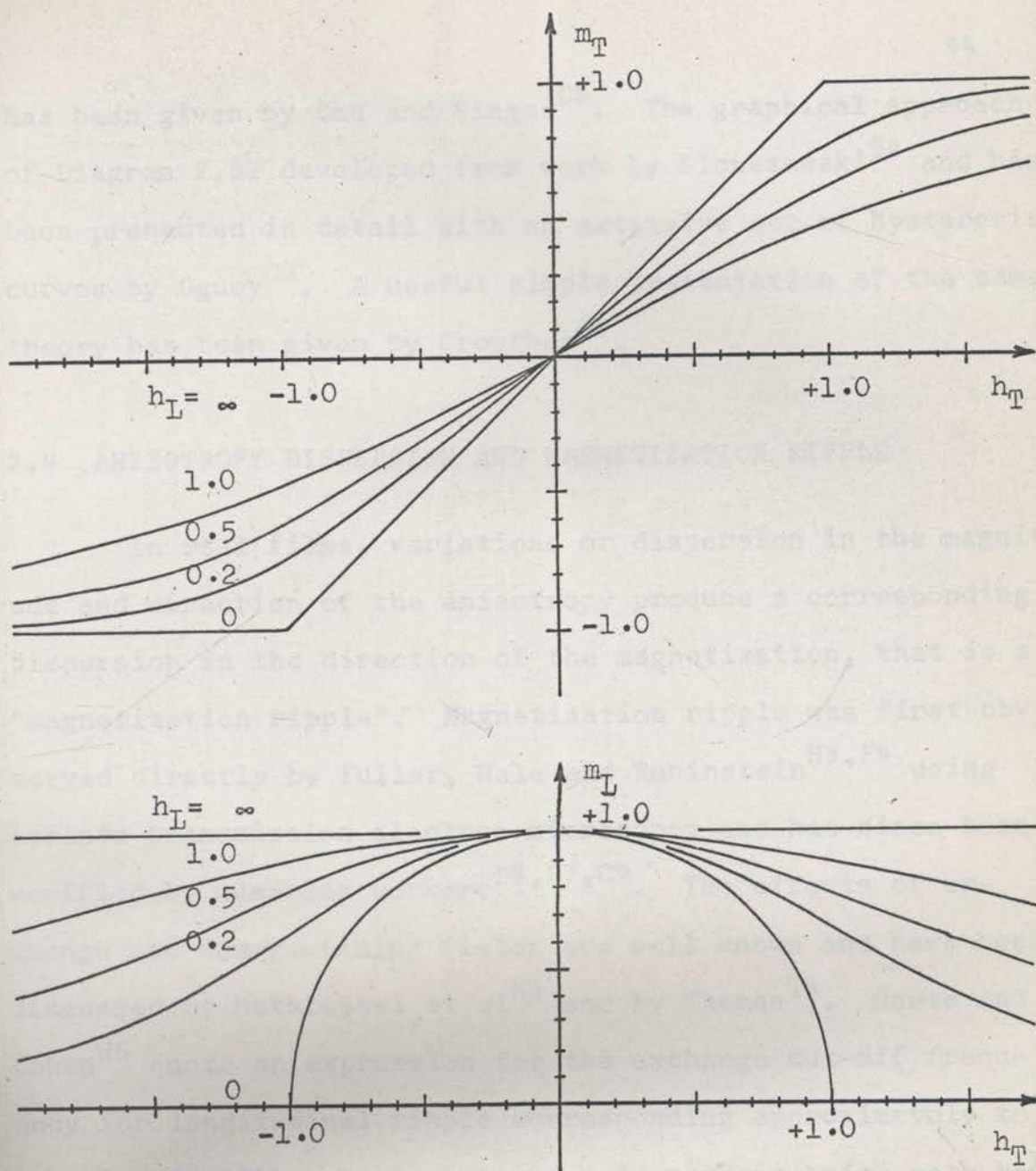


Fig. 2.33b Coherent Rotational Hysteresis Curves as a Function of the Hard Axis Field  $h_T$  with the Easy Axis Field  $h_L$  as Parameter.

has been given by Chu and Singer<sup>C5</sup>. The graphical approach of Diagram 2.32 developed from work by Slonezewski<sup>S4</sup> and has been presented in detail with an extensive set of hysteresis curves by Oguey<sup>O3</sup>. A useful simple presentation of the same theory has been given by Crowther<sup>C6</sup>.

#### 2.4 ANISOTROPY DISPERSION AND MAGNETIZATION RIPPLE

In real films, variations or dispersion in the magnitude and direction of the anisotropy produce a corresponding dispersion in the direction of the magnetization, that is a "magnetization ripple". Magnetization ripple was first observed directly by Fuller, Hale and Rubinstein<sup>H3,F4</sup> using Lorentz transmission electron microscopy and has since been verified by numerous workers<sup>F6,F7,C9</sup>. The effects of exchange and demagnetizing fields are well known and have been discussed by Methfessel et al<sup>M6</sup> and by Thomas<sup>T4</sup>. Harte and Cohen<sup>H5</sup> quote an expression for the exchange cut-off frequency for longitudinal ripple corresponding approximately to equation (2.425). It is not clear from their brief note how magnetostatic energy has been considered. The present section introduces a new and useful concept of a vector anisotropy and gives a more rigorous statistical treatment of anisotropy dispersion and ripple than available in the

literature. The result of equation (2.422) has, it is believed, not been given elsewhere.

## 2.41 A Statistical Representation of Anisotropy Dispersion

In the general case the anisotropy of a film must be represented by an energy density function  $\epsilon(\underline{r})$  which is a function of position  $\underline{r}$  over the area of the film. It is consistent with certain models of the causes of anisotropy (see Chapter 3), that  $\epsilon(\underline{r})$  is of uniaxial form,

$$\epsilon(\underline{r}) = K(\underline{r}) \sin^2(\phi - \beta(\underline{r})) \quad (2.41)$$

Neglecting a constant independent of  $\phi$ , equation (2.41) can be written

$$\epsilon(\underline{r}) = K'(\underline{r}) \sin^2 \phi + K''(\underline{r}) \sin^2(\phi - \frac{\pi}{4}) \quad (2.42)$$

where

$$K(\underline{r})^2 = K'(\underline{r})^2 + K''(\underline{r})^2, \text{ and}$$

$$\tan 2\beta(\underline{r}) = K''(\underline{r}) / K'(\underline{r}).$$

The form of equation (2.41), where  $K(\underline{r})$  is the magnitude and  $\beta(\underline{r})$  the direction of the anisotropy, is the form of the energy function normally found in the literature. The form of equation (2.42) indicates that the energy function can be resolved into component anisotropies  $K'(\underline{r})$  and  $K''(\underline{r})$  along



the directions  $\beta=0$  and  $\beta=\frac{\pi}{4}$ , respectively, and in this sense may be considered as a vector  $\underline{\epsilon}(\underline{r})$ . Certain important results follow immediately, for example:

"The sum of any number of arbitrary uniaxial energy functions is itself a uniaxial energy function whose components are the linear sum of the components of the added functions."

It is then possible to define an average energy function over the whole film (the average energy function will give the energy, if the magnetization is everywhere over the film uniform and in the direction  $\phi$ ) and to write the energy at any point as the sum of the average energy plus a variable term whose average value is zero.

$$\underline{\epsilon}(\underline{r}) = \overline{\underline{\epsilon}(\underline{r})} + \underline{\epsilon}'(\underline{r}) = \underline{\epsilon}_0(\underline{r}) + \underline{\epsilon}'(\underline{r}) \quad (2.43)$$

where, by definition,  $\overline{\underline{\epsilon}'(\underline{r})}$  must equal zero.

Further, the variable energy term, since linear superposition applies, can be resolved into a series of plane waves in two-dimensional  $\underline{k}$  space

$$\underline{\epsilon}'(\underline{r}) = \int_{\underline{k} \text{ space}} \underline{\epsilon}'(\underline{k}) e^{j\underline{k} \cdot \underline{r}} d\underline{k} \quad (2.44)$$

Standard statistical methods can now be used to determine the amplitude distribution of the components  $\underline{\epsilon}'(\underline{k})$ . From consideration of the physical model, the variable energy  $\underline{\epsilon}'(\underline{r})$  can be considered to be correlated over a region of characteristic dimension  $r_0=1/k_0$  and uncorrelated otherwise  $r_0$  is perhaps related to the scale of microscopic centres in the film, or to other inhomogeneities such as crystallite size or fluctuations in alloy composition. The auto-correlation function<sup>T1</sup> of  $\underline{\epsilon}'(\underline{r})$  may then be assumed to be of the form

$$\phi_{11}(\underline{r}) = \overline{\underline{\epsilon}'^2(\underline{r})} e^{-rk_0} = \{ \overline{K'^2(\underline{r})} + \overline{K''^2(\underline{r})} \} e^{-rk_0} \quad (2.45)$$

where  $\underline{\epsilon}'(\underline{r})$  is expressed in terms of the "vector" components  $K'(\underline{r})$  and  $K''(\underline{r})$ .

The power density function in  $\underline{k}$  space is

$$\underline{\epsilon}'^2(\underline{k}) = \frac{1}{(2\pi)^2} \int_{\underline{r} \text{ space}} \phi_{11}(\underline{r}) e^{-j\underline{k} \cdot \underline{r}} d\underline{r} \quad (2.46)$$

If all directions are the same in the plane of the film, that is  $\underline{k}$  space is isotropic, then  $e^{-j\underline{k} \cdot \underline{r}}$  may be replaced by its value averaged over all directions in  $\underline{k}$  space

$$e^{-jk \cdot r} \Big|_{\text{average}} = \frac{1}{2\pi} \int_{-\pi}^{\pi} e^{-jkr \cos \theta} d\theta = J_0(kr) \quad (2.47)$$

where  $J_0(kr)$  is the Bessel function of zero order. Substituting equation (2.47) in (2.46), the amplitude distribution of the anisotropy components is thus\*

$$\underline{\underline{\epsilon}}'^2(\underline{k}) = K'^2(\underline{k}) + K''^2(\underline{k}) = \overline{\underline{\underline{\epsilon}}'^2(\underline{r})} \cdot \frac{1}{(2\pi)^2} \cdot \frac{2\pi r_0^2}{(1+k^2 r_0^2)^{\frac{3}{2}}} \quad (2.48)$$

Equations (2.44) and (2.48) express the anisotropy variations in terms of dispersion waves in the "vector" components  $K'(\underline{k})$  and  $K''(\underline{k})$ . To interpret these in terms of the more common "magnitude and angular dispersion" of films, note that, provided  $K'(\underline{k})$  and  $K''(\underline{k})$  are both small compared to the average anisotropy  $K_0$ ,

---

\* Integration of  $\underline{\underline{\epsilon}}'^2(\underline{k})$  over all  $\underline{k}$  space gives  $\overline{\underline{\underline{\epsilon}}'^2(\underline{r})}$  as required

$$\int_{\underline{k} \text{ space}} \underline{\underline{\epsilon}}'^2(\underline{k}) d\underline{k} = \overline{\underline{\underline{\epsilon}}'^2(\underline{r})} \int_0^{\infty} \frac{1}{(2\pi)^2} \cdot \frac{2\pi r_0^2}{(1+k^2 r_0^2)^{\frac{3}{2}}} \cdot 2\pi k dk$$

$$= \overline{\underline{\underline{\epsilon}}'^2(\underline{r})}$$


---

$$K_0 \sin^2 \phi + K'(\underline{k}) \sin^2 \phi + K''(\underline{k}) \sin^2 (\phi - \frac{\pi}{4}) = (K_0 + K'(\underline{k})) \sin^2 (\phi - \beta(\underline{k})) \quad (2.49)$$

where

$$2\beta(\underline{k}) + \tan 2\beta(\underline{k}) = K''(\underline{k})/K_0$$

Thus  $K'(\underline{k})/K_0$  and  $\frac{1}{2}K''(\underline{k})/K_0$  are respectively the fractional magnitude and angular dispersions discussed in the literature.

The concept of magnitude and angular dispersion as uniaxial dispersion components along the easy axis and at  $\frac{\pi}{4}$  to the easy axis allows certain predictions. If the variable anisotropy term of equation (2.43) is random in direction  $\beta$  over the film, then for any given wave  $\underline{k}$ ,  $K'(\underline{k})=K''(\underline{k})$  and the fractional magnitude dispersion should be twice the angular dispersion. It is commonly found in thin films that, while magnitude and angular dispersion are related in that one increases with the other, the relation is not linear and further, the fractional magnitude dispersion is much larger (by factors of 3 to 7 times) than the angular dispersion<sup>S10,C8,T5</sup>. A possible explanation may be with the assumption of the "independent region model" implicit in these dispersion measurements. Alternatively, the random distribution assumed for the variable anisotropy  $\epsilon'(r)$  may not be

correct. The results of Smith<sup>S9</sup>, that regions of "-ve  $H_K$ " (that is regions in which the local anisotropy direction is along the mean easy axis, but  $K$  has a negative value) exist in films and that these regions themselves have a small angular dispersion, are suggestive in this regard. It is, however, extremely difficult to postulate any mechanism whereby these -ve  $H_K$  regions, rather than an isotropic distribution, might occur.

#### 2.42 Magnetization Ripple

The magnitude of the magnetization ripple produced by anisotropy fluctuations may be found by equating to zero the sum of the anisotropy, magnetostatic and exchange torques per unit volume at all points in the film. The general equation of torque equilibrium in a ferromagnet has been given by Brown<sup>B2</sup>,

$$-\vec{T} = \vec{v} \times \left( \frac{\partial \epsilon}{\partial \vec{v}} - \vec{M} \times \vec{H}_t - 2A \nabla^2 \vec{v} \right) = 0 \quad (2.410)$$

where

$\vec{v}$  is a unit vector in the direction of  $\vec{M}$ ,  
 $\frac{\partial \epsilon}{\partial \vec{v}}$  is a vector whose components are the partial derivatives of the anisotropy energy  $\epsilon$  with respect to the directional cosines of  $\vec{v}$ ,

$\vec{H}_t$  is the total field including the external applied field  $\vec{H}$  and the internal field  $\vec{H}_i$  due to surface poles and poles produced by fluctuations in  $\vec{M}$ , and  $A$  is the exchange constant.

At the surface of the ferromagnet we must also satisfy the exchange boundary condition

$$\vec{v} \times \frac{\partial \vec{v}}{\partial n} = 0 \quad (2.411)$$

where  $\frac{\partial}{\partial n}$  denotes differentiation along the outward normal to the surface.

For a thin film  $\vec{M}$  may be considered as uniform across the film thickness. In the present treatment we shall consider only external fields  $\vec{H}$  in the plane of the film and shall assume that  $\vec{M}$  lies solely in the film plane, variations out of the plane being suppressed by the large demagnetizing field produced\*. In this case the boundary condition (2.411) is automatically satisfied, and equation (2.410) reduces to a single equation in the z-component of torque. Referring to Fig. 2.41,

$$-T_z = \frac{\partial \epsilon}{\partial \phi} - \vec{M} \cdot \vec{H}_t - 2A\nabla^2 \phi = 0 \quad (2.412)$$

---

\* Such an assumption will scarcely apply for example to films showing rotatable anisotropy properties<sup>L3</sup>.

---

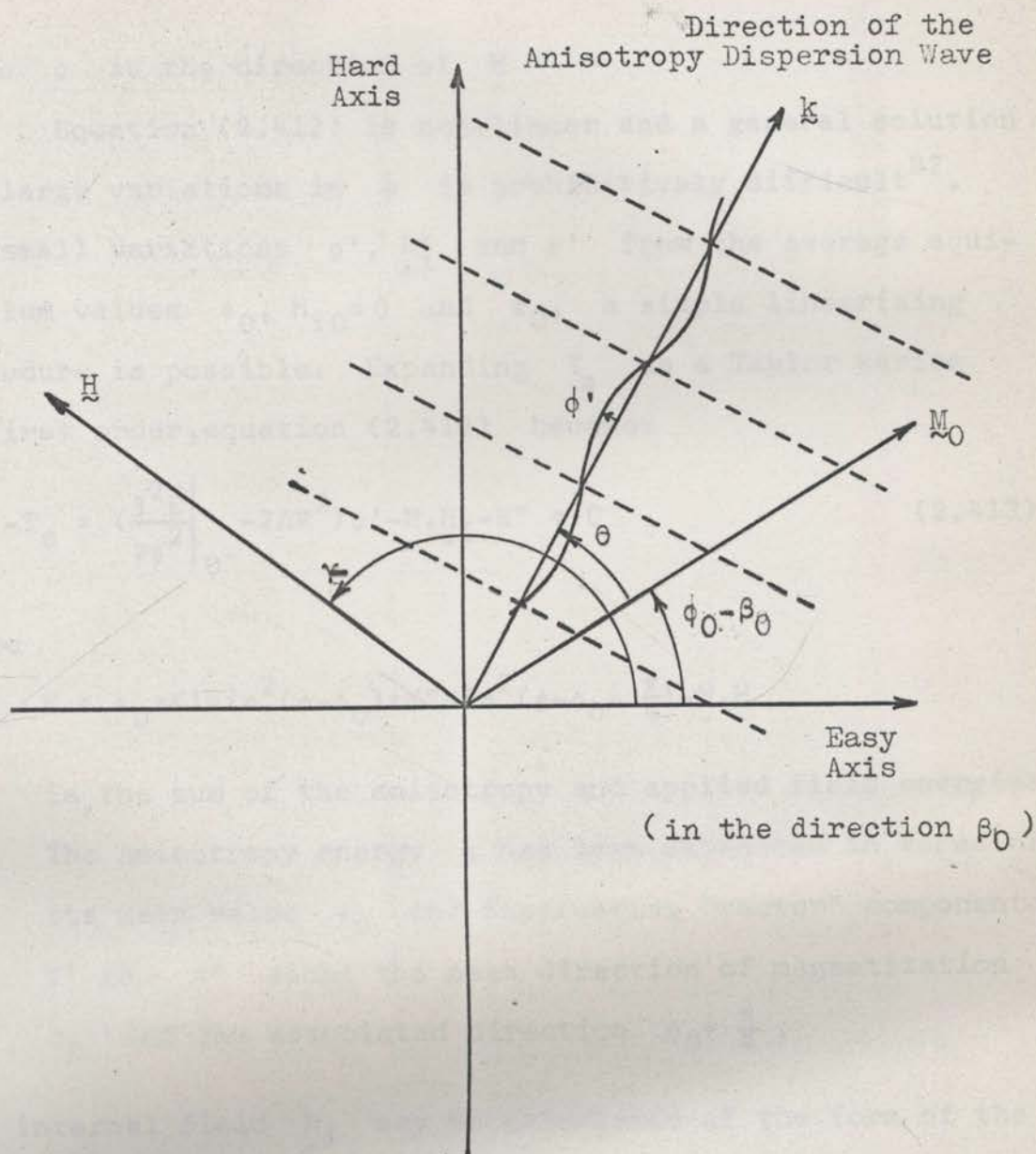


Fig. 2.41 Figure Illustrating Magnetizational Ripple.

where  $\phi$  is the direction of  $\underline{M}$

Equation (2.412) is non-linear and a general solution for large variations in  $\phi$  is prohibitively difficult<sup>B2</sup>.

For small variations  $\phi'$ ,  $\underline{H}_i$  and  $\epsilon'$  from the average equilibrium values  $\phi_0$ ,  $\underline{H}_i = 0$  and  $\epsilon_0$ , a simple linearizing procedure is possible. Expanding  $T_z$  as a Taylor series to first order, equation (2.412) becomes

$$-T_z = \left( \frac{\partial^2 E}{\partial \phi^2} \right)_0 - 2A \nabla^2 \phi' - \underline{M} \cdot \underline{H}_i - K'' = 0 \quad (2.413)$$

where

$$E = \epsilon_0 + K' \sin^2(\phi - \phi_0) + K'' \sin^2(\phi - \phi_0 - \frac{\pi}{4}) - \underline{M} \cdot \underline{H}$$

is the sum of the anisotropy and applied field energies.

The anisotropy energy  $\epsilon$  has been expressed in terms of its mean value  $\epsilon_0$  and fluctuating "vector" components

$K'$  and  $K''$  along the mean direction of magnetization

$\phi_0$  and the associated direction  $\phi_0 + \frac{\pi}{4}$ .

The internal field  $\underline{H}_i$  may be calculated if the form of the variation in  $\phi'$  is known. Assuming sincoidal plane wave variations in  $K''$ , and consequently in  $\phi'$ , of the form  $\sin k \cdot r$ , then the component of  $\underline{H}_i$  in the plane of the film is, to first order,



$$\underline{H}_i = -2\pi t M \phi' k \sin \theta \quad (2.414)$$

where

$$\phi' \propto \sin k \cdot r ,$$

$t$  is the thickness of the film, and

$\theta$  is the angle between the wave propagation vector  $\underline{k}$  and the direction of average magnetization  $\phi_0$ .

Substituting (2.414) into (2.413),

$$\phi' = \frac{K''}{\left. \frac{\partial^2 E}{\partial \phi^2} \right|_0 + 2Ak^2 + 2\pi(tk)M^2 \sin^2 \theta} \quad (2.415)$$

For randomly orientated dispersion centres the value of  $K''$  will be independent of direction, and  $\phi'$  will depend on  $\phi_0$  only through the denominator term  $\left. \frac{\partial^2 E}{\partial \phi^2} \right|_0$ .

Equation (2.415) illustrates the economy of expression and conceptual simplicity resulting from the use of the vector anisotropy. In terms of the more common magnitude angular dispersions  $\Delta K$  and  $\Delta \beta$  about the mean easy axis direction  $\beta_0$ ,

$$K'' = 2\Delta\beta K_0 \cos 2(\phi_0 - \beta_0) - \Delta K \sin 2(\phi_0 - \beta_0) \quad (2.416)$$

Examination of equation (2.415) shows that internal magnetization fields will suppress lateral magnetization

variations (that is, variations in which the propagation vector  $\underline{k}$  is normal to the average direction of  $\underline{M}$ ) of wavelength  $\lambda$  shorter than a magnetostatic cut-off wavelength  $\lambda_M$  defined as

$$\lambda_M = \frac{2\pi}{k_M} = 4\pi^2 M^2 t \left( \frac{\partial^2 E}{\partial \phi^2} \Big|_0 \right)^{-1} \quad (2.417)$$

$$\doteq 500 \mu$$

for a 200 Å permalloy film with the magnetization at remanence along the easy axis, assuming  $4\pi M = 10^4$  cgs units,  $K_0 = 10^3$  ergs  $\text{cm}^{-3}$  and  $A = 2 \times 10^{-6}$  ergs  $\text{cm}^{-1}$ . Further exchange forces will suppress all variations with a wavelength  $\lambda$  shorter than an exchange cut-off wavelength  $\lambda_A$  defined as

$$\lambda_A = \frac{2\pi}{k_A} = 2\pi(2A)^{\frac{1}{2}} \left( \frac{\partial^2 E}{\partial \phi^2} \Big|_0 \right)^{-\frac{1}{2}} \quad (2.418)$$

$$\doteq 2 \mu$$

for a 200 Å permalloy film under the same conditions as previously. Thus, the observed ripple will be very closely a longitudinal variation (that is, a variation in which the propagation vector  $\underline{k}$  is parallel to the average direction of  $\underline{M}$ ) at a wavelength  $\doteq \lambda_M$ . We shall now consider these predictions more rigorously.

Equation (2.415) may be written

$$\phi' = \frac{K''}{\left. \frac{\partial^2 E}{\partial \phi^2} \right|_0} \cdot \frac{1}{1 + \frac{\lambda_A^2}{\lambda^2} + \frac{\lambda_M \sin^2 \theta}{\lambda}} \quad (2.419)$$

The mean squared ripples amplitude may be obtained by summing  $\phi'^2(k)$  over all  $k$  space, where the distribution function of  $K''^2(k)$  follows from equation (2.48). Thus,

$$\overline{\phi'^2} = \int_{\tilde{k} \text{ space}} \frac{K''^2(k) d\tilde{k}}{\left( \left. \frac{\partial^2 E}{\partial \phi^2} \right|_0 \right)^2 \left( 1 + \frac{\lambda_A^2}{\lambda^2} + \frac{\lambda_M \sin^2 \theta}{\lambda} \right)^2} \quad (2.420)$$

Since  $\tilde{k}$  space is isotropic, the factor  $\left( 1 + \frac{\lambda_A^2}{\lambda^2} + \frac{\lambda_M \sin^2 \theta}{\lambda} \right)^{-2}$  may be replaced by its value averaged over all directions of  $\theta$ .

$$\begin{aligned} \left( 1 + \frac{\lambda_A^2}{\lambda^2} + \frac{\lambda_M \sin^2 \theta}{\lambda} \right)^{-2} \Big|_{\text{average}} &= \frac{1}{2\pi} \int_{-\pi}^{\pi} \left( 1 + \frac{\lambda_A^2}{\lambda^2} + \frac{\lambda_M \sin^2 \theta}{\lambda} \right)^{-2} d\theta \\ &\doteq \frac{1}{2} \left( \frac{\lambda}{\lambda_M} \right)^{\frac{1}{2}} \left( 1 + \frac{\lambda_A^2}{\lambda^2} \right)^{-\frac{3}{2}} \end{aligned} \quad (2.421)$$

where the approximation is accurate over the range

$$0.02\mu = \frac{2\lambda_A^2}{\lambda_M} < \lambda < \lambda_M = 500\mu. \quad \text{Since contributions to the integral}$$

of equation (2.421) outside the limits of this approximation are negligible, then closely

$$\overline{\phi'^2} \div \frac{\overline{K''^2}}{\left(\frac{\partial^2 E}{\partial \phi^2}\right)_0^2} \cdot \frac{2\pi^2 r_0^2}{\lambda_M \lambda_A^{\frac{3}{2}}} \cdot \int_{k'=0}^{\infty} \frac{k'^{\frac{1}{2}} dk'}{(1+r_0^2 k_A^2 k'^2)^{\frac{3}{2}} (1+k'^2)^{\frac{3}{2}}} \quad (2.422)$$

where  $k' = k/k_A$ .

The integral of equation (2.422) can be evaluated numerically as a function of  $r_0^2 k_A^2$ . In the case, where the correlation distance  $r_0 \ll \lambda_A$  (if for example  $r_0$  corresponds to the size of individual crystallites in the film,  $r_0$  will be of the order of  $100 \text{ \AA} \ll 2\mu$ ), equation (2.422) simplifies to

$$\begin{aligned} \overline{\phi'^2} \div 0.85 \cdot \frac{\overline{K''^2}}{\left(\frac{\partial^2 E}{\partial \phi^2}\right)_0^2} \cdot \frac{2\pi^2 r_0^2}{\lambda_M \lambda_A^{\frac{3}{2}}} \\ = \frac{0.10 \overline{K''^2} r_0^2}{M t^{\frac{1}{2}} \lambda_A^{\frac{3}{4}} \left(\frac{\partial^2 E}{\partial \phi^2}\right)_0^{\frac{3}{4}}} \quad (2.423) \end{aligned}$$

For  $r_0 = 100 \text{ \AA}$  and the values of  $\lambda_M$  and  $\lambda_A$  from equations (2.417) and (2.418),

$$\sqrt{\phi'^2} = 0.45^\circ \cdot \frac{\sqrt{K''^2}}{K_0} \quad (2.424)$$

for the magnetization at remanence along the easy axis.

We may define the mean ripple wavelength from the relation

$$\bar{\lambda} = \frac{2\pi}{\bar{K}} = \frac{2\pi}{k\phi'^2/\phi'^2} \quad (2.423),$$

With the same approximations as in equation

$$\bar{\lambda} = \frac{2\pi}{\bar{K}} = 0.68 \cdot \frac{2\pi}{k_A} = 0.68\lambda_A \quad (2.425)$$

Fuller and Hale<sup>F4</sup> have given experimental values for a 200 Å permalloy film of  $\phi' = 10^{-2} \text{ rad} = 0.6^\circ$  and  $\bar{\lambda} = 2\mu$ . Agreement with the theoretical value of  $\bar{\lambda}$  is excellent.

From equation (2.424) a value of

$\sqrt{K''^2} = 1.3K_0$  is predicted, which seems not unreasonable for permalloy. It is difficult to compare this value with the results  $\Delta K \approx 0.1K_0$  obtained by dispersion measurements using the Crowther technique. Clearly, the latter are greatly reduced by exchange and magnetostatic couplings. Though not directly applicable to the present case, an order of magnitude reduction by interactions has also been reported by Crowther<sup>C8</sup> in connection with dispersion measurements on a strained permalloy film of known chemical inhomogeneity over  $12\mu$

intervals. From the form of equation (2.419) only components of the mean ripple having

$$\sin^2 \theta < \frac{\bar{\lambda}}{\lambda_M} \left(1 + \frac{\lambda_A^2}{\bar{\lambda}^2}\right) \quad (2.426)$$

will be significant. Substituting numerical values, the ripple is indeed very closely a pure longitudinal variation with  $\theta < 5.3^\circ$ . Present data reported in the literature does not allow a more detailed examination of the predictions of either equations (2.423) or (2.426).

While longitudinal ripple produces no demagnetizing field to first order ( $\theta=0$ ), evaluation of second order terms gives a magnetostatic energy of approximately  $M^2(kt)\phi'^4$ . Comparison with the exchange energy  $\frac{1}{2}Ak^2\phi'^2$  for  $k=\frac{2\pi}{\bar{\lambda}}$  shows that the magnetostatic term may be neglected for  $\phi' < 6^\circ$ . The present analysis is thus adequate for a description of magnetization ripple ( $\phi' \approx 0.6^\circ$ ), but clearly breaks down if large angle switching is considered. The magnetostatic interaction model of Thomas<sup>14</sup> suggests the importance of magnetostatic fields in this case.

## 2.43 Switching Thresholds and the Unstable Growth of Magnetization Ripple

If a film is being switched, then as the coherent rotational switching threshold is approached, the restoring torque for small magnetization disturbances tends to zero, or mathematically  $\left. \frac{\partial^2 E}{\partial \phi^2} \right|_0 \rightarrow 0$ . Thus equations (2.423) and (2.418)

with (2.425) predict the infinite growth of a longitudinal ripple at increasingly greater wavelength ( $>2\mu$ ) as the switching threshold is approached. While these results cannot be interpreted too exactly, as the present analysis is necessarily invalid in this limiting case, it is of value in an understanding of the initial course of partial switching and labyrinth propagation processes.

## 2.5 SWITCHING BY WALL MOTION FOR FIELDS NEAR THE EASY AXIS

Ni-Fe films, for switching fields applied at small angles  $\gamma < \gamma_c$  to the easy axis, reverse by domain wall motion. If the film is saturated by an external field  $H$  and  $H$  is then reduced to zero and increased in the opposite direction, small domains of reverse magnetization will be created about inhomogeneities in the film at a "nucleation" field  $H_n$ .  $H_n$  is defined as positive, if the field  $H$  must be reversed

from its previous saturation direction before nucleation occurs. The external field at which these nuclei begin to grow irreversibly may be called the critical or threshold field for wall expansion and denoted by  $H_{sw}$ .  $H_{sw}$  is not necessarily equal to the critical or threshold field  $H_{Ow}$  for the motion of a free domain wall through the material according to the equation of Sixtus and Tonks<sup>S1</sup>

$$v_w = \theta(H - H_{Ow}) \quad (2.51)$$

where

$v_w$  is the wall velocity, and  
 $\theta$  is a constant of the material measuring the viscous damping force on the wall.

Clearly, however,  $H_{Ow} \leq H_{sw}$ .

In normal permalloy films nucleation of reverse domains occurs at the edges of the film due to edge imperfections and demagnetizing fields\*.  $H_n > 0$  and the remanence is high. Reversal takes place at  $H = H_{sw}$  by growth of these nuclei into large  $180^\circ$  domains with walls parallel to the easy axis.

---

\* The behaviour of films of high dispersion (Type 2, RIS films described by Cohen<sup>C7</sup>) or subject to special edge preparation<sup>M4</sup> may be very different.

---



The domains expand by motion of the walls in the direction of the outward wall normal.  $H_{Ow}$  is of the order of  $H_{sw}$ , and the walls thus move by a series of Barkhausen wall jumps rather than a single step. The sides of the hysteresis loop are correspondingly somewhat sloped. A measure of  $H_{sw}$  and  $H_{Ow}$  is often taken as the coercive force  $H_C$  of the  $(m_L, H_L)$  hysteresis loop. A more detailed consideration of the relationship between  $H_{sw}$ ,  $H_{Ow}$  and  $H_C$  is given in Section 4.6.  $H_n$  as defined above corresponds to the "nucleation field" of Goodenough<sup>G1</sup>.  $H_{sw}$  corresponds to the "critical field for irreversible wall motion" of Goodenough or to the "starting field" of Methfessel et al<sup>M4</sup>.  $H_{Ow}$  is commonly called the wall coercive force. Unless otherwise stated,  $H_n$ ,  $H_{sw}$ ,  $H_{Ow}$  and  $H_C$  may be taken as the values obtained for an external field applied along the easy axis, that is at  $\gamma=0$ . Permalloy films deposited under suitable conditions\* have anisotropy field values  $H_K$  in the range 1 to approximately 6 oe and show small anisotropy dispersion. The normalized coercive force  $h_C = H_C/H_K$  of such "normal" films is less than unity as opposed to "inverted" films having  $h_C > 1$ .

---

\* Deposition rate  $\geq 5 \text{ \AA sec}^{-1}$ , vacuum  $\leq 10^{-5}$  mm of Hg, substrate temperature  $\pm 300^\circ\text{C}$ .

---

If  $H_C$  is measured as a function of the angle  $\gamma$  of the applied field, then the resulting "threshold" curve may be conveniently plotted on a  $(h_L, h_T)$  diagram as in Fig. 2.51. A threshold curve can also be obtained by switching  $H_L$  with various traverse bias fields  $H_T$  applied. Since processes up to the threshold are reversible, then experimentally a unique curve is obtained independent of the particular locus of the field vector in the  $(h_L, h_T)$  plane. For some films the curve will show a marked discontinuity in slope on approaching the theoretical threshold for coherent rotation (see Fig. 4.41<sup>\*</sup>). If this discontinuity occurs at an angle  $\gamma = \gamma_C$ , then  $\gamma_C$  represents a critical angle below which reversal takes place by parallel wall motion and above which additional rotational processes occur. These further mechanisms are discussed in Section 2.6 and 2.7.

The domain processes described above have been verified by many workers using both Bitter patterns and the Kerr magneto-optical effect. Bitter patterns of edge domains and expanding  $180^\circ$  domains are given by Smith<sup>S10</sup> and Middelhoek<sup>M7</sup>.  $H_w$  has been measured using low frequency BH plotters and

---

\* In other cases no such discontinuity is apparent and the transition point can be found only from Bitter pattern examination.

---

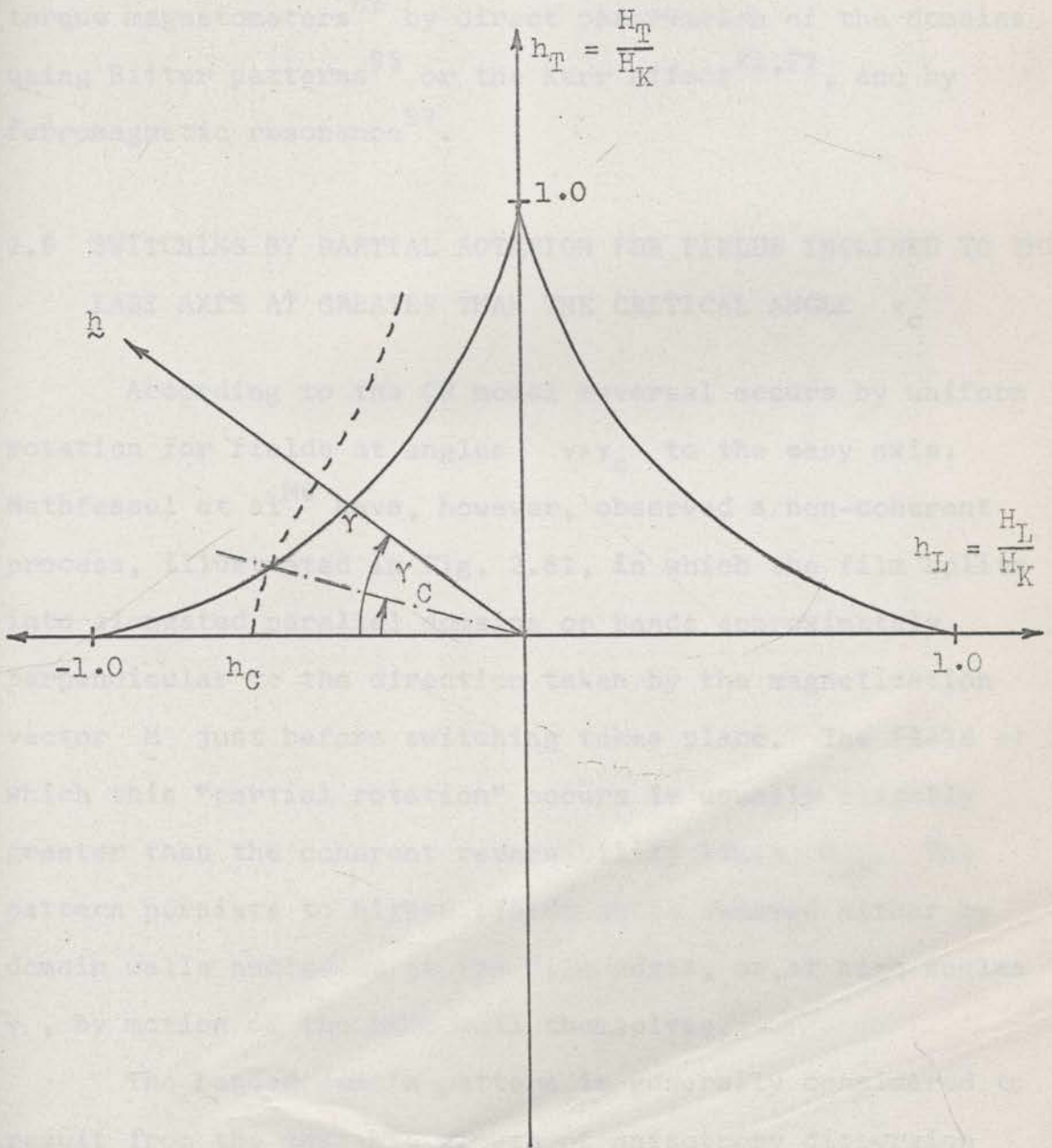


Fig. 2.51 The Threshold Curve and Critical Angle  $\gamma_C$  for Domain Wall Motion.

torque magnetometers<sup>H6</sup> by direct observation of the domains using Bitter patterns<sup>S5</sup> or the Kerr effect<sup>F1,F2</sup>, and by ferromagnetic resonance<sup>S7</sup>.

## 2.6 SWITCHING BY PARTIAL ROTATION FOR FIELDS INCLINED TO THE EASY AXIS AT GREATER THAN THE CRITICAL ANGLE $\gamma_c$

According to the CR model reversal occurs by uniform rotation for fields at angles  $\gamma > \gamma_c$  to the easy axis. Methfessel et al<sup>M6</sup> have, however, observed a non-coherent process, illustrated in Fig. 2.61, in which the film splits into elongated parallel domains or bands approximately perpendicular to the direction taken by the magnetization vector  $\underline{M}$  just before switching takes place. The field at which this "partial rotation" occurs is usually slightly greater than the coherent reversibility limit  $H_{cr}$ . The pattern persists to higher fields until removed either by domain walls nucleated at the film edges, or, at high angles  $\gamma$ , by motion of the band wall themselves.

The banded domain pattern is generally considered to result from the unstable growth of anisotropy dispersion induced magnetization ripple as the rotational threshold is approached (see Section 2.4 on magnetization ripple). As the field increases, the rotational threshold for some of the

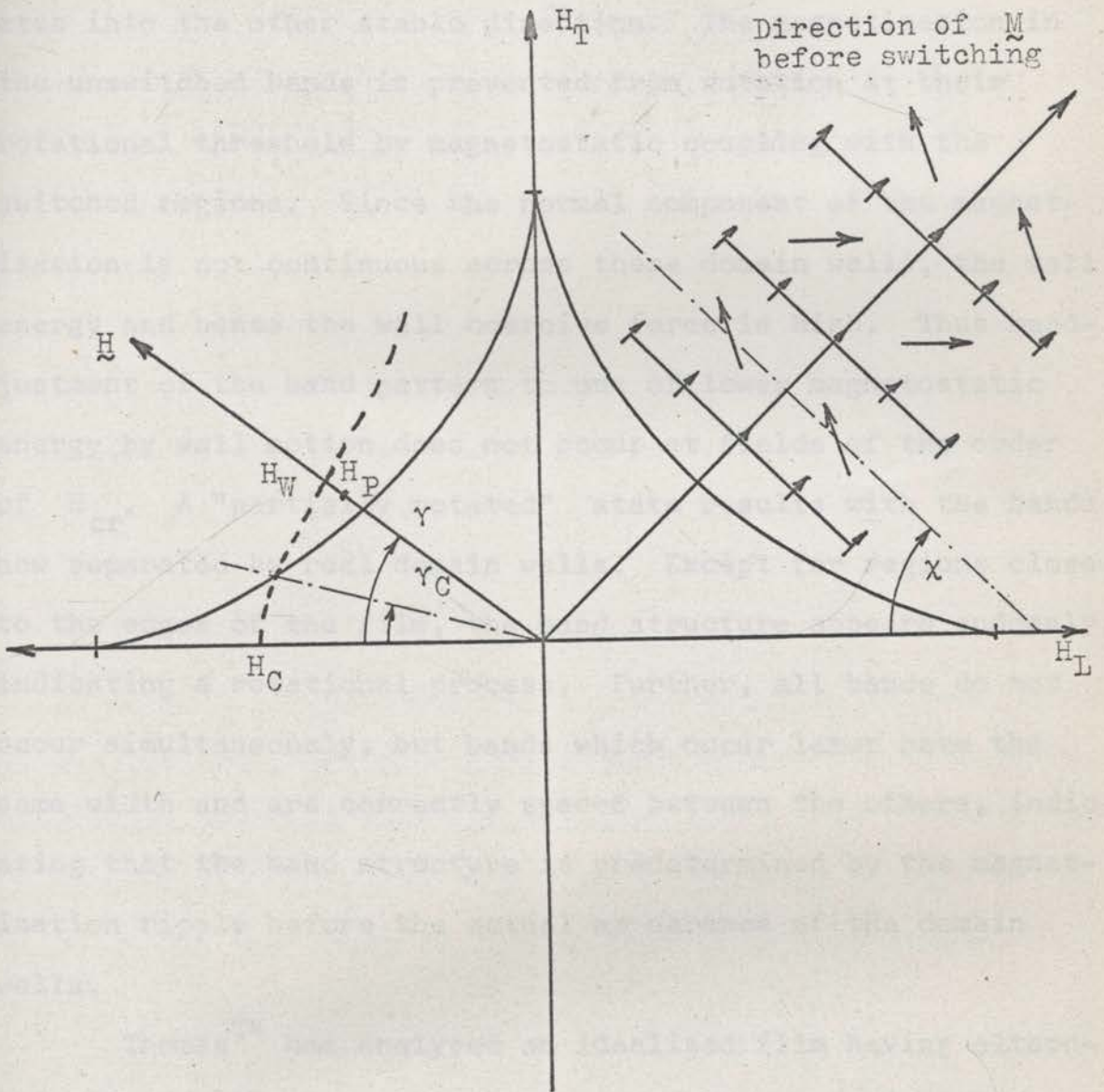


Fig. 2.61 Switching by Partial Rotation.

bands is exceeded, and the magnetization in these bands rotates into the other stable direction. The magnetization in the unswitched bands is prevented from rotation at their rotational threshold by magnetostatic coupling with the switched regions. Since the normal component of the magnetization is not continuous across these domain walls, the wall energy and hence the wall coercive force is high. Thus readjustment of the band pattern to one of lower magnetostatic energy by wall motion does not occur at fields of the order of  $H_{cr}$ . A "partially rotated" state results with the bands now separated by real domain walls. Except for regions close to the edges of the film, the band structure appears suddenly, indicating a rotational process. Further, all bands do not occur simultaneously, but bands which occur later have the same width and are correctly spaced between the others, indicating that the band structure is predetermined by the magnetization ripple before the actual appearance of the domain walls.

Thomas<sup>T4</sup> has analysed an idealized film having alternating bands of anisotropies  $K_1$  and  $K_2$ , perpendicular to the magnetization direction just before switching. Considering magnetostatic interaction between the bands, Thomas predicts theoretically a stable partially reversed state similar

to that just discussed.

## 2.61 Deficiencies of the Simple Theory

When the partial rotation of thin films is considered in detail, several important deviations from the simple theory arise.

Referring to Fig. 6.21, the angle  $\chi$  between the band pattern and the easy axis for reversal by a field  $H$  at the angle  $\gamma$  is given by

$$\tan \chi = \tan^{\frac{1}{3}} \gamma \quad (2.61)$$

where we have assumed that the bands are formed perpendicular to the direction of  $M$  at the switching threshold. Experimental data has been given by Middelhoeck<sup>M7</sup> and by Smith<sup>S10</sup> and is in part reproduced in Fig. 2.62. Agreement is very good for films of the order of  $1000 \text{ \AA}$ , but is clearly inadequate for the thinner films.

Measurements of the wall density<sup>M7</sup> also show a marked dependence on thickness, the average width of a domain band decreasing with increasing thickness, tending to a limiting value of about  $70\mu$  for films greater than  $1000 \text{ \AA}$ . No explanation is given by the present model. Indeed, Section 2.43 predicts that the wavelength of the principle component

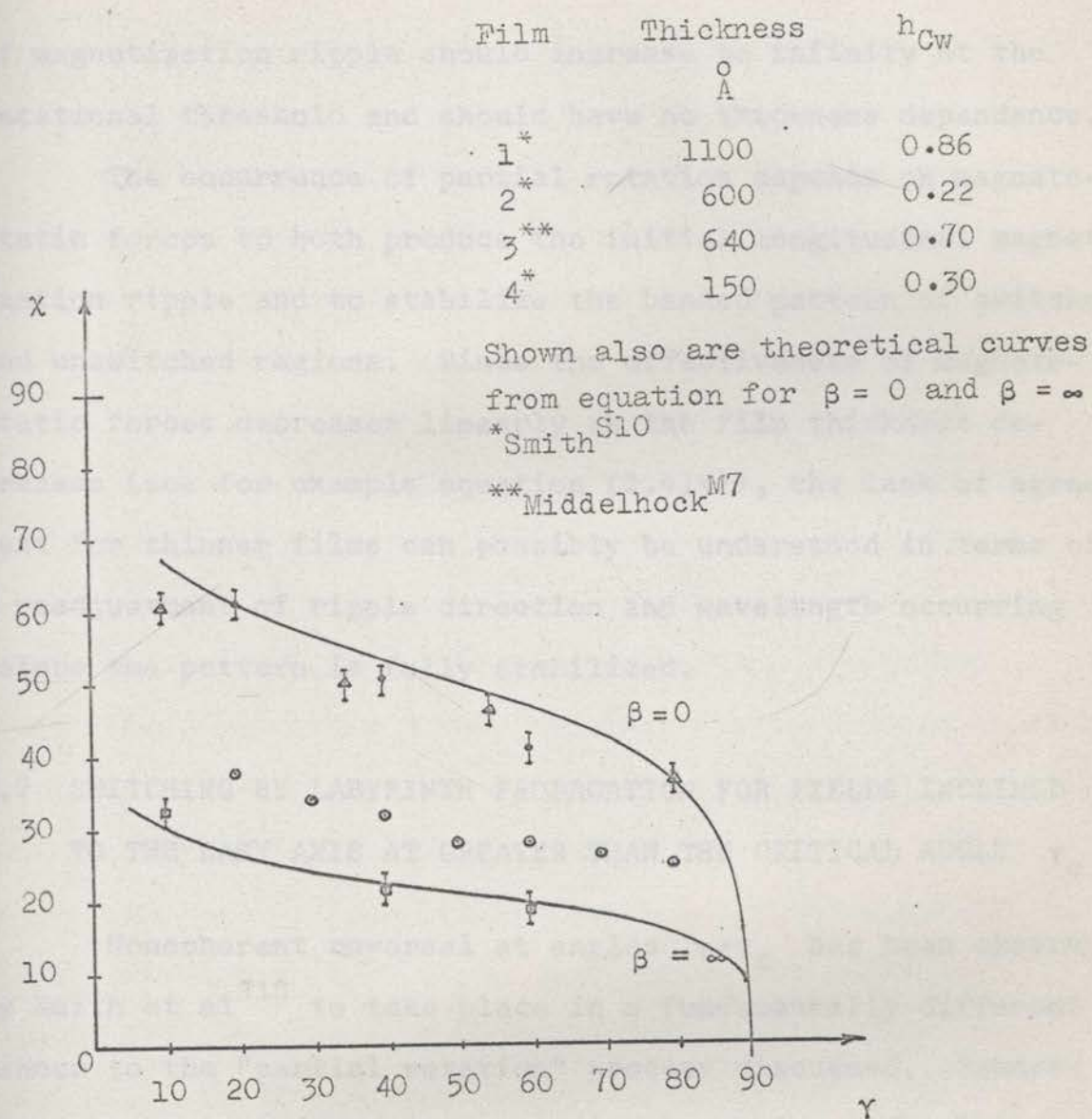


Fig. 2.62 The Direction  $\chi$  of Partial Rotation Bands or Labyrinth Propagation Domains as a Function of the Angle  $\gamma$  of the Applied Field



of magnetization ripple should increase to infinity at the rotational threshold and should have no thickness dependence.

The occurrence of partial rotation depends on magneto-static forces to both produce the initial longitudinal magnetization ripple and to stabilize the banded pattern of switched and unswitched regions. Since the effectiveness of magneto-static forces decreases linearly as the film thickness decreases (see for example equation (2.414)), the lack of agreement for thinner films can possibly be understood in terms of a readjustment of ripple direction and wavelength occurring before the pattern is fully stabilized.

## 2.7 SWITCHING BY LABYRINTH PROPAGATION FOR FIELDS INCLINED TO THE EASY AXIS AT GREATER THAN THE CRITICAL ANGLE $\gamma_c$

Noncoherent reversal at angles  $\gamma > \gamma_c$  has been observed by Smith et al<sup>S10</sup> to take place in a fundamentally different manner to the "partial rotation" process discussed. Reverse bands are not produced by a rotational process occurring simultaneously across the whole film. Instead reverse centres are nucleated at the film edges and propagate across the film as long filamentary domains, giving a "labyrinth" like flux pattern of switched and unswitched regions.

The sequential propagating nature of labyrinth switch-

ing indicates magnetostatic coupling between the last switched region and the region to be switched next\*. In the model proposed by Smith et al the film is considered as consisting (due to anisotropy dispersion) of a large number of regions of slightly different rotational thresholds. The switching behaviour of any region is independently determined in the first instance by its own local anisotropy while magnetostatic interaction between the regions is included later by a standard perturbation procedure. A rigorous derivation of these perturbation equations has been given by Harte and Smith<sup>H7</sup>. We shall reproduce here a somewhat simplified and, it is hoped, somewhat clearer treatment as an illustration of the use of perturbation methods with the Independent Region model.

In Fig. 2.71, (1), (2) and (3) are three regions of local anisotropy  $K_1, K_2, K_3$ . Region (1) has switched; region (2) situated at a characteristic distance  $R$  from region (1) is at its switching threshold; region (3) has not

---

\* It may be noted that lateral magnetostatic coupling is also responsible for the longitudinal magnetization ripple which initiates a partial rotation pattern.

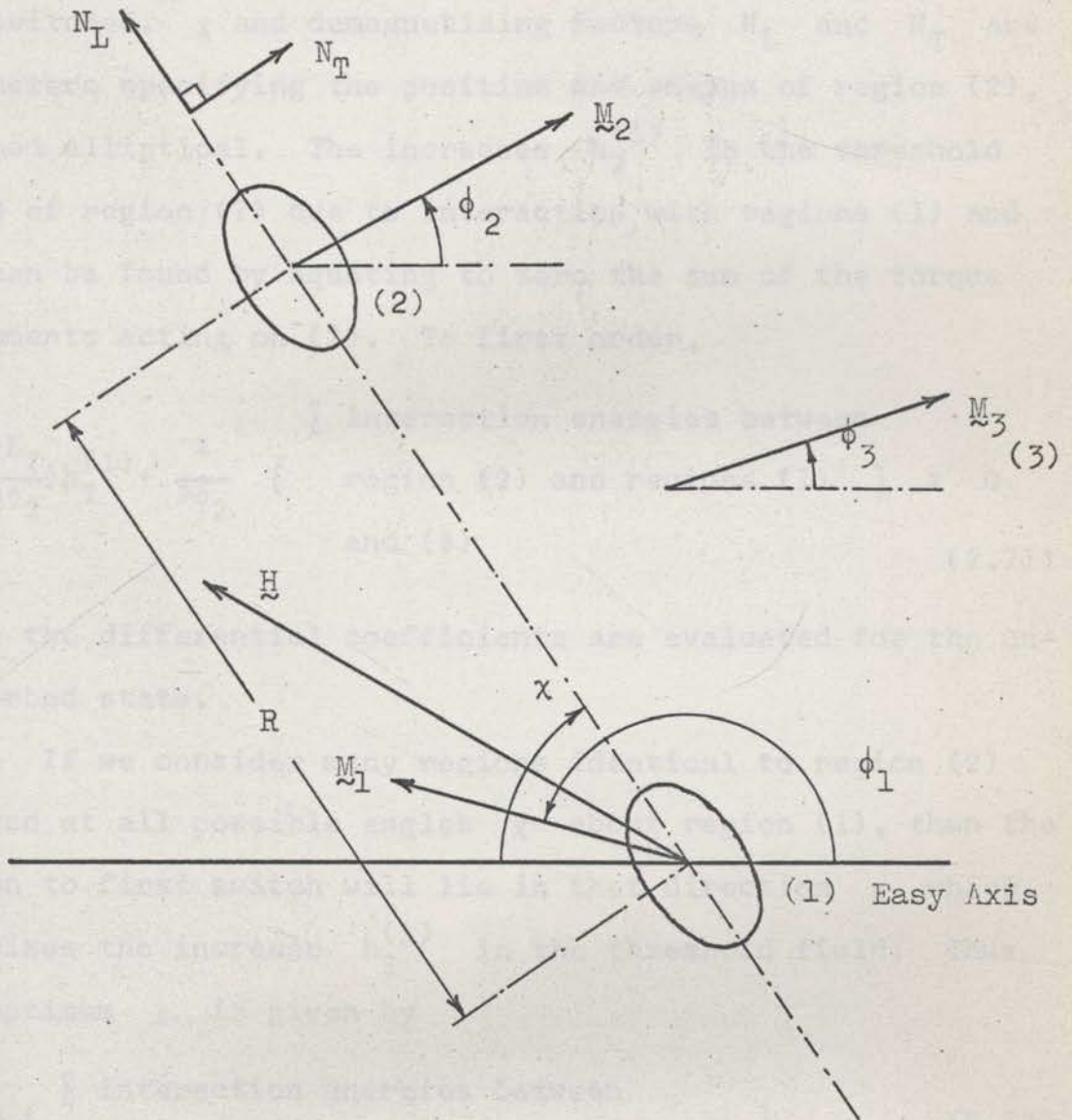


Fig. 2.71 Figure Illustrating Labyrinth Switching

yet switched.  $\chi$  and demagnetizing factors  $N_L$  and  $N_T$  are parameters specifying the position and shapes of region (2), assumed elliptical. The increases  $h_2^{(1)}$  in the threshold field of region (2) due to interaction with regions (1) and (3) can be found by equating to zero the sum of the torque increments acting on (2). To first order,

$$\frac{\partial}{\partial h_2} \left( \frac{\partial E_2}{\partial \phi_2} \right) h_2^{(1)} + \frac{\partial}{\partial \phi_2} \left( \begin{array}{l} \sum \text{interaction energies between} \\ \text{region (2) and regions (1)} \\ \text{and (3)} \end{array} \right) = 0 \quad (2.71)$$

where the differential coefficients are evaluated for the unperturbed state.

If we consider many regions identical to region (2) located at all possible angles  $\chi$  about region (1), then the region to first switch will lie in that direction  $\chi$  which minimizes the increase  $h_2^{(1)}$  in the threshold field. Thus the optimum  $\chi$  is given by

$$\frac{\partial^2}{\partial \chi \partial \phi_2} \left( \begin{array}{l} \sum \text{interaction energies between} \\ \text{region (2) and regions (1) and (3)} \end{array} \right) \quad (2.72)$$

The interaction energies per unit volume of (2),  $E_{21}$  and  $E_{23}$  are

$$E_{21} = \frac{V_1 M_s^2}{R^3} \{ \cos(\phi_2 - \phi_1) - 3 \cos(\chi + \phi_2) \cos(\chi + \phi_1) \}$$

$$E_{23} = 2\pi M_s^2 \{ N_T (\sin(\chi + \phi_2) - \sin(\chi + \phi_3))^2 + N_L (\cos(\chi + \phi_2) - \cos(\chi + \phi_3))^2 \}$$

$$- \frac{V_1 M_s^2}{R^3} \{ \cos(\phi_2 - \phi_3) - 3 \cos(\chi + \phi_2) \cos(\chi + \phi_3) \} \quad (2.73)$$

where

$V_1$  is the volume of region (1), and

$M_s$  is the saturation magnetism for the film material.

$E_{23}$  is calculated as the energy of a magnetized ellipse in a uniform sheet minus a dipole - dipole term representing the missing portion of the sheet, region (1). Substituting equation (2.73) into (2.72), then

$$\tan 2\chi = \frac{\cos 2\phi_2 - \cos(\phi_2 + \phi_3) + \beta \{ \cos(\phi_1 + \phi_2) - \cos(\phi_2 + \phi_3) \}}{\sin 2\phi_2 - \sin(\phi_2 + \phi_3) + \beta \{ \sin(\phi_1 + \phi_2) - \sin(\phi_2 + \phi_3) \}} \quad (2.74)$$

where

$\phi_1, \phi_2, \phi_3$  are unperturbed values, and

$$\beta = \frac{3V_1}{R^3 4\pi(N_T - N_L)}$$

Two cases arise.

2.71  $\beta=0$  : Shape Anisotropy and  $\chi$  for Thick Films

If the shape anisotropy energy of region (2) itself is of much more importance than propagation effects due to coupling to region (1), then  $\beta$  may be taken equal to zero in equation (2.74), giving

$$\chi = \frac{\pi}{2} - \frac{3\phi_2 + \phi_3}{4} \quad (2.75)$$

$$\div \frac{\pi}{2} - \phi$$

where  $\phi$  is the magnetization angle calculated at the rotational threshold for the average anisotropy of the film.

Equation (2.75) is just the result obtained by Middelhoek (equation (2.61)) and applies well to thicker films.

The increase in the threshold field  $h_2^{(1)}$  for  $\beta=0$

and  $\chi = \frac{\pi}{2} - \frac{3\phi_2 + \phi_3}{4}$  may be evaluated from equation (2.71) as

$$h_2^{(1)} = \frac{8\pi M_S^2 \sin \frac{1}{2}(\phi_2 - \phi_3) \{N_L \cos^2 \frac{2\phi_2 - \phi_3}{4} - N_T \sin^2 \frac{2\phi_2 - \phi_3}{4}\}}{2K_2 \sin(\gamma - \phi_2)} \quad (2.76)$$

$\phi_2 - \phi_3$  is small, but +ve so that  $\sin \frac{1}{2}(\phi_2 - \phi_3) > 0$ ,

$\cos^2 \frac{2\phi_2 - \phi_3}{4} \div 1$  and  $\sin^2 \frac{2\phi_2 - \phi_3}{4} \div 0$ . Thus the minimum increase

in the threshold will occur for those regions for which  $N_L$  is small, that is for long elongated domains in the direction  $\chi$ . Because of the uncertainties in the values of  $\phi_2 - \phi_3$  and of  $N_L$  and  $N_T$ , numerical evaluation of  $h_2^{(1)}$  is scarcely justified.

## 2.72. $\beta = \infty$ : Propagation Effects and $\chi$ for Thin Films

If the shape anisotropy energy of region (2) itself is of much less importance than propagation effects due to coupling to region (1), then  $\beta$  may be taken equal to infinity in equation (2.74), giving

$$\chi = \frac{\pi}{2} - \frac{\phi_1 + \phi_3 + 2\phi_2}{4} \quad (2.77)$$

If the anisotropy dispersion is small, we may put

$$\phi_2, \phi_3 \doteq \phi \quad \text{and} \quad \phi_1 \doteq \phi_s$$

where

$\phi$ ,  $\phi_s$  are the magnetization angles calculated at the rotational threshold for the average anisotropy of the film.  $\phi$  is the angle immediately before,  $\phi_s$  the angle immediately after switching occurs.

Thus

$$\chi = \frac{\pi}{2} - \frac{3\phi + \phi_s}{4} \quad (2.78)$$

Equation (2.78) is plotted in Fig. 2.62 and is seen to apply well to thinner films.

Reasons for the thickness dependence of  $\chi$  are not as yet well understood<sup>S10</sup>. If only magnetostatic forces are involved, the whole pattern should scale linearly with film thickness  $t$  while  $\beta$ , as a dimensionless product, must remain constant. Experimentally, this does not happen, the traverse width  $w$  of a switched band instead decreasing with increasing thickness. Smith<sup>S10</sup> has thus proposed the following tentative explanation. The range of magnetostatic forces increases with increasing thickness (see equation (2.414)). If then the characteristic distance  $R$  is assumed proportional to  $t$ ,

$$\beta \propto \frac{V/R^3}{N_T - N_L} \propto \frac{tRw/R^3}{N_T - N_L} \propto \frac{w/t}{N_T - N_L}$$

Since experimentally  $w$  decreases and also  $N_T - N_L$  increases (to the limiting value of  $4\pi$ ) with increasing  $t$ , then  $\beta$  decreases with increasing  $t$  as  $\frac{1}{t}$  at least. Thus, small values of  $\beta$  might be expected from thick films, large values of  $\beta$



from thin films.

The increase in the threshold field  $h_2^{(1)}$  for  $\beta = \infty$   
 $\chi = \frac{\pi}{2} - \frac{\phi_1 + \phi_3 + 2\phi_2}{4}$  may be evaluated from equation (2.71) as

$$h_2^{(1)} = - \frac{\frac{VM_s^2}{R^3} \sin \frac{\phi_1 - \phi_3}{2} \cos \frac{\phi_1 + \phi_3 - 2\phi_2}{2}}{2K_2 \sin(\gamma - \phi_2)}$$

$$\dagger - \frac{\frac{1}{2} \frac{VM_s^2}{R^3} \sin(\phi_s - \phi)}{2K \sin(\gamma - \phi)} \quad (2.79)$$

Numerical evaluation shows that  $h_2^{(1)}$  is approximately independent of  $\gamma$  for  $\pi - 70^\circ < \gamma < \pi$  and in this range

$$h_2^{(1)} \dagger - \frac{\frac{1}{2} \frac{VM_s^2}{R^3}}{2K} \dagger - \frac{\frac{1}{2} \frac{wt_s M_s^2}{R^2}}{2K} \quad (2.710)$$

For a permalloy film of thickness  $t = 150 \text{ \AA}$ , taking  $w = 25 \mu$ ,  $R = 50 \mu$ ,  $M_s = 800$  cgs units, and  $K = 10^3$  ergs  $\text{cm}^{-3}$ , then  $h_2^{(1)} \dagger - 0.25$ . Though the above analysis is inexact, it is an indication that, for thin films, the switching threshold may be appreciably lowered by the labyrinth mechanism.

## 2.73 Reconciliation of Partial Rotation and Labyrinth Propagation Processes

Middelhoek<sup>M7</sup> has stated that the labyrinth pattern is not inherent in the reversal process itself, but appears only when the reversing field is decreased due to demagnetizing effects within the switched bands. It appears, however, that this is not true. Cohen<sup>C9</sup> has investigated a single film in which the anisotropy dispersion has been progressively increased by heat treatment. At low dispersion labyrinth propagation occurs. At high dispersion, simultaneous reversal at many centres throughout the film is possible without requiring a lowering of the threshold by magnetostatic interaction with a labyrinth tip. Partial rotation then occurs. Cohen's work underlines the importance of not only the uniaxial anisotropy, but of the magnitude and scale of the anisotropy dispersion in deciding film behaviour.

## 2.8 TORQUE MEASUREMENTS AND ROTATIONAL HYSTERESIS

Referring to Fig. 2.81, then in normalized notation,  $T = \sin\phi \cos\phi = h \sin(\gamma - \phi)$  is the torque acting on a film due to a field  $h$  applied at an angle  $\gamma$  to the easy axis. The film has been previously saturated along the easy axis in the direction shown. Torque curves of  $T$  against  $\gamma$  are common-

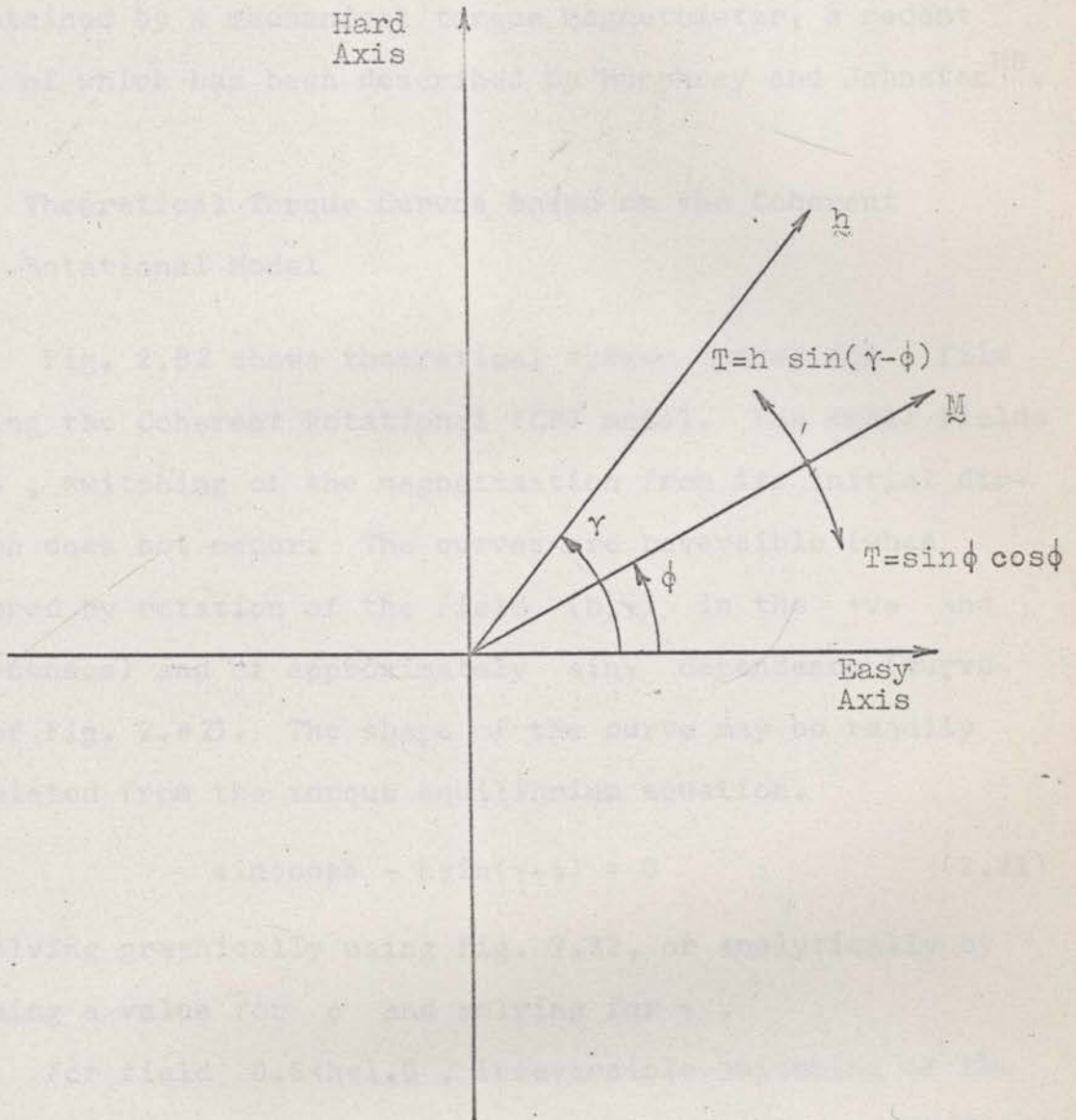


Fig. 2.81 Figure Illustrating the Torque Acting on the Magnetization.

ly obtained by a mechanical torque magnetometer, a recent model of which has been described by Humphrey and Johnston<sup>H6</sup>.

## 2.81 Theoretical Torque Curves Based on the Coherent Rotational Model

Fig. 2.82 shows theoretical torque curves for a film obeying the Coherent Rotational (CR) model. For small fields  $h < 0.5$ , switching of the magnetization from its initial direction does not occur. The curves are reversible (when measured by rotation of the field  $(h, \gamma)$  in the +ve and -ve senses) and of approximately  $\sin \gamma$  dependence (curve (1) of Fig. 2.82). The shape of the curve may be readily calculated from the torque equilibrium equation.

$$\sin \phi \cos \phi - h \sin(\gamma - \phi) = 0 \quad (2.81)$$

by solving graphically using Fig. 2.32, or analytically by assuming a value for  $\phi$  and solving for  $\gamma$ .

For field  $0.5 < h < 1.0$ , irreversible switching of the magnetization occurs at a critical angle  $\phi_r(h)$  as the field  $(h, \gamma)$  rotates into the reverse quadrant. The curves are no longer reversible, but show discontinuous jumps (as switching occurs) between the two branches of the curve calculated for  $-\phi_r < \phi < \phi_r$  and for  $\pi - \phi_r < \phi < \pi + \phi_r$  (curve (2) of Fig. 2.82). A considerable rotational hysteresis loss  $w_r = \oint T d\gamma$  is indic-

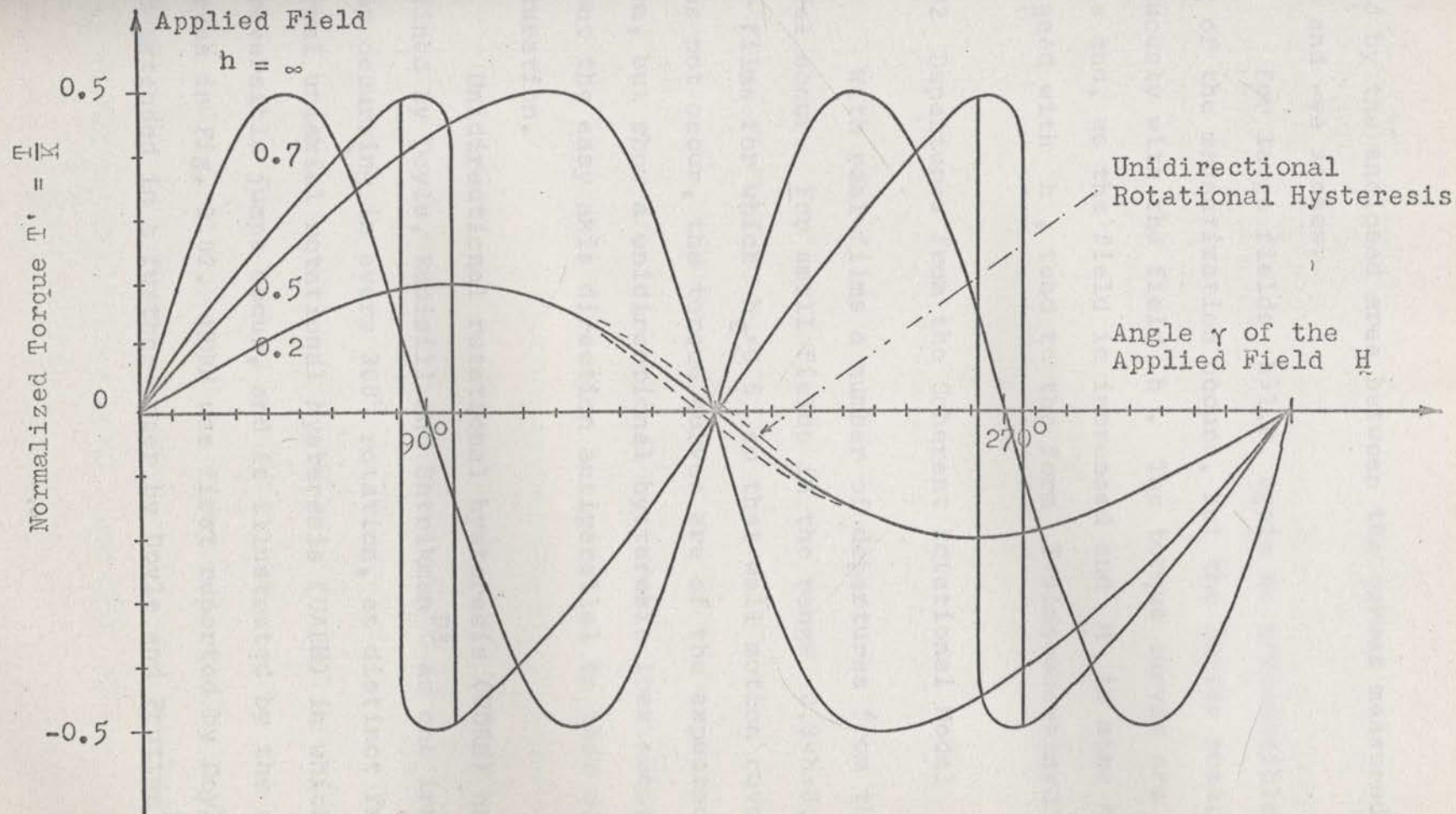


Fig. 2.82 Rotational Torque Curves Assuming Coherent Rotation of the Magnetization.

ated by the enclosed area between the curves measured in the +ve and -ve senses.

For large fields  $h > 1.0$ , again no irreversible switching of the magnetization occurs, but the latter rotates continuously with the field  $h$ . The torque curves are reversible and, as the field is increased and  $\vec{M}$  is more closely aligned with  $\vec{h}$ , tend to the form  $T = \sin\phi \cos\phi + \sin\gamma \cos\gamma$ .

## 2.82 Departures from the Coherent Rotational Model

With real films a number of departures from the CR model occur. For small fields in the range  $0.3 < h < 0.5$  and for films for which  $h_c > 0.5$  so that wall motion reversal does not occur, the torque curves are of the expected CR form, but show a unidirectional hysteresis loss occurring about the easy axis direction antiparallel to that of initial saturation.

Unidirectional rotational hysteresis (UDRH) has been defined by Doyle, Rudisill and Shtrikman<sup>D3</sup> as one irreversible jump occurring in every  $360^\circ$  rotation, as distinct from the normal uniaxial rotational hysteresis (UARH) in which two irreversible jumps occur, and is illustrated by the dotted curves in Fig. 2.82. UDRH was first reported by Doyle et al<sup>D3</sup> and extended in a further paper by Doyle and Prutton<sup>D4</sup>. An

adequate explanation appears to have been provided in terms of irreversible switching of anisotropy dispersion regions (orientated approximately  $90^\circ$  from the average easy axis) under the sum of the applied field and a local effective field due to the bulk film magnetization. Consistent with this model, Doyle et al<sup>D3</sup> report a continuous increase in UDRH with increasing film coercive force and dispersion.

Uniaxial rotational hysteresis has been reported by Doyle, Rudisill and Shtrikman<sup>D2</sup> and more recently by a large number of workers. Since magnetization reversal occurs by wall processes at fields below the rotational threshold, large hysteresis loss occurs for these films at fields (typically down to  $h=0.2$ ) considerably lower than the range  $0.5 < h < 1.0$  of the CR model. Doyle et al<sup>D2</sup> have discussed the low field difference in terms of a wall motion model of Kondorsky<sup>K1</sup> and a non-coherent magnetization curling model of Shtrikman and Treves<sup>S8</sup>. However, in view of the multiple reversal processes occurring in real films, it is perhaps best to determine the points of discontinuity of the torque curves from an experimental plot of the film switching curve in the  $(h_L, h_T)$  plane as in Fig. 2.51.

For large fields  $h > 1.0$  the torque curves tend to the expected CR form  $\sin\gamma\cos\gamma$ , but have a residual hysteresis loss occurring about the  $\gamma=90^\circ$  and  $270^\circ$  directions. This

can be attributed to irreversible switching of regions in which the magnitude of the anisotropy is greater than average. In addition, films of very high dispersion (such as found in inverted films or films possessing rotatable anisotropy in which a new easy axis direction can be established by a large saturating field) show isotropic rotational hysteresis (IRH). Typical curves (showing a residual uniaxial component) are shown in Fig. 2.83 and are readily explained as the averaged hysteresis loss for a film consisting of randomly orientated uniaxial regions. Alternatively, the slightly different view may be taken that the field produces a rotatable anisotropy with the anisotropy axis slightly lagging the field direction. The torque measured then corresponds to that required to move the anisotropy axis over a local energy minimum (in a similar manner to the coercive force for domain wall motion). High field hysteresis loss and IRH have been reported by Bozorth<sup>B1</sup> for bulk material and by Jacobs and Luborsky<sup>J1</sup> for permanent magnet material consisting of randomly orientated uniaxial particles. For films, investigations have been made by numerous workers including Takahashi, Watanabe, Kono and Ogawa<sup>T2</sup>, Robinson<sup>R2</sup>, Cohen<sup>C7</sup>, Lommel and Graham<sup>L2</sup>, Flanders, Prutton and Doyle<sup>F8</sup> and in somewhat greater detail by Lehrer<sup>L3</sup>. Mayfield<sup>M2</sup> has measured the hysteresis loss by a different method employing a rotating AC field. Doyle



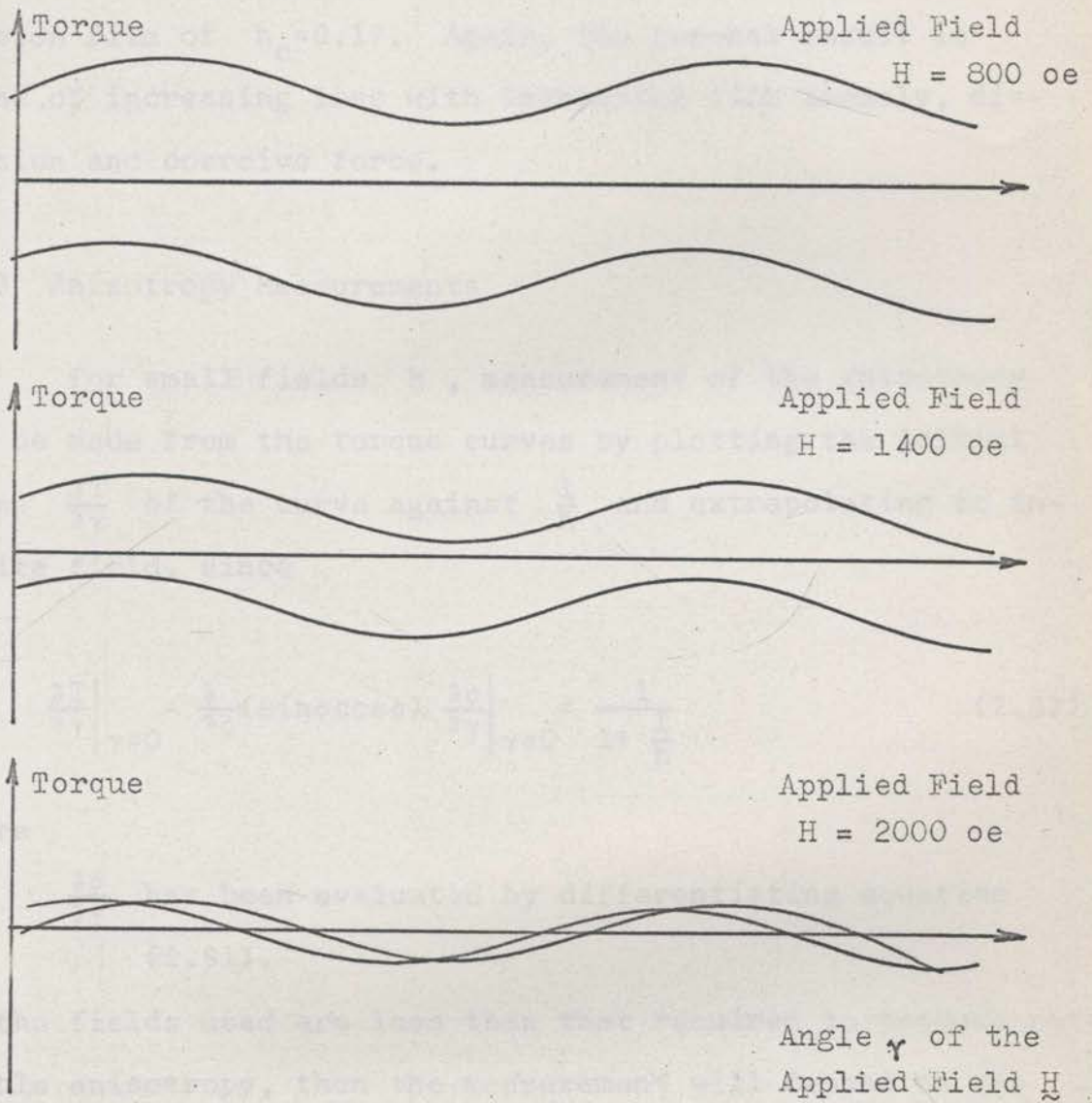


Fig. 2.83 Isotropic Rotational Hysteresis with a Residual High Field Uniaxial Component.  
(after Lehrer <sup>L3</sup>)

et al<sup>D2</sup> report a very small high field loss for a low dispersion film of  $h_c=0.17$ . Again, the general result is found of increasing loss with increasing film anomaly, dispersion and coercive force.

### 2.83 Anisotropy Measurements

For small fields  $h$ , measurement of the anisotropy can be made from the torque curves by plotting the initial slope  $\frac{\partial T}{\partial \gamma}$  of the curve against  $\frac{1}{h}$  and extrapolating to infinite field, since

$$\left. \frac{\partial T}{\partial \gamma} \right|_{\gamma=0} = \frac{\partial}{\partial \phi} (\sin \phi \cos \phi) \left. \frac{\partial \phi}{\partial \gamma} \right|_{\gamma=0} = \frac{1}{1 + \frac{1}{h}} \quad (2.82)$$

where

$$\frac{\partial \phi}{\partial \gamma} \text{ has been evaluated by differentiating equation (2.81).}$$

If the fields used are less than that required to produce rotatable anisotropy, then the measurement will depend on the previous magnetic history of the sample and the measured anisotropy will be the sum of both fixed and rotatable components. For large fields, measurement can be made of both the rotatable and fixed uniaxial anisotropies by separating the constant and  $\sin \gamma \cos \gamma$  components of the torque curves (Fig. 2.83).

## 2.9 LIST OF REFERENCES

- B1 Bozorth, R.M.,  
"Ferromagnetism".  
D.Van Nostrand Company Inc., New York, p. 514, (1951).
- B2 Brown, W.F., Jr.,  
"Micromagnetics, Domains and Resonance".  
J.Appl.Phys., (Suppl.), 30, 625, (1959).
- B3 Boersch, H.,  
"Electron-optics Investigations of Weiss Domains in  
Thin Iron Films".  
Z.Phys., 159, 388, (1960).
- C1 Crittenden, E.C., Jr., Hudimac, A.A., Strough, R.J.,  
"Magnetization Hysteresis Loop Tracer for Long Specimens  
of Extremely Small Cross Section".  
Rev.Sci.Instrum., 22, 872, (1951).
- C2 Crittenden, E. C., Jr., Hoffman, R.W.,  
"Thin Films of Ferromagnetic Materials".  
Rev.Mod.Phys., 25, 310, (1953).
- C3 Conger, R.T.,  
"Magnetisational Reversal in Thin Films".  
Phys.Rev., 98, 1752, (1955).
- C4 Conger, R.T., Essig, F.C.,  
"Resonance and Reversal Phenomena in Ferromagnetic Films".  
Phys.Rev., 104, 915, (1956).
- C5 Chu, K., Singer, J.R.,  
"Thin Films Magnetisation Analysis".  
Proc.Inst.Radio Engrs., 47, 1237, (1959).
- C6 Crowther, T.S.,  
"Techniques for Measuring the Angular Dispersion of the  
Easy Axis of Magnetic Films".  
Group Report No. 51-2, Lincoln Lab., Massachusetts  
Institute of Technology, (1959).
- C7 Cohen, J.A.,  
"Anomalous Magnetic Films".  
J.Appl.Phys., 33, 2968, (1962).

- C8 Crowther, T.S.,  
"Angular and Magnitude Dispersion of the Anisotropy  
in Thin Magnetic Films".  
J.Appl.Phys., 34, 580, (1963).
- C9 Cohen, M.S.,  
"Influence of Anisotropy Dispersion on Magnetic  
Properties of Ni-Fe Films".  
J.Appl.Phys., 34, 1841, (1963).
- D1 Dietrich, W., Proebster, W.E., Wolf, P.,  
"Nanosecond Switching in Thin Magnetic Films".  
IBM J.Res.Developm., 4, 189, (1960).
- D2 Doyle, W.D., Rudisill, J.E., Shtrikman, S.,  
"Angular Dependence of Torque in Anisotropic Permalloy  
Films".  
J.Appl.Phys., 32, 1785, (1961).
- D3 Doyle, W.D., Rudisill, J.E., Shtrikman, S.,  
"Unidirectional Hysteresis in Thin Permalloy Films".  
J.Appl.Phys. (Suppl.), 33, 1162, (1962).
- D4 Doyle, W.D., Prutton, M.,  
"Anisotropy Distributions and Unidirectional Hysteresis  
in Thin Permalloy Films".  
J.Appl.Phys. (Suppl.), 34, 1077, (1963).
- F1 Fowler, C.A., Jr., Fryer, E.M.,  
"Magnetic Domains by the Longitudinal Kerr Effect".  
Phys.Rev., 94, 52, (1954).
- F2 Fowler, C.A., Jr., Fryer, E.M.,  
"Magnetic Domains in Thin Films of Nickel-Iron".  
Phys.Rev., 100, 746, (1955).
- F3 Fowler, C.A., Jr., Stevens, J.R., Fryer, E.M.,  
"Magnetic Domains in Evaporated Thin Films of Nickel-  
Iron".  
Phys.Rev., 104, 645, (1956).
- F4 Fuller, H.W., Hale, M.E.,  
"Determination of Magnetisation Distribution in Thin  
Films Using Electron Microscopy".  
J.Appl.Phys., 31, 238, (1960).

- F5 Fuchs, E.,  
"Display of Weiss Domains in Thin Ferromagnetic Films  
by Means of an Electromagnetic Electron Microscope".  
Naturviso, 47, 392, (1960).
- F6 Feldtkeller, E.,  
"Magnetisation Ripple in Thin Films Using Electron  
Microscopy".  
Elektron. Rechenanlagen, 3, 167, (1961).
- F7 Fuchs, E.,  
"Magnetic Structures in Thin Ferromagnetic Films,  
Investigated by the Electron Microscope".  
Z. angew. Physik, 13, 157, (1961).
- F8 Flanders, P.J., Prutton, M., Doyle, W.D.,  
"Relationship Between Uniaxial, Inverted and Rotatable  
Initial Susceptibility in Permalloy Films".  
J.Appl.Phys. (Suppl.), 34, 1075, (1963).
- G1 Goodenough, J.B.,  
"A Theory of Domain Creation and Coercive Force in  
Polycrystalline Ferromagnetics".  
Phys.Rev., 95, 917, (1954).
- G2 Garrod, J.R.,  
"Methods of Improving the Sensitivity of the Bitter  
Technique".  
Proc.Phys.Soc. (London), 79, 1252, (1962).
- H1 Humphrey, F.B.,  
"Traverse Flux Change in Soft Ferromagnetics".  
J.Appl.Phys., 29, 284, (1958).
- H2 Huber, E.E., Smith, D.O., Goodenough, J.B.,  
"Domain Wall Structure in Permalloy Films".  
J.Appl.Phys., 29, 294, (1958).
- H3 Hale, M.E., Fuller, H.W., Rubinstein, H.,  
"Magnetic Domain Observations by Electron Microscopy".  
J.Appl.Phys., 30, 789, (1959).
- H4 Honde, H.J.,  
"Observations of Cross Tie Domain Walls by the  
Faraday Effect".  
J.Appl.Phys., 32, 1234, (1961).

- H5 Harte, K., Cohen, M.S.,  
"Anisotropy Dispersion and Magnetisation Ripple in  
Magnetic Films".  
Quarterly Res.Rept. on Solid State Research, Lincoln  
Lab., Massachusetts Institute of Technology, No.2,  
p.57, (1962).
- H6 Humphrey, F.B., Johnston, A.R.,  
"Sensitive Automatic Torque Balance for Thin Magnetic  
Films".  
Rev.Sci.Instrum., 34, 348, (1963).
- H7 Harte, K.J., Smith, D.O.,  
"Switching Thresholds of Weakly Coupled Ferromagnetic  
Domains".  
J.Appl.Phys., 34, 442, (1963).
- J1 Jacobs, I.S., Luborsky, F.E.,  
"Magnetic Anisotropy and Rotational Hysteresis in  
Elongated Fine-particle Magnets".  
J.Appl.Phys., 28, 467, (1957).
- K1 Kondorsky  
"On Hysteresis in Ferromagnetics".  
J.Phys. (U.S.S.R.), 2, 161, (1940).
- K2 Kittel, C.,  
"Theory of the Structure of Ferromagnetic Domains in  
Films and Small Particles".  
Phys.Rev., 70, 965, (1946).
- K3 Kittel, C., Galt, J.K.,  
"Ferromagnetic Domain Theory".  
Solid State Physics, Academic Press Inc., New York,  
V 3, p. 439, (1956).
- L1 Landau, L., Lifshitz, E.,  
"Theory of the Dispersion of Magnetic Permeability in  
Ferromagnetic Bodies".  
Physik. Z. Sowjetunion, 8, 153, (1935), (in English).
- L2 Lommel, J.M., Graham, C.D., Jr.,  
"Rotatable Anisotropy in Composite Films".  
J.Appl.Phys., 33, 1160, (1963).

- L3 Lehrer, S.S.,  
"Rotatable Anisotropy in Negative Magneto-striction  
Ni-Fe Films".  
J.Appl.Phys., 34, 1207, (1963).
- M1 Moon, R.M.,  
"Internal Structure of Cross-Tie Walls in Thin Permalloy  
Films Through High Resolution Bitter Techniques".  
J.Appl.Phys. (Suppl.), 30, 82S, (1959).
- M2 Mayfield, J.R.,  
"Rotational Hysteresis in Thin Films".  
J.Appl.Phys., (Suppl.), 30, 256S, (1959).
- M3 Methfessel, S., Middlehoek, S., Thomas, H.,  
"Domain Walls in Thin Ni-Fe Films".  
IBM J.Res.Developm., 4, 96, (1960).
- M4 Methfessel, S., Middlehoek, S., Thomas, H.,  
"Nucleation Processes in Thin Permalloy Films".  
J.Appl.Phys. (Suppl.), 32, 294S, (1961).
- M5 Michalak, J.T., Glenn, R.C.,  
"Transmission Electron Microscope Observations of  
Magnetic Domain Walls".  
J.Appl.Phys., 32, 1261, (1961).
- M6 Methfessel, S., Middlehoek, S., Thomas, H.,  
"Partial Rotation in Permalloy Films".  
J.Appl.Phys., 32, 1959, (1961).
- M7 Middlehoek, S.,  
"Static Reversal Processes in Thin Ni-Fe Films".  
IBM J.Res.Developm., 6, 394, (1962).
- O1 Olson, C.D., Pohm, A.V.,  
Progress Report No.5 on Deposited Core Matrix.  
Remington Rand Univac, PX72004-5, (May, 1956).
- O2 Olson, C.D., Pohm, A.V.,  
"Flux Reversal in Thin Films of 82% Ni, 18% Fe".  
J.Appl.Phys., 29, 274, (1958).
- O3 Oguey, H.J.,  
"Theoretical Hysteresis Loops of Thin Magnetic Films".  
Proc.Inst.Radio Engrs., 48, 1165, (1960).

- P1 Prutton, M.,  
"The Observation of Domain Structure in Magnetic Thin Films by Means of the Kerr Magneto-Optic Effect".  
Phil.Mag., 4, 1063, (1959).
- R1 Roberts, B.W., Bean, C.P.,  
"Large Magnetic Kerr Rotation in Bi Mn Alloy".  
Phys.Rev., 96, 1494, (1954).
- R2 Robinson, G.,  
"Anisotropy in Polycrystalline Nickel Iron Thin Films in the Compositional Range 40-100% Nickel".  
Proc.International Conference on Magnetism and Crystallography, Kyots, p. 558, (1961).
- S1 Sixtus, K.J., Tonks, L.,  
"Propagation of Large Barkhausen Discontinuities".  
Part I, Phys.Rev., 37, 930, (1931);  
Part II, Phys.Rev., 42, 419, (1932).
- S2 Stoner, E.C., Wohlfarth, E.P.,  
"A Mechanism of Magnetic Hysteresis in Heterogeneous Alloys".  
Phil.Trans.Roy.Soc., A, 240, 599, (1948).
- S3 Smith, D.O.,  
"Switching Behaviour of Thin Permalloy Films".  
Proc.Second Conf. on Magnetism and Magnetic Materials, Boston, (Oct., 1956).
- S4 Slonczewski, J.C.,  
"Analysis of the Rotational Hysteresis Curves of Thin Films".  
IBM Res.Rept. No. RM003, 111, 224, (Oct., 1956).
- S5 Sherwood, R.C., Williams, H.J.,  
"Magnetic Domain Patterns on Thin Films".  
J.Appl.Phys., 28, 548, (1957).
- S6 Smith, D.O.,  
"Static and Dynamic Behaviour of Thin Permalloy Films".  
J.Appl.Phys., 29, 264, (1958).
- "The Determination of Domain Wall Thickness in Ferrimagnetic Films by Electron Microscopy".  
Proc.Phys.Soc. (London), 73, 1237, (1957).



- S7 Smith, D.O.,  
"Some Structure Sensitive Properties of Permalloy Films".  
Proc.Int.Conference on the Structure and Properties of  
Thin Films, Lake George, p. 380, (1959).
- S8 Shtrikman, S., Treves, D.,  
"The Coercive Force and Rotational Hysteresis of  
Elongated Ferromagnetic Particles".  
J.de Physique et le Radium, 20, 286, (1959).
- S9 Smith, D.O.,  
"Anisotropy in Nickel-Iron Films".  
J.Appl.Phys., (Suppl.), 32, 70S, (1961).
- S10 Smith, D.O., Harte, H.J.,  
"Noncoherent Switching in Permalloy Films".  
J.Appl.Phys., 33, 1399, (1962).
- T1 Truxal, J.G.,  
"Automatic Feedback Control System Synthesis".  
McGraw Hill, Inc., New York, p.441, (1955).
- T2 Takahashi, M., Watanabe, D., Kono, T., Ogawa, S.,  
"Induced Magnetic Anisotropy of Evaporated Ni-Fe Films".  
J.Phys.Soc., Japan, 15, 1351, (1960).
- T3 Treves, D.,  
"Limitations of the Magneto-Optic Technique in the Study  
of Microscopic Magnetic Domain Structures".  
J.Appl.Phys., 32, 358, (1961).
- T4 Thomas, H.,  
"A Theoretical Model for Partial Rotation".  
J.Appl.Phys. (Suppl.), 33, 1117, (1962).
- T5 Torak, E.J., White, R.A., Hunt, A.J., Oredson, H.N.,  
"Measurement of the Easy Axis and  $H_k$  Probability  
Density Function for Thin Ferromagnetic Films Using the  
Longitudinal Permeability Hysteresis Loop".  
J.Appl.Phys., 33, 3037, (1962).
- W1 Wade, R.H.,  
"The Determination of Domain Wall Thickness in Ferro-  
magnetic Film by Electron Microscopy".  
Proc.Phys.Soc. (London), 79, 1237, (1962).

## CHAPTER 3

THE ORIGIN OF MAGNETIC ANISOTROPY IN  
THIN EVAPORATED NICKEL-IRON FILMS

## 3.1 INTRODUCTION

The origin of the uniaxial magnetic anisotropy in thin evaporated Fe-Ni films is imperfectly understood at the present time. The problem is related to the magnetic annealing of bulk material, but differs in several important respects. Firstly, while Fe and Ni films show strong anisotropy, magnetic annealing of pure bulk metals has not been reported.\* For bulk Ni-Fe alloys the anisotropy is in the range  $1-10 \times 10^3$  ergs  $\text{cm}^{-3}$ , compositions from 65 to 85 per cent Ni responding strongly, compositions from 90 to 92 per cent to a lesser extent, and compositions outside this range not at all. Secondly, anneal of bulk Ni-Fe alloys occurs only at high temperature ( $\geq 450^\circ\text{C}$ )<sup>F1</sup>, in contrast to the low temperature ( $\leq 300^\circ\text{C}$ )<sup>M3, S10</sup> annealing and, more obviously, the rotatable anisotropy found in thin films. While low temperature ordering of interstitial impurities, such as carbon and nitrogen, is well established for bulk materials, the magnitude of the anisotropy involved ( $\div 10^2$  ergs  $\text{cm}^{-3}$ ) is inadequate to account

---

\* With the possible exception of Fe, where a small effect may exist.

---

for that observed in films. Further, Graham<sup>G4</sup> has found no anisotropy ( $<10^2$  ergs  $\text{cm}^{-2}$ ) in Ni foils prepared from the bulk, indicating that anisotropy is due to some inherent property of evaporated films rather than their thinness as such. A number of theories have been advanced for bulk material over a space of many years. A proposal which appears at the present time to be most promising is the directional ordering theory developed by Néel<sup>N1-5</sup>, Taniguchi et al<sup>T2</sup> and Chikazumi et al<sup>C2</sup>. Reviews of bulk anneal have been given by Becker and Döring (in German)<sup>B2</sup>, Chikazumi (in Japanese)<sup>C4</sup>, Bozorth<sup>B10</sup> and Graham<sup>G2</sup>.

A discussion will thus be given here of some of the features and possible causes of film anisotropy. In view of their importance to the general problem, sections 3.2 and 3.3 are devoted to a review of reported results on film microstructure and on film stress, respectively. Section 3.5 is a review of certain aspects of directional ordering theory needed in an explanation of anisotropy in films. Section 3.4 discusses the anisotropies observed in Ni and Fe with emphasis on a clear separation of the non-rotatable anisotropy  $K_u$  and the pseudo rotatable anisotropy  $K_r$ . Some confusion has resulted in the past from failure to make this distinction. The non-rotatable anisotropy  $K_u$  of normally incident films is most likely due to a combination of

- directional Fe-Ni pair ordering,
- directional ordering of imperfections, and
- anisotropic elastic stress and magneto-striction.

Section 3.7 discusses evidence for directional pair and imperfection ordering in zero magneto-striction permalloy and indicates the importance of magnetic anneal experiments in providing information on the different imperfections contributing. Section 3.8 discusses the compositional variation  $K_u$  in terms of pair ordering and an "equivalent" anisotropic stress which may arise either from elastic stress, or from imperfection ordering. Section 3.6 has been added for completeness and shows that crystalline texture does not contribute to the anisotropy  $K_u$ . Crystalline texture has been discussed in the literature principally for oblique incident films and certain of the arguments used there are inapplicable in the present case. Pseudo-rotatable anisotropy  $K_r$  seems most likely to result from a distribution throughout the film of randomly orientated centres of high anisotropy. Anisotropy is established by magnetic interaction rather than by a structural anisotropy of the film. Section 3.9 discusses various features of this model. Finally, Section 3.10 is a brief review of the causes of anisotropy in oblique incident films, which appear well understood at the present time.

## 3.2 CRYSTAL ORIENTATION AND MICROSTRUCTURE

### 3.2.1 Crystallite Size, Shape and Orientation

The microstructure of thin films has been extensively investigated<sup>E1,K5,V2,A2,P4,P5,H5,C7,M5,Y2</sup> using a range of techniques including transmission electron microscopy (TEM), transmission electron diffraction (TED), reflection electron diffraction (RED) and X-ray diffraction (XD). A very useful article on general film microstructure with a review of TEM and ED techniques has been given by Basset et al<sup>B12</sup>.

TEM investigations<sup>A2,H5,C7,M5</sup> show that Fe-Ni films are polycrystalline with a crystallite size of 200-1000 Å. A slow deposition rate, or an increased substrate temperature ( $\geq 300^{\circ}\text{C}$ ), favours an increased crystallite size due to the lower initial nucleation density<sup>C10,S7</sup>. Crystallite size may also be increased by annealing at  $\geq 300^{\circ}\text{C}$ <sup>C10</sup>. No geometrical anisotropy in crystallite shape has been reported in normally incident films. Oblique incident films show a "chain" structure<sup>H5,S7</sup> whose long axis is normal to the incident vapour plane, with elongation of the individual crystallites in the vapour direction for very large angles of incidence<sup>C9</sup>.

TED, RED and XD studies indicate the normal body centred (alloys < 25 per cent Ni), or face centred

(alloy > 25 per cent Ni) cubic lattice with no evidence of addition phases such as ordered  $\text{Ni}_3\text{Fe}$ . Crystal orientation is either random or sometimes shows a texture axis formation. The details of the texture structure is subject to considerable disagreement<sup>P4</sup> and while some workers have found no structure<sup>H5, M5</sup>, persistent reports of texture have been made. Knorr et al<sup>K5</sup> and Yelon et al<sup>Y2</sup> (using XD) report [111], [221] and [110] texture in Fe; Verderber<sup>V2</sup> (using XD) reports [111] and [311] texture in alloys from 50 to 82 per cent Ni; Adamsky<sup>A2</sup> (using XD and ED) reports [111] texture in Fe, permalloy and Ni; Smith<sup>C7</sup> (using RED) reports [110] texture in permalloy. Heidenreich<sup>H5</sup> suggests that RED is unreliable and that the apparent texture may be a surface effect due to an orientated oxide layer. It appears that texture, principally [111], may occur for Ni, permalloy and Fe. It is important to note that no reports of a [100] texture have been made. The most extensive texture reported occurs for Fe and involves some 50 per cent of the material. For Ni and permalloy a 20 per cent texture seems a more probable figure. Texture tends to form more readily for higher substrate temperatures ( $\geq 200^\circ\text{C}$ ) and for thicker films (though see Yelon et al<sup>Y2</sup>). For normally incident films the texture axis is found normal to the film plane (the accuracy of such a determination is probably  $\pm 2^\circ$ ), while for oblique incident films the texture axis lies in the

plane of incidence as shown in Fig. 3.21 and may be tilted up to approximately  $10^\circ$  toward the vapour source.

### 3.22 Oxide and Other Impurities

The existence of oxide in technical films deposited on glass is well established (films deposited in a "technical" vacuum of the order of  $10^{-5}$  mm of Hg). Reports of oxide have been made by numerous workers including Moore et al<sup>M5</sup> (permalloy films, TED); Prosen et al<sup>P6,P7,P8</sup> (NiO in Ni films, TED); Adamsky<sup>A2</sup> ( $\text{Fe}_2\text{O}_3$  in Fe films); Heidenreich et al<sup>H5</sup> (Fe, permalloy and perminvar films, RED) and Smith et al<sup>C7</sup> (permalloy films, RED). Heidenreich<sup>H5</sup> reports that the oxide has a preferential orientation with a [220] texture axis and moreover that no magnetic anisotropy is developed in films showing no presence of oxide. While the effect of oxygen on film anisotropy is important, it appears now that it is by no means necessary. Further, aware of Heidenreich's results, both Moore<sup>M5</sup> and Smith<sup>C7</sup> have investigated films which were anisotropic, but for which no preferential oxide orientation could be detected.

The importance of small quantities of other impurities is also firmly established. Prutton et al<sup>A4</sup> reported that the anisotropy of Ni-Fe films is extremely dependent on the

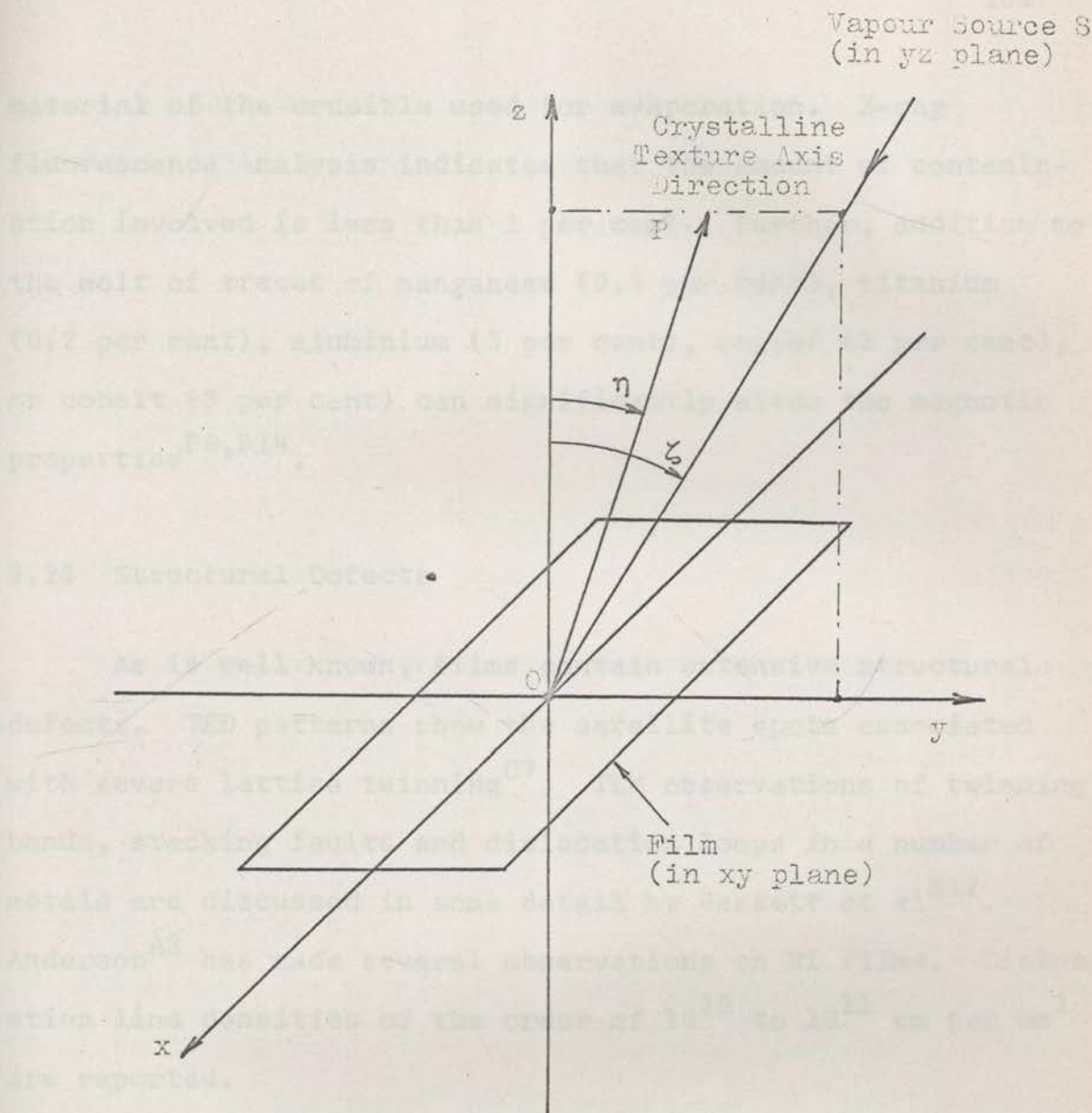


Fig. 3.21 Diagram Illustrating a Film Deposited at an Oblique Angle of Incidence of  $\zeta$

The direction  $OP$  of the crystalline texture axis is inclined at an angle  $\eta$  towards  $S$  and lies in the "plane of incidence" ( $yz$ ). Anisotropic mechanical stress will be taken as positive if the film is in tension along the  $x$ -axis. The magnetic anisotropy constant  $K$  will be taken as positive if the easy axis lies in the  $x$ -axis direction.



material of the crucible used for evaporation. X-ray fluorescence analysis indicates that the amount of contamination involved is less than 1 per cent. Further, addition to the melt of traces of manganese (0.5 per cent), titanium (0.2 per cent), aluminium (3 per cent), copper (3 per cent), or cobalt (3 per cent) can significantly alter the magnetic properties<sup>P9, B14</sup>.

### 3.23 Structural Defects

As is well known, films contain extensive structural defects. TED patterns show the satellite spots associated with severe lattice twinning<sup>C7</sup>. TEM observations of twinning bands, stacking faults and dislocation loops in a number of metals are discussed in some detail by Bassett et al<sup>B12</sup>. Anderson<sup>A3</sup> has made several observations on Ni films. Dislocation line densities of the order of  $10^{10}$  to  $10^{11}$  cm per  $\text{cm}^3$  are reported.

### 3.24 Chemical Inhomogeneity

Alloy films show considerable chemical inhomogeneity. Chu et al<sup>C6</sup> report for permalloy films variations in composition of up to 3 per cent at 0.001 in. intervals. Films of nominally zero average magneto-striction may be strain

sensitive on a microscopic scale. Further information on film inhomogeneity and stratification has been given by Hermitage et al<sup>H8</sup>.

### 3.3 MECHANICAL STRESS

#### 3.3.1 Causes of Stress

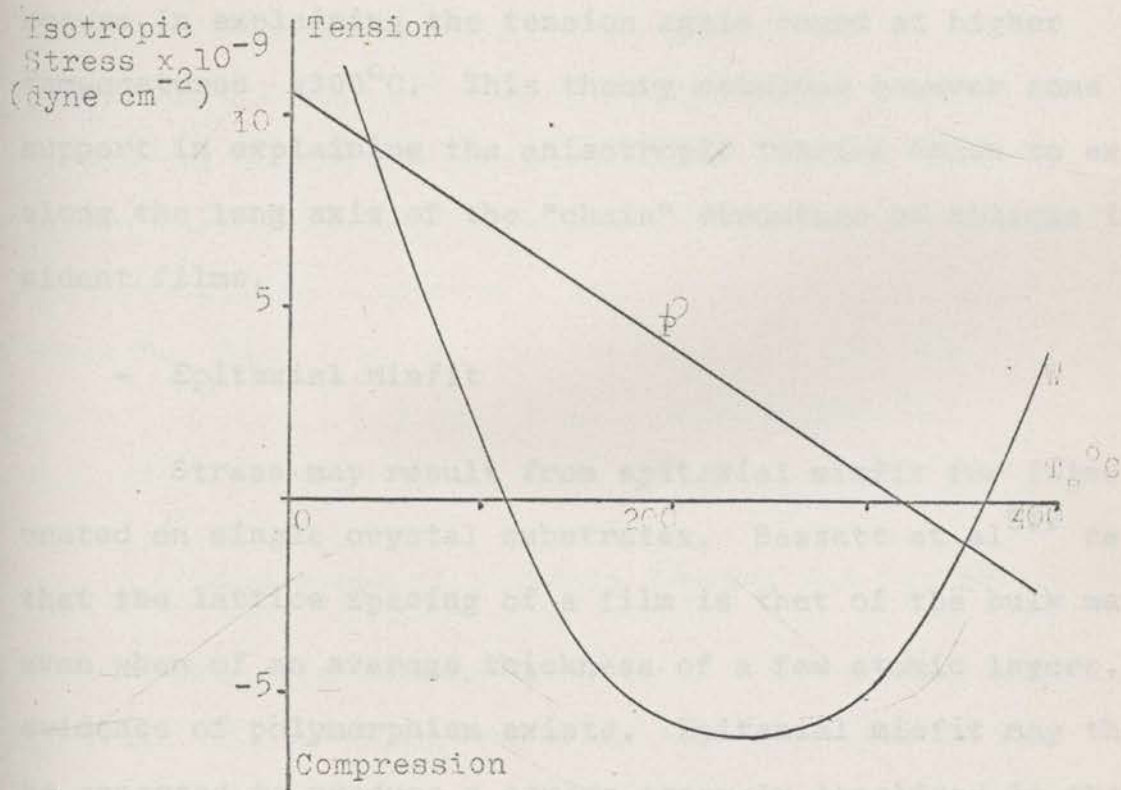
It is likely that stress in an evaporated film is the net result of a number of different contributing mechanisms.

#### - Differential Thermal Expansion between Film and Substrate

Stress may result from differential thermal expansion between the film and substrate as the former cools below the recrystallization temperature. Differential expansion was first proposed by Murbach et al<sup>M1</sup> to explain a correlation between stress and recrystallization temperature for evaporated films of a number of different metals. Support is given by the work of Freedman<sup>F6</sup> on Ni evaporated on single crystal NaCl, for which a reversible appearance and disappearance of wrinkles occurred on heating and cooling of a film partially relieved from the substrate. Such a reversible dependence of strain on temperature is consistent with a differential expansion model.

- Intrinsic Film Stress, Lattice Defects and Crystallite Surface Energies

Differential thermal expansion alone however does not provide a complete description. The magnitude of the stress in permalloy (81 per cent Ni, 19 per cent Fe) on soda glass, both of which have a coefficient of linear expansion of approximately  $1.2 \times 10^{-5} \text{ } ^\circ\text{C}^{-1}$ , cannot be explained. Nor is it consistent with the irreversible stress anneal behaviour in the temperature range  $100\text{-}300^\circ\text{C}$  observed in Ni films by Hoffman et al<sup>C1,H1,H2</sup>. Hoffman et al proposed instead a qualitative explanation in terms of the initial diffusion and aggregation of vacancies and their final coalescence into dislocation rings. Smith et al<sup>W5</sup> have measured stress as a function of evaporating rate and substrate temperature during deposition (see Fig. 3.31) and propose a different model based on crystallite surface energy. Smith suggests that at low temperatures tensile stress results from a tendency for neighbouring crystallites to coalesce to reduce surface energy. At temperatures of the order of  $200^\circ\text{C}$ , crystallite size is larger and a compressive stress may result from the surface tension of the individual crystallite. Smith<sup>S7</sup> has calculated that the surface energy involved is more than adequate to supply the elastic strain energy observed. Difficulty



Data:

Prutton <sup>P10</sup>; 81.2 per cent Fe; 800 to 1200  $\text{\AA}$ ; substrate glass;  $10^{-5}$  mm of Hg; deposition rate  $40 \text{ \AA sec}^{-1}$

Weiss and Smith <sup>W4</sup>; 83 per cent Ni; 17 per cent Fe in melt; 200 to 2000  $\text{\AA}$ ; substrate glass or mica;  $10^{-5}$  mm Hg; deposition rate  $4 \text{ \AA sec}^{-1}$

Fig. 3.31 The Variation of Stress in Permalloy Films with Substrate Temperature  $T_s$

occurs in explaining the tension again found at higher temperatures  $\geq 300^{\circ}\text{C}$ . This theory receives however some support in explaining the anisotropic tension known to exist along the long axis of the "chain" structure of oblique incident films.

#### - Epitaxial Misfit

Stress may result from epitaxial misfit for films evaporated on single crystal substrates. Bassett et al<sup>B12</sup> report that the lattice spacing of a film is that of the bulk material even when of an average thickness of a few atomic layers. No evidence of polymorphism exists. Epitaxial misfit may thus be expected to produce a stress strongly localized in the surface layer. The independence of stress on film thickness<sup>F14</sup> is an indication that this is not a significant mechanism in most cases.

### 3.32 Methods of Measuring Stress

#### Reported Experimental Data

Methods of measurement of film stresses can be divided into two classes:

#### - Measurement of Crystal Lattice Strain

For single crystal films the elastic strain can con-

veniently be found from a measurement of the lattice parameter by standard electron<sup>M4,P2</sup>, or X-ray<sup>F6</sup> diffraction techniques. Difficulty occurs for polycrystalline films. The X-ray diffraction method of Warren et al<sup>W2</sup> for determining rms strain and crystallite size from a Fourier analysis of line profiles fails for thin films as usually only one line can be measured. Techniques using a single line only<sup>S9</sup> suffer from considerable error<sup>S11</sup>.

- Measurement of Stresses Transmitted to the Substrate

The stress transmitted by a film to the substrate can be found by depositing the film on a thin elastic substrate and determining the resulting substrate curvature. The substrate may be a cantilever beam whose deflection is measured, or a plate whose curvature can be found by the optical Newton ring technique. The latter allows stress anisotropy to be also determined.

Stresses arising from differential expansion or epitaxial misfit may be expected to be transmitted to the substrate. For intrinsic stresses it is conceivable that significant stresses internal to the film will also be present. The changes in lattice parameter<sup>F6</sup> and in various magnetic properties<sup>S7,F6,Y1,H7</sup> on stripping films from their substrates are

consistent with the almost complete relief on any average stress component. Randomly orientated micro-stress centres most likely still remain.

Stresses in normally incident permalloy films have been measured by Smith et al<sup>W5</sup> (cantilever beam technique)\* and by Prutton<sup>P10</sup> (Newton ring technique), and for comparison have been replotted in Fig. 3.31. Both Smith and Prutton report a stress essentially independent of film thickness and of composition (near 81 per cent Ni, 10 per cent Fe), but dependent on substrate temperature and deposition rate. The different temperature dependence is unexplained. Prutton also finds any anisotropic stress component to be less than  $10^8$  dynes  $\text{cm}^{-2}$ .

Hoffman et al<sup>F4</sup> (Newton ring technique)\*\* have investigated obliquely deposited Fe films (substrate temperature  $75^\circ\text{C}$ , deposition rate  $\pm 60 \text{ \AA sec}^{-1}$ ) at angles of incidence  $\zeta$  up to  $36.5^\circ$ . Hoffman et al report an isotropic tension and an

---

\* Earlier work (by the Newton ring technique) of an inconclusive nature has been briefly reported in references H7, C7, S7.

\*\* A detailed account of the Newton ring technique is given. An earlier and less extensive investigation is reported in reference F2.

---

anisotropic tension, the latter approximately proportional to  $(1-\cos\zeta)$  and normal to the plane of incidence (along the x-axis in Fig. 3.21). A maximum stress occurs at a film thickness of  $700 \text{ \AA}$ . For a  $1000 \text{ \AA}$  film at  $\zeta = 36.5^\circ$ , isotropic and anisotropic stresses are  $6 \times 10^9$  and  $8 \times 10^8$  dynes  $\text{cm}^{-2}$  respectively. The accuracy of the results infers that any anisotropic stress existing in normally incident films is less than  $10^8$  dynes  $\text{cm}^{-2}$ .

Macdonald<sup>M2</sup> has reported an anisotropic stress of  $5 \times 10^8$  dynes  $\text{cm}^{-2}$  for Ni film deposited at normal incidence in a magnetic field. It is felt<sup>P10</sup>, in view of the failure by many workers to detect anisotropic stress of this magnitude in normally deposited films, that Macdonald's results may have been due to anisotropy of the single crystal mica substrates used. However, anisotropic stress  $< 10^8$  dynes  $\text{cm}^{-2}$  may well be present. The results of stripping of normally incident films<sup>Y1</sup> are suggestive.

Additional indirect evidence for film stress is provided by a number of magnetic measurements. Anomalous values have been reported for "out of the plane" film anisotropy<sup>F6,N6</sup> and for the crystalline anisotropy constant  $K_1$  of single crystal films<sup>F6,C8</sup>. A detailed analysis of these effects is given by Freedman<sup>F6</sup>. Again, an isotropic stress of the order of  $10^{10}$  dynes  $\text{cm}^{-2}$  is indicated.



### 3.4 SOME PROPERTIES OF Ni AND Fe FILMS.

#### PSEUDO-ROTATABLE AND ROTATABLE ANISOTROPIES

Both Ni and Fe films normally show a pseudo-rotatable anisotropy (PRA), in that the direction of the anisotropy can be rotated by saturating fields of the order of the anisotropy field itself. Thus for "initial" measurements\*, PRA films will appear to have a fixed uniaxial anisotropy. For saturated measurements, for example the measurement of saturated hysteresis loops, PRA films will appear isotropic in any direction.

Fig. 3.41 shows typical results of torque studies on PRA films. The magnitude of the  $\sin\gamma$  and  $\sin 2\gamma$  torque components and of the rotational hysteresis  $W_r$  is

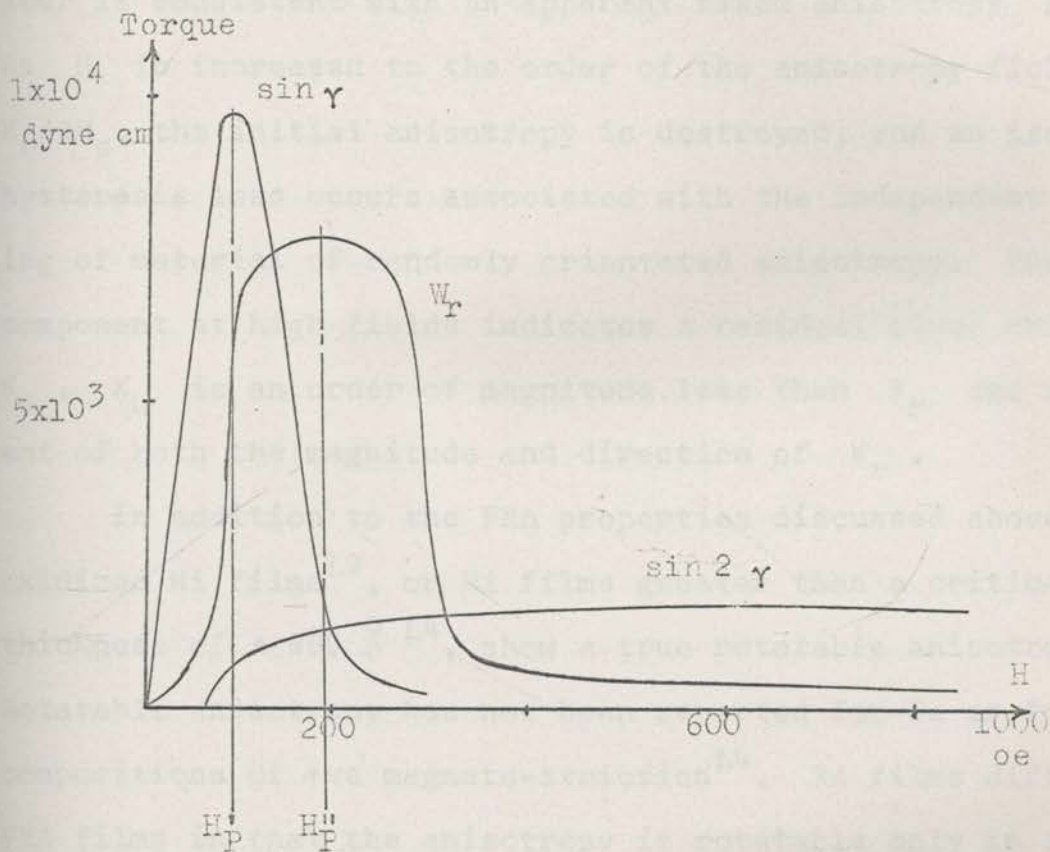
---

\* Examples of "initial" measurements are

- the direction of the remanent magnetization,
- the hysteresigraph initial susceptibility,
- the  $\sin\gamma$  component of low field torque curves.

All these properties are measured with small applied fields, and the term "rotatable initial susceptance" (RIS) is conveniently used to collectively describe them.

---



Data by Graham and Lommel<sup>G4</sup>.

Fig. 3.41 Torque Curves Illustrating Pseudo-rotatable Anisotropy.

plotted against the applied field  $H$ . The low field behaviour is consistent with an apparent fixed anisotropy  $K_r$ . As  $H$  is increased to the order of the anisotropy field  $K_r/2M_s$ , the initial anisotropy is destroyed, and an isotropic hysteresis loss occurs associated with the independent switching of material of randomly orientated anisotropy. The  $\sin 2\gamma$  component at high fields indicates a residual fixed anisotropy  $K_u$ .  $K_u$  is an order of magnitude less than  $K_r$  and independent of both the magnitude and direction of  $K_r$ .

In addition to the PRA properties discussed above, oxidized Ni films<sup>L3</sup>, or Ni films greater than a critical thickness of  $\approx 900 \text{ \AA}$ <sup>L4</sup>, show a true rotatable anisotropy (RA). Rotatable anisotropy has not been reported for Fe or for compositions of +ve magneto-striction<sup>L4</sup>. RA films differ from PRA films in that the anisotropy is rotatable only in fields of magnitude greater than the anisotropy field itself.\*

Torque curves show a  $\sin 2\gamma$  component corresponding to  $K_r$  before the anisotropy is destroyed. The curve of loss  $W_r$  against field  $H$  shows two peaks. The first is associated with normal irreversible switching of the film considered as having a fixed anisotropy  $K_r$ . The second is due to the

---

\* Differences in hysteresigraph behaviour for PRA and RA films have been discussed by Lehrer<sup>L1</sup>.

---

destruction of  $K_r$  and the increase of isotropic hysteresis. At high fields a residual fixed anisotropy  $K_u$  is found as before.

For PRA films  $K_r$  may be found from the hysteresigraph initial susceptance. Alternatively,  $K_r$  may be estimated using torque curve data from the field  $H'_p$  at which the  $\sin\gamma$  torque component is a maximum, or from the field  $H''_p$  at which the loss  $W_r$  is a maximum. It may be expected that  $H'_p \approx \frac{1}{2}H_{K_r}$ , while  $H''_p$  will be somewhat greater than  $\frac{1}{2}H_{K_r}$ . ( $H''_p = \frac{1}{2}H_K$  for a film obeying the CR model.  $H''_p$  is  $\approx \frac{1}{2}H_K$  for a non-ideal film with  $h_c \approx 1.0$ , respectively). For RA films,  $K_r$  may be estimated from the field  $H'_p$  at which the torque reaches 14, its maximum value, from the amplitude of the  $\sin 2\gamma$  curve corresponding to  $K_r$ , or from the field  $H''_p$  at the lower peak of the  $W_r$  curve. Data for Ni and Fe collected from various sources is given in Tables 3.42 and 3.43.

### 3.5 DIRECTIONAL ORDERING

In substitutional alloys of the Fe-Ni type, the average spatial distribution of the three possible bond types Fe-Fe, Ni-Ni, and Fe-Ni is normally isotropic. If, however, the bond energies are differently dependent on the angle between the bond and a reference direction established, for example by a

Table 3.42 DATA ON THE ANISOTROPY OF Ni FILMS

Substrate and Subst. Temp.	Pressure mm of Hg	Evap. Rate Å sec <sup>-1</sup>	Thick-ness Å	Quantity Measured *
Glass 240°C	10 <sup>-5</sup>	~	1000	<p><math>K_u</math> <math>3 \times 10^3</math> ergs cm<sup>-3</sup></p> <p><math>H_P''</math> 50 oe equivalent to <math>12 \times 10^3</math> ergs cm<sup>-3</sup> *</p> <p>The results quoted are from torque magnetometer measurements by Robinson<sup>R2</sup>. The films showed PRA properties.</p>
Glass 50°C	~	8	600 to 2500	<p><math>K_u</math> <math>3 \times 10^3</math> ergs cm<sup>-3</sup></p> <p><math>H_P''</math> 500 oe equivalent to <math>117 \times 10^3</math> ergs cm<sup>-3</sup>.</p> <p>The results quoted are from torque magnetometer measurements by Lehrer<sup>L4</sup>. The films showed RA properties.</p>
Glass 20°C	~	~	~	<p><math>K_u</math> <math>3 \times 10^3</math> ergs cm<sup>-3</sup></p> <p><math>H_P'</math> 50 oe equivalent to <math>11.7 \times 10^3</math> ergs cm<sup>-3</sup>.</p> <p>The results quoted are from torque magnetometer measurements by Graham and Lommel<sup>G4, G5</sup>.</p> <p>The films showed PRA properties with <math>H_P'</math> varying from 10 to 100 oe. The results given indicate that <math>H_P + 2H_P'</math>.</p>

Table 3.42 cont.

Substrate and Temp.	Pressure mm of Hg	Evap. Rate $\text{\AA} \text{ sec}^{-1}$	Thick-ness $\text{\AA}$	Quantity Measured*	
				$K_u$	$K_r$
Evaporated Molybdenum underlayer on glass	$10^{-5}$ or $10^{-10}$	~	~	$3.5 \times 10^3$ ergs $\text{cm}^{-3}$	$30 \times 10^3$ ergs $\text{cm}^{-3}$

The results quoted are from torque magnetometer measurements by Lommel and Graham<sup>L3</sup>. The films showed RA properties.  $K_u$  and  $K_i$  have been estimated from torque curves given for the applied fields  $H=750$  and  $2400$  oe, respectively.

NOTES:

- Definitions of  $K_r$ ,  $K_u$ ,  $H_p'$  and  $H_p''$  are given in the text of Section 3.4.
- If  $H_K$  is the normal anisotropy field obtained by extrapolating the initial hard axis hysteresis loop to saturation, then  $H_K = 2(K_r + K_u)/M + 2K_r/M_s$ .
- All anisotropy values quoted have been measured at room temperature.

\* Conversion has been made between anisotropy field values  $H$  and the "equivalent" anisotropy energy densities  $K$  using the formulae  $H = 2K/M_s$ , where the saturation magnetization  $M_s$  has the value 486 cgs units for Ni at  $20^\circ\text{C}$ .

Table 3.43 DATA ON THE ANISOTROPY OF Fe FILMS

Substrate and Subst. Temp.	Pressure mm of Hg	Evap. Rate Å sec <sup>-1</sup>	Thick-ness Å	Quantity Measured*
Glass	10 <sup>-5</sup>	~	600	$K_u$ 2.7x10 <sup>3</sup> ergs cm <sup>-3</sup> . $H_p'$ 19 oe equivalent to 16.3x10 <sup>3</sup> ergs cm <sup>-3</sup> * $H_p''$ 26 oe equivalent to 22.3x10 <sup>3</sup> ergs cm <sup>-3</sup> .

The results quoted are from torque magnetometer measurements by Takahashi<sup>T3</sup>. The films showed PRA properties.

Glass 75°C	10 <sup>-6</sup>	60	350	$K_u$ ~ $H_c$ 35 oe $K_r$ 30x10 <sup>3</sup> ergs cm <sup>-3</sup> .
---------------	------------------	----	-----	--

The results quoted are from hysteresisgraph measurements by Knorr and Hoffman<sup>K4</sup>. The films showed PRA properties. The value of  $K_r$  has been inferred from the BH curves given in Fig. 4 of reference K4.

Table 3.43 cont.

Substrate and Subst. Temp.	Pressure mm of Hg	Evap. Rate $\text{\AA sec}^{-1}$	Thick- ness $\text{\AA}$	Quantity Measured*
Glass	~	~	790	$K_u$ $1.5 \times 10^3$ ergs $\text{cm}^{-3}$

$H_c$  42 oe

The results quoted are from hysteresisgraph measurements by Vrambout and de Greve<sup>V3</sup> and are the averages of the values for film samples 1 to 11 of that reference. The films showed PRA properties.

NOTES:

- Definitions of  $K_r$ ,  $K_u$ ,  $H_P^I$  and  $H_P^{II}$  are given in the text of Section 3.4 .
- If  $H_K$  is the normal anisotropy field obtained by extrapolating the initial hard axis hysteresis loop to saturation, then  $H_K = 2(K_r + K_u)/M \div 2K_r/M$ .
- $H_c$  is the normal coercive force measured in the easy axis direction.
- All anisotropy values quoted have been measured at room temperature.

\* Conversion has been made between anisotropy field values  $H$  and the "equivalent" anisotropy energy densities  $K$  using the formulae  $H = 2K/M_s$ , where the saturation magnetization  $M_s$  has the value 1714 cgs units for Fe at 20°C.



magnetic field<sup>N4, T2, C2</sup>, or an applied stress<sup>Z1</sup>, a short range directional order or anisotropy will result. Further, in addition to the normal pair ordering of the substitutional alloy constituents, pair ordering of vacancies or of substitutional impurities will occur. These may be expected to contribute to the anisotropy in both alloys and pure metals. The effective number of possible pairs will be proportional to

$$nc_1^2 c_2^2 \text{ per unit volume,}$$

where  $n$  is the number of atoms per unit volume, and  $c_1, c_2$  are the fractional concentration of the relevant constituents.

Interstitial impurities or other defects which may singularly define a direction in space will also directionally order. In this case the effective number will be simply proportional to

$$nc \text{ per unit volume,}$$

where  $c$  is the fractional impurity concentration.

At any temperature  $T_A$ , the equilibrium spatial distribution of pairs or interstitials will be given by the Boltzmann function at that temperature. Since the ordering energies involved (of the order of  $10^{-15}$  to  $10^{-16}$  ergs) are small compared to the thermal energy ( $kT_A = 10^{-13}$  ergs at  $T_A = 450^\circ\text{C}$ ),

the effective number of aligned pairs or interstitials will be

$$\Delta n_{\infty} \propto n c_1^2 c_2^2 \cdot \frac{w(T_A)}{3kT_A} \quad \text{for substitutionals} \quad (3.51)$$

and

$$\Delta n_{\infty} \propto n c \cdot \frac{w(T_A)}{3kT_A} \quad \text{for interstitials,}$$

where  $w(T_A)$  is a measure of the ordering energy per pair or interstitial.

The approach to equilibrium with time  $t$  is given by

$$\Delta n = \Delta n_{\infty} (1 - \exp(-\frac{t}{\tau_A}))$$

where

$$\tau_A = A \exp \frac{T_0}{T_A},$$

$A$  is a constant, and

$T_0$  is a measure of the activation energy required for diffusion of the substitutionals, or interstitials, between the possible sites.

If a magnetic anneal is carried out at  $T_A$  for time  $t$  and the material cooled to temperature  $T$  such that the equilibrium distribution at  $T_A$  is quenched in, the anisotropy energy produced will be

$$K = K_{\infty} \left(1 - \exp\left(-\frac{t}{\tau_A}\right)\right) \quad (3.52)$$

where  $K_{\infty} = \Delta n_{\infty} w(T)$

$$\propto n c_1^2 c_2^2 \frac{w(T)w(T_A)}{3kT_A} \quad \text{for substitutionals}$$

and

$$K_{\infty} \propto n c \frac{w(T)w(T_A)}{3kT_A} \quad \text{for interstitials.}$$

### 3.51 Ordering in Bulk Materials

Directional ordering of the alloy constituents has been applied to bulk materials with some success. Neel<sup>N4</sup> and Taniguchi et al<sup>T2</sup> have predicted the angular dependence of the anisotropy in crystals in approximate agreement with experiment. Experimental data by Ferguson<sup>F1</sup> on Fe-Ni alloys is in good agreement, giving anisotropies of the correct magnitude (of the order of  $2 \times 10^3$  ergs  $\text{cm}^{-3}$ ) and a time constant  $\tau_A$  (independent of composition in the range 40-100 per cent Ni) of  $10^4$  secs. at  $T_A = 450^\circ\text{C}$ . Table 3.51 gives data on the anisotropy expected from various types of substitutional impurities<sup>P9, F5</sup>. Ordering of interstitial carbon<sup>N5, R1</sup> in iron has been well established and is the

Material	Atomic Radius A	Anisotropy <sub>-1</sub> ergs cm <sup>-1</sup>
Al	1.43	200
C	0.77	1300
Co	1.26	300
Cu	1.27	300
Fe	1.26	300
Mn	1.29	300
N	0.71	1600
O	0.60	2600
Si	1.18	350

Fig. 3.51 Induced Anisotropies for Various Substitutional Impurities in Iron

Data: Prutton<sup>P9</sup>.

cause of diffusion "after-effect". For carbon at room temperature the relaxation time is approximately 1sec, and the magnitude of the anisotropy at the solid solubility limit\* is  $\pm 10^2$  ergs  $\text{cm}^{-2}$ . It appears that carbon is hence unimportant in thin films (however, see Matcovich et al<sup>M6</sup>). Similar effects for nitrogen have been reported<sup>R1</sup>. Directional ordering of vacancies in pure Ni has been discussed by Seeger et al<sup>S6</sup> and Klein et al<sup>K6</sup>.

### 3.52 The Origin of the Ordering Interaction Energy

The origin of the interaction energy  $w$  is at present in some doubt. A useful review has been given by Rathenau<sup>R1</sup>. Both substitutionals and interstitials will produce some distortion of the normal lattice and hence an energy through magneto-strictive coupling with the resultant stress. In addition, the distribution of nearest neighbours at such points is no longer isotropic. An exchange energy contribution can then arise<sup>N4, B13</sup>. Néel has presented a simple classical phenomenological theory of crystalline anisotropy and magneto-striction which relates this exchange energy to

---

\* 0.01 per cent at room temperature. Carbon at concentrations above the solubility limit is not effective.

---

the magneto-striction constants,  $\lambda_{100}$ ,  $\lambda_{111}$ , and the elastic constants,  $C_{11}$ ,  $C_{12}$ ,  $C_{44}$ , of the material as

$$n\ell = \frac{1}{4}(2B_1 - B_2) = -\frac{3}{4}(\lambda_{100}(C_{11} - C_{12}) - \lambda_{111}C_{44}) \quad (3.53)$$

where

$\ell$  is the exchange energy per atom, and

$n$  is the number of atoms per unit volume.

Thus, in both cases an interaction energy proportional to the magneto-striction is predicted. Gross defects such as voids, dislocation planes and regions of impurity segregation, etc., will also have an interaction energy associated with them.

In principle, ordering will result at temperatures at which the mobility of the defect is sufficient for ordering to take place during the time of the anneal. Such defects will have, as before, a magneto-strictive and an exchange "surface" energy associated with them. They may also have a demagnetizing energy. The latter will be proportional to  $M_s^2$ . For Ni rich alloys the temperature variation of  $M_s^2$  is very similar to that of the magneto-striction, however, a distinction can be made by the compositional variation particularly in the permalloy region of zero magneto-striction.

### 3.6 ANISOTROPY IN NORMALLY INCIDENT FILMS

#### PREFERRED CRYSTALLINE ALIGNMENT AND ISOTROPIC STRESS

Uniaxial anisotropy can arise due to crystalline anisotropy if a preferential crystal alignment takes place. In addition, a further component will result from the now anisotropic magneto-strictive properties of the material and the large isotropic stress known to exist in thin films. It has been convincingly shown<sup>P4</sup> that crystalline texture axis formation gives an anisotropy both in the wrong direction and an order of magnitude too small to explain the anisotropy  $K$  of oblique incident films. It is, however, still possible on these grounds that crystal alignment may contribute to the smaller fixed anisotropy  $K_u$  of normally incident films, if we are prepared to assume that a weak texture structure is formed in the correct direction. While electron and X-ray diffraction evidence cast serious doubt on the existence of an inclined texture axis in normally incident films, the results of these studies have been somewhat contradictory (see Section 3.2). It is thus worthwhile to consider the predictions of such a mechanism more fully for the normally-incident case, and to show that it is in fact deficient on numerous other counts.

### 3.61 Calculation of the Anisotropy Produced by a Crystalline Texture Axis

The anisotropy due to a texture axis structure may be calculated from the phenomenological equation for the magnetic anisotropy energy of a cubic crystal as given by Kittel<sup>K2</sup>,

$$\begin{aligned}
 f = & K_1(\alpha_1^2\alpha_2^2 + \alpha_2^2\alpha_3^2 + \alpha_3^2\alpha_1^2) + K_2\alpha_1^2\alpha_2^2\alpha_3^2 \\
 & + B_1(\alpha_1^2e_{xx}^2 + \alpha_2^2e_{yy}^2 + \alpha_3^2e_{zz}^2) + B_2(\alpha_1\alpha_2e_{xy} + \alpha_2\alpha_3e_{yz} + \alpha_3\alpha_1e_{zx}) \\
 & + \frac{1}{2}C_{11}(e_{xx}^2 + e_{yy}^2 + e_{zz}^2) + \frac{1}{2}C_{44}(e_{xy}^2 + e_{yz}^2 + e_{zx}^2) \\
 & + C_{12}(e_{yy}e_{zz} + e_{zz}e_{xx} + e_{xx}e_{yy})
 \end{aligned} \tag{3.61}$$

where

$\alpha_1, \alpha_2, \alpha_3$  are the directional cosines of the magnetization vector  $\underline{M}$  with respect to the crystallographic [100] axes,

$e_{xx}, e_{yy}, e_{zz}, e_{yz}, e_{zx}, e_{xy}$  are the strain components relative to the same axes,

$K_1, K_2$  are the crystalline anisotropy constants,

$B_1 = -\frac{3}{2}\lambda_{100}(C_{11} - C_{12}), B_2 = -3\lambda_{111}C_{44}$  are the magneto-elastic coupling coefficients, and



$C_{11}, C_{12}, C_{44}$  are the elastic constants.

The energy is averaged over all possible crystal orientations by deriving an unstable coordinate transformation between the crystallographic [100] axes and axes (x,y,z) fixed to the plane of the film as in Fig. 3.21, such that an arbitrary rotation may be performed around the texture axes direction. For small angles of tilt  $\eta$  of the texture axis from the normal to the film, the anisotropy energy is closely of uniaxial  $K\sin^2$  form, where the anisotropy constant  $K$  is given by<sup>P4</sup>

$$\begin{aligned} K &= -A\sigma_x + B\sigma_y - C \\ &= -(\sigma_x + \sigma_y)(A-B) - (\sigma_x - \sigma_y)(A+B) - C \end{aligned} \quad (3.62)$$

where, referring to Fig. 3.21,

$\sigma_x, \sigma_y$  are the stress components in the plane of the film,

$A, B, C$  are constants depending on the angle  $\eta$

such that  $A-B$  and  $C$  are proportional to

$\sin^2 \eta$  and

$K$  is considered positive if the easy axis lies along the x-axis direction.

If magneto-striction may be neglected, the averaging procedure is very simple. Goodenough<sup>G3</sup> and Kittel<sup>K4</sup> have given explicit details of this calculation. Knorr and Hoffman<sup>K5</sup> have described the analysis for the more general case, where magneto-striction cannot be neglected. For a [111] texture axis a solution can only be obtained numerically, and Pugh et al<sup>P4</sup> have given curves of A, B and C as functions of  $\eta$  for Fe and Ni. For [hk0] texture an analytic solution has been obtained by Yelon et al<sup>Y2</sup>.

### 3.62 Anisotropies in Fe and Ni

#### Contradictions of the Texture Axis Theory with Experiment

Table 3.61 gives the anisotropy values, calculated from the data of references P4 and Y2, which may be expected for various texture axis structures, if the texture involves 20 per cent of the total material, is inclined at  $\eta=10^\circ$  to the normal, and the film is under an isotropic stress of  $10^{10}$  dynes  $\text{cm}^{-2}$ . In the case of pure Fe and Ni (see Tables 3.42 and 3.43), the predicted anisotropy is comparable to the fixed anisotropy  $K_u$ , but inadequate by an order of magnitude to explain the initial anisotropy  $K_r$ . In the case of permalloy the predicted anisotropy is too small by several

Table 3.61 ANISOTROPIES PRODUCED BY VARIOUS CRYSTALLINE TEXTURE AXIS STRUCTURES

Material	[111] Texture			[110] Texture			[100] Texture		
	Crystalline Component	Isotropic Stress Component	Total	Crystalline Component	Isotropic Stress Component	Total	Crystalline Component	Isotropic Stress Component	Total
	ergs $\text{cm}^{-3} \times 10^{-3}$			ergs $\text{cm}^{-3} \times 10^{-3}$			ergs $\text{cm}^{-3} \times 10^{-3}$		
Fe	-1.4	-3.4	-4.9	-0.60	+1.7	+1.1	+2.1	+4.9	-7.0
Ni	+0.14	+2.4	+2.5	+0.02	-2.4	-2.4	-0.19	-4.1	-4.3
Permalloy	+0.03	~	+0.03	+0.01	~	+0.01	-0.05	~	-0.05

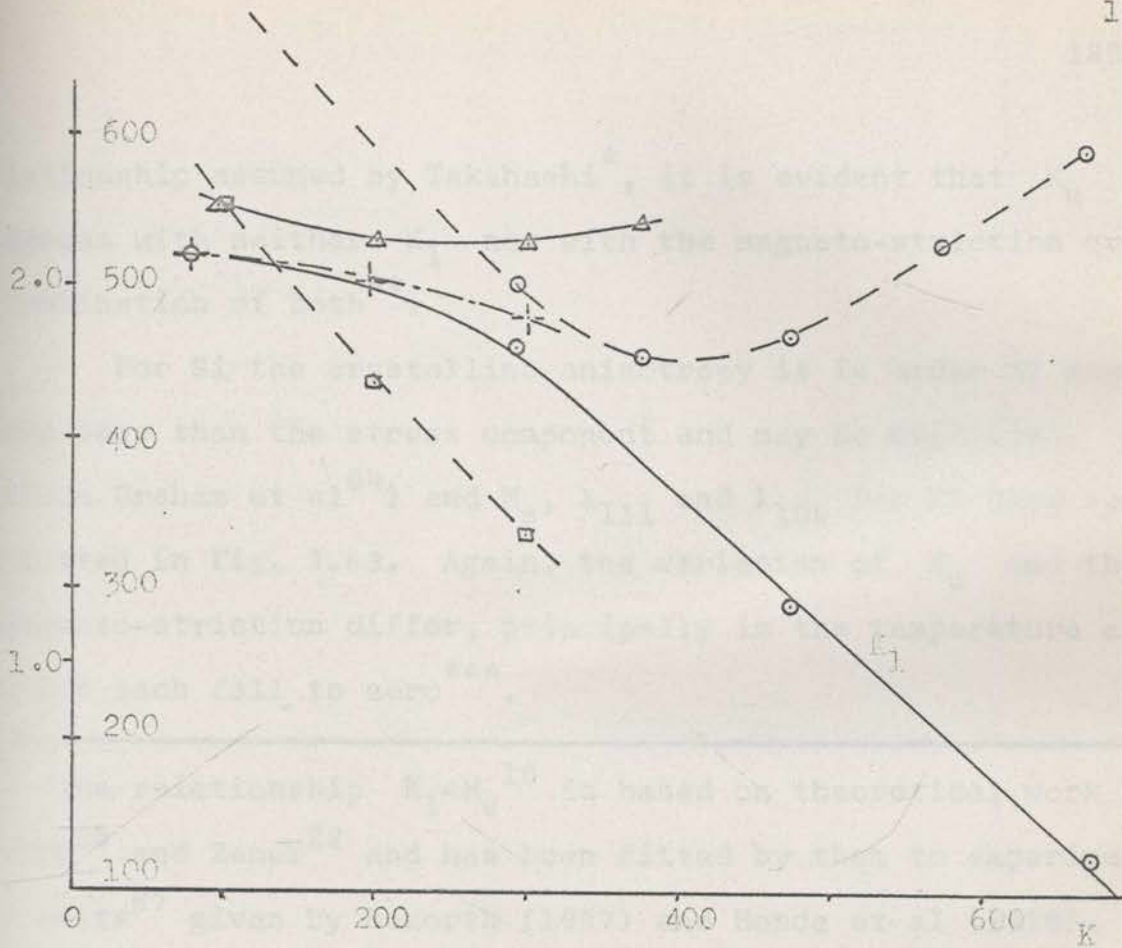
NOTES:

This Table gives the values of the anisotropies produced by various crystalline texture axis structures. It is assumed that the texture axis involves 20 per cent of the total film material, is inclined at  $10^0$  to the normal and that the film is under an isotropic tensile stress of  $10^{10}$  dynes  $\text{cm}^{-2}$ . The values of the constants  $K_1, K_2; \lambda_{100}, \lambda_{111}; C_{11}, C_{12}, C_{44}$  used are as given by Pugh et al<sup>P4</sup>. The anisotropy is denoted as +ve, if the easy axis lies in the direction normal to the plane of incidence containing the texture axis (see Fig. 3.21).

orders of magnitude to be of any significance. Various workers have reported no correlation between the amount of texture in a film and the observed anisotropy, but these observations have generally been made for oblique incident films. However, an explanation of  $K_u$  in Fe and Ni fails on several additional counts;

- Takahashi<sup>T3</sup> reports that  $K_u$  for Fe decreases with increasing substrate temperature during deposition, whereas the best texture is formed as the temperature increases. Similar measurements for Ni do not appear to have been made.

- Takahashi also reports that the temperature variation of the  $K_u$  for Fe does not agree with the temperature dependence of the bulk crystalline anisotropy constant  $K_1$  (the effect of  $K_2$  may be neglected). From Table 3.61, however, the principle contribution to  $K_u$  arises through the isotropic stress.  $K_u$  has been plotted against temperature (from Takahashi) in Fig. 3.62, together with the variation of  $M_s$ ,  $K_1$ ,  $\lambda_{111}$  and  $\lambda_{100}$  for bulk Fe. While recent determinations of  $K_1$  depart considerably from the  $K_1 \propto M_s^{10}$  re-



Data:  
 $\Delta-\Delta$   $K_u$ , Takahashi<sup>T3</sup>, 600Å, Glass,  $T_s$  20°C,  $10^{-5}$  mm of Hg  
 ---  $M_s/M_s(0)$ , Bozorth<sup>B11</sup>  
 —  $K_1, K_2$ , Bozorth<sup>B11</sup>, Graham<sup>G1</sup>, room temperatures values<sup>S4</sup>,  
 $K_1 = 450 \times 10^3 \text{ erg cm}^{-3}$   
 $\ominus$  ---  $\lambda_{110}, \lambda_{111}$ , Takaki<sup>T1</sup>, room temperature values<sup>H4</sup>  $\lambda_{100} = 20 \times 10^{-6}$   
 $\lambda_{111} = -16 \times 10^{-6}$

Fig. 3.62 The Variation of the Fixed Anisotropy  $K_u$  and the Constants  $M_s, K_1, \lambda_{111}, \lambda_{100}$  for Iron Films with the Temperature of Measurement.

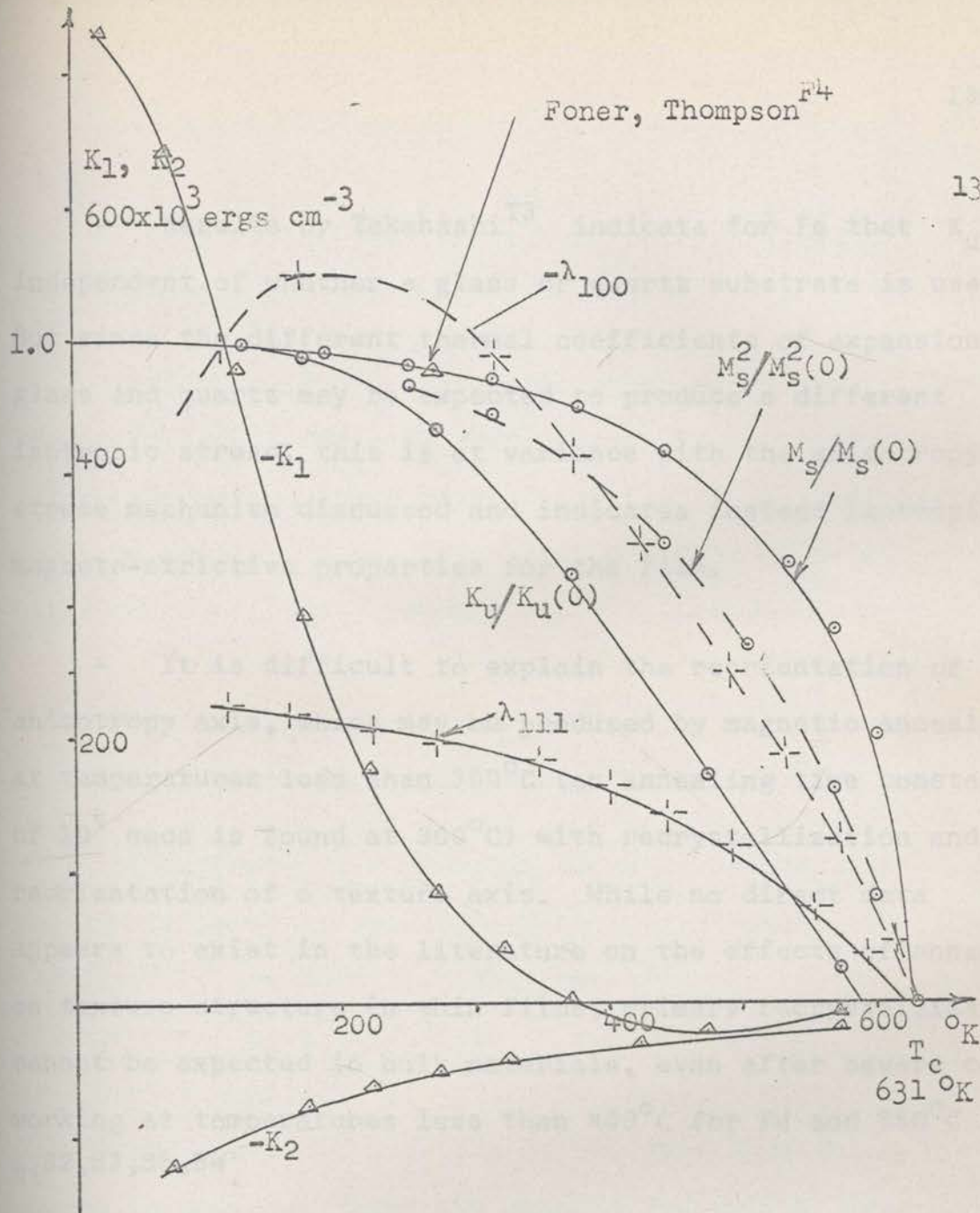
relationship assumed by Takahashi\*, it is evident that  $K_u$  agrees with neither  $K_1$  nor with the magneto-striction or a combination of both\*\*.

For Ni the crystalline anisotropy is in order of magnitude less than the stress component and may be neglected.  $K_u$  (from Graham et al<sup>G4</sup>) and  $M_s$ ,  $\lambda_{111}$  and  $\lambda_{100}$  for Ni have been plotted in Fig. 3.63. Again, the variation of  $K_u$  and the magneto-striction differ, principally in the temperature at which each fall to zero\*\*\*.

\* The relationship  $K_1 = M_s^{10}$  is based on theoretical work by Carr<sup>C5</sup> and Zener<sup>Z2</sup> and has been fitted by them to experimental results<sup>B7</sup> given by Bozorth (1937) and Honda et al (1928). More recent data indicates a  $M_s^5$  or  $M_s^4$  dependence<sup>B11, G1</sup>.

\*\* The exact temperature variation of the stress component can only be found by a calculation of the anisotropy as outlined in Section 3.61 for the values of the magneto-striction and elastic constants at each temperature for the particular crystallographic texture concerned. It is reasonable, however, for the present argument to assume an approximate variation as the magneto-striction constants themselves.

\*\*\* The temperature uncertainty in the data for  $K_u$  is estimated by Lemmel and Graham as  $10^\circ\text{C}$ .



Data:

$K_u/K_u(0)$  Gramham, Lommel<sup>G4</sup>, 300-400 Å, glass  $20^{\circ}C$ ,  $10^{-8}$  mm of Hg.

$M_s/M(0)$  Bozorth<sup>B11</sup>, Neugebauer<sup>N6</sup>

$K_1, K_2$ , Bozorth<sup>B8</sup>, room temperature values<sup>S4</sup>,  $K_1 = -45 \times 10^3 \text{ erg cm}^{-3}$ ,  $K_2 = 23 \times 10^3 \text{ erg cm}^{-3}$

$\lambda_{111}, \lambda_{100}$ , Corner, Hunt<sup>C3</sup>, room temperature values  
 $\lambda_{111} = -24 \times 10^{-6}$ ,  $\lambda_{100} = -58 \times 10^{-6}$

Fig. 3.63 The Temperature Dependence of the Fixed Anisotropy  $K_u$

- Results by Takahashi<sup>T3</sup> indicate for Fe that  $K_u$  is independent of whether a glass or quartz substrate is used. But since the different thermal coefficients of expansion of glass and quartz may be expected to produce a different isotropic stress, this is at variance with the anisotropy stress mechanism discussed and indicates instead isotropic magneto-strictive properties for the film.

- It is difficult to explain the reorientation of the anisotropy axis, which may be produced by magnetic annealing at temperatures less than  $300^{\circ}\text{C}$  (an annealing time constant of  $10^4$  secs is found at  $300^{\circ}\text{C}$ ) with recrystallization and reorientation of a texture axis. While no direct data appears to exist in the literature on the effects of anneal on texture structure in thin films, primary recrystallization cannot be expected in bulk materials, even after severe cold working at temperatures less than  $400^{\circ}\text{C}$  for Fe and  $550^{\circ}\text{C}$  for Ni<sup>S2,S3,S5,B4</sup>.



### 3.7 ANISOTROPY IN NORMALLY INCIDENT PERMALLOY FILMS.

#### DIRECTIONAL ORDERING

Permalloy films, evaporated under normal conditions, show a small non-rotatable anisotropy  $K_u$ . Since permalloy films have zero average magnetostriction,  $K_u$  may be expected to be solely due to directional ordering of either Fe-Ni pairs or impurities. Several observations may be made.

#### 3.71 Fixed Anisotropies and Anisotropies Rotatable by Low Temperature Magnetic Anneal

Directional pair ordering alone is inconsistent with the low temperature annealing behaviour of technical films. Segmüller<sup>S10</sup> reports that the temperature variation of the anisotropy of permalloy films is reversible up to 300°C, if no field is applied. If a field is applied along the hard direction, a gradual rotation of the easy axis into the new direction occurs. Segmüller reports relaxation times associated with this anneal as ranging from approximately 1 sec at 300°C (for a small irreversible anisotropy decrease which occurs immediately on applying the field) to a time constant of approximately  $10^4$  secs at 300°C associated with the main rotation. If repeated anneals are carried out

(provided the temperature is not excessively high); the rotatable anisotropy component is often found to decrease in magnitude<sup>T3</sup>. In addition, for alloys, a "memory" effect is observed in which, if annealed without a field, the anisotropy returns to the original easy direction<sup>L1, T3</sup>. The memory effect has been found not to occur for Fe<sup>T3</sup>, nor has it been reported for Ni. Low temperature anneal has been verified by numerous workers for permalloy<sup>M3</sup>, Fe<sup>T3</sup> and Ni<sup>G4</sup>.

These results have been explained by Takahashi<sup>T3</sup> in terms of two different anisotropy sources,

- An anisotropy  $K_{up}$  not rotatable by low temperature anneal

It is suggested that  $K_{up}$  is due to directional ordering of Fe-Ni pairs and provides the "memory" of the original easy direction.

- An anisotropy  $K_{ud}$  rotatable by low temperature anneal

It is suggested that  $K_{ud}$  is a combination of directional ordering of various types of defects such as dislocation, vacancies, substitutional or interstitial

impurity atoms which occur in high density in technical films. The decrease in  $K_{ud}$  after repeated anneals may be explained by a reduction of the number of imperfections. The results of Chu et al<sup>C6</sup> on the spread of  $K$  values for a number of technical permalloy films before and after anneal, suggest that  $K_{ud}$  is associated with much of the variability found in films. While the ordering energy of impurities will vary approximately as the magneto-striction, an exact zero energy at the zero magneto-striction composition can hardly be expected. The results of Chu<sup>C6</sup> on the chemical inhomogeneity found in permalloy films is also relevant.

Low temperature anneal is consistent with recovery and stress relief in bulk materials arising from diffusion of lattice imperfections. Stress annealing in Ni films has been reported by Hoffman et al<sup>H1</sup>. A minimum stress was found at 200°C. It is well known that the resistivity of evaporated films is a critically dependent function of the deposition conditions<sup>A1</sup>. The resistivity may be written

$$\rho = \rho_l + \rho_s + \rho_m + \rho_i \quad (3.71)$$

where

$\rho_l$  is due to scattering of the conduction electrons by thermal lattice vibrations,

$\rho_s$  is a surface scattering effect,

$\rho_m$  may arise from scattering at domain walls in a magnetic film, if a saturated reference state is not established, and

$\rho_d$  is due to scattering at lattice imperfections.

Thin films of all metals show irreversible decreases in  $\rho_d$  on annealing<sup>V1,W1</sup> ("island" formation may, however, occur for thinner films and higher temperatures). Hoffman et al.<sup>H1</sup> report such a decrease in the range 100-200°C for Ni films.

Considerable support of the above interpretation is given by the work of Methfessel et al.<sup>M7</sup> on permalloy films evaporated from a thorium oxide crucible at rates of 100 Å sec<sup>-1</sup> at 10<sup>-9</sup> mm of Hg onto quartz or artificial sapphire substrates precleaned by heating in vacuum to 900°C. Such films may be expected to be free from contamination due to the residual atmosphere, the substrate and the evaporation crucible. Such films do not show low temperature magnetic anneal. For higher temperature anneals (>400°C) the magnitude of the induced anisotropy and the relaxation times involved agree very well indeed with the data by Furgeson<sup>F1</sup> and others for Fe-Ni pair formation in bulk permalloy. The anneal data is similar to that reported by Segmüller<sup>S10</sup> for "recovered" films in which presumably the low temperature mechanisms have been annealed out by heating above 400°C.

### 3.72 The Variation of Anisotropy with Substrate Temperature

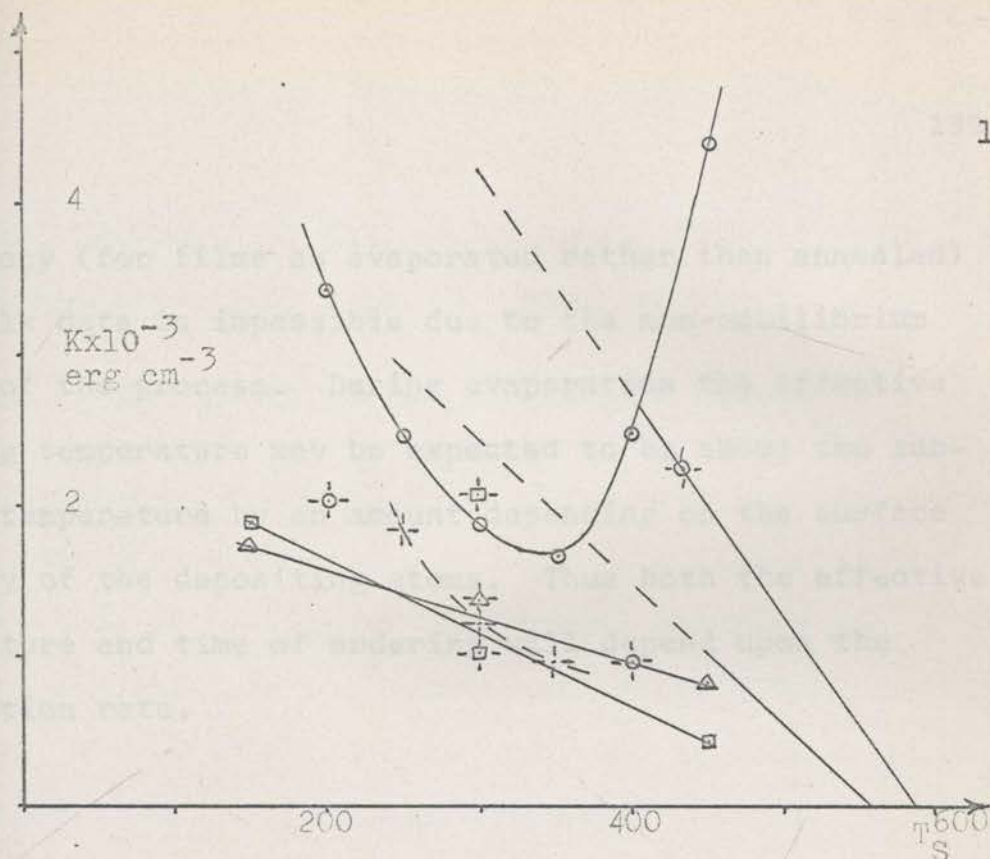
The variation of  $K=K_r+K_u$  with substrate temperature as reported by a number of workers is given in Fig. 3.71, together with bulk data for Fe-Ni pair anisotropy. The results of Prutton et al<sup>P3</sup> cannot be interpreted in terms of Fe-Ni pair ordering, and suggest a high density of imperfections or contamination by the vacuum or silica crucible used\*. Similar high values of  $K$  are reported for films showing low temperature anneal<sup>S10,C6</sup>. More recent results<sup>L2,01</sup> using tungsten sources show an entirely different temperature variation. The values of  $K$  are lower in magnitude and are not significantly different from those shown by films after low temperature anneal or from the values reported by Methfessel et al<sup>M7</sup> for evaporated UHV films. Less imperfection is suggested, and data on the anneal behaviour of these films would be interesting\*\*. A detailed prediction of the

---

\* Crucible contamination is indicated by the different variation of  $K$  with film composition for films evaporated from different crucible materials<sup>A4</sup>.

\*\* Such information does not appear to have been reported in the literature.

---



Data:

- Bradley, Prutton,<sup>P9</sup> 82 per cent Ni in melt, silica crucible, 1500 Å, glass,  $3 \times 10^{-4}$  mm of Hg,  $4 \text{ Å sec}^{-1}$
- Lemke, Morrison<sup>L2</sup>, 83 per cent wire, tungsten filament, 1500 Å, glass,  $10^{-6}$  mm of Hg,  $50 \text{ Å sec}^{-1}$
- △—△— Olmen<sup>O1</sup>, 85.9 per cent wire, tungsten ring source, 1100 Å, glass,  $< 10^{-5}$  mm of Hg,  $20 \text{ Å sec}^{-1}$ .
- Methfessel<sup>M7</sup>, 76 per cent Ni, thoria crucible, 3000 Å  $\text{sec}^{-1}$ , annealed at temperature shown
- Segmuller, 80 per cent Ni in Melt, 2000 Å, glass,  $300^{\circ}\text{C}$ ,  $10^{-5}$  mm of Hg,  $8 \text{ Å sec}^{-1}$
- △ Chu<sup>C6</sup> 75 per cent Ni, glass, annealed  $300^{\circ}\text{C}$
- Ferguson<sup>F1</sup> Bulk anneal data.

Fig. 3.71 The Variation of  $K = K_u + K_r$  with substrate Temperature  $T_s$

anisotropy (for films as evaporated rather than annealed) from bulk data is impossible due to the non-equilibrium nature of the process. During evaporation the effective ordering temperature may be expected to be above the substrate temperature by an amount depending on the surface mobility of the depositing atoms. Thus both the effective temperature and time of ordering will depend upon the evaporation rate.

The stress magnetostriction theory was originally proposed for bulk alloys by Benarath<sup>21</sup>. For polycrystalline material magnetically annealed at temperature  $T_A$ , magnetostrictive strain produces local stresses which are removed by plastic flow. On cooling to a lower temperature  $T$ , the local strains are frozen in, resulting in a mean anisotropic stress in the demagnetized state of  $\frac{1}{2}Y(T)\epsilon(T)$ , where  $Y(T)$  is Young's modulus at temperature  $T$ . A uniaxial magnetic anisotropy is produced of magnitude

$$K(T) = \frac{1}{2}Y(T)\epsilon(T) \quad (3.83)$$

In bulk material several objections arise including the anisotropy found in unconstrained single crystals, the lack of

### 3.8 THE DEPENDENCE OF THE NON-ROTATABLE ANISOTROPY $K_u$ OF NORMALLY INCIDENT FILMS ON COMPOSITION.

#### DIRECTIONAL ORDERING AND ANISOTROPIC STRESS

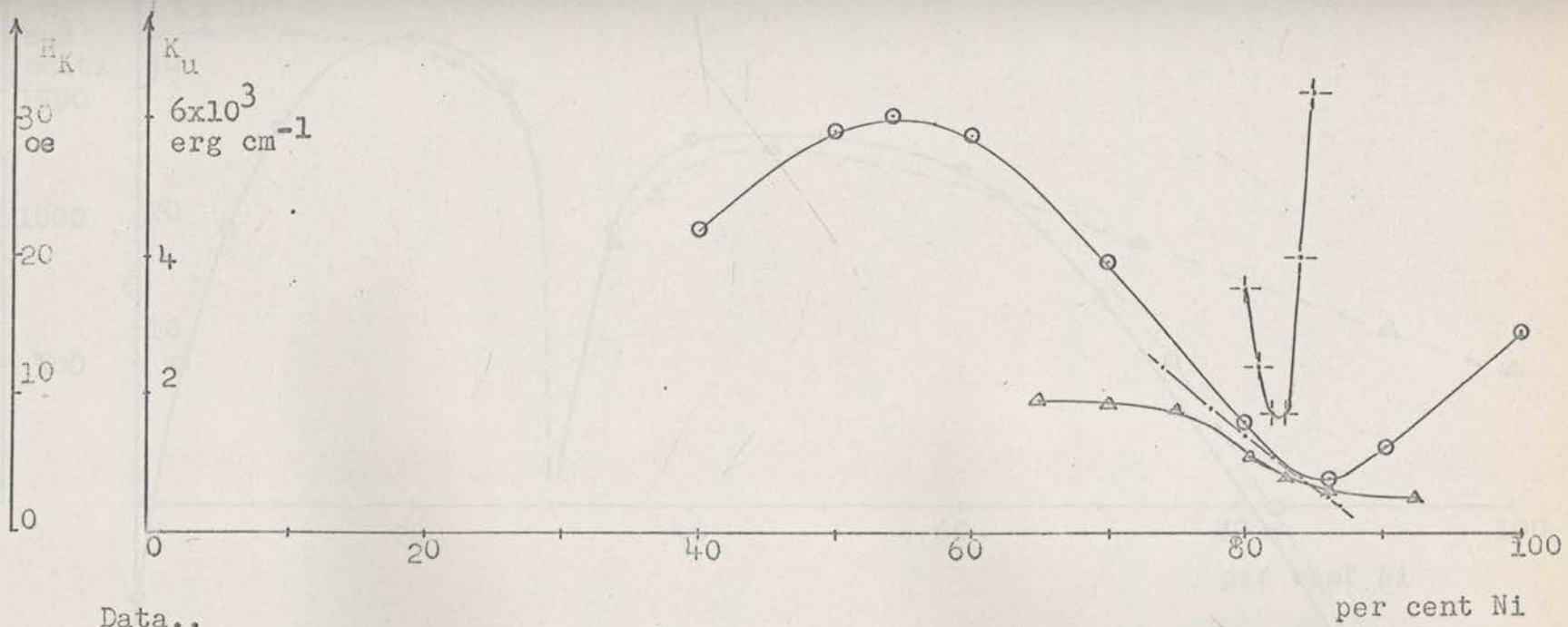
A number of workers<sup>R2,P3,01</sup> have explained the variation of the non-rotatable anisotropy  $K_u$  with film composition as a combination of Fe-Ni pair directional ordering and of stress anisotropy coupled to the magneto-striction. Typical reported data for  $K_u$  is shown in Fig. 3.81 and for comparison the compositional variation of the magneto-striction and saturation magnetization is included in Fig. 3.82.

The stress magneto-striction theory was originally proposed for bulk alloys by Bozorth<sup>B1</sup>. For polycrystalline material magnetically annealed at temperature  $T_A$ , magneto-strictive strain produces local stresses which are removed by plastic flow. On cooling to a lower temperature  $T$ , the local strains are frozen in, resulting in a mean anisotropic stress in the demagnetized state of  $\lambda(T_A)Y(T)$ , where  $Y(T)$  is Young's modulus at temperature  $T$ . A uniaxial magnetic anisotropy is produced of magnitude

$$K(T) = \frac{3}{2}Y(T)\lambda(T)\lambda(T_A) \quad (3.81)$$

In bulk material several objections arise including the anisotropy found in unconstrained single crystals, the lack of





- Data..
- $K_u$  Robinson <sup>R2</sup>, 1000 Å, substrate glass at  $T_s$  240°C,  $10^{-5}$  mm of Hg
  - $H_{Kr}$  Smith <sup>S3</sup>, 1200 Å,  $T$  250°C
  - |— Prutton and Bradley <sup>SP3</sup>, 1500 Å,  $T_s$  300°C
  - △— Olmen <sup>O1</sup>, 1200 Å,  $T_s$  300°C

Fig. 3.71 The Variation of  $K_u$  and the Total Anisotropy Field  $H_K$  with Composition

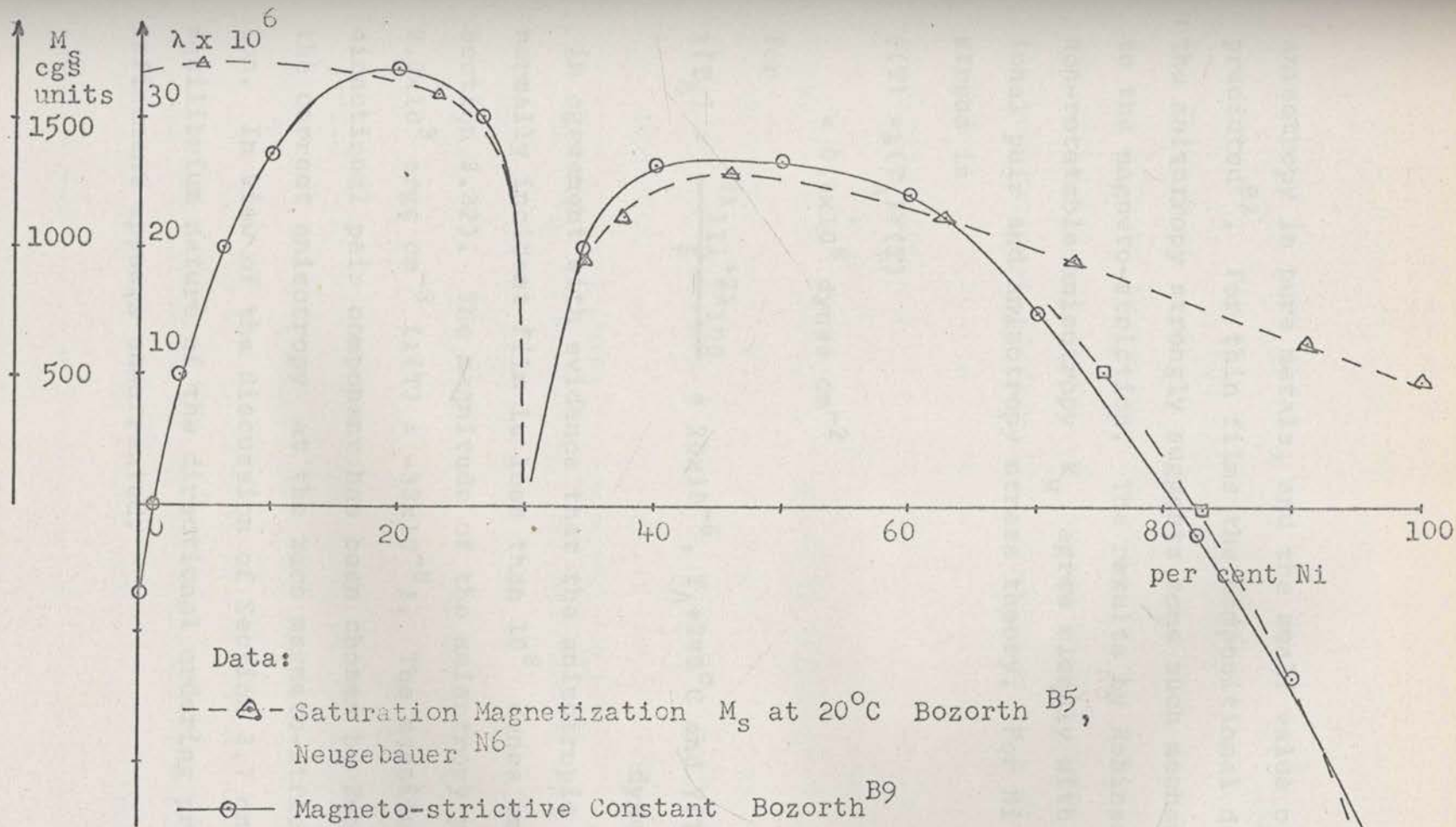


Fig.3.82 Compositional Variation of the Saturation Magnetization and the Magnetostriction

□/

anisotropy in pure metals, and the small value of anisotropy predicted<sup>B3</sup>. For thin films the compositional dependence of the anisotropy strongly suggests some such mechanism coupled to the magneto-striction. The results by Robinson for the non-rotatable anisotropy  $K_u$  agree closely with the directional pair and anisotropy stress theory. For Ni the anisotropy stress is

$$\begin{aligned}\sigma(T) &= \lambda(T_A) Y(T) \\ &= 0.4 \times 10^8 \text{ dynes cm}^{-2}\end{aligned}$$

for

$$\lambda(T_A) = \frac{3\lambda_{111} + 2\lambda_{100}}{5} = 20 \times 10^{-6}, \quad T_A = 240^\circ\text{C} \text{ and } Y(T) = 2 \times 10^{12} \text{ dynes cm}^{-2},$$

in agreement with evidence that the anisotropic stress in normally incident film is less than  $10^8$  dynes  $\text{cm}^{-2}$  (see Section 3.32). The magnitude of the anisotropy predicted is  $2.0 \times 10^3$  ergs  $\text{cm}^{-3}$  ( $\lambda(T) = -33 \times 10^{-6}$ ). The magnitude of the directional pair component has been chosen by Robinson to give the correct anisotropy at the zero magneto-strictive composition. In view of the discussion of Section 3.7 on the non-equilibrium nature of the directional ordering process further refinement appears unwarranted.

### 3.81 An Interpretation of Anisotropic Stress in Terms of Directional Ordering of Imperfections

It is of importance to consider whether the anisotropic stress postulated above arises solely from elastic strain or whether there exists a wider interpretation. Such an interpretation is possible in terms of directional ordering of impurities and imperfections as discussed in Section 3.5. If the ordering energy is due to either magneto-striction or exchange<sup>\*</sup>, then writing  $w(T) = \lambda(T)$  in equation (3.52), the resultant expression for  $K$  is identical in form to that of equation (3.81). The results by Prutton et al on crucible contamination<sup>A4</sup> and the effects of trace additives to the

---

\* Voids, and inclusions may be expected to have also a contribution to the ordering energy due to demagnetizing energy. (The voids may be uniformly or randomly elongated). For Ni, voids involving only 1 per cent of the total material, if uniformly elongated by 20 per cent, fully aligned and non-interacting, will produce an anisotropy of  $2.2 \times 10^3$  ergs  $\text{cm}^{-3}$ . However, in view of the incorrect compositional variation predicted, the influence of any such mechanism is in serious doubt (compare  $K_u$ , Fig. 3.81 and  $M_s$ , Fig. 3.82).

---

mechanisms have been suggested including

melt<sup>P9</sup> clearly indicate the importance of impurities. Further, they indicate that the effect of any given impurity is approximately proportional to the magneto-striction, in agreement with the above.

All mechanisms contributing to the apparent or equivalent anisotropic stress will thus have the same temperature and compositional variation. A separation may be expected on the basis of the relaxation time or times involved in magnetic anneal. Considerable work is at the moment proceeding to determine accurately the relaxation time spectrum by dynamic annealing in alternating fields<sup>S12, S13</sup>. It might be noted that the anneal behaviour of Ni films reported by Graham et al<sup>G4</sup> suggests at least two mechanisms (both of the order of  $1.5 \times 10^3$  ergs  $\text{cm}^{-3}$ ). The relation of work by Graham et al<sup>G4</sup> on Ni films to that of Methfessel et al<sup>M7</sup> (Section 3.71) on permalloy is not clear. In the former case it is possible that anisotropy may be due to structural defects or to substrate or crucible contamination.

### 3.82 The Effects of Oxygen

Finally, mention should be made of the confused situation with regard to the importance of oxygen. Various mechanisms have been suggested including

- ferromagnetic-antiferromagnetic exchange with oxide inclusions or surface layers<sup>P6,L3</sup>. The persistence of  $K_u$  for Ni (Fig. 3.62) at temperatures above the anti-ferromagnetic Néel point for NiO ( $+520^\circ\text{K}$ , reference B6) casts considerable doubt on this mechanism.

- surface exchange across ferromagnetic non-magnetic interfaces due to condensed oxygen fault planes<sup>H6,B13</sup>.

- stresses resulting from oxide inclusions or surface layers<sup>P6,L3</sup>, or from intergranular diffusion of oxygen in a preferred pattern<sup>P7</sup>.

A brief review and a calculation of the anisotropy energies produced by the above mechanisms has been given by Prutton<sup>P9</sup>. The significance of oxygen in produced Ni<sup>L3</sup> and permalloy<sup>P6</sup> films with rotatable anisotropy is extremely provoking.

### 3.9 PSEUDO-ROTATABLE ANISOTROPY IN NORMALLY INCIDENT FILMS.

#### RANDOM ANISOTROPY CENTRES

In Section 3.8 an explanation of the non-rotatable anisotropy  $K_u$  was given in terms of Fe-Ni pair directional ordering and an equivalent anisotropic stress due to elastic

strain or imperfection ordering. Attempts have been made at various times<sup>P3, S8</sup> to explain the total anisotropy  $K=K_r+K_u$  (both non-rotatable and rotatable components) on a similar basis. Such a theory encounters severe difficulties both in suggesting an origin for the stress<sup>S8</sup> and in the magnitude of the stress required. For Ni,  $K=20 \times 10^3$  ergs  $\text{cm}^{-3}$  requires a stress of  $4 \times 10^8$  dynes  $\text{cm}^{-2}$ . Anisotropic stresses of this magnitude are not found in normally incident films (see Section 3.32). Further the relaxation time\* associated with the rotation of the anisotropy and the independence of this time on temperature\*\* does not indicate a diffusion process (as would be involved in reorientating any structural ani-

\* Smith and others<sup>H7</sup> report that if a saturating alternating field is suddenly applied and the hysteresis loop of the film measured, relaxation effects occur which indicate that rotation of the anisotropy takes place in a few cycles of the applied field. Matcovich<sup>M6</sup> et al report relaxation times of the order of 10 milli-secs.

\*\* Posen et al<sup>P6</sup> report that the relaxation time for RA perm-alloy films is independent of temperature from 77°K to room temperature.

sotropy of the film). Rather a model based on a magnetic interaction is suggested.

It seems most likely that pseudo-rotatable anisotropy should be explained on the basis of an isotropic distribution of small centres of high uniaxial anisotropy. After saturation in any direction, a pseudo-anisotropy is established by the magnetization relaxing symmetrically about that direction into a minimum energy configuration in which the magnetization at any point tends to be in the direction of the local easy axis. Similar PRA behaviour occurs in bulk material of high anisotropy and in the field of fine particle magnets, where a large amount of work has been done<sup>P1,K4,J1,J2,S1</sup>

Several points may be noted:

- A discussion of various mechanisms causing random anisotropy centres has been given by Cohen<sup>C10</sup>. The compositional (Fig. 3.81) and temperature\* dependence of  $K_r$  indicate an "equivalent stress" mechanism as discussed in Section 3.81. Either elastic strain or ferromagnetic to non-magnetic surface anisotropy may be important. No difficulty now exists to postulating simple elastic strain centres, for as these are random, no anisotropy stress results. The isotropic stress

---

\* Found for example by measuring the temperature dependence of the rotational hysteresis loss<sup>C10,R2</sup>.

---



found in films is of sufficient magnitude to provide the anisotropy centres found (for Ni,  $\lambda = -34 \times 10^{-6}$ , a stress of  $10^{10}$  dynes  $\text{cm}^{-2}$  gives an anisotropy  $K$  of  $51 \times 10^3$  ergs  $\text{cm}^{-3}$ ).

- For a two-dimensional isotropic distribution of non-interacting uniaxial particles it is readily shown (see Section 5.61) that

$$m_r = \frac{2}{\pi} = 0.64$$

and

$$K_r = \frac{2}{\left(\frac{1}{K}\right)} \quad (3.91)$$

where

- $m_r$  is the fractional remanent magnetization,
- $K_r$  is the pseudo-rotatable anisotropy, and
- $K$  is the anisotropy of the film at any point.

Experimental values of  $m_r$  reported by Robinson<sup>R2</sup> agree well with the predicted value 0.64 for alloys >90 per cent Ni. For alloys <80 per cent Ni, however, a random cubic anisotropy is indicated. The high remanence PRA films reported by Cohen<sup>C10</sup> cannot be explained for non-interacting particles.

- If interaction takes place between the anisotropy centres, variation of the magnetization into the local easy axis directions will be suppressed. The remanent magnetization will be increased and the anisotropy and coercive force

decreased. Interaction may be magnetostatic or more likely (in view of the wavelength of the magnetization ripple seen by Lorentz electron microscope, see Section 2.4) due to exchange. From equation 2.418 of Section 2.4 exchange may be expected to average anisotropy variations below a critical size or wavelength  $\lambda_A$ . Thus, as a rough approximation,

$$m_r = 1 - \frac{0.36}{1 + \frac{\lambda_A^2}{\lambda^2}}$$

and

$$K_r = \frac{2}{\left(\frac{1}{K}\right) \left(1 + \frac{\lambda_A^2}{\lambda^2}\right)} \quad (3.92)$$

where

$$\lambda_A = 2\pi \left(\frac{A}{K}\right)^{\frac{1}{2}}, \quad A = 2 \times 10^{-6} \text{ ergs cm}^{-1}, \text{ and}$$

$\lambda$  is a measure of the scale of the anisotropy dispersion.

For Ni the value of  $m_r = 0.65$  indicates that the independent particle model may be reasonably valid in this case. For  $K_r = 20 \times 10^3 \text{ ergs cm}^{-3}$ , anisotropy centres of  $K = 40 \times 10^3 \text{ ergs cm}^{-3}$  and of size  $\lambda > \lambda_A = 4000 \text{ \AA}$  are indicated. High remanence PRA films<sup>C10</sup> can perhaps result, if the anisotropy dispersion

is on a sufficiently fine scale. For example, if again  $K=40 \times 10^3$  ergs  $\text{cm}^{-3}$ , but  $\lambda=2000 \text{ \AA}$ , then  $m_r=0.93$  and  $K_r=4 \times 10^3$  ergs  $\text{cm}^{-3}$ .

- Bulk materials or fine particle magnets do not appear to show the rotatable anisotropy properties (as distinct from PRA) found in certain films. No explanation of rotatable anisotropy can be given at the present time. The progressive change from PRA to RA behaviour reported by Cohen<sup>C10</sup> suggests that no new mechanism is involved. Results by Lehrer<sup>L4</sup> again emphasize a compositional variation similar to the magnetostriction. No explanation has yet been produced, but it is suggested that RA may be associated with twisting of the magnetization out of the plane of the film<sup>H7</sup>. The existence of a critical thickness and the fact that RA behaviour is found only in -ve magneto-strictive compositions\* (permalloy films may show RA behaviour if subject to special treatment or preparation) is suggestive of such a model.

### 3.10 ANISOTROPY IN OBLIQUE INCIDENT FILMS

A large anisotropy arises in films evaporated at oblique angles of incidence  $\zeta$ . Data on the compositional variation

---

\* Isotropic tension for -ve magneto-contraction will produce an easy axis perpendicular to the film plane.

of  $K(\zeta)$  for  $\zeta=34^\circ$  is given in Fig. 3.(10)1. Smith<sup>S7</sup> has determined the variation of  $K(\zeta)$  with angle  $\zeta$  for perm-alloy, and his results are well fitted by the relation  $K(\zeta) \propto \sin^{2.5} \zeta$  (which has been used to correct Smith's results for  $\zeta=45^\circ$  to  $\zeta=34^\circ$  in Fig. 3.(10)1). In addition,  $K(\zeta)$  depends on evaporation rate and decreases rapidly as substrate temperature is increased<sup>P4</sup>.

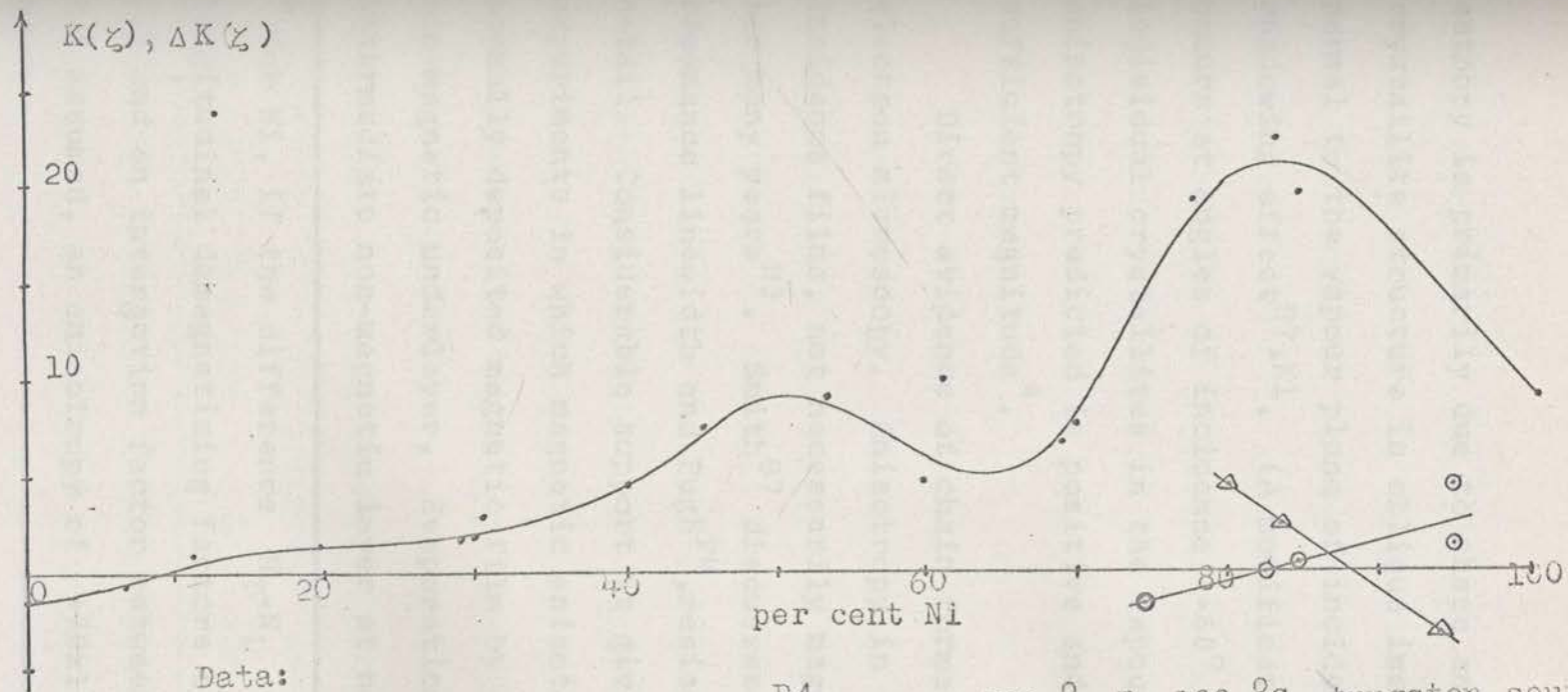
Various models have been suggested:

### 3.(10)1 Crystalline Texture

The formation of a crystalline texture axis has been discussed in Section 3.6. Again, the anisotropy predicted is an order of magnitude too small and increases rather than decreases with substrate temperature. Moreover, as discussed in detail by Pugh et al<sup>P4</sup>, the anisotropy for any of the textures  $[111]$ ,  $[110]$ ,  $[211]$ , etc. is of the wrong sign for both Fe and Ni films (the anisotropy is taken as +ve if the easy axis is normal to the plane of the incident vapour as in Fig.3.21). Only for a  $[100]$  texture is the correct direction predicted, and this texture has never been reported (see Section 3.21).

### 3.(10)2 The Formation of an Anisotropic Crystallite Chain Structure and Anisotropic Stress

It is generally accepted that angle of incidence ani-



Data:

- $K(z)$  , Push et al.<sup>P4</sup>, approx. 700 Å,  $T_s$  100 °C, tungsten source.
  - ▲  $K(z)$  Smith et al.<sup>S7</sup>, approx. 700 Å,  $T_s$  200 °C , also
  - $\Delta K(z)$  , change in  $K(z)$  on stripping,
- all data at  $z = 34^\circ$ .

Fig. 3.(10)1 The Compositional Variation of the Oblique Angle of Incidence Anisotropy  $K(z)$  for  $z = 34^\circ$ .

sotropy is primarily due to shape anisotropy of the chain crystallite structure in oblique incident films produced normal to the vapour plane of incidence by a geometrical self-shadowing effect<sup>S7,K1</sup>. (A modification of the shape anisotropy occurs at angles of incidence  $>60^\circ$  due to elongation of the individual crystallites in the vapour direction<sup>C9</sup>). The anisotropy predicted is positive and appears to be of sufficient magnitude\*.

Direct evidence of chain formation has been obtained by electron microscopy. Anisotropy in the properties of oblique incidence films, not necessarily magnetic, have been observed for many years<sup>H3</sup>. Smith<sup>S7</sup> discusses optical dichroism and resonance linewidth and Pugh<sup>P4</sup>, resistive anisotropy, in some detail. Considerable support is given by magnetic replica experiments in which magnetic anisotropy is transmitted to a normally deposited magnetic film by an obliquely deposited non-magnetic underlayer. Evaporation over a sufficient intermediate non-magnetic layer at normal incidence causes

---

\* For Ni, if the difference  $N_T - N_L$  of the traverse and longitudinal demagnetizing factors of the chains be taken as 0.5 and an interaction factor between neighbouring chains of 0.1 assumed, an anisotropy of  $+70 \times 10^3$  ergs  $\text{cm}^{-3}$  is predicted.

---

the correspondence to be lost.

The change in sign of  $K(\zeta)$  (Fig. 3.(10)1) at the 90 per cent Ni composition results from magnetostriction and the anisotropy tensile stress found normal to the deposition plane in oblique incident films (shape anisotropy alone cannot explain such a change in sign). The anisotropy, calculated from reported values of anisotropic stress (see Section 3.3) again appears to be of the correct magnitude\*\*.

If the simple assumption is made that the shape and stress anisotropies are independent of composition, the compositional variation of  $K(\zeta)$  predicted by the shape and stress anisotropy model is in fair qualitative agreement with experiment over the whole range 0 to 100 per cent Ni. Resistivity data by Pugh<sup>P4</sup> may suggest that the geometric anisotropy is also composition dependent. In this case even better agreement is possible, but there is as yet insufficient evidence to support a more detailed estimate along these lines. Collaborating evidence is provided by the change in  $K$  found by Smith on stripping a number of films (compositional range 75-95 per cent Ni) from their substrates. These

---

\*\* For Ni,  $\lambda = -34 \times 10^{-6}$ , assuming an anisotropy stress of  $7 \times 10^8$  dynes  $\text{cm}^{-2}$  at  $\zeta = 34^\circ$ , an anisotropy of  $-35 \times 10^3$  ergs  $\text{cm}^{-3}$  is predicted.

---

results have been plotted in Fig. 3.(10)1 and show a remarkable similarity to the variation of the magnetostriction. On the other hand, others<sup>P4,H5</sup> have found no correlation in anisotropy change on stripping. No explanation of this contradiction can be given, but nevertheless the stress mechanism appears most likely correct. Finally, the anneal behaviour of oblique incident films<sup>W4</sup> is well explained by the above model.

- Single Crystal Nickel Films,  
Trans. Eighth Vacuum Symposium, American Vacuum Soc.,  
p. 939, (1961).
- 40 Astwood, D., Frutton, N.,  
"The Influence of Crucible Material Upon the Magnetic  
Anisotropy of Evaporated Ferralloy Films",  
Brit. J. Appl. Phys., 34, 48, (1963).
- 41 Bosworth, R.M.,  
"Theory of the Heat Treatment of Magnetic Materials",  
Phys. Rev., 48, 232, (1934).
- 42 Becker, R., Döring, W.,  
"Ferromagnetismus",  
Julius Springer, Berlin, p. 411, (1939).
- 43 Becker, R., Döring, W.,  
"Ferromagnetismus",  
Julius Springer, Berlin, p. 416, (1939).
- 44 Bosworth, R.M.,  
"Ferromagnetism",  
D. Van Nostrand Company Inc., New York, p. 43, (1951).
- 45 Bosworth, R.M.,  
"Ferromagnetism",  
D. Van Nostrand Company Inc., New York, p. 105, (1951).
- 46 Bosworth, R.M.,  
"Ferromagnetism",  
D. Van Nostrand Company Inc., New York, p. 470, (1951).



## 3.11 LIST OF REFERENCES

- A1 Alderson, R.H., Ashworth, F.,  
"Vacuum Deposited Films of Nickel-Chromium Alloy".  
Brit.J.Appl.Phys., 8, 205, (1957).
- A2 Adamsky, R.F.,  
"Preferred Orientation and Ordering in Evaporated Films  
of Fe, Ni and Fe-Ni".  
J.Appl.Phys., (Suppl.), 31, 289S, (1960).
- A3 Anderson, J.C.,  
"Preparation and Magnetic Anisotropy of Continuous  
Single Crystal Nickel Films".  
Trans. Eighth Vacuum Symposium, American Vacuum Soc.,  
p.930, (1961).
- A4 Astwood, D., Prutton, M.,  
"The Influence of Crucible Material Upon the Magnetic  
Anisotropy of Evaporated Permalloy Films".  
Brit.J.Appl.Phys., 14, 48, (1963).
- B1 Bozorth, R.M.,  
"Theory of the Heat Treatment of Magnetic Materials".  
Phys.Rev., 46, 232, (1934).
- B2 Becker, R., Döring, W.,  
"Ferromagnetismus".  
Julius Springer, Berlin, p.411, (1939).
- B3 Becker, R., Döring, W.,  
"Ferromagnetismus".  
Julius Springer, Berlin, p. 418, (1939).
- B4 Bozorth, R.M.,  
"Ferromagnetism".  
D. Van Nostrand Company Inc., New York, p.43, (1951).
- B5 Bozorth, R.M.,  
"Ferromagnetism".  
D. Van Nostrand Company Inc., New York, p.109, (1951).
- B6 Bozorth, R.M.,  
"Ferromagnetism".  
D. Van Nostrand Company Inc., New York, p.470, (1951).

- B7 Bozorth, R.M.,  
"Ferromagnetism".  
D. Van Nostrand Company Inc., New York, p.568, (1951).
- B8 Bozorth, R.M.,  
"Ferromagnetism".  
D. Van Nostrand Company Inc., New York, p.569, (1951).
- B9 Bozorth, R.M.,  
"Ferromagnetism".  
D. Van Nostrand Company Inc., New York, p.667, (1951).
- B10 Bozorth, R.M.,  
"Review of Magnet Annealing".  
Proc.Second Conference on Magnetism and Magnetic  
Materials, Boston, p.69, (1956).
- B11 Bozorth, R.M.,  
"Magnetic Properties of Materials".  
American Institute of Physics Handbook, p.5-164, (1957).
- B12 Bassett, G.A., Mentor, J.W., Pashley, D.W.,  
"The Nucleation, Growth and Microstructure of Thin Films".  
Proc.International Conference on the Structure and  
Properties of Thin Films, Lake George, p.11, (1959).
- B13 Bean, C.P.,  
"Aspects of the Ferromagnetism of Thin Films".  
Proc.International Conference on the Structure and  
Properties of Thin Films, Lake George, p.331, (1959).
- B14 Bradley, E.M.,  
"Properties of Magnetic Films for Memory Systems".  
J.Appl.Phys., (Suppl.), 33, 1051S, (1962).
- C1 Crittenden, E.C., Jr., Hoffman, R.W.,  
"Determination of Stress in Evaporated Metal Films".  
Phys.Rev., 78, 349, (1950).
- C2 Chikazumi, S., Oomura, T.,  
"On the Origin of Magnetic Anisotropy Induced by  
Magnetic Annealing".  
J.Phys.Soc.of Japan, 10, 842, (1955).

- C3 Corner, W.D., Hunt, G.H.,  
"Temperature Dependence of Magnetostriction in Nickel  
Crystal".  
Proc.Phys.Soc., London, 68A, 133, (1955).
- C4 Chikazumi, S.,  
"Review on Magnetic Annealing Effect".  
Japan Butsuri Gakkai-Shi., 11, 92, (1956).
- C5 Carr, W.J.,  
"Temperature Dependence of Ferromagnetic Anisotropy".  
J.Appl.Phys., 29, 436, (1958).
- C6 Chu, W.W.L., Wolfe, J.E., Wagner, B.C.,  
"Some Observations on Evaporated Permalloy Films".  
J.Appl.Phys., (Suppl.), 30, 272S, (1959).
- C7 Cohen, M.S., Huber, E.E., Weiss, G.P., Smith, D.O.,  
"Investigations into the Origin of Anisotropy in  
Oblique-Incidence Films".  
J.Appl.Phys., (Suppl.), 31, 291S, (1960).
- C8 Chikazumi, S.,  
"Epitaxial Growth and Magnetic Properties of Single-  
Crystal Films of Iron, Nickel and Permalloy".  
J.Appl.Phys., (Suppl.), 32, 81S, (1961).
- C9 Cohen, M.S.,  
"Anisotropy in Permalloy Films Evaporated at Grazing  
Incidence".  
J.Appl.Phys., (Suppl.), 32, 87S, (1961).
- C10 Cohen, M.S.,  
"Anomalous Magnetic Films".  
J.Appl.Phys., (Suppl.), 33, 2968, (1962).
- E1 Evans, D.M., Wilman, H.,  
"Crystal Growth and Orientation in Deposits Condensed  
from the Vapour".  
Acta., Cryst., 5, 731, (1952).
- F1 Ferguson, E.T.,  
"Uniaxial Magnetic Anisotropy Induced in Fe-Ni  
Alloys by Magnetic Anneal".  
J.Appl.Phys., 29, 252, (1958).

- F2 Finegan, J.D., Hoffman, R.W.,  
"Stress Anisotropy in Evaporated Iron Films",  
J.Appl.Phys., 30, 597, (1959).
- F3 Foner, S., Thompson, E.D.,  
"Test of Spin Wave Theory with Precision Magnetisation  
Measurements".  
J.Appl.Phys., (Suppl.), 30, 229S, (1959).
- F4 Finegan, J.D., Hoffman, R.W.,  
"Stress and Stress Anisotropy in Iron Films".  
Trans.Eighth Vacuum Symposium, American Vacuum Soc.,  
p.935, (1961).
- F5 Ferrer, A., Mazzetti, P., Montalenti, G.,  
"Experiments on Magnetic Viscosity due to Different  
Solute Atom Pairs in Iron Alloys".  
Il Nuovo Cimento, 23, 280, (1962).
- F6 Freedman, J.F.,  
"Residual Stress in Single-Crystal Nickel Films".  
IBM J.Res.Developm., 6, 449, (1962).
- G1 Graham, C.D.,  
"Magnetocrystalline Anisotropy Constants of Iron at  
Room Temperature and Below".  
Phys.Rev.112,1117, (1958).
- G2 Graham, C.D.,  
"Magnetic Annealing".  
"Magnet Properties of Metals and Alloys",  
American Soc. of Metals, Cleveland, p.288, (1959).
- G3 Goodenough, J.B., Smith, D.O.,  
"Magnetic Properties of Thin Films".  
"Magnetic Properties of Metals and Alloys".  
American Soc. of Metals, Cleveland, p.337, (1959).
- G4 Graham, C.D., Lommel, J.M.,  
"Effect of Pressure During Evaporation on Magnetic  
Properties of Nickel Films".  
Proc.International Conference on Magnetism and  
Crystallography, Kyoto, p.570, (1961).

- G5 Graham, C.D., Lommell, J.M.,  
"Magnetic Anisotropies of Nickel Films Evaporated and  
Measured at  $10^{-8}$  mm Hg and Below".  
J.Appl.Phys., (Suppl.), 32, 83S, (1961).
- H1 Hoffman, R.W., Anders, F.J., Crittenden, E.C., Jr.,  
"Evidence of Collapse of Lattice Vacancy Aggregates  
to Form Dislocation Rings".  
J.Appl.Phys., 24, 231, (1953).
- H2 Hoffman, R.W., Daniels, R.D., Crittenden, E.C., Jr.,  
"The Cause of Stress in Evaporated Metal Films".  
Proc.Phys.Soc. (London), B67, 497, (1954).
- H3 Holland, L.,  
"Vacuum Deposition of Thin Films".  
Chapman and Hall Ltd., London, p.330, (1956).
- H4 Hall, R.C.,  
"Single Crystal Anisotropy and Magnetostriction Con-  
stants of Several Ferromagnetic Material Including  
Alloys of NiFe, SiFe, AiFe, CoNi and CoFe".  
J.Appl.Phys., 30, 816, (1959).
- H5 Heidenreich, R.D., Reynolds, F.W.,  
"Uniaxial Magnetic Anisotropy and Microstructure of  
Ferromagnetic Metal Films".  
Proc.International Conference on the Structure and  
Properties of Thin Films, Lake George, p.402, (1959).
- H6 Heidenreich, R.D., Nesbitt, E.A., Burbank, R.D.,  
"Magnetic Annealing in Perminvar".  
J.Appl.Phys., 30, 995, (1959).
- H7 Huber, E.E., Smith, D.O.,  
"Properties of Permalloy Films having a Magneto-  
elastic Easy Axis Normal to the Film".  
J.Appl.Phys., (Suppl.), 30, 267S, (1959).
- H8 Hermitage, R.J., Young, N.S.,  
"Compositional Studies of Evaporated Ni-Fe Layers".  
British J.Appl.Phys., 14, 439, (1963).

- H9 Hodges, J.A.,  
"The Influence of Crucible Material on the Induced Anisotropy of Evaporated Iron Films".  
Brit.J.Appl.Phys., 14, 340, (1963).
- J1 Jacobs, J.S., Bean, C.P.,  
"An Approach to Elongated Fine Particle Magnets".  
Phys.Rev., 100, 1060, (1955).
- J2 Jacobs, J.S., Luborsky, F.E.,  
"Magnetic Anisotropy and Rotational Hysteresis in Elongated Fine Particle Magnets".  
J.Appl.Phys., 28, 467, (1957).
- K1 König, H., Helwig, G.,  
"The Structure of Obliquely Evaporated Films and Their Influence on the Formation of Sub-microscopic Surface Irregularities".  
Optik, 6, 111, (1950).
- K2 Kittel, C.,  
"Physical Theory of Ferromagnetic Domains".  
Rev.Mod.Phys., 21, 541, (1949).
- K3 Katayama, T.,  
"On the Temperature Dependence of the Magnetostrictive Constants of Iron".  
Science Rept., Research Institute of Tokôhu University, 3A, 341, (1951).
- K4 Kittel, C., Galt, J.K.,  
"Ferromagnetic Domain Theory".  
Solid State Physics, Academic Press Inc., New York, V 3, p. 439, (1956).
- K5 Knorr, T.G., Hoffman, R.W.,  
"Dependence of Geometric Magnetic Anisotropy in Thin Iron Films".  
Phys.Rev., 113, 1039, (1959).
- K6 Klein, M.V., Kronmuller, H.,  
"Contribution of Divacancies to Magnetic After Effects in Nickel".  
J.Appl.Phys., 33, 2191, (1962).

- L1 Lehrer, S.S.,  
"Magnetic Annealing".  
Quarterly Res.Rept.on Solid State Research, Lincoln  
Lab., Massachusetts Institute of Technology, p.69,  
(July, 1961).
- L2 Lemke, J.S., Morrison, R.D.,  
"The Influence of Deposition Temperatures on Magnetic  
Parameters of Permalloy Thin Films".  
Res.Rept. PX 2308, Remington Rand Univac.
- L3 Lommel, J.M., Graham, C.D.,  
"Rotatable Anisotropy in Composite Films".  
J.Appl.Phys., (Suppl.), 33, 1160, (1962).
- L4 Lehrer, S.S.,  
"Rotatable Anisotropy in Negative Magnetostriction  
Ni-Fe Films".  
J.Appl.Phys., (Suppl.), 34, 1207, (1963).
- M1 Murbach, H.P., Wilman, H.,  
"The Origin of Stress in Metal Layers Condensed from  
the Vapour in High Vacuum".  
Proc.Phys.Soc., London, B66, 905, (1953).
- M2 Macdonald, J.R.,  
"Stress in Evaporated Ferromagnetic Films".  
Phys.Rev., 106, 890, (1957).
- M3 Mitchell, E.N.,  
"Effects of Heat Treatment on Thin Ferromagnetic Films  
at Intermediate Temperatures".  
J.Appl.Phys., 29, 286, (1958).
- M4 Menter, J.W., Pashley, D.W.,  
"The Microstructure and Mechanical Properties of Thin  
Films".  
Proc.International Conference on the Structure and  
Properties of Thin Films, Lake George, p.111, (1959).
- M5 Moore, A.C., Young, A.S.,  
"Some Physical Properties of Thin Magnetic Films".  
J.Appl.Phys., (Suppl.), 31, 279S, (1960).

- M6 Matcovich, T., Korostoff, E., Schmeckenbecher, A.,  
 "Anisotropy Rotation in Thin Permalloy Films at  
 Room Temperature".  
 J.Appl.Phys., (Suppl.), 32, 93S, (1961).
- M7 Methfessel, S., Segmuller, A., Sommerhalder, R.,  
 "Magnetic Properties of Thin Films Evaporated in  
 Ultrahigh Vacuum".  
 Proc.International Conference on Magnetism and  
 Crystallography, Kyoto, p. 575, (1961).
- N1 Néel, L.,  
 "Surface Anisotropy of Ferromagnetic Materials".  
 Comptes Rendus, 237, 1468, (1953).
- N2 Néel, L.,  
 "Oriented Superstructures (Directional Order)".  
 Comptes Rendus, 237, 1613, (1953).
- N3 Néel, L.,  
 "Oriented Superstructures (Directional Order) Resulting  
 from Mechanical Deformation".  
 Comptes Rendus, 238, 305, (1954).
- N4 Néel, L.,  
 "Magnetic Surface Anisotropy and Oriented Superstructures  
 (Directional Order)".  
 J.de Physique et le Radium, 15, 225, (1954).
- N5 Néel, L.,  
 "Directional Order and Diffusion Aftereffect".  
 J.Appl.Phys., (Suppl.), 30, 3S, (1959).
- N6 Neugebauer, C.A.,  
 "The Saturation Magnetisation of Nickel Films of  
 Thickness less than 100 Å".  
 Proc.International Conference on the Structure and  
 Properties of Thin Films, Lake George, p.358, (1959).
- O1 Olmen, R.W.,  
 "The Characteristics of Nickel-Iron Films Deposited  
 in an Orientating Field using a Tungsten Ring Source".  
 Res.Rept.PX 2308, Remington Rand, Attachment 11, (1962).
- "Stress and Magnetic Anisotropy in Thin Permalloy Films".  
 Nature, 193, 505, (1962).



- P1 Paine, T.O.,  
"Magnetic Properties of Fine Particles".  
"Magnetic Properties of Metals and Alloys".  
American Soc.of Metals, Clevelend, 146, (1959).
- P2 Pashley, D.W.,  
"The Observation of Dislocations in Thin Single Crystal  
Films of Gold Prepared by Evaporation".  
Phil.Mag., 4, 324, (1959).
- P3 Prutton, M., Bradley, E.M.,  
"The Induced Magnetic Anisotropy in Evaporated Films  
of Nickel-Iron Alloys".  
Proc.Phys.Soc., London, 75, 557, (1960).
- P4 Pugh, E.W., Boyd, E.L., Freedman, J.F.,  
"Angle of Incidence Anisotropy in Evaporated Nickel-  
Iron Films".  
IBM J.Res.Developm., 4, 163, (1960).
- P5 Pugh, E.W., Matisoo, J., Speliotis, D.E., Boyd, E.L.,  
"Magnetic Anisotropy in Evaporated Iron Films".  
J.Appl.Phys., (Suppl.), 31, 293S, (1960).
- P6 Prosen, R.J., Holmen, J.O., Gran, B.E.,  
"Rotatable Anisotropy in Thin Permalloy Films".  
J.Appl.Phys., (Suppl.), 32, 91S, (1961).
- P7 Prosen, R.J., Holmen, J.O., Gran, B.E., Cebulla, T.J.,  
"Influence of Minor Constituents in Ferromagnetic Films",  
Proc.International Conference on Magnetism and  
Crystallography, Kyoto, p. 580, (1961).
- P8 Prosen, R.J., Holmen, J.O., Gran, B.E., Cebulla, T.J.,  
"Stratification in Thin Permalloy Films".  
J.Appl.Phys., 33, 1150, (1962).
- P9 Prutton, M.,  
"Structure and Anisotropy in Magnetic Films".  
Trans.Ninth Vacuum Symposium, American Vacuum Soc.,  
p.59, (1962).
- P10 Prutton, M.,  
"Stress and Magnetic Anisotropy in Thin Permalloy Films".  
Nature, 193, 565, (1962).

- R1 Rathenau, G.W.,  
"Time Effects in Magnetisation".  
"Magnetic Properties of Metals and Alloys".  
American Soc. of Metals, Cleveland, p. 168, (1959).
- R2 Robinson, G.,  
"Anisotropy in Polycrystalline Nickel-Iron Thin Films  
in the Compositional Range 40-100 per cent Nickel".  
Proc. International Conference on Magnetism and  
Crystallography, Kyoto, p. 558, (1961).
- S1 Stoner, E.C., Wohlfarth, E.P.,  
"A Mechanism of Magnetic Hysteresis in Heterogeneous  
Alloys".  
Phil. Trans. Royal Soc., (London), A240, 599, (1948).
- S2 Smoluchowski, R., Turner, R.W.,  
"Influence of Magnetic Field on Recrystallisation".  
J. Appl. Phys., 20, 745, (1949).
- S3 Smoluchowski, R., Turner, R.W.,  
"Continuous Pole Figure Studies of Magnetic Recrystallisation".  
Physica, 16, 397, (1950).
- S4 Sato, H., Chandrasekhar, B.S.,  
"Determination of the Magnetic Anisotropy Constant  $K_2$   
of Cubic Ferromagnetic Substances".  
The Phys. and Chem. of Solids, 1, 228, (1957).
- S5 Sawyer, B., Smoluchowski, R.,  
"Magnetic Influence on the Recrystallised Grain  
Texture of a Ferromagnetic Alloy".  
J. Appl. Phys., 28, 1069, (1957).
- S6 Seeger, A., Schiller, P., Kronmüller, H.,  
"Observation of Interstitial Atoms in F.C.C. Metals".  
Phil. Mag., 5, 853, (1960).
- S7 Smith, D.O., Cohen, M.S., Weiss, G.P.,  
"Oblique-Incidence Anisotropy in Evaporated Permalloy  
Films".  
J. Appl. Phys., 31, 1755, (1960).

- S8 Smith, D.O.,  
"A Model for M Induced Anisotropy in Fe-Ni Films".  
Quarterly Res. Rept. on Solid State Research, Lincoln  
Lab., Massachusetts Institute of Technology, p.75,  
(July, 1960).
- S9 Smith, R.S.,  
"Measurement of Crystallite Size and Strain of  
Electroplated Films".  
IBM J.Res. and Developm., 4, 205, (1960).
- S10 Segmüller, A.,  
"Annealing Behaviour and Temperature Dependence of  
the Magnetic Properties of Thin Permalloy Films".  
J.Appl.Phys., (Suppl.), 32, 89S, (1961).
- S11 Segmüller, A.,  
"Determination of Lattice Strain and Crystallite  
Size in Thin Films".  
IBM J.Res.and Developm., 6, 464, (1962).
- S12 Smith, D.O., Weiss, G.P.,  
"Dynamic Magnetic Anneal".  
Quarterly Research Rept. on Solid State Research,  
Lincoln Lab., Massachusetts Institute of Technology,  
No.4, p.65, (1962).
- S13 Smith, D.O., Weiss, G.P.,  
"Dynamic Annealing of Magnetic Films".  
Quarterly Research Rept. on Solid State Research,  
Lincoln Lab., Massachusetts Institute of Technology,  
No.1, p.55, (1963).
- T1 Takaki, H.,  
"Ueber die Magnetostriktion der Eisenkristalle bei  
hoher Temperatur".  
Zeitschrift für Physik, 105, 92, (1937).
- T2 Taniguchi, S.,  
"A Theory of the Uniaxial Ferromagnetic Anisotropy  
Induced by Magnetic Annealing in Cubic Solid Solutions".  
Science Reports, Research Institute of Tohoku University,  
A7, 269, (1955).

- T3 Takahashi, M.,  
"Induced Magnetic Anisotropy of Evaporated Films  
Formed in a Magnetic Field".  
J.Appl.Phys., (Suppl.), 33, 1101, (1962).
- V1 Vand, V.,  
"A Theory of the Irreversible Electrical Resistances  
Changes of Metallic Films Evaporated in Vacuum",  
Proc.Phys.Soc., London, 55, 222, (1943).
- V2 Verderber, R.R.,  
"Texture of Evaporated Ni-Fe Thin Films".  
J.Appl.Phys., 30, 1359, (1959).
- V3 Vrambout, R., De Greve, L.,  
"Measurements on the Magnetic Anisotropy in Evaporated  
Iron Films".  
App.Scientific Research, 9B, 102, (1961).
- W1 Wilkinson, P.G.,  
"Lattice Distortion Spectrum of Evaporated Gold".  
J.Appl.Phys., 22, 419, (1949).
- W2 Warren, B.E., Averback, B.T.,  
"The Separation of Cold-Work Distortion and Particle  
Size Broadening in X-ray Patterns".  
J.Appl.Phys., 23, 497, (1952).
- W3 Williams, H.J., Sherwood, R.C.,  
"Magnetic Domain Patterns on Films".  
J.Appl.Phys., 28, 548, (1957).
- W4 Weiss, G.P., Smith, D.O.,  
"Annealing of Oblique Incidence Permalloy Films".  
J.Appl.Phys., (Suppl.), 32, 85S, (1961).
- W5 Weiss, G.P., Smith, D.O.,  
"Isotropic Stress Measurements in Permalloy Films".  
J.Appl.Phys., (Suppl.), 33, 1166, (1962).
- Y1 Yee, W.F., Weiss, G.P.,  
"Stripping of Normal-Incidence Films".  
Quarterly Research Rept. on Solid State Research,  
Lincoln Lab., Massachusetts Institute of Technology,  
p.81, (July, 1960).

- Y2 Yelon, A., Asik, J.R., Hoffman, R.W.,  
"Fibre Texture and Magnetic Anisotropy in Evaporated  
Iron Films".  
J.Appl.Phys., 33, 949, (1962).
- Z1 Zener, C.,  
"Stress Induced Preferential Orientation of Pairs of  
Solute Atoms in Metallic Solid Solutions".  
Phys.Rev., 71, 34, (1947).
- Z2 Zener, C.,  
"Classical Theory of the Temperature Dependence of  
Magnetic Anisotropy Energy".  
Phys.Rev., 96, 1335, (1954).

## CHAPTER 4

BH PLOTTER HYSTERESIS LOOPS AND LOW FREQUENCY SWITCHING  
BEHAVIOUR OF THIN FILMS

## 4.1 INTRODUCTION

The present chapter investigates the low frequency switching behaviour of films using BH plotter measurements of their voltage switching waveforms and hysteresis loops. The non-coherent nature of this switching is discussed in Section 4.4. Voltage switching waveforms are examined in Section 4.5. These waveforms show multiple peaks indicating that more than one reversal mechanism is present. Transitions from one to the other occur with increasing traverse field  $h_T$  and plots are given of the threshold curves for each process on a  $(h_L, h_T)$  diagram. The time required for switching is considered in Section 4.6. It is not negligible in 1000 c/s BH plotter measurements which thus cannot be regarded as truly quasistatic. Different processes proceed at different rates, and the coercive force consequently varies with the frequency and amplitude of the applied field.

## 4.2 TYPICAL SWITCHING WAVEFORMS AND HYSTERESIS CURVES

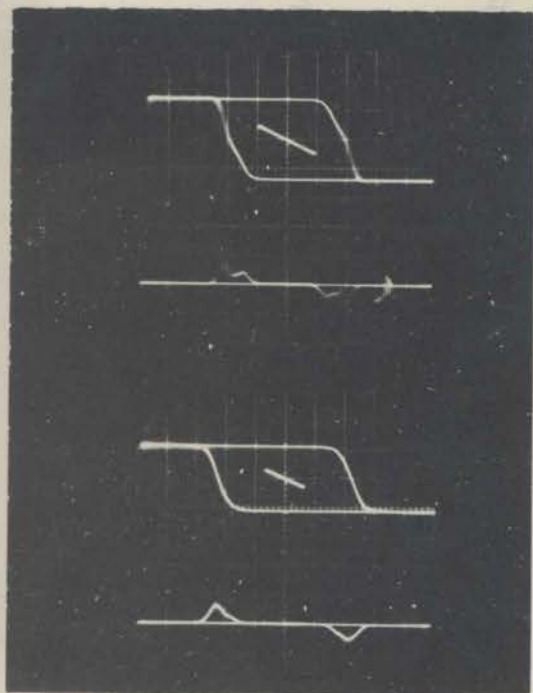
Fig. 4.21 shows the easy direction linear hysteresis  $(m_L, H_L)$  and the switching voltage waveforms  $(\dot{m}_L, H_L)$  for four typical film samples, S2P17, S2P18, S2P9 and S2P7. The loops have been measured at a frequency of 1000 c/s by the audio frequency (AF) MH plotter described in Chapter 6. The initial hard direction curves  $(m_T, H_T)$  have been superposed on the photograph so that the total anisotropy field  $H_K$  and the normalized coercive force  $h_C = H_C/H_K$  may be found. The photographs show that all films are "normal" with  $h_C < 1.0$ . A summary of the physical and magnetic properties of the four samples is given in Table 4.22.

The switching behaviour of films is changed, if a static traverse field  $H_T$  is applied. As discussed in Section 2.5, the switching process is fundamentally altered at higher  $h_T = H_T/H_K$ . The behaviour of film S2P17 is typical in this respect. Fig. 4.23 shows experimental 1000 c/s  $(m_L, H_L)$ ,  $(\dot{m}_T, H_L)$ ,  $(m_T, H_L)$  and  $(\dot{m}_T, H_L)$  curves for film S2P17 taken with increasing values of the field  $h_T$ . Fig. 4.24 gives the same results taken at 230 c/s.

## 4.3 INSTRUMENTATIONAL ERRORS

The 1000 c/s curves show small errors due to the high

Fig. 4.21 1000 c/s EASY AXIS LINEAR HYSTERESIS LOOPS  
 $(m_L, H_L)$  AND SWITCHING VOLTAGE WAVEFORMS  $(\dot{m}_L, H_L)$   
 OF TYPICAL THIN PERMALLOY FILMS.



AF field, 1000 c/s, 12.7 oe pp

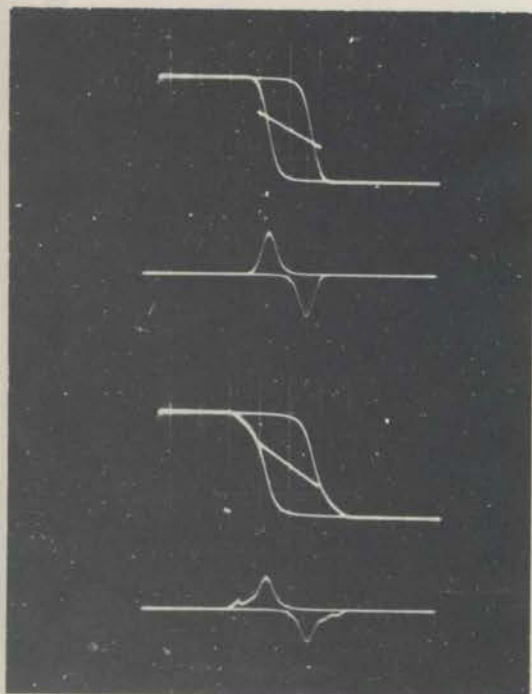
Scales: m 2 mV/cm +

$\dot{m}$  50 mV/cm +

H 1.27 oe/cm

Frame 1: Film S2P17

Frame 2: Film S2P18



AF field, 1000 c/s, 12.7 oe pp

Scales: m 5 mV/cm +

$\dot{m}$  100 mV/cm +

H 1.27 oe/cm

Frame 1: Film S2P9

Frame 2: Film S2P7

+ referred to the terminals  
 of the sense coil of the MH  
 plotter by the gain at 1000 c/s



Fig. 4.22 Measured Properties of Film Samples

Sample No.	Film Thickness	Easy Axis Hysteresis Loop Meas.			Hard Axis Hysteresis Loop Meas.			Anisotropy Data			Dispersion Data			Easy Axis Skew	
		$M_s$	$h_c$	$h_c$	$m_r$	$H'_c$	$h'_c$	$m'_r$	$H_{K_i}$	$H_{K_{torq}}$	R	$\beta$	$\beta$		$\beta$
Units	$\text{\AA}$	mV	oe	oe	oe	oe	oe	oe	oe	$\times 10^2$	$\times 10^3$	$\times 10^3$	demag	deg.	
Error		$\pm .05$	$\pm .05$		$\pm .05$			$\pm .05$	$\pm .01$		$\pm 5\%$	$\pm 5\%$			
S2P17	1070	2.85	2.48	.69	.98	.26	.075	.15	3.57	3.49	1.0	19.5	19.5	19	2.1
S2P18	880	2.32	2.85	.93	.98	.71	.239	.42	3.00	2.83	6.0	62	62	19	3.7
S2P14	1420	3.70	1.91	.54	.98	.35	.099	.18	3.54	3.67		22.5	23.8	25	2.4
S2P15	1390	3.70	2.02	.57	.99	.35	.098	.18	3.56	3.64		20.7	18.4	23	2.9
S2P4	1010	2.70	2.65	.67	.98	.35	.089	.18	3.93	4.18		30.0	25.4	15	0.4
S2P9	3470	9.05	0.89	.23	.93	.15	.037	.07	4.01	3.56	0.0	58	54	57	1.3
S2P7	3470	9.05	1.10	.36	.90	.29	.095	.14	3.09	2.65	1.0	123	123	69	1.2
S2P8	3500	9.20	0.95	.27	.93	.26	.074	.07	3.50	4.31		57	57	65	2.5

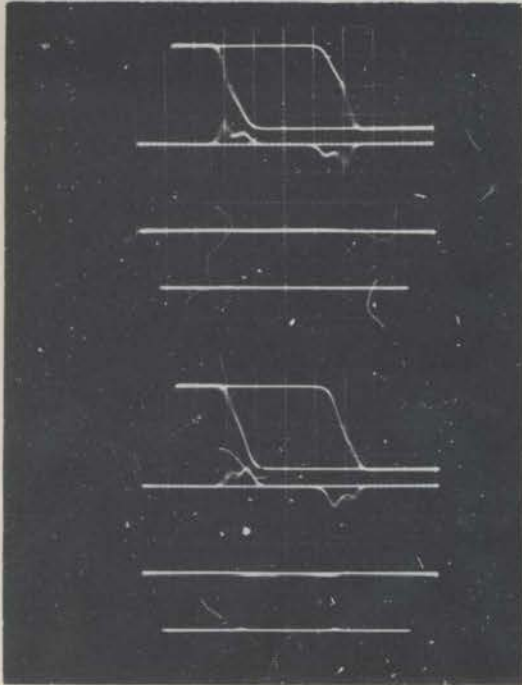
Notes:

- Conditions of deposition: 81 per cent Ni 19 per cent Fe in melt, soft glass substrates at  $300^{\circ}\text{C}$ , source to substrate distance 9 in., deposition rate  $4 \text{ \AA sec}^{-1}$ , pressure  $10^{-5}$  mm of Hg rising to  $10^{-4}$  mm of Hg, orientating field 75 oe.
- Relative thicknesses are accurate, being based on the measurement of  $M_s$ . Absolute thicknesses were determined to  $\pm 10$  per cent using a Taylor-Hobson Talysurf Model 2.
- All hysteresis loop quantities were measured using the MH plotter of Chapter 6 with a 1000 c/s, 12.5 oe pp audio field.
- $H_{K_i}$  measured from the extrapolated initial hard axis susceptibility.
- $H_{K_{\text{torq}}}$  is the torque anisotropy measured by the method of Section 5.4 and R a parameter measuring the departure of the anisotropy torque from a  $\sin 2\theta$  form (defined in Section 5.4).
- $\beta_{\frac{1}{2}}^{\phi}$  and  $\beta_{\frac{1}{2}}^{hT}$  are the angular dispersions measured by the Crowther first and second methods.  $\beta_{\text{demag}}$  is the apparent dispersion due to the demagnetising field of the film given by  $\beta_{\text{demag}}$  equals  $\pi^2 M_s t / H_{K_i} D$ , where t and D are the film thickness and diameter. Low dispersion values measured by the Crowther technique must be regarded with caution.

Figure 3:  $H_c = 0.20$

\* referred to the terminals of the sense coil of the MH plotter by the gain at 1000 c/s

Fig. 4.23 1000 c/s EASY AXIS LINEAR HYSTERESIS LOOPS ( $m_L, H_L$ ),  
 $(m_T, H_L)$  AND SWITCHING VOLTAGE WAVEFORMS ( $\dot{m}_L, H_L$ ), ( $\dot{m}_T, H_L$ )  
 AS A FUNCTION OF TRAVERSE FIELD  $h_T$  FOR FILM S2P17



AF field, 1000 c/s, 12.7 oe pp

Scales: m 2 mV/cm †

$\dot{m}$  50 mV/cm †

H 1.27 oe/cm

The traces shown are ( $m_L, H_L$ ),  
 $(\dot{m}_L, H_L)$ , ( $m_T, H_L$ ), ( $\dot{m}_T, H_L$ ) respecti-  
 vely for varying  $h_T = H_T/H_K$  torque

Frame 6:  $h_T = 0.0$

Frame 1 :  $h_T = 0.00$

Frame 2 :  $h_T = 0.05$

Frame 7:  $h_T = 0.9$

Frame 3 :  $h_T = 0.10$

Frame 4 :  $h_T = 0.20$

† referred to the terminals  
 of the sense coil of the MH  
 plotter by the gain at 1000 c/s

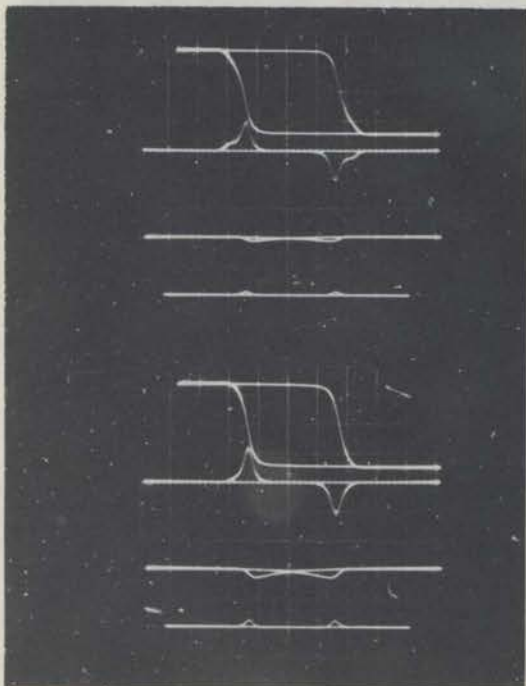
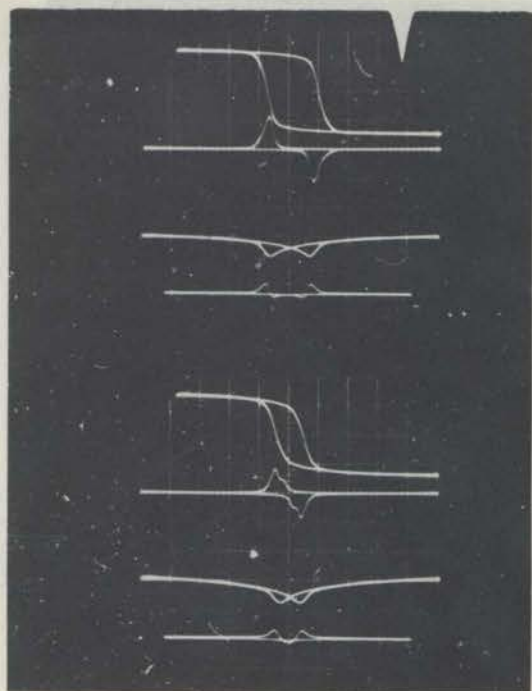
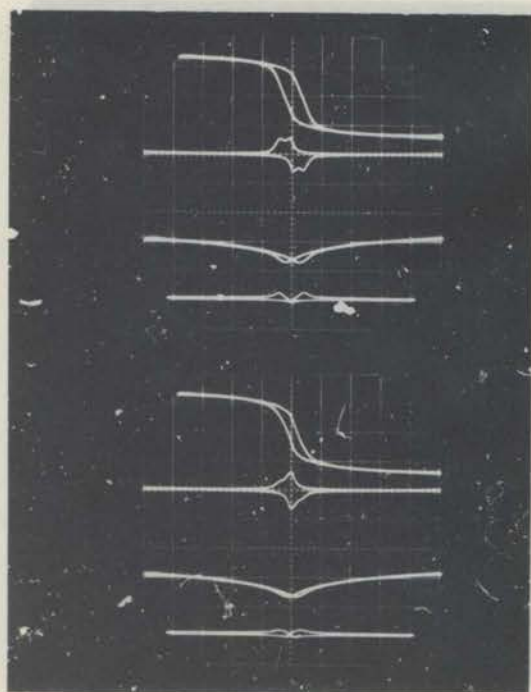


Fig. 4.23 cont.



Frame 5:  $h_T = 0.5$

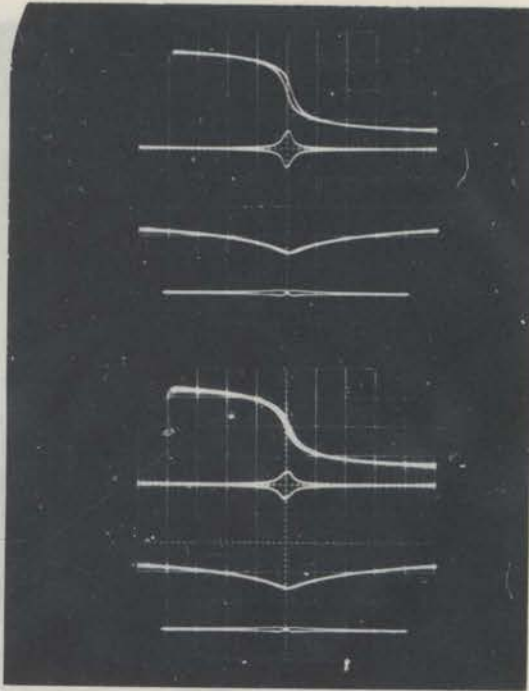
Frame 6:  $h_T = 0.8$



Frame 7:  $h_T = 0.9$

Frame 8:  $h_T = 1.0$

Fig. 4.23 cont. EASY AXIS LINEAR HYPERBOLIC LOOPS  $(m_{11}, H_L)$ ,  
 $(m_{21}, H_L)$  AND SWITCHING VOLTAGE WAVEFORMS  $(A_L, H_L)$ ,  $(E_T, E_L)$   
 AS A FUNCTION OF TRANSVERSE FIELD  $h_T$  FOR FILM 22117.



Frame 9:  $h_T = 1.10$  6 sec pp  
 Scales:  $a = 2 \text{ mV/cm}$   
 $b = 20 \text{ mV/cm}$   
 $H = 1.36 \text{ sec/cm}$

The traces shown are  $(m_{11}, H_L)$ ,  
 $(m_{21}, H_L)$ ,  $(A_L, H_L)$ ,  $(E_T, E_L)$  respectively  
 for varying  $h_T = H_T/H_L$  starting

Frame 10:  $h_T = 1.20$

Frame 14:  $h_T = 0.00$

Frame 2:  $h_T = 0.05$



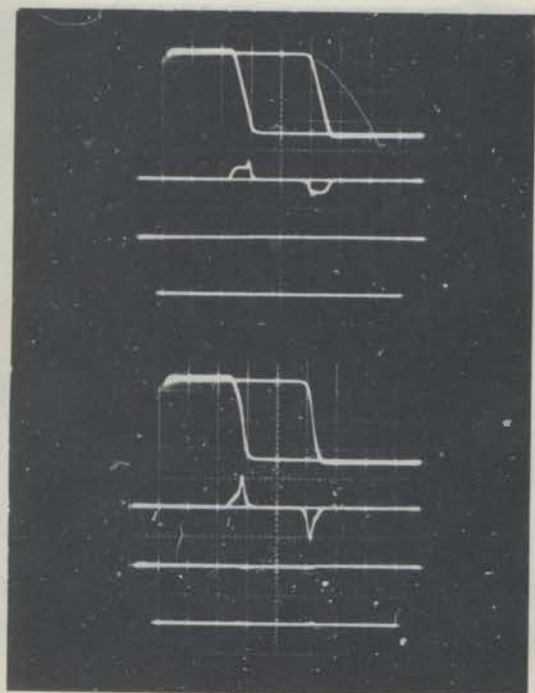
Frame 11:  $h_T = 1.30$

Frame 3:  $h_T = 0.10$

Frame 4:  $h_T = 0.20$

\* referred to the terminals  
 of the sense coil of the MI  
 plotter by the gain at 230 c/s

Fig. 4.24 230 c/s EASY AXIS LINEAR HYSTERESIS LOOPS  $(m_L, H_L)$ ,  
 $(m_T, H_L)$  AND SWITCHING VOLTAGE WAVEFORMS  $(\dot{m}_L, H_L)$ ,  $(\dot{m}_T, H_L)$   
 AS A FUNCTION OF TRAVERSE FIELD  $h_T$  FOR FILM S2P17.



AF field, 230 c/s, 13.6 oe pp

Scales:  $m$  2 mV/cm †

$\dot{m}$  20 mV/cm †

$H$  1.36 oe/cm

The traces shown are  $(m_L, H_L)$ ,  
 $(\dot{m}_L, H_L)$ ,  $(m_T, H_L)$ ,  $(\dot{m}_T, H_L)$  respectively  
 for varying  $h_T = H_T/H_{K\text{torque}}$

Frame 0:  $h_T = 0.00$

Frame 1:  $h_T = 0.00$

Frame 2:  $h_T = 0.05$

Frame 3:  $h_T = 0.10$

Frame 3:  $h_T = 0.10$

Frame 4:  $h_T = 0.20$

† referred to the terminals  
 of the sense coil of the MH  
 plotter by the gain at 230 c/s

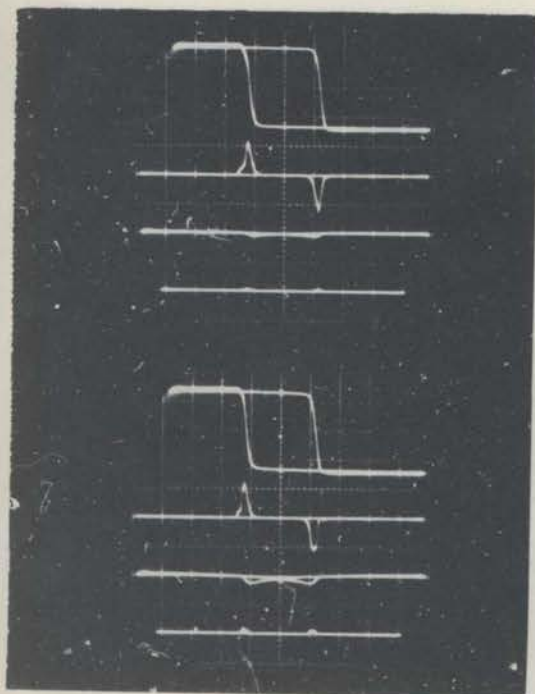
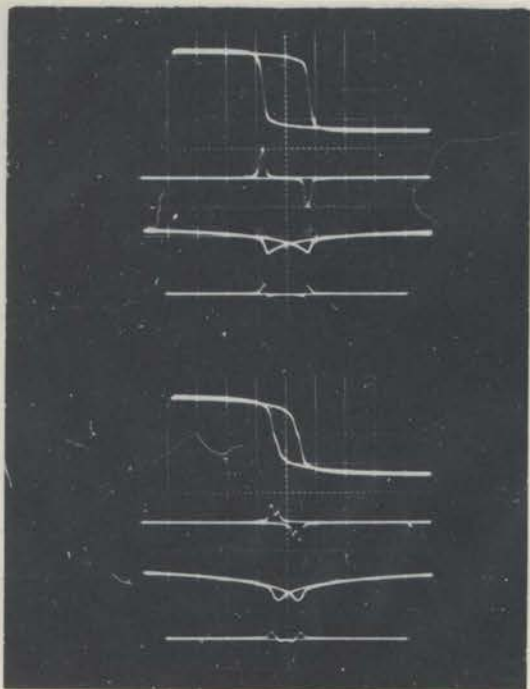
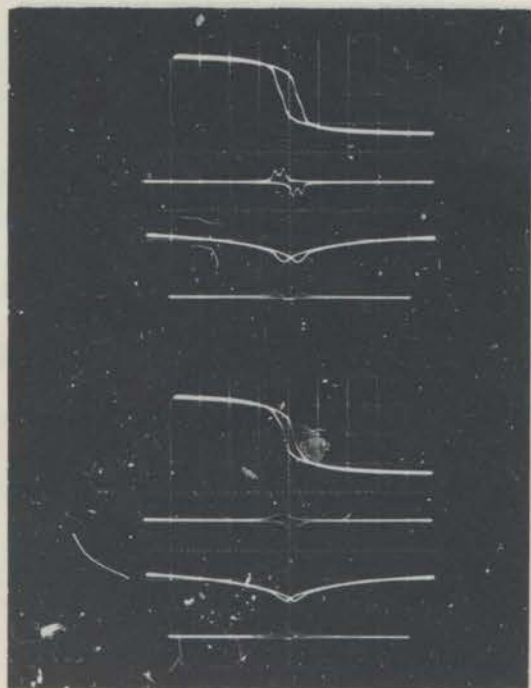


Fig. 4.24 cont.



Frame 5:  $h_T = 0.50$

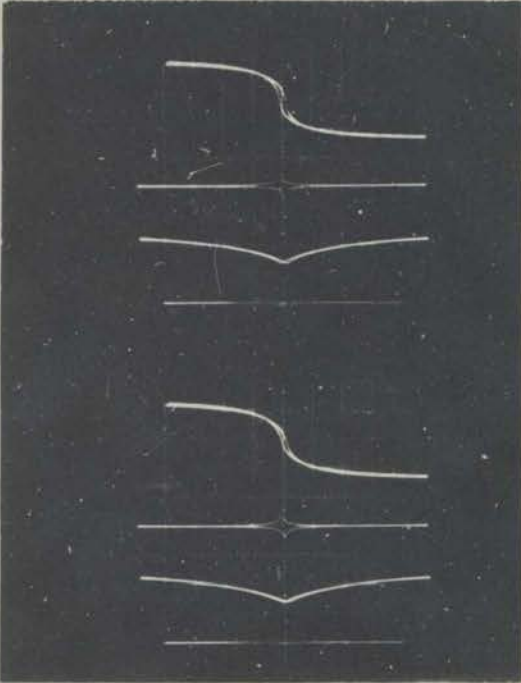
Frame 6:  $h_T = 0.80$



Frame 7:  $h_T = 0.90$

Frame 8:  $h_T = 1.00$

Fig. 4.24 cont.



Frame 9:  $h_T = 1.10$

Frame 10:  $h_T = 1.20$



Frame 11:  $h_T = 1.30$



frequency limitations of the MH plotter (arising from the inductance and self-capacitance of the sense coil). Their interpretation must be made with this in mind. An idealized square hysteresis loop will show instead a finite interval of rise  $\Delta H$  (from the 10 per cent to 90 per cent value) and an associated error  $\Delta H_C$  in the coercive force  $H_C$ . Using formula (6.73) and the data on the high frequency response of the MH plotter given in Section 6.72,  $\Delta H=0.4$  oe and  $\Delta H_C=0.2$  oe for a 1000 c/s applied field  $H$  of 12.5 oe pp assuming  $H_C \ll H$ . 0.4 oe and 0.2 oe are equivalent to 0.30 and 0.15, respectively, of a "centimetre" division (or one large division) on the photographs shown. The switching voltage peaks will show a finite rise and a broadening over a similar interval. For the 230 c/s curves the high frequency error is negligible, being  $\Delta H=0.09$  oe equivalent to 0.07 cm divisions and  $\Delta H_C=0.045$  oe equivalent to 0.035 cm divisions.

The hysteresis curves of the present chapter have been taken with the "basic" integrator of Section 8.4, equation (8.42). Phase compensations of the transfer function has not been used in this case. The effects of low frequency sag is shown in Fig. 6.73 and with reference to that figure, is approximately 15 per cent for the 230 c/s curves reducing to 4 per cent for the 1000 c/s curves.

The facility of measuring hysteresis curves at different frequencies provides a useful check on the effects and interpretation of instrumental errors.

#### 4.4 DEPARTURES FROM THE COHERENT ROTATIONAL MODEL

Experimental  $(m_L, H_L)$  and  $(m_T, H_L)$  hysteresis curves depart significantly from the coherent rotational (CR) model. An examination of Fig. 4.23 and Fig. 4.24 shows that the CR model adequately describes the reversible rotation of the magnetization up to the point where switching occurs. The switching threshold and the nature of the irreversible switching process itself is, however, in considerable disagreement. In this connection the following differences may be listed showing clearly that the switching process cannot be one of coherent rotation.

- It is convenient in a first approximation to define the switching threshold field as the coercive force  $H_C$  of the  $(m_L, H_L)$  hysteresis loop. Plots of  $H_C$  as a function of  $H_T$  are given in Fig. 4.41. For small  $H_T$ , that is for fields near the easy axis,  $H_C$  is well below the coherent rotational threshold  $H_{cr}$ . In particular (except for film S2P18),

Threshold fields  $H_1, H_2, H_3$  on the  $(H_1, H_2)$   
plane for film S2P17.

The fields are normalized in terms of the anisotropy  
field  $H_K = 3.57$  Oe.

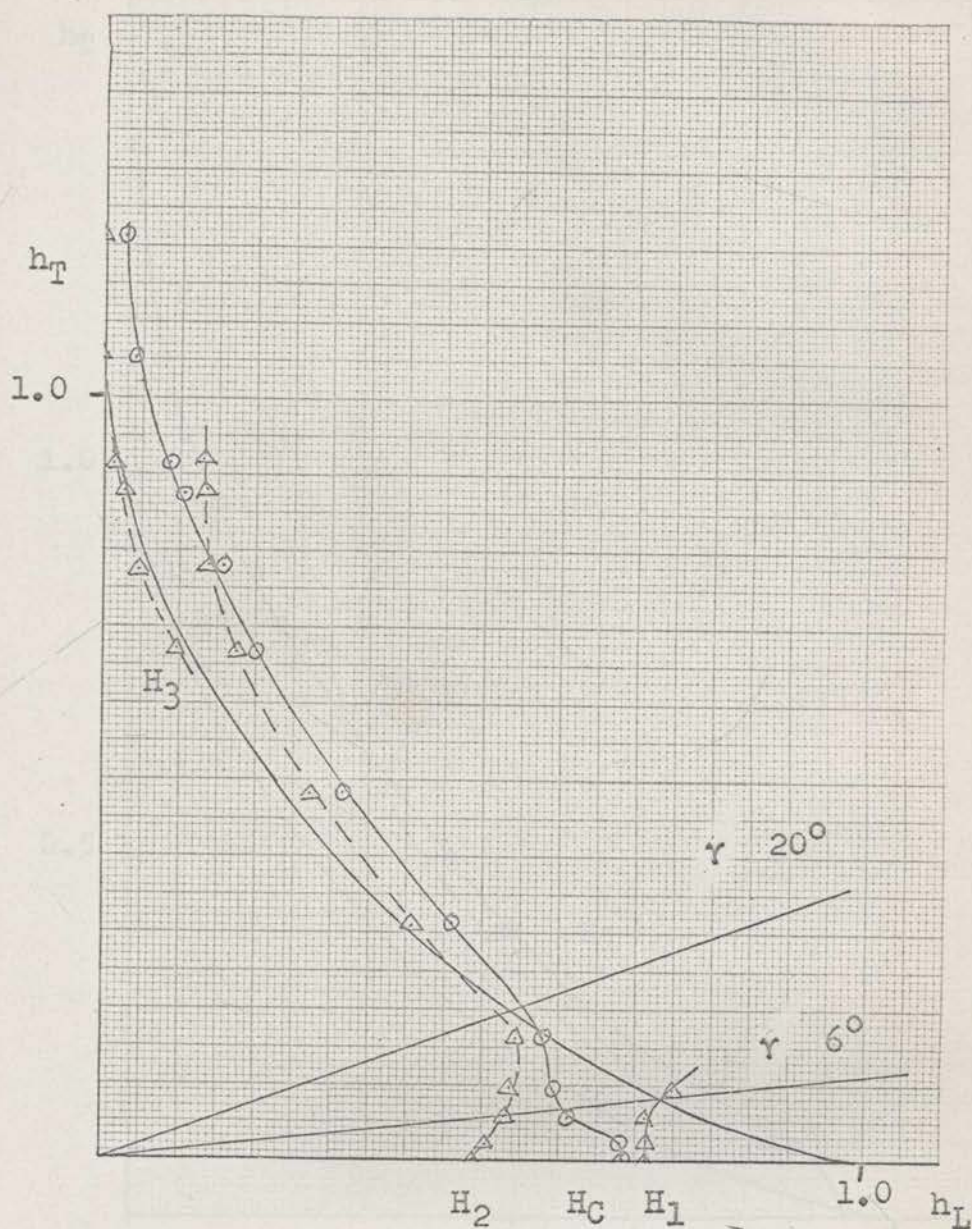


Fig. 4.41a Plot of the Coercive Force  $H_C$  and the Switching Threshold Fields  $H_1$ ,  $H_2$ ,  $H_3$  on the  $(h_L, h_T)$  Plane for Film S2P17.

The fields are normalised in terms of the anisotropy field  $H_{K1}$  3.57 oe.

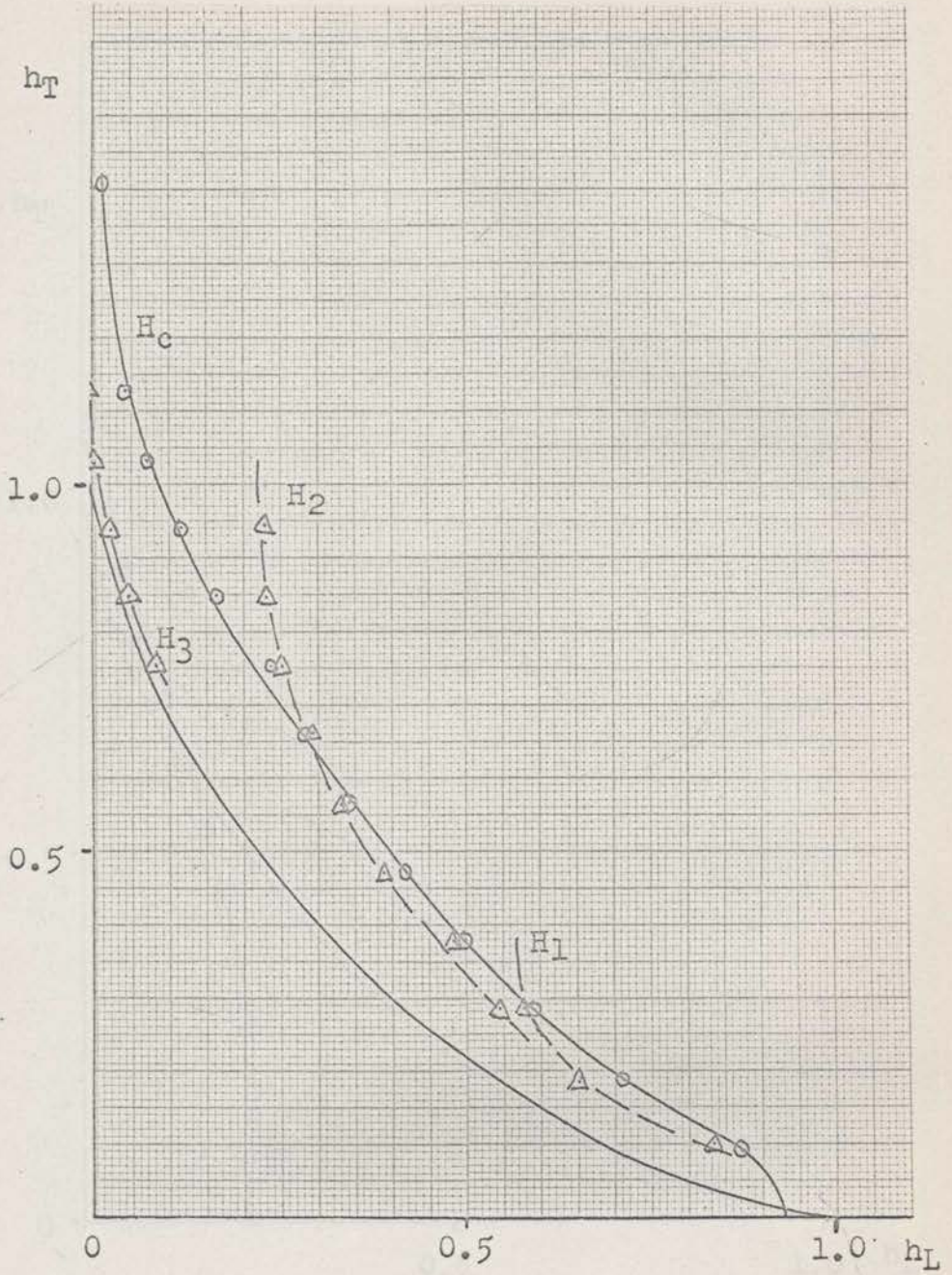


Fig. 4.41b (continued). Film S2P18.

The fields are normalised in terms of the anisotropy field  $H_{K1}$  3.00 oe.

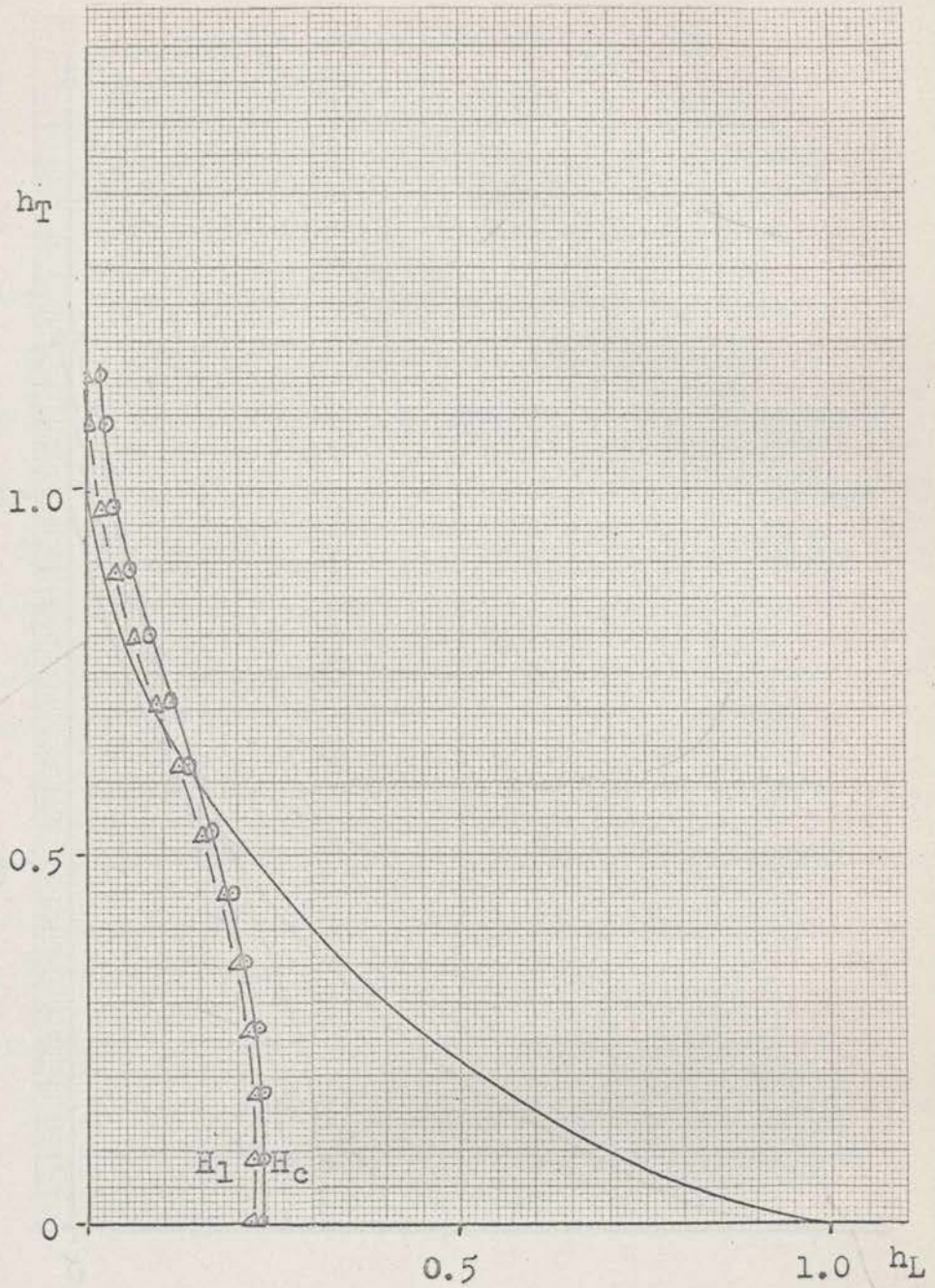


Fig. 4.41c (continued). Film S2P9.

The fields are normalised in terms of the anisotropy field  $H_{K1}$  4.01 oe.

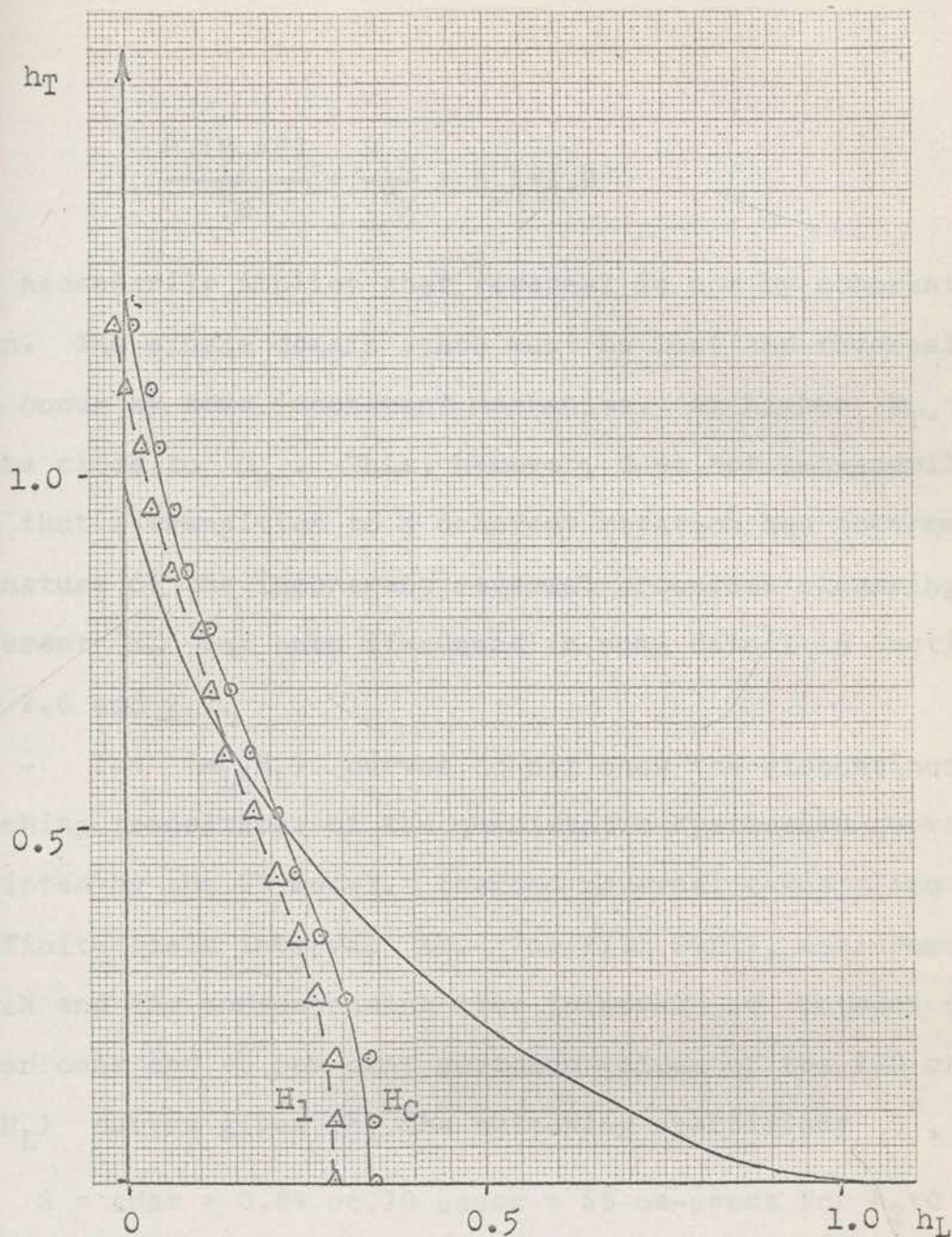


Fig. 4.41d (continued). Film S2P7.

The fields are normalised in terms of the anisotropy field  $H_K$  3.09 oe.

$$\frac{H_C(H_T=0)}{H_K} = \frac{H_{CO}}{H_K} = h_{CO} < 1.0$$

This necessarily implies that reversal is not by coherent rotation. The single domain state must be lost and reversal must then occur by some incoherent mechanism. At higher  $H_T$ ,  $H_C$  may be close to  $H_r$ . This, however, does not necessarily mean that a transition to a coherent rotation has occurred. The nature of the incoherent reversal processes occurring for different  $H_T$  has been discussed in some detail in Sections 2.5, 2.6 and 2.7.

The  $(m_L, H_L)$  curves do not show the discontinuous switching transitions of the quasistatic hysteresis curves predicted by the CR model. Instead reversal takes place over a definite field interval  $\Delta H$ . For film S2P17, measurement of  $\Delta H$  and the corresponding time interval  $\Delta t$  between the 10 per cent and 90 per cent switched values of the 230 c/s  $(m_L, H_L)$  curves gives for the switching coefficient  $S^*$ ,

$$\begin{aligned} S &= \Delta H \Delta t = 0.84 \text{ oe} \cdot 70 \text{ } \mu\text{secs} = 59 \text{ oe} \cdot \mu\text{secs for } h_T=0 \\ &= 0.37 \text{ oe} \cdot 40 \text{ } \mu\text{secs} = 15 \text{ oe} \cdot \mu\text{secs for } h_T=0.2 \end{aligned}$$

---

\* The data quoted for  $\Delta t$  has been measured directly. Alternatively,  $\Delta t$  may be deduced from  $\Delta H$  using equation (6.73). Both values agree to within 10 per cent.

---

Thus  $\Delta H$  cannot be due to the finite rise time ( $\pm 10 \mu\text{secs}$ ) of the MH plotter, since the times involved are too long. The switching process itself must have either a variation in the switching threshold of  $\Delta H$  over the area of the film, or require a finite time  $\Delta t$  for the completion of the process. This question is further discussed in Section 4.6. For the present, a coherent process cannot, ad hoc, have a variation in the threshold field. Further, the above values of  $S$  are several orders of magnitude larger than the values expected for a coherent rotation (typically values of  $S$  of  $\pm 0.01$  or  $\mu\text{secs}$  are obtained from pulse switching experiments<sup>S2</sup>).

- The coherent rotational  $(m_T, H_L)$  curves of Fig. 2.33 show a transient spike reaching to  $m_L=1.0$  as the magnetization rotates past the hard axis direction. With an AF MH plotter of normal high frequency response, this spike will not be seen even if a coherent rotation were to take place. h43

If we assume for the moment that the magnetization does rotate coherently in a time  $\Delta t$  short compared to the time constants of the MH plotter, then the spike may be represented by a delta function of magnitude in normalized notation of  $\Delta t u_0(t) \text{secs}$ . If the overall transfer function  $T(s)$  of the instrument (defined as in Section 6.72) has a double pole at



$w_r = 1/\tau_r^*$ , that is  $T(s) = 1/(1 + S\tau_r)^2$ , then it is readily shown that the maximum value of the output pulse produces is
 
$$m_0 \Big|_{\max} = 0.367 \Delta T / \tau_r.$$
 For  $\Delta t = 0.01 \text{ oe} - \mu\text{sec} / 0.1 \text{ oe} = 0.1 \mu\text{secs}$  and  $\tau_r = 3 \mu\text{secs}$ , then  $m_0 \Big|_{\max} \approx 0.01$ . If only a fraction of the film switches coherently, and the remainder of the film switches in a time of say  $0.1\tau_0$ , where  $w_0 = \frac{1}{\tau_0}$  is the repetition frequency of the applied AF field, then the spike will be accentuated in the  $(\dot{m}_T, H_L)$  display relative to the remainder of the pulse by the factor  $0.1\tau_0/\tau_r$ . If this factor is of the order of 10, it may be expected that the spike (strictly the spike will now occur as a differentiated delta function) may just be seen in this case. However, in the region of higher  $h_T$ , where a coherent rotation is most likely,  $m_0 \Big|_{\max}$  will be reduced by a further factor  $(1 - h_T^2)^{\frac{1}{2}}$ . It is thus possible that some small fraction of the flux may rotate coherently at high  $h_T$ . The experimental curves of Fig. 4.23 and Fig. 4.24 show no evidence of any such spike.

#### 4.5 SWITCHING VOLTAGE WAVEFORMS AND THE OCCURRENCE OF MULTIPLE REVERSAL PROCESSES

The switching voltage waveforms can show details of the

---

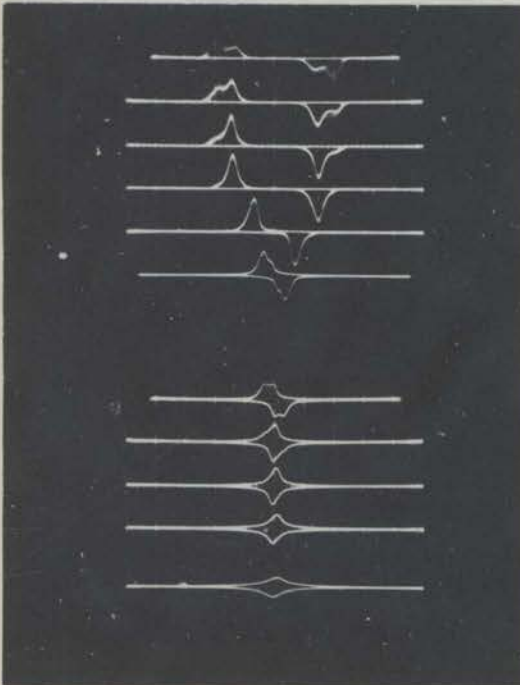
\* A double order pole will be produced by the sense coil.

switching voltage process which are not readily visible from the integrated hysteresis curves.

$(\dot{m}_L, H_L)$  and  $(\dot{m}_T, H_L)$  curves have been included amongst the curves for film S2P17 given in Figs. 4.23 and 4.24. The curves are, however, more conveniently studied if displayed separately.  $(\dot{m}_L, H_L)$  curves for film S2P17, taken for increasing traverse field  $h_T$ , are given in Fig. 4.51a. Curves at both 1000 c/s and 230 c/s are shown. The same data is given for films S2P10, S2P9 and S2P7 in Figs. 4.51b, 4.51c and 4.51d, respectively.

For film S2P17, Fig. 4.51a shows two distinct switching peaks occurring near  $h_T=0.9$  at fields  $H_2, H_3$  (where  $H_2 > H_3$ ). The peaks are partially masked by rise time limitations in the 1000 c/s series, but are very much clearer at 230 c/s. The occurrence of two peaks indicates that reversal is not a simple single process, but rather that two different mechanisms occur. Reversal proceeds by process  $H_2$  for  $h_T \leq 0.8$ , but is then progressively transferred to the lower threshold process  $H_3$  as  $h_T$  increases. Fields  $H_2$  and  $H_3$  are plotted as a function of  $h_T$  in Fig. 4.41a. The almost exact agreement of the  $H_3$  threshold with the coherent rotational threshold  $H_{cr}$  suggests that  $H_3$  is very close to a coherent rotational process itself. Unfortunately, it has not been possible to verify the nature of the processes

Fig.4.51a 1000 c/s AND 230 c/s SWITCHING VOLTAGE WAVEFORMS ( $\dot{m}_L, H_L$ )  
AS A FUNCTION OF TRAVERSE FIELD  $h_T$  FOR FILM S2P17



## 1000 c/s WAVEFORMS

AF field, 1000 c/s, 12.7 oe pp

Scales:  $\dot{m}$  50 mV/cm †

H 1.27 oe/cm

The traces shown are taken for

$h_T = H_T/H_{K_{torque}}$	= 0.00
	0.05
	0.10
	0.20
	0.50
	0.80
	0.90
	1.00
	1.10
	1.20
	1.35

## 230 c/s WAVEFORMS

Scales:  $\dot{m}$  20 mV/cm †

H 1.36 oe/cm

the traces shown are taken for

$h_T = H_T/H_{K_{torque}}$	= 0.00
	0.05
	0.10
	0.20
	0.50
	0.80
	0.90
	1.00
	1.10
	1.20
	1.35

† referred to the terminals  
of the sense coil of the MH  
plotter by the gain of 1000 c/s  
and 230 c/s respectively.

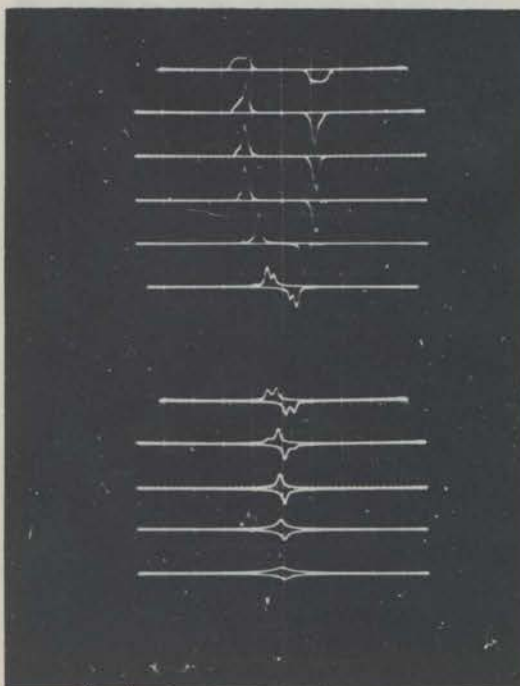
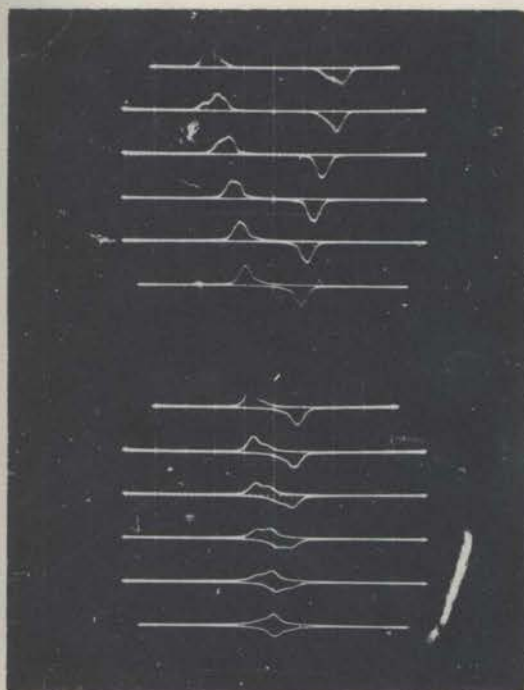


Fig.4.51b 1000 c/s AND 230 c/s SWITCHING VOLTAGE WAVEFORMS ( $\dot{m}_L, H_L$ )  
AS A FUNCTION OF TRAVERSE FIELD  $h_T$  FOR FILM S2P18



## 1000 c/s WAVEFORMS

AF field, 1000 c/s, 12.7 oe pp

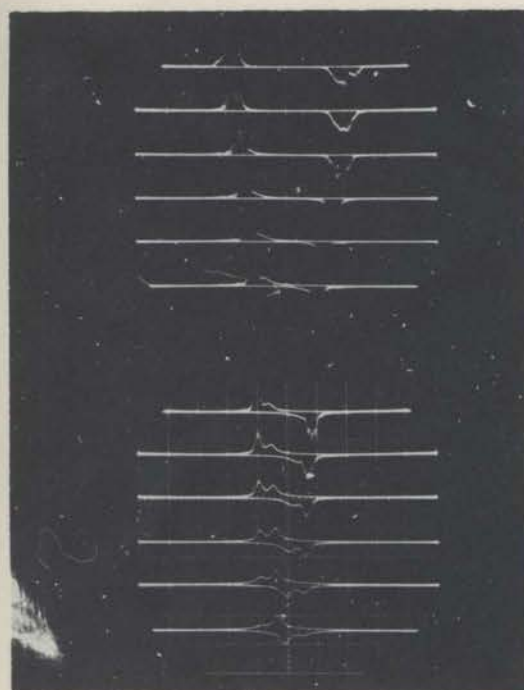
Scales:  $\dot{m}$  50 mV/cm †

H 1.27 oe/cm

The traces shown are taken for

$h_T = H_T / H_{Ktorque} =$

0.0
0.1
0.2
0.3
0.4
0.5
0.6
0.7
0.8
0.9
1.0
1.1



## 230 c/s WAVEFORMS

AF field, 230 c/s, 12.7 oe pp

Scales:  $\dot{m}$  10 mV/cm †

H 1.27 oe/cm

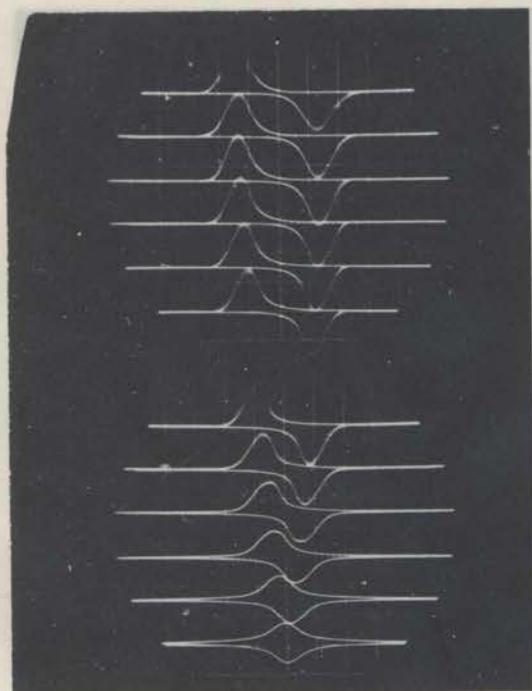
The traces shown are taken for

$h_T = H_T / H_{Ktorque} =$

0.0
0.1
0.2
0.3
0.4
0.5
0.6
0.7
0.8
0.9
1.0
1.1

† referred to the terminals of the sense coil of the MH plotter by the gain of 1000 c/s and 230 c/s respectively.

Fig. 4.51c 1000 c/s AND 230 c/s SWITCHING VOLTAGE WAVEFORMS ( $\dot{m}_L, H_L$ )  
AS A FUNCTION OF TRAVERSE FIELD  $h_T$  FOR FILM S2P9



## 1000 c/s WAVEFORMS

AF field, 1000 c/s, 12.7 oe pp

Scales:  $\dot{m}$  100 mV/cm †

H 1.27 oe/cm

The traces shown are taken for

$h_T = H_T/H_{K_{torque}}$	=	0.0
		0.1
		0.2
		0.3
		0.4
		0.5
		0.6
		0.7
		0.8
		0.9
		1.0
		1.1

## 230 c/s WAVEFORMS

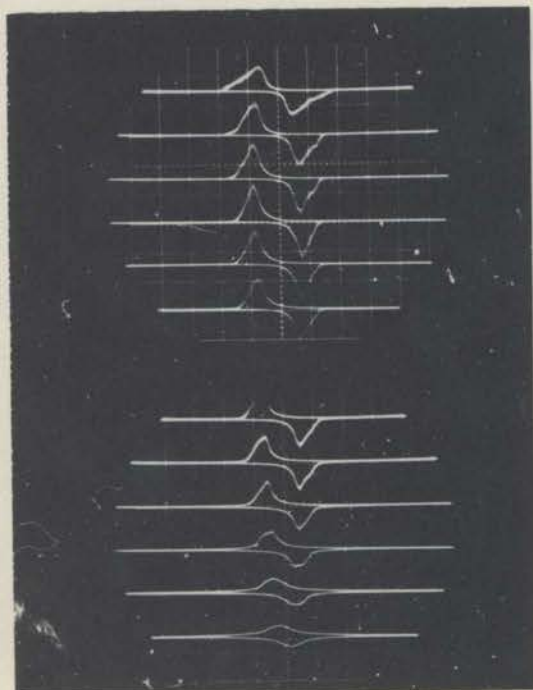
AF field, 230 c/s, 12.7 oe pp

Scales:  $\dot{m}$  50 mV/cm †

H 1.27 oe/cm

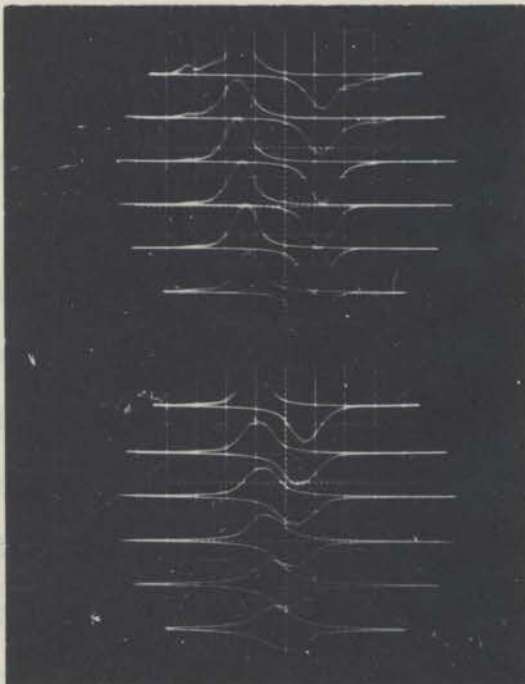
The traces shown are taken for

$h_T = H_T/H_{K_{torque}}$	=	0.0
		0.1
		0.2
		0.3
		0.4
		0.5
		0.6
		0.7
		0.8
		0.9
		1.0
		1.1

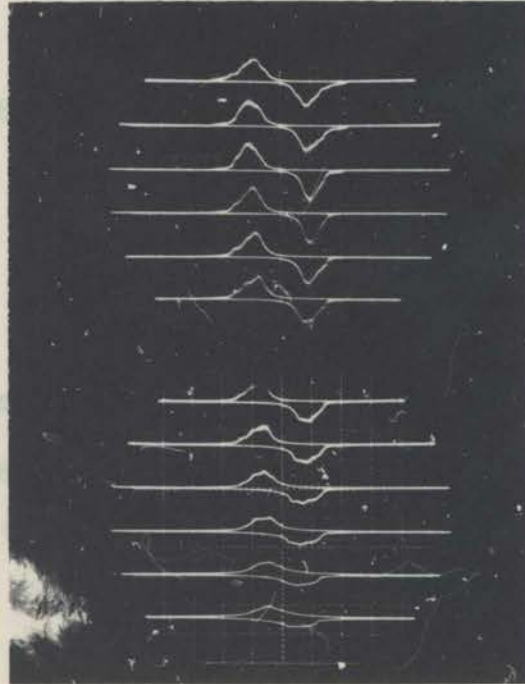


† referred to the terminals of the sense coil of the MH plotter by the gain of 1000 c/s and 230 c/s respectively.

Fig.4.51d 1000 c/s AND 230 c/s SWITCHING VOLTAGE WAVEFORMS ( $\dot{m}_L, H_L$ )  
 AS A FUNCTION OF TRAVERSE FIELD  $h_T$  FOR FILM S2P7



1000 c/s WAVEFORMS  
 AF field, 1000 c/s, 12.7 oe pp  
 Scales:  $\dot{m}$  100 mV/cm †  
 H 1.27 oe/cm  
 The traces shown are taken for  
 $h_T = H_T / H_{Ktorque} =$   
 0.0  
 0.1  
 0.2  
 0.3  
 0.4  
 0.5  
 0.6  
 0.7  
 0.8  
 0.9  
 1.0  
 1.1



230 c/s WAVEFORMS  
 AF field, 230 c/s, 12.7 oe pp  
 Scales:  $\dot{m}$  50 mV/cm †  
 H 1.27 oe/cm  
 The traces shown are taken for  
 $h_T = H_T / H_{Ktorque} =$   
 0.0  
 0.1  
 0.2  
 0.3  
 0.4  
 0.5  
 0.6  
 0.7  
 0.8  
 0.9  
 1.0  
 1.1

† referred to the terminals of the sense coil of the MH plotter by the gain of 1000 c/s and 230 c/s respectively.

involved by direct observation of the domains using the Bitter technique or otherwise.

Multiple peaks of the above type occur generally for films in the thickness range near  $1000 \text{ \AA}$ . For example, film S2P18 shows identical behaviour in Figs. 4.41b and 4.51b. No such multiple peaks occur for thicker films near  $3500 \text{ \AA}$ . Films S2P9 and S2P7 are typical of the behaviour in this case (see Figs. 4.41c, 4.51c; 4.41d, 4.51d). The reasons for the difference is not known. For thicker films, however, the  $H_2$  threshold itself approaches very closely to  $H_{cr}$  for high  $h_T$  values. Possibly (and not entirely unexpectedly) the  $H_2$  process may be basically different for the two film thicknesses. In any case, a more gradually transition from the  $H_2$  to the  $H_3$  process is indicated.

#### 4.6 THE TIME DEPENDENCE OF CERTAIN REVERSAL PROCESSES AND THE ASSOCIATED DEPENDENCE OF COERCIVE FORCES ON THE FREQUENCY AND AMPLITUDE OF THE APPLIED AF FIELD

The behaviour of film S2P17 for fields near  $h_T=0$  is particularly interesting. The  $1000 \text{ c/s } h_T=0$  trace of Fig. 4.51a shows two peaks occurring at fields  $H_1$  and  $H_2$  ( $H_1 > H_2$ ).  $H_1$  and  $H_2$  are plotted as a function of  $H_T$  in Fig. 4.41a. Again, a multiple switching process is

suggested. However, in this case the  $H_1$  peak, clearly visible in the 1000 c/s trace of Fig. 4.51a, is absent from the same trace of Fig. 4.51a taken at 230 c/s.

The above results are caused by the dependence of the switching process on the time rate of change  $\frac{dH}{dt}$  of the applied field  $H$ .  $\frac{dH}{dt}$  may be varied by varying the field frequency, or more conveniently, by varying the field amplitude. Fig. 4.61a shows the switching waveforms for S2P17 as a function of field amplitude at both 1000 and 230 c/s. The 230 c/s switching waveforms are given to an enlarged scale in Fig. 4.62. The switching voltage is shown against both a field scale and a time scale. Fig. 4.61b presents the same data for film S2P18 as is given for S2P17 in Fig. 4.61a. The 230 c/s,  $H=2.5$  cm pp trace of Figs. 4.61a and 4.62 is blurred. Close examination shows individual pulses, suggestive of Barkhausen domain wall jumps. The waveform has a triangular shape beginning at a field  $H'$  and extending over only a small field interval  $\Delta H$ . Since

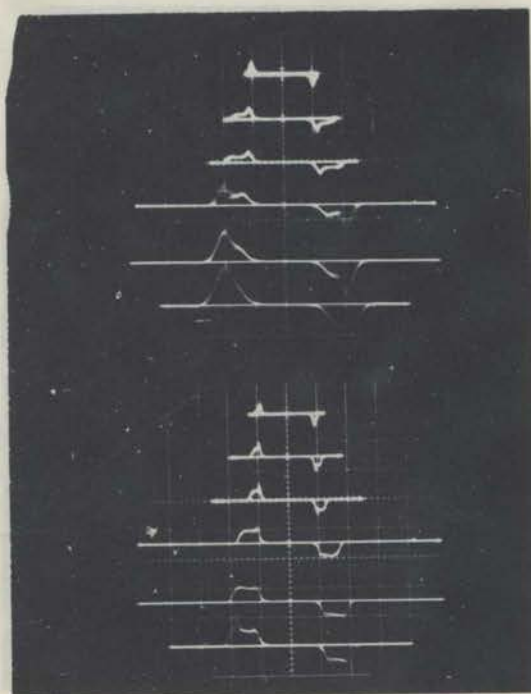
$$\frac{dm}{dt} = \lambda_w v_w \quad (4.61)$$

where

$v_w$  is the domain wall velocity, and  
 $\lambda_w$  an effective domain wall length,



Fig.4.61a 1000 c/s AND 230 c/s SWITCHING VOLTAGE WAVEFORMS  
 $(\dot{m}_L, H_L)$  AS A FUNCTION OF THE AMPLITUDE OF THE  
 APPLIED FIELD  $H_L$  FOR FILM S2P17



The traces shown are taken for various amplitudes of the applied AF field  $H_L = 2.5$  cm pp  
 3.8  
 5.0  
 10.0  
 15.0  
 20.0  
 in equivalent cm field units.

Frame 1: 1000 c/s WAVEFORMS

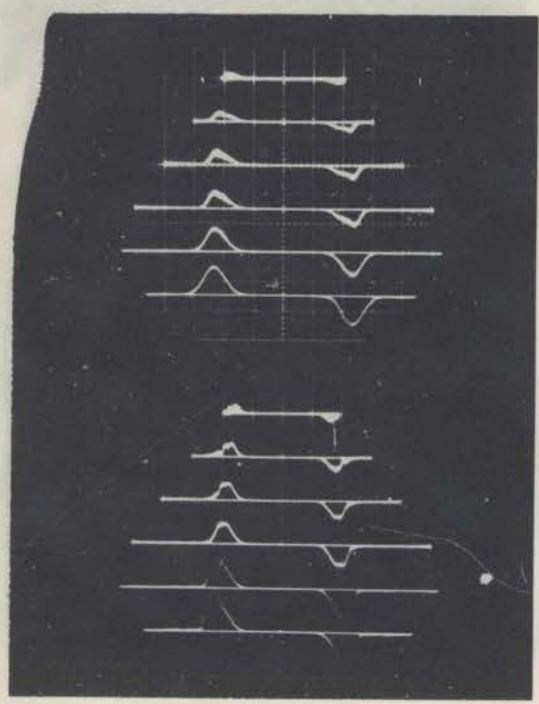
Scales:  $\dot{m}$  50 mV/cm †  
 H 1.27 oe/cm

Frame 2: 230 c/s WAVEFORMS

Scales:  $\dot{m}$  20 mV/cm †  
 H 1.36 oe/cm

† referred to the terminals of the sense coil of the MH plotter by the gain of 1000 c/s and 230 c/s respectively.

Fig.4.61b 1000 c/s AND 230 c/s SWITCHING VOLTAGE WAVEFORMS  
( $\dot{m}_L, H_L$ ) AS A FUNCTION OF THE AMPLITUDE OF THE  
APPLIED FIELD  $H_L$  FOR FILM S2P18



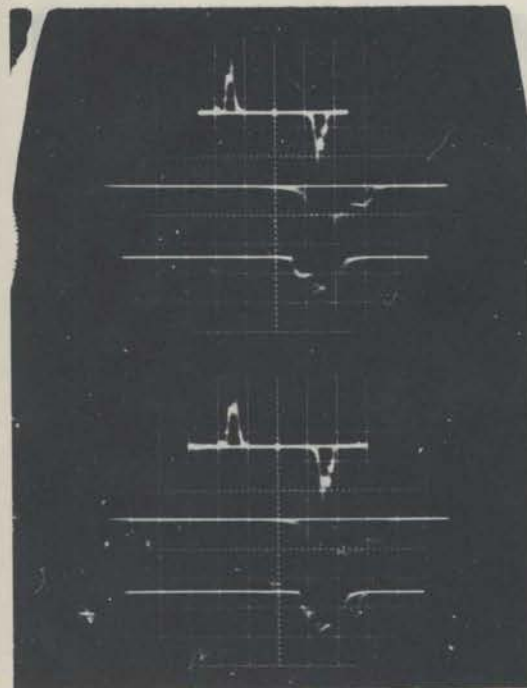
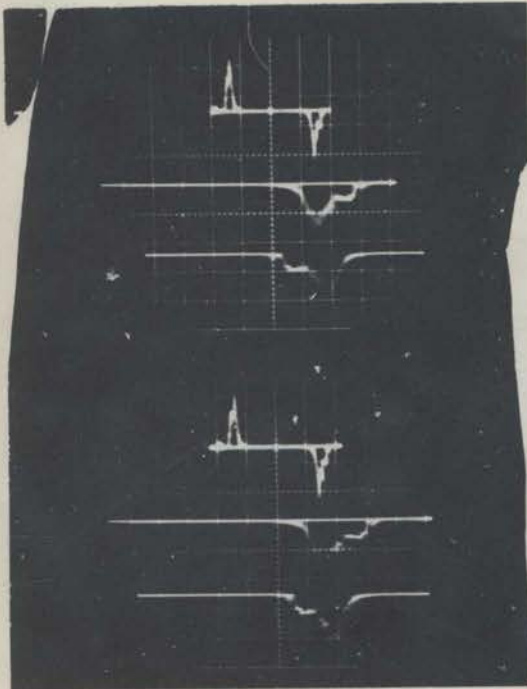
The traces shown are taken for various amplitudes of the applied AF field  $H_L = 4$  cm pp  
6  
8  
10  
15  
20  
in equivalent cm field units.

Frame 1: 1000 c/s WAVEFORMS  
Scales:  $\dot{m}$  50 mV/cm †  
H 1.27 oe/cm

Frame 2: 230 c/s WAVEFORMS  
Scales:  $\dot{m}$  10 mV/cm †  
H 1.27 oe/cm

† referred to the terminals of the sense coil of the MH plotter by the gain of 1000 c/s and 230 c/s respectively.

Fig. 4.62 230 c/s SWITCHING VOLTAGE WAVEFORMS ( $\dot{m}_L, H_L$ )  
AS A FUNCTION OF THE AMPLITUDE OF THE  
APPLIED FIELD  $H_L$  FOR FILM S2P17.



The traces shown are

- ( $\dot{m}_L, H_L$ ) Scales:  $\dot{m}$  20 mV/cm +  
H .63 oe/cm
- ( $\dot{m}_L, H_L$ ) Scales:  $\dot{m}$  20 mV/cm +  
H 0.25 oe/cm
- ( $\dot{m}_L, t$ ) Scales:  $\dot{m}$  20 mV/cm +  
t 100 sec/cm

taken for varying amplitudes of  
the applied field  $H_L$ .

Frame 1:  $H_L$  4 cm pp  
in equivalent cm field  
units\*

Frame 2:  $H_L$  4.5 cm pp  
in equivalent cm field  
units

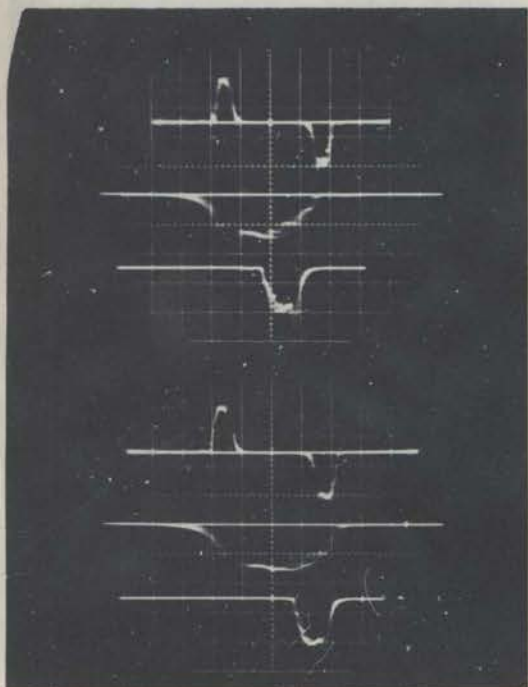
Frame 3:  $H_L$  5 cm pp  
in equivalent cm field  
units

Frame 4:  $H_L$  6 cm pp  
in equivalent cm field  
units

+ referred to the terminals of  
the sense coil of the MH plotter  
by the gain at 230 c/s.

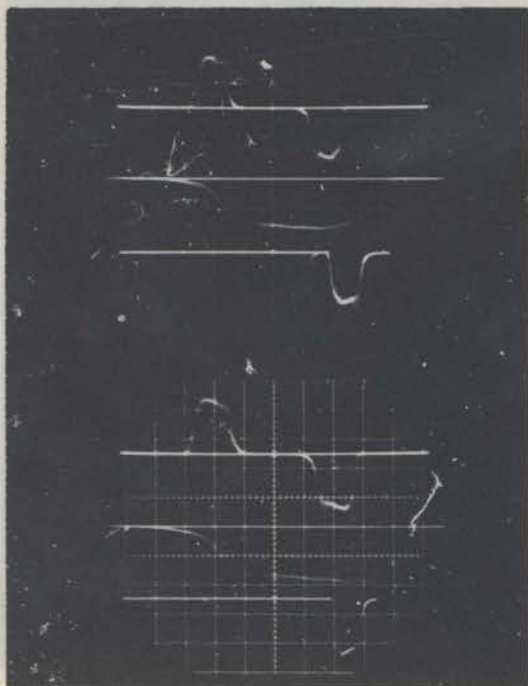
\* in terms of the scale of trace

Fig. 4.62 cont.



Frame 5:  $H_L$  8 cm pp  
in equivalent cm field  
units.

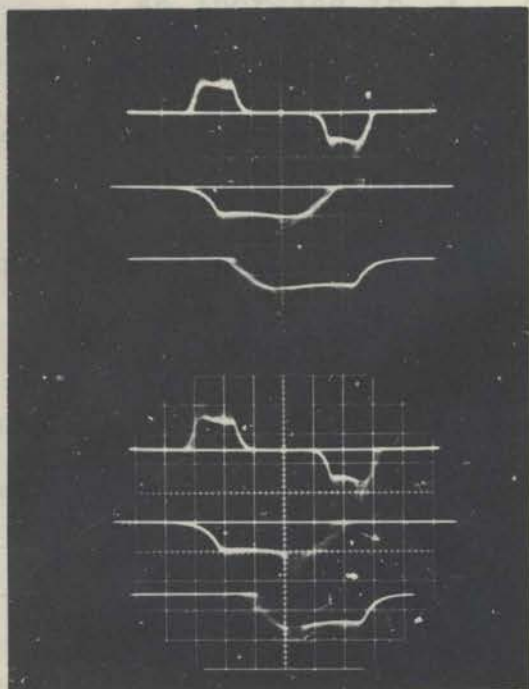
Frame 6:  $H_L$  10 cm pp  
in equivalent cm field  
units.



Frame 7:  $H_L$  15 cm pp  
in equivalent cm field  
units.

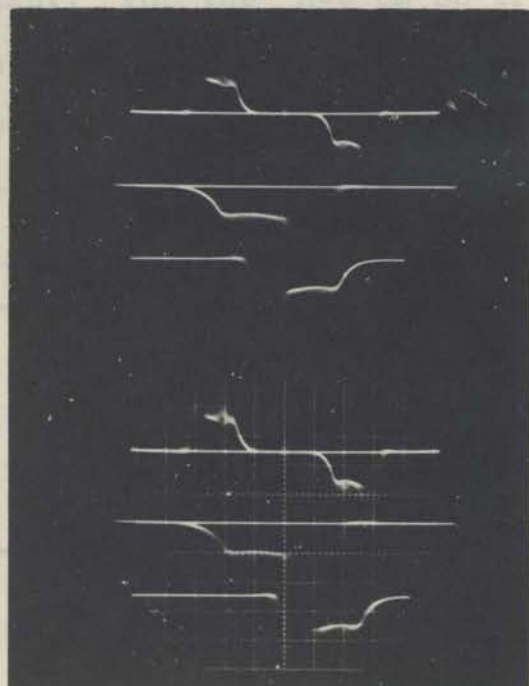
Frame 8:  $H_L$  20 cm pp  
in equivalent cm field  
units.

Fig. 4.62 cont.



Frame 9:  $H_L$  25 cm pp  
in equivalent cm field  
units.

Frame 10:  $H_L$  30 cm pp  
in equivalent cm field  
units.



Frame 11:  $H_L$  35 cm pp  
in equivalent cm field  
units.

Frame 12:  $H_L$  40 cm pp  
in equivalent cm field  
units.

then the initial linear rise may be explained by

- an increase in  $\ell_w$  due to a distribution of values of the critical field  $H_{sw}$  for the expansion of reverse nuclei (see Section 2.5), or

- more likely by an increase in  $v_w$  according to the Sixtus Tonks equation<sup>S1</sup> (see Section 2.5)

$$v_w = \theta(H-H') \quad (4.62)$$

The fall is due to the decrease in  $\ell_w$  as the reversal nears completion.

As  $H$  increases in Fig. 4.61a, the threshold field  $H'$  for the beginning of the reversal pulse is unchanged, but the pulse lengthens. The pulse height  $\frac{dm}{dt}$  is almost constant. For the  $H=5$  cm pp trace,  $\frac{dm}{dt}$  is constant for the duration of the pulse even though the field almost doubles over this interval. The pulse width  $\Delta H$  in field units increases roughly linearly with  $\frac{dH}{dt}$  while the width  $\Delta t$  in time units remains approximately constant\*.  $1/\Delta t$  has been

---

\* Constancy of  $\frac{dm}{dt}$  requires constancy of  $\Delta t$ , since

$$2.0 = \int \left(\frac{dm}{dt}\right) dt = \left(\frac{dm}{dt}\right) \int dt = \left(\frac{dm}{dt}\right) \Delta t$$


---

plotted against  $\frac{dH}{dt}$  in Fig. 4.63. From equation (4.61), if  $\frac{dm}{dt}$  is constant, the wall length-velocity product  $\ell_w v_w$  must also be constant.

It may be expected that  $\Delta H$  will have a minimum value of  $2H_D$ , where  $H_D = \pi^2 M_s \frac{t}{d}$  is the demagnetizing field of the film sample. For a 1 cm diameter, 1000 Å permalloy film,  $2H_D = 0.16$  oe. The experimental pulse width  $\Delta H$  is both larger than  $2H_D$  and varies with  $\frac{dH}{dt}$ . Also, as  $\Delta H$  varies, with  $\frac{dH}{dt}$ , the results cannot be explained by a variation in the threshold field over the film. Nor is it likely that  $\ell_w$  decreases. Examination of the  $(\frac{dm}{dt}, t)$  trace of Fig. 4.62 for  $H_C = 2.5$  cm pp shows that the plateau occurs when only a small fraction of the film has reversed. It is thus suggested that a limiting wall velocity  $v_{w \max}$  is reached.

The existence of a limiting velocity is in contradiction to the Sixtus Tonks equation and to numerous results for bulk materials. For permalloy thin films, Olmen and Mitchell<sup>01</sup> have reported a variation of wall velocity as  $v = v_0(T) \exp(8.8(H-H'))$  for very low velocities  $< 10^{-1}$  cm sec<sup>-1</sup>. Other workers<sup>F1, C1</sup> using pulsed field techniques, have reported agreement with the Sixtus Tonks equation over a range of switching times from 5 to 100 μsecs, of fields  $H-H'$  from 0.1 to ±1 oe and of wall velocities from 1500 to 15000 cm sec<sup>-1</sup>.

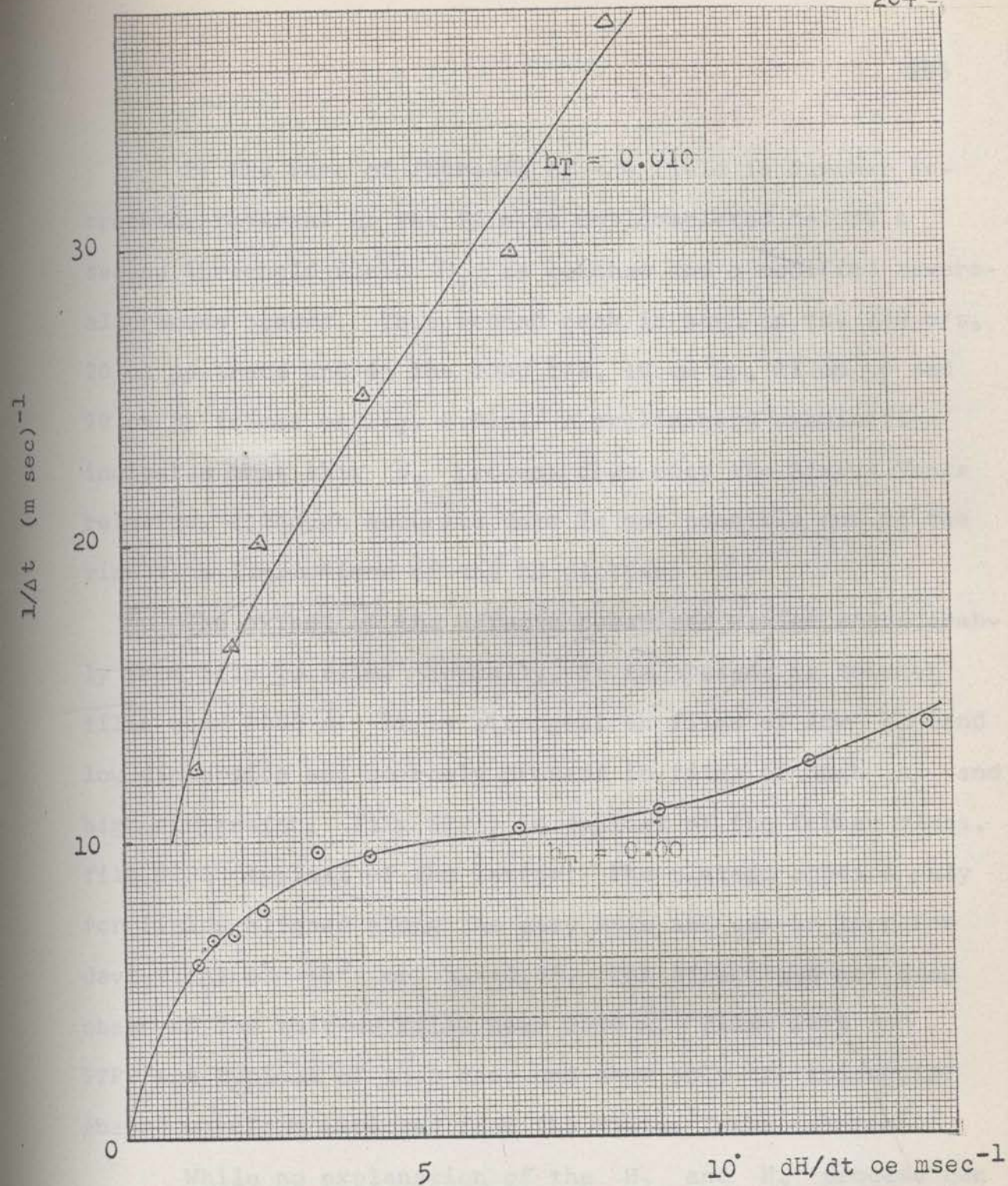


Fig. 4.63 Inverse Switching Time  $1/t$  as a Function of the Time Rate of Change of Field  $dH/dt$  at the Switching Point for Film S2P17



If the rate of increase of the field is further increased, reversal of the film is not completed before a second threshold field  $H_1$  is reached and a modified reversal process occurs. This second peak is seen in the 230 c/s, 20 cm pp trace and in the 1000 c/s, 10 cm pp, 15 cm pp and 20 cm pp traces of Fig. 4.61a. A preliminary examination indicates that this  $H_1$  process does obey the Sixtus Tonks relation, although accurate data is not possible due to the rise time limitations of the MH plotter.

The extent of the effects described varies considerably from film to film. Normally, it is present in thinner films near  $1000 \text{ \AA}$ . It is strongest in films of low  $h_c$  and low dispersion and scarcely present in films of high  $h_c$  and high dispersion. Film S2P17 is typical of the former class, film S2P18 typical of the latter. The plateau appears only for fields aligned along the easy axis and can be lost for deviations of  $\pm 3^\circ$  or  $h_T = \pm 0.05$ . The effect has not been observed for thicker films near  $3500 \text{ \AA}$ . Films S2P9 and S2P7 are typical of this case and show only the triangular shaped waveform expected from the Sixtus Tonks relation.

While no explanation of the  $H_1$  and  $H_2$  process can be given, the results do indicate a number of important points,

- Hysteresis loops as common measured by AF MH plotters

cannot be regarded as quasistatic. Examination of Figs. 4.23 and 4.24 show clearly the difference in shape and coercive force between 1000 c/s and 230 c/s loops for fields near the easy axis.

- It is suggested that the reversal process examined under static conditions, for example by the Bitter technique, may be modified for even AF switching. (Certainly, this is true for high speed nano-second switching as shown by the increasing approach to coherent rotational behaviour<sup>D1</sup>).

- If the reversal of a film requires a finite time for completion, then, necessarily, the coercive force  $H_C$  will depend on the field amplitude and frequency. Both of these should be specified in any measurement. Formally, if the rate of change of magnetization can be written as a function of the applied field  $H(t)$ , then

$$\frac{dm}{dt} = f(H(t)) \quad (4.63)$$

and the coercive force  $H_C$  is given from the equation

$$\begin{aligned} 1.0 = m - m(-\infty) &= \int_{t=-\infty}^{t_C} f(H(t)) dt \\ &= \int_{H=-\infty}^{H_C} \frac{f(H)}{\frac{dH}{dt}} \cdot dH \end{aligned} \quad (4.64)$$

If  $\frac{dH}{dt}$  may be taken as constant over the interval in which switching occurs, then

$$H_C = H' + (2.0 \frac{dH}{dt} \frac{l_w}{v_w})^{\frac{1}{2}} \quad (4.65)$$

for a film obeying the Sixtus Tonks law and

$$H_C = H' + \frac{\frac{dH}{dt}}{(l_w v_w)} \quad (4.66)$$

for a film for which the wall length-velocity product  $l_w v_w$  is constant above the threshold  $H'$ .

Data in the literature on the variation of the coercive force  $H_C$  with field amplitude is small. Smith<sup>S2</sup> gives photographed hysteresis loops showing a large change\*. A latter publication<sup>G1</sup> indicates that the apparent dependence of  $H_C$  may be due to a phase error in the field display. For a sinoidal field, phase error will give a variation of  $H_C$  identical in form to that of equation (4.66). However, the hysteresis loops of Figs. 4.23 and 4.24 are accurate to approximately 5 per cent, and the variation of pulse width shown in Fig. 4.61 is unambiguous.

---

\* The change in slope of the sides of the hysteresis loops given indicate a time dependence of the switching process.

---

## 4.7 LIST OF REFERENCES

- C1 Copeland, J.A., Humphrey, F.B.,  
"Flux Reversal by Néel Wall Motion".  
J.Appl.Phys.(Suppl.), 34, 1211, (1963).
- D1 Dietrich, W., Proebster, W.E., Wolf, P.,  
"Nanosecond Switching in Thin Magnetic Films".  
IBM J.Res.Developm., 4, 189, (1960).
- F1 Ford, N.C., Jr.,  
"Domain Wall Velocities in Thin Iron-Nickel Films".  
J.Appl.Phys., 31, 300S, (1960).
- G1 Goodenough, J.B., Smith, D.O.,  
"Magnetic Properties of Thin Films".  
"Magnetic Properties of Metals and Alloys".  
American Soc.Metals, Cleveland, (1958).
- M1 Methfessel, S., Middelhoek, S., Thomas, H.,  
"Domain Walls in Thin Ni-Fe Films".  
IBM J.Res.Developm., 4, 96, (1960).
- O1 Olmen, R.W., Mitchell, E.N.,  
"Slow Domain Wall Motion in Homogeneous Vacuum-  
Deposited Iron-Nickel Films".  
J.Appl.Phys.(Suppl.), 30, 258S, (1959).
- S1 Sixtus, K.J., Tonks, L.,  
"Propagation of Large Barkhausen Discontinuities".  
Part I, Phys.Rev., 37, 930, (1931).  
Part II, Phys.Rev., 42, 419, (1932).
- S2 Smith, D.O.,  
"Static and Dynamic Behaviour of Thin Permalloy Films".  
J.Appl.Phys., 29, 264, (1958).

CHAPTER 5  
MEASUREMENT OF TORQUE CURVES AND OF THE ANISOTROPY  
ENERGY FUNCTION OF THIN FILMS

5.1 INTRODUCTION

The following chapter presents in Section 5.4 a new method whereby torque curves and the anisotropy energy function  $\frac{\partial \epsilon}{\partial \phi}$  of a film may be determined to an accuracy of 0.1 per cent using an ordinary MH plotter\*. Such a method is particularly attractive, since mechanical torque balances of the sensitivity required for thin film measurements are not readily available, and are further costly, delicate and sensitive to vibration. For completeness Sections 5.2 and 5.3 give a brief review of previous film torque curve measurements and classifies these, according to the method used, into three basic groups.

---

\* The method of Section 5.4 extends to measurement of bulk samples. All that is required is a large saturating field (> 1000 oe) which may be deeply modulated. Such a field is possible with the magnet supply described in Appendix B.

---

In the past, some confusion has existed between the various ways in which the anisotropy energy can be determined. Doyle<sup>DI</sup> has found that different methods give significantly different answers. An attempt has been made in the present chapter to establish these measurements on a firmer footing by giving precise definitions of the quantities actually measured and by considering the departures of real films from the ideal Coherent Rotational (CR) model. Thus, Section 5.44 discusses the effects of anisotropy dispersion on the present torque curve measurements. It was originally hoped that the high accuracy of these torque measurements would allow  $H_K$  to be determined for increasing fields and that the resulting "approach to saturation" would give details of the anisotropy magnitude dispersion. However, experimentally, such is not the case; instead, an irreversible "ripple jump" phenomenon occurs. The high accuracy, however, does allow some interesting experimental torque curves to be obtained which show small but significant departures of the anisotropy energy function from the true uniaxial  $K\sin^2\phi$  form (see Section 5.46).

Section 5.5 discusses the difference between "initial" and "saturated" anisotropy measurements. Section 5.6 considers in some detail the effects of anisotropy dispersion

on the well known "initial" method of determining the anisotropy field  $H_{Ki}$  in which the initial reversible hard axis direction hysteresis loop is extrapolated to the saturation value. Experimental results for  $H_{Ki}$  for a number of films are compared with their anisotropy field values obtained from saturated torque curve measurements. Small differences are found which, while compatible with the theory presented, show no convincing correlation with dispersion measurements (by the Crowther technique<sup>C1</sup>), nor can values of dispersion be estimated from them. The results reflect the inadequacy of the models so far available (see Section 2.2) to describe the details of film behaviour.

## 5.2 BASIC METHODS OF MEASURING TORQUE CURVES

It is in principle possible to calculate the anisotropy torque  $\frac{\partial \epsilon}{\partial \phi}$  as a function of the angle  $\phi$  between the magnetization and the easy axis direction from the linear hysteresis curves. For example, if the film remains single domain, the hard direction hysteresis loop of  $m_T$  against  $H_T$  gives

$$\phi = \sin^{-1} m_T$$

$$\frac{\partial \epsilon}{\partial \phi} = (1 - m_T^2)^{\frac{1}{2}} H_T M \quad (5.21)$$

Using an audio frequency MH plotter, measurements can be made only at fields  $H_T$  less than the irreversibility limit  $H_r \approx 0.5 H_K$ , as the film then splits into a multi-domain state. With a VCS magnetometer (see Section 6.23),  $H_T$  can be taken to higher values, although a multi-domain state may still be expected for  $H_T$  near  $H_K$  due to anisotropy dispersion.

Such indirect determinations of  $\frac{\partial \epsilon}{\partial \phi}$  are of low accuracy. Further, interpretation is complicated by anisotropy dispersion and fixed and pseudo-rotatable anisotropy components. The basic MH plotter is thus unsuitable for a detailed examination of  $\frac{\partial \epsilon}{\partial \phi}$ . Torque curves can be accurately measured by the mechanical torque balance. As discussed, a balance of the sensitivity required for thin films is, however, rarely available, and is delicate and sensitive to vibration. Since the MH plotter is a relatively simple instrument, a number of variations of the basic design have been proposed for such torque measurements. The following section reviews three basic methods of torque curve measurement and discusses in particular their application to MH plotter type instruments.

Referring to Fig. 5.21,  $(H, \gamma)$  is an applied field and  $M$  has been rotated into the direction of  $\phi$  by the torque

$$T = \frac{\partial \epsilon}{\partial \phi} = MH \sin(\gamma - \phi) \quad (5.22)$$



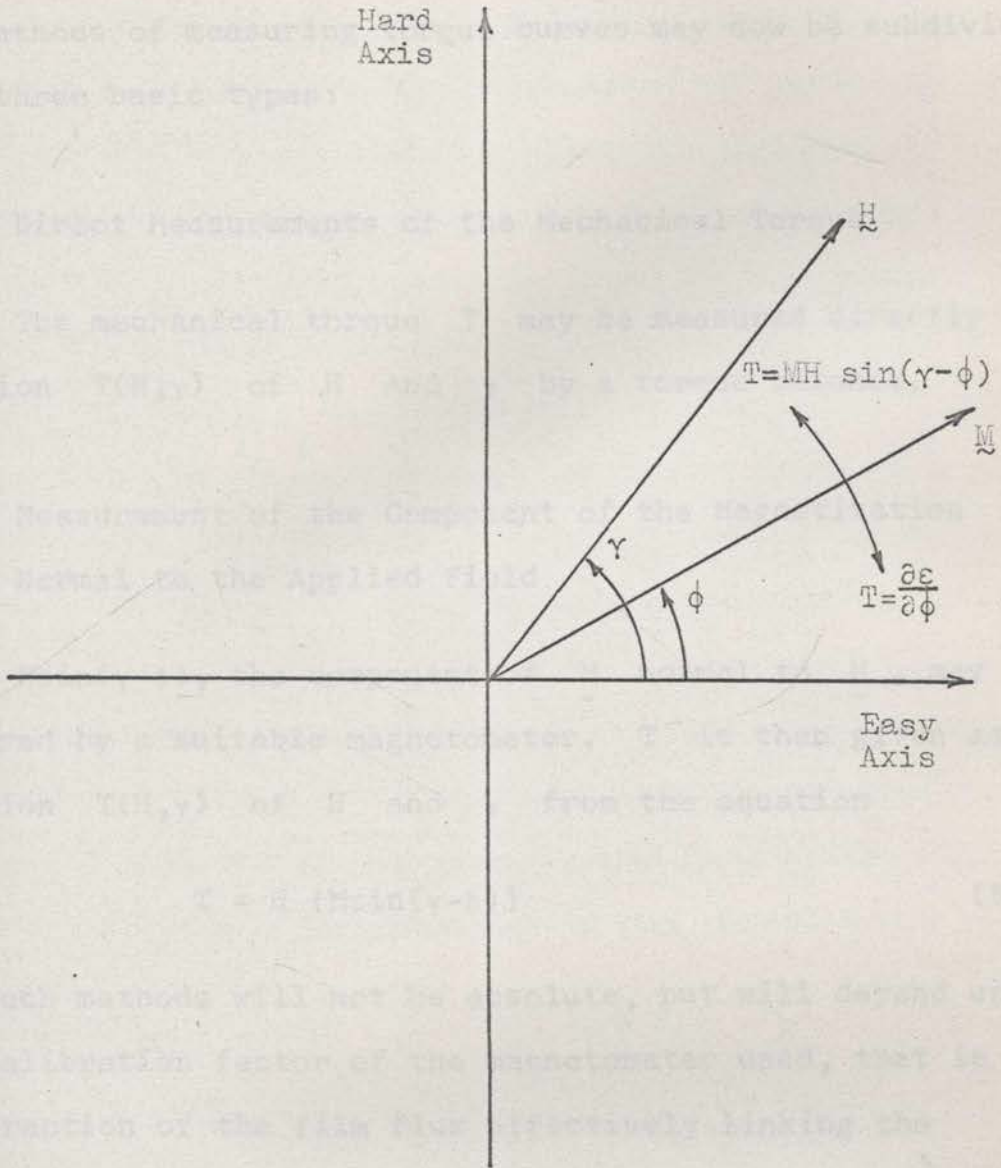


Fig. 5.21 Figure Illustrating the Torque Acting on the Magnetization.

The methods of measuring torque curves may now be subdivided into three basic types:

#### 5.21 Direct Measurements of the Mechanical Torque

The mechanical torque  $T$  may be measured directly as a function  $T(H, \gamma)$  of  $H$  and  $\gamma$  by a torque balance.

#### 5.22 Measurement of the Component of the Magnetization Normal to the Applied Field

$M \sin(\gamma - \phi)$ , the component of  $\underline{M}$  normal to  $\underline{H}$ , may be measured by a suitable magnetometer.  $T$  is then given as a function  $T(H, \gamma)$  of  $H$  and  $\gamma$  from the equation

$$T = H \{M \sin(\gamma - \phi)\} \quad (5.23)$$

All such methods will not be absolute, but will depend upon the calibration factor of the magnetometer used, that is upon the fraction of the film flux effectively linking the instrument.

If the static value of  $M \sin(\gamma - \phi)$  is measured, for example by a VCS magnetometer, torque curves of  $T(\gamma)$  against  $\gamma$  may be plotted which are identical to those of a torque balance. Alternatively, an MH plotter may be used by applying,

along the direction of  $(H, \gamma)$ , a field alternating from zero to saturation. The varying component of  $\underline{M}$  normal to  $(H, \gamma)$  can be detected by a suitable sense coil, the peak to peak amplitude of this signal being just  $M \sin(\gamma - \phi)$ . Low field or "initial" torque curves cannot be found by this method. As the film is alternately saturated in the direction  $\gamma$ , pseudo-rotatable anisotropy components will be eliminated. Collette<sup>C2</sup> has described an MH plotter type instrument overcoming this disadvantage. The sample is rotated at 200 c/s by an air turbine\*.  $M \sin(\gamma - \phi)$  is detected by a sense coil and displayed on an oscilloscope against the angle of rotation  $\gamma$ . In this case any isotropic component of  $T(\gamma)$  (that is a component independent of  $\gamma$  which hence produces no time variation of  $M \sin(\gamma - \phi)$ ) will not be detected. Assuming that the film obeys the CR model, the magnitude of the detected signal is

$$M \sin(\gamma - \phi) \Big|_{\max} = \frac{T_{\max}}{H} = M \quad \text{for } H \leq \frac{1}{2} H_K$$

$$= M \cdot \frac{1}{2} \frac{H_K}{H} \quad \text{for } H \geq \frac{1}{2} H_K$$

---

\* It is irrelevant whether the film is rotated as in Collette's instrument, or the field  $(H, \gamma)$  is rotated as in a torque balance.

---

Thus, for low fields the sensitivity is comparable to that of a normal MH plotter (or as discussed in Section 6.23, to that of a good torque balance). At high fields, the sensitivity decreases rapidly as  $1/H$ .

### 5.23 Measurement of the Angular Position of the Magnetization

The angular position  $\phi$  of  $M$  may be measured.  $T$  will then be given as a function  $T(H, \gamma)$  of  $H$  and  $\gamma$  or as a function  $T(H, \phi)$  of  $H$  and  $\phi$  from the equation

$$T = HM \sin(\gamma - \phi)$$

provided that  $M$  is known. For a real film with anisotropy dispersion,  $M$  in the general case will not be equal to the saturation value  $M_s$ , but will depend upon the applied field  $(H, \gamma)^*$ . The results are thus best expressed in terms of an equivalent field  $H_t$  defined by

$$T = H_t M = HM \sin(\gamma - \phi) \quad (5.24)$$

---

\* For permalloy films in which the anisotropy dispersion is small,  $M$  may be nearly equal to  $M_s$ . Experimental values of the easy direction remanence of a number of permalloy films are given in Table 4.22 and range from 0.90 to 0.98. For Ni films on the other hand,  $M \approx 0.65 M_s$ .

---

For an ideal film obeying the CR model,  $\epsilon = K \sin^2 \phi$  and  $M = M_S$  and the above definition gives:

$$H_t = \frac{1}{M_S} \cdot \frac{\partial^2 \epsilon}{\partial \phi^2} = H_{K_S} \sin \phi \cos \phi \quad (5.25)$$

where  $H_{K_S} = 2K/M_S$  is the saturated anisotropy field of the film.

The direction of  $\underline{M}$  may be determined by a number of methods, for example, by use of a VCS magnetometer, by RF methods<sup>B1</sup>, or by ferromagnetic resonance<sup>H1,S3</sup>. Rossing and Stolen<sup>R1</sup> have described an MH plotter type instrument using an AF "probe" field. All are equivalent. The method of Rossing and Stolen is closely related to the new method described in Section 5.4 and is hence discussed in some detail in the following section.

### 5.3 MEASUREMENT OF TORQUE CURVES BY DETERMINING THE ANGULAR POSITION OF THE MAGNETIZATION

#### THE METHOD OF ROSSING AND STOLEN

#### 5.31 A Description of the Method

The method of Rossing and Stolen<sup>R1</sup> is illustrated in Fig. 5.31.  $(H', \gamma)$  is a steady DC field.  $(H'', \theta)$  is an

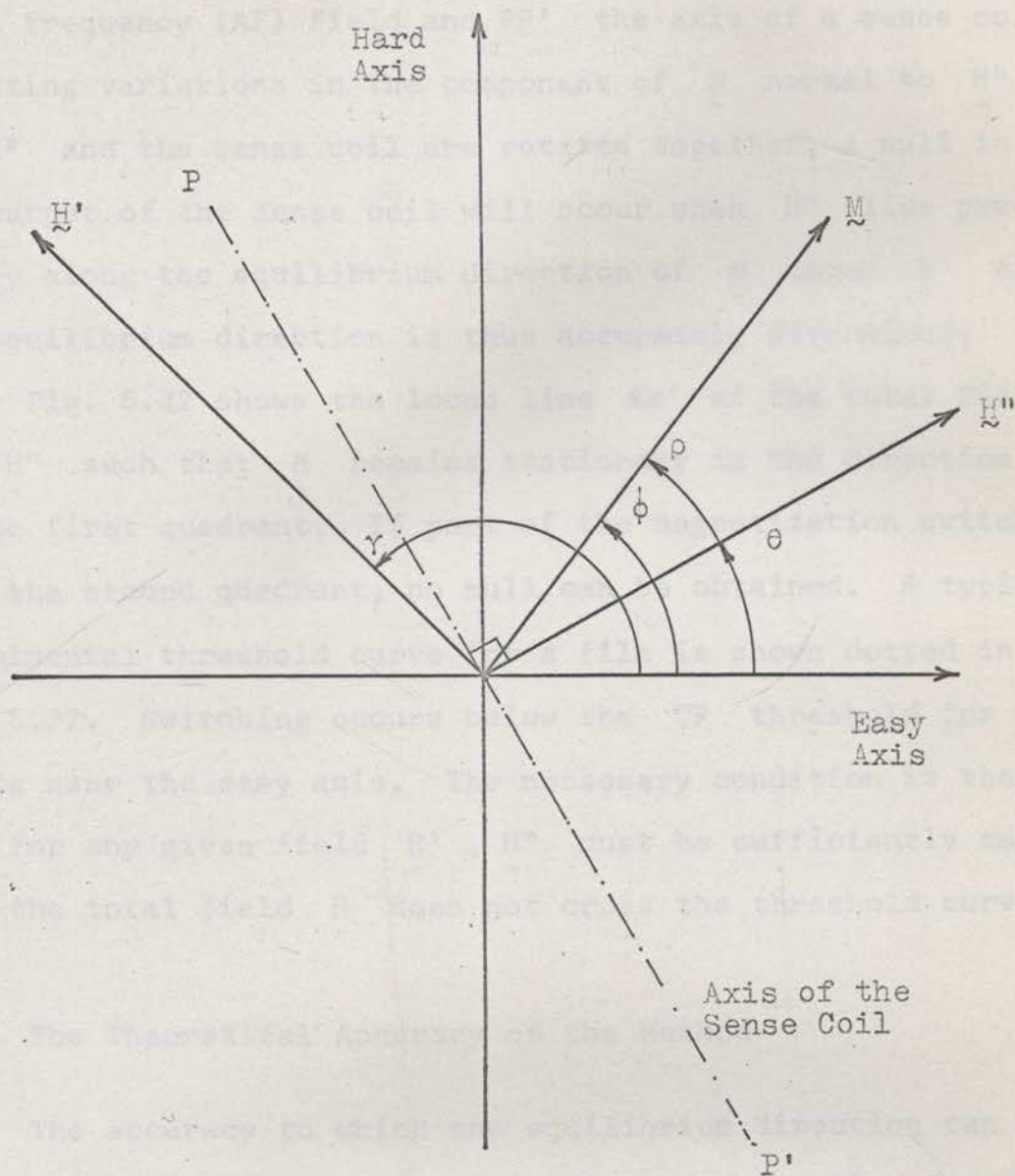


Fig. 5.31 The Method of Rossing and Stolen for Determining the Angular Position of the Magnetization.

audio frequency (AF) field and  $PP'$  the axis of a sense coil detecting variations in the component of  $\underline{M}$  normal to  $\underline{H}''$ . If  $\underline{H}''$  and the sense coil are rotated together, a null in the output of the sense coil will occur when  $\underline{H}''$  lies precisely along the equilibrium direction of  $\underline{M}$  under  $\underline{H}'$  alone. The equilibrium direction is thus accurately determined.

Fig. 5.32 shows the locus line  $xx'$  of the total field  $\underline{H} = \underline{H}' + \underline{H}''$  such that  $\underline{M}$  remains stationary in the direction  $\phi$  in the first quadrant. If part of the magnetization switches into the second quadrant, no null can be obtained. A typical experimental threshold curve for a film is shown dotted in Fig. 5.32. Switching occurs below the CR threshold for fields near the easy axis. The necessary condition is then that for any given field  $\underline{H}'$ ,  $\underline{H}''$  must be sufficiently small that the total field  $\underline{H}$  does not cross the threshold curve.

### 5.32 The Theoretical Accuracy of the Method

The accuracy to which the equilibrium direction can be found is determined by the sensitivity of the null. For the purposes of calculating the sensitivity, the film will be assumed to be ideal and to obey the CR model. Referring to Fig. 5.31,  $\phi$  is the direction of  $\underline{M}$  under the steady field  $(H', \gamma)$  and the small AF probe field  $(H'', \theta)$ . To first order

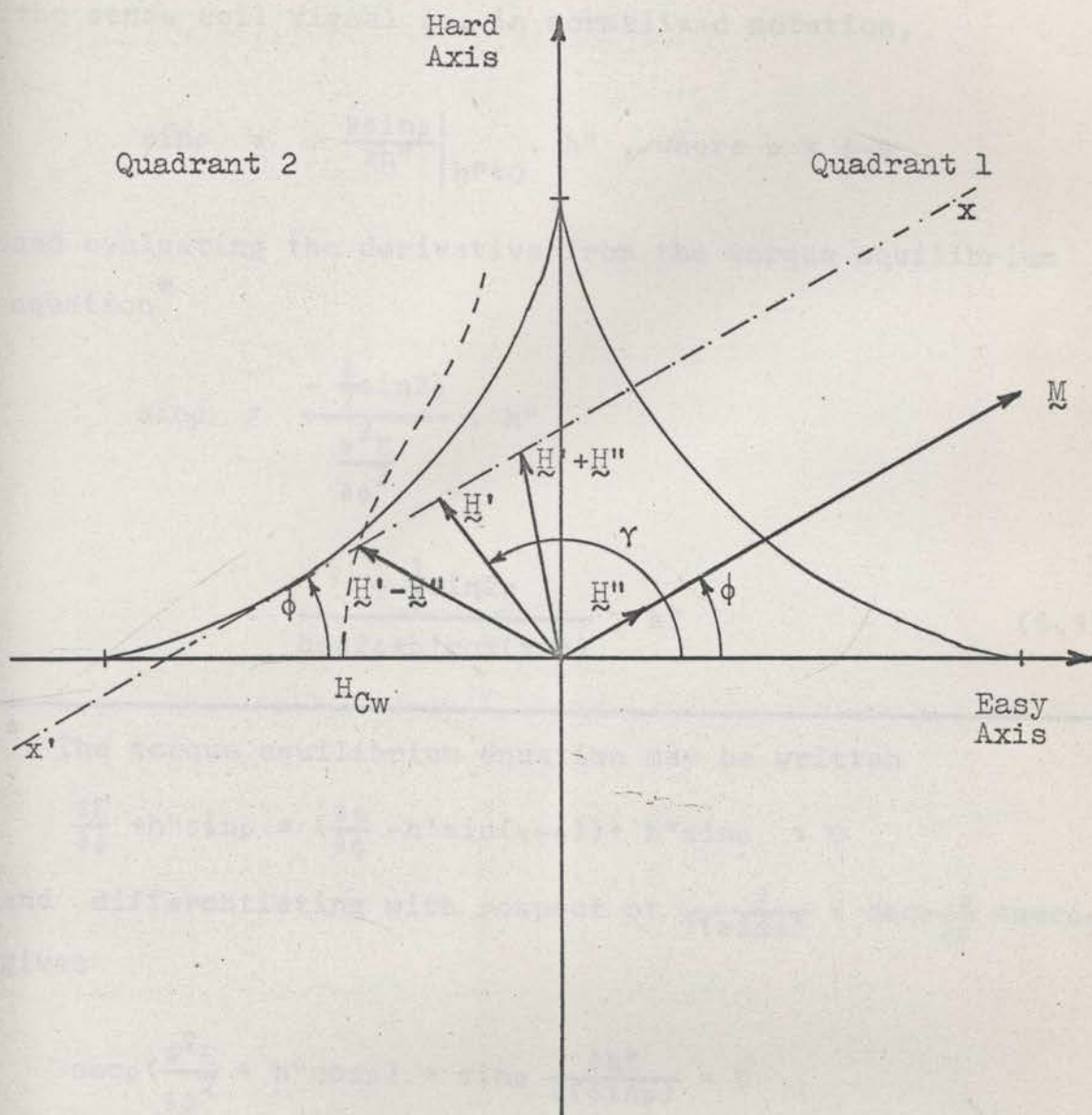


Fig. 5.32 Figure Illustrating Possible Irreversible Switching with the Method of Rossing and Stolen.



the sense coil signal is, in normalized notation,

$$\sin\rho = \left. \frac{\partial \sin\rho}{\partial h''} \right|_{h''=0} \cdot h'' , \text{ where } \rho = \phi - \theta \quad (5.32)$$

and evaluating the derivative from the torque equilibrium equation\*

$$\begin{aligned} \sin\rho &= \frac{-\frac{1}{2}\sin 2\rho}{\frac{\partial^2 E}{\partial \phi^2}} \cdot h'' \\ &= \frac{-\frac{1}{2}\sin 2\rho}{\cos 2\phi + h' \cos(\gamma - \phi)} \cdot h'' \end{aligned} \quad (5.31)$$

\* The torque equilibrium equation may be written

$$\frac{\partial E}{\partial \phi} + h'' \sin\rho = \left( \frac{\partial \epsilon}{\partial \phi} - h' \sin(\gamma - \phi) \right) + h'' \sin\rho = 0$$

and differentiating with respect to  $\frac{\partial}{\partial(\sin\rho)} = \sec\rho \frac{\partial}{\partial\rho} = \sec\rho \frac{\partial}{\partial\phi}$  gives

$$\sec\rho \left( \frac{\partial^2 E}{\partial \phi^2} + h'' \cos\rho \right) + \sin\rho \frac{\partial h''}{\partial(\sin\rho)} = 0$$

The null sensitivity  $Q$  is given by

$$Q = \left. \frac{\partial \sin \rho}{\partial \rho} \right|_{\rho=0} = \frac{h''}{\left. \frac{\partial^2 E}{\partial \phi^2} \right|_{\phi=\theta}} \quad (5.32)$$

If  $\frac{S}{N}$  is the signal to noise ratio of the MH plotter when measuring the full saturation flux, then  $d(\sin \rho)$  can be set zero to the order of  $1/\left(\frac{S}{N}\right)$ .

$$\therefore d\rho = \frac{d(\sin \rho)}{Q} = \frac{1}{Q\left(\frac{S}{N}\right)} \quad (5.33)$$

Since  $Q$  increases with  $h''$ , the most sensitivity condition is with  $h''$  as large as possible, provided that switching does not occur. For fields  $H'$  close to the critical curve,  $h''$  may be  $\pm 0.05$  with  $\frac{\partial^2 E}{\partial \phi^2} \div 0.5$  giving  $Q \div 0.1$ . For large fields  $H'$ ,  $Q \rightarrow h''/h'$ , and the sensitivity rapidly decreases if  $h''$  is maintained small. If  $h''$  is made large,  $Q$  may still be  $\pm 1$ . However, in this case the above small signal analysis is invalid. Further, it is more convenient to use a modified method which is described in detail in the following section.

## 5.4 MEASUREMENT OF HIGH FIELD TORQUE CURVES BY DETERMINING THE ANGULAR POSITION OF THE MAGNETIZATION

### 5.41 Introduction

Both the methods of Colette and of Rossing and Stolen are most suitable for low field torque curve studies. At high fields the sensitivity of Colette's method decreases as  $1/H$ , as also does the method of Rossing and Stolen if the probe signal  $H''$  is kept small.

This section describes a method, based on determining the position of  $\underline{M}$ , suitable for measuring high field torque curves. The method is similar in principle to that of Rossing and Stolen, but has the following advantages:

- An ordinary MH plotter is used. No additional rotating AF field is required. Further, in the method of Rossing and Stolen, the  $H'$  and  $H''$  field coils are not necessarily orthogonal and large AF currents may be induced in the  $H'$  coils, if special precautions are not taken (see Section 6.45).

- A large probe signal is used, giving a null sharpness factor  $Q$  of the order of unity for all fields. The sensitivity is thus comparable to that of the basic MH plotter.

- A direct and accurate reading of the anisotropy torque  $\frac{\partial \epsilon}{\partial \phi}$  may be obtained in terms of a DC field  $H'$  (that is in

terms of a DC current measurement). No calculation of  $\sin(\rho - \phi)$  is necessary.

-  $\frac{\partial \varepsilon}{\partial \phi}$  may be determined directly as a function of  $\phi$ .

#### 5.42 A Description of the Method

Referring to Fig. 5.41,  $(H'', \theta)$  is a field varying from  $H''_{\min}$  to  $H''_{\max}$ .  $H''$  may be produced by passing both a DC and an AC current through the same field coil.  $PP'$  is the axis of a sense coil detecting variations in the component of  $\underline{M}$  in the direction  $\frac{\pi}{2} + \theta$  normal to  $H''$ . If a static field  $H'$  is then applied in the direction  $\frac{\pi}{2} + \theta$ , a null in the output of the sense coil will occur when the equilibrium position of  $\underline{M}$  under  $H'$  lies in the direction of  $H''$ . If  $H''_{\max}$  is sufficiently large, then  $\rho$  will be zero for  $H'' = H''_{\max}$  regardless of  $H'$ . The null condition is then that  $\rho$  be zero for  $H'' = H''_{\min}$  also.

That is

$$\rho = 0 \text{ evaluated at } H'' = H''_{\min} \quad (5.41)$$

which, from the torque equilibrium equation, requires,

$$H'_n(\theta)M = \frac{\partial \varepsilon}{\partial \phi} \Big|_{\phi = \theta} \text{ evaluated at } H'' = H''_{\min} \quad (5.42)$$

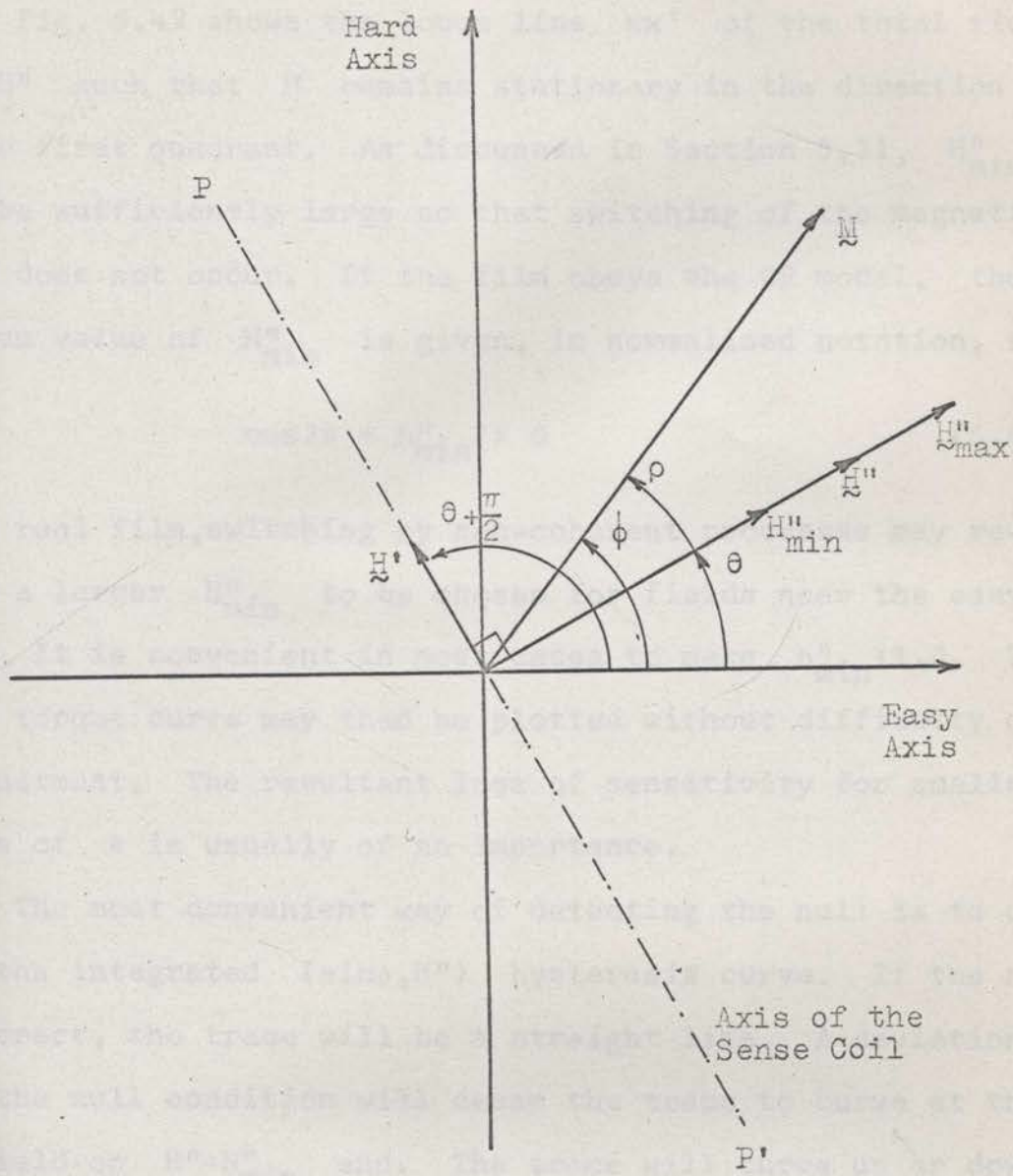


Fig. 5.41 A Method for Determining the Angular Position of the Magnetization.

Fig. 5.42 shows the locus line  $xx'$  of the total field  $H = H' + H''$  such that  $M$  remains stationary in the direction  $\phi$  in the first quadrant. As discussed in Section 5.31,  $H''_{\min}$  must be sufficiently large so that switching of the magnetization does not occur. If the film obeys the CR model, the minimum value of  $H''_{\min}$  is given, in normalized notation, by

$$\cos 2\theta + h''_{\min} = 0 \quad (5.43)$$

For a real film, switching by non-coherent processes may require a larger  $H''_{\min}$  to be chosen for fields near the easy axis. It is convenient in most cases to make  $h''_{\min} \doteq 1.0$ . The whole torque curve may then be plotted without difficulty or readjustment. The resultant loss of sensitivity for smaller values of  $\theta$  is usually of no importance.

The most convenient way of detecting the null is to display the integrated  $(\sin\phi, H'')$  hysteresis curve. If the null is correct, the trace will be a straight line. A deviation from the null condition will cause the trace to curve at the low field or  $H'' = H''_{\min}$  end. The trace will curve up or down depending on the sign of the error. Curvature of a straight line in this manner is very readily apparent even in the presence of considerable noise. Traces taken experimentally for a typical 1000 Å permalloy film are shown in Fig. 5.43

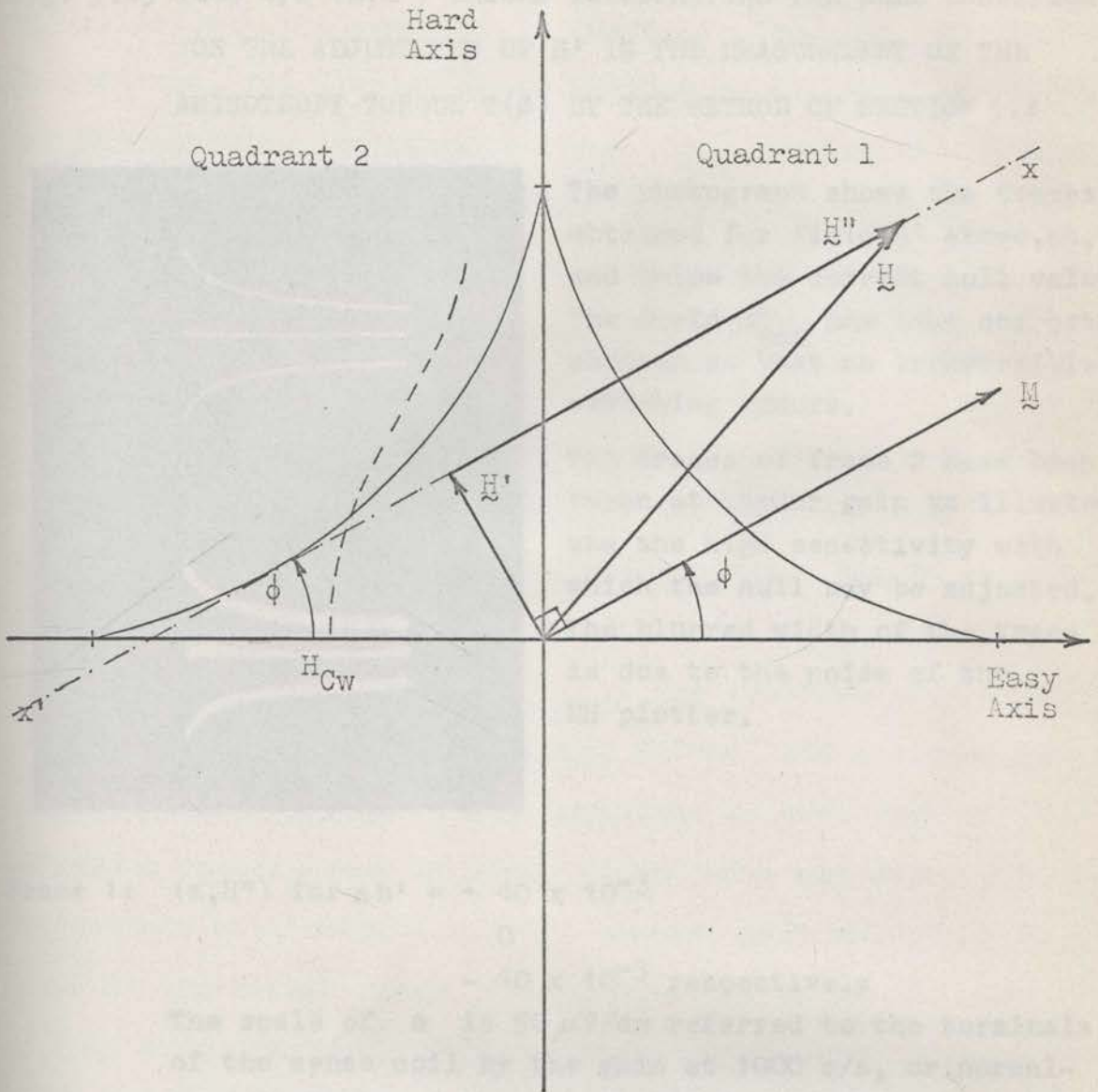


Fig. 5.42 Figure Illustrating Possible Irreversible Switching.

Fig. 5.43 1000 c/s ( $m, H''$ ) TRACES ILLUSTRATING THE NULL CONDITION FOR THE ADJUSTMENT OF  $H'$  IN THE MEASUREMENT OF THE ANISOTROPY TORQUE  $T(\theta)$  BY THE METHOD OF SECTION 5.4



The photograph shows the traces obtained for field  $H'$  above, at, and below the correct null value. The field  $H''_{\min}$  has been correctly chosen so that no irreversible switching occurs.

The traces of frame 2 have been taken at higher gain to illustrate the high sensitivity with which the null may be adjusted. The blurred width of the trace is due to the noise of the MH plotter.

Frame 1: ( $m, H''$ ) for  $\Delta h' = + 40 \times 10^{-3}$

0

-  $40 \times 10^{-3}$  respectively

The scale of  $m$  is  $50 \mu\text{V}/\text{cm}$  referred to the terminals of the sense coil by the gain at 1000 c/s, or normalised in terms of the saturation magnetisation of the film,  $17 \times 10^{-3}$  parts/cm.

Frame 2: ( $m, H''$ ) for  $\Delta h' = + 7.5 \times 10^{-3}$

0

-  $7.5 \times 10^{-3}$  respectively

The scale of  $m$  is  $10 \mu\text{V}/\text{cm}$  or  $3.4 \times 10^{-3}$  parts/cm.

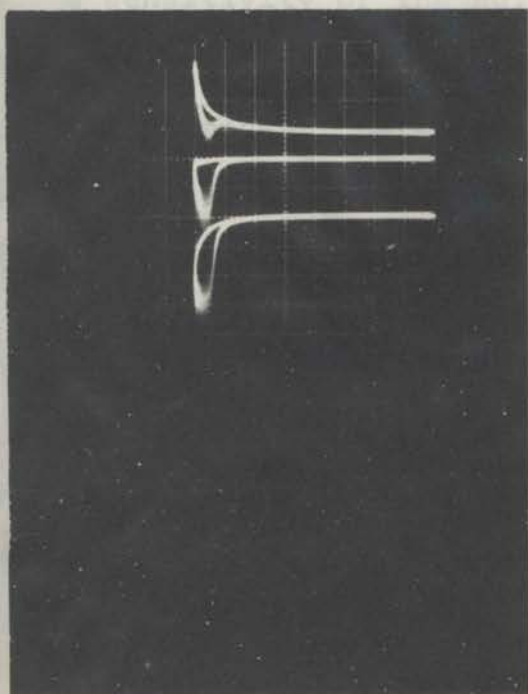
Data: Film S2P17, thickness  $1000 \text{ \AA}$ ,  $H_{K\text{torque}}$  3.49 oe,  $h''_{\min} = 1.0$ ,  $h''_{\max} = 8.3$  and  $H''$  is in the direction  $\theta = 45^\circ$



and illustrate the accuracy to which the null can be adjusted. In addition, the display shows whether or not partial switching is occurring and hence whether  $H''_{\min}$  satisfies the conditions discussed in the previous paragraph. Experimental traces showing the onset of switching are given in Fig. 5.44.

It is also possible to detect the null from the unintegrated output using a suitable synchronous phase sensitive detector. However, the most convenient way is rather to first integrate and display the signal as before. A check is thus provided that switching is not taking place. The DC restorer of the MH plotter itself can then be used to synchronously DC restore the trace at  $H''=H''_{\max}$ . The restorer output is passed through a suitable low pass filter, and a signed DC error signal obtained. It is important to note that if switching occurs, zero DC error signal will not correspond to the correct null condition. The correct null condition is shown in the second trace of Fig. 5.44 and it can be seen that it does not have equal positive and negative areas above and below the straight line section of the trace. The method is capable of very high sensitivity depending on the narrowness of the bandwidth used. Further, automatic balancing is easily arranged by a simple feedback control of  $H'$ , if this is desired.

Fig. 5.44 1000 c/s ( $m, H''$ ) TRACES ILLUSTRATING THE NULL CONDITION FOR THE ADJUSTMENT OF  $H'$  IN THE MEASUREMENT OF THE ANISOTROPY TORQUE  $T(\theta)$  BY THE METHOD OF SECTION 5.4



The photograph shows the traces obtained for fields  $H'$  above, at, and below the correct null value when the field  $H''_{\min}$  is incorrectly chosen. The occurrence of irreversible switching is clearly seen.

Frame 1: ( $m, H''$ ) for  $h' = + 6 \times 10^{-3}$

0

The torque equilibrium -  $12 \times 10^{-3}$  respectively

The scale of  $m$  is  $50 \mu\text{V}/\text{cm}$  referred to the terminals of the sense coil by the gain at 1000 c/s, or normalised in terms of the saturation magnetisation of the film,  $17 \times 10^{-3}$  parts/cm.

Data: Film S2P17, thickness  $1000 \text{ \AA}$ ,  $H_{K_{\text{torque}}}^0$  3.49 oe,  $h''_{\min} = 0.2$ ,  $h''_{\max} = 7.5$  and  $H''$  is in the direction  $\theta = 45^\circ$ .

## 5.43 The Theoretical Accuracy of the Method

The accuracy to which  $H'$  can be adjusted is determined by the sensitivity of the null. For the purpose of calculating the sensitivity, the film will be assumed to be ideal and to obey the CR model. Referring to Fig. 5.41, the sense coil signal, in normalized notation, will be  $\sin\rho$  evaluated at  $h''=h''_{\min}$  and the null sensitivity is hence

$$Q = \left. \frac{\partial(\sin\rho)}{\frac{\partial h'}{h'}} \right|_{\rho=0, h''=h''_{\min}}$$

Evaluating the derivative from the torque equilibrium equation\*,

$$\begin{aligned} Q &= \frac{h'_n}{\left. \frac{\partial^2 E}{\partial \phi^2} \right|_{\phi=\theta, h''=h''_{\min}}} & (5.44) \\ &= \frac{h'_n}{\cos 2\theta + h''_{\min}} \end{aligned}$$

\* The torque equilibrium equation may be written

$$\frac{\partial E}{\partial \phi} - h' \cos \rho = \left( \frac{\partial \epsilon}{\partial \phi} + h'' \sin \rho \right) - h' \cos \rho = 0$$

and differentiating with respect to

$$\frac{\partial}{(\sin \rho)} = \sec \rho \frac{\partial}{\partial \rho} = \sec \rho \frac{\partial}{\partial \rho}$$

gives

$$\sec \rho \left( \frac{\partial^2 E}{\partial \phi^2} + h'' \sin \rho \right) - \cos \rho \frac{\partial h'}{\partial (\sin \rho)} = 0$$

As in Section 5.32, if  $\frac{S}{N}$  is the signal to noise ratio of the MH plotter when measuring the full saturation flux, then  $d(\sin\rho)$  can be made zero to the order of  $1/(\frac{S}{N})$ .

Therefore,

$$\frac{dh'_n}{h'_n} = \frac{d(\sin\rho)}{Q} = \frac{1}{Q(\frac{S}{N})} \quad (5.45)$$

Experimental measurements of the error signal  $d(\sin\rho)$  caused by deliberately introduced deviations  $dh'_n$  from the null condition have been plotted in Fig. 5.45 for film S2P17 at  $h''_{\min} \pm 1.0$ . The slope of the lines  $d(\sin\rho)/dh'_n = Q/h'_n$  agrees very closely with the theoretical result of equation (5.44).

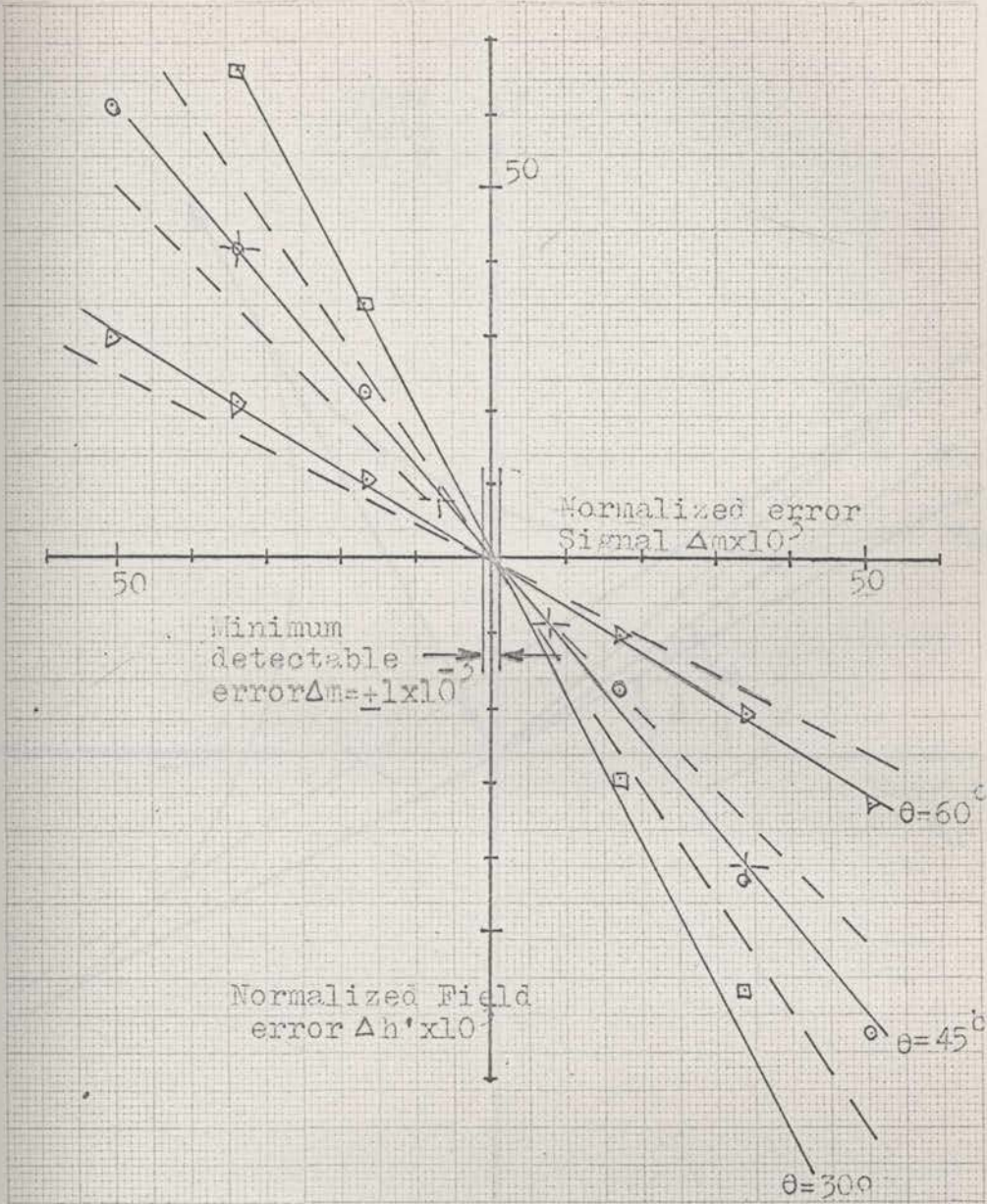
If the film has rotatable anisotropy properties, the expression for the sensitivity is slightly modified. Referring to Fig. 5.46, suppose the film has a fixed anisotropy  $K_u$  along the  $x$ -axis and also a rotatable anisotropy  $K_r$  which will be established in the direction of saturation of the film, that is in the direction  $\theta$ . Then the total anisotropy will be (see Section 2.41)

$$K \sin^2(\phi - \beta)$$

where

$$K^2 = K_u^2 + K_r^2 + 2K_u K_r \cos 2\theta$$

and



Experimental curves ,ratio of slopes 31: 60: 95

Theoretical curves ,ratio of slopes 0.5: 1: 1.5

Data of film S2P17, at  $h''_{\min} = 1.0$ ,  $h''_{\max} = 8.3$

Fig. 5.45 The Variation of the Normalized Error Signal  $\Delta m$  with the Deviation  $\Delta h'$  from the Null Value.

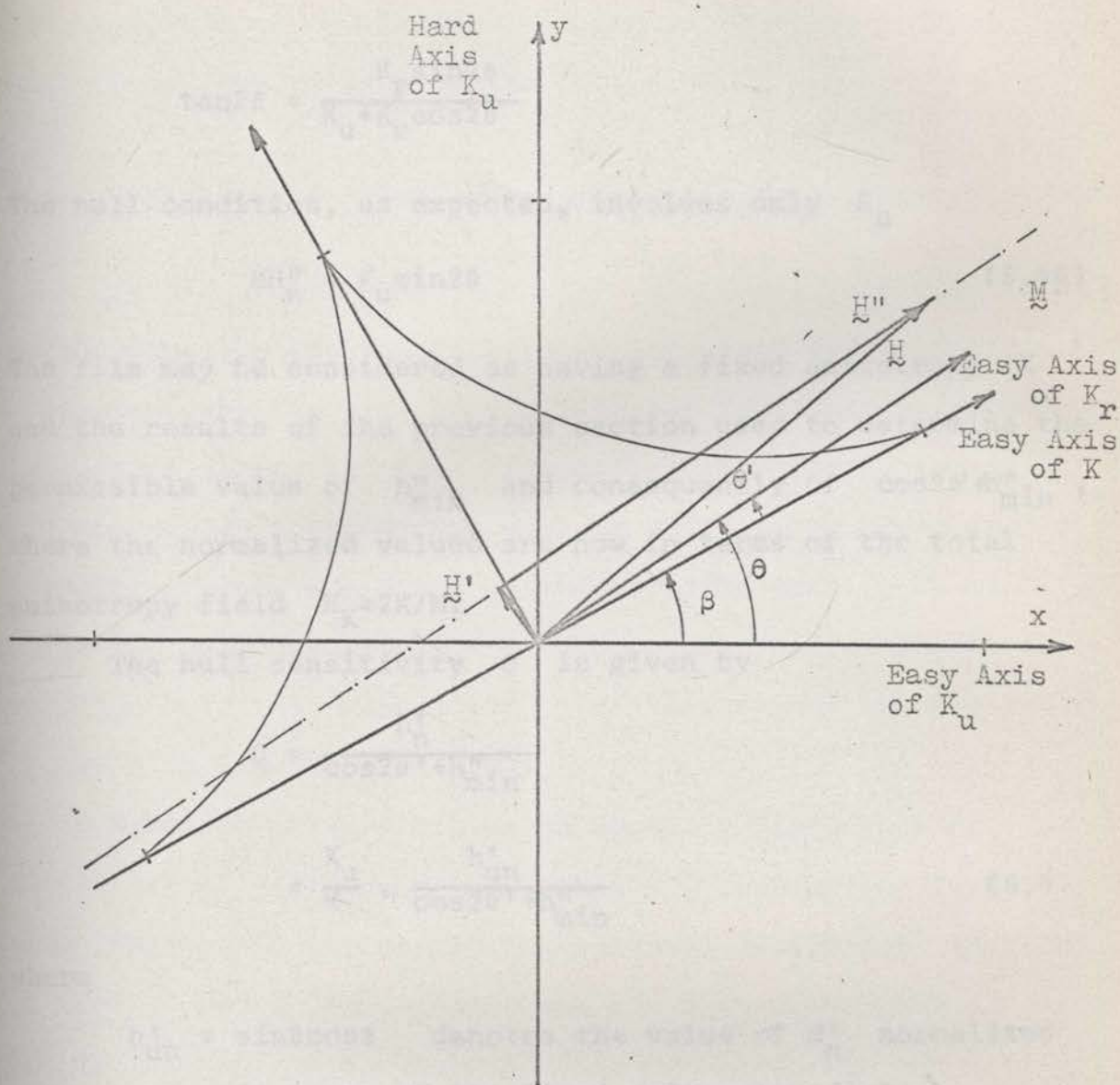


Fig. 5.46 The Null Condition for Films having Pseudo-rotatable Anisotropy.

$$\tan 2\beta = \frac{K_r \sin 2\theta}{K_u + K_r \cos 2\theta}$$

The null condition, as expected, involves only  $K_u$

$$MH_n'' = K_u \sin 2\theta \quad (5.46)$$

The film may be considered as having a fixed anisotropy  $K$  and the results of the previous section used to determine the permissible value of  $h_{\min}''$  and consequently of  $\cos 2\theta' + h_{\min}''$ , where the normalized values are now in terms of the total anisotropy field  $H_K = 2K/M$ .

The null sensitivity  $Q$  is given by

$$Q = \frac{h_n'}{\cos 2\theta' + h_{\min}''}$$

$$= \frac{K_u}{K} \cdot \frac{h_{un}'}{\cos 2\theta' + h_{\min}''} \quad (5.47)$$

where

$h_{un}' = \sin\theta \cos\theta$  denotes the value of  $H_n'$  normalized in terms of the fixed anisotropy field

$$H_{Ku} = 2K_u/M \text{ only.}$$

If  $K \gg K_u$ , then  $\theta' \rightarrow 0$  and

$$Q \div \frac{K_u}{K} \cdot \frac{h_{un}'}{1 + h_{\min}''}$$

The magnitude of  $Q$  is thus similar to that for a fixed anisotropy, but reduced by the factor  $K_u/K$ .

#### 5.44 A Discussion of the Null Condition for Real Films

In the general case,  $M$  and  $\frac{\partial \epsilon}{\partial \phi}$  for a real film will depend upon the applied fields and upon the past magnetic history of the sample. If the film has rotatable anisotropy properties, then, if  $H''_{\max}$  is sufficiently large, the axis of the rotatable anisotropy will be established along the  $\theta$  direction. Only the fixed anisotropy component  $\frac{\partial \epsilon_u}{\partial \phi}$  will enter the null equation. The torque curve measured will correspond to the "high field" or "saturated" torque curve of the film (see Section 2.8).

Equation (5.42) implies an implicit dependence of  $H'_n(\theta)$  on  $H''_{\min}$  through the factors  $M$  and  $\frac{\partial \epsilon}{\partial \phi}$ . It is thus simplest to express an experimental measurement in terms of  $H'_n(\theta)$  and to state the value of  $H''_{\min}$  used. It is also possible to define a saturated "torque" field by

$$H'_{ns}(\theta) = \lim_{H''_{\min} \rightarrow \infty} H'_n(\theta) \quad (5.48)$$

where

$H'_{ns}(\theta)$  is then independent of the conditions of measurement.



For an ideal film obeying the CR model,  $\epsilon = K \sin^2 \phi$  and  $M = M_s$ . Equation (5.42) reduces to

$$H'_n(\theta) = H_{Ks} \sin \phi \cos \phi, \quad \text{where } H_{Ks} = \frac{2K}{M_s}$$

The dependence of  $H'_n(\theta)$  on  $H''_{\min}$  for a real film is of interest, both in relating the measured torque curve to the saturated curve through equation (5.48) and as a possible means of measuring the anisotropy dispersion. For a film obeying the Independent Region (IR) model of Section 2.2 we may derive an expression for  $H'_n$  in terms of  $H''_{\min}$  and the normalized standard deviations  $\sigma_K$  and  $\sigma_\beta$  of the anisotropy distribution.

The behaviour of  $H'_n$  for the special case of  $\theta = \frac{\pi}{4}$  is typical of the general behaviour for any  $\theta$ . In view of the simpler resulting expressions and the importance of this case in measuring the anisotropy field  $H_K$  (see Section 5.46) only  $\theta = \frac{\pi}{4}$  will be considered here.

Thus, for  $\theta = \frac{\pi}{4}$ , referring to Fig. 5.47, the torque equilibrium equation for a typical region  $(H_K, \beta)$  may be written

$$H_K \sin\left(\frac{\pi}{4} + \rho + \beta\right) \cos\left(\frac{\pi}{4} + \rho + \beta\right) + H'' \sin \rho - H' \cos \rho = 0$$

giving

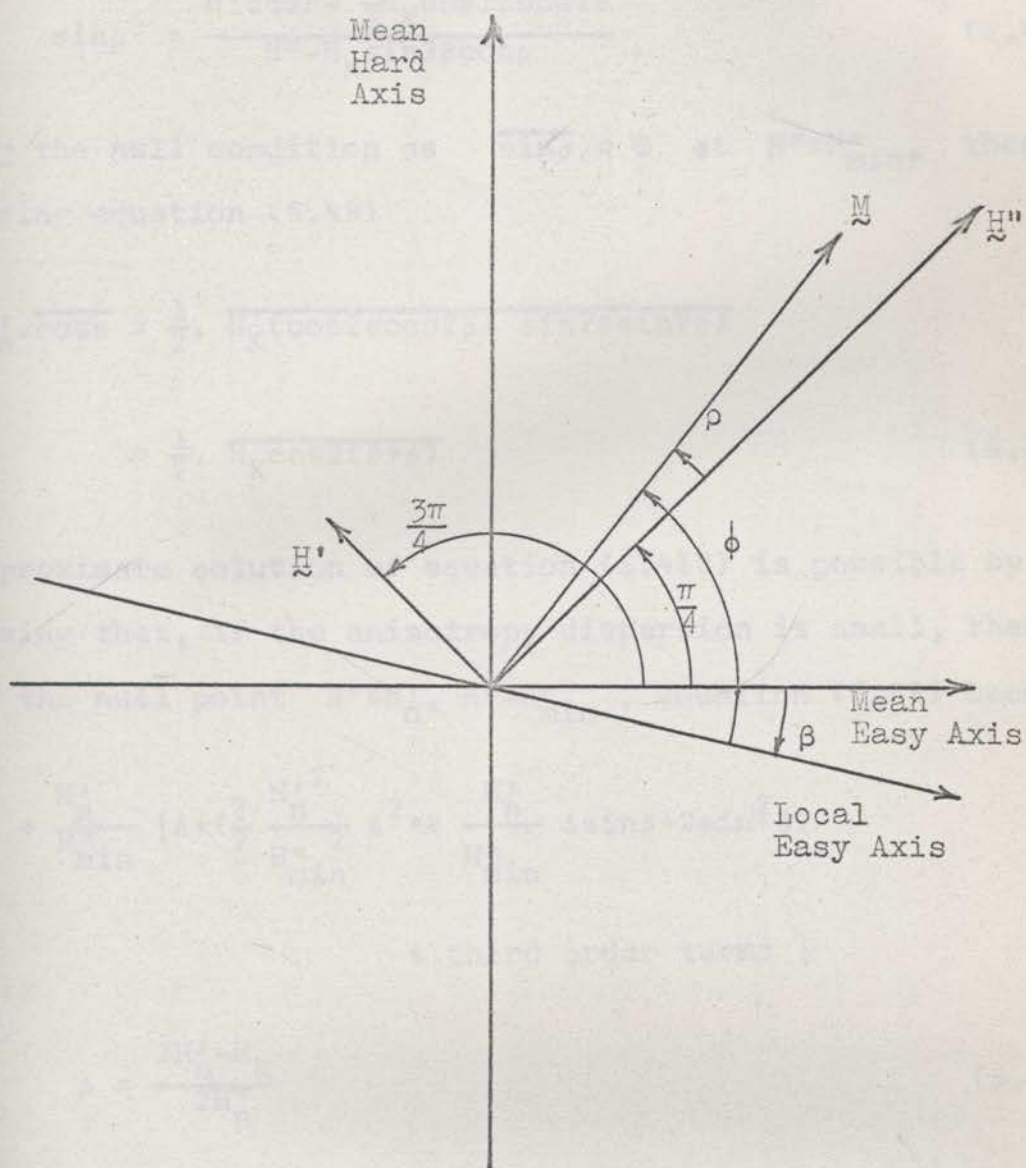


Fig. 5.47 Figure Illustrating the Effects of Anisotropy Dispersion.

$$\sin \rho = \frac{H' \cos \rho - \frac{1}{2} H_K \cos 2\beta \cos 2\rho}{H'' - H_K \sin 2\beta \cos \rho} \quad (5.49)$$

Taking the null condition as  $\overline{\sin \rho} = 0$  at  $H'' = H''_{\min}$ , then averaging equation (5.49)

$$\begin{aligned} H'_n \overline{\cos \rho} &= \frac{1}{2} \cdot \overline{H_K (\cos 2\beta \cos 2\rho - \sin 2\beta \sin 2\rho)} \\ &= \frac{1}{2} \cdot \overline{H_K \cos 2(\beta + \rho)} \end{aligned} \quad (5.410)$$

An approximate solution of equation (5.410) is possible by observing that, if the anisotropy dispersion is small, then about the null point  $H' = H'_n$ ,  $H'' = H''_{\min}$ , equation (5.49) becomes

$$\begin{aligned} \sin \rho &= \frac{H'_n}{H''_{\min}} \left\{ \Delta + \left( \frac{3}{2} \frac{H_n'^2}{H''_{\min}} \Delta^2 + 4 \frac{H'_n}{H''_{\min}} \Delta \sin \beta + 2 \sin^2 \beta \right) \right. \\ &\quad \left. + \text{third order terms} \right\} \end{aligned} \quad (5.411)$$

where

$$\Delta = \frac{2H'_n - H_K}{2H'_n} \quad (5.411)$$

Thus,  $\sin \rho$  is independent of  $\beta$  to first order. If the  $H_K$  and  $\beta$  distribution are independent and  $\overline{\sin 2\beta} = 0$ , then equation (5.410) reduces to

$$H'_n \overline{\cos \rho} = \frac{1}{2} \cdot \overline{H_K \cos 2\rho} \cdot \overline{\cos 2\beta}$$

$\cos\rho$  and  $H_K \cos 2\rho$  may be evaluated in terms of  $\Delta$  and  $\beta$  from equation (5.411). Taking the average values and performing the division

$$\frac{\overline{H_K \cos 2\rho}}{\overline{\cos\rho}} = \overline{H_K} \left( 1 - \frac{3}{2} \frac{H_n'^2}{H_{\min}''^2} \sigma_K^2 \right)$$

where

$\sigma_K$  is the normalized standard deviation of  $H_K$ .

The approximation is correct to the fourth order in  $\Delta$  and  $\beta$ .

Hence

$$\begin{aligned} H_n'(\theta = \frac{\pi}{4}) &= \frac{1}{2} \cdot \overline{H_K \cos 2\beta} \cdot \left( 1 - \frac{3}{2} \frac{H_n'^2}{H_{\min}''^2} \sigma_K^2 \right) \\ &= \frac{1}{2} H_{Ks} \left( 1 - \frac{3}{2} \frac{H_n'^2}{H_{\min}''^2} \sigma_K^2 \right) \end{aligned} \quad (5.412)$$

Finally, the value of  $\overline{\sin\rho}$  as a function of  $H''$  for the null value of  $H_n'$  given by (5.412), may be obtained by replacing  $H_{\min}''$  by  $H''$  in (5.411), then substituting (5.412) into the resulting equation and averaging

$$\overline{\sin\rho} = - \frac{3}{2} \frac{H_n'^3}{H_{\min}''^2 H''} \left( 1 - \frac{H_{\min}''^2}{H''^2} \right) \sigma_K^2$$

which has a minimum value of

$$\overline{\sin\phi}_{\max} = \frac{1}{\sqrt{3}} \cdot \frac{H'_n{}^3}{H''_{\min}{}^3} \cdot \sigma_K^2 \text{ occurring at } H'' = \sqrt{3}H''_{\min} \quad (5.413)$$

Attempts to experimentally verify equations (5.412) and (5.413) for permalloy films have not been successful\*. For example, the  $(\sin\phi, H'')$  trace shown in Fig. 5.43 for film S2P17 is, at the correct null condition, very close to a straight line. Any curvature is less than 1 part in  $10^3$  at  $h''_{\min} = 1.0$ , that is  $H'_n/H''_{\min} = 0.5$ . From equation (5.413) then

$$\sigma_K < 0.11$$

Further measurements on film S2P17 have, in fact, shown that curvature of the trace is less than 1 part in  $10^3$  down to  $h''_{\min} = 0.65$  giving

$$\sigma_K < 0.03$$

When at lower fields the trace does depart from a straight line, the reversible curvature predicted by the previous model is not observed. Rather a hysteresis effect occurs. An open hysteresis loop similar to those shown in Fig. 5.44 is observed down to the smallest detectable signal.

---

\* The effect should be larger in Ni films. However, none were available.

---

The normalized amplitude of the hysteresis loop  $m'$ , is shown as a function of  $h''_{\min}$  for four film samples in Fig. 5.48.

The cause of the hysteresis effect is not understood in detail. There are, however, several features of the behaviour which may be noted.

The curves of Fig. 5.48 show two regions. At high fields  $h''_{\min}$  there is a long exponential tail. As  $h''_{\min}$  is decreased, there is a sudden and rapid increase in  $m'$  as the film switches in the normal manner. The transition on a linear plot is much more marked. If the threshold switching field is taken as the value of  $h''_{\min}$  for  $m'=0.5$ , then there is satisfactory agreement for all four films with the threshold fields predicted by drawing the appropriate  $45^\circ$  field locus line on Fig. 5.42.

The high field tail is of interest. In particular, for films S2P9 and S2P7 hysteresis is present at fields much higher than that at which domain walls might normally be expected. A model may be derived based on the IR model of Section 2.2 in which the hysteresis is associated with the irreversible rotational switching of regions whose anisotropy is suitably dispersed from the mean.

Referring to Fig. 5.49, suppose the total field

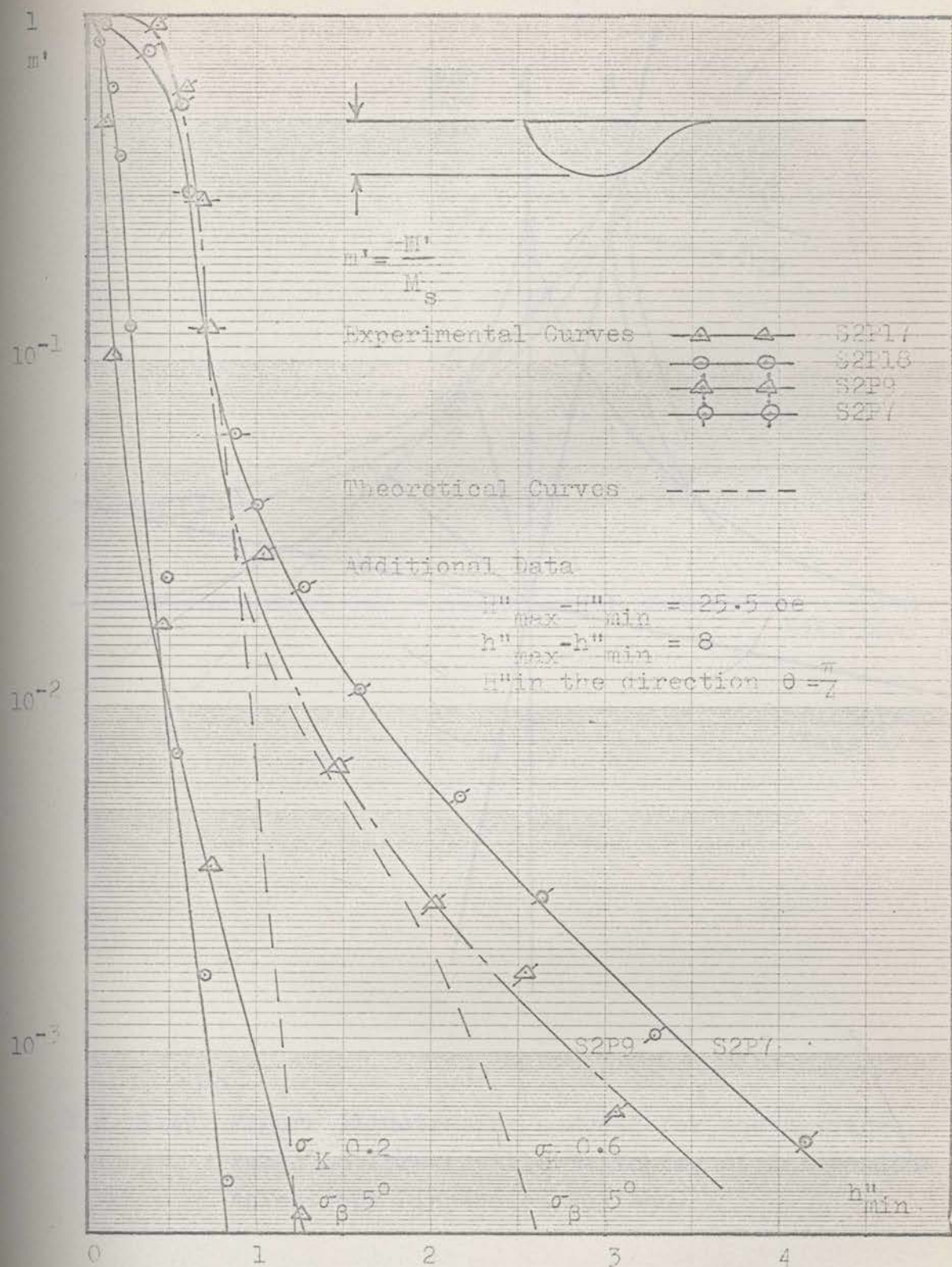


Fig. 5.48 The Normalized Amplitude of the Minor Hysteresis Loop  $m' = (M'/M_s)$  as a Function of the Minimum Field  $h''_{\min}$  for Four Films S2P17, S2P18, S2P9, S2P7.

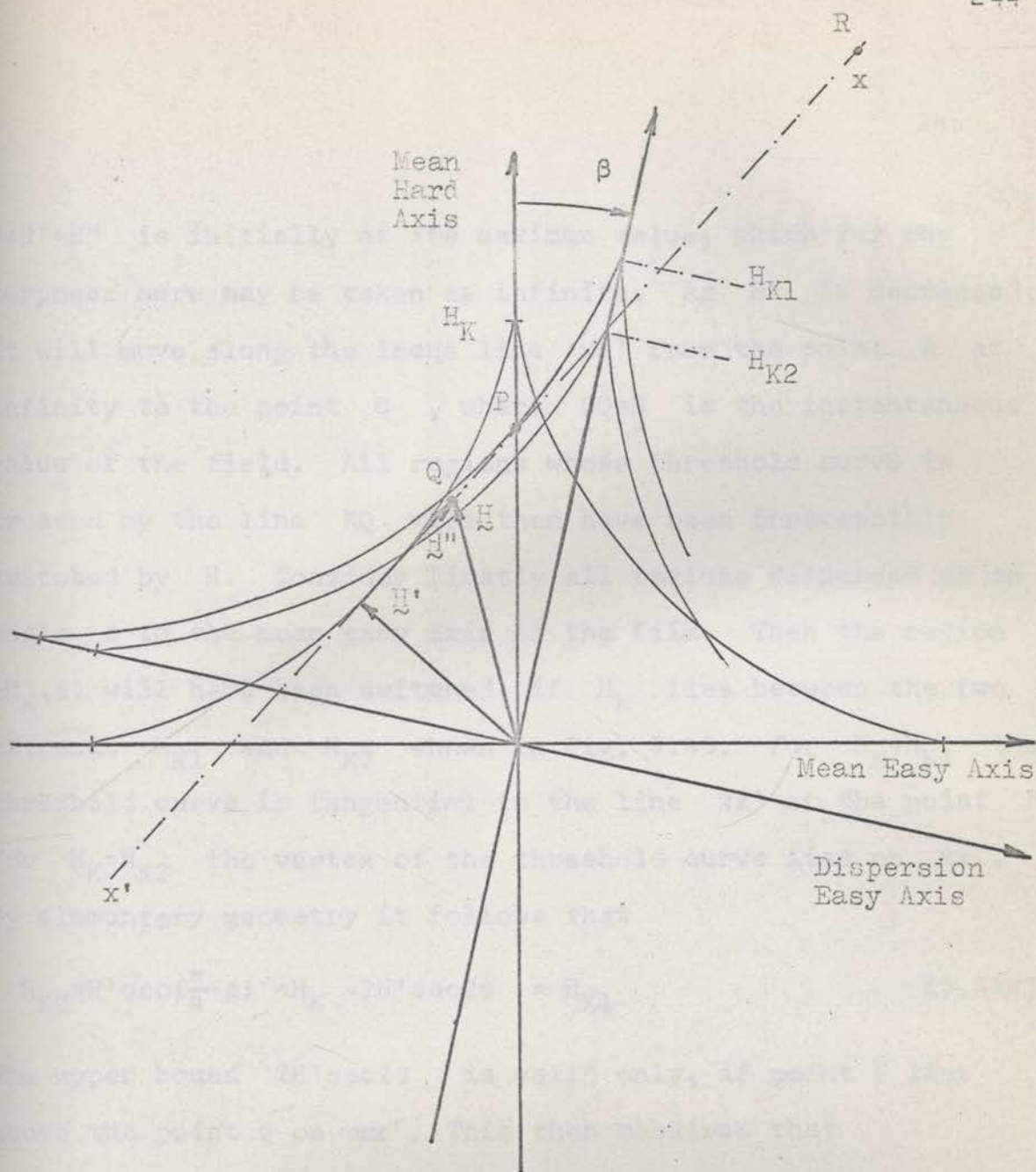


Fig. 5.49 Figure Illustrating a Model for the Hysteresis Loss Based on Irreversible Switching of Independent Anisotropy Dispersion Regions.



$\underline{H} = \underline{H}' + \underline{H}''$  is initially at its maximum value, which for the purposes here may be taken as infinite. As  $\underline{H}''$  is decreased, it will move along the locus line  $\underline{xx}'$  from the point  $R$  at infinity to the point  $Q$ , where  $\underline{OQ} = \underline{H}$  is the instantaneous value of the field. All regions whose threshold curve is crossed by the line  $RQ$  will then have been irreversibly switched by  $\underline{H}$ . Consider firstly all regions dispersed at an angle  $\beta$  to the mean easy axis of the film. Then the region  $(H_K, \beta)$  will have been switched, if  $H_K$  lies between the two extremes  $H_{K1}$  and  $H_{K2}$  shown in Fig. 5.49. For  $H_K = H_{K1}$  the threshold curve is tangential to the line  $\underline{xx}'$  at the point  $P$ . For  $H_K = H_{K2}$  the vertex of the threshold curve lies on  $\underline{xx}$ . By elementary geometry it follows that

$$H_{K2} = H' \sec\left(\frac{\pi}{4} + \beta\right) < H_K < 2H' \sec 2\beta = H_{K1} \quad (5.414)$$

The upper bound  $2H' \sec 2\beta$  is valid only, if point  $P$  lies above the point  $Q$  on  $\underline{xx}'$ . This then requires that

$$\beta > \beta_1 = \frac{1}{2} \tan^{-1} \frac{H''_{\min}}{2H'}$$

If not, it must be replaced by the bound  $H'_{K1} > H_K$ , where  $H'_{K1}$  is given as a function of  $\beta$  in terms of the parameter  $\phi$  from the equations

$$-H'_{K1} \cos^3 \phi = -H' \sin\left(\frac{\pi}{4} + \beta\right) + H''_{\min} \cos\left(\frac{\pi}{4} + \beta\right)$$

$$H'_{K1} \sin^3 \phi = H' \cos\left(\frac{\pi}{4} + \beta\right) + H''_{\min} \sin\left(\frac{\pi}{4} + \beta\right) \quad (5.415)$$

Equation (5.415) is then valid over the range

$$\beta_2 < \beta < \beta_1$$

$$\frac{\pi}{2} > \phi > \frac{\pi}{4} + \beta_1$$

and intersects the lower bound of equation (5.414) for  $\beta$  given by

$$\beta = \beta_2 = \tan^{-1} \frac{H''_{\min}}{H'} - \frac{\pi}{4}$$

The region bounded by these curves is conveniently shown on a  $(\beta, H_K)$  diagram as in Fig. 5.410. If the field has decreased from infinite to the value  $\underline{H}$ , all regions in the shaded area  $R_S$  will have switched, all regions in the unshaded area  $R$  will remain unswitched.

The sense coil signal will be given as a function of  $\underline{H}$  by

$$\overline{\sin \rho} = \int_R \sin \rho p(H_K, \beta) dH_K d\beta + \int_{R_S} \sin \rho_S p(H_K, \beta) dH_K d\beta \quad (5.416)$$

where

$p(H_K, \beta)$  is the probability distribution function of the regions  $(H_K, \beta)$  and  $\int p(H_K, \beta) dH_K d\beta = 1.0$ ,  $\sin \rho$  is calcul-

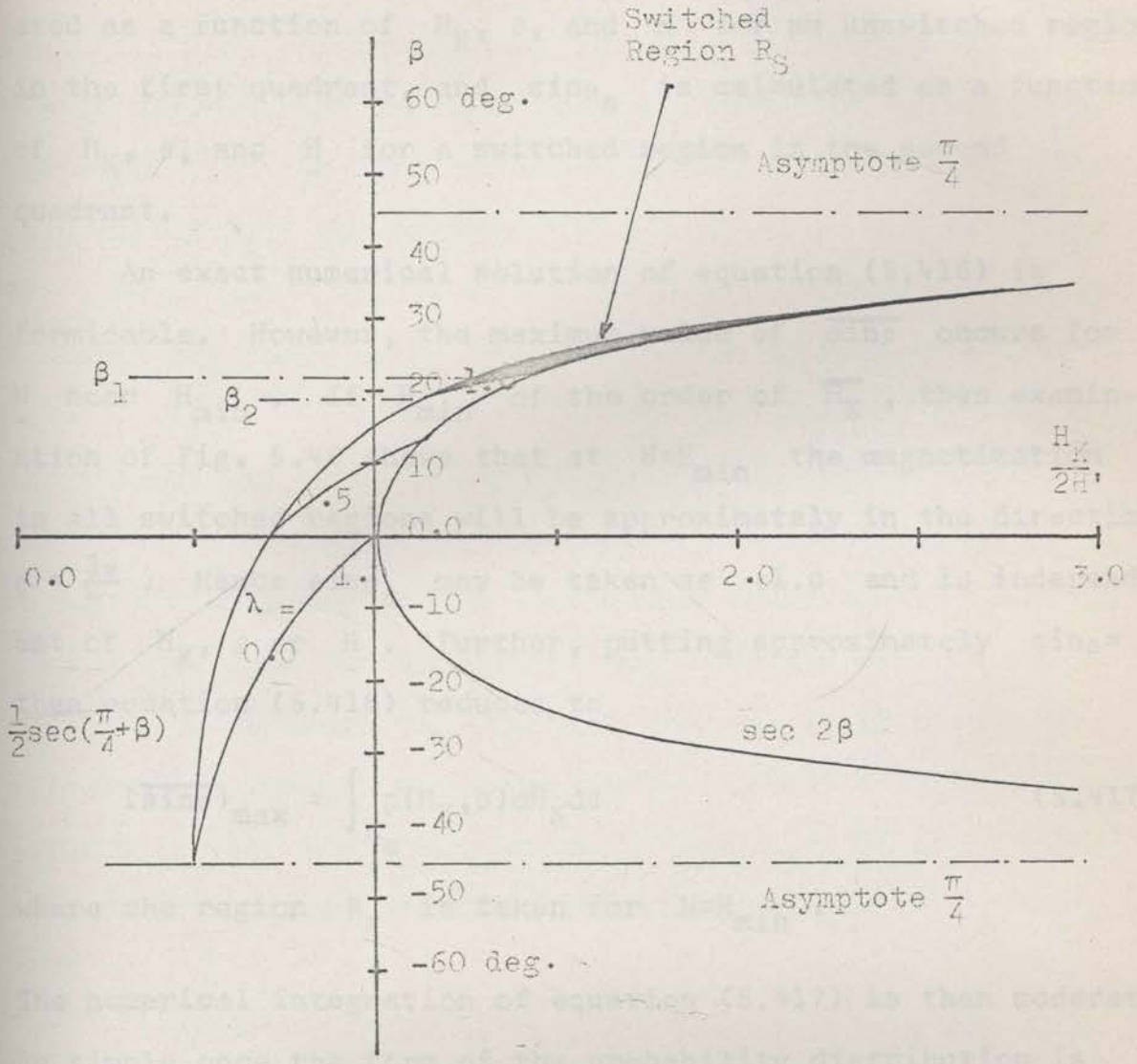


Fig. 5.410 The Region  $R_S$  in the  $(H_K, \beta)$  Plane for which Irreversible Switching occurs as  $H''$  decreases to  $H''_{min}$ .

The  $H_K$  axis is normalized in terms  $2H'$  with the parameter  $\lambda$  specifying the Region  $R_S$  given by  $\lambda = H''_{min}/2H'$

ated as a function of  $H_K$ ,  $\beta$ , and  $H$  for an unswitched region in the first quadrant, and  $\sin\rho_S$  is calculated as a function of  $H_K$ ,  $\beta$ , and  $H$  for a switched region in the second quadrant.

An exact numerical solution of equation (5.416) is formidable. However, the maximum value of  $\overline{\sin\rho}$  occurs for  $H$  near  $H_{\min}$ . If  $H_{\min}$  is of the order of  $H_K$ , then examination of Fig. 5.49 shows that at  $H=H_{\min}$  the magnetization in all switched regions will be approximately in the direction  $\phi = \frac{3\pi}{4}$ . Hence  $\sin\rho_S$  may be taken as  $\pm 1.0$  and is independent of  $H_K$ ,  $\beta$  or  $H$ . Further, putting approximately  $\sin\rho = 0$ , then equation (5.416) reduces to

$$(\overline{\sin\rho})_{\max} = \int_{R_S} p(H_K, \beta) dH_K d\beta \quad (5.417)$$

where the region  $R_S$  is taken for  $H=H_{\min}$ .

The numerical integration of equation (5.417) is then moderately simple once the form of the probability distribution is known.

It is commonly assumed that  $H_K$  and  $\beta$  are independent and that they both satisfy a normal probability distribution. Fig. 5.48 shows curves of  $(\overline{\sin\rho})_{\max}$  against  $H_{\min}''$  calculated for  $\sigma_K=0.2$ ,  $\sigma_\beta=5^\circ$ , and for  $\sigma_K=0.6$ ,  $\sigma_\beta=15^\circ$ , where  $\sigma_K$ ,  $\sigma_\beta$  are the respective normalized standard deviations.

From Fig. 5.48 the theoretical curves do show some similarity to the experimental results, however, agreement is not good. For films S2P9 and S2P7 the experimental curve is moderately well fitted over the central region only if we assume values of  $\sigma_K=0.6$  and  $\sigma_\beta=15^\circ$ , values which are greater than those measured for these films by the Crowther technique (see Table 4.22, where  $\sigma_\beta=3.1^\circ$  for S2P9 and  $7.0^\circ$  for S2P7). Even so, the theoretical curve falls too steeply at higher fields.

Better agreement is obtained if the distribution of  $\sigma_K$  is not strictly normal, but has a high field tail. There is some evidence in the literature that such may well be the case<sup>S4,C3</sup>. However, the greatest argument against such an approach and against the simple model presented is that the results for the four films shown in Fig. 5.48 do not correlate with their measured values of anisotropy dispersion (Table 4.22).

In deriving equation (5.417), the model used has assumed the independent irreversible switching of dispersed regions throughout the film. As discussed in Section 2.2, both exchange and magnetostatic coupling exists which produces an averaging effect over the random dispersion regions. The extent to which regions of a film can be considered independent depends on both the scale and on the nature of the dist-

urbance. For example, variations which produce a lateral magnetizational ripple are much more effectively suppressed than those causing a longitudinal ripple. The irreversible switching of the present model should rather be interpreted as irreversible ripple jumps. The manner in which a ripple jump occurs is easily understood from Fig. 5.411. Fig. 5.411 shows the magnetization configuration about a small region whose easy axis is at  $90^\circ$  at the mean easy axis of the film. Configurations (1) and (2) both represent equally likely equilibrium configurations at which the total energy has a local minimum. A transition from one to the other may be produced by a traverse field  $H_T$ , and will occur as an irreversible jump. The magnitude of  $H_T$  required will depend upon the anisotropies and upon the effective coupling between the dispersion region and the remainder of the film. A similar ripple jump phenomenon has been suggested by Feldtkeller<sup>F1</sup> to explain the residual opening of very small amplitude hard axis direction hysteresis loops.

Anisotropy dispersion as measured by the Crowther technique is essentially the measurement of longitudinal variations of the magnetization whose wavelength corresponds to the scale of the domains into which the film splits. This scale may be much greater than the wavelength involved in the ripple jumps considered here. In this case there is some doubt in

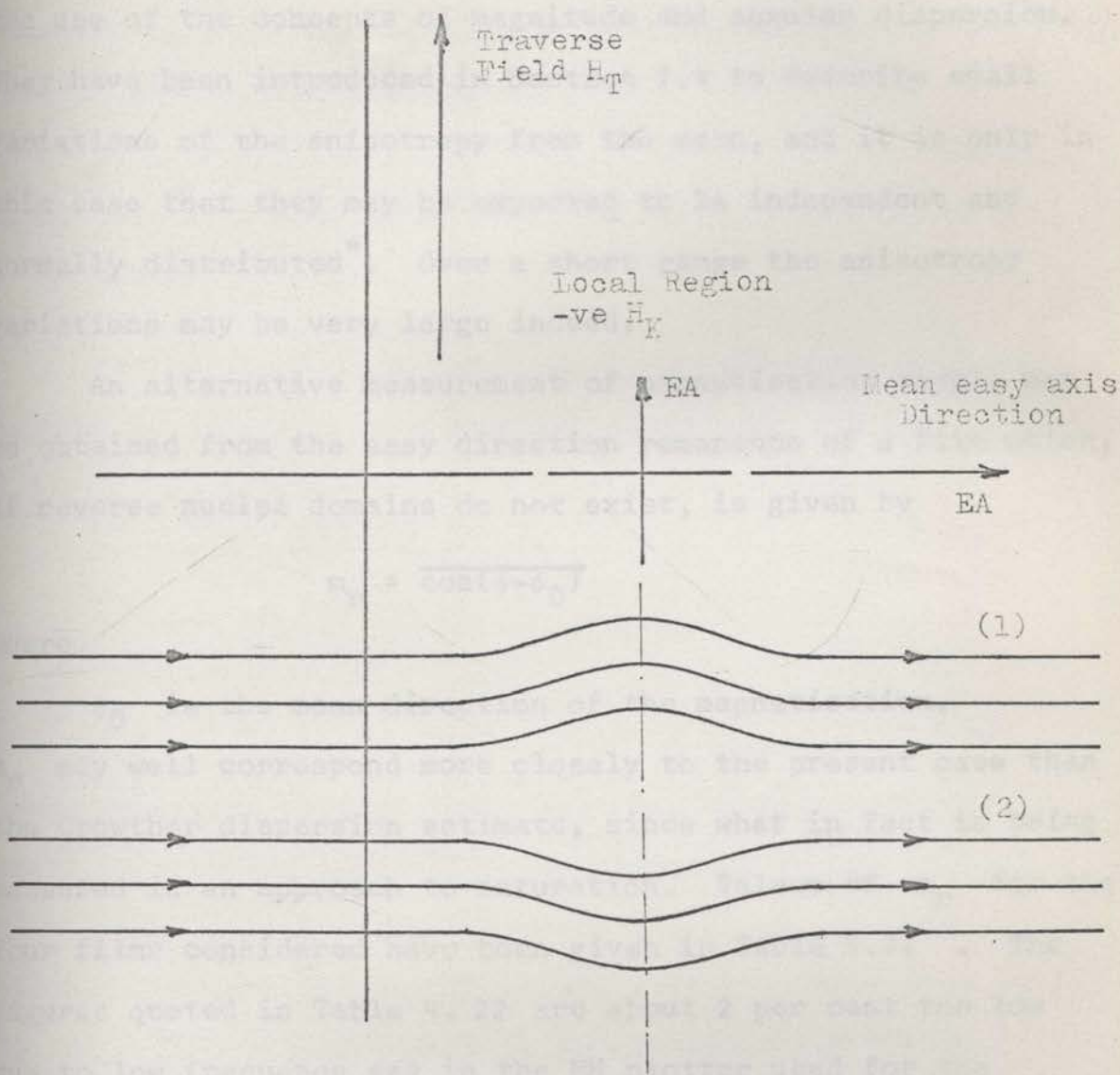


Fig. 5.411 Figure Illustrating "Ripple Jump" Hysteresis

(1) and (2) represent two stable equilibrium configurations of the magnetisation near a dispersion region of -ve  $H_K$  : A transition from one to the other may be produced by applying a traverse field  $H_T$  .

the use of the concepts of magnitude and angular dispersion. They have been introduced in Section 2.4 to describe small variations of the anisotropy from the mean, and it is only in this case that they may be expected to be independent and normally distributed\*. Over a short range the anisotropy variations may be very large indeed.

An alternative measurement of magnetization ripple may be obtained from the easy direction remanence of a film which, if reverse nuclei domains do not exist, is given by

$$m_r = \overline{\cos(\phi - \phi_0)}$$

where

$\phi_0$  is the mean direction of the magnetization.

$m_r$  may well correspond more closely to the present case than the Crowther dispersion estimate, since what in fact is being measured is an approach to saturation. Values of  $m_r$  for the four films considered have been given in Table 4.22. The figures quoted in Table 4.22 are about 2 per cent too low due to low frequency sag in the MH plotter used for the measurement. Thus  $m_r$  for films S2P17 and S2P18 is very close to 1.00. There appears to be some correlation between the high field hysteresis tail, between  $m_r$  and

---

\* The same conclusion has been given by Crowther<sup>C3</sup>.

---



between the film thickness. The small sample tested does not justify any further comparison.

#### 5.45 Some Practical Details of the Method and Experimental Errors

For an ideal film the accuracy to which the null may be determined is given from equation (5.44) and equation (5.45) as

$$\frac{dh'_n}{h'_n} = \frac{d(\sin\theta)}{Q} = \frac{1}{Q\left(\frac{S}{N}\right)}$$

where

$$Q = \frac{h'_n}{\cos^2\theta + h''_{\min}}$$

These equations suggest that  $\frac{dh'_n}{h'_n}$  may be made arbitrarily small by choosing  $\cos^2\theta + h''_{\min}$  sufficiently small. However, the  $(\sin\theta, H'')$  null trace of practical films shows (as previously described) a hysteresis effect at the lower values of  $h''_{\min}$ . The uncertainty in the error signal  $d(\sin\theta)$  is no longer  $\frac{1}{\left(\frac{S}{N}\right)}$ , but is determined by the amplitude of the hysteresis loop and this rapidly increases with decreasing  $h''_{\min}$ . There thus exists an optimum  $h''_{\min}$  for which  $\frac{1}{\left(\frac{S}{N}\right)}$  and the amplitude of the hysteresis loop are approximately equal. As a typical example, the 1000 Å film S2P17 can be measured by the MH plotter used here with an error of

$d(\sin\theta) = \frac{1}{\left(\frac{S}{N}\right)}$  of about  $5 \times 10^{-4}$ . From Fig. 5.48 a  $h''_{\min}$  of the order of 0.75 may be chosen giving  $Q \approx 0.66$  and  $\frac{dh'_n}{h'_n} \approx 7.5 \times 10^{-4}$ .

The principal measurement errors arise from

- Measurement of the Field  $H'_n$

$H'_n$  is directly measurable in terms of a DC current and in the present work was determined to 1 part in  $10^3$  using a precision manganin standard resistor and a digital voltmeter. Stray static magnetic fields (such as the earth's field) will produce a systematic error in  $H'_n$  equal to the component of the stray field in the  $H'_n$  direction. This error may be eliminated by taking the mean of two readings for  $H'_n$  taken with the direction of the field  $H''$  reversed. An error in  $H'_n$  will occur if the fields  $H'$  and  $H''$  are not precisely at right angles. This is a second order effect and in the present instrument is less than 1 part in  $10^4$ .

- Measurement of the Angle  $\theta$

The true angle  $\theta$  to the easy axis will depend upon both the mechanical accuracy and limit of reading of the plotter and upon the accuracy to which the hard axis of the film can be found by the Crowther cross field technique<sup>C1</sup> (see

Section 6.5). For the present instrument these errors are together less than  $\pm 0.20^\circ$  or 0.004 rad.

Experimentally, a series of 20 independent measurements of  $H'_n$  were made on the same sample S2P17. The measurements were taken for the angle  $\theta = \frac{\pi}{4}$ . Angular errors are therefore of second order and will be less than  $0.004^2 + 2 \times 10^{-5}$ . The sample was removed from and then replaced in the MH plotter between each measurement. The root mean square error was 0.15 per cent and the maximum error of any of the readings was 0.23 per cent. An error of 0.15 per cent corresponds to an error of one unit in the last digit of the digital voltmeter used. Several different films have been measured and all give the above accuracy. A further check of the accuracy may be made by measuring  $H'_n$  for the two directions  $\theta = \frac{\pi}{4}$  and  $\theta = \frac{\pi}{4} + \pi$ . The maximum error between any two such measurements was 0.35 per cent.

#### 5.46 Experimental Torque Curves for a Number of Films

Experimental torque curves of  $(H'_n, \phi)$  are shown for the four films S2P17, S2P18, S2P9 and S2P7 in Fig. 5.412a, 5.412b, 5.412c and 5.412d, respectively. A sufficiently high  $H''_{\min}$  has been used so that the curves correspond to the saturated torque curves of the films. The curves are very closely

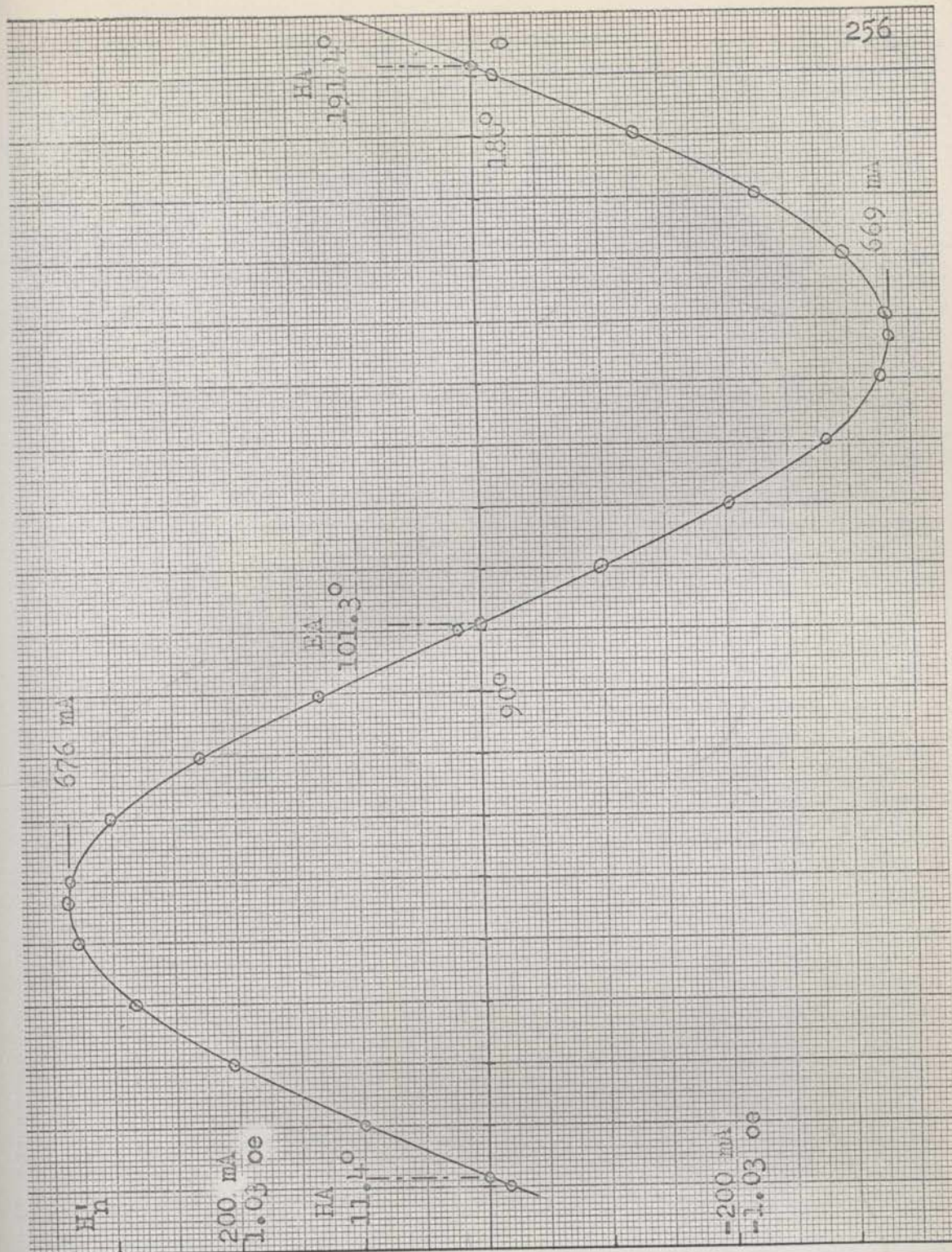


Fig. 5.412a Experimental Saturated Torque Curve for Film S2P17  $R = 1 \times 10^{-2}$

$H'_n$  is given in terms of a DC current, the conversion factor being 5.16 oe/amp. The accuracy of determining  $H'_n$  at any point is better than the accuracy of plotting the points on this diagram.

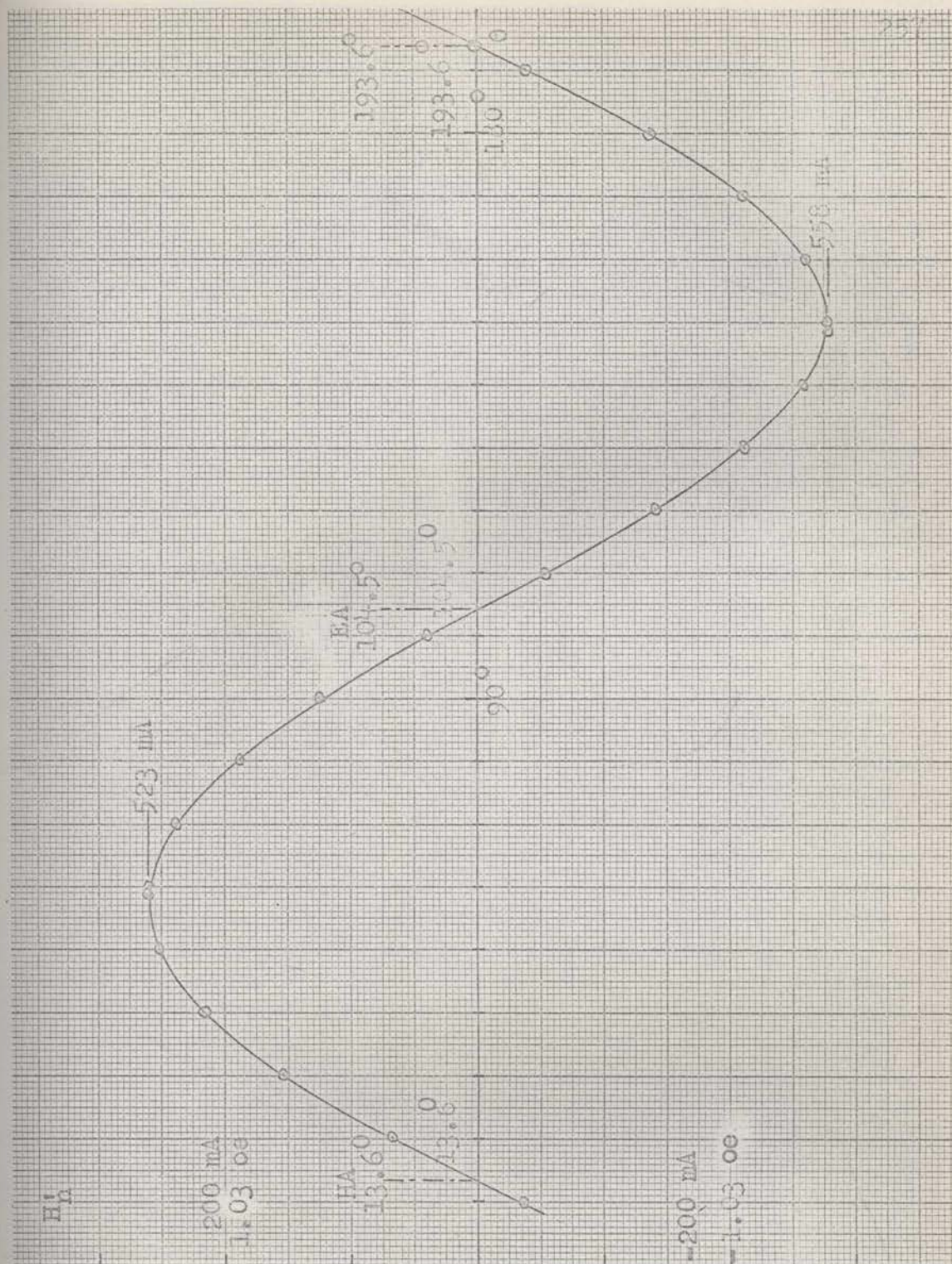


Fig. 5.412b Experimental Saturated Torque Curve for Film S2P18 ,  $R = 6.5 \times 10^{-2}$

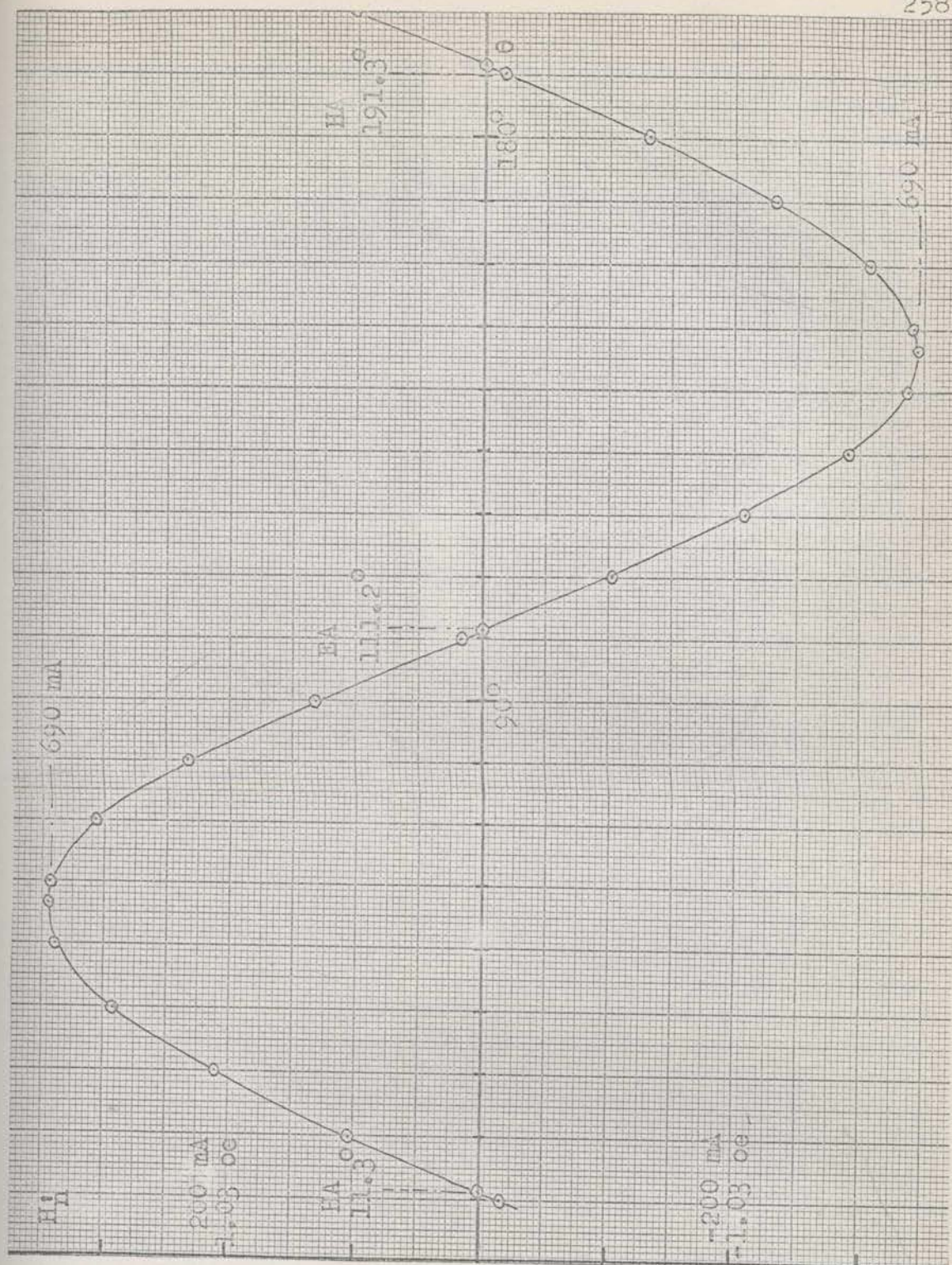


Fig. 5.412c Experimental Saturated Torque Curve for Film S2P9 ,  $R = 0.0 \times 10^{-2}$

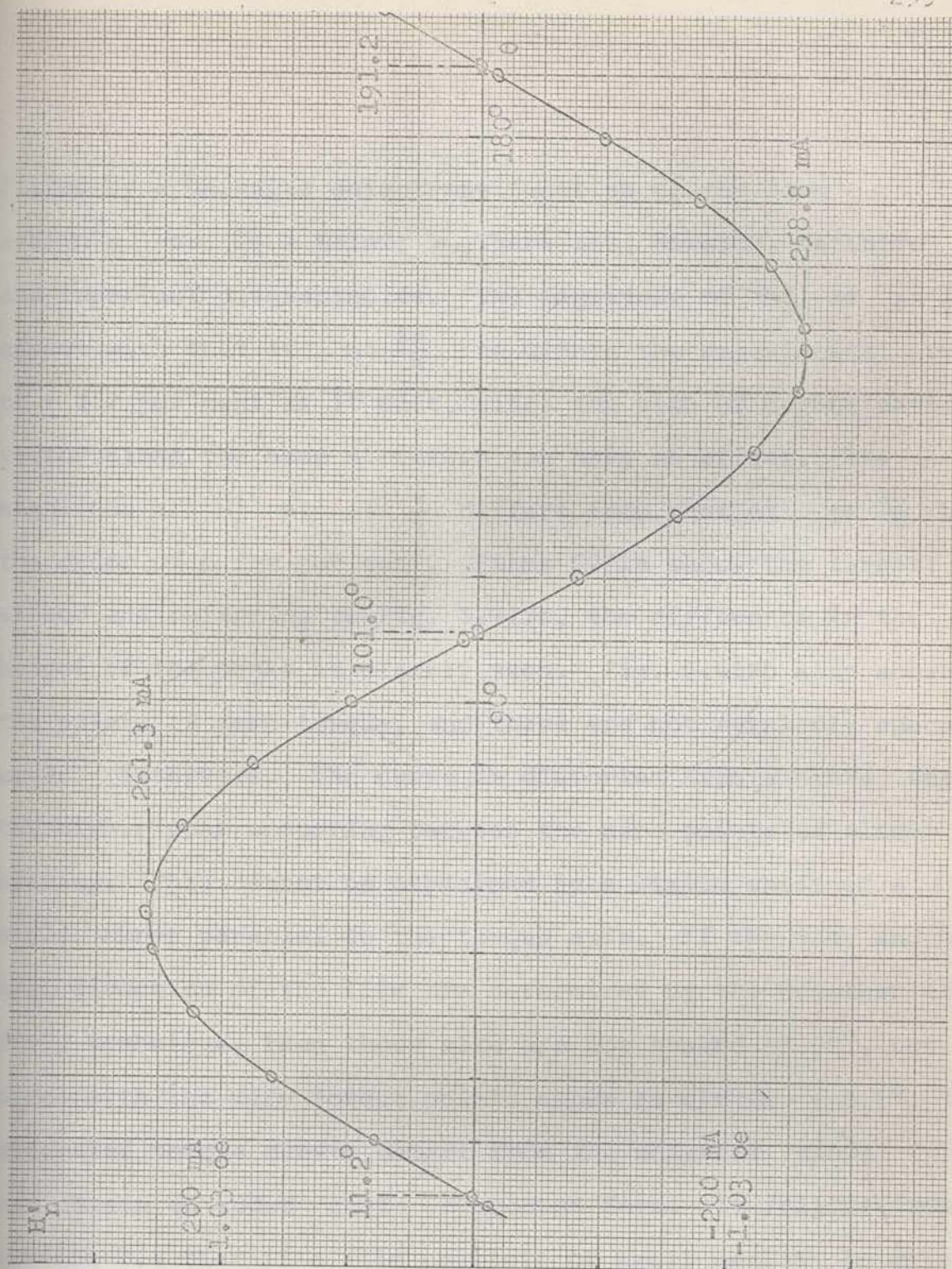


Fig. 5.412a Experimental Saturated Torque Curve for Film S2P7,  $R = 1.0 \times 10^{-2}$

fitted by a uniaxial anisotropy function of the form  $\epsilon = K \sin^2 \phi$  or  $\frac{\partial \epsilon}{\partial \phi} = K \sin 2\phi$ . There are, however, definite and important discrepancies. The magnitude of  $H'_n$  at  $\phi = \frac{\pi}{4}$  agrees with that at  $\phi = \frac{5\pi}{4}$  to within the experimental error of  $\pm 0.2$  per cent as it must, since the sign of magnetization vector along the same direction can have no effect. The magnitude of  $H'_n$  at  $\phi = \frac{\pi}{4}$  differs from that at  $\phi = \frac{3\pi}{4}$  by the order of a few per cent. Films S2P18 shows the largest effect and referring to Fig. 5.412b, the difference in the height of the peaks is clearly seen. Fig. 5.412b also shows the points of zero torque, and these are not regularly spaced at  $90^\circ$  intervals. The curve is distorted from a  $\sin 2\phi$  shape, the higher peak occurring between the zero points of closer spacing. This cannot be explained by a simple shift of a  $\sin 2\phi$  curve parallel to the torque axis. If the easy and hard axis direction of the film are determined by the Crowther cross field technique, then these also are not spaced at  $90^\circ$ , but agree with the zero torque points above to within  $\pm 0.1^\circ$ . The saturated torque curves depart from the uniaxial  $\sin 2\phi$  form and obtain an added  $\cos 2\phi$  component form. It follows from Section 2.4 that if a film consists of small regions in which the anisotropy is random but still uniaxial, then the saturated anisotropy of the whole film will be uniaxial also. Thus it appears that other than uniaxial anisotropies are present in



films of higher dispersion, the  $\cos 4\phi$  form possibly suggesting crystalline anisotropy centres.

The ratio

$$R = \frac{\Delta H'_n}{H'_{nm}}$$

where

$$\Delta H'_n = \left| H'_n(\phi = \frac{\pi}{4}) \right| - \left| H'_n(\phi = \frac{3\pi}{4}) \right|$$

and

$$H'_{nm} = \frac{1}{2} \left\{ \left| H'_n(\phi = \frac{\pi}{4}) \right| + \left| H'_n(\phi = \frac{3\pi}{4}) \right| \right\}$$

is given in Table 4.22 for a number of film samples. The number is too small to show any definite correlation. The results however suggest that  $R$  is much larger in thinner films near  $1000 \text{ \AA}$  than in thicker films near  $3500 \text{ \AA}$  and that for films of the same thickness,  $R$  increases with increasing dispersion.

#### 5.47 A Variation of the Method for the Measurement of the Saturation Magnetization of a Film

A variation of the present method can be performed with the fields  $H'$  and  $H''$  applied at a known angle  $\theta$  out of the plane of the film as in Fig. 5.413. The restoring torque is now provided by the demagnetizing energy of the magnetiz-

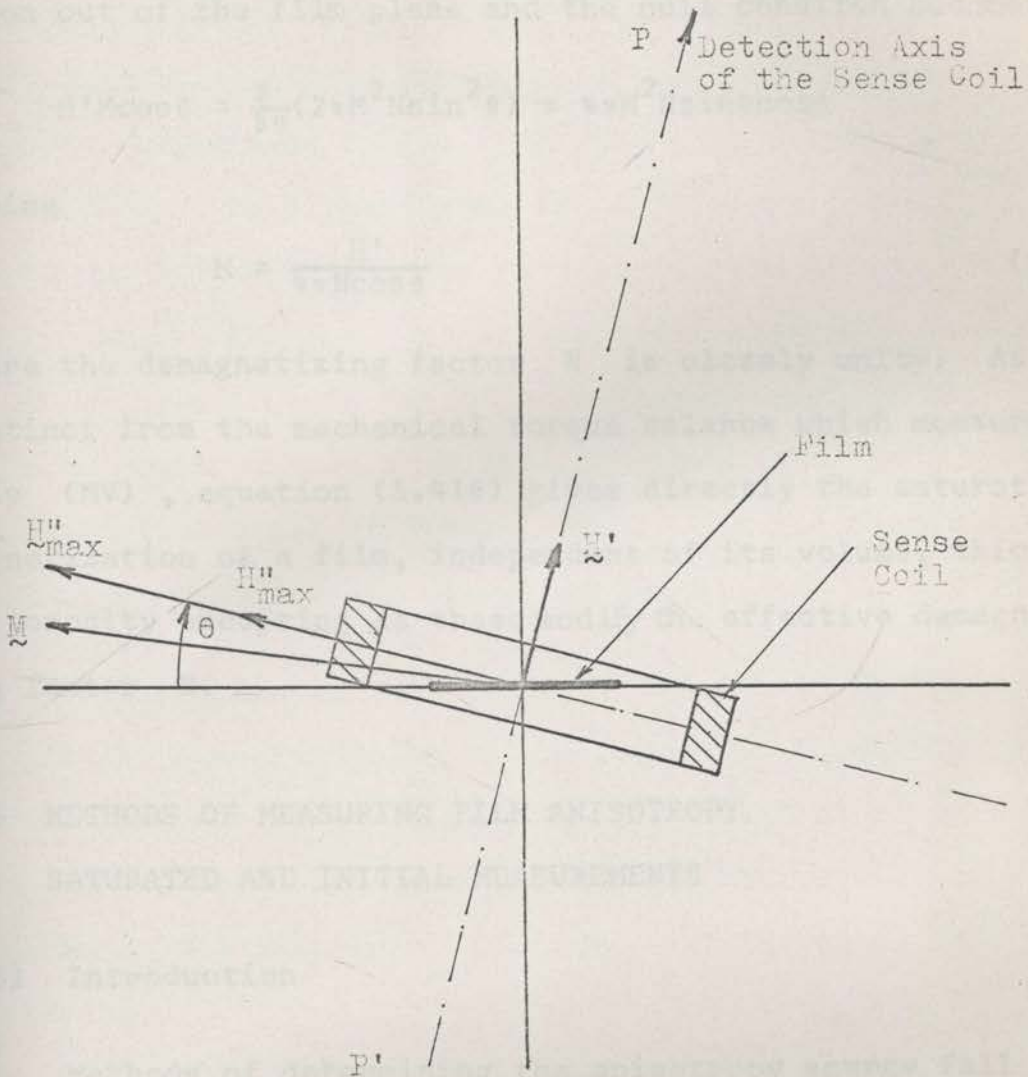


Fig. 5.413 A Method of Measuring the Saturation Magnetization of a Film

ation out of the film plane and the null condition becomes

$$H'M\cos\theta = \frac{\partial}{\partial\theta}(2\pi M^2 N \sin^2\theta) = 4\pi M^2 N \sin\theta\cos\theta$$

giving

$$M = \frac{H'}{4\pi N\cos\theta} \quad (5.418)$$

where the demagnetizing factor  $N$  is closely unity. As distinct from the mechanical torque balance which measures only  $(MV)$ , equation (5.418) gives directly the saturation magnetization of a film, independent of its volume, thickness, or porosity excepting as these modify the effective demagnetizing factor  $N$ .

## 5.5 METHODS OF MEASURING FILM ANISOTROPY

### SATURATED AND INITIAL MEASUREMENTS

#### 5.51 Introduction

Methods of determining the anisotropy energy fall into two classes:

#### Initial Measurements

"Initial" measurements are those involving only small rotations  $\phi$  of the magnetization about its equilibrium direction along the apparent easy axis of the film. The easy

axis may be fixed, or may be determined by the direction in which the film was last saturated if the film has pseudo-rotatable anisotropy (PRA). (PRA has been discussed in Section 3.4). In either case, for sufficiently small  $\phi$ , an anisotropy energy  $\epsilon(\phi)$  may be associated with the position of the magnetization.  $\epsilon(\phi)$  is the total anisotropy energy, and is the sum of both fixed and rotatable components. All "initial" measurements then have in common that they measure only the total local stiffness  $\left. \frac{\partial \epsilon}{\partial \phi} \right|_{\phi=0}$  of the magnetization. A number of examples are discussed below;

- The anisotropy is commonly determined by measuring the initial susceptibility in the hard axis direction by an MH plotter or other suitable method. The field at which the extrapolated low drive trace intersects the saturation level is taken as the anisotropy field  $H_{Ki}$  of the film. Thus, by definition

$$\begin{aligned}
 H_{Ki} &= \frac{M_s}{\left. \frac{d}{dH}(M \sin \phi) \right|_{H=0}} \\
 &= \frac{M_s}{M_r} \cdot \left. \frac{\partial^2 \epsilon}{\partial \phi^2} \right|_{H=0, \phi=0} \quad (5.51)
 \end{aligned}$$

where

$M_r$  is the remanent magnetization,

$M_s$  is the saturation magnetization, and

$H$  is the applied field in the hard direction.

The proof of equation (5.51) is discussed in detail in Section 5.61. In practice the low drive trace is usually a straight line up to  $H=H_r+0.5 H_K$ . This then also implies that  $\epsilon(\phi)$  is of the form  $K\sin^2\phi$  at least for  $\phi < \sin^{-1}(H_r/H_K)$ .

- The anisotropy may be calculated from the low field torque curves found by any of the methods of Section 5.2. If  $(H,\gamma)$  is the applied field, then the initial slope of the curve,  $\left. \frac{\partial T}{\partial \gamma} \right|_{\gamma=0}$ , is plotted against  $1/H$  and extrapolated to infinite field.

$$\text{Since } T = \frac{\partial \epsilon}{\partial \phi} = HM \sin(\gamma - \phi) \quad (5.52)$$

then

$$\left. \frac{\partial T}{\partial \gamma} \right|_{\gamma=0} = V \cdot \frac{\left. \frac{\partial^2 \epsilon}{\partial \phi^2} \right|_{\phi=0}}{1 + \frac{\left. \frac{\partial^2 \epsilon}{\partial \phi^2} \right|_{\phi=0}}{HM_r \cos(\gamma - \phi)}} \quad \gamma=0, \phi=0$$

$$= V \cdot \frac{\left. \frac{\partial^2 \epsilon}{\partial \phi^2} \right|_{\phi=0}}{1 + \frac{\left. \frac{\partial^2 \epsilon}{\partial \phi^2} \right|_{\phi=0}}{HM_r}}$$

$$\rightarrow V \cdot \left. \frac{\partial^2 \epsilon}{\partial \phi^2} \right|_{H=\infty, \phi=0} \quad \text{as } H \rightarrow \infty \quad (5.53)$$

The anisotropy may also be found by a number of indirect means such as the torsion pendulum method<sup>S1</sup>, or ferromagnetic resonance<sup>S3</sup>. In either case the period of oscillation or the resonant frequency depends upon the local stiffness

$$\left. \frac{\partial^2 \epsilon}{\partial \phi^2} \right|_{\phi=0} .$$

### High Field Measurements of the film,

These involve large rotations of the magnetization and measure essentially the fixed anisotropy component  $\epsilon_u(\phi)$  only. The basic method of finding  $\epsilon_u(\phi)$  is to measure the high field torque curve of the film in any of the ways of Section 5.2. Experiment shows that  $\epsilon_u(\phi)$  is closely of the form  $\epsilon_u(\phi) = K_u \sin^2 \phi$  (see Fig. 5.412).  $\epsilon_u(\phi)$  is thus specified by the value of the anisotropy constant  $K_u$ .

## 5.6 MEASUREMENT OF THE ANISOTROPY BY THE HARD AXIS INITIAL SUSCEPTIBILITY METHOD USING AN MH PLOTTER

### 5.61 The Effects of Anisotropy Dispersion

As discussed in Section 5.5, the anisotropy is commonly determined by measuring the uniaxial susceptibility in the hard axis direction by an MH plotter<sup>S2, B2</sup>. The field at which the

extrapolated low drive trace intersects the saturation level is taken as the anisotropy field  $H_{Ki}$  of the film. By this definition

$$H_{Ki} = \frac{M_s}{\left. \frac{d}{dH}(M \sin \phi) \right|_{H=0}} \quad (5.61)$$

where

$(M, \phi)$  is the magnetization of the film,

$M_s$  is the saturation magnetization, and

$H$  is the applied field in the hard direction.

The torque equilibrium equation for the film may be written

$$\frac{\partial \epsilon}{\partial \phi} - H M \sin(\gamma - \phi) = 0, \quad \gamma = \frac{\pi}{2} \quad (5.62)$$

As previously discussed in Sections 5.23 and 5.44, for real films both the anisotropy energy  $\epsilon$  and the magnetization  $M$  will in the general case depend not only on  $\phi$ , but also on the applied field  $(H, \gamma)$ . Two independent variables are needed which may conveniently be taken as  $\phi$  and  $\gamma$ . The derivative in equation (5.61) may be evaluated from equation (5.62) to give

$$H_{Ki} = \frac{M_s}{\frac{M \cos \phi (M \cos \phi + \sin \phi \frac{\partial M}{\partial \phi})}{\frac{\partial^2 \epsilon}{\partial \phi^2} + H (M \sin \phi - \cos \phi \frac{\partial M}{\partial \phi})} \Big|_{H=0, \phi=0}$$

where the total derivative  $\frac{d}{d\phi}$  has been replaced by the partial derivative  $\frac{\partial}{\partial\phi}$ , since  $\gamma$  is constant.

Thus,

$$\begin{aligned}
 H_{Ki} &= \frac{M_s}{\frac{M_r^2}{\frac{\partial^2 \epsilon}{\partial \phi^2}} \Big|_{H=0, \phi=0}} \\
 &= \frac{M_s}{M_r^2} \cdot \frac{\partial^2 \epsilon}{\partial \phi^2} \Big|_r
 \end{aligned} \tag{5.63}$$

where

$M_r$  is the remanent magnetization, and

$\frac{\partial^2 \epsilon}{\partial \phi^2} \Big|_r$  is the initial stiffness evaluated at the remanent condition.

$H_{Ki}$  thus might alternatively be called the remanent anisotropy field.

For an ideal film obeying the CR model,  $\epsilon = K \sin^2 \phi$ ,  $M_r = M_s$  and from equation (5.63),  $H_{Ki} = H_{Ks}$ , where  $H_{Ks} = 2K/M_s$  is the saturated anisotropy field of the film. The relation of  $H_{Ki}$  to  $H_{Ks}$  for a real film having anisotropy dispersion is of great importance. For a film obeying the Independent Region (IR) model of Section 2.2, then referring to Fig. 5.61, it follows that if  $(H_K, \beta)$  is the anisotropy of a typical region, then



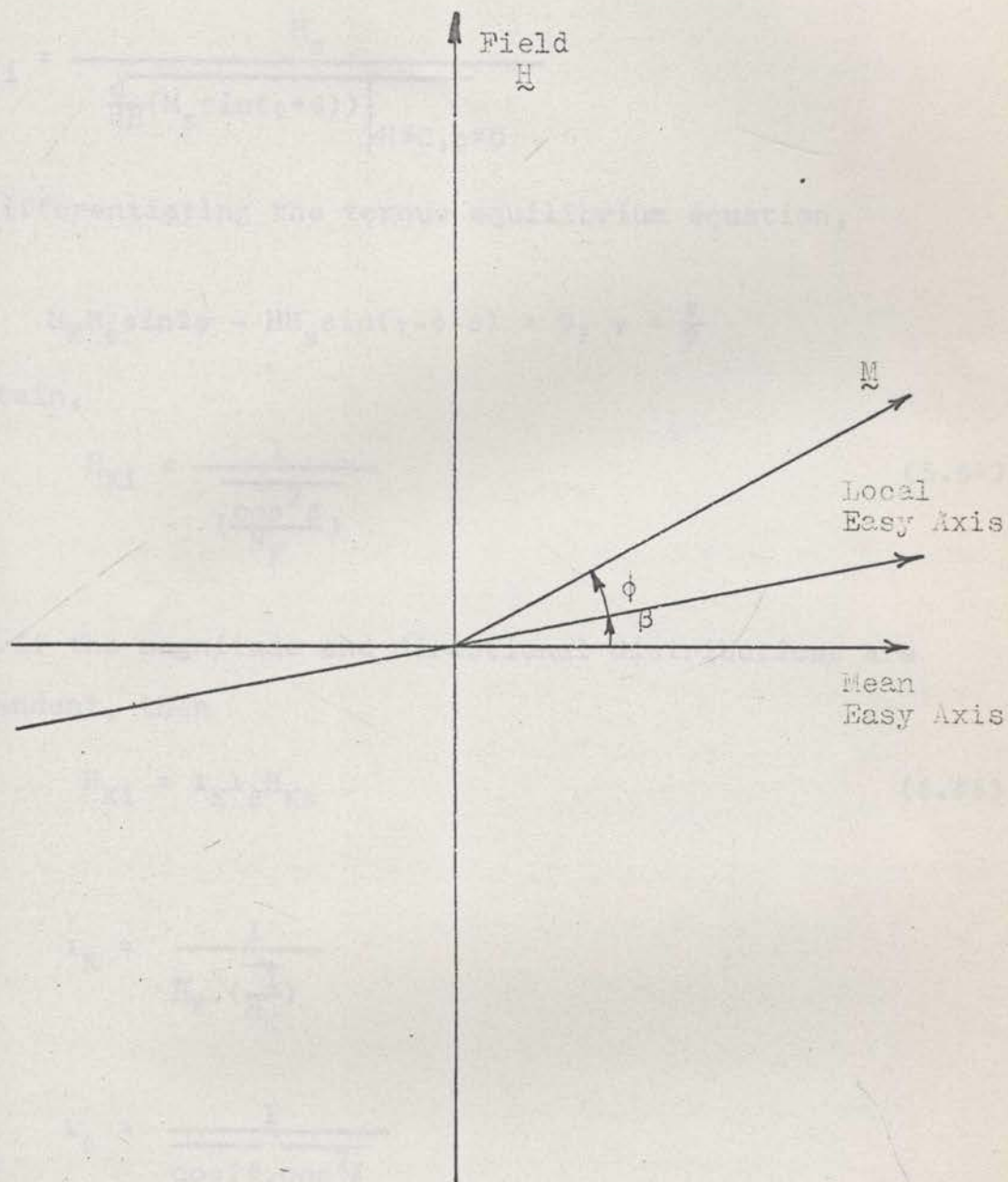


Fig. 5.61 Diagram for Calculating  $H_{Ki}$  for a Film Consisting of Independent Dispersion Regions.

$$H_{Ki} = \frac{M_s}{\left. \frac{d}{dH}(M_s \sin(\phi + \beta)) \right|_{H=0, \phi=0}}$$

and differentiating the torque equilibrium equation,

$$H_K M_s \sin 2\phi - H M_s \sin(\gamma - \phi - \beta) = 0, \quad \gamma = \frac{\pi}{2}$$

we obtain,

$$H_{Ki} = \frac{1}{\left( \frac{\cos^2 \beta}{H_K} \right)} \quad (5.64)$$

If the magnitude and directional distributions are independent, then

$$H_{Ki} = \lambda_K \lambda_\beta H_{Ks} \quad (5.65)$$

where

$$\lambda_K = \frac{1}{\bar{H}_K \cdot \left( \frac{1}{H_K} \right)}$$

$$\lambda_\beta = \frac{1}{\cos 2\beta \cdot \cos^2 \beta}$$

and

$H_{Ks} = \frac{H_K \cos 2\beta}{\cos^2 \beta}$  is the saturated anisotropy field of the film.

$\lambda_K$  and  $\lambda_\beta$  may be evaluated for a normal distribution in terms of the respective normalized standard deviations  $\sigma_K$  and  $\sigma_\beta$ . The calculation is outlined in Appendix A and values of  $\lambda_K$  and  $\lambda_\beta$  have been plotted against  $\sigma_K$  and  $\sigma_\beta$  in Fig. 5.62.  $\lambda_K$  is less than 1, while  $\lambda_\beta$  is greater than 1. Thus,  $H_{Ki}$  can be either greater or less than  $H_{Ks}$  depending on whether the angular dispersion factor  $\lambda_\beta$  or the magnitude dispersion factor  $\lambda_K$  is dominant.

Experimental measurements of  $H_{Ki}$  have been plotted against the angular dispersion  $\beta_{\frac{1}{2}}$  for a number of film samples in Fig. 5.63. Plotted also in Fig. 5.63 are the values of  $H_{Ks}$  for the same films found from measurement of the saturated torque curves as in Section 5.4. The two values agree moderately well.  $H_{Ki}$  is as often smaller than  $H_{Ks}$  as it is larger. As expected, these permalloy films show no evidence of any significant pseudo-rotatable anisotropy component. Though the sample number is small, it would appear that agreement is best for thinner films near  $1000 \text{ \AA}$  and somewhat worse for thicker films near  $3500 \text{ \AA}$ . There appears to be no correlation with the dispersion  $\beta$ .  $H_{Ki}$  and  $H_{Ks}$  have also been measured by Doyle<sup>D1</sup> who similarly reports approximate agreement between the two, but a lack of correlation with  $\beta$ . It does not seem profitable to discuss

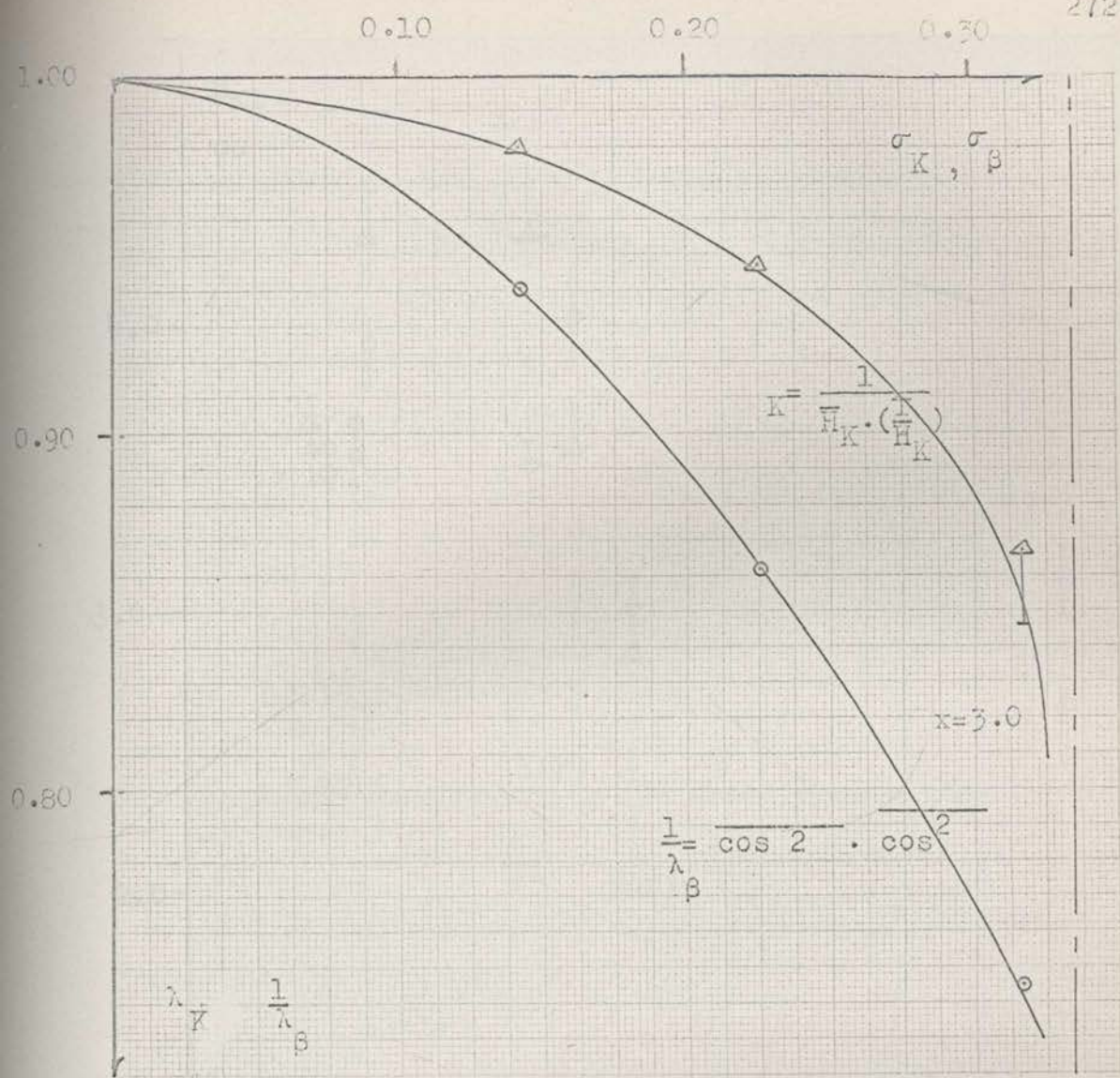


Fig. 562 Graph of  $\lambda_K$ ,  $\frac{1}{\lambda_\beta}$  against  $\sigma_K$ ,  $\sigma_\beta$

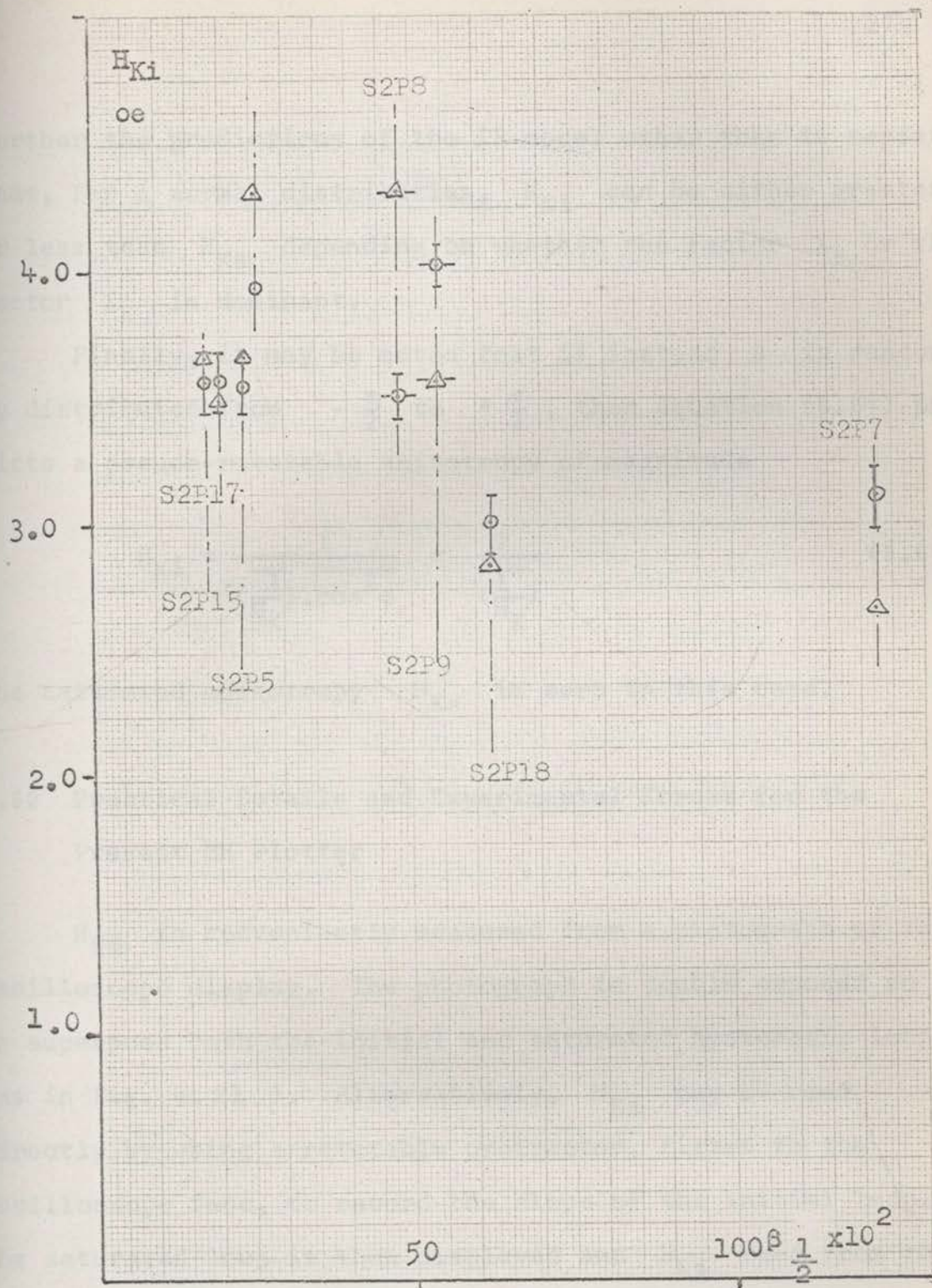


Fig. 5.63 Experimental Measurements of  $H_{Ki}$  and  $H_{Ks}$  plotted against the Angular Dispersion  $\beta_{\frac{1}{2}}$ .

further the predictions of the IR model other than to repeat that, for a normal distribution,  $H_{Ki}$  can be either greater or less than  $H_{Ks}$  depending on whether the factor  $\lambda_\beta$  or the factor  $\lambda_K$  is dominant.

Finally, it may be noted that if instead  $\beta$  is randomly distributed from  $-\frac{\pi}{2}$  to  $+\frac{\pi}{2}$ , then equation (5.64) predicts a pseudo-rotatable anisotropy of magnitude

$$H_{Ki} = \frac{1}{\left(\frac{1}{H_K}\right) \cdot \cos^2 \beta} = \frac{2}{\left(\frac{1}{H_K}\right)} \quad (5.66)$$

The saturated anisotropy  $H_{Ks}$  is zero in this case.

## 5.62 Practical Details and Experimental Errors for the Present MH Plotter

$H_{Ki}$  is conveniently measured from a photograph of the oscilloscope display. The photograph is double exposed so as to superpose both the initial and saturated hysteresis loops (as in Fig. 4.21). Alternatively,  $H_{Ki}$  may be read directly by using a rotatable protractor, fitted to the oscilloscope face, to record the slope of the initial loop. The saturated loop is then displayed and  $H_{Ki}$  read from the slope of the protractor and the value of the saturation

magnetization. Other variations of this method are possible. Once a standard measurement procedure has been adopted, random errors are small. It is found in practice that the slope can be set to 2 per cent, the oscilloscope scale read to 1 per cent and  $H_{Ki}$  thus determined with a relative error of approximately 3 per cent. Experimentally, a series of 20 independent measurements of  $H_{Ki}$  were made on the same sample S2P17. The sample was removed from and then replaced in the MH plotter between each measurement. The root mean square error was 2 per cent, and the maximum error in any of the readings was 5 per cent. Several different films have been measured and all give the above accuracy.

Additional errors in  $H_{Ki}$  may arise from

- the calibration of the field scale of the oscilloscope display. This may readily be calibrated in terms of a DC current by comparing the voltage produced across the field current monitoring resistor  $R_M$  of the MH plotter (see Fig. 6.22) when passing both an AF and DC current simultaneously through the field coils. An accuracy of 1 per cent is obtainable.

- the effect of the small but non-zero value of the measuring field on the reversibility and slope of the initial hysteresis loop. Typical experimental results for

the variation of  $H_{Ki}$  with the field amplitude are shown in Fig. 5.64.

- incomplete cancellation of stray static magnetic fields (such as the earth's field).
- inaccurate alignment of either the film or the sense coil with the field direction.

In Fig. 5.65  $\beta$  and  $\alpha$  are small errors in the alignment of the film easy axis and the sense coil, respectively.  $(H', \gamma')$  is an uncancelled static field. Equations (5.61) and (5.62) then become

$$H'_{Ki} = \frac{M_s \cos \alpha}{\left. \frac{d}{dH} (M \sin(\phi + \beta - \alpha)) \right|_{H=0}} \quad (5.67)$$

and

$$\frac{\partial \epsilon}{\partial \phi} - HM \sin(\gamma - \phi - \beta) - H' M \sin(\gamma' - \phi - \beta) = 0, \quad \gamma = \frac{\pi}{2} \quad (5.68)$$

The derivative may be evaluated as previously. For the purpose of calculating errors it is sufficient to assume that

$$\left. \frac{\partial^2 \epsilon}{\partial \phi^2} \right|_{H=0} = \left. \frac{\partial^2 \epsilon}{\partial \phi^2} \right|_r \quad \text{is unaltered by the field } (H', \gamma') \text{ and also}$$

$$\text{that } \frac{\partial M}{\partial \phi} = 0.$$

Finally, writing  $h' = \frac{H' M}{\left. \frac{\partial^2 \epsilon}{\partial \phi^2} \right|_r}$ , then



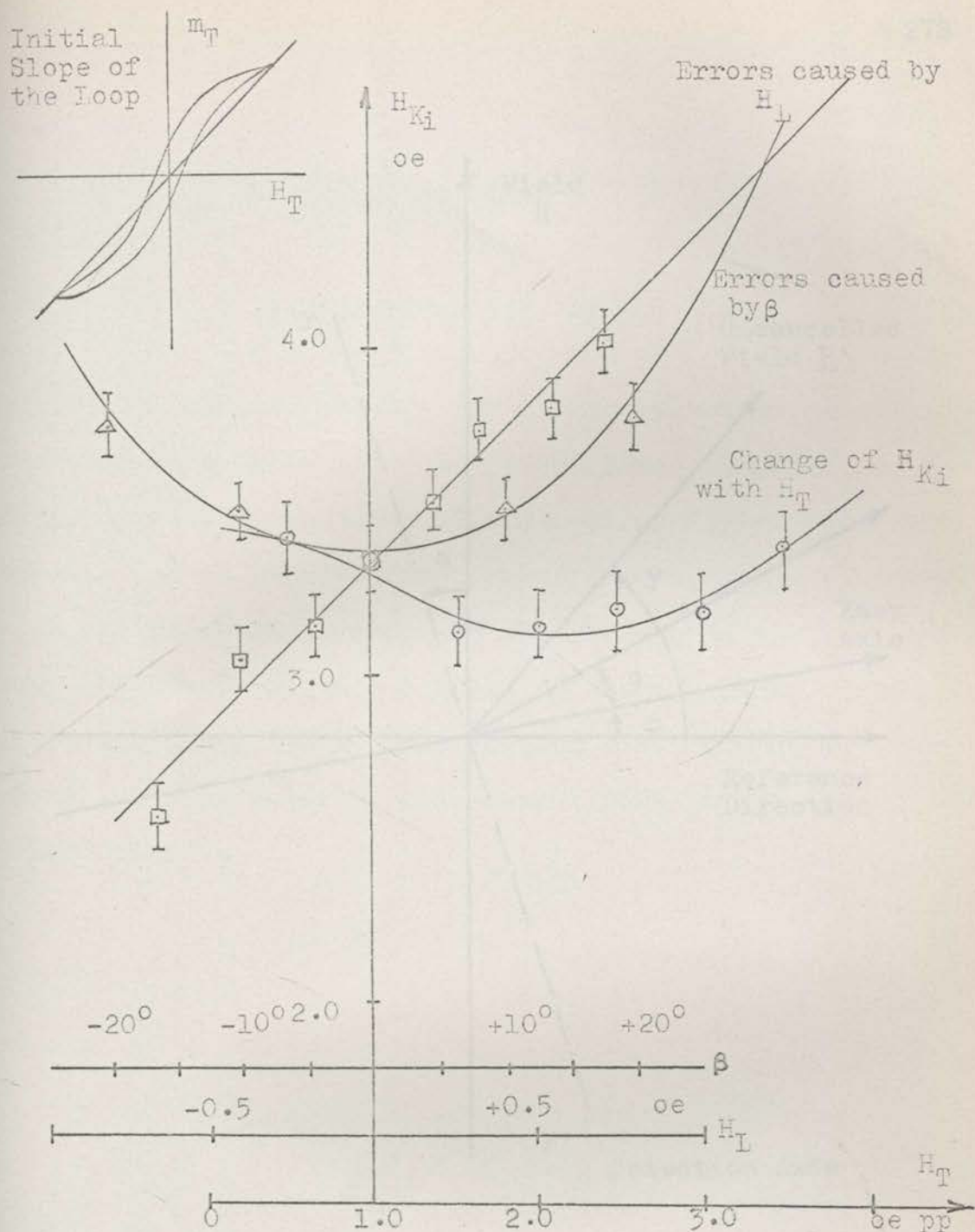


Fig. 5.64 Experimental Measurements of the Errors Caused by a Finite Magnitude of the Field  $H=H_T$  on the Value of  $H_{Ki}$ .  
 Experimental Measurements of the Error in  $H_{Ki}$  produced by Alignment Errors and Uncancelled Stray Fields.

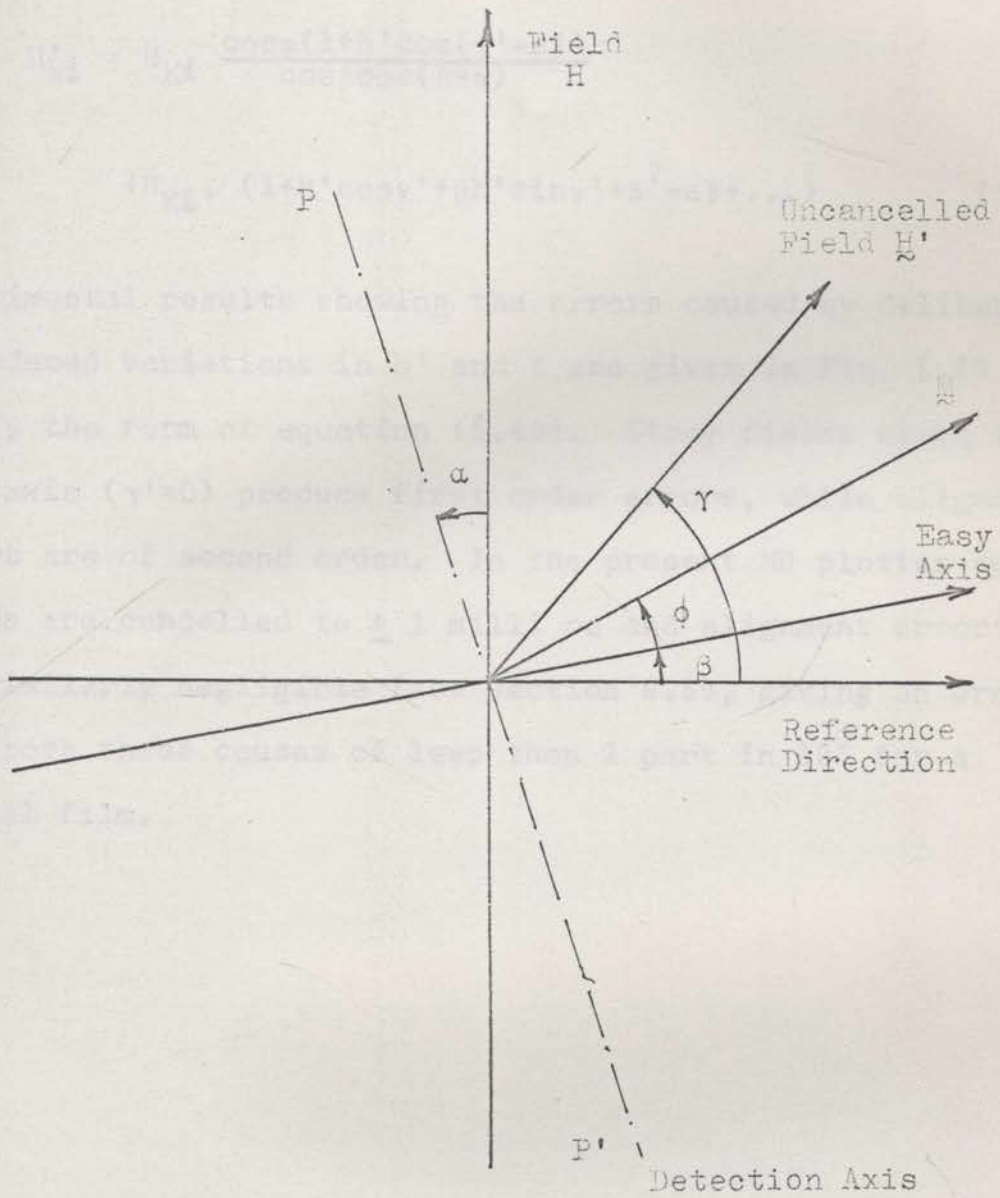


Fig. 5.65 The Effect of Alignment Errors and Uncanceled Stray Fields on the Measurement of  $H_{Ki}$

$$H'_{Ki} = H_{Ki} \frac{\cos\alpha(1+h'\cos(\gamma'-\beta))}{\cos\beta\cos(\beta-\alpha)}$$

$$\approx H_{Ki} \cdot (1+h'\cos\gamma'+\beta h'\sin\gamma'+\beta^2-\alpha\beta+\dots) \quad (5.69)$$

Experimental results showing the errors caused by deliberately introduced variations in  $h'$  and  $\beta$  are given in Fig. 5.64 and verify the form of equation (5.69). Stray fields along the easy axis ( $\gamma'=0$ ) produce first order errors, while alignment errors are of second order. In the present MH plotter such fields are cancelled to  $\pm 1$  milli oe and alignment errors are similarly negligible (see Section 6.5), giving an error from both these causes of less than 1 part in  $10^3$  for a typical film.

"Determination of the Anisotropy in Thin Permalloy Films".  
*J. Appl. Phys.*, 35, 1964, (1964).

21. Feldtkeller, E.,  
 "Whipple Hysteresis in Thin Magnetic Films".  
*J. Appl. Phys.*, 34, 2646, (1963).

22. Huber, E.E., Cohen, M.L., Weiss, G.S., Bellin, R.O.,  
 "Resonance Studies of Inverted Films".  
 Quarterly Rep. Rept. on Solid State Research, IBM T. J. Watson  
 Massachusetts Institute of Technology, 3-24, 1960, 1961.

23. Rossing, T.D., Stoler, F.,  
 "Method for Measuring the Anisotropy Function of Thin  
 Magnetic Films".  
*Rev. Sci. Instrum.*, 31, 782, (1960).

- B1 Bader, C.J., Ellis, D.M.,  
"Instrument for the Observation of Magnetisation Vector  
Position in Thin Magnetic Films".  
J.Sci.Instrum., 33, 1429, (1962).
- B2 Beeforth, T.H.,  
"The Importance of Secondary Effects when Measuring  
Thin Films Anisotropy Fields".  
J.Electronics and Control, 13, 437, (1962).
- C1 Crowther, T.S.,  
"Techniques for Measuring the Angular Dispersion of the  
Easy Axis of Magnetic Films".  
Group Report No. 51-2, Lincoln Lab., Massachusetts  
Institute of Technology, p. 51, (1959).
- C2 Collette, R.,  
"A New Anisotropy Recorder for Ferromagnetic Thin Films".  
Rev.Sci.Instrum., 33, 450, (1962).
- C3 Crowther, T.S.,  
"Angular and Magnetic Dispersion of the Anisotropy  
in Magnetic Films".  
J.Appl.Phys., 34, 580, (1963).
- D1 Doyle, W.D.,  
"Determination of the Anisotropy in Thin Permalloy  
Films".  
J.Appl.Phys., 33, 1769, (1962).
- F1 Feldtkeller, E.,  
"Ripple Hysteresis in Thin Magnetic Films".  
J.Appl.Phys., 34, 264b, (1963).
- H1 Huber, E.E., Cohen, M.S., Weiss, G.P., Smith, D.O.,  
"Resonance Studies of Inverted Films".  
Quarterly Res.Rept.on Solid State Research, Lincoln Lab.,  
Massachusetts Institute of Technology, p.96, (Oct., 1959).
- R1 Rossing, T.D., Stoler, R.,  
"Method for Measuring the Anisotropy Function of Thin  
Magnetic Films".  
Rev.Sci.Instrum., 32, 752, (1961).

CHAPTER 6

- S1 Smit, J., Wyn, H.P.J.,  
"Ferrites".  
John Wiley and Sons Inc., New York, p.118, (1958).
- S2 Smith, D.O.,  
"Static and Dynamic Behaviour of Thin Permalloy Films".  
J.Appl.Phys., 29, 264, (1958).
- S3 Smith, D.O., Weiss, G.P.,  
"Resonance Studies on Oblique Incident Films".  
Quarterly Res.Rept.on Solid State Research, Loncoln Lab.,  
Massachusetts Institute of Technology, p. 82, (July,'60).
- S4 Smith, D.O., Harte, K.J.,  
"Noncoherent Switching in Permalloy Films".  
J.Appl.Phys., 33, 1399, (1962).

The instrument is suitable for the measurement of planar films of thickness from 100 Å to 3000 Å deposited on a flat non-conducting substrate and has a noise level corresponding to the signal obtained from a film of 1 cm diameter and 0.0 Å in thickness. Provision has been made for variable frequency operation from 100 c/s to 1000 c/s to enable study of the effects of frequency on film behaviour.

A prime object of the present investigation of thin films has been to extend the range and accuracy with which film properties can be studied by MR plotter techniques. An integral part of this work has been an examination of theoretical and practical factors limiting the performance of an instrument of this type. In the construction of the present MR plotter, particular attention has been paid to

## CHAPTER 6

THE DESIGN OF AN MH PLOTTER FOR THE ACCURATE  
MEASUREMENT OF THIN FILMS

## 6.1 INTRODUCTION

In the course of the present research, it has been necessary to design and construct a sensitive audio frequency MH plotter or hysteresigraph for the measurement of thin magnetic films. The instrument is suitable for the measurement of planar films of thickness from 100 Å to 3000 Å deposited on a flat non-conducting substrate and has a noise level corresponding to the signal obtained from a film of 1 cm diameter and 0.6 Å in thickness. Provision has been made for variable frequency operation from 100 c/s to 1000 c/s to enable study of the effects of frequency on film behaviour.

A prime object of the present investigation of thin films has been to extend the range and accuracy with which film properties can be studied by MH plotter techniques. An integral part of this work has been an examination of theoretical and practical factors limiting the performance of an instrument of this type. In the construction of the present MH plotter, particular attention has been paid to

mechanical accuracy, faithful reproduction of the hysteresis loops and high sensitivity.

The basic principles in measuring the hysteresis loops of magnetic materials are well understood. A comprehensive survey up to 1950 has been presented by Bozorth<sup>B1</sup>. Alternating field instruments suitable for the oscilloscope display of MH curves of small samples have been described by a number of workers<sup>C1, C2, C3, M1, H1, W1</sup>. Instruments have been constructed<sup>S3, O1, O2, B3</sup>, especially for measurements on Ni-Fe films in which provision has been made for orientating the sample and for applying traverse magnetic fields. Instruments have been described for measurements on films deposited on other than flat substrates. In particular, the MH plotter reported by Bryzinski and Sahba<sup>B3</sup> allows the film to be positioned to within  $0.1^\circ$ , but the mechanical construction is complicated, the sense coil large and its resonant frequency low (8.3 Kc/s). The most sensitive instrument is a recent design by Oguey<sup>O1</sup> who has obtained a noise level corresponding to the signal from a 1 cm diameter film of  $2 \text{ \AA}$  thickness. Oguey has discussed the optimum design for maximum sensitivity and has given a brief description of the choice of the integration characteristic and a restricted analysis of the correct sense coil shape. Neither of these aspects has been fully treated. Further, as much as any theoretically optimum

design, the success of an MH plotter depends upon its lack of critical adjustments, its stability and absence of drift, and the accuracy, reliability and ease with which measurements can be made. The purpose of the present treatment is thus twofold;

- to extend certain features of the optimum theoretical design, in particular the choice of the repetition frequency  $f_0$ , the design of the sense coil and the choice of the integration transfer function. These matters are considered later in Chapter 7. Details of the preamplifier and integrator used in the present instrument, and embodying the theoretical principles outlined, are given in Chapter 8.

- to record those aspects of a practical nature which are of importance in the overall performance of the instrument.

The present chapter is concerned with these latter practical considerations. Section 6.2 briefly outlines the principles of operation of the MH plotter. Section 6.3 describes the mechanical construction of the MH plotter, the sense and cancellation coil assembly and the film holder. The use of a sense coil positioned on one side only of the film simplifies the mechanical construction and allows a greater



accuracy in positioning the film. Section 6.4 discusses features of the field coil design including the size, impedance level, tuning, and orthogonality of the coils. A method is given for producing, using the same field coils, an audio frequency (AF) field and a simultaneous DC field necessary for the saturation of the film while cancellation of the air flux voltage is made. Section 6.5 outlines a method of orientating the film and cancelling the earth's magnetic field using the film itself as an indicator of the null field condition. The latter is cancelled by passing a current through auxiliary windings on the normal field coils, avoiding the additional Helmholtz coils<sup>B3</sup>, or magnetically shielded boxes<sup>02</sup> used in some previous designs. Section 6.6 considers the cancellation of the air flux voltage and other stray voltages other than the signal from the film induced in the sense coil circuit. It cannot be too strongly emphasized that the lack of perfect cancellation, in particular of harmonic distortion components in the drive field, imposes one of the principal limitations on the useful sensitivity of an MH plotter. Section 6.7 discusses and establishes tolerable limits for the effects on a hysteresis loop display of limited frequency response of the flux detecting system and of phase errors in the field display. The latter is particularly undesirable as a hysteresis loop may appear normal yet be grossly in error. An adjust-

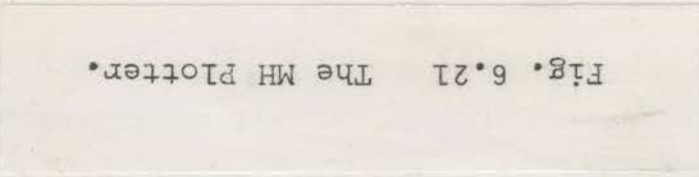
ment procedure is given. It may be noted that adjustment is only possible if the flux detecting amplifier and integrator are designed as in Chapter 8 to have zero phase error.

## 6.2 THE BASIC PRINCIPLES OF OPERATION

### 6.2.1 A description of the System

A photograph of the MH plotter is given in Fig. 6.21, and a block diagram of the circuit is shown in Fig. 6.22. The method of operation is readily understood. Referring to Fig. 6.22, the film  $F$  is placed in a sinusoidally varying magnetic field produced by the Helmholtz coils  $D_1$ . Repetition frequencies  $f_0$  from 100 c/s to 1000 c/s can be used, variable frequency operation being of value in interpreting certain time dependent features of film behaviour (see Section 4.6). The second Helmholtz coil pair  $D_2$  provides a steady DC field at right angles to the field of  $D_1$ , necessary for traverse field studies of thin films.

The flux of the film is detected by the sense coil  $S$  placed near the film.  $S$  has a voltage induced in it proportional to the rate of change of the component of flux along the coil axis. The signal is amplified and displayed on an oscilloscope against the instantaneous applied field

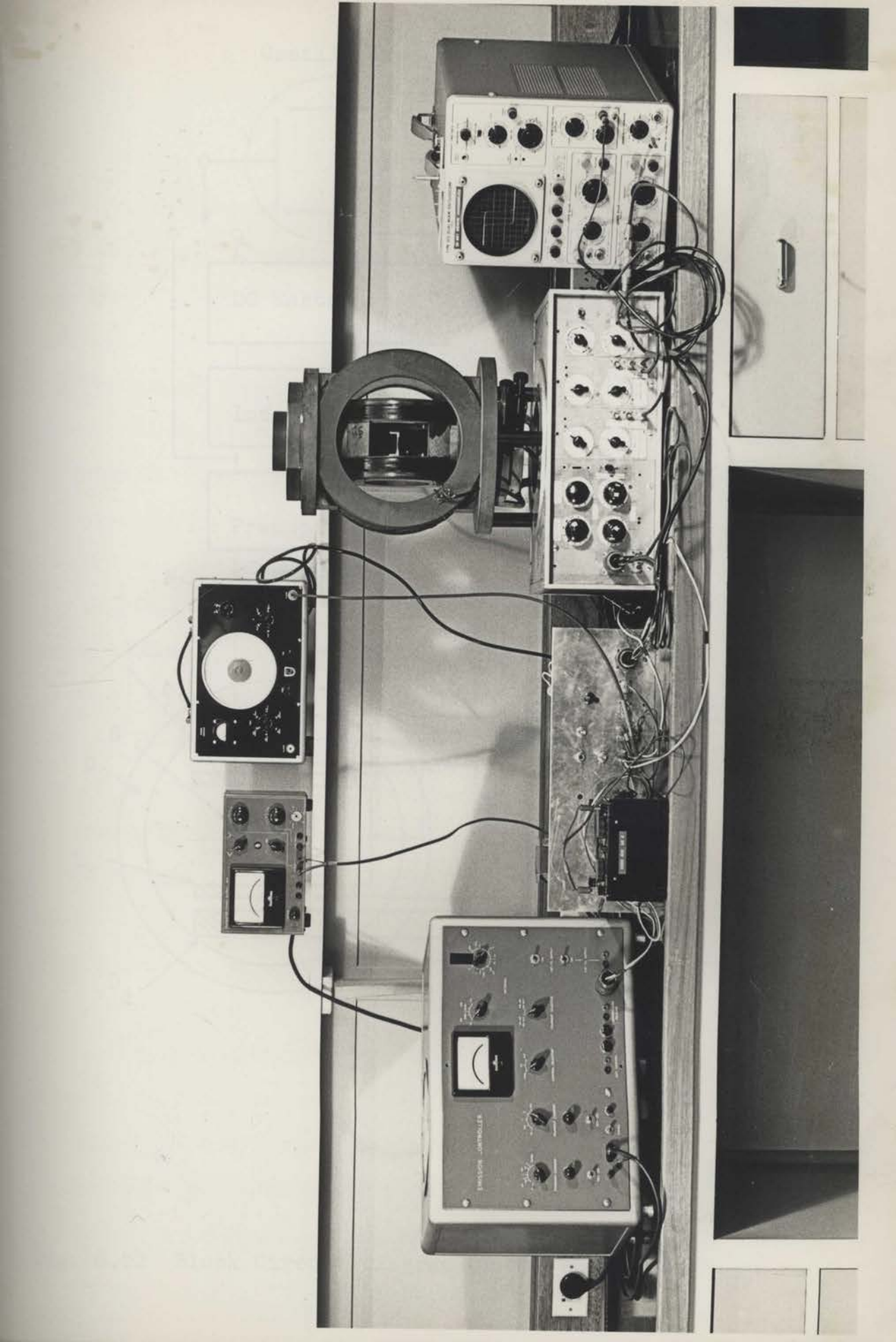


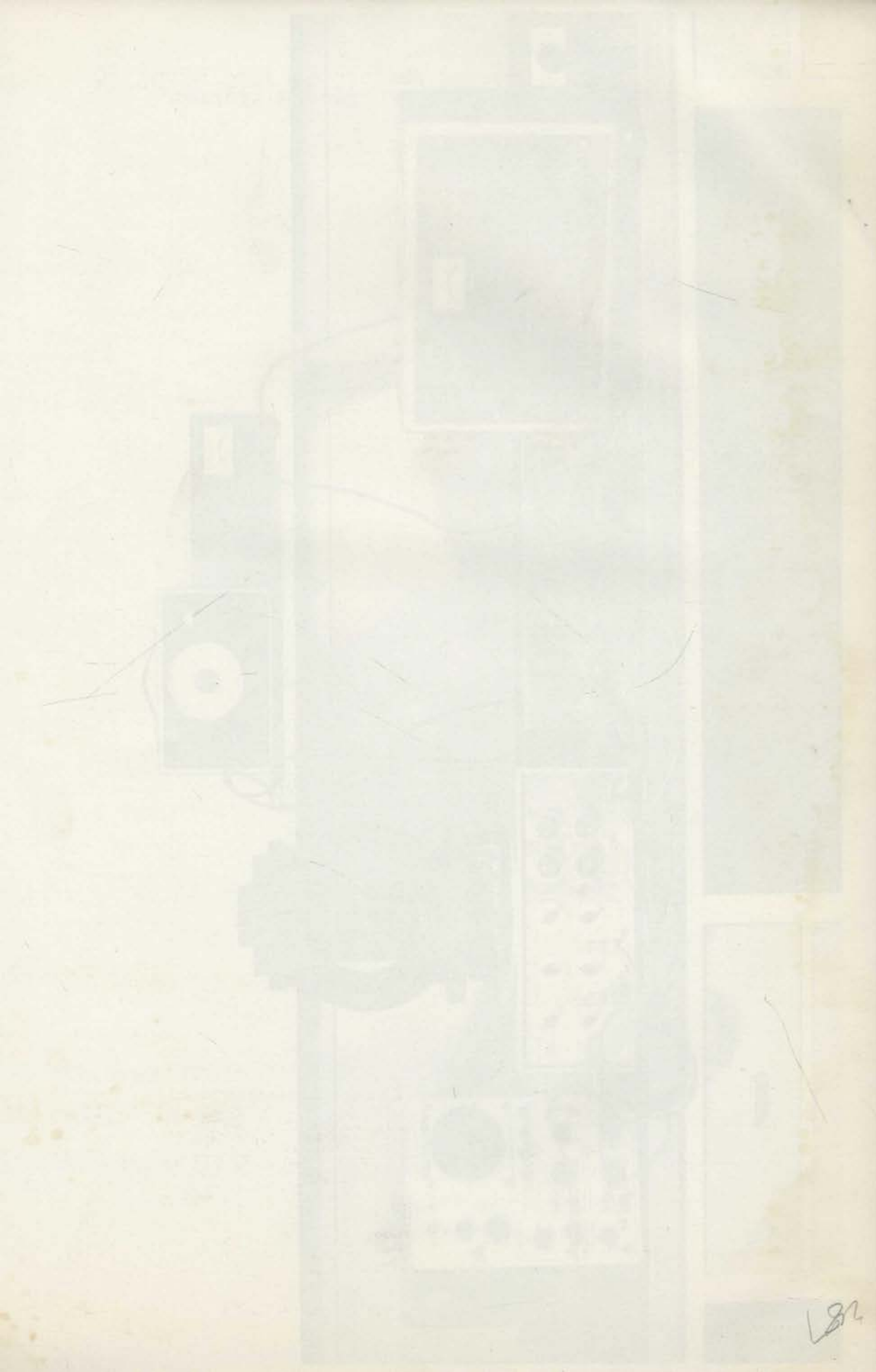
The MH plotter is a device used for plotting the magnitude of the transfer function of a system. It consists of a network of resistors and capacitors, which is connected to a sinusoidal input. The output of the network is measured, and the magnitude of the transfer function is plotted against the frequency of the input. The plot shows a series of peaks and valleys, which correspond to the poles and zeros of the transfer function. The plot is used to determine the stability and performance of the system.

and a plot of the magnitude of the transfer function.

### THE BASIC PRINCIPLES OF OBSERVATION

The basic principles of observation are the same as those of the MH plotter. The magnitude of the transfer function is plotted against the frequency of the input. The plot shows a series of peaks and valleys, which correspond to the poles and zeros of the transfer function. The plot is used to determine the stability and performance of the system.





## Oscilloscope

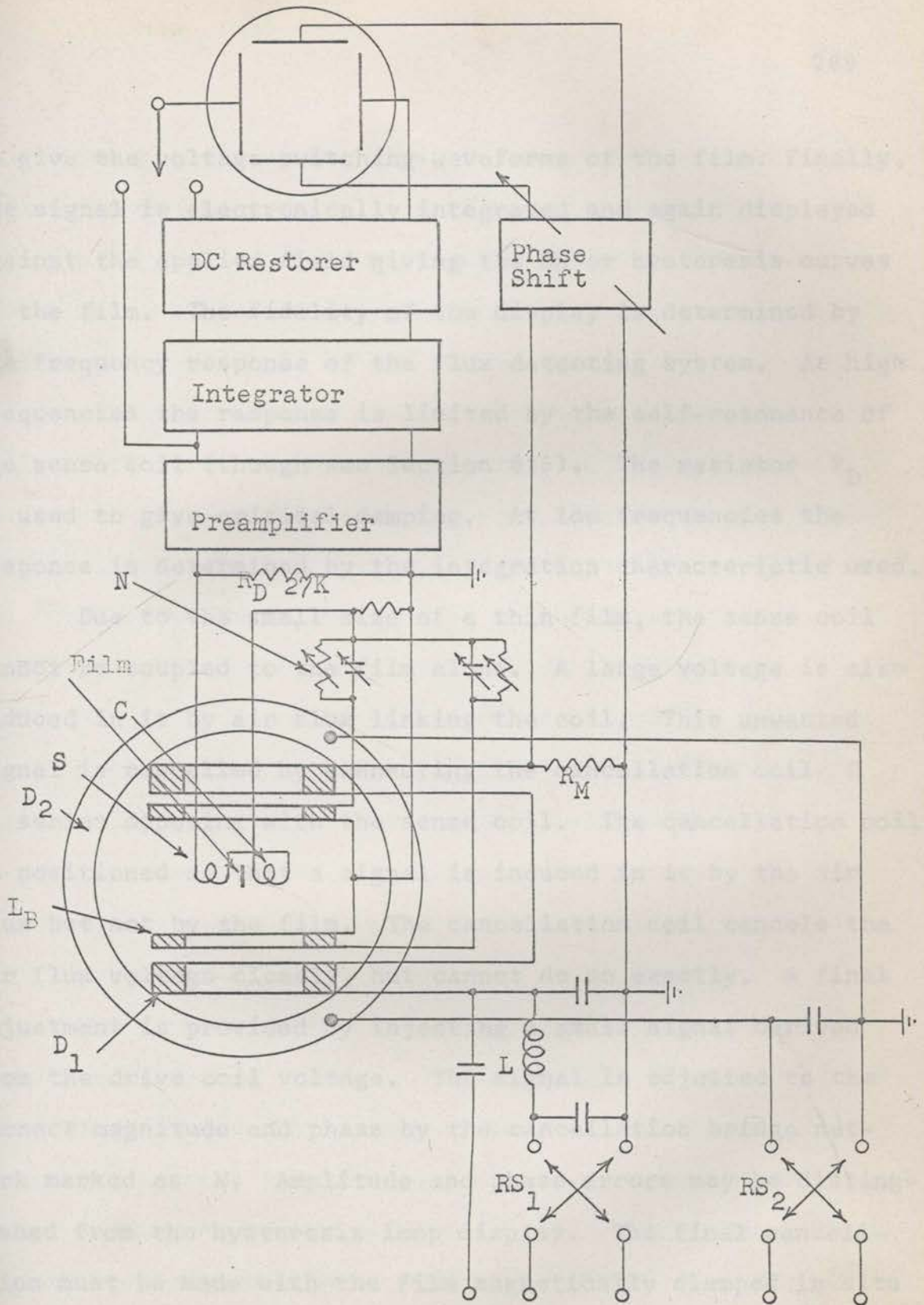


Fig. 6.22 Block Circuit Diagram of the MH Plotter

to give the voltage switching waveforms of the film. Finally, the signal is electronically integrated and again displayed against the applied field giving the MH or hysteresis curves of the film. The fidelity of the display is determined by the frequency response of the flux detecting system. At high frequencies the response is limited by the self-resonance of the sense coil (though see Section 8.6). The resistor  $R_D$  is used to give critical damping. At low frequencies the response is determined by the integration characteristic used.

Due to the small size of a thin film, the sense coil cannot be coupled to the film alone. A large voltage is also induced in it by air flux linking the coil. This unwanted signal is cancelled by connecting the cancellation coil C in series opposing with the sense coil. The cancellation coil is positioned so that a signal is induced in it by the air flux but not by the film. The cancellation coil cancels the air flux voltage closely, but cannot do so exactly. A final adjustment is provided by injecting a small signal derived from the drive coil voltage. The signal is adjusted to the correct magnitude and phase by the cancellation bridge network marked as N. Amplitude and phase errors may be distinguished from the hysteresis loop display. The final cancellation must be made with the film magnetically clamped in situ by a large saturating DC field. While the air flux voltage

is very much the largest, other drive frequency voltages are induced in the sense coil circuit by stray capacitive, magnetic, and common lead couplings. The final balance should thus be made after all other settings, for example the position of the sample holder or the gain of the sense amplifier, have been first completed. In the present instrument, while these voltages are small, being less than 1 part in  $10^4$  of the air flux signal, they are very apparent at the highest sensitivities. Capacitive couplings in particular eliminate any final adjustment procedure in which an object, for example an adjusting tool or a hand, is brought into the immediate region of the sense coil. Likewise any procedure in which the film sample is removed, the balance made, and the sample then replaced, is in serious doubt. Apart from possible mechanical disturbances, capacitive effects caused by the introduction of even a plain glass sample slide are again very apparent at high sensitivities.

The DC saturating field is best produced in the same direction as the AF field by passing both a DC and AF current simultaneously through the field coils  $D_1$ . The design of a coupling network for this purpose is discussed in Section 6.44. The magnetization will tend to lie along the DC field direction and the torque exerted on it by the AF field will



be small. For fields precisely along the easy or hard directions, there is ideally no signal from the film if the minimum field exceeds  $H_K$ . If instead the DC field is produced via coils  $D_2$  and is traverse to the AF field, the latter will always exert a torque on the magnetization. A very much larger DC field will be required for effective saturation.

## 6.22 The Limiting Sensitivity

The sensitivity of the MH plotter is limited by thermal noise in the sense coil resistance and the input noise of the preamplifier. Hum, imperfectly cancelled air flux voltages and other extraneous interference have been reduced to a negligible level. The theoretical aspects of achieving the maximum signal to noise ratio  $\frac{S}{N}$  are discussed in Chapter 7. It is sufficient here to say that the signal from the film will be given by the time rate of change of the fraction  $\psi = 0.13$  (see Section 7.48) of the flux effective in linking the sense coil, giving, for a 1000 Å, 1 cm diameter permalloy film ( $4\pi M_s = 10^4$  ergs units) and a repetition frequency  $f_0 = 1$  Kc/s, a saturated signal of 6.3 mV pp at the sense coil terminals.

The measured noise of the preamplifier and integration, also referred to the terminal of the sense coil by the gain at  $f_0 = 1 \text{ Kc/s}$ , is (see Section 8.2)  $40 \mu\text{V pp}$ . The noise level of the MH plotter thus corresponds to the signal from a 1 cm diameter film of thickness  $7 \overset{\circ}{\text{A}}$ . With synchronous DC restoration (see Section 8.7), the noise level is reduced to  $3.5 \mu\text{V pp}$ , giving an "equivalent thickness" of  $0.6 \overset{\circ}{\text{A}}$ .

### 6.23 A Comparison with the Vibrating Sample Magnetometer and the Mechanical Torque Balance.

The low frequency properties of thin films are also commonly measured using vibrating coil or vibrating sample (VCS) magnetometers  $S_1, D_1, F_1, F_2$  and mechanical torque balances  $B_2, H_2$ .

#### The VCS Magnetometer

The VCS magnetometer is identical to an audio frequency MH plotter in that the measured quantity is the film flux component in a given direction, with however the difference that the measurement can be made with steady fields applied to the film. This latter feature can have advantages in certain cases. For example, hysteresis curves as measured

by an MH plotter may not be truly quasistatic (Section 4.6). As a second example, the measurement of anisotropy magnitude dispersion by the Crowther technique<sup>C4</sup> is simplified, since no read pulses are required to determine the remanent magnetization component along the easy axis.

With an MH plotter, a permanent record of the data can be made photographically, or using synchronous time sampling of the display, an X-Y recorder can be used. The latter need involve only a small modification of the DC restorer given in Section 8.7). In presenting hysteresis loops, an oscilloscope display is useful if adjustments are to be made by observing changes in the pattern. The sensitivity of either an MH plotter or a VCS magnetometer, other factors being equal (for example, the coil shape and relative position to the film), is proportional to  $B/\omega_0^2$ ,

where

$B$  is the detector bandwidth,

$\omega_0^2$  is the AF field frequency or the frequency of the component vibration.

$B$  for an oscilloscope display is necessarily large ( $> 100 \omega_0$ ) but need not be if an X-Y recorder is used. In this case the lower limit on  $B$  is the same for both MH plotter and magnetometer and is set by the time allowed for a recording

to be taken. The MH plotter normally has the advantage that the AF field frequency can be made higher than that for a mechanical vibration. Also for the MH plotter the sense coil flux linkage varies from maximum in one direction to maximum in the opposite direction. The amplitude of vibration of a VCS magnetometer is usually small\* and the flux change correspondingly less than the optimum of maximum to zero. It is not difficult, however, to find a design where the optimum flux change does occur. Fig. 6.23 shows a possible moving coil arrangement. The stationary sample allows accurate orientation with respect to the field. Further only a continuous rotation is required giving a simpler mechanical design and a higher frequency  $\omega_0$ .

### The Mechanical Torque Balance

In the torsion balance also, a steady field  $H$  is applied to the film. The balance then measures mechanically the component of the torque vector  $\underline{T} = \underline{M} \times \underline{H}$  along the torsion axis of the instrument. The torque is proportional to  $M_s V$ ,

---

\* In the vibrating sample instrument described by Flanders and Doyle<sup>F2</sup> the amplitude of the vibration can be varied from 0.5 to 4 mm.

---

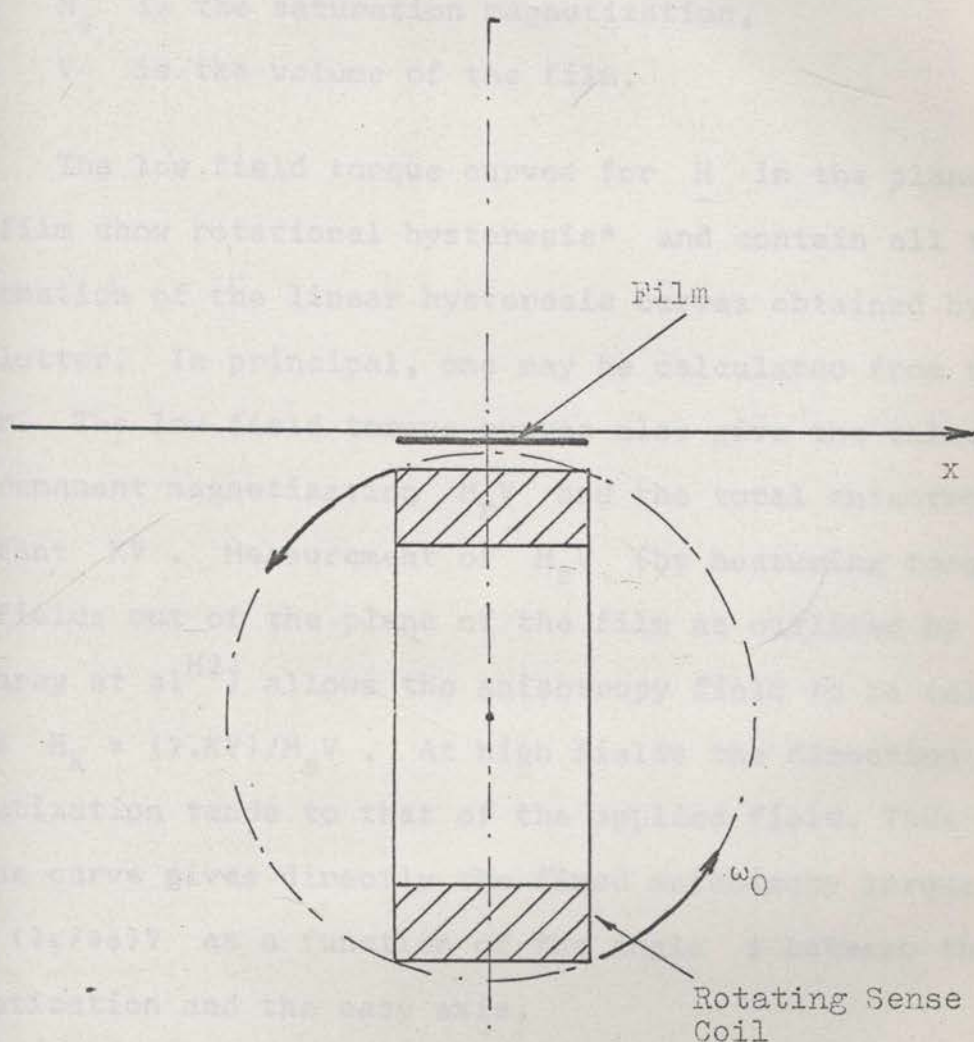


Fig. 6.23 A Rotating Coil Arrangement Measuring the Steady x-axis Component of the Magnetization of the Film Sample shown.

where

$M_S$  is the saturation magnetization,

$V$  is the volume of the film.

The low field torque curves for  $\vec{H}$  in the plane of the film show rotational hysteresis\* and contain all the information of the linear hysteresis curves obtained by an MH plotter. In principal, one may be calculated from the other. The low field torque curves also give the values of the remanent magnetization  $M_r V$  and the total anisotropy constant  $KV$ . Measurement of  $M_S V$  (by measuring torques for fields out of the plane of the film as outlined by Humphrey et al<sup>H2</sup>) allows the anisotropy field to be calculated as  $H_K = (2.KV)/M_S V$ . At high fields the direction of the magnetization tends to that of the applied field. Thus the torque curve gives directly the fixed anisotropy torque  $TV = (\partial\epsilon/\partial\phi)V$  as a function of the angle  $\phi$  between the magnetization and the easy axis.

For thin films the torque balance may also be used to plot directly the magnetization in any given direction against an applied field, thus exactly duplicating all the

---

\* A detailed account of torque measurements and rotational hysteresis has been given in Section 2.8 .

---

uses of an MH plotter or VCS magnetometer. The method is a variation of that given by Humphrey et al for determining  $H_C$  and is illustrated in Fig. 6.24. A small fixed field  $H_{\perp}$  ( $\div$  few oersteds) is applied perpendicular to the plane of the film. Rotation of  $\underline{M}$  out of the plane of the film is negligible ( $\div H_{\perp}/4\pi M_S$ ) and the torque component  $T_y$  about the y axis is closely equal to the product of  $H_{\perp}$  and the x component of the magnetization. The film may be rotated in the xy plane and additional fields  $H_L$  or  $H_T$  in the xy plane applied as required.

#### A Comparison of the Sensitivities of the Three Instruments

The sensitivity of a torsion balance is not directly comparable to the sensitivity of an MH plotter or a VCS magnetometer. For the former the torque is KV while for the latter, assuming a circular film of thickness t and diameter d, the output signal will be proportional to  $4\pi M_S t d$ . For a 1 cm diameter film, taking  $K=10^3$  erg  $\text{cm}^{-3}$  and  $4\pi M_S = 10^4$  cgs units =  $10^{-4}$  volt secs.,

$$KV = 10^3 V \text{ dyne cm}$$

$$4\pi M_S t d = \frac{4}{\pi} \cdot 4\pi M_S \cdot \frac{V}{d} \div 10^{-4} V \text{ volt secs.}$$

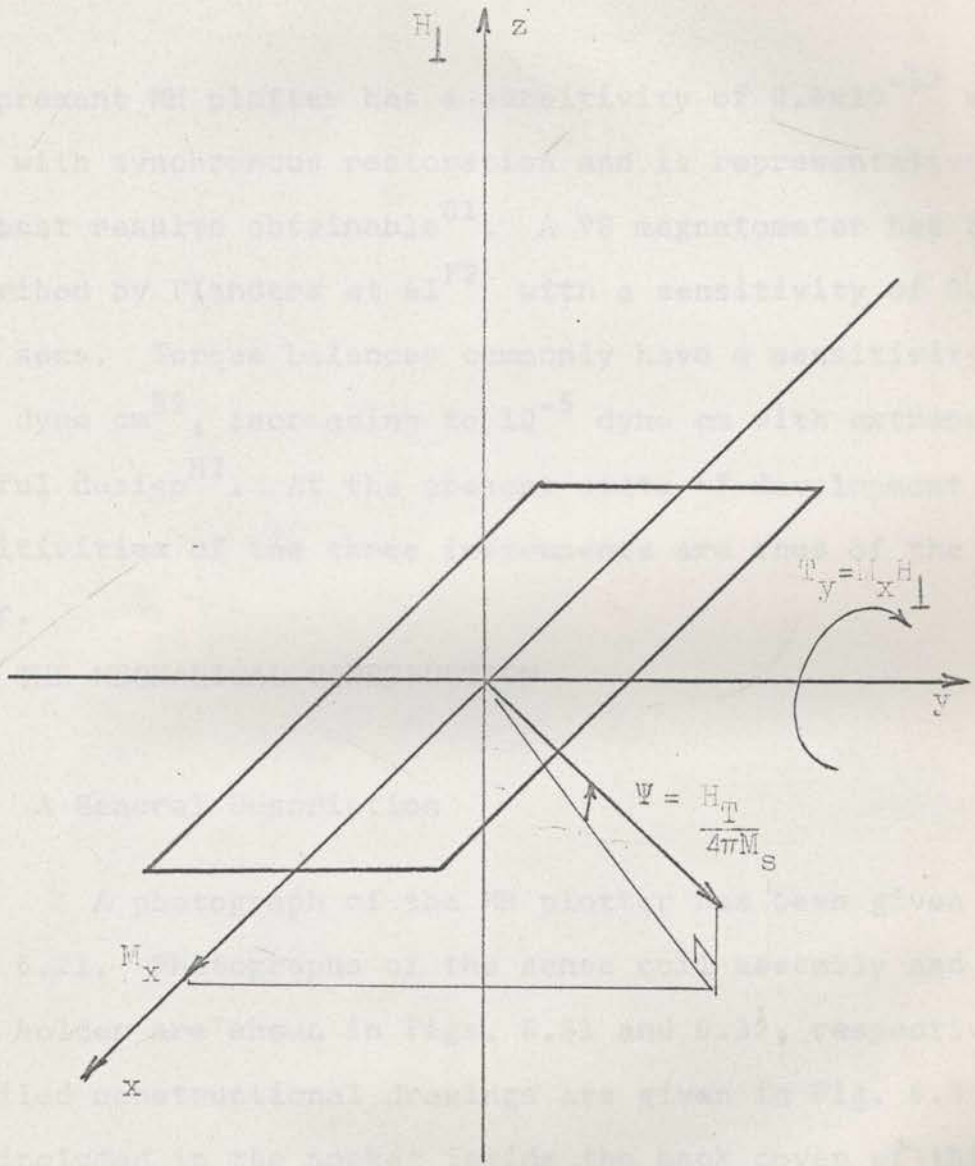


Fig. 6.24 Figure Illustrating the Use of a Mechanical Torsion Balance to Measure Magnetization Components in the Phase of the Film.



The present MH plotter has a sensitivity of  $0.6 \times 10^{-12}$  volt secs with synchronous restoration and is representative of the best results obtainable<sup>01</sup>. A VS magnetometer has been described by Flanders et al<sup>F2</sup> with a sensitivity of  $0.5 \times 10^{-12}$  volt secs. Torque balances commonly have a sensitivity of  $10^{-3}$  dyne cm<sup>B2</sup>, increasing to  $10^{-5}$  dyne cm with extremely careful design<sup>H2</sup>. At the present state of development the sensitivities of the three instruments are thus of the same order.

### 6.3 THE MECHANICAL CONSTRUCTION

#### 6.31 A General Description

A photograph of the MH plotter has been given in Fig. 6.21. Photographs of the sense coil assembly and the film holder are shown in Figs. 6.31 and 6.32, respectively. Detailed constructional drawings are given in Fig. 6.33 and are included in the pocket inside the back cover of this volume.

The coil assembly is fabricated from Novasteen D201 supplied by the W.J. Manufacturing Co., Australia. This material is a coarse weave linen based, phenolic bonded laminate available in sheet and in rolled rod form. It has good machining properties, mechanical rigidity and dimensional stability.



Fig. 6.31 The Sense and Cancellation  
Coil Assembly.



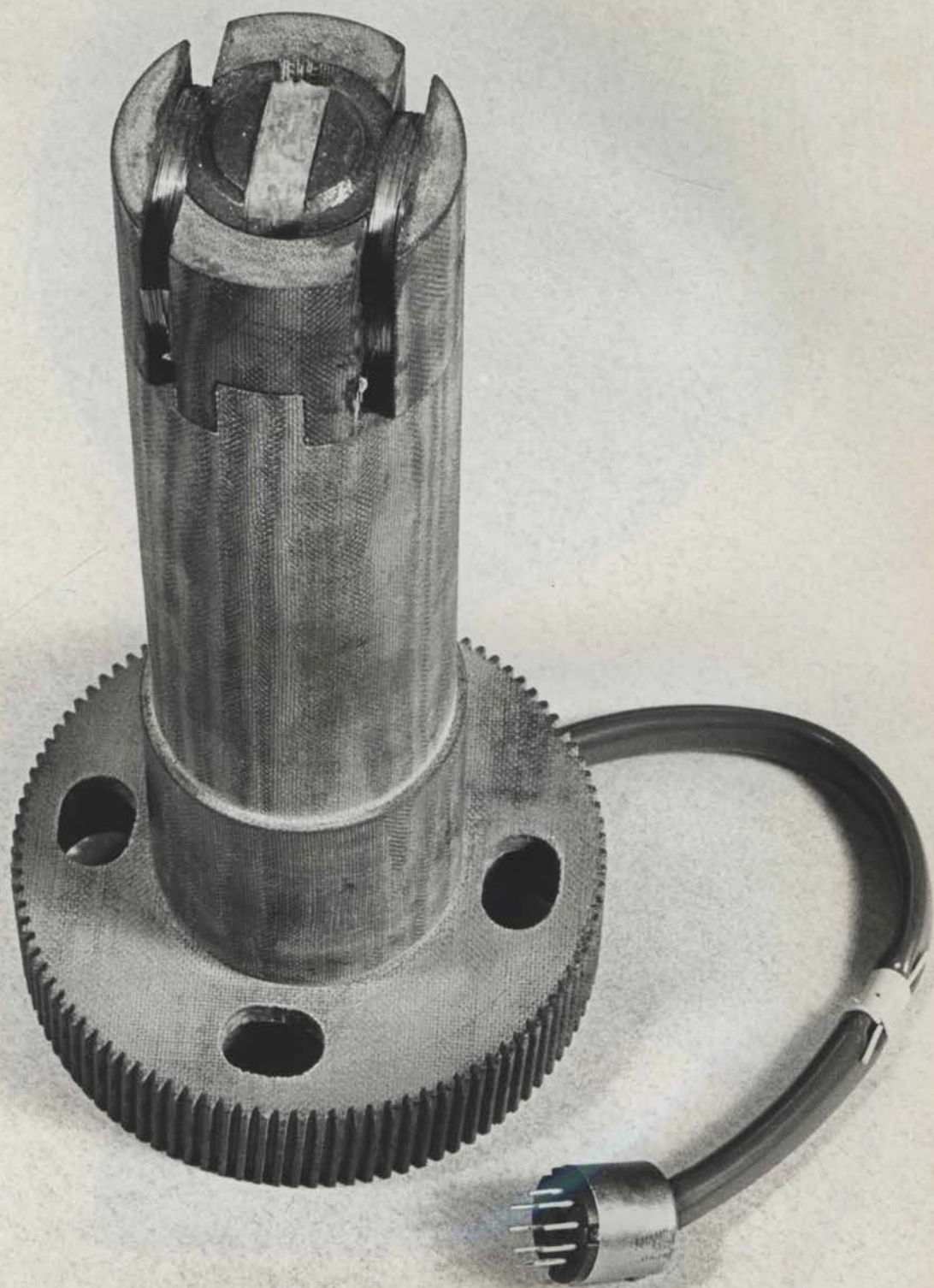
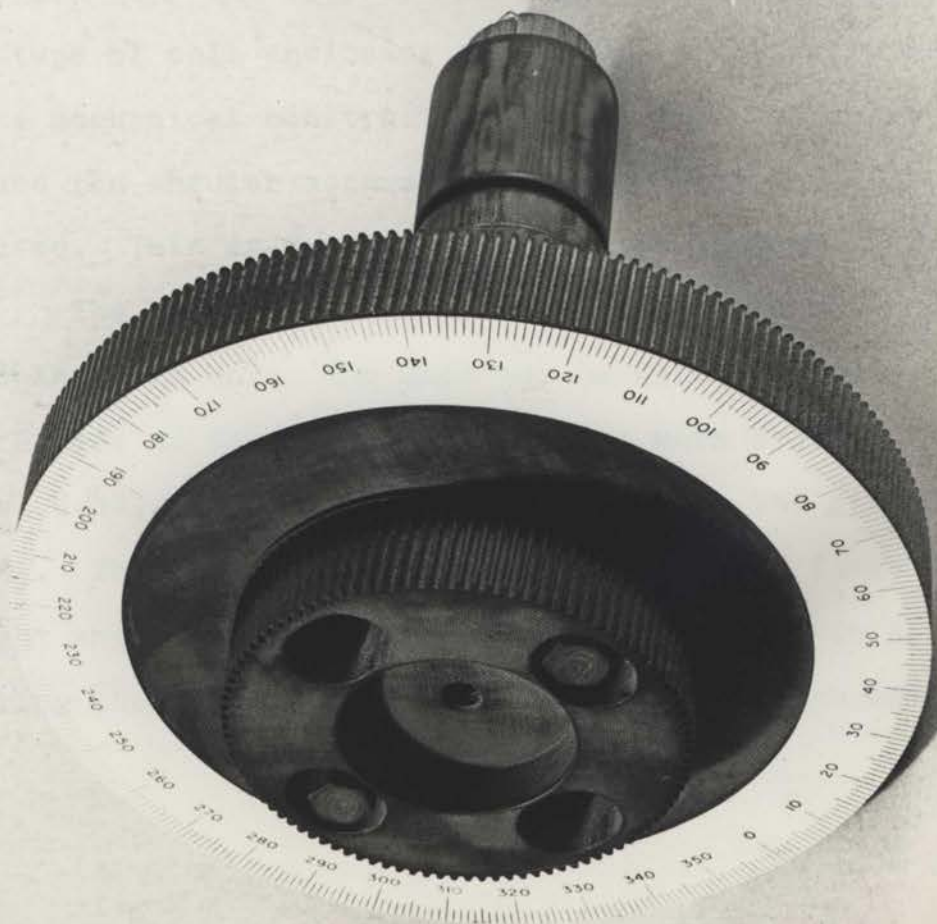
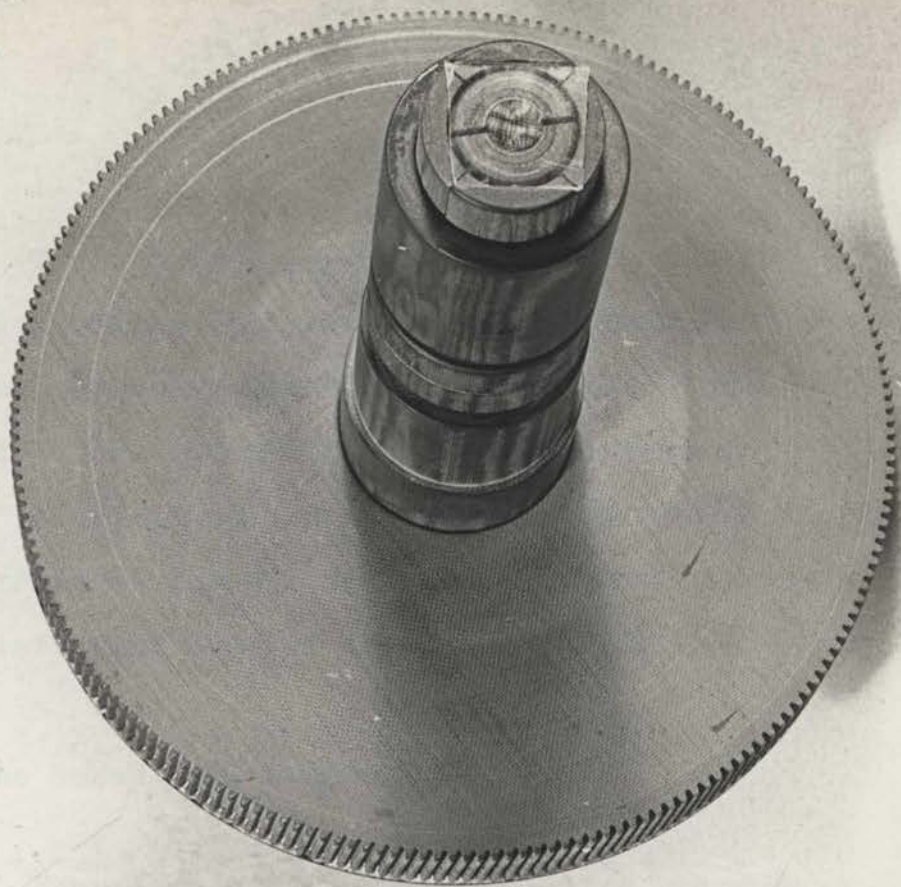


Fig. 6.32 The Film Holder.





The complete assembly is rigidly mounted on top of a cabinet housing the sense coil amplifier, integrator and all other necessary circuitry except the AF and DC field supplies. This construction gives the minimum pick up of hum and interference and the maximum operating convenience. The controls of the air flux cancellation bridge are grouped at the left hand side of the front panel.

### 6.32 The Sense Coil Assembly

The sense coil is positioned on one side only and just below the film sample. In comparison to the more usual type of coil enclosing the film, sensitivity is less, but the mechanical construction of the film holder is simplified and the angular accuracy in positioning the film greatly increased. This is further discussed in Section 7.42.

The sense and cancellation coils form one rigid, interchangeable unit. The unit may be rotated through  $100^\circ$  with respect to the field coils by the worm drive  $J_2$  shown in Fig. 6.33, the angle being measured from the graduated disc  $M_2$ . The  $90^\circ$  position with the sense and field coils at right angles can be located to within 1 part in  $10^4$  by adjusting the sense coil for zero induced voltage across it.

## 6.33 The Film Holder

The film is held by the film holder just above the sense coil. The holder rotates through  $360^\circ$  with respect to the field coils, the angle being read to  $\pm 0.020^\circ$  from the graduated disc  $M_1$  using the vernier  $V^*$ . The holder will take either 1 in diameter circular glass slides or 1 in wide rectangular slides. The former is held by the four jaws A, B, C and D, and the latter by the flat faces on the jaws A and C. The slide is located at a reproducible height above the sense coil by being pressed against the button E. The height is adjustable by means of the spacer H. For rectangular slides, the film spot is centrally positioned by aligning it through the glass with a series of concentric circles inscribed on the face of button E. The variation in the apparent saturation flux of the film with angular position is less than 1 per cent. The jaws are flexible, and the holding pressure, adjustable by means of the collet G, should be no more than just sufficient to retain the slide. Surprisingly little pressure is required to distort a 1/32 in thick glass slide and changes in  $H_K$  of up to several per cent may occur, even for permalloy films of nominally zero magnetostrictive coefficient.

---

\* The measurement of angular dispersion of a film with  $\sigma_\beta = 20 \times 10^{-3}$  or  $1^\circ$  using Crowther's first method<sup>C4</sup> requires an accuracy of  $\pm 0.05^\circ$  at least.

---

#### 6.4 THE FIELD COILS $D_1$ AND $D_2$

As outlined in Section 6.21, the fields of the MH plotter are produced by the two Helmholtz field coils  $D_1$  and  $D_2$ ;

- the coils  $D_1$  of 7 ins diameter produce either an AF field, a DC field, or both simultaneously; the latter being required for magnetic clamping of the film during air flux cancellation, in partial switching experiments<sup>M2</sup> and in the measurement of torque curves by the method of Section 5.4

- the coils  $D_2$  of 11 ins diameter produce a steady field at right angles to that of the coils  $D_1$ .

These two sets of mutually orthogonal coils are all that are required for almost all possible measurements which might be made on a film (one exception being the method of Rossing and Stolen outlined in Section 5.3).

Winding data, measured electrical parameters and other details of the field coils have been collected in Table 6.41. Formulae for the design of Helmholtz coils, including the effects and optimum proportions for a winding of finite cross section, have been given by numerous authors<sup>R1, S2</sup> and will not be repeated here. The design of



Table 6.41 DETAILS OF THE FIELD COILS,  
THE EARTH'S FIELD COMPENSATING COILS,  
AND THE BRIDGE CANCELLATION COILS. \*

THE FIELD COILS \*\*

	Inner Coils $D_1$	Outer Coils $D_2$
Mean Diameter	7 ins	11 ins
Winding Data	Each half, 80 turns of 48 strand 33 SWG litz	
Field Calibration Factor (field per unit current)	8.12 oe amp <sup>-1</sup>	5.16 oe amp <sup>-1</sup>
DC Resistance 18° C	0.63 ohms	0.98 ohms
Inductance	3.76 mH	6.96 mH
Self Resonant Frequency	100 kc/s	61 kc/s
Q at 1 kc/s	31.2	37.1
Parallel Resonance Impedance	740 ohms	1640 ohms

THE COILS FOR COMPENSATING THE EARTH'S MAGNETIC FIELD \*\*

	Inner Coils D	Outer Coils $D_4$
Mean Diameter	7.8 ins	11.8 ins
Winding Data	Each half, 36 turns 23 SWG' enamel	
Field Calibration Factor	3.65 oe amp <sup>-1</sup>	2.41 oe amp <sup>-1</sup>
DC Resistance 18° C	2.76 $\Omega$	4.05 $\Omega$

# THE CANCELLATION BRIDGE COILS \*\*

	Inner coils $D_3$	Outer coils $D_6$
Mean Diameter	7.5 ins	11.5 ins
Winding Data	Each half, 6 turns enamel	23 SWG'
DC Resistance $18^{\circ}$ C	0.67 $\Omega$	0.87 $\Omega$
Inductance	41 $\mu$ H	69 $\mu$ H
Mutual Inductance to the Field Coils $D_1$ and $D_2$	215 $\mu$ H	435 $\mu$ H

---

\* the present MH plotter was originally designed so that either the inner or outer coils could be used as the AF field coil, thus windings  $D_2, D_4, D_6$  duplicate  $D_1, D_3, D_5$  respectively. For normal use it has been found more convenient to use the inner coils  $D_1$  as the AF field coils, and this is the mode of operation which has been described in the text.

\*\* unless otherwise stated all values quoted apply to the two halves of each coil pair connected in series

the coils  $D_1$  ,  $D_2$  are determined by a number of considerations which are briefly listed in Sections 6.41 to 6.47 below.

#### 6.41 The Diameter of the Coils

The 7 ins diameter is set by

- the minimum field uniformity required over the region of the cancellation coil for successful cancellation of spatial harmonics in the induced air flux voltage as discussed in Section 6.63.
- the provision of a working space inside the coil large enough for easy handling of the film sample. It may also be necessary to measure individual spots on a large glass plate, or to bend a long slide in determining the magneto-strictive properties of a film.

The field homogeneity of 1 part in  $10^4$  over a 1 cm diameter film is more than adequate for normal applications\*.

---

\* The measurement of anisotropy dispersion will require the highest uniformity. For a film of  $\sigma_\beta = 20 \times 10^{-3}$  or  $1^\circ$ , a uniformity of 1 part in  $10^3$  is desirable.

---

#### 6.42 AF Power Requirements of

The AF power requirements have been made small, consistent with 7 ins coil diameter, by the use of a large winding cross section. For a given field, the power required by a Helmholtz pair increases as the first power of the diameter if both diameter and winding cross section are scaled together. It becomes increasingly difficult to provide large amounts of distortion free power. Harmonics in the drive field can prevent complete cancellation of the air flux signal. Undue thermal changes can effect the stability of the cancellation.

#### 6.43 The Impedance Level and Tuning of $D_1$

The impedance level of  $D_1$  has been made low to reduce capacitively coupled voltages in the sense coil circuit. A balanced drive has not been found necessary in this regard.  $D_1$  is parallel tuned to reduce distortion and to provide a suitable load for the driving amplifier. At the lower frequencies near 100 c/s the tuning capacity is large. AC "motor start" electrolytics have been satisfactorily used for this purpose.

#### 6.44 The Production of Simultaneous AF and DC Fields

A DC supply cannot be connected directly across the coils  $D_1$  as a large AF voltage would be impressed upon the supply. For the same current, the ratio of the AF to DC voltages would equal the  $Q$  of the coil, about 30 at  $f_0 = 1 \text{ Kc/s.}$  A current, regulated supply would be needed with the regulating element absorbing the full AF voltage. The problem is not avoided by using separate windings, since if the windings produce coincident fields, then necessarily they must be magnetically coupled.

In the present instrument  $D_1$  is decoupled by the DC supply by the choke-capacitor filter shown in Fig. 6.22. The iron cored choke  $L$  is designed to avoid excessive inductance change and consequent detuning of the AF circuit when a DC current is passed. Both the current monitoring resistor  $R_M$  and the AF supply are earthed. Any convenient AF or DC supplies may be used. Other coupling methods are possible (see Appendix B), but are not as convenient as the above.

### 6.45 The Orthogonality of the Field Coils and Induced AF Currents

The field coils  $D_1$  and  $D_2$  must be set accurately at right angles to prevent magnetically induced currents flowing in  $D_2$ . If a mutual inductance  $M$  exists between the coils, the total field will be

$$\begin{aligned} \vec{H} &= \vec{n}_1 H_1 + \vec{n}_2 H_2 \\ &= H_1 (\vec{n}_1 + \vec{n}_2 \cdot \frac{\gamma_2}{\gamma_1} \cdot \frac{sM}{Z_2}) \end{aligned} \quad (6.41)$$

where

$H_1$ ,  $H_2$  are the fields of  $D_1$ ,  $D_2$ , respectively,

$\gamma_1$ ,  $\gamma_2$  are the field calibration factors (field per unit current) of  $D_1$ ,  $D_2$ , respectively,

$\vec{n}_1$ ,  $\vec{n}_2$  are unit vectors along the axis of  $D_1$ ,  $D_2$ , respectively, and

$Z_2$  is the total impedance in the circuit of  $D_2$ .

A current monitoring resistor used in series with coils  $D_1$  to measure the AF field will detect only  $H_1$  not  $H_2$ . Similarly, field sensing coils will measure only  $H_1$  and not  $H_2$  which is normal to their axis. Variations in  $Z_2$  and consequently  $H_2$  can cause the air flux cancellation to change with the DC current through  $D_2$ . Certain film measurements

will be effected by  $H_2$  .

It seems desirable to set a limit of  $H_2/H_1 < 1 \times 10^{-3}$  . If the coils  $D_2$  are supplied from a high impedance current source so that  $Z_2$  is large, the induced voltage in  $D_2$  needs only to be sufficiently small to be absorbed across the current regulating element. The simplest arrangement, however, is, as in the present instrument, to short circuit coils  $D_2$  by a large capacitor. The AF operation of the MH plotter is then independent of the DC source and any convenient variable DC supply may be used<sup>A1</sup>. In this case equation 6.41 reduces to

$$H \div H_1 (n_1 + n_2 \cdot \frac{Y_2}{Y_1} \cdot \frac{M}{L_2}) \quad (6.42)$$

where  $L_2$  is the inductance of  $D_2$  , and it may be calculated from the measured parameters of the field coils (Table 6.41) that for  $H_2/H_1 < 1 \times 10^{-3}$  ,  $D_1$  and  $D_2$  must be orthogonal to within an angular error of approximately  $3 \times 10^{-3}$  rad. This is easily obtained in the present instrument by adjusting  $D_1$  relative to  $D_2$  using the worm drive  $J_3$  (Fig. 6.33) to give zero induced voltage across  $D_2$  .  $H_2/H_1$  can be made  $< 1 \times 10^{-4}$  and the adjustment is stable over a period of months. Nevertheless, as discussed in Section 6.46, a fixed coil design offers definite advantages and an angular error of  $< 3 \times 10^{-3}$

rad. does not seem unreasonable with accurate construction.

Adjustment of  $D_1$  and  $D_2$  for zero voltage across  $D_2$  will not, due to constructional irregularities and nearby metal objects, necessarily ensure that the fields at the film are orthogonal. With the present instrument this has been checked by mounting the sense coil assembly in place of the film holder in the graduated measuring plate  $M_1$  (Fig. 6.33), and measuring the position of the sense coil nulls for an AF field produced by first  $D_1$ , then  $D_2$ . Experimentally, the error in orthogonality is  $0.23 \pm 0.02^\circ$ .

#### 6.46 Possible Modifications

In the present instrument the inner coils  $D_1$  can be rotated through  $360^\circ$  inside the outer coils  $D_2$ . This facility has not been found necessary and a decrease in size and an increase in rigidity and simplicity is possible if the coils are permanently fixed at right angles to each other.

A design in which the inner coils are used as the AF coils tends to give the lowest AF power requirements for a given working space inside the coils, at the expense of an increased overall size. While not used in the present case, the alternative design in which the outer coils are used as the AF coils can have certain advantages. The larger outer



coils can give a uniform AF field necessary for correct air flux cancellation, while the smaller inner coils, to which this requirement does not apply, will still give adequate field homogeneity over the film area. The earthed inner coils will reduce capacitive coupling between the AF coils and the sense coil circuit. Temperature changes of the sense coil assembly will be less. Such a design tends to give a smaller overall size at the expense of increased AF power and a decreased working space inside the coil.

## 6.5 THE ORIENTATION OF A FILM AND CANCELLATION OF THE EARTH'S MAGNETIC FIELD

### 6.51 Determining the Easy and Hard Axis Directions of a Film

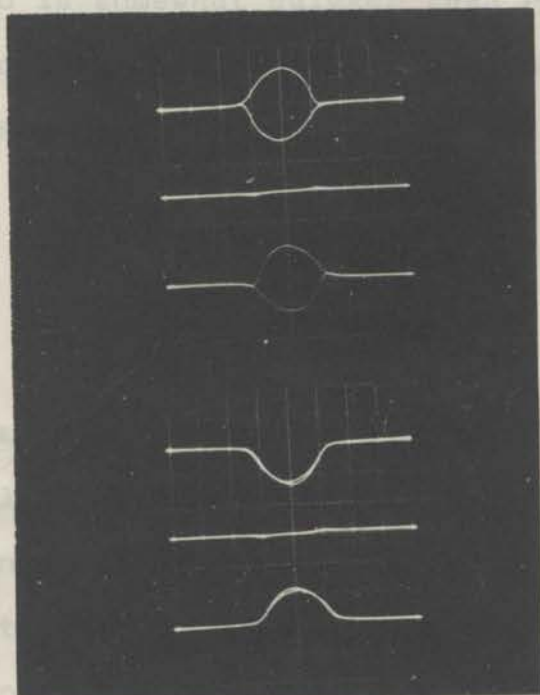
The orientation of a film is best determined by the cross field technique originally described by Crowther<sup>C4</sup>. For films with high dispersion, or with a large pseudo-rotatable anisotropy component the orientation may be found in this way even though the normal( $m_L$ ,  $H_L$ ) hysteresis loop may indicate no orientation at all.

In the cross-field method the magnetization is measured in the direction normal to the applied AF field. If the AF field is orientated precisely along the hard axis

of the film, and if there is no stray DC field component normal to it, then the magnetization will rotate equally in opposite directions and a straight line null will be observed. If there is either a small error in film orientation, or a small non-zero traverse field  $H_T$ , then the magnetization will rotate preferentially in one direction. The nature of the hysteresis loops observed in this case are shown in Fig. 6.51. Angular and field errors are readily distinguished by the different hysteresis loops produced. The precision in locating the null is high, the error in angle or in normalized traverse field  $h_T = H_T/H_K$  being of the order of a few per cent of the angular dispersion  $\sigma_\beta$  for films  $\geq 500 \text{ \AA}$ . For low dispersion films, where  $\sigma_\beta$  is of the order of  $1^\circ$ , the error in angle is set by the limit of reading  $\pm 0.02^\circ$  of the MH plotter while the field  $H_T$  can be set to zero to within  $\pm 1$  milli.oe.. It is also possible to measure cross field hysteresis loops with the AF field applied near the easy axis of the film. The method is however less sensitive than the previous hard direction measurements.

The approximate orientation of a low dispersion film can be found to within  $\pm 1^\circ$  or  $\pm 2^\circ$  without the use of the cross field technique by examining the hard axis ( $\dot{m}_T, \dot{u}_T$ ) switching waveforms. These waveforms normally show a series of peaks due to domain wall transitions which change

Fig. 6.51 HARD AXIS 1000 c/s CROSS FIELD HYSTERESIS LOOPS OF A 1000 Å PERMALLOY FILM S2P17 SHOWING THE METHOD OF ORIENTATING THE FILM AND CANCELLING THE EARTH'S MAGNETIC FIELD.



Frame 1: is taken at zero traverse field for varying angles the hard direction

$$\begin{array}{ccc} + 0.50^\circ & & + 8.7 \times 10^{-3} \text{rads} \\ 0 & \text{or} & 0 \\ - 0.50^\circ & & - 8.7 \end{array}$$

Frame 2: is taken along the hard direction for varying traverse fields  $H_T$  of

$$\begin{array}{ccc} + 31 \text{ milli oe} & & + 8.7 \times 10^{-3} \text{in normalised notation} \\ 0 & \text{or} & 0 \\ - 31 & & - 8.7 \end{array}$$

Scales: m 1 mV/cm \*  
H 3.18 oe/cm \*

\* referred to the terminals of the sense coil by the gain at 1000 c/s

asymmetrically for angular deviations from the hard axis. They vanish altogether when the magnetization begins to rotate coherently at deviations of the order of  $\sigma_{\beta}$ . This method is somewhat quicker than rotating the sense coil and recancelling the air flux as is necessary for a cross-field measurement.

#### 6.52 Cancellation of the Earth's Magnetic Field

The behaviour of low anisotropy is seriously affected by the earth's magnetic field. The field component normal to the plane of the film has a negligible effect; the field component along the AF field direction, that is the longitudinal component, is not critical\*; however the component traverse to the AF field must be accurately cancelled. The simplest way to make this adjustment is to measure the hard axis cross-field hysteresis loops of a low dispersion film as just discussed, and to use the behaviour of the film itself to indicate the zero field. The traverse

---

\* In the display of saturated hysteresis loops, the loop will be unchanged, but slightly displaced along the field axis. In the measurement of the hard direction initial susceptibility, such an uncancelled field has only a second order effect.

---

component is cancelled by passing a small current through an additional winding  $D_4$  wound on the same coil former as the traverse field coils  $D_2$  (see Fig. 6.22). While this current could be passed through the main field winding, the use of a separate winding simplifies the design of the necessary DC current supplies. The winding  $D_4$  requires little power (75 mA, 0.3 V) and can be supplied by an adjustable dropping resistor from the - 12 V regulated voltage supply used for the transistor electronics. The adjustment is stable to within  $\pm 1$  milli.o.e.. Cancellation of the longitudinal component is more difficult. An additional winding cannot be used, since AF currents will be induced in it by magnetic coupling with the main field winding (see Section 6.45). The simplest way is to position the MH plotter on the bench so that the earth's field in the longitudinal direction is zero. Alternatively, a current can be passed through the main field winding via the AF decoupling network. However, two constant current supplies will be required if the reversing switch  $RS_1$  is to reverse only the additional DC current and not the current cancelling the earth's field.

In numerous measurements (for example the measurement of torque curves as in Section 5.4) it is very convenient to either eliminate the effect of the earth's field,

or to check that it is correctly cancelled by taking two readings with the directions of all other applied fields reversed. It is sufficient to reverse only the DC fields by the reversing switches  $RS_1$  and  $RS_2$  shown in Fig. 6.22. Reversal of the AF fields corresponds merely to a change of phase. The field coils themselves should not be reversed as stray couplings to the sense coil circuit, and consequently the cancellation adjustment, will be altered.

## 6.6 FACTORS IN THE STABLE CANCELLATION OF THE AIR FLUX VOLTAGE

### 6.6.1 Introduction

It cannot be too strongly emphasized that the lack of a perfect cancellation of the air flux voltage imposes one of the principle practical limitations on the useful sensitivity of an MH plotter. Nor can it be reduced by correlation techniques as with random noise in Section 8.7. Cancellation must be both

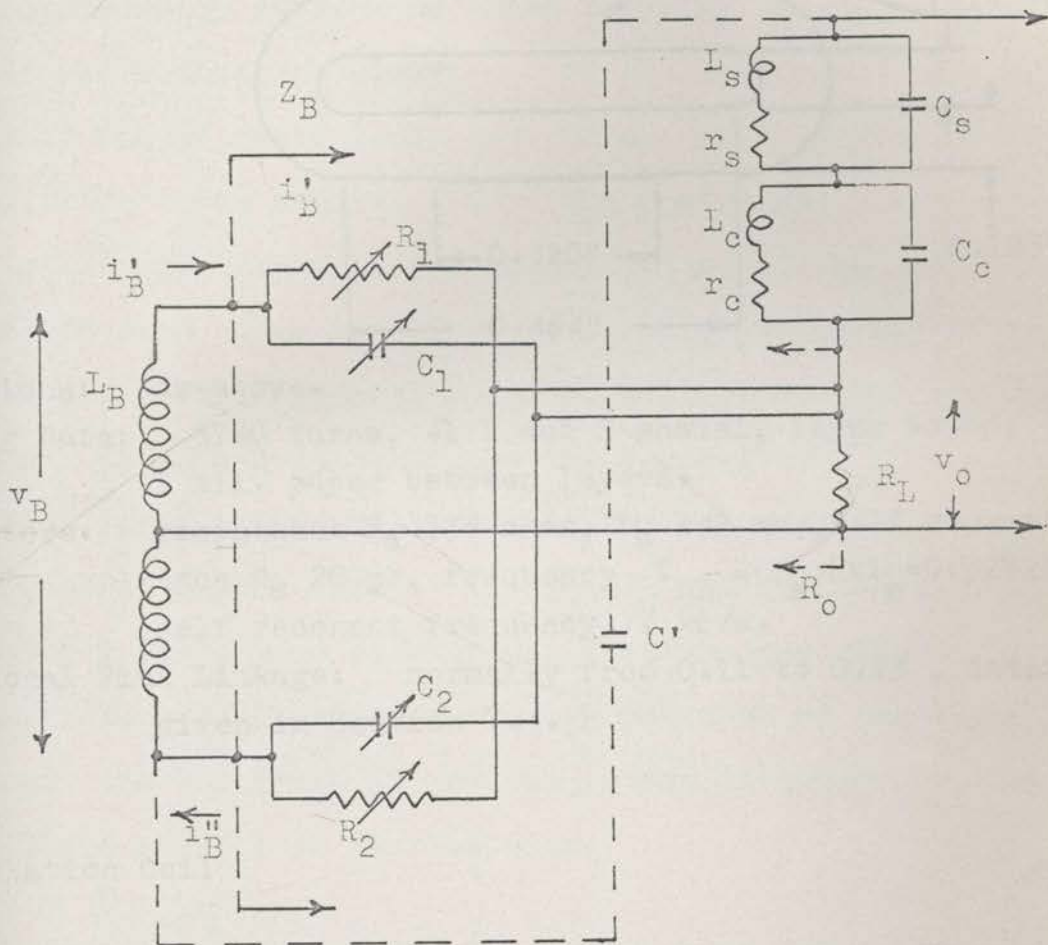
- stable and
- insensitive to the frequency of the drive field.

Cancellation of the fundamental will otherwise still

leave a residual signal due to higher harmonic distortion components in the field. Harmonics have been a definite limitation in some previous designs<sup>S3</sup>.

The cancellation system has been shown in the block diagram of Fig. 6.22 and is given in greater detail in Fig. 6.61. Winding data, measured electrical parameters and other details of the sense and cancellation coils have been collected in Table 6.62. As outlined in Section 6.21, the air flux voltage induced in the sense coil  $S$  is cancelled by a series connected cancellation coil  $C$ , a final adjustment being made by injecting a small variable voltage via the cancellation bridge  $N$ . Injection of this signal in series with  $S$  rather than at a latter point in the amplifier<sup>S3</sup> makes the adjustment independent of all following circuitry, in particular of the coil damping resistor  $R_D$  and the amplifier input impedance and gain.

Section 6.62 below derives an expression for the residual voltage across the sense and cancellation coils, and examines the conditions for a frequency independent balance. Section 6.63 considers the principle unbalance component, the first order amplitude term and its relation to the overall cancellation stability. Practical constructional details and experimental measurements of stabili-



$R_1$  82 K precision WW resistor

$R_1, R_2$  switched bank of 9 18 K precision WW resistors

$C_1, C_2$  switched bank of 9 330 pF capacitors

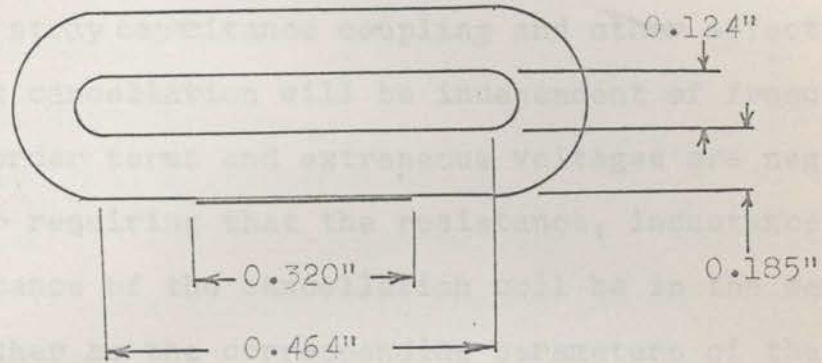
A fine adjustment is provided by a second higher impedance decade with a final continuously variable shunt across  $R_1, C_1$

Fig. 5.61 Details of the Cancellation Bridge



Fig. 6.62 Properties of the Sense and Cancellation Coils

## The Sense Coil



Dimensions: as above.

Winding Data: 3740 turns, 41 B and S enamel, layer wound, 1 mil. paper between layers.

Parameters: resistance  $R_s$  738 ohms,  $L_s$  142 mH, self capacitance  $C_s$  28 pF, frequency  $f_{LR} = R_s / 2\pi L_s = 0.825$  kc/s, self resonant frequency 77 kc/s.

Fractional Flux Linkage: normally from 0.11 to 0.13, details given in Section 7.4.

## Cancellation Coil

Dimensions: as given in detailed mechanical drawing Fig. 6.33

Winding data: 2 x 405 turns per half, 38 SWG

Parameters: resistance  $R_c$  75 ohms,  $L_c$  14.8 mH, self capacitance  $C_c$  25 pF, frequency  $f_{LR} = R_c / 2\pi L_c = 0.810$  kc/s added capacitance for 77 kc/s self resonant frequency 260 pF.

ty are given. Section 6.64 discusses the second order phase unbalance, higher order unbalance terms and extraneous voltage produced by stray capacitance coupling and other effects. It is shown that cancellation will be independent of frequency only if higher order terms and extraneous voltages are negligible, the former requiring that the resistance, inductance and self-capacitance of the cancellation coil be in the same ratio to each other as the corresponding parameters of the sense coil. Experimental results on harmonic rejection are given. Section 6.65 describes the cancellation bridge design to give first order amplitude and second order phase correction without higher terms. The conditions for the minimum "reaction field" are discussed. Finally, the effects of the cancellation coil on the frequency response of the sense coil circuit and its value in reducing stray interference are mentioned briefly in Section 6.66.

#### 6.62 Conditions for Stable and Frequency Independent Cancellation

The induced air flux voltage in the sense coil will produce a voltage  $v_s$  across the terminals of the coil given by

$$v_s = \frac{sM_s i_f}{1+sR_s C_s + s^2 L_s C_s} \quad (6.61)$$

where

$M_s$  is the mutual inductance between the sense coil and the field coils  $D_1$ ,

$i_f$  is the current through  $D_1$ ,

$s$  is the complex frequency of  $i_f$ ,

$R_s$ ,  $L_s$  and  $C_s$  are the series resistance, inductance and self-capacitance of the sense coil.

A similar expression may be written from the voltage  $v_c$  across the cancellation coil. The residual voltage across the combination is thus

$$v = v_s - v_c$$

$$= si_f \left( \frac{\Delta M}{1+sRC+s^2LC} + M \Delta \left( \frac{1}{1+sRC+s^2LC} \right) \right)$$

where

$$M = \frac{1}{2}(M_s + M_c)$$

$$\Delta M = (M_s - M_c)$$

$$\left( \frac{1}{1+sRC+s^2LC} \right) = \frac{1}{2} \left( \frac{1}{1+sR_s C_s + s^2 L_s C_s} + \frac{1}{1+sR_c C_c + s^2 L_c C_c} \right)$$

$$\Delta \left( \frac{1}{1+sRC+s^2LC} \right) = \left( \frac{1}{1+sR_s C_s + s^2 L_s C_s} - \frac{1}{1+sR_c C_c + s^2 L_c C_c} \right)$$

At the fundamental and low harmonics of the drive frequency both  $1/(1+sR_sC_s+s^2L_sC_s)$  and  $1/(1+sR_cC_c+s^2L_cC_c)$  will be close to unity giving

$$v + s i_f (\Delta M - s \Delta(RC) - s^2 \Delta(LC)) \quad (6.62)$$

where

$$\Delta(RC) = R_s C_s - R_c C_c$$

$$\Delta(LC) = L_s C_s - L_c C_c$$

The various terms in  $v$  may be classified as

$s i_f \Delta M$  - first order amplitude term,

$-s^2 i_f \Delta(RC)$  - second order phase term,

$-s^3 i_f \Delta(LC)$  - third order amplitude term,

..... - fourth order phase term,

..... (6.63)

In a simple cancellation procedure as outlined in Section 6.21, it is possible to distinguish only total amplitude and phase errors. Since the relative ratio of terms of different order depends upon frequency, cancellation of the fundamental drive frequency will not necessarily result in the cancellation of harmonic frequencies unless all third and higher order terms are negligible.

We shall now consider the various terms of equation 6.62 and their influence on the quality of cancellation.

### 6.63 Cancellation Stability

#### First Order Amplitude Unbalance

With correct design the first order amplitude term determines the limiting cancellation stability. Stability is high, depending only on relative dimensional changes between the two coils. For the present instrument, with the sense coil aligned in the field direction, a 12.5 oe.pp.1000c/s field gives an air flux voltage of 5 V pp. This may be cancelled to below the amplifier noise level of 3.5  $\mu$ V pp. (Table 8.22 with synchronous DC restoration). Drift, measured under normal room conditions, is  $\pm$  3  $\mu$ V per hour or 1 part in  $2 \times 10^6$  per hour after a 1 hour warm up period. For comparison the saturated signal from a 1000  $\text{\AA}$  film is 6.3 mV pp. Practical points which may be noted are

- the rigid one piece construction of sense and cancellation coils preventing relative motion between them

- the uniformity of the AF field making cancellation independent of the exact position of the sensing assembly
- the rigid mounting of connecting leads to the coils eliminating variable voltages from this source.

The limiting stability is achieved only if the initial cancellation between the sense and cancellation coils makes  $si_f\Delta M$  so small that drift in the cancellation bridge does not become significant. It is convenient to be able to measure hysteresis loops at any angle  $\theta$  to the drive field, in particular at the  $\theta = 0^\circ$  and  $90^\circ$  positions.  $si_f\Delta M$  should thus be small at all values of  $\theta$ . Further a knowledge of variation of  $si_f\Delta M$  with  $\theta$  assists in the interpretation of various phase error terms (see Section 6.64). We shall hence consider this variation in further detail.

#### The Variation of $si_f\Delta M$ with Angle $\theta$

Fig. 6.63 shows schematically the sense coil S and cancellation coil C positioned with their axis of rotation  $zz'$  in the median plane of the Helmholtz coil pair  $D_1$ . The axis of both coils makes an angle  $\theta$  with the axis  $xx'$  of  $D_1$ .

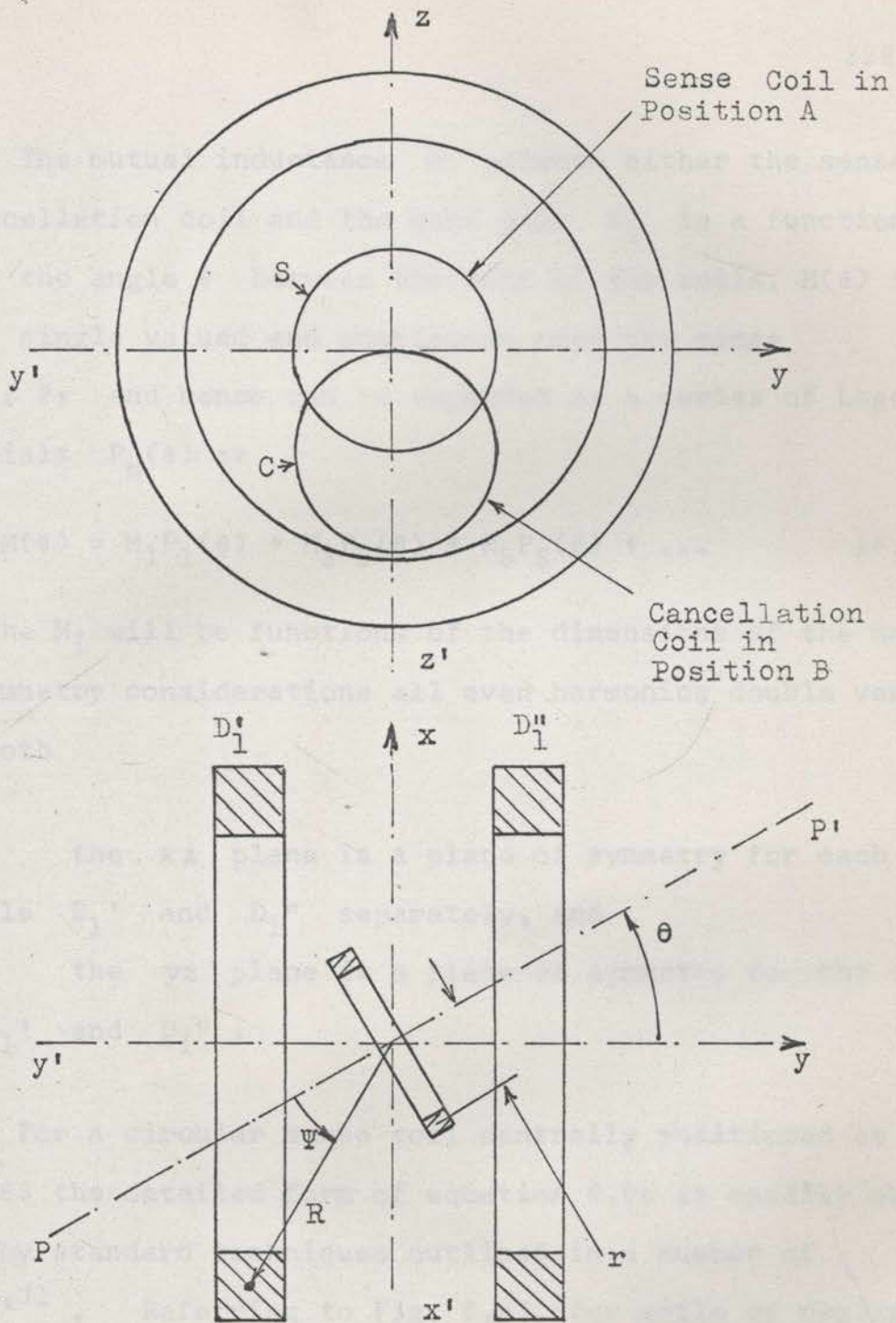


Fig. 6.64<sub>1</sub> Figure Illustrating the Variation of the Mutual Coupling between the Sense and Cancellation Coils and the Drive Coils  $D_1'$  and  $D_1''$ .

The mutual inductance  $M$  between either the sense or the cancellation coil and the coil pair  $D_1$  is a function  $M(\theta)$  of the angle  $\theta$  between the axis of the coils.  $M(\theta)$  is finite, single valued and continuous over the range  $0 \leq \theta \leq 2\pi$  and hence can be expanded as a series of Legendre polynomials  $P_n(\theta)$  as

$$M(\theta) = M_1 P_1(\theta) + M_3 P_3(\theta) + M_5 P_5(\theta) + \dots \quad (6.64)$$

where the  $M_i$  will be functions of the dimensions of the coils. From symmetry considerations all even harmonics double vanish, since both

- the  $xz$  plane is a plane of symmetry for each of the coils  $D_1'$  and  $D_1''$  separately, and
- if the  $yz$  plane is a plane of symmetry for the coil pair  $D_1'$  and  $D_1''$ .

For a circular sense coil centrally positioned as in Fig. 6.63 the detailed form of equation 6.64 is readily obtained by standard techniques outlined in a number of texts<sup>G1, J1</sup>. Referring to Fig. 6.63, for coils of negligible cross section,



$$M_n = 4\pi^2 \sin^2 \psi \, r \sum_n \frac{P'_n(\theta) P'_n(\frac{\pi}{2})}{n(n+1)} \left(\frac{r}{R}\right)^n \quad (6.65)$$

for  $n = 1, 3, 5, \dots$ , valid for  $r < R$ ,

where

$r$  is the radius of the smaller sense coil,

$R$  is the distance from the arc of the field coil to the origin  $O$ ,

$\psi$  is the angle subtended by a radius of the field coil at the origin  $O$ , and

$$P'_n(\theta) = \frac{dP_n(\theta)}{d(\cos\theta)} \quad \text{is the derivative of } n^{\text{th}} \text{ Legendre}$$

polynomial with respect to  $\cos \theta$ .

If the coils  $D_1$  form a Helmholtz pair, then  $\cos^2 \psi = 1/5$  and  $P'_3(\psi) = 0$ . After the first harmonic term, only the fifth remains and

$$\frac{M_5}{M_1} = \frac{9}{40} \left(\frac{r}{R}\right)^4 = \frac{18}{125} \left(\frac{r}{A}\right)^4 \quad (6.66)$$

where  $A$  is the radius of the field coils  $D_1$ .

For the case of the cancellation coil positioned off centre as in Fig. 6.63, the calculation of the coefficients  $M_n$  is extremely difficult. In this case the third harmonic

term  $M_3 P_3(\theta)$  will be present, whether or not the coils  $D_1$  form a Helmholtz pair. From the nature of the expansion in spherical harmonics of a field satisfying Laplace's equation,  $M_n$  will still be proportional to  $(r/R)^n$ .

If the mutual inductances of both the sense and cancellation coils are expanded in a series such as in equation 6.64 and if further the axis of the sense and cancellation coils are malaligned by the angle  $\epsilon$ , and if the sense coil is smaller than the cancellation coil so that higher order harmonics of  $M_s$  can be neglected, then

$$\frac{\Delta M}{M_1} = \left( \frac{\Delta M_1}{M_1} \cos\theta - \epsilon \sin\theta \right) - \frac{M_{3c}}{M_{1c}} Z_{3c}(\theta) - \frac{M_{5c}}{M_{1c}} Z_{5c}(\theta) - \dots \quad (6.67)$$

where

$$M_1 = M_{1s} - M_{1c}$$

and

$$M_1 \div M_{1s} \div M_{1c} \quad \text{provided that } \Delta M/M_1 \text{ is small.}$$

The solid curve of Fig. 6.64 shows experimental values

of

$$\begin{aligned} \frac{\Delta v}{v(\theta=0)} &= \frac{\Delta M}{M_1} \\ &= \left( \frac{\Delta M_1}{M_1} \cos\theta - \epsilon \sin\theta \right) - \frac{M_{3c}}{M_1} Z_{3c}(\theta) - \frac{M_{5c}}{M_1} Z_{5c}(\theta) \dots \end{aligned}$$

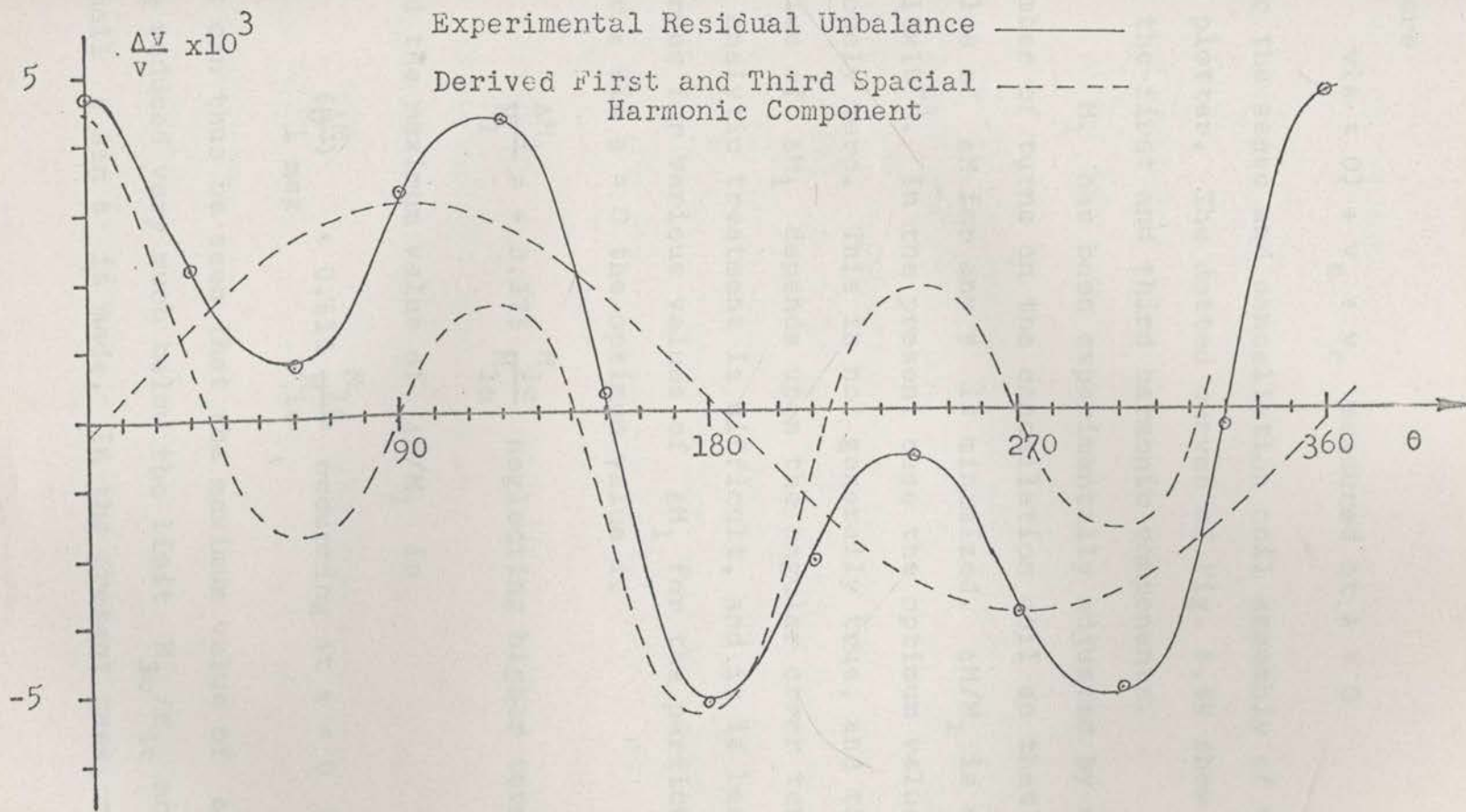


Fig. 6.64 The Variation of the Residual Cancellation Voltage with the Angle  $\theta$  between the Sense and Field Coils

where

$$v(\theta = 0) \div v_s \div v_c \text{ measured at } \theta = 0$$

for the sense and cancellation coil assembly of the present MH plotter. The dotted curves of Fig. 6.64 show the amplitudes of the first and third harmonic components.

$M_1$  has been experimentally adjusted by varying the number of turns on the cancellation coil so that the maximum value of  $\Delta M$  for any  $\theta$  is minimized.  $\Delta M/M_1$  is everywhere  $< 15 \times 10^{-3}$ . In the present case the optimum value of  $\Delta M_1$  is closely zero. This is not generally true, and the optimum value of  $\Delta M_1$  depends upon the angular error term  $\epsilon \sin \theta$ . An analytic treatment is difficult, and it is best to draw curves for various values of  $\Delta M_1$  for the particular case. For  $\epsilon \sin \theta = 0$  the optimum value is

$$\frac{\Delta M_1}{M_1} = + 0.375 \frac{M_{3c}}{M_{1c}} \text{ neglecting higher terms,}$$

and the maximum value of  $\Delta M/M_1$  is

$$\left(\frac{\Delta M}{M_1}\right)_{\max} = 0.615 \frac{M_{3c}}{M_{1c}} \text{ occurring at } \theta = 0 \text{ and } 60^\circ.$$

It can thus be seen that the maximum value of  $\Delta M/M_1$  cannot be reduced very much below the limit  $M_{3c}/M_{1c}$  no matter how small  $\epsilon \sin \theta$  is made. In the present case, reduction of

$\epsilon$  by a more complicated construction of the sense and cancellation coil assemblies is not justified.

#### 6.64 Cancellation Frequency Dependence

##### First Order Phase Unbalance, Higher Order Terms and Other Extraneous Voltages

Both the second order phase term  $-s^2 i_f M \Delta(RC)$  and the third order amplitude term  $-s^3 i_f M \Delta(LC)$  of equation 6.63 may be made small by ensuring that the frequencies  $1/RC$  and  $1/\sqrt{LC}$  of the two coils are both sufficiently high and well matched. In the present instrument the frequencies  $1/R_c C_c$  and  $1/\sqrt{L_c C_c}$  of the cancellation coil have been adjusted to within  $\pm 2$  per cent of the  $7.1 \text{ Mc/s}$   $1/R_s C_s$  frequency and the  $77 \text{ Kc/s}$   $1/\sqrt{L_s C_s}$  resonance frequency of the sense coil by the capacitor  $C'_c$  and resistor  $R'_c$  of Fig. 6.61. The resulting fractional unbalance components,  $-s^2 i_f M \Delta(RC) / s i_f M$  and  $-s^3 i_f M \Delta(LC) / s i_f M$  are both of the order of  $\pm 3 \times 10^{-6}$  at  $|s| = 2\pi \times 10^3 \text{ rad sec}^{-1}$ . As discussed in Section 6.62, the third order amplitude term is a direct cause of frequency dependent cancellation.

In addition to the magnetically induced air flux voltage just discussed, extraneous drive frequency voltages

result from stray capacitive couplings, secondary inductive circuits, common earth impedances and induced voltages in early amplifier stages. Expressions for these voltages are given in Fig. 6.65. Other than first and second order terms are present and thus all voltages must be reduced to a negligible level if cancellation is to be independent of frequency. The latter three components are negligible with correct design. The largest component is that due to stray capacitance. It may be reduced by using low impedance drive coils and, if necessary, a balanced drive. Ideally, it may be cancelled by connecting a small capacitor  $C'$  from the top of the sense coil to the appropriate side (or phase) of the bridge coil  $L_B$  as shown in Fig. 6.61. However, in practice it is difficult to separate the phase error due to stray capacitance from other components.

Fig. 6.66 shows experimental measurements of the phase error as a function of  $\theta$  found by first obtaining an exact amplitude balance with the cancellation bridge. The capacitors of the bridge were disconnected for this measurement. There are clearly a number of components;

- a variable term following the form of the first order amplitude unbalance of Fig. 6.64. This voltage arises from the inductive characteristics of the high stability wire

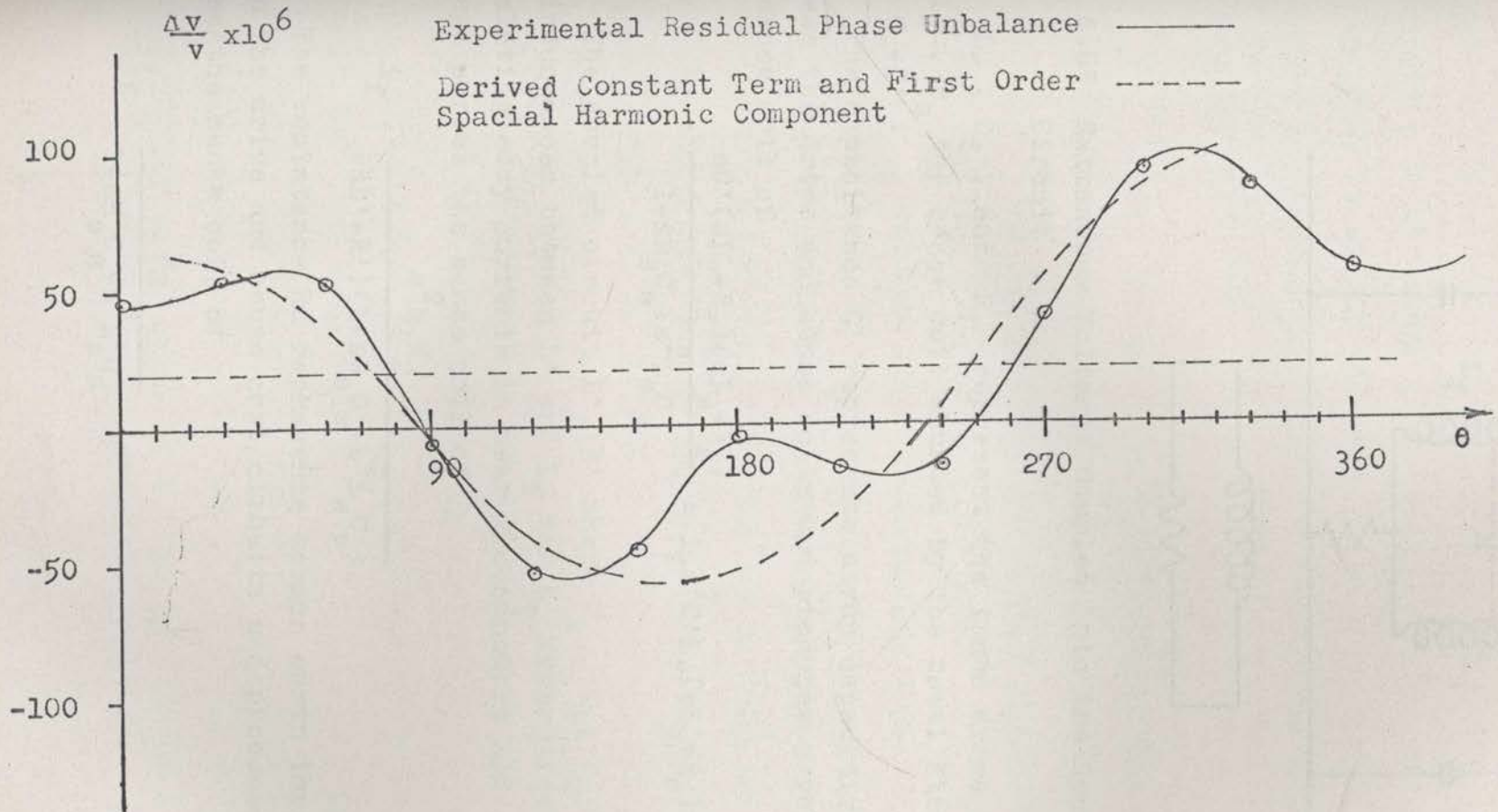


Fig. 6.66 The Variation of the Phase Component of the Residual Cancellation Voltage with the Angle  $\theta$  between the Sense and Field Coils.

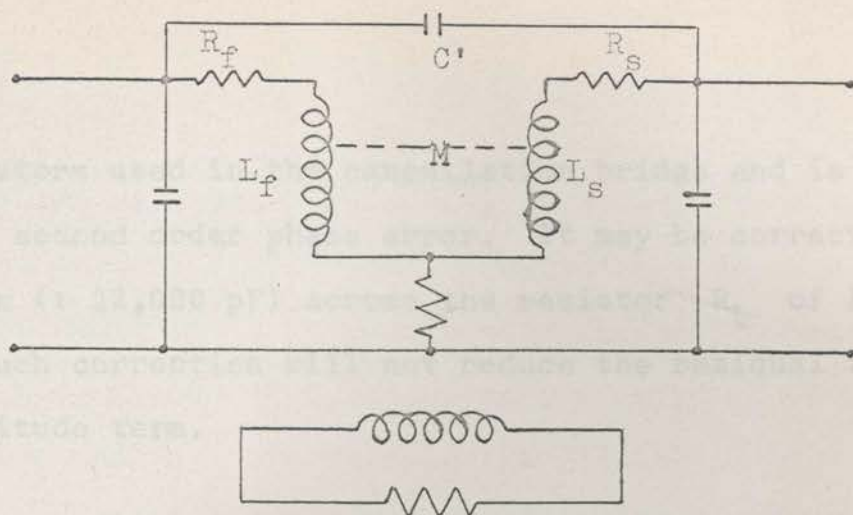


Fig. 6.65 Extraneous Voltages Coupled into the Sense Coil Circuit.

$L_f$ ,  $C_f$ , and  $R_f$  represent the tuned drive coil circuit and  $L_s$ ,  $R_s$  the sense coil shunted by the total stray capacitance  $C_s + C'$ .

The capacitance  $C'$  represents stray capacitive coupling between the drive and sense coils and produces a voltage across the sense coil of

$$i_f \cdot \frac{sC'(sL_f + R_f)(sL_s + R_s)}{1 + sR_s C_s + s^2 L_s C_s} = i_f s^2 C' L_f (sL_s + R_s)$$

The coupled circuit  $L'$ ,  $R'$  where  $M_1$ ,  $M_1$ ,  $M_2$  are the mutual inductances between  $L'$  and  $L_f$  and  $L_s$  respectively represents circulating eddy currents in nearby conductors and produces a voltage across the sense coil of

$$i_f \cdot \frac{s^2 M_1 M_2}{(sL' + R')(1 + sR_s C_s + s^2 L_s C_s)}$$

The resistance  $R_E$  represents common earth impedance between the drive and sense coil circuits and produces a voltage across the sense coil of

$$i_f \cdot \frac{R_E}{1 + sR_s C_s + s^2 L_s C_s}$$



wound resistors used in the cancellation bridge and is almost entirely a second order phase error. It may be corrected by a capacitor ( $\pm 22,000$  pF) across the resistor  $R_L$  of Fig. 6.61, however, such correction will not reduce the residual third order amplitude term.

- a smaller variable term possibly due to changes in the effective stray capacitance with the angle of the sense coil. The second order phase term produced by the air flux voltage is, as discussed,  $< \pm 3 \times 10^{-6}$ .
- a constant stray capacitance term.

In the present instrument no attempt has been made to reduce these phase errors further and a phase adjustment of suitable range has been incorporated in the cancellation bridge. This has proved satisfactory in all respects. From Fig. 6.66 and equation 6.68 of Fig. 6.65, noting that  $|sL_s| \div R_s$  at  $|s| = 2\pi \times 10^3$  rad sec<sup>-1</sup>, it may be concluded that third order amplitude terms are  $< \pm 50 \times 10^{-6}$ . Experimentally, for a 12.5 oe.pp., 1000 c/s field and 4 amps DC flowing through the iron cored choke  $L$  of Fig. 6.22,  $i_f$  contains a 1 per cent third harmonic component. The air flux voltage of 5 V pp. shows a residual harmonic content of the order of the amplifier noise level of 3.5  $\mu$ V pp., or as a fraction of

the uncancelled voltage,  $\pm 0.7 \times 10^{-6}$ , in satisfactory agreement with the theoretical predictions. While not a problem, it may be mentioned that it is possible to further suppress harmonics by carrying out a balancing procedure at two different frequencies, for example the initial balance may be made at 1 Kc/s and the frequency then increased to 3 Kc/s. The resulting unbalance amplitude and phase terms at 3 Kc/s are cancelled by adjusting the capacitors  $C'$  and  $C_c$ , respectively of Fig. 6.61.

#### 6.65 The Cancellation Bridge

The circuit of the cancellation bridge has been shown in Fig. 6.61. A voltage  $V_B$  is induced across a centre tapped "bridge" coil  $L_B$  inductively coupled to the AF driven coils. Amplitude and phase adjustments are made by varying the resistors  $R_1$  and  $R_2$  and the capacitors  $C_1$  and  $C_2$ , respectively. The circuit is intended for a stepped adjustment in which resistors (or capacitors) are switched from  $R_2$  and added to  $R_1$  such that  $R_1$  and  $R_2$  vary from 0 to  $R_t$  and from  $R_t$  to 0, respectively, while  $R_1 || R_2 = R_t$  remains constant. All resistors are precision wire wound and switching of  $R_1$  and  $R_2$  is readily done by a progressively shorting Oak type switch.

Neglecting  $L_B$ , the output voltage across  $R_L$  may be written

$$v_0 = sM_B i_f (\lambda_1 + s\lambda_2) \quad (6.611)$$

where

$M_B$  is the mutual inductance between the bridge and field coils and  $\lambda_1$ ,  $\lambda_2$  are variable constants.

$v_0$  has thus the correct frequency dependence for a cancellation of first order amplitude and second order phase errors, and ideally introduces no higher order terms.

An alternative circuit<sup>01</sup> is shown in Fig. 6.67.  $R_1$  and  $R_2$  should be precision helical potentiometers. There is little to choose between the two circuits. The costs of each are comparable.

If balanced field coils are used, the field coils themselves can be used as the bridge coil  $L_B$ . Since the voltage across the field coils and the true induced voltage will have a phase difference determined by the  $Q$  of the coil, a compensating capacitor must be connected across the output terminals 22' of the bridge. In this case the circuit of Fig. 6.61 is preferred as the output resistance  $R_0$  is closely a constant for any setting of the bridge controls. If a compensation capacitor is not used, then the amplitude correction signal will introduce an additional phase error,

typically an order of magnitude larger than that actually present. The required range of the gain cancellation network is then increased.

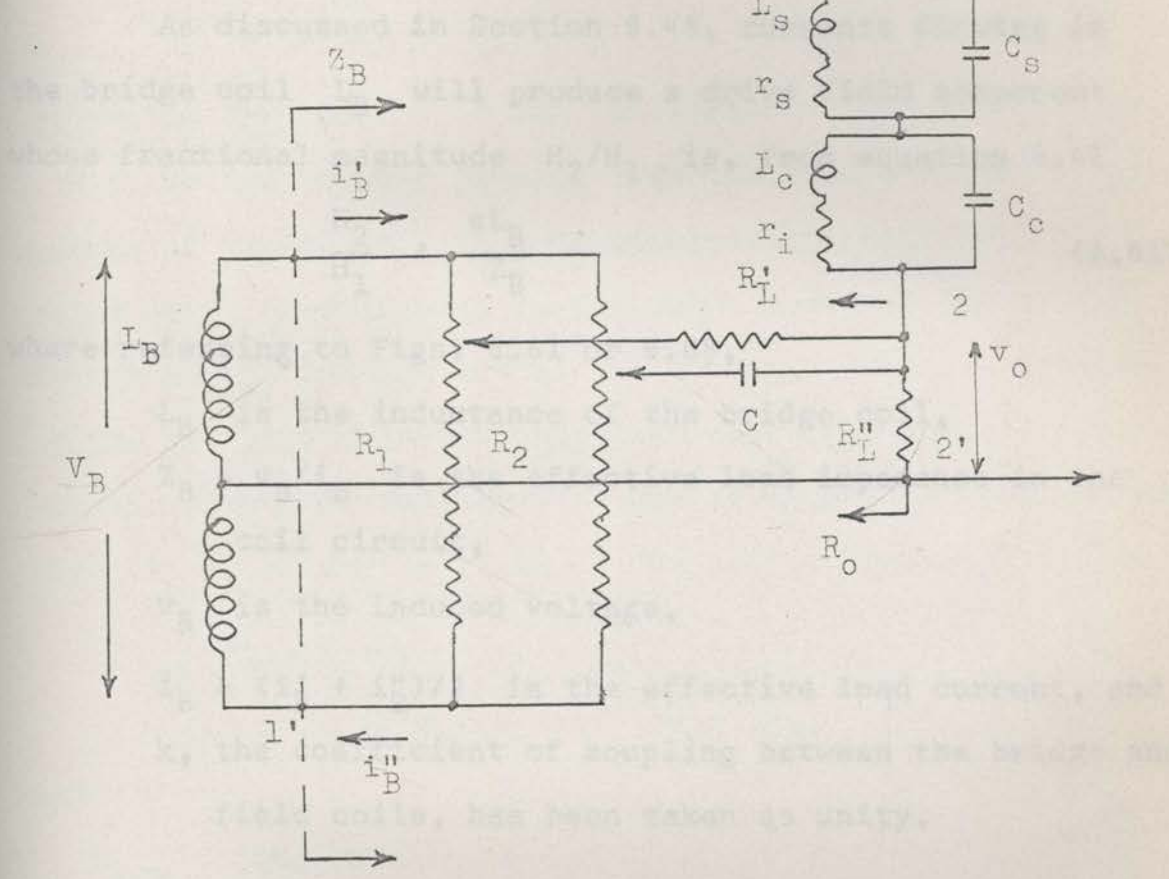


Fig. 6.67 An Alternative Cancellation Bridge Circuit.

The design of the cancellation bridge must provide a... conditions that the reaction field  $H_r$ , and the voltages  $V_p$ ... added in series with the sense and cancellation coils, shall... both be sufficiently small. A large value of  $H_r$  will in-... across the input noise. Equation 6.67 may be rewritten as

typically an order of magnitude larger than that normally present. The required range of the phase correction network is then increased.

As discussed in Section 6.45, currents flowing in the bridge coil  $L_B$  will produce a drive field component whose fractional magnitude  $H_2/H_1$  is, from equation 6.41

$$\frac{H_2}{H_1} \div \frac{sL_B}{Z_B} \quad (6.612)$$

where referring to Figs. 6.61 or 6.68,

$L_B$  is the inductance of the bridge coil,

$Z_B = v_B/i_B$  is the effective load impedance in the coil circuit,

$v_B$  is the induced voltage,

$i_B = (i_B' + i_B'')/2$  is the effective load current, and  $k$ , the coefficient of coupling between the bridge and field coils, has been taken as unity.

The design of the cancellation bridge must provide a cancellation signal of the necessary magnitude, subject to the conditions that the reaction field  $H_2$ , and the resistance  $R_0$ , added in series with the sense and cancellation coils, shall both be sufficiently small. A large value of  $R_0$  will increase the input noise. Equation 6.612 may be rewritten as

$$\frac{H_2}{H_1} = \frac{\frac{v_B^2}{z_B}}{\frac{v_B^2}{sL_B}} = \frac{P}{P_B} \quad (6.613)$$

Neglecting the inductance and resistance of the bridge coil,  $P$  will be the "power" flowing into the bridge network. For a given AF field,  $P_B$  is a geometrical constant of the bridge coil, proportional to the third power of the linear dimensions and independent of the number of turns. Considering the resistance bridge component only (the phase error is normally very much smaller), it may be shown that the maximum value of  $P$  at any settling of the bridge controls will be

$$\begin{aligned} P_{\max} &= \eta P_0 \\ &= \eta \lambda^2 P_S \quad \text{for the circuit of Fig. 6.61,} \end{aligned}$$

and

$$\begin{aligned} P_{\max} &= \eta P_0 (1 + 4\beta(1 - 1/\eta)) \\ &= \eta \lambda^2 P_S (1 + 4\beta(1 - 1/\eta)) \quad \text{for the circuit of Fig. 6.67} \end{aligned}$$

(6.614)

where

$$P_0 = v_{0 \max}^2 / R_{0 \max}$$

$$P_S = v_S^2 / R_{0 \max}$$

$v_S$  is the sense coil voltage,

$v_{0 \max} = \lambda v_s$  is the maximum required correction voltage across the terminals 22' ,

$R_{0 \max}$  is the maximum allowable resistance measured across the terminal 22' ,

$$2\eta = \frac{v_B}{v_{0 \max}} = 2 \cdot \frac{R_1 \parallel (R_2 + R_L)}{R_L} \quad \text{for the circuit of Fig. 6.61,}$$

$$= 2 \cdot \frac{R_L' + R_L''}{R_L'} \quad \text{for the circuit of Fig. 6.67,}$$

and  $\beta = (R_L' + R_L'')/R_1$  is a parameter, defined in the diagram and graph of Fig. 6.68, determining the "evenness" of the potentiometer adjustment. A value of  $\beta = 1$  is reasonable.

Hence, combining equations 6.613 and 6.614, then

$$\begin{aligned} \frac{H_2}{H_1} &= \eta \lambda^2 \left( \frac{P_s}{P_B} \right) \quad \text{for the circuit of Fig. 6.61} \\ &= \eta \lambda^2 \left( \frac{P_s}{P_B} \right) [1 + 4\beta(1 - 1/\eta)] \quad \text{for the circuit of Fig. 6.67.} \end{aligned} \quad (6.615)$$

The method of design is now clear.  $P_s/P_B$  is a constant depending on the geometry of the bridge coil, on the design of the sense coil, and on the maximum tolerable resistance  $R_{0 \max}$ . The shunting effect of the phase

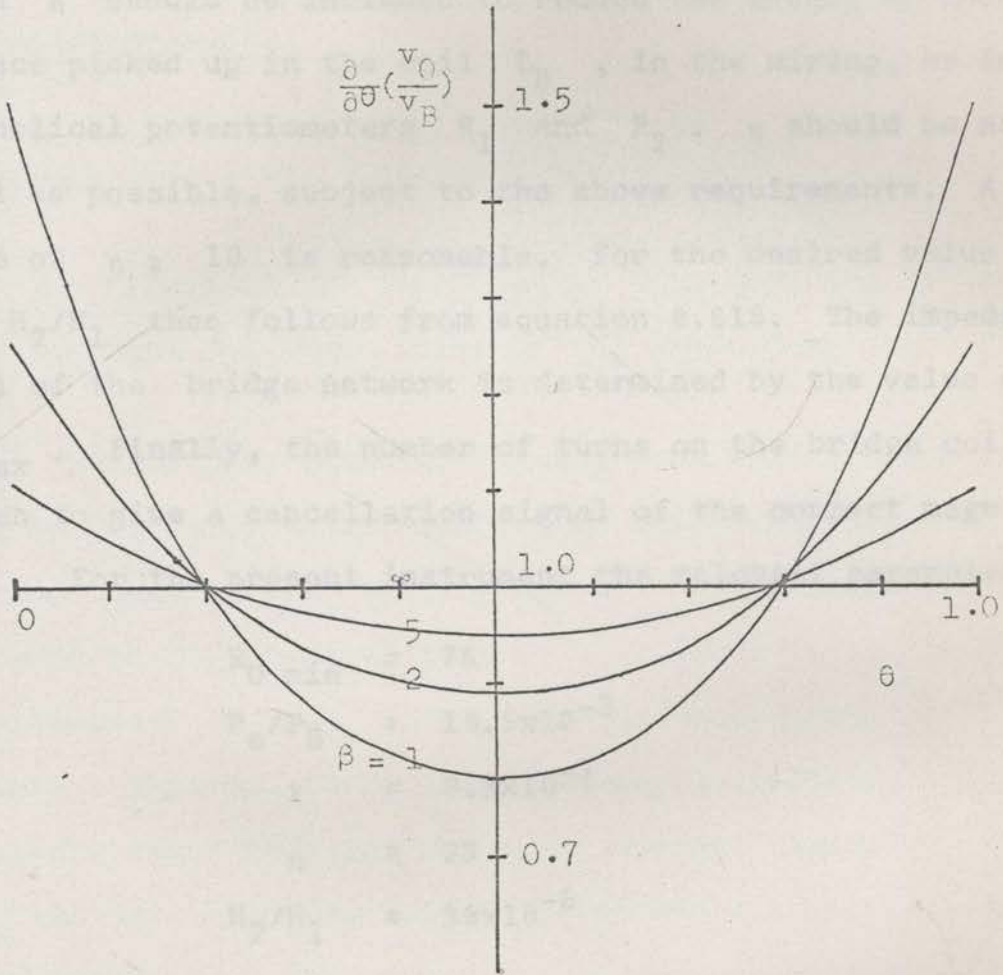
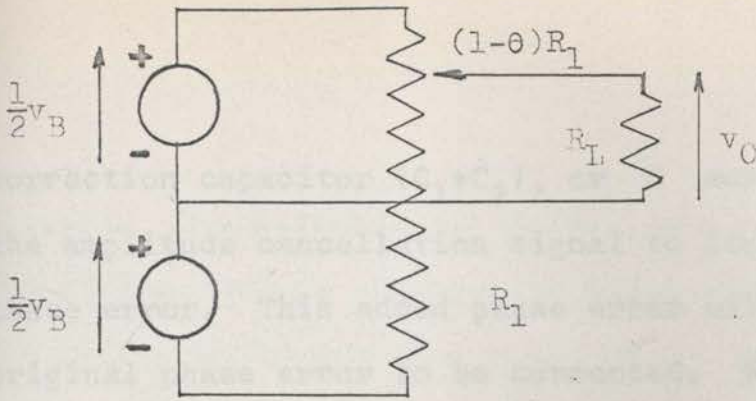


Fig. 6.68 The Evenness of a Potentiometer Adjustment

The graph shows the variation of the evenness of the adjustment, defined as  $\frac{\partial}{\partial \theta} (v_O/v_B)$ , with the potentiometer setting  $(0 < \theta < 1)$  for various values of the ratio  $\beta = (R_L/R_1)$  of the "load" impedance to the potentiometer impedance.



correction capacitor ( $C_1+C_2$ ), or  $C$  across  $R_0$  will cause the amplitude cancellation signal to itself produce a small phase error. This added phase error will be  $\pm 1/\eta$  of the original phase error to be corrected. Further some attenuation  $\eta$  should be included to reduce the effect of interference picked up in the coil  $L_B$ , in the wiring, or in the helical potentiometers  $R_1$  and  $R_2$ .  $\eta$  should be as small as possible, subject to the above requirements. A value of  $\eta \geq 10$  is reasonable. For the desired value of  $\lambda$ ,  $H_2/H_1$  then follows from equation 6.615. The impedance level of the bridge network is determined by the value of  $R_{0 \text{ max}}$ . Finally, the number of turns on the bridge coil is chosen to give a cancellation signal of the correct magnitude.

For the present instrument the relevant parameters are

$$\begin{aligned}
 R_{0 \text{ min}} &= 75 \\
 P_S/P_B &= 19.5 \times 10^{-3} \\
 \lambda &= 9.3 \times 10^{-3} \\
 \eta &= 23 \\
 H_2/H_1 &= 38 \times 10^{-6}
 \end{aligned}$$

Since  $H_2$  is closely  $90^\circ$  out of phase with  $H_1$ ,  $H_2$  is best measured by the change in the phase difference (using the method of Section 6.73) between the sense coil voltage and the AF field current through  $D_1$  on connecting the bridge

network. Experimentally,  $H_2/H_1 < 1 \times 10^{-3}$ , the limit of reading of the method. Connecting lower value resistors across the bridge coils produces a change of  $H_2/H_1 = 150 \times 10^{-3}$  parts per mho in satisfactory agreement with the predicted value from equation 6.612.

### 6.66 Some Additional Considerations

#### The Effect of the Cancellation Coil Upon the Frequency Response and Input Noise of the Sense Coil Circuit

It has been shown in Section 6.64 that if cancellation is to be frequency independent, then the resistance, inductance and capacitance,  $R_c$ ,  $L_c$  and  $C_c$  of the cancellation coil must be in the same ratio to each other as the corresponding parameters  $R_s$ ,  $L_s$  and  $C_s$  of the sense coil. By Thévenin's theorem, the combination may be replaced by an equivalent sense coil for which the voltage induced by the film flux is unchanged, but whose impedance level is raised by the factor  $\sigma$ . The parameters of the equivalent coil are

$$R_i = \sigma R_s, \quad L_i = \sigma L_s, \quad \frac{1}{C_i} = \sigma \frac{1}{C_s} \quad (6.616)$$

where

$$\sigma = \frac{R_s + R_c}{R_s} = \frac{L_s + L_c}{L_s} = \frac{C_s + C_c}{C_s}$$

Since the same air flux voltage must be induced in both coils,  $\sigma$  is a geometrical constant, independent of the number of turns, which tends to unity as the diameter of the cancellation coil is made larger than that of the sense coil. For the present instrument  $\sigma = 1.1$ .

Connection of the cancellation coil will thus leave unaltered the nature of the transfer function

$\omega_r^2 / (\omega_r^2 + 2\xi\omega_r s + s^2)$  of the input circuit (see Section 6.72).

However, the resonant frequency  $\omega_r$  will be lowered by the factor

$$(1 + \sigma \frac{C_A}{C_S})^{\frac{1}{2}} (1 + \frac{C_A}{C_S})^{-\frac{1}{2}} < \sigma^{\frac{1}{2}}$$

where  $C_A$  is the input capacitance of the sense amplifier.

The ratio  $\frac{S}{N}$  of the signal from the film to the input noise (see Section 7.1) will be decreased by the factor  $\sigma$ .

### The Reduction of Interference

The cancellation coil significantly reduces stray interference by

- acting as an earthed electrostatic screen about the higher impedance sense coil and
- by cancelling magnetically induced interference for which the interfering field is uniform over the region

of the sense and cancellation. The construction of the sensing assembly with sense and cancellation coils positioned close to each other assists in this regard.

Fig. 6.6.9 shows photographs of the interference level of the present instrument. Connection of the cancellation coil reduces 50 c/s interference by a factor of  $10^2$  to below the limit set by the input noise of the preamplifier. ( $< 0.5 \mu\text{V pp.}$  referred to the input by the gain at 50 c/s without DC restoration).

## 6.7 FREQUENCY RESPONSE ERRORS IN HYSTERESIS LOOP DISPLAYS

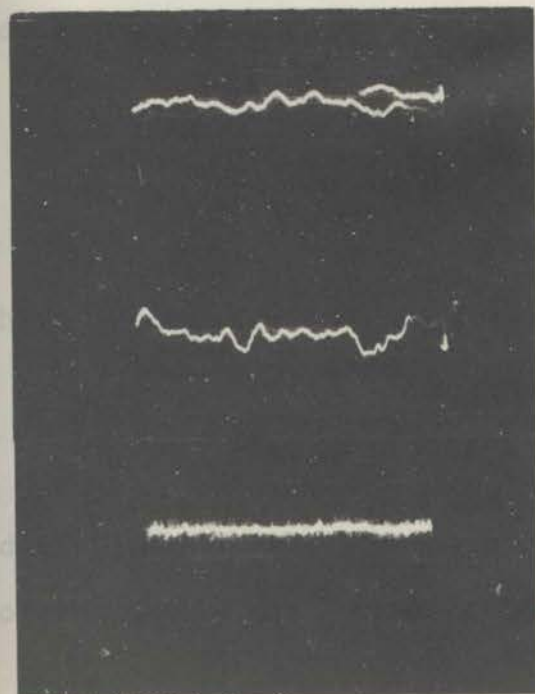
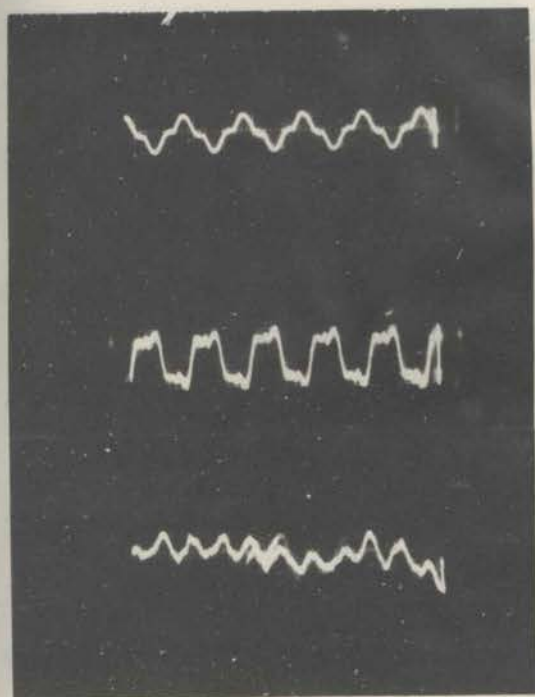
### 6.7.1 Introduction

Of the various measurements which may be performed using an MH plotter, the display of hysteresis loops places the highest requirements on faithful reproduction. Errors will be produced by both

- inadequate high or low frequency response in the flux detection and amplification system, or "sensing system".
- phase errors in the field display.

In the present section we shall discuss the nature

Fig. 6.69 THE HUM, INTERFERENCE AND THERMAL NOISE LEVEL  
OF THE MH PLOTTER.



The traces show the output noise of the MH plotter referred to the terminals of the sense coil by the gain at  $f_0 = 1$  kc/s. The MH plotter has been rotated on the bench through  $360^\circ$  to find the positions of maximum and minimum interference,

Trace 1: Maximum interference, cancellation coil disconnected.  
Scales: 1 mV/cm, 10 m sec/cm

Trace 2: Minimum interference, cancellation coil disconnected.  
Scales: 100  $\mu$ V/cm, 10 m sec/cm

Trace 3: Maximum interference, cancellation coil connected.  
Scales: 20  $\mu$ V/cm, 20 m sec/cm

Trace 4: Minimum interference, cancellation coil connected.  
Scales: 20  $\mu$ V/cm, 20 m sec/cm

Trace 5: Reference noise level of amplifier in "calibrate" position, 1 k resistive source impedance.  
Scales: 20  $\mu$ V/cm, 20 m sec/cm

Trace 6: Minimum interference, cancellation coil connected, with 1000 c/s synchronous DC restoration (Section 8.7).  
Scales: 5  $\mu$ V/cm, 20 m sec/cm

and magnitude of these errors so that they may be readily recognized in a hysteresis loop display and a possible invalid interpretation of film behaviour avoided.

## 6.72 Errors Due to Limited Frequency Response of the Flux Detection System

We may define the overall transfer function of the system  $T(s)$  as the transfer function measured from the flux  $\phi_i$  linking the sense coil to the output oscilloscope display. Thus

$$T(s) = s A(s) \quad (6.71)$$

where  $A(s)$  is the transfer function of the amplifier system measured from the induced coil voltage to the output oscilloscope display

### High Frequency Response

In the present instrument  $T(s)$  has the form at high frequencies of

$$T(s) = \frac{\omega_r^2}{\omega_r^2 + 2\xi\omega_r s + s^2} = \frac{1}{1 + 2\xi\tau_r s + \tau_r^2 s^2} \quad (6.72)$$

determined by the resonant circuit formed by the inductance of the sense and cancellation coils with the coil self-

capacitance and the input capacitance of the preamplifier. The resonant frequency  $f_r$  is 60 Kc/s; values of coil inductance and capacitance have been given in Table 6.62. The 27 k $\Omega$  damping resistor  $R_D$  of Fig. 6.22 chosen to give a critically damped ( $\xi = 1$ ) response, the overall transient response being measured directly by passing a square wave current through a few turns of wire held near the sense coil. The measured 10 per cent to 90 per cent rise time  $\Delta\tau$  is 10  $\mu$ secs. and the 0 per cent to 50 per cent rise time  $\Delta\tau_{1/2}$  is 5  $\mu$ secs. As discussed in Section 7.2, the resonance of  $\frac{1}{2}$  the sense coil should not be regarded as a fundamental limitation on the high frequency response. Since the poles produced by the sense coil can be compensated by a network later in the amplifier<sup>S3</sup>, the limitation is of a practical nature depending on how accurately compensation can be achieved.

Fig. 6.71 shows the nature of the errors produced. The solid line represents the true hysteresis loop, in which an idealized linear change in flux over the field interval  $H_1$  to  $H_2$  is assumed. The results may be applied to either an easy or hard axis loop by an appropriate choice of  $H_1$  and  $H_2$ . The error  $H'_c - H_c$  in the apparent coercive force can be obtained if it is assumed that the rate of change of field

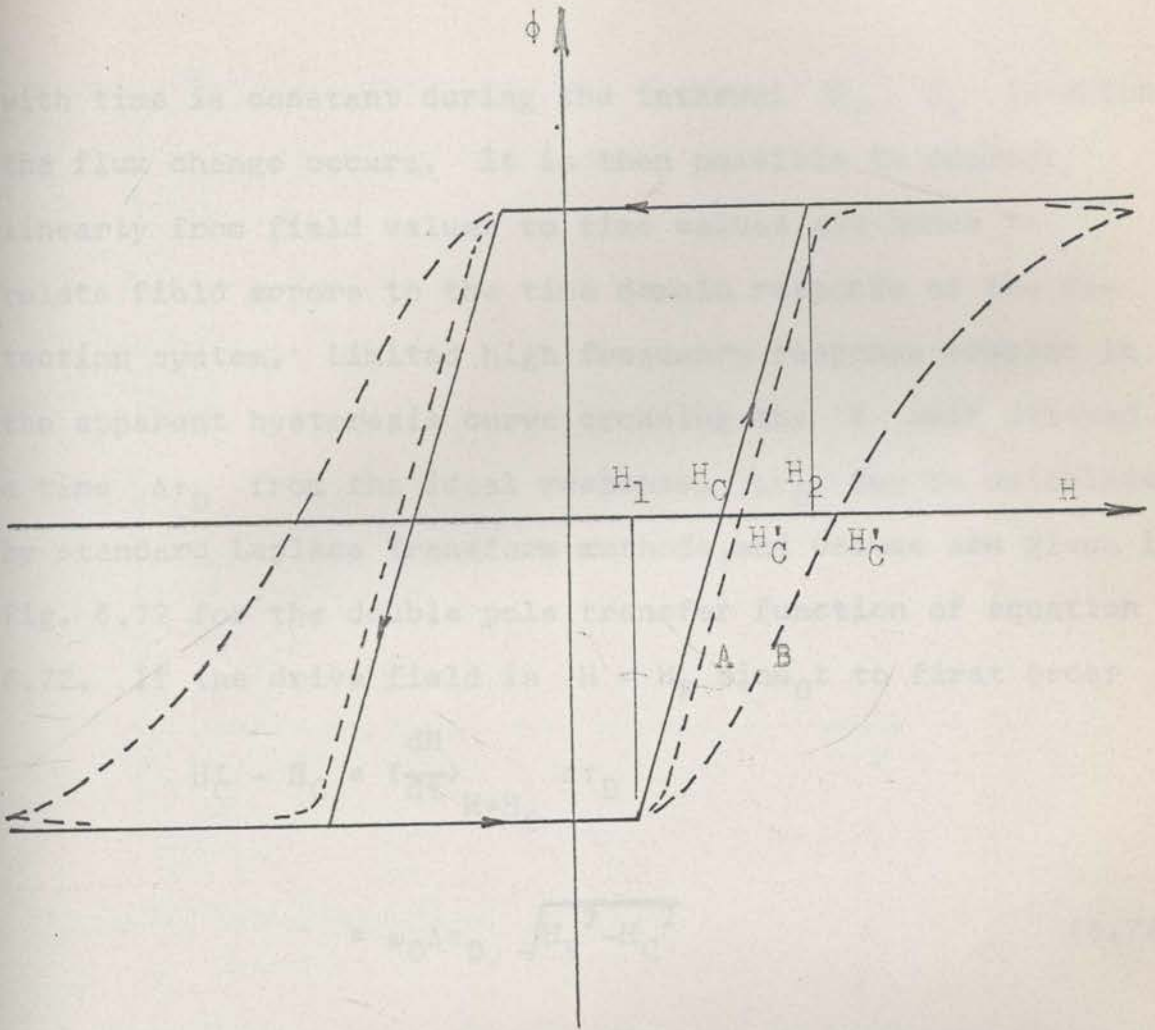


Fig. 6.71 Errors in the Display of a Hysteresis Loop due to Limited High Frequency Response of the Film Detection System

The dotted curves show the error from the true response (represented by the solid line).

Curve A shows the case where the rise time of the flux detection system is less than the time  $t_2 - t_1$  over which the flux takes place.

Curve B shows the case where the rise time is greater than the time  $t_2 - t_1$



with time is constant during the interval  $H_2 - H_1$  in which the flux change occurs. It is then possible to convert linearly from field values to time values and hence to relate field errors to the time domain response of the detection system. Limited high frequency response results in the apparent hysteresis curve crossing the  $H$  axis delayed a time  $\Delta\tau_D$  from the ideal response.  $\Delta\tau_D$  may be calculated by standard Laplace Transform methods, and values are given in Fig. 6.72 for the double pole transfer function of equation 6.72. If the drive field is  $H = H_p \sin\omega_0 t$  to first order

$$\begin{aligned} H'_C - H_C &= \left( \frac{dH}{dt} \right)_{H=H_C} \Delta\tau_D \\ &= \omega_0 \Delta\tau_D \sqrt{H_p^2 - H_C^2} \end{aligned} \quad (6.73)$$

An easy axis hysteresis curve will show an increased slope of the sides and an error in coercive force given by equation 6.73. A hard axis curve will similarly show an increased coercive force or opening of the loop. Further, and most important, these effects will vary with the magnitude  $H_p$  of the applied field.

In an experimental measurement of  $H_C$ ,  $H_p/H_C$  is typically of the order of 2.5. For the present instrument  $f_p = 60$  Kc/s and  $\Delta\tau_D = 1.2 \frac{\Delta\tau_1}{2} = 6$   $\mu$ secs. for Case A of

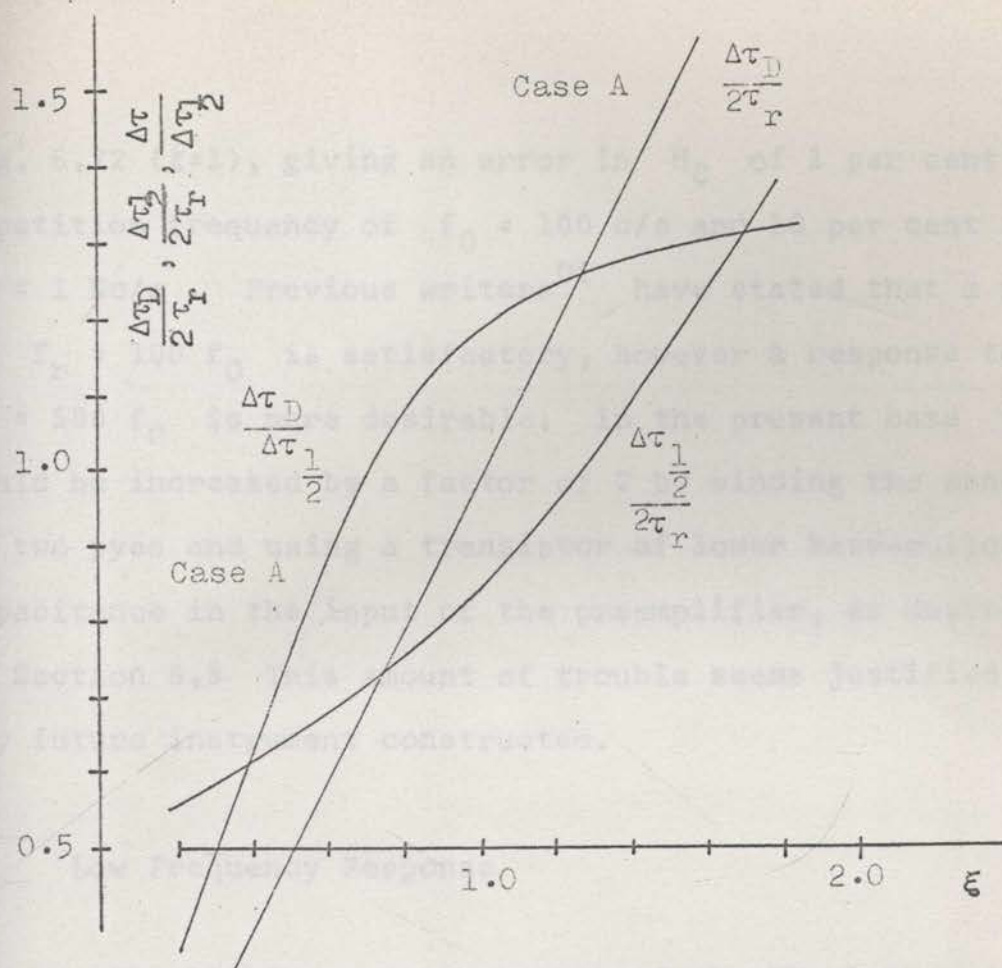


Fig.6.72 The Delay Time  $\Delta\tau_D$  due to Limited High Frequency Response of the Flux Detection System.

The graph gives the value of  $\Delta\tau_D$  for the two pole transfer function  $1/(1+2\xi\tau_r s+\tau_r^2 s^2)$

There are two cases:

Case A:  $\Delta\tau_D \ll$  the time  $t_2 - t_1$  over which the flux change occurs.

$\Delta\tau_D/2\tau_r$  is given as a function of the damping parameter  $\xi$ . Since experimentally the 0 to 50 per cent rise time  $\Delta\tau_{1/2}$  is the easiest to measure, the graph also gives curves  $\frac{\Delta\tau_{1/2}}{2\tau_r}$  and  $\frac{\Delta\tau_D}{\Delta\tau_{1/2}}$  against  $\xi$ .

Case B:  $\Delta\tau_D \gg$  the time  $t_2 - t_1$  over which the flux change occurs. Here, as might be expected,  $\Delta\tau_D = \Delta\tau_{1/2}$

Fig. 6.72 ( $\xi=1$ ), giving an error in  $H_C$  of 1 per cent at a repetition frequency of  $f_0 = 100$  c/s and 10 per cent at  $f_0 = 1$  Kc/s. Previous writers<sup>01</sup> have stated that a response to  $f_r = 100 f_0$  is satisfactory, however a response to  $f_r = 500 f_0$  is more desirable. In the present case  $f_r$  could be increased by a factor of 2 by winding the sense coil in two pyes and using a transistor of lower base-collector capacitance in the input of the preamplifier, as described in Section 8.3 This amount of trouble seems justified in any future instrument constructed.

#### Low Frequency Response

The low frequency response of the MH plotter is determined by the integrator characteristics used. A detailed theory of integrator transfer functions has been given in Section 7.3.

Fig. 6.73 shows the nature of the errors produced in a hysteresis loop display if, in the terminology of Section 7.3, the dominant error of the integrator characteristic is the first order phase term  $P_{-1}$  (see equation 7.34). As in Fig. 6.71, an idealized linear change in flux over the field interval  $H_1$  to  $H_2$  is assumed and the results may be applied to either an easy or hard axis type loop by an

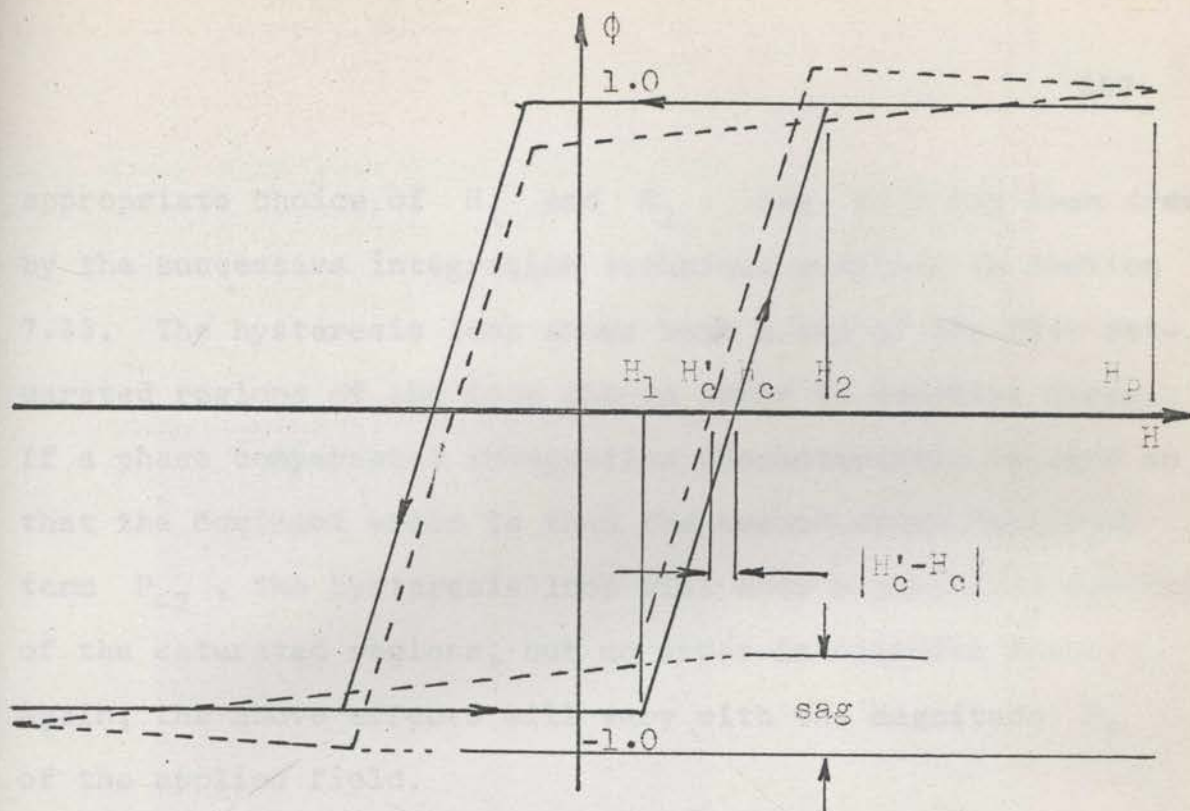


Fig. 6.73 Errors in the Display of a Hysteresis Loop due to Limited Low Frequency Response of the Film Detection System

The dotted line shows the error from the true hysteresis loop (represented by the solid line) for an integrator characteristic having at low frequencies a dominant first order phase error  $P_{-1}^*$ . The hysteresis loop shows both sag and an error in coercive force of

$$\text{sag} \doteq \frac{1}{2} T_0 P_{-1}$$

$$H'_c - H_c = \omega_0 D \sqrt{H^2 - H_c^2}$$

where

$$\tau_D = \frac{1}{8} (t_2 - t_1) (T_0 - (t_2 - t_1)) P_{-1}$$

and

$T_0 = 2\pi/\omega_0$  is the repetition period of the hysteresis loop

\* For the single pole transfer function  $s/(s + \omega_{L1})$

appropriate choice of  $H_1$  and  $H_2$ . Fig. 6.73 has been drawn by the successive integration technique outlined in Section 7.33. The hysteresis loop shows both a sag of the flat saturated regions of the loop and an error in coercive force. If a phase compensated integration characteristic is used so that the dominant error is then the second order amplitude term  $P_{-2}$ , the hysteresis loop will show a parabolic curvature of the saturated regions, but no error in coercive force. Again, the above effects will vary with the magnitude  $H_p$  of the applied field.

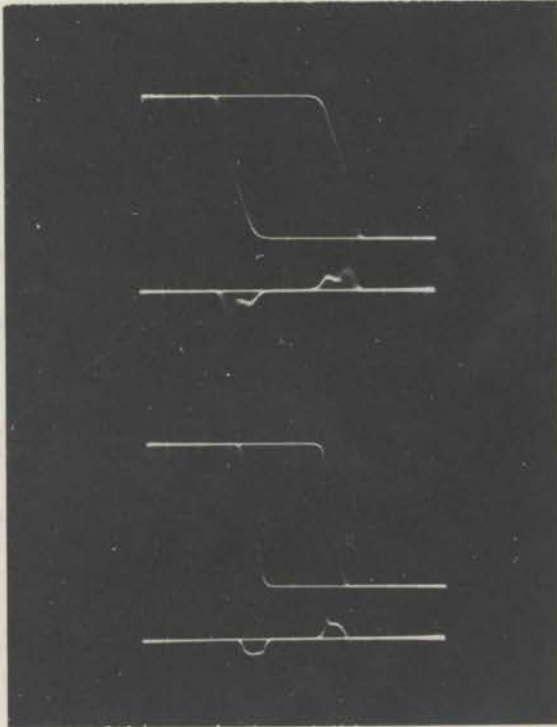
Fig. 6.74 shows photographs of MH curves taken at 1000 c/s and 230 c/s, using the phase compensated response of equation 8.41 and having sags of 0.01 per cent and 0.2 per cent, respectively. These may be compared with the MH curves of Fig. 4.21 taken with the basic two pole characteristic

$T(s) = 1/(1 + \frac{2\pi \times 5.78}{s})^2$  without phase compensations. There the error at  $f_0 = 1$  Kc/s is 1 per cent and, as can be seen, is still barely noticeable. Hence it appears that a 1 per cent integration error is adequate for most applications.

### 6.73 Phase Errors in the Field Display

An additional error occurs if the field display is not the same as the applied field itself. If the display has a phase error  $\theta$  and is delayed a time  $\Delta\tau'_D = -\theta/\omega_0$  with

Fig. 6.74 EASY AXIS LINEAR HYSTERESIS LOOPS ( $m_L, H_L$ ) OF A  
 1000 Å PERMALLOY FILM S2P17 ILLUSTRATING THE  
 FIDELITY OF THE MH PLOTTER



The photographs were taken using the phase compensated response of equation 8.41

Frame 1: is taken at 1000 c/s. The calculated low frequency sag is 0.01 per cent

Frame 2: is taken at 230 c/s. The calculated low frequency sag is 0.2 per cent

respect to the applied field, then the error in coercive force is, as in equation 6.73,

$$\begin{aligned}
 H'_C - H_C &= - \left( \frac{dH}{d\tau} \right)_{H=H_C} \Delta\tau'_D \\
 &= -\omega_0 \Delta\tau'_D \sqrt{H_P^2 - H_C^2} = \theta \sqrt{H_P^2 - H_C^2} \quad (6.74)
 \end{aligned}$$

The apparent coercive force of a film will thus vary with field amplitude without, however, any increasing in the slope of the sides of the loop or of the apparent sag. The present case may hence be distinguished from errors due to the frequency response of the detection system.

In practice it is almost impossible to avoid some phase shift. Phase shift will occur in the field display amplifier circuitry. Even with bifilar winding, the inductance of the wire wound  $0.1 \Omega$  field current sampling resistor  $R_M$  cannot be reduced below  $0.1 \mu\text{H}$ , giving a phase shift of  $+5 \times 10^{-3}$  rad at  $f_0 = 1 \text{ Kc/s}$ . (Self-capacitance of the drive coils is not a problem in the present instrument, the  $100 \text{ Kc/s}$  self-resonant frequency  $f'_r$ , giving a phase error of  $-f_0^2/Q f_r'^2 = -3 \times 10^{-6}$  rad at  $f_0 = 1 \text{ Kc/s}$ ). It is thus necessary to incorporate a phase adjustment and it is desirable that this should be possible without an associate

change in gain and field calibration. A suitable network is shown in Fig. 6.75, giving a first order phase adjustment of  $\pm 3 \times 10^{-2}$  rad at  $f_0 = 1$  Kc/s with a second order fractional change of gain of  $\pm 2 \times 10^{-3}$ .

The phase adjustment may be made by displaying either the integrated air flux voltage induced in the sense coil, or an initial or unsaturated hard axis hysteresis loop of a low dispersion film, against the field and adjusting to give a closed straight line trace. The former method allows the adjustment to be made within  $\pm 1 \times 10^{-3}$ , and the later to within  $\pm 3 \times 10^{-3}$ , the limit being set by noise in the hysteresis loop display. Both agree to within the experimental error. It is essential when making this adjustment to disconnect the damping resistor  $R_D$  from across the sense coil, otherwise a large lagging phase error will be introduced. The error in the field display will now be just the phase error of the sense coil amplification and detection system, and this can be independently set to zero by the procedure described in Section 8.5. Note that it is not sufficient to merely adjust the flux and field displays for the same error at the repetition frequency  $f_0$ . For example, if the flux detection system has a phase error at  $f_0$  due to low fall off, then the sides of a perfectly square hysteresis loop will not be effected. However, if the flux and field



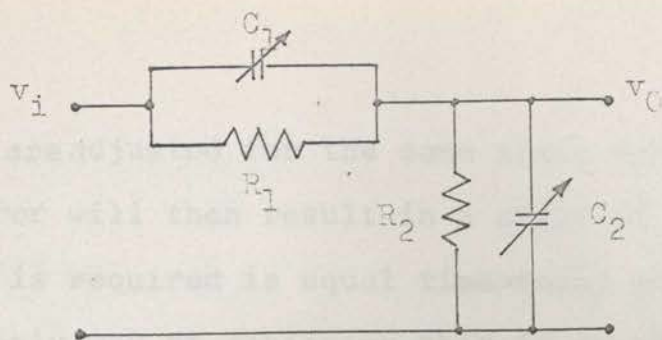


Fig 6.75 A NETWORK FOR PHASE

$$\begin{aligned}
 \text{Transfer function } \frac{V_o(s)}{V_i(s)} &= \frac{R_1}{R_1 + R_2} \cdot \frac{1 + sC_1R_1}{1 + s(C_1 + C_2) \frac{R_1R_2}{R_1 + R_2}} \\
 &= \frac{R_1}{R_1 + R_2} \left[ 1 + s \frac{R_1}{R_1 + R_2} (C_1R_1 - C_2R_2) \right. \\
 &\quad \left. + s^2 \frac{R_1}{R_1 + R_2} (C_1R_1 - C_2R_2) \frac{R_1R_2}{R_1 + R_2} (C_1 + C_2) \right. \\
 &\quad \left. + \dots \dots \dots \right]
 \end{aligned}$$

Variation of  $C_2$  gives a first order phase adjustment with only a small second order amplitude change. Suitable values for a phase change of  $\pm 3 \times 10^{-2}$  rad at  $f_0 = 1$  kc/s are

$$R_1 = R_2 = 22 \text{ k}$$

$$C_1 = 470 \text{ pF}$$

$$C_2 = 30 \text{ to } 1000 \text{ pF}$$

The associated fractional change of gain is  $\pm 2 \times 10^{-3}$

displays are adjusted for the same phase error, the field phase error will then result in a shift of the sides. What, in fact, is required is equal time delay at all frequencies and the only way of achieving this is to avoid phase shift altogether.

1. R.M.,  
"Prognostic",  
D. Van Nostrand Company Inc., New York, 1958, (1958).
21. Boyd, E.L.,  
"Magnetic Anisotropy in Single-Crystal Thin Films",  
IBM Journ. Res. and Develop., 4, 115, (1959).
22. Bryzinski, T.F., Sahba, D.R.,  
"Hysteresis Curve Tracer for Magnetic Thin Films",  
IRE International Convention Record, V3, Pt. 3,  
p. 145, (1951).
23. Crittenden, E.C., Smith, C.S., Olsen, L.O.,  
"E-H Meter for Samples of Small Cross Sectional Area",  
Rev. Sci. Instrum., 17, 372, (1946).
24. Crittenden, E.C., Strough, R.J.,  
"Limiting Sensitivity of Instruments for Measuring  
Magnetic Hysteresis Loop",  
Phys. Rev., 75, 1836, (1949).
25. Crittenden, E.C., Rudman, R.H., et al.,  
"Magnetization Hysteresis Loop Tracer for Loop Measurements  
of Extremely Small Cross Section",  
Rev. Sci. Instrum., 21, 172, (1950).
26. Crowther, T.E.,  
"Angular and Magnitude Measurements of the Hysteresis Loop  
in Magnetic Films",  
J. Appl. Phys., 34, 140, (1963).
27. Dwight, K., Manyak, K.,  
"Further Developments of the Hysteresis Loop Magnetometer",  
J. Appl. Phys., 28, 491, (1957).
28. Foner, S.,  
"A Versatile and Sensitive Vibrating Coil Magnetometer",  
Rev. Sci. Instrum., 30, 546, (1959).

## 6.8 LIST OF REFERENCES

- A1 Aitchison, R.E., Murray, C.T.,  
"A Simple DC Power Supply Using Transistors".  
Proc.Instn.Radio Engrs., Australia, 19, 174, (1958).
- B1 Bozorth, R.M.,  
"Ferromagnetism".  
D. Van Nostrand Company Inc., New York, p.838, (1951).
- B2 Boyd, E.L.,  
"Magnetic Anisotropy in Single-Crystal Thin Films".  
IBM Journ.Res. and Developm., 4, 116, (1960).
- B3 Bryzinski, T.F., Sahba, D.R.,  
"Hysteresis Curve Tracer for Magnetic Thin Films".  
IRE International Convention Record, V9, Pt.9,  
p.249, (1961).
- C1 Crittenden, E.C., Smith, C.S., Olsen, L.O.,  
"B-H Meter for Samples of Small Cross Sectional Area".  
Rev.Sec.Instrum., 17, 372, (1946).
- C2 Crittenden, E.C., Strough, R.J.,  
"Limiting Sensitivity of Instruments for Displaying  
Magnetic Hysteresis Loop".  
Phys.Rev., 75, 1630, (1949).
- C3 Crittenden, E.C., Hudimac, A.A., Strough, R.J.,  
"Magnetisation Hysteresis Loop Tracer for Long Specimens  
of Extremely Small Cross Section".  
Rev.Sec.Instrum., 22, 172, (1951).
- C4 Crowther, T.S.,  
"Angular and Magnitude Dispersion of the Anisotropy  
in Magnetic Films".  
J.Appl.Phys., 34, 580, (1963).
- D1 Dwight, K., Menyuk, N., Smith, D.O.,  
"Further Developments of Vibrating Coil Magnetometer".  
J.Appl.Phys., 29, 491, (1958).
- F1 Foner, S.,  
"A Versatile and Sensitive Vibrating Coil Magnetometer".  
Rev.Soc.Instrum., 30, 548, (1959).

- F2 Flanders, P.J., Doyle, W.D.,  
"Motor Driven Magnetometer for Thin Magnetic Films".  
Rev.Sci.Instrum., 33, 691, (1962).
- G1 Gray, A.,  
"Absolute Measurements in Electricity and Magnetism".  
MacMillan and Co., London, 1st Edition, V2, Pt.1,  
p.267, (1893).
- H1 Howling, D.H.,  
"A Simple 60 c/s Hysteresis Loop Tracer for Magnetic  
Materials of High or Low Permeability".  
Rev.Sci.Instrum., 27, 952, (1956).
- H2 Humphrey, F.B., Johnston, A.R.,  
"A Sensitive Automatic Torque Balance for Thin Magnetic  
Film".  
Rev.Sci.Instrum., 34, 348, (1963).
- J1 Jeans, J.,  
"The Mathematical Theory of Electricity and Magnetism".  
Cambridge University Press, London, p. 225, (1946).
- M1 Melville, W.S.,  
"The Measurement and Calculation of Pulse Magnetisation  
Characteristics of Nickel-Irons from 0.1 to 5 Micro-  
seconds".  
Proc.Inst.Elect.Engrs., (London), 97II, 165, (1950).
- M2 Methfessel, S., Middlehoek, S., Thomas, H.,  
"Partial Rotation in Permalloy Films".  
J.Appl.Phys., 32, 1959, (1961).
- O1 Oguey, H.J.,  
"Sensitive Flux Measurement of Thin Magnetic Films".  
Rev.Sci.Instrum., 31, 701, (1960).
- O2 Oguey, H.J.,  
"Measurement of Hysteresis Loops of Thin Magnetic Films".  
Proc.Fifth International Conference on Instruments and  
Measurements, Stockholm, Sweden, p.907, Sept.13, (1960).
- R1 Ruark, A.E., Peters, M.F.,  
"Helmholtz Coils for Producing Uniform Magnetic Fields".  
J.Opt.Soc.Am., 13, 205, (1926).

- S1 Smith, D.O.,  
 "Development of a Vibrating Coil Magnetometer".  
 Rev.Sci.Instrum., 27, 261, (1956).
- S2 Scott, G.G.,  
 "Compensation of the Earth's Magnetic Field".  
 Rev.Sci.Instrum., 28, 270, (1957).
- S3 Strassberg, D.D.,  
 "An Audio Frequency Hysteresisgraph for Thin  
 Magnetic Films".  
 Group Report No. 51-10, Lincoln Lab., Massachusetts  
 Institute of Technology, (1959).
- W1 Wiegand, D.W., Hansen, W.W.,  
 "A 60 Cycle Hysteresis Loop Tracer".  
 Jr.Am.Inst.Elec.Engrs., 66, 119-31, (1947).

## CHAPTER 7

FACTORS IN OBTAINING THE MAXIMUM SENSITIVITY OR SIGNAL  
TO NOISE RATIO IN THE DETECTION OF THE FILM FLUX

## 7.1 INTRODUCTION

## AN EXPRESSION FOR THE SIGNAL TO NOISE RATIO

It is clearly desirable to obtain a hysteresis loop display as free as possible from noise and extraneous interference. The following section discusses those factors important in achieving the maximum possible sensitivity as limited by thermal noise in the resistance of the sense coil and by input noise in the amplifiers used to detect the film signal. A general theoretical treatment is developed, illustrated by reference to the present MH plotter. In this instrument, by attention to the points outlined, a limiting sensitivity has been obtained corresponding to the signal from a film of 1 cm diameter and  $0.6 \text{ \AA}$  in thickness (for repetition frequencies  $f_0$  from 0.1 to 1.0 Kc/s).

The sensitivity or signal to noise ratio  $\frac{S}{N}$  may be written as the ratio of the mean squared signal voltage produced by the film flux to the mean squared noise voltage, measured at the output oscilloscope display<sup>01</sup>.

Thus

$$\frac{S}{N} = \frac{\omega_0^2 |A(\omega_0)|^2 \overline{\phi_i^2}}{\frac{2}{\pi} \cdot kTR_i \int_0^{\infty} F(\omega) |A(\omega)|^2 d\omega} \quad (7.11)$$

where

- $\omega_0$  is the repetition frequency of the MH plotter,  
 $k$  is the Boltzman's constant,  
 $T$  is the absolute temperature,  
 $R_i$  is the equivalent resistance of the sense coil\*,  
 $F(\omega)$  is the spot amplifier noise figure at the frequency  $\omega$ ,  
 $A(\omega)$  is the transfer function of the sense channel measured from the induced coil voltage to the output oscilloscope display, and  
 $\overline{\phi_i^2}$  is the mean squared film flux linking the total turns of the sense coil (and is thus proportional to  $n^2$ , where  $n$  is the number of turns).

The expression  $\omega_0^2 |A(\omega_0)|^2 \overline{\phi_i^2}$  for the mean squared output voltage follows from the fact that, if a hysteresis

---

\* Strictly,  $R_i$  will be the total input resistance and is the sum of the sense and cancellation coil resistances as discussed in Section 6.66 plus the output impedance  $R_0$  of the air flux cancellation bridge.

---

curve is to be accurately displayed, the overall transfer function  $sA(s)$  must be constant for all frequencies of interest in  $\phi_i$ . As discussed in Section 6.72, the transfer function is determined by the permissible errors in the hysteresis loop display and is thus a function of the relative frequency  $\omega/\omega_0$  rather than of  $\omega_0$ . It is convenient to normalize equation 7.11 in terms of  $\omega_0$  to give

$$\frac{S}{N} = \frac{\omega_0^2 \overline{\phi_i^2}}{\frac{2}{\pi} kTR_i(\omega_0 \beta) F} \quad (7.12)$$

where

$$\beta = \frac{\int_0^{\infty} |A(\omega)|^2 d\left(\frac{\omega}{\omega_0}\right)}{|A(\omega_0)|^2}$$

is the normalized noise bandwidth<sup>T1</sup> and

$$F = \frac{\int_0^{\infty} F(\omega) |A(\omega)|^2 d\left(\frac{\omega}{\omega_0}\right)}{\int_0^{\infty} |A(\omega)|^2 d\left(\frac{\omega}{\omega_0}\right)}$$

is the averaged amplifier noise figure.

Equation(7.12)is in a form which allows a convenient separation of the various factors involved. These are



- the repetition frequency  $\omega_0$ , the impedance level of the coil and the design of the detecting amplifier. These factors effect the  $\frac{S}{N}$  ratio through the terms  $\omega_0/F$  and are discussed in Section 7.2 below. Both transistor and valve amplifiers are compared and the former shown to be clearly superior.

- the transfer function  $A(s)$  effects the  $\frac{S}{N}$  ratio principally through the normalized bandwidth  $\beta$  and to a small extent through the noise figure  $F$ . A choice of  $A(s)$  which decreases  $\beta$  will produce a net decrease in  $\beta F$ . Thus Section 7.3 discusses the approximation problem in choosing  $A(s)$  to minimize  $\beta$  subject to preserving the necessary frequency response and fidelity in the transmission of the film signal.

- the geometrical shape and size of the sense coil which effects the  $\frac{S}{N}$  ratio through the factor

$\frac{\overline{\phi_i^2}}{R_i} \cdot \frac{\overline{\phi_i^2}}{R_i}$  is a measure of the fraction of the flux effective in linking the sense coil to the winding resistance per turn. A detailed analysis is given in Section 7.4 including design curves for a coil both enclosing the film and located on one side of the film only.

## 7.2 THE CHOICE OF THE REPETITION FREQUENCY $\omega_0$ THE AMPLIFIER NOISE FIGURE $F$ AND THE OPTIMUM IMPEDANCE LEVEL OF THE SENSE COIL

### 7.21 Introduction

The choice of  $\omega_0$  will be determined by both instrumental considerations and by the effect of frequency on the properties of the films measured. For example, at high frequencies the switching of a film will no longer be quasi-static. Section 4.6 discussed some experimental results illustrating such non-quasistatic behaviour. It is for this reason that variable frequency operation (and the range 0.1 to 1.0 Kc/s appears the most suitable in practice) is of such value.

In regard to instrumental difficulties, previous writers<sup>C1,01</sup> have limited  $\omega_0$  to a small fraction, typically 0.01, of the sense coil resonant frequency  $\omega_r$ , so that the flux waveform is accurately reproduced with a sufficiently fast rise time and satisfactory overshoot. Since poles produced by the sense coil can be compensated by networks later in the amplifier<sup>S1,B3</sup>, or by other methods\*, this limitation becomes

---

\* For example, the input impedance of the sense amplifier may be made to appear as a negative capacitance by suitable positive feedback, or the low input impedance circuit described in Section 8.6 may be used.

of a practical nature depending on the accuracy with which compensation can be achieved (for example, poles at  $10 \omega_0$  compensated to within 10 percent will have an effect comparable to uncompensated poles at  $100 \omega_0$ ). A more definite criterion is required. From equation 7.12 it can be seen that as  $\omega_0$  is increased,  $\frac{S}{N}$  initially increases as  $\omega_0$ , but then decreases as the noise figure  $F$  begins to increase due to the coil inductance and shunt capacitance. Thus an optimum  $\omega_0$  exists simply on the basis of an optimum  $\frac{S}{N}$  ratio. It remains to develop a quantitative analysis of the variation of  $\frac{S}{N}$  with frequency. Such an analysis is given for transistor amplifiers in Section 7.22 and for valve amplifiers in Section 7.23.

For valve amplifiers the previous situation has been obscure, normal practice being to make the sense coil impedance as high as possible subject to a specified value of  $\omega_r/\omega_0$ . The question then arises as to what penalty is paid by specifying  $\omega_r/\omega_0$  and if a lower impedance and higher  $\omega_0$  should instead be used for the same value of  $\omega_r/\omega_0$ . The present analysis was originally undertaken in connection with an earlier MH plotter using the E180F valve preamplifier described in Section 7.23. Clear and definite answers are provided. Both an optimum  $\omega_0$  and an optimum coil impedance  $R_i$  are predicted and these values are practically useful ( $f_0 \doteq 2$  Kc/s,  $R_i \doteq 10$  k $\Omega$ , see Fig. 7.27). For white noise,

specifying  $\omega_r/\omega_0$  decreases the possible  $\frac{S}{N}$  ratio by the factor  $\omega_r/\omega_0 K_4$ , where  $K_4$  is a dimensionless constant of the order of 20 describing the shape of the transfer function  $A(s)$ . Further low frequency  $\frac{1}{f}$  noise may be readily included in the analysis.

Section 7.24 discusses the relative advantages of transistor and valve amplifiers and shows that on numerous practical considerations, the former are clearly preferred. For transistor amplifiers, Section 7.22 gives an operating frequency in the range 500 c/s to 1 Kc/s. The optimum impedance in this case is not greatly different from the normal optimum resistive source impedance of a transistor amplifier for minimum noise figure. Most previous MH plotters have in fact used frequencies in the range 500 c/s to 1 Kc/s to obtain an acceptable  $\omega_r/\omega_0$  <sup>01</sup>. Nevertheless, it is useful to show that this is also the optimum frequency from the quite general consideration of  $\frac{S}{N}$  ratio and to set a figure to the maximum realizable value of  $\frac{S}{N}$ .

## 7.22 Transistor Amplifiers

For transistor amplifiers the impedance of the coil is sufficiently low so that coil self-capacitance may be neglected in the noise figure calculations. The effects of white noise can be analysed almost exactly, and low frequency  $\frac{1}{f}$  noise can be included with lesser accuracy if certain simpli-

fying assumptions are made. The spot noise figure  $F(\omega)$  may be written as the sum of separate white noise and  $\frac{1}{F}$  noise components,  $\Delta F_W(\omega)$  and  $\Delta F_L(\omega)$  respectively;

$$F(\omega) = 1 + \Delta F_W(\omega) + \Delta F_L(\omega) \quad (7.21)$$

The coil inductance  $L_i$  has a significant effect on the noise figure only at frequencies  $\omega > R_i/L_i$ . For a practical coil design,  $R_i/L_i$  is of the order of  $2\pi \times 10^3$  rad sec<sup>-1</sup>.  $\frac{1}{F}$  noise is negligible at these frequencies and  $\Delta F_L(\omega)$  in equation (7.21) can be replaced by  $\Delta F_{Lt}(\omega)$ , the  $\frac{1}{F}$  noise for a purely resistive source  $R_i$  alone. Using the independent current generator model for white noise proposed by Giacoletto<sup>G1</sup>,  $F(\omega)$  becomes

$$F(\omega) = 1 + \Delta F_{Lt}(\omega) + \frac{r_{bb'}}{R_i} + \frac{|r_{bb'} + R_i + j\omega L_i|^2}{R_i} \cdot \frac{(\frac{I_{ec}}{\beta_t} + a^2 I_{ec} + I_{bc})}{2\phi_t} \quad (7.22)$$

where

$$a = \frac{\phi_t}{I_{ec}} \frac{1}{|r_{bb'} + R_i + j\omega L_i|}$$

$R_i$  is the resistance of the equivalent sense coil,

$L_i$  is the inductance of the equivalent sense coil,

$r_{bb'}$  is the extrinsic base resistance,

$I_{ec}$  is the emitter to collector current,  
 $I_{bc}$  is the base to collector saturation current,  
 $\beta_t$  is the common emitter current amplification factor,  
 $\phi_t = kT/q$  is the thermal equilibrium potential, and  
 $q$  is the electronic charge.

Performing the integration of equation (7.22), the average noise figure  $F$  is given by

$$F = 1 + \Delta F_{Lt}(\omega_0) + \frac{r_{bb'}}{R_i} + \frac{(r_{bb'} + R_i)^2 + \omega_0^2 L_i^2 K_2^2}{R_i} \cdot \frac{\left(\frac{I_{ec}}{\beta_t} + a'^2 I_{ec} + I_{bc}\right)}{2\phi_t} \quad (7.23)$$

where

$$\Delta F_{Lt}(\omega_0) = \frac{\int_0^{\infty} \Delta F_{Lt}(\omega) |A(\omega)|^2 d\left(\frac{\omega}{\omega_0}\right)}{\int_0^{\infty} |A(\omega)|^2 d\left(\frac{\omega}{\omega_0}\right)}$$

is the average  $\frac{1}{F}$  noise component for a resistive source  $R_i$ .  
 If  $\Delta F_{Lt}(\omega)$  varies as  $1/\omega^m$ , then for a given shape of the response function  $A(\omega)$ ,  $\Delta F_{Lt}(\omega_0)$  will vary as  $1/\omega_0^m$ .

$$a'^2 = \frac{\left(\frac{\phi_t}{I_{ec}}\right)^2}{(r_{bb'} + R_i)^2 + \omega_0^2 L_i^2 K_2^2}$$

and

$$K_2^2 = \frac{\int_0^{\infty} \left(\frac{\omega}{\omega_0}\right)^2 |A(\omega)|^2 d\left(\frac{\omega}{\omega_0}\right)}{\int_0^{\infty} |A(\omega)|^2 d\left(\frac{\omega}{\omega_0}\right)}$$

$K_2$  is a constant, normally of the order of unity, depending only on the shape of the response function  $A(\omega)$ . Formulae and typical values for  $K_2$  for various integrator transfer function are given in Table 7.21.

#### The Optimum Impedance Level of the Sense Coil and the Optimum Repetition Frequency $\omega_0$

The number of turns  $n$  of the sense coil effects the  $\frac{N}{S}$  ratio of equation (7.12) only through the factor  $F$ . Since  $R_i$  and  $L_i$  are proportional to  $n^2$ , then minimizing the white noise component of  $F$  with respect to both  $n$ , that is the impedance level of the coil, and the transistor operating current  $I_{ec}$ ,

$$F = 1 + F_{Lt}(\omega_0) + \Delta F_{Wt} \left( 1 + \frac{\omega_0^2}{\omega_{LR}^2} K_2^2 \right)^{\frac{1}{2}} \quad (7.24)$$

and the minimum occurs for

Table 7.21 FORMULAE FOR THE CONSTANTS  $K_{-1}, K_1, K_2, K_3$  and  $K_4$  AS DEFINED BY EQUATION (7.212) FOR THE PHASE COMPENSATED TRANSFER FUNCTION

$$A(s) = \frac{(1 + \frac{\omega_3}{s})}{s(1 + \frac{\omega_1}{s}) (1 + \frac{s}{\omega_2})}$$

In terms of the normalized frequencies  $\omega_1' = \omega_1/\omega_0$ ,  $\omega_2' = \omega_2/\omega_0$ ,  $\omega_3' = \omega_3/\omega_0$ , then in the case  $\omega_1', \omega_3' \ll 1, \omega_2' \gg 1$ , integration gives to a very good approximation

$$\beta K_{-1} \div \frac{1}{2\omega_1^2} (1 + \frac{1}{2} \frac{\omega_3^2 - \omega_1^2}{\omega_1^2}) + \frac{1}{2} (1 - \frac{2}{\omega_2^2} \log_e \omega_2^2)$$

$$\beta K_1 \div \log_e \frac{1}{\omega_1} + \frac{1}{4} \frac{\omega_3^2 - \omega_1^2}{\omega_1^2} + \log_e \omega_2 - 1$$

$$\beta K_2^2 \div \frac{\pi}{4} \omega_2$$

$$\beta K_3^3 \div \frac{1}{2} \omega_2^2$$

$$\beta K_4^4 \div \frac{\pi}{4} \omega_2^3$$

Numerical Values

$$\omega_1' = 0.58 \times 10^{-2}$$

$$\omega_3' = 1.73 \times 10^{-2}$$

$$\omega_2' = 2 \times 10^2$$

$$\beta = 2.60 \frac{\pi}{2} \times 10^2$$

$$K_{-1} = 182$$

$$K_1 = 0.0255$$

$$K_2 = 0.619$$

$$K_3 = 3.65$$

$$K_4 = 11.1$$

$$K_2^2 = 0.384$$

$$K_3^3 = 4.87$$

$$K_4^4 = 1.54 \times 10^4$$

where  $\beta$  is the normalized noise bandwidth defined in equation (7.22) and for which a general expression has been given in equation (7.38).



Table 7.21 cont.

If synchronous DC restoration is used, then from equation (8.72),  $A(s)$  contains the additional pole factor  $(1 + \frac{\omega_4}{s})$ , where  $\omega_4 = \omega_0/5.05$ . Only the formulae of  $\beta K_{-1}$  and  $\beta K_1$  are significantly ordered. The latter remains negligibly small while  $\beta K_{-1}$  becomes

$$\beta K_{-1} \div \frac{1}{2\omega_4^2} \left( \log \frac{\omega_4^2}{\omega_1^2} + \frac{1}{2} \frac{\omega_3^2 - 3\omega_1^2}{\omega_1^2} \right)$$

Formulae for  $\beta K_2$ ,  $\beta K_3$  and  $\beta K_4$

as previously.

Numerical Values for  
(synchronous restoration)

$$\omega_1' = 0.58 \times 10^{-2}$$

$$\omega_3' = 1.73 \times 10^{-2}$$

$$\omega_2' = 2 \times 10^2$$

$$\omega_4' = 1/5.05$$

$$\beta = 5.05 \frac{\pi}{2}$$

$$K_{-1} = 11.4$$

$$K_2^2 = 19.8, \quad K_2 = 4.45$$

$$K_3^3 = 2.5 \times 10^3, \quad K_3 = 13.6$$

$$K_4^4 = 79.3 \times 10^4, \quad K_4 = 29.8$$

$$R_i = \frac{R_{iWt}}{\left(1 + \frac{\omega_0^2}{\omega_{LR}^2} K_2^2\right)^{\frac{1}{2}}}$$

$$I_{ec} = \frac{I_{ecWt}}{\left(1 + \frac{\omega_0^2}{\omega_{LR}^2} K_2^2\right)^{\frac{1}{2}}}$$

where

$\omega_{LR} = L_i/R_i$  is a geometrical constant of the coil independent of the number of turns

$$\Delta F_{Wt} = \frac{1}{\sqrt{\beta_t}} + 2 \left( r_{bb'} \frac{I_{bc}}{2\phi_t} \right)^{\frac{1}{2}}$$

$$R_{iWt} = \left( r_{bb'} \frac{2\phi_t}{I_{bc}} \right)^{\frac{1}{2}}$$

and

$$I_{ecWt} = \frac{\phi_t}{(R_{iWt} + r_{bb'})\sqrt{\beta_t}}$$

In deriving equation (7.24), the usual approximation of

$$(r_{bb'} + R_i)^2 + \omega_0^2 L_i^2 K_2^2 \div R_i^2 + \omega_0^2 L_i^2 K_2^2$$

has been made.

$\Delta F_{Wt}$ ,  $R_{iWt}$ ,  $I_{ecWt}$  are the minimum noise figure increment, the optimum source resistance and the optimum operating current of the transistor for a purely resistive source and considering white noise only. They are best measured directly for the transistor type used rather than calculated from the formulae of equation(7.24). Equation(7.24) represents a minimum of the total noise figure  $F$  only if the values given for  $R_i$  and  $I_{ec}$  simultaneously minimize the  $\frac{1}{F}$  noise component  $\Delta F_{Lt}(\omega_0)$ . While this is not so, it may be expected that the error involved is not great. The optimum source impedance and operating current for  $\frac{1}{F}$  noise are both a little lower than the values  $R_{iWt}$  and  $I_{ecWt}$   $F_1, F_2$ . Further  $\Delta F_{Lt}(\omega_0)$  varies only slowly about the optimum point.

From equation 7.12, the  $\frac{S}{N}$  ratio depends on  $\omega_0$  through the terms

$$\frac{S}{N} \propto \frac{\omega_0}{F} = \frac{\omega_0}{1 + \Delta F_{Lt}(\omega_0) + \Delta F_{Wt} \left\{ 1 + \frac{\omega_0^2}{\omega_{LR}^2} K_2^2 \right\}^{\frac{1}{2}}} \quad (7.25)$$

At low frequencies  $\omega_0 \ll \omega_{LR}/K_2$ ,  $\omega_0/F$  reduces to

$$\frac{\omega_0}{1 + \Delta F_{Lt}(\omega_0) + \Delta F_{Wt}} = \frac{\omega_0}{F_t}$$

as might be expected. At high frequencies  $\omega_0 \gg \omega_{LR}/K_2$ ,  $\omega_0/F$

tends to a limiting value  $(\omega_0/F)_{\max} = \omega_{LR}/K_2 \Delta F_{Wt}$  independent of the  $\frac{1}{F}$  noise. Little is gained by increasing  $\omega_0$  much above the value  $(\omega_0)\frac{1}{2}$  for which  $(\omega_0/F) = \frac{1}{2}(\omega_0/F)_{\max}$ . Thus, as stated in Section 7.21, an optimum repetition frequency may be determined purely on the basis of the maximum  $\frac{S}{N}$  ratio.

#### The Optimum Conditions for White Noise Only

In the case  $\Delta F_{Lt}(\omega_0) \equiv 0$ , where  $\frac{1}{F}$  noise may be neglected, equation (7.25) simplifies to

$$\begin{aligned} \frac{\omega_0}{F} &= \frac{\omega_0}{1 + \Delta F_{Wt} \left( 1 + \frac{\omega_0^2}{\omega_{LR}^2} K_2^2 \right)^{\frac{1}{2}}} & (7.26) \\ &= \frac{\omega_0}{1 + \Delta F_{Wt} \left( 1 + \frac{\omega_0^2}{\omega'_{LR}{}^2} \right)^{\frac{1}{2}}} \end{aligned}$$

where  $\omega'_{LR} = \omega_{LR}/K_2$  is a characteristic frequency depending on the coil shape (but independent of the number of turns) and on the constant  $K_2$  describing the shape of the transfer function.

Writing

$$\frac{\left(\frac{\omega_0}{F}\right)}{\left(\frac{\omega_0}{F}\right)_{\max}} = \frac{\left(\frac{\omega_0}{\omega'_{LR}}\right) \Delta F_{Wt}}{1 + \Delta F_{Wt} \left(1 + \frac{\omega_0^2}{\omega'^2_{LR}}\right)^{\frac{1}{2}}} \quad (7.27)$$

then a series of universal curves of  $(\omega_0/F)/(\omega_0/F)_{\max}$  can be plotted against the normalized frequency  $\omega_0/\omega'_{LR}$  with  $\Delta F_{Wt}$  as parameter. These curves are shown in Fig. 7.22.

In the derivation of equation (7.22) it has been assumed that the self-resonant frequency  $\omega_r$  of the sense coil is sufficiently above the frequency  $\omega_0$  that self-capacitance of the coil can be neglected. It is of interest to verify that this is true. For the optimum coil impedance of equation (7.24) it may be shown that

$$\frac{\omega'_r}{\omega_0} = \frac{\omega'_{LR}}{\omega_0} \left(1 + \frac{\omega_0^2}{\omega'^2_{LR}}\right)^{\frac{1}{4}} \left(\frac{Z_{0i}^2}{R_i R_{it}}\right)^{\frac{1}{2}} \quad (7.28)$$

where

$$\omega'_r = \frac{\omega_r}{K_2}$$

and

$$Z_{0i} = \left(\frac{L_i}{C_i}\right)^{\frac{1}{2}}$$

$\left(Z_{0i}^2/R_i R_{it}\right)^{\frac{1}{2}}$  is a dimensionless constant depending on the

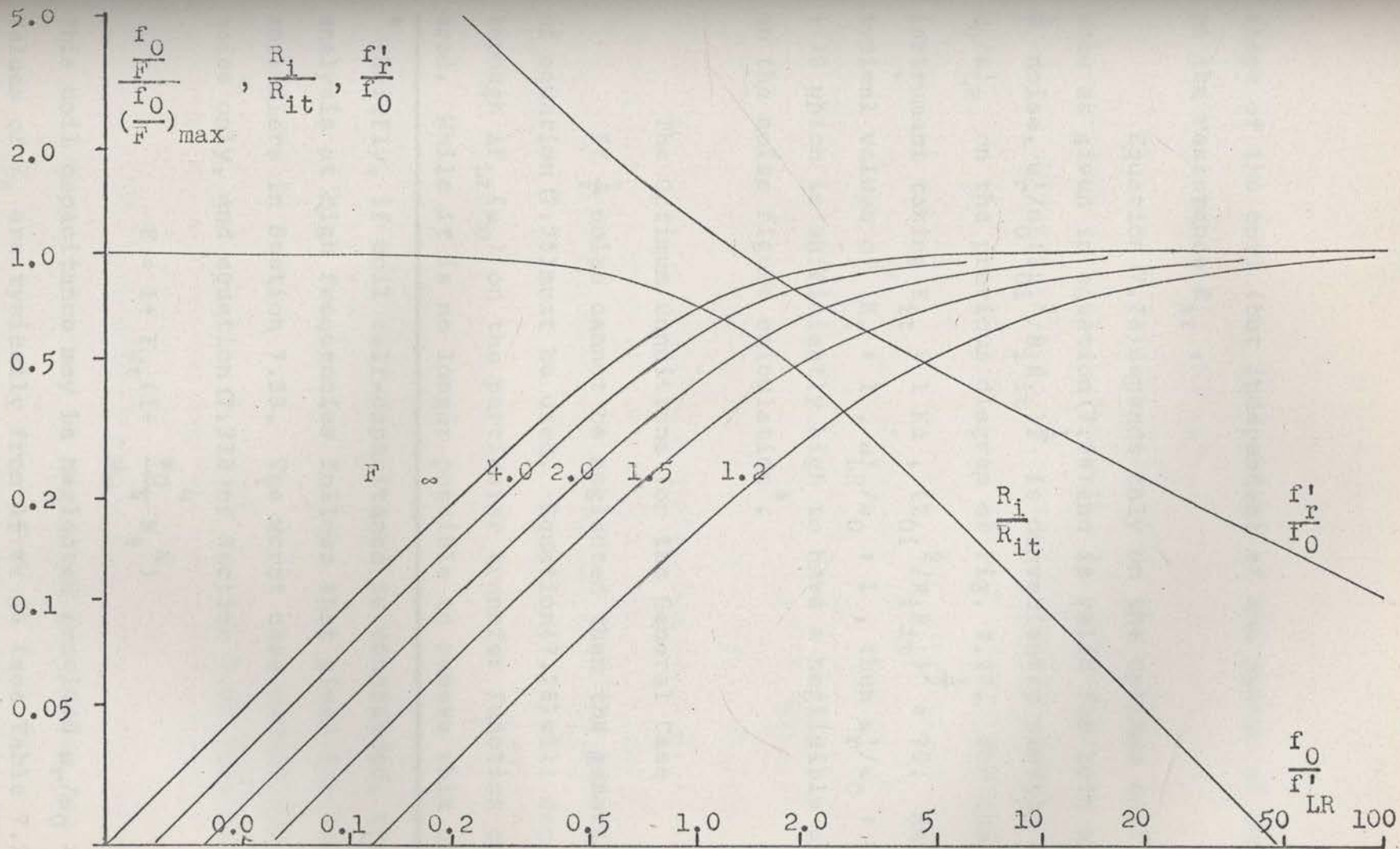


Fig. 7.22 Universal Curves of  $\frac{f_0}{F} / \left(\frac{f_0}{F}\right)_{\max}$  against the Normalized Frequency  $f_0/f'_{LR}$  for a Transistor Amplifier in the case of White Noise only.

shape of the coil (but independent of the number of turns) and on the resistance  $R_{it}$ .

Equation (7.28) depends only on the optimum coil impedance as given in equation (7.24) and is valid for both white and  $\frac{1}{f}$  noise.  $\omega_r'/\omega_0 (Z_{oi}^2/R_i R_{it})^{\frac{1}{2}}$  is conveniently plotted against  $\omega_0/\omega_{LR}'$  on the previous diagram of Fig. 7.22. For the present instrument taking  $R_{it} = 1 \text{ K}\Omega$ ,  $(Z_{oi}^2/R_i R_{it})^{\frac{1}{2}} = 70$ . Assuming typical values of  $K_2 \div 1$ ,  $\omega_{LR}'/\omega_0 \div 1$ , then  $\omega_r'/\omega_0 \div \omega_r/\omega_0 \div 70$  which is sufficiently high to have a negligible effect on the noise figure calculation\*.

#### The Optimum Conditions for the General Case

If  $\frac{1}{f}$  noise cannot be neglected then the general form of equation (7.25) must be used. Equation (7.25) will depend through  $\Delta F_{Lt}(\omega_0)$  on the particular transfer function considered. While it is no longer possible to remove this depend-

---

\* Briefly, if coil self-capacitance is considered, then the analysis at high frequencies follows that given for valve amplifiers in Section 7.23. The worst case occurs for white noise only, and equation (7.213) of Section 7.23 then becomes

$$F = 1 + F_{Wt} \left( 1 + \frac{\omega_0^4}{\omega_r^4} K_4^4 \right)$$

This coil capacitance may be neglected provided  $\omega_r/\omega_0 > K_4$ . Values of  $K_4$  are typically from 15 to 25 (see Table 7.21).

---

ance by normalization, the normalized scales of Fig. 7.22 are still the most convenient way of drawing curves of  $\omega_0/F$  against  $\omega_0$ . In Fig. 7.24 discussed below, normalization has not been used so that the results for transistor amplifiers might be more conveniently compared with those for valve amplifiers in Section 7.23. The nature of the curves are not significantly altered by  $\frac{1}{F}$  noise. The limiting value  $(\omega_0/F)_{\max}$  is as before  $\omega_{LR}/K_2 \Delta F_{Wt}$  independent of  $\Delta F_{Lt}(\omega_0)$ , however the frequency  $(\omega_0)_{\frac{1}{2}}$  for which  $(\omega_0/F) = \frac{1}{2}(\omega_0/F)_{\max}$  is raised.

The above discussion can be best illustrated by reference to the specific case of the present MH plotter. We shall consider two possible transfer functions  $A(s)$ , corresponding approximately to those normally used with the instrument with and without synchronous DC restoration (see Sections 8.41 and 8.71)

- without synchronous restoration  $A(s)$  is of the form

$$A(s) = \frac{1}{s} \cdot \frac{\left(1 + \frac{1.73 \times 10^{-2} \omega_0}{s}\right)}{\left(1 + \frac{0.58 \times 10^{-2} \omega_0}{s}\right)^3 \left(1 + \frac{s}{200 \omega_0}\right)^2} \quad (7.29)$$

giving from Table 7.21,  $K_2 = 0.62$ . Using the measured frequency  $f_{LR} = 0.825$  Kc/s of the sense coil,  $f_{LR}/K_2 = 1.33$  Kc/s.

- with synchronous restoration the effective transfer function for the calculation of noise is from equation (8.72),



$$A(s) = \frac{1}{s} \cdot \frac{(1 + \frac{1.73 \times 10^{-2} \omega_0}{s})}{(1 + \frac{0.58 \times 10^{-2} \omega_0^3}{s}) (1 + \frac{\omega_0}{5.05s}) (1 + \frac{s}{200\omega_0})^2} \quad (7.210)$$

giving from Table 7.21,  $K_2 = 4.45$ . Using the measured frequency  $f_{LR} = 0.825$  Kc/s of the sense coil,  $f_{LR}/K_2 = 0.185$  Kc/s.

The transfer functions of equations 7.29 and 7.210 give a 0.01 per cent low frequency sag error at  $\omega_0$  increasing to 1 per cent at  $0.1 \omega_0$ . These are representative of the tolerances which might be set in a practical case. Measured noise figure data for the transistorized preamplifier of the MH plotter is shown in Fig. 7.23.  $F_{Wt} = 0.25$  and  $F_{Lt}(\omega_0)$  is plotted against the repetition frequency  $f_0$  for each of the transfer functions of equations 7.29 and 7.210.

Calculated curves of  $f_0/F$  against  $f_0$  for the above data are shown in Fig. 7.24, together with the corresponding curves for the two cases considering white noise only ( $\Delta F_{Wt} = 0.25$ ,  $\Delta F_{Lt}(\omega_0) \equiv 0$ ). As previously stated  $\frac{1}{F}$  noise raises only the frequency  $(\omega_0) \frac{1}{2}$  leaving the limiting value  $(\omega_0/F)_{max}$  unaltered. With DC synchronous restoration, the lower frequency components are suppressed and  $(\omega_0) \frac{1}{2}$  is lowered. With restoration and considering  $\frac{1}{F}$  noise,  $(\omega_0) \frac{1}{2} = 0.83$  Kc/s which is near the upper limit of the

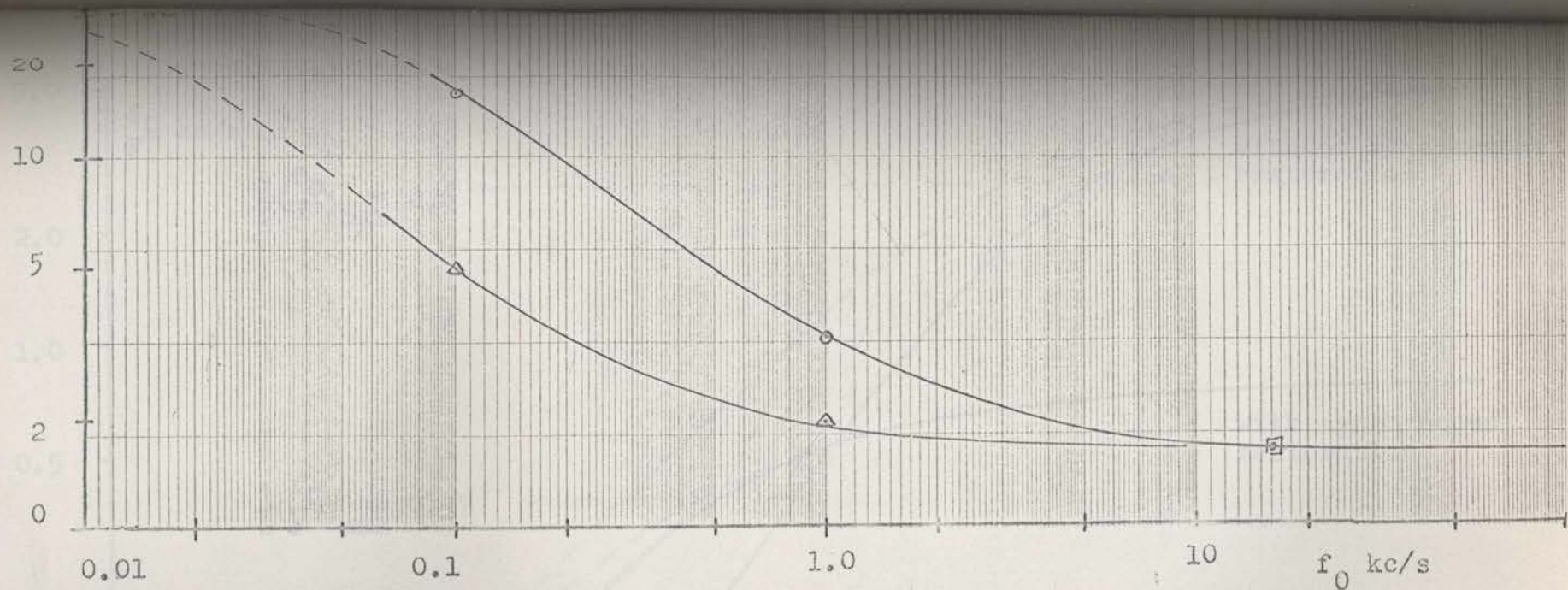


Fig. 7.23 Noise Figure Measurements for the MH Plotter Transistor Preamplifier.

The equivalent or average noise figure  $F$  is defined in equation 7.12. Points marked  $\odot$  and  $\triangle$  are measurements of  $F$  for the transfer functions of equations (7.209) and (7.210) respectively at  $f_0 = 1$  kc/s and 10 kc/s. The point marked  $\square$  is for a flat response from 20 c/s to 15 kc/s. The measurement at  $f_0 = 1$  kc/s for the transfer function (7.209) was made by estimating the peak noise from an oscilloscope display (see Fig. 6.69) and dividing by 3.5 to obtain the rms value. All other measurements were made using the Ballantine 310 voltmeter (low frequency 3 db point 20 c/s) and correcting 1.05 db for the average rather than rms reading properties of the instrument.

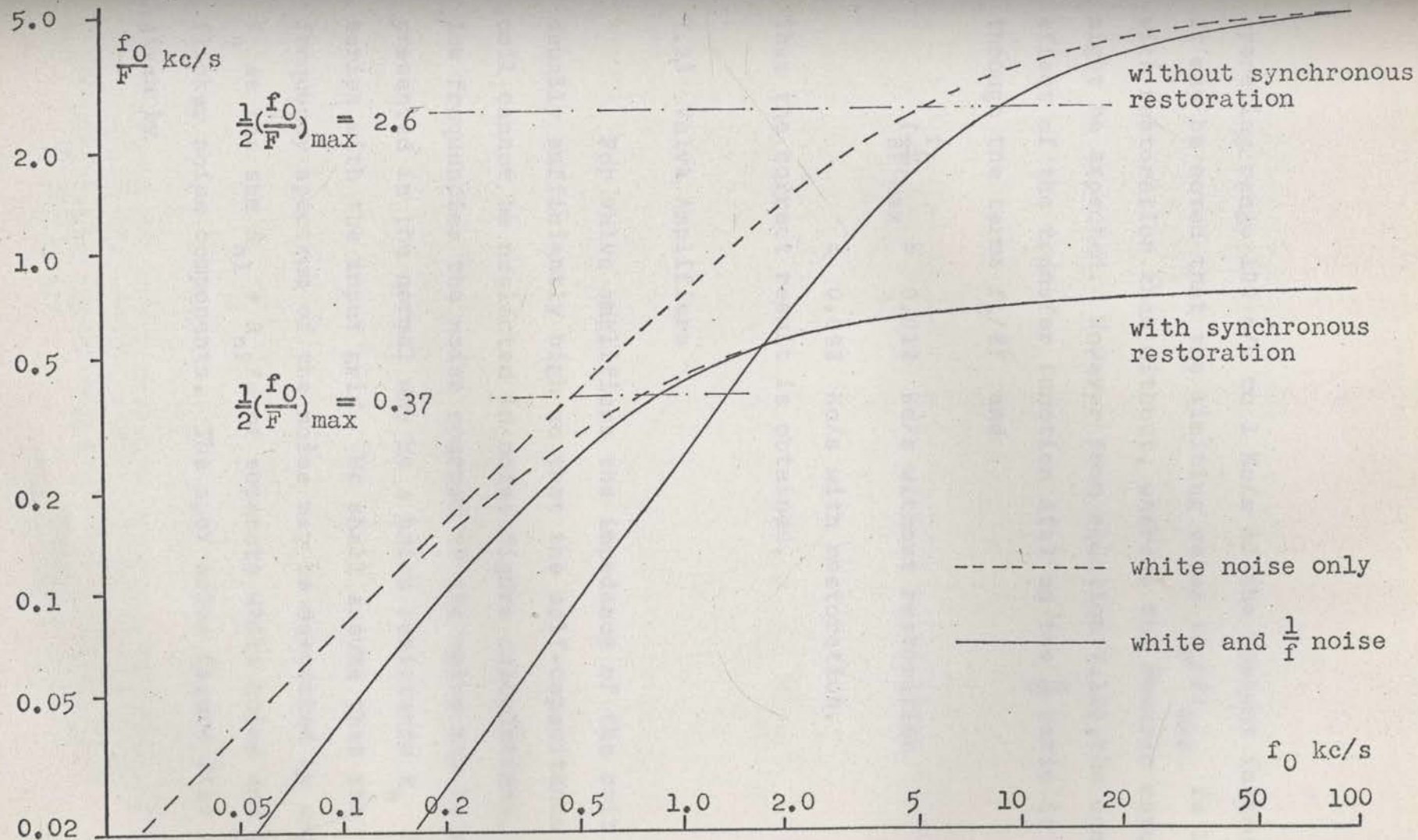


Fig. 7.24  $f_0/F$  Against Repetition Frequency  $f_0$  for a Transistor Amplifier

operating range 100 c/s to 1 Kc/s of the present instrument. It may be noted that the limiting value  $(f_0/F)_{\max}$  is less with restoration than without, whereas the reverse result might be expected. However from equation (7.12), the complete effect of the transfer function  $A(s)$  on the  $\frac{S}{N}$  ratio is through the terms  $f_0/\beta F$  and

$$\begin{aligned} \left(\frac{f_0}{\beta F}\right)_{\max} &= 0.013 \text{ Kc/s without restoration} \\ &= 0.093 \text{ Kc/s with restoration.} \end{aligned}$$

Thus the correct result is obtained.

### 7.23 Valve Amplifiers

For valve amplifiers the impedance of the coil is usually sufficiently high so that the self-capacitance of the coil cannot be neglected in noise figure calculations. At low frequencies the noise sources of the valve may be represented in the normal way by a noise resistance  $R_n$  in series with the input grid. We shall assume that the frequency spectrum of the noise may be described by writing  $R_n$  as the sum  $R_{n1} + R_{n2}/\omega$  of separate white noise and  $\frac{1}{f}$  flicker noise components. The spot noise figure  $F(\omega)$  is given by

$$F(\omega) = 1 + \frac{R_{n1} + \frac{R_{n2}}{\omega}}{R_i} \left\{ (1 - \omega^2 L_i C_i)^2 + \omega^2 R_i C_i \right\} \quad (7.211)$$

where  $C_i$  is the total capacitance across the coil.

Performing the integration of equation (7.211), the average noise figure  $F$  becomes

$$F = 1 + \frac{R_{n1}}{R_i} \left( 1 - 2 \frac{\omega_0^2}{\omega_r^2} K_2^2 + \frac{\omega_0^4}{\omega_r^4} K_4^4 + \frac{\omega_0^2}{\omega_r^2} \cdot \frac{\omega_{RL}^2}{\omega_r^2} K_2^2 \right) + \frac{R_{n2}}{\omega_0 R_i} \left( K_{-1} - 2 \frac{\omega_0^2}{\omega_r^2} K_1 + \frac{\omega_0^4}{\omega_r^4} K_3^3 + \frac{\omega_0^2}{\omega_r^2} \cdot \frac{\omega_{RL}^2}{\omega_r^2} K_1 \right) \quad (7.212)$$

where

$\omega_{LR} = R_i/L_i$  is a geometrical constant of the coil independent of the number of turns

$\omega_r = 1/\sqrt{L_i C_i}$  is the resonant frequency of the coil

and

$$K_m^m = \frac{\int \left(\frac{\omega}{\omega_0}\right)^m |A(\omega)|^2 d\left(\frac{\omega}{\omega_0}\right)}{\int |A(\omega)|^2 d\left(\frac{\omega}{\omega_0}\right)}$$

$K_{-1}$ ,  $K_1$ ,  $K_2$ ,  $K_3$  and  $K_4$  are constants depending only on the shape of the transfer function  $A(\omega)$ . Formulae and typical values for  $K_{-1}$  . . . . .  $K_4$  are given in Table 7.21. In

practice  $\omega_{LR}$  is normally less than or of the order of  $\omega_r$ ,  $K_4^4 \gg K_2^2$  and  $K_{-1}$  is of the order of  $K_3^3$  and both  $\gg K_1$ . To a close approximation equation (7.212) simplifies to

$$F = 1 + \frac{R_{n1}}{R_i} \left(1 + \frac{\omega_0^4}{\omega_r^4} K_4^4\right) + \frac{R_{n2}}{\omega_0 R_i} \left(K_{-1} + \frac{\omega_0^4}{\omega_r^4} K_3^3\right) \quad (7.213)$$

The Optimum Impedance Level of the Sense Coil and the Optimum Repetition Frequency  $\omega_0$

The number of turns  $n$  of the sense coil, that is the impedance level of the coil, effects the  $\frac{S}{N}$  ratio of equation (7.12) only through the factor  $F$ . Now  $R_i \propto n^2$  and for fixed values of  $\omega_{LR} = R_i/L_i$  and  $C_i$ ,  $\omega_r^2 = \omega_{LR}/R_i C_i \propto 1/n^2$ . Hence minimizing  $F$  with respect to  $n$

$$F = 1 + 2 \frac{R_{n1} + \frac{R_{n2}}{\omega_0} K_{-1}}{R_i} \quad (7.214)$$

$$= 1 + 2 \frac{C_i}{\omega_{LR}} \left(R_{n1} + \frac{R_{n2} K_{-1}}{\omega_0}\right)^{\frac{1}{2}} \left(R_{n1} K_4^4 + \frac{R_{n2} K_3^3}{\omega_0}\right)^{\frac{1}{2}} \omega_0^2$$

and the minimum occurs for\*

---

\* since  $\omega_r^2 = \omega_{LR}/R_i C_i$  and  $\omega_{LR}$  and  $C_i$  are fixed, we may consider either  $R_i$  or  $\omega_r$  as interchangeably specifying the coil impedance level.

---

$$\omega_r = \omega_0 \frac{R_{n1} K_4^4 + \frac{R_{n2}}{\omega_0} K_3^3}{R_{n1} + \frac{R_{n2}}{\omega_0} K_{-1}} \quad (7.215)$$

From equation (7.12), the  $\frac{S}{N}$  ratio then depends on  $\omega_0$  through the terms

$$\frac{S}{N} \propto \frac{\omega_0}{F} = \frac{\omega_0}{1 + 2 \frac{C_i}{\omega_{LR}} \left( R_{n1} + \frac{R_{n2} K_{-1}}{\omega_0} \right)^{\frac{1}{2}} \left( R_{n1} K_4^4 + \frac{R_{n2} K_3^3}{\omega_0} \right)^{\frac{1}{2}}} \quad (7.216)$$

$\omega_0/F$  passes through a maximum with respect to  $\omega_0$ , the position of this maximum being given by the simultaneous equations

$$\omega_0 = \frac{\omega_r}{K_4} \left\{ 1 + \frac{R_{n2}}{\omega_0 R_{n1}} \left( K_{-1} - \frac{\omega_0^4}{\omega_r^4} K_3^3 \right) \right\}^{\frac{1}{4}} \quad (7.217)$$

$$R_i = 2R_{n1} + \frac{R_{n2}}{\omega_0} \left( K_{-1} - \frac{\omega_0^4}{\omega_r^4} K_3^3 \right)$$

In practice it may not be possible to make the impedance level of the coil equal to the optimum value given by equation (7.215). For example,

- it may be preferred to avoid the added complicati

of compensating high frequency poles produced by the sense coil, in which case the variation of  $\omega_0/F$  must be considered subject to a fixed value of  $\omega_r/\omega_0$ . For a specified  $\omega_r/\omega_0$  and fixed  $\omega_0$ ,  $F$  is completely determined from equation (7.213) and equation (7.216) is replaced by

$$\frac{\omega_0}{F} = \frac{\omega_0}{1 + \frac{R_{n1}}{R_i} \left(1 + \frac{\omega_0^4}{\omega_r^4} K_4^4\right) + \frac{R_{n2}}{\omega_0 R_i} \left(K_{-1} + \frac{\omega_0^4}{\omega_r^4} K_3^3\right)} \quad (7.218)$$

As before,  $\omega_0/F$  passes through a maximum with respect to  $\omega_0$ . Noting that for fixed  $\omega_r/\omega_0$ ,  $\omega_0^2 R_i$  is independent of  $\omega_0$ , the maximum occurs for\*

$$R_i = R_{n1} \left(1 + \frac{\omega_0^4}{\omega_r^4} K_4^4\right) \quad (7.219)$$

- alternatively at low frequencies  $\omega_0$ , the resistance  $R_i$  given by equation (7.215) becomes large. A maximum  $R_i$  will be set by difficulties in winding the sense coil. For a coil of  $R_i = 5 \text{ K}\Omega$ , 50 SWG wire must be used. For a specified  $R_i$  and fixed  $\omega_0$ ,  $F$  is completely determined from equation

---

\* Since  $\omega_r^2 = \omega_{LR}/R_i C_i$  and  $\omega_{LR}$ ,  $C_i$  and  $\omega_r/\omega_0$  are fixed, then specifying  $R_i$  specifies also  $\omega_0$ .

---



(7.213), and equation (7.216) is, as before, replaced by equation (7.218).

Again  $\omega_0/F$  passes through a maximum with respect to  $\omega_0$  now occurring for

$$\omega_r = \omega_0 \cdot \frac{3R_{n1}K_4^4 + 2 \frac{R_{n2}}{\omega_0} K_3^3}{R_i + R_{n1} + 2 \frac{R_{n2}}{\omega_0} K_{-1}} \quad \frac{1}{4} \quad (7.220)$$

Thus in all cases, as stated in Section 7.21, an optimum repetition frequency exists purely on the basis of the maximum  $\frac{S}{N}$  ratio.

#### The Optimum Conditions for White Noise Only and the Effect of Specifying $\omega_r/\omega_0$

In the case  $R_{n2} \equiv 0$ , where  $\frac{1}{F}$  noise may be neglected, equation (7.216) simplifies to

$$\frac{\omega_0}{F} = \frac{\omega_0}{1 + 2 \frac{C_i R_{ni} K_4^2}{\omega_{LR}} \omega_0^2} \quad (7.221)$$

$\omega_0/F$  passes through a maximum with respect to  $\omega_0$  given by

$$\left(\frac{\omega_0}{F}\right)_{\max} = \frac{1}{2} \left(\frac{\omega_{LR}}{2C_i R_{nl} K_4}\right)^{\frac{1}{2}} = \frac{1}{2} \omega_n \quad (7.222)$$

occurring for

$$\omega_0^2 = \frac{\omega_{LR}}{2C_i R_{nl} K_4} = \omega_n^2$$

where  $\omega_n$  is a characteristic frequency depending on the coil shape (but independent of the number of turns), on the noise resistance  $R_{nl}$  and on the constant  $K_4$  describing the shape of the transfer function.

Writing

$$\frac{\frac{\omega_0}{F}}{\left(\frac{\omega_0}{F}\right)_{\max}} = 2 \cdot \frac{\frac{\omega_0}{\omega_n}}{1 + \left(\frac{\omega_0}{\omega_n}\right)^2} \quad (7.223)$$

then a single universal curve of  $(\omega_0/F)/(\omega_0/F)_{\max}$  can be plotted against the normalized frequency  $\omega_0/\omega_n$  as shown in Fig. 7.25.

Substituting  $R_i = \omega_{LR}/C_i \omega_r^2$ , equation (7.218) giving the optimum  $\omega_0/F$  for fixed  $\omega_0/\omega_r$ , reduces to

$$\frac{\omega_0}{F} = \frac{\omega_0}{1 + \frac{C_i R_{nl}}{\omega_{LR}} \left(\frac{\omega_r}{\omega_0}\right)^2 \left(1 + \frac{\omega_0^4}{\omega_r^4} K_4\right) \cdot \omega_0^2} \quad (7.224)$$

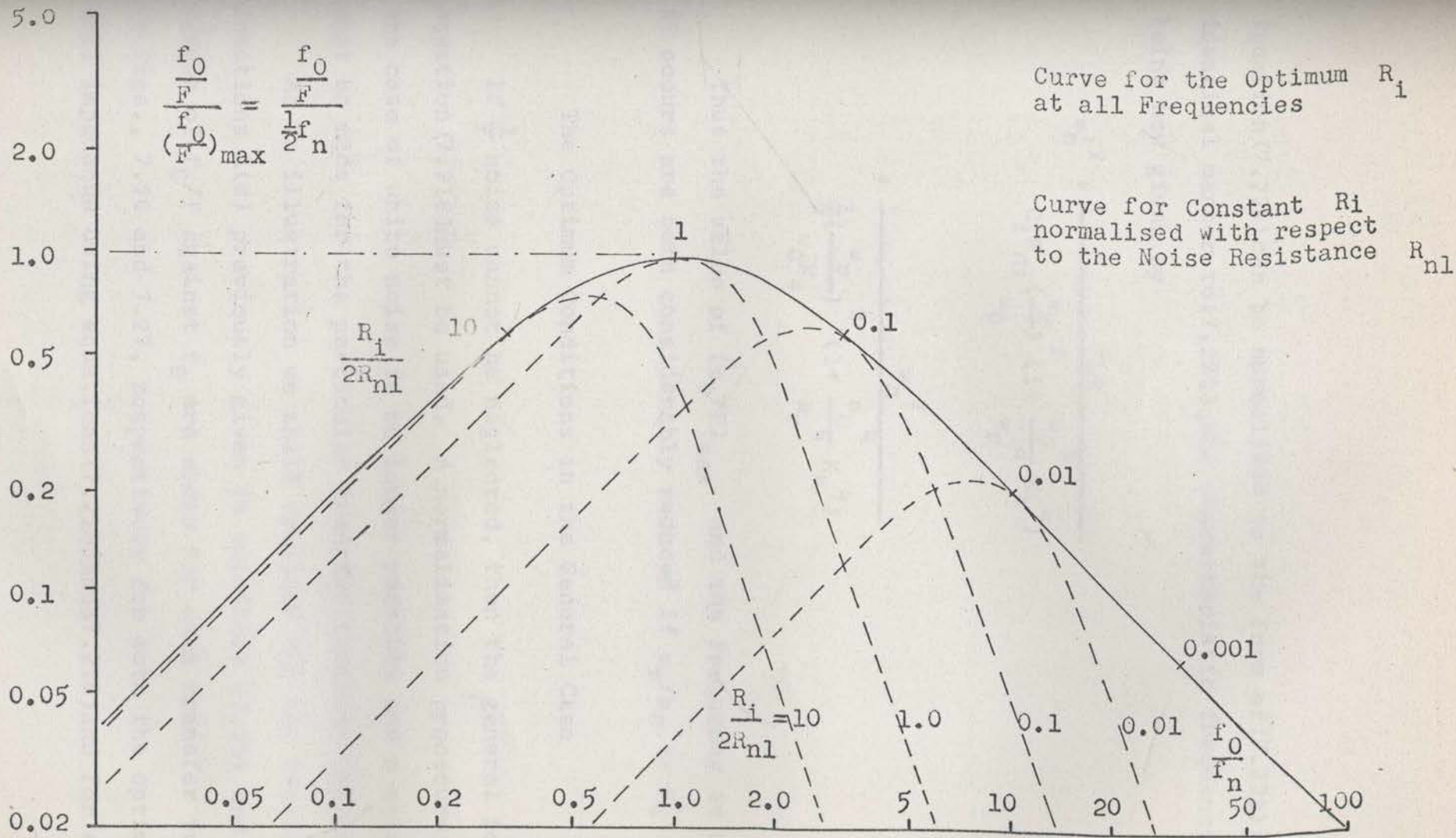


Fig. 7.25 Universal Curves of  $\left(\frac{f_0}{F}\right) / \left(\frac{f_0}{F}\right)_{\max}$  against the Normalized Frequency  $f_0/f_n$  for a Valve Amplifier in the Case of White Noise only.

Equation (7.224) can be normalized to the form of (7.223) in an identical manner to (7.221), the characteristic frequency  $\omega'_n$  being now given by

$$\begin{aligned} \omega'_n{}^2 &= \frac{\omega_{LR}}{C_i R_{ni} \left(\frac{\omega_r}{\omega_0}\right)^2 \left(1 + \frac{\omega_0^4}{\omega_r^4} K_4^4\right)} \\ &= \frac{\omega_n^2}{\frac{1}{2} \left(\frac{\omega_r}{\omega_0 K_4}\right)^2 \left(1 + \frac{\omega_0^4}{\omega_r^4} K_4^4\right)} \end{aligned} \quad (7.225)$$

Thus the value of  $(\omega_0/F)_{\max}$  and the frequency at which it occurs are both considerably reduced if  $\omega_r/\omega_0 \gg K_4$ .

#### The Optimum Conditions in the General Case

If  $\frac{1}{F}$  noise cannot be neglected, then the general form of equation (7.216) must be used. A normalization procedure as in the case of white noise is no longer possible and a calculation must be made for the particular transfer function considered.

As an illustration we shall consider the two transfer functions  $A(s)$  previously given in equations (7.29) and (7.210). Curves of  $f_0/F$  against  $f_0$  are shown for each transfer function in Figs., 7.26 and 7.27, respectively for both the optimum coil impedance using equations (7.215) and (7.216) and for a

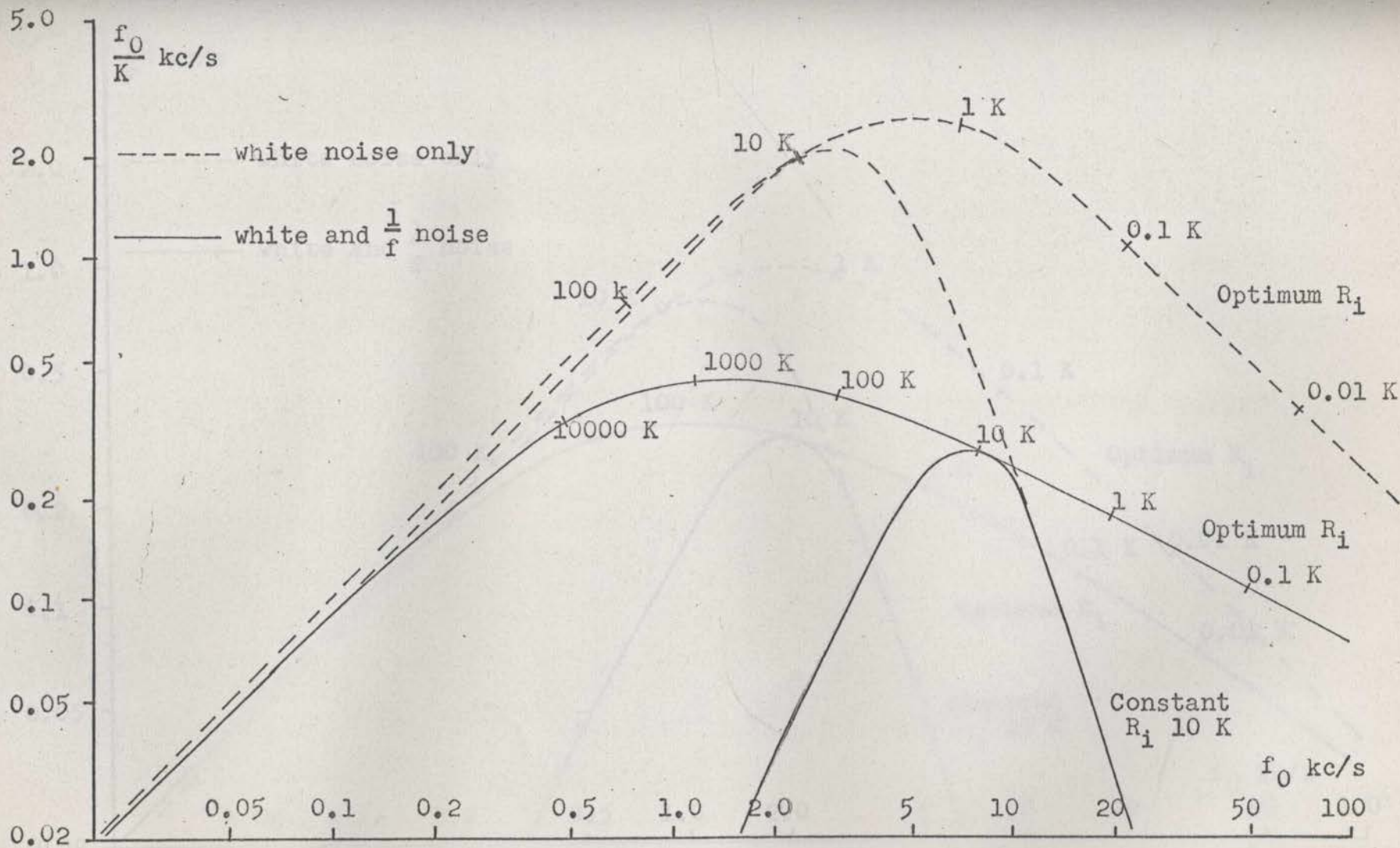


Fig. 7.26  $f_0/F$  Against Repetition Frequency  $f_0$  for a Valve Amplifier and the Transfer Characteristic of Equation 7.29 (without Synchronous DC Restoration)

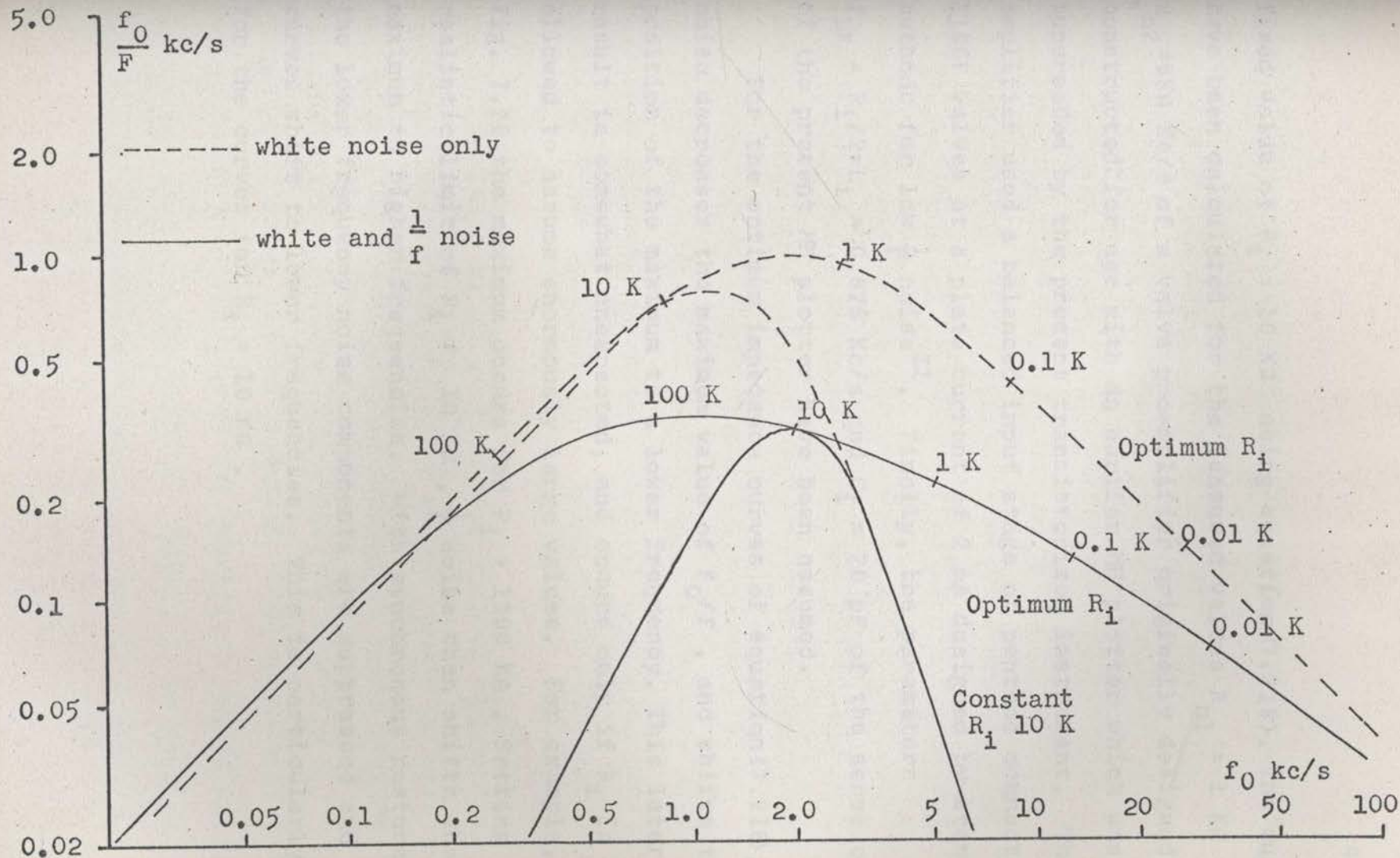


Fig. 7.27  $f_0/F$  Against Repetition Frequency  $f_0$  for a Valve Amplifier and the Transfer Characteristic of Equation 7.210 (without Synchronous DC Restoration)

fixed value of  $R_i = 10 \text{ K}\Omega$  using equation (7.218). The curves have been calculated for the measured values  $R_{n1} = 1 \text{ K}\Omega$  and  $R_{n2} = 6 \text{ K}\Omega$  Kc/s of a valve preamplifier originally designed and constructed for use with an earlier MH plotter which was superseded by the present transistorized instrument. The amplifier used a balanced input stage of pentode connected E180F valves at a plate current of 2 mA designed by standard methods for low  $\frac{1}{F}$  noise<sup>Z1</sup>. Finally, the parameters  $f_{LR} = R_i/2\pi L_i = 0.825 \text{ Kc/s}$  and  $C_i = 20 \text{ pF}$  of the sense coil of the present MH plotter have been assumed.

For the optimum impedance curves of equation (7.216),  $\frac{1}{F}$  noise decreases the maximum value of  $f_0/F$ , and shifts the position of the maximum to a lower frequency. This later result is somewhat unexpected, and occurs only if  $R_i$  is allowed to assume enormously large values. For example, in Fig. 7.26 the maximum occurs for  $R_i > 1000 \text{ K}\Omega$ . Setting a realistic limit of  $R_i \neq 10 \text{ K}\Omega$ ,  $\frac{1}{F}$  noise then shifts the maximum to higher frequencies. With synchronous restoration, the lower frequency noise components are suppressed and the curves shift to lower frequencies. This is particularly so for the curves for  $R_i = 10 \text{ K}\Omega$ .

## 7.24 A Comparison Between Transistor and Valve Preamplifiers

Fig. 7.24 and Figs. 7.26 and 7.27 allow a ready comparison to be made between the use of transistor and valve preamplifiers. It is felt that the two preamplifiers considered here are representative of the noise performance readily obtained, though in the case of the valve preamplifier lower  $\frac{1}{F}$  noise is possible. A number of different valves have been investigated during the present work, and it has been found that the  $\frac{1}{F}$  noise resistance  $R_{n2}$  of the E180F stage is of the same order as obtained for 12AX7 or 12AT7 triode stages, but that the white noise resistance  $R_{n1}$  is lower. The above values of  $R_{n2}$  agree with similar results reported by Brophy<sup>B1</sup> for 12AX7 triodes, but are an order of magnitude greater than obtained by the same author<sup>B2</sup> using a modified triode connected 6CB6.

Limiting  $R_i$  to 10 K $\Omega$ , then without synchronous restoration, the transistor amplifier is two orders of magnitude better at 1 Kc/s and improves further at lower frequencies. With synchronous restoration, where the higher  $\frac{1}{F}$  noise of the valve amplifier is not so important, then comparable results are obtained at 1 Kc/s, with the transistor amplifier again the better at lower frequencies. However, the greatest advantages of the transistor amplifier are of a practical nature



and result simply from the lower impedance level of the transistor circuit (that is the lower optimum source impedance  $R_i < 1 \text{ K}\Omega$  required). The lower impedance automatically locates the coil self-resonant frequency  $f_r$  well above  $f_0$ . While, as discussed, it is possible to compensate these poles, it is far more convenient if this can be avoided while still obtaining the optimum  $\frac{S}{N}$  ratio. If for a valve amplifier a ratio  $f_r/f_0 > K_4$  is required, equations (7.218) or (7.224) apply and the signal to noise ratio decreases as  $f_0/f_r$ . The valve amplifier then compares even less favourably with the transistor amplifier. Further, and most important, a low impedance greatly simplifies the manufacture of the sense coil. High impedances require small wire gauges which are almost impossible to wind without breakage. Finally, it may be mentioned that a transistor amplifier is in any case simpler to construct and avoids the hum problems (accentuated by the integration characteristic used) and the DC heater supply necessary in a valve amplifier.

The noise output is a minimum while causing only a small fractional error from the ideal integrated signal. For white noise, the noise performance of  $h(s)$  can be described, as in Section 7.1, by the effective noise bandwidth  $\Delta$ , normalized in terms of the repetition frequency  $\omega_0$ .

## 7.3 THE CHOICE OF THE TRANSFER FUNCTION $A(s)$

### 7.31 Introduction

The choice of the transfer characteristic  $A(s)$  of the sense channel is a compromise between requirements of accurate integration and minimum noise. An ideal integrator has the transfer function

$$A(s) = \frac{\omega_0}{s} \quad (7.31)$$

where for convenience, since only the form of the transfer function is to be considered, we have normalized  $A(s)$  to unity at the repetition frequency  $\omega_0$ .

Since  $A(s) \rightarrow \infty$  as  $s \rightarrow 0$ , such a characteristic is both physically unrealizable and undesirable in practice as low frequency noise and DC drift will be greatly accentuated. Since, however, only a repetitive signal is to be integrated, it is possible to modify  $A(s)$  at frequencies below the repetitive frequency  $\omega_0$  so that the noise output is a minimum while causing only a small fractional error  $\epsilon$  from the ideal integrated signal. For white noise, the noise performance of  $A(s)$  can be described, as in Section 7.1, by the effective noise bandwidth  $\beta$ , normalized in terms of the repetition frequency  $\omega_0$

$$\beta = \frac{\int_0^{\infty} |A(j\omega)|^2 d\left(\frac{\omega}{\omega_0}\right)}{|A(j\omega_0)|^2} \quad (7.32)$$

The present section thus deals with the approximation problem in deriving a physically realizable transfer function  $A(s)$  such that for a given error  $\beta$ , the noise bandwidth has the minimum possible value. It is shown that an error bandwidth product  $\epsilon\beta$  can be defined which is a constant characterizing the number of poles and zeros, that is the "complexity", of  $A(s)$ . Thus for any particular network, bandwidth can be traded against the integration error.

The use of more complex integration characteristics than that of a single CR section is not new. Dunstan and Somerville<sup>D1</sup> have described a feedback integration producing, in the terminology of the present section, a "two pole" transfer function and also an integrator producing a "two pole single zero phase compensated" transfer function. Oguey<sup>O1</sup> has discussed the use of these two transfer functions in MH plotters and has given the element values of certain passive networks realizing them. The value of the present section lies in the clear separation of the approximation and realization problems. In the work of Dunstan and Somerville no

distinction is made between choosing the transfer function and the design of the feedback amplifier circuits. Much unnecessary confusion is caused. The present treatment is quite general and extends readily to transfer functions of higher complexity. Since the transfer function is visualized in terms of pole positions, the effects of extraneous poles, produced in a practical amplifier system by interstage coupling capacitors and by-pass capacitors, are readily seen. The necessary adjustments to the pole positions of  $A(s)$  to preserve phase compensation are clear. In particular, Section 7.36 derives a three pole one zero phase compensated response which makes possible the design of the feedback integration of the present MH plotter discussed in Section 8.4. This integrator represents a considerable advance on previous designs<sup>01</sup>; giving reduced white and low frequency  $\frac{1}{f}$  noise and completely overcoming overload problems due to DC drift of the amplifier output.

### 7.32 The Form of $A(s)$ for Physical Realizability

The transfer function of a practical integrator may be written

$$\begin{aligned}
 A(s) &= \frac{\omega_0}{s} P(s) \\
 &= \frac{\omega_0}{s} \frac{\prod_{m=1}^M (1 - \frac{s'_m}{s})}{\prod_{n=1}^N (1 - \frac{s_n}{s})}
 \end{aligned} \tag{7.33}$$

where the poles and zeros  $s_n$  and  $s'_m$  may be real or complex.  $A(s)$  is physically realizable if  $N - M \geq 1$ .

### 7.33 The Fractional Integration Error

If  $v_0(t)$  is the integrated output signal for the ideal transfer function  $\omega_0/s$ , the actual output  $v'_0(t)$  may be obtained by expanding  $P(s)$  as a function of  $1/s$

$$P(s) = \sum_{i=0}^{\infty} \frac{P_{-i}}{s^i} \tag{7.34}$$

where

$$P_0 = 1$$

$$P_{-1} = \sum s_n - \sum s'_m$$

$$P_{-2} = \{(\sum s_n)^2 - \sum s_n s_p\} - \sum s_n \sum s'_m + \sum s'_m s'_q$$

• • • • •

and  $\sum s_n$ ,  $\sum s_n s_p$ , . . . denotes the sum of the poles and  $\sum s'_m$ ,  $\sum s'_m s'_q$ , . . . the sum of the zeros taken one, two, . . . at a time, respectively. It follows from well known properties of the Laplace transform<sup>V1</sup> that

$$v'_0(t) = v_0(t) + P_{-1}v_{-1}(t) + P_{-2}v_{-2}(t) + \dots \quad (7.35)$$

where

$$v_{-1}(t) = \int_0^t v_0(t) dt$$

$$v_{-2}(t) = \int_0^t v_{-1}(t) dt$$

. . . . .

For a periodic function  $v_0(t)$  of frequency  $s_0$ , then depending on the choice of the time origin,  $v_{-i}(t)$  as defined in equation (7.35) may contain non-periodic terms of the form  $t^{i-1}$ ,  $t^{i-2}$ , . . . . ,  $t^0$  as well as the periodic component. These are transient terms corresponding to the pole  $1/s^i$  and are to be neglected in obtaining the steady state solution. The expansion of equation (7.34) is valid provided only that  $|s_n/s| < 1$  for all  $s_n$ .

From equation (7.35) fractional error components may be defined as

$$\epsilon_{-1} = P_{-1} \frac{|v_{-1}(t)|_{\max}}{|v_0(t)|_{\max}} \quad (7.36)$$

$$\epsilon_{-2} = P_{-2} \frac{|v_{-2}(t)|_{\max}}{|v_0(t)|_{\max}}$$

• • • • •

To calculate the  $v_{-1}(t)$  it is necessary to specify the particular waveform  $v_0(t)$ . If  $v_0(t)$  is a sine wave of frequency  $\omega_0$ , then simply

$$\epsilon_{-1} = \frac{P_{-1}}{\omega_0}, \quad \epsilon_{-2} = \frac{P_{-2}}{\omega_0}, \quad \dots \quad (7.37)$$

To second order,  $\epsilon_{-1}$  and  $\epsilon_{-2}$  are just the phase and fractional amplitude errors, respectively, at the frequency  $\omega_0$ . In the measurement of MH curves,  $v_0(t)$  is often more closely approximated by a square wave. Fig. 7.31 shows the form of the error terms in this case and lists the values of the error coefficients  $\epsilon_{-i}$ . These values of  $\epsilon_{-i}$  differ from the  $\epsilon_{-i}$  of equation 7.37 only by a numerical factor near unity. For simplicity then the following analysis will be in terms of the sine wave errors of equation 7.37. This is in keeping with the conventional usage.

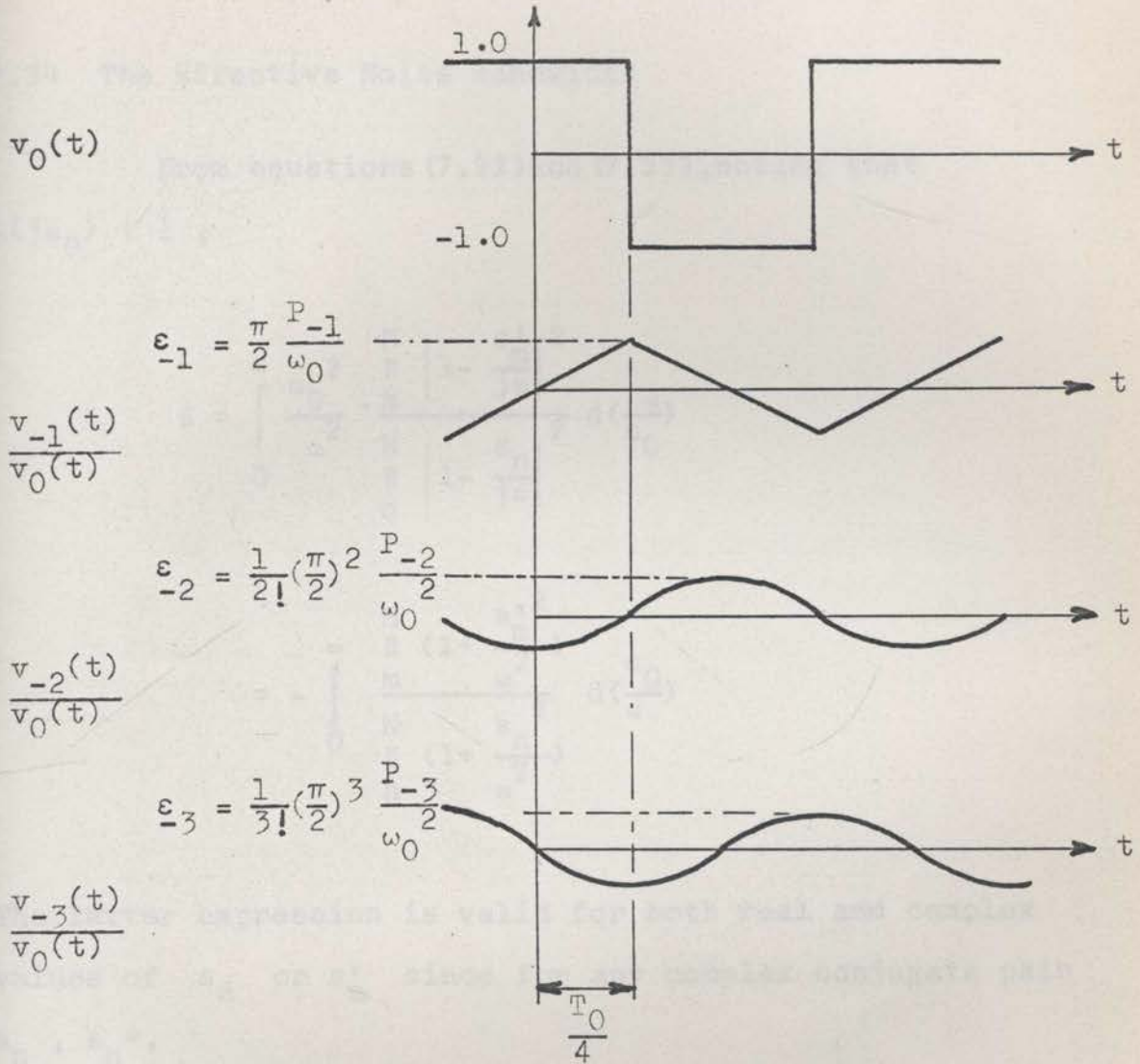


Fig. 7.31 Intergration Error Terms produced in an Ideal Square Wave Output.

Analytic expressions for the error voltages  $V_i(t)$  are, for the range  $0 < t < \frac{T_0}{4}$ , given by

$$v_0(t) = 1.0$$

$$v_{-1}(t) = t$$

$$v_{-2}(t) = \frac{t^2}{2!} - \frac{1}{2} \left(\frac{T_0}{4}\right)^2$$

$$v_{-3}(t) = \frac{t^3}{3!} - \frac{1}{2} t \left(\frac{T_0}{4}\right)^2$$



## 7.34 The Effective Noise Bandwidth

From equations (7.32) and (7.33), noting that

$$A(j\omega_0) \doteq 1,$$

$$\beta = \int_0^{\infty} \frac{\omega_0^2}{\omega^2} \cdot \frac{\prod_m \left| 1 - \frac{s'_m}{j\omega} \right|^2}{\prod_n \left| 1 - \frac{s_n}{j\omega} \right|^2} d\left(\frac{\omega}{\omega_0}\right)$$

$$= - \int_0^{\infty} \frac{\prod_m \left( 1 + \frac{s'_m}{\omega^2} \right)}{\prod_n \left( 1 + \frac{s_n}{\omega^2} \right)} d\left(\frac{\omega_0}{\omega}\right)$$

The latter expression is valid for both real and complex values of  $s_n$  or  $s'_m$  since for any complex conjugate pair  $s_n, s_n^*$ ,

$$\begin{aligned} \left| 1 - \frac{s_n}{j\omega} \right|^2 \left| 1 - \frac{s_n^*}{j\omega} \right|^2 &= \left( 1 - \frac{s_n}{j\omega} \right) \left( 1 + \frac{s_n^*}{j\omega} \right) \cdot \left( 1 - \frac{s_n^*}{j\omega} \right) \left( 1 + \frac{s_n}{j\omega} \right) \\ &= \left( 1 + \frac{s_n}{\omega^2} \right) \left( 1 + \frac{s_n^*}{\omega^2} \right) \end{aligned}$$

Since  $N > M$ , which is just the condition for physical realizability, the integrand may be expanded in partial fractions with no integral term. By elementary integration

$$\beta = -\frac{\pi}{2} \sum_{i=n}^N \frac{\omega_0}{s_i} \cdot \frac{\prod_{m=1}^M (1 - \frac{s_m'^2}{s_i^2})}{\prod_{n=1}^N (1 - \frac{s_n^2}{s_i^2})} \quad (7.38)$$

### 7.35 Uncompensated Transfer Functions

The simplest possible integrator characteristic is the one pole transfer function

$$A(s) = \frac{\omega_0}{s} \cdot \frac{1}{1 - \frac{s_1}{s}} \quad (7.39)$$

From equations (7.34), (7.37) and (7.38) the dominant error is the phase term  $\epsilon_{-1}$  and

$$\epsilon_{-1} = -\frac{s_1}{\omega_0}$$

$$\beta = -\frac{\pi}{2} \frac{\omega_0}{s_1}$$

and  $\beta \epsilon_{-1} = \frac{\pi}{2}$  (7.310)

Low frequency  $\frac{1}{F}$  noise and DC drift may be suppressed by the addition of a second pole such that

$$A(s) = \frac{\omega_0}{s} \cdot \frac{1}{\left(1 - \frac{s_1}{s}\right)\left(1 - \frac{s_2}{s}\right)} \quad (7.311)$$

$$= \frac{\omega_0}{s} \cdot \frac{1}{1 + \frac{2\xi\omega_r}{s} + \frac{\omega_r^2}{s^2}}$$

$$\rightarrow 0 \text{ as } s \rightarrow 0$$

For white noise there is no advantage over the one pole transfer function since from equations (7.34), (7.37) and (7.38)

$$\epsilon_{-1} = - \frac{\sum s_n}{\omega_0} = \frac{2\xi\omega_r}{\omega_0}$$

$$\beta = - \frac{\pi}{2} \frac{\omega_0}{\sum s_n} = \frac{\pi}{2} \frac{\omega_0}{2\xi\omega_r} \quad (7.312)$$

and  $\beta\epsilon_{-1} = \frac{\pi}{2}$

$\beta\epsilon_{-1}$  is entirely independent of the choice of the pole positions. It should be noted that the phase error  $\epsilon_{-1}$  dominates the amplitude error  $\epsilon_{-2}$  only if the pole damping factor  $\xi$  is sufficiently large that

$$\frac{2\xi\omega_r}{\omega_0} > \frac{\omega_r^2}{\omega_0^2}, \text{ that is } 2\xi > \frac{\omega_r^2}{\omega_0^2}$$

Smaller values of  $\xi$  should not be used since the  $\beta\epsilon$  product is increased.

Fig. 7.32 shows curves of  $|A(j\omega)|$  against normalized frequency  $\omega/\omega_0$  calculated for an error  $\epsilon$  (that is  $\epsilon_{-1}$ ) of 0.01. Curve A is for the one pole function of equation (7.39), and curves B, C and D for the two pole function of equation (7.311) for  $\xi = 1.0, 0.5$  and  $0.1$ , respectively. Characteristic D is not desirable in a 1000 c/s MH plotter, since the peak occurs in the 50 c/s region and a significantly increased hum interference level can result.

### 7.36 Phase Compensated Transfer Functions

The noise output is substantially decreased if the dominant phase error  $\epsilon_{-1}$  is compensated by adding a suitable pole and zero pair. The compensated equivalent of equation (7.39) is the two pole, one zero transfer function

$$A(s) = \frac{\omega_0}{s} \cdot \frac{1 - \frac{s_1}{s}}{\left(1 - \frac{s_1}{s}\right)\left(1 - \frac{s_2}{s}\right)} \quad (7.313)$$

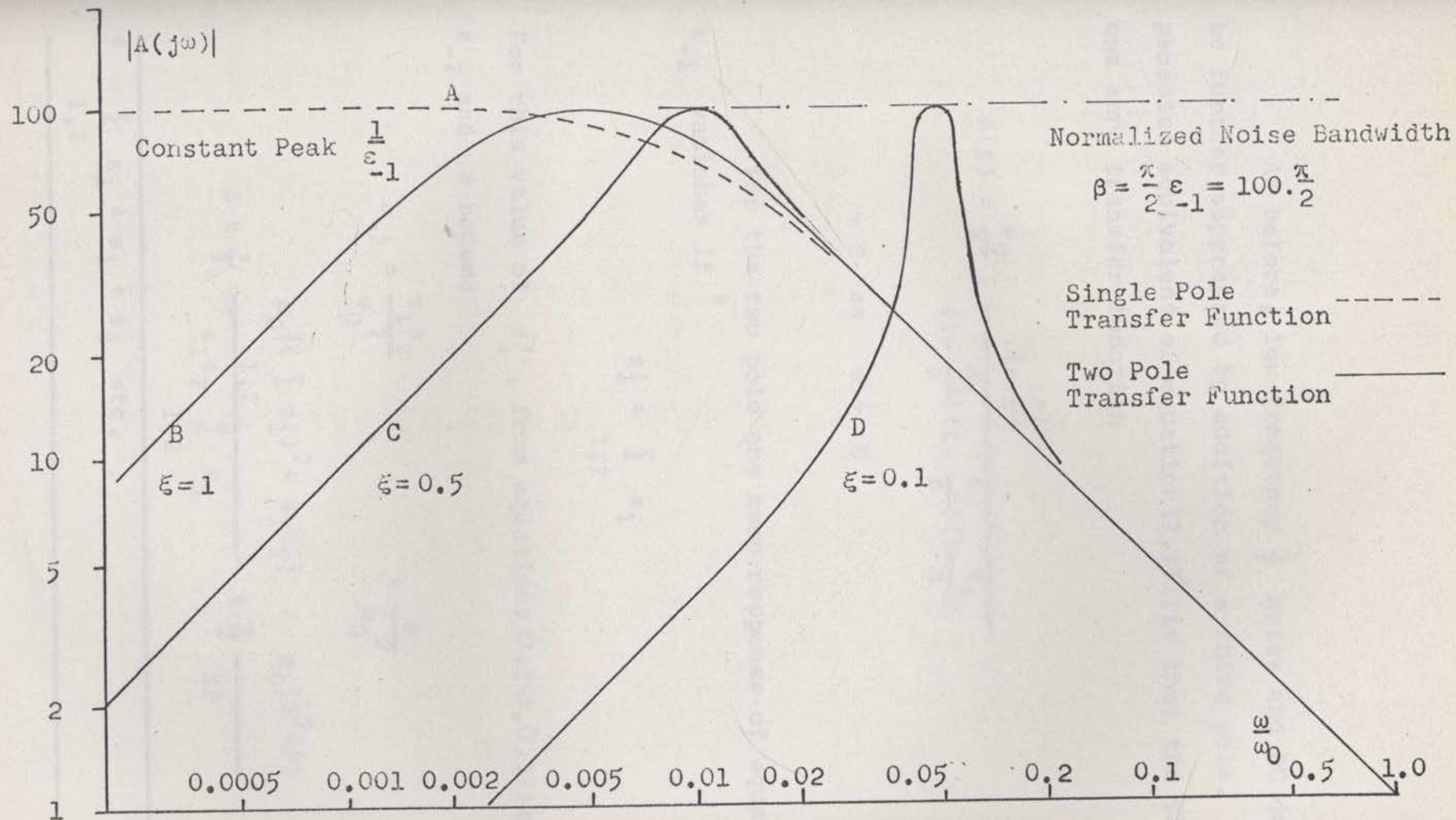


Fig. 7.32 Curves of  $A(j\omega)$  against Normalized Frequency  $\omega/\omega_0$  for the Single Pole and Two Pole Uncompensated Transfer Functions of Equations (7.39) and (7.311) respectively Calculated for an Error of  $\epsilon_{-1} = 0.01$

As before, low frequency  $\frac{1}{f}$  noise and DC drift may be further suppressed by addition of a third pole. The compensated equivalent of equation (7.311) is thus the three pole, one zero transfer function

$$A(s) = \frac{\omega_0}{s} \cdot \frac{1 - \frac{s_1'}{s}}{\left(1 - \frac{s_1}{s}\right)\left(1 - \frac{s_2}{s}\right)\left(1 - \frac{s_3}{s}\right)} \quad (7.314)$$

$$\rightarrow 0 \text{ as } s \rightarrow 0$$

For the two pole one zero response of equation (7.313),  $\epsilon_{-1}$  vanishes if \*

$$s_1' = \sum_{1,2} s_1$$

For this value of  $s_1'$ , from equations (7.34), (7.37) and (7.38),  $\epsilon_{-2}$  and  $\beta$  become

$$\epsilon_{-2} = \frac{s_1 s_2}{\omega_0^2} = \frac{P}{\omega_0^2}$$

$$\beta = \frac{\pi}{2} \frac{\omega_0 \left\{ \left( \sum_{1,2} s_1 \right)^2 + s_1 s_2 \right\}}{s_1 s_2 \sum_{1,2} s_1} = \frac{\pi}{2} \frac{\omega_0 (S^2 + P)}{SP}$$

---

\*  $\sum_{1,2} s_1 = s_1 + s_2$  etc.

---

where  $S = \sum_{1,2} s_1$  is the sum of the poles and  $P = s_1 s_2$  is the product of the poles.

To determine the optimum positions of the poles  $s_1, s_2$ , it is most convenient to consider  $\epsilon_{-2}$  and  $\beta$  as functions of the two independent variables  $S$  and  $P$ .  $S$  and  $P$  are real, and the optimization procedure is hence valid, irrespective of whether real or complex poles are considered. Minimizing  $\beta$  subject to the condition that  $\epsilon_{-1}$ , that is  $P$ , remains constant gives

$$S^2 = P, \text{ or } \xi = 0.5 \quad (7.315)$$

At the optimum pole position

$$\beta = 2.0 \frac{\pi}{2} \frac{\omega_0}{\sqrt{P}}$$

and we may define a modified error bandwidth product as

$$\beta \sqrt{\epsilon_{-2}} = 2.0 \frac{\pi}{2} \quad (7.316)$$

If the transfer function is to be realized by a passive RC network, the poles  $s_1$  and  $s_2$  must be restricted to real values. The minimum  $\beta$  then occurs when the two poles coincide so that

$$S^2 = 4P, \text{ or } \xi = 1.0 \quad (7.317)$$

and in this case

$$\beta\sqrt{\epsilon_{-2}} = 2.5 \frac{\pi}{2} \quad (7.313)$$

This is only slightly worse than the optimum value, however complex poles may be preferred if low frequency  $\frac{1}{f}$  noise and DC drift are a problem, since

$$A(s=0) = \frac{\omega_0 S}{P} = \frac{\omega_0}{\sqrt{P}} \quad \text{for } S^2 = P$$

$$= 2.0 \frac{\omega_0}{\sqrt{P}} \quad \text{for } S^2 = 4P$$

For the three pole, one zero response of equation (7.314),  $\epsilon_{-1}$  again vanishes, if

$$s_1' = \sum_{1,2,3} s_1$$

For this value of  $s_1'$ ,  $\epsilon_{-2}$  and  $\beta$  become



$$\epsilon_{-2} = \frac{\sum_{1,2,3} s_1 s_2}{\omega_0^2} = \frac{P}{\omega_0^2}$$

$$\beta = \frac{\pi}{2} \frac{\omega_0 \left\{ \left( \sum_{1,2,3} s_1 \right)^2 + \sum_{1,2,3} s_1 s_2 \right\}}{(\omega_1 + \omega_2)(\omega_2 + \omega_3)(\omega_3 + \omega_1)} = \frac{\pi}{2} \frac{\omega_0 (S^2 + P)}{SP - Q}$$

where \*

$$S = \sum_{1,2,3} s_1$$

$$P = \sum_{1,2,3} s_1 s_2$$

$$Q = s_1 s_2 s_3$$

Subject to the condition that  $\epsilon_{-2}$ , that is  $P$  remains constant,  $\beta$  is monotonically decreasing with  $Q$ , and the minimum  $\beta$  occurs for

$$Q = 0$$

$$S^2 = P$$

---

\*  $\sum_{1,2,3} s_1 s_2 = s_1 s_2 + s_2 s_3 + s_3 s_1$  etc.

---

These are just the necessary conditions to remove the third pole and to reduce the transfer function to the optimum two pole one zero configuration previously discussed. Since the third pole must be retained for the suppression of  $\frac{1}{f}$  noise and DC drift,  $\beta$  must instead be minimized subject to a specified value  $s_3$  of the third real pole .

Writing

$$S = s_3 + S'$$

$$P = s_3 S' + P'$$

$$Q = s_3 P'$$

where

$$S' = \sum_{1,2} s_1$$

$$P' = s_1 s_2$$

then

$$\beta = \frac{\pi}{2} \omega_0 \frac{(s_3 + S')^2 + P}{(s_3 + S')P - s_3 P'} \quad (7.319)$$

By the method of Lagrangian multipliers, then minimizing  $\beta$  with respect to  $S'$  and  $P'$  subject to the condition

$$P = s_3 S' + P' = \text{a constant} \quad (7.320)$$

gives the further conditions

$$\frac{(s_3 + S')^2 P - P^2 - 2s_3(s_3 + S')P'}{\{(s_3 + S')P - s_3 P'\}^2} + \lambda s_3 = 0 \quad (7.321)$$

$$\frac{s_3(s_3 + S')^2 + s_3 P}{\{(s_3 + S')P - s_3 P'\}^2} + \lambda = 0 \quad (7.322)$$

Eliminating first  $\lambda$ , then  $P'$  from equations (7.320), (7.321) and (7.322), gives finally

$$S'^2 = P + s_3^2 \quad (7.323)$$

Equations (7.320) and (7.323) may be readily solved to give the optimum position of the poles  $s_1$  and  $s_2$  in terms of  $P$  and  $s_3$ . The value of  $\beta$  at the optimum point follows from equation (7.319) as

$$\beta = 2 \frac{\pi}{2} \omega_0 \cdot \frac{s_3 + \sqrt{s_3^2 + P}}{s_3^2 + P}$$

giving

$$\beta \sqrt{\epsilon_{-2}} = 2 \frac{\pi}{2} \cdot \frac{\{s_3 + \sqrt{s_3^2 + P}\} \sqrt{P}}{s_3^2 + P} \quad (7.324)$$

The above results are most conveniently shown as a root locus plot on the normalized frequency plane  $s/\sqrt{P}$ , values of  $\beta \sqrt{\epsilon_{-2}}$  being marked at corresponding points along the loci. Such a

plot is given in Fig. 7.33.  $\beta\sqrt{\epsilon_{-2}}$  ranges from

$$\beta\sqrt{\epsilon_{-2}} = 2.00 \frac{\pi}{2} \text{ for } \frac{s_3}{\sqrt{P}} = 0 \quad (7.325)$$

to

$$\beta\sqrt{\epsilon_{-2}} = \frac{3\sqrt{3}}{2} \frac{\pi}{2} = 2.60 \frac{\pi}{2} \text{ for } \frac{s_1}{\sqrt{P}} = \frac{s_2}{\sqrt{P}} = \frac{s_3}{\sqrt{P}} = -\frac{1}{\sqrt{3}} = -0.577 \quad (7.326)$$

Clearly equation (7.326) gives the desired pole positions since this provides the largest attenuation of the lower frequency  $\frac{1}{f}$  noise.

Fig. 7.34 shows curves of  $|A(j\omega)|$  against normalized frequency  $\omega/\omega_0$  calculated for an error of  $\epsilon$  (that is  $\epsilon_{-2}$ ) of 0.01. Curves E and F are for the two pole one zero transfer function of equation (7.313) calculated for pole damping factors of  $\xi = 1.0$  and 0.5, respectively. Curve G is for the three pole one zero transfer function of equation 7.314 calculated for three coincident poles at  $s/\sqrt{P} = -0.577$  as given in equation (7.326). For comparison curves A, B and D of Fig. 7.32 are shown dotted and a list of numerical values of  $\beta$  is given. The improved noise performance possible with the phase compensated characteristics, curves E, F and G, of the present section is apparent. When, as occurs in practise,  $\frac{1}{f}$  noise is also present, curve G is very much superior. Coupled with the active network realization of Section 7.38, character-

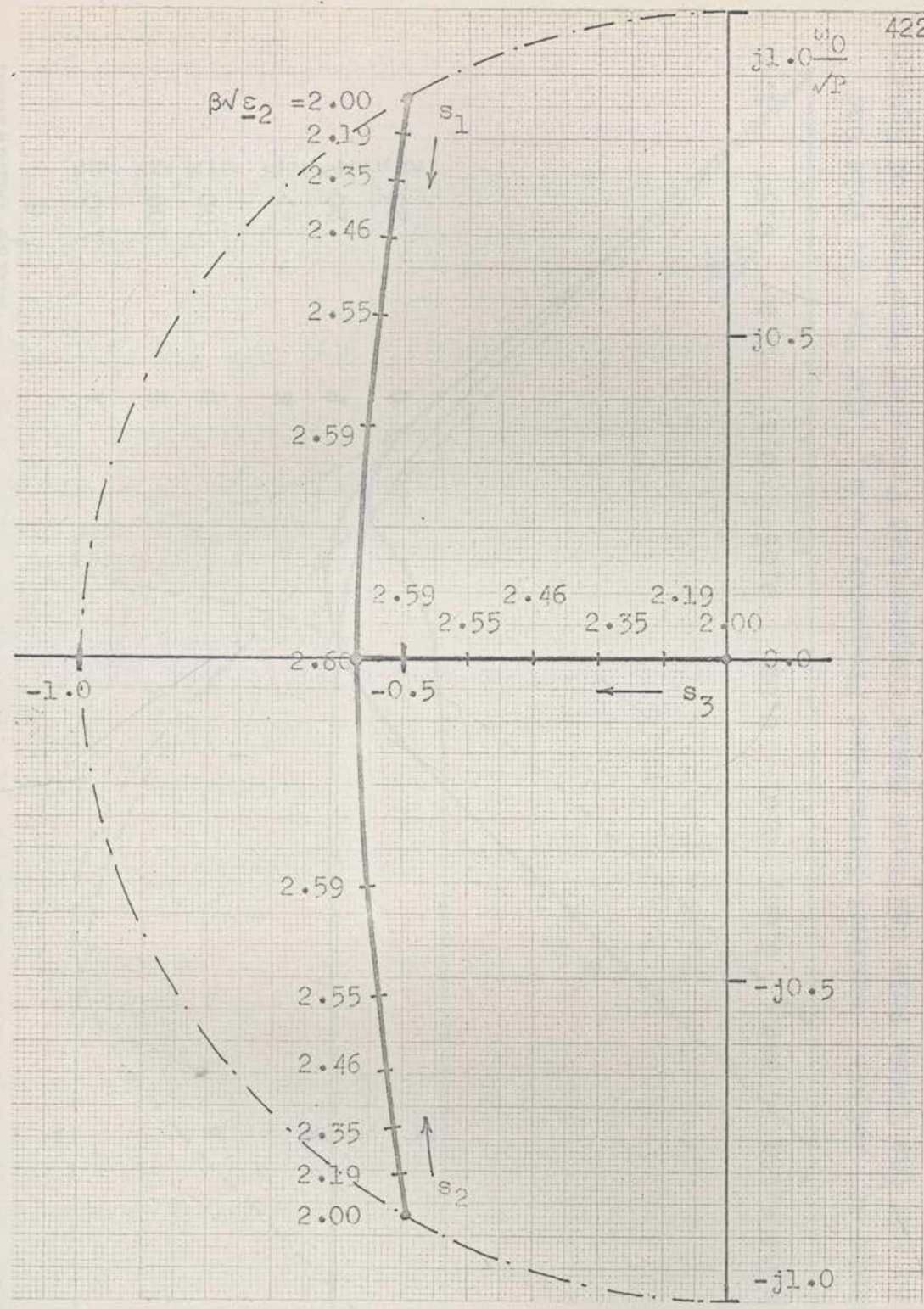


Fig. 7.33 Root Locus Plot of the Pole Positions of the Three Pole Single Zero Phase Compensated Transfer Function of Equation 7.314. The Frequency Plane is Normalized in Terms of the Frequency  $\sqrt{P}$  where the Value of  $\sqrt{P}$  is given from the required Fractional Error as  $\sqrt{P} = \omega_0 \sqrt{\epsilon_2}$

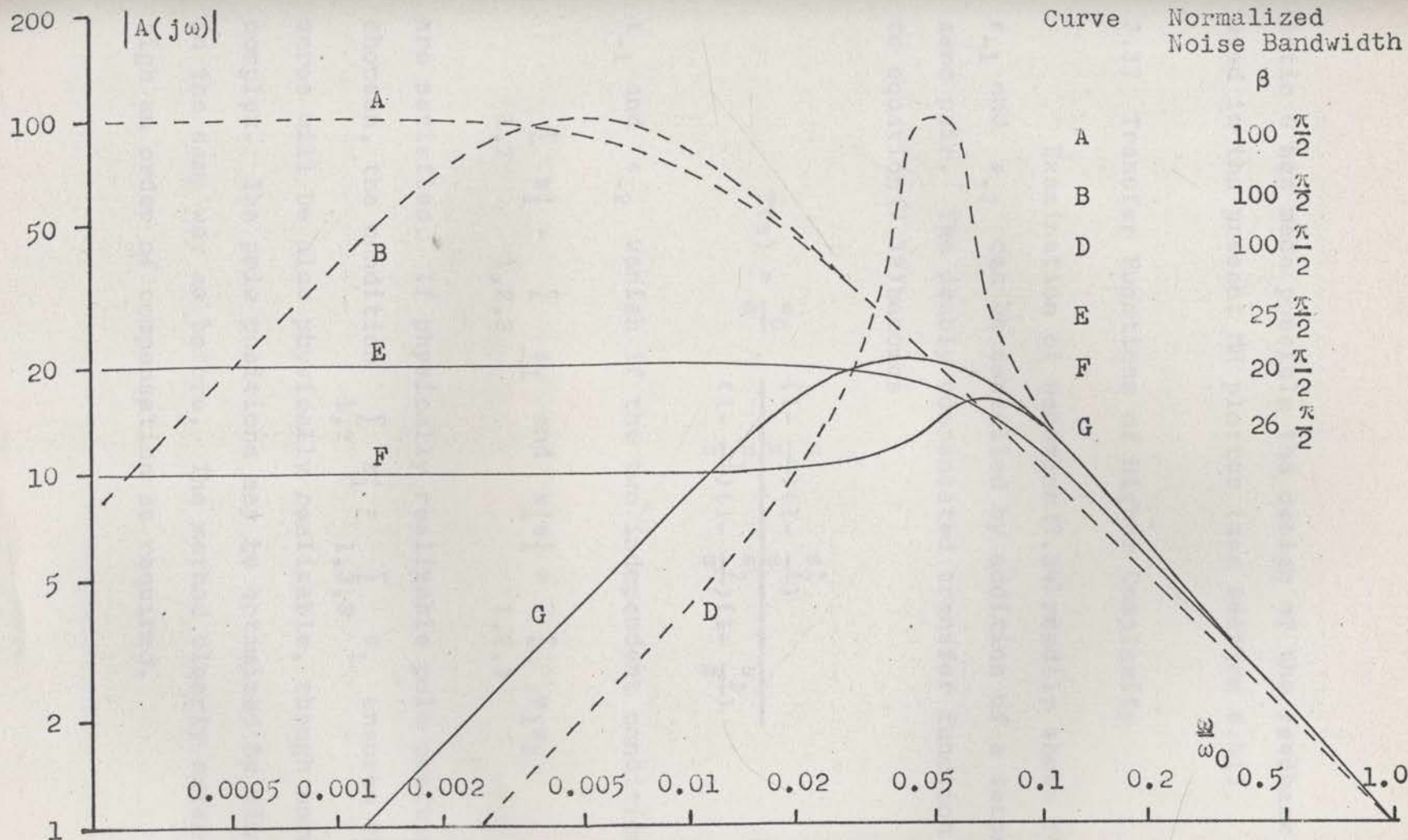


Fig. 7.34 Curves of  $|A(j\omega)|$  against Normalized Frequency  $\omega/\omega_0$  for the Two Pole One Zero and the Three Pole One Zero Phase Compensated Transfer Functions of Equations (7.313) and (7.314) Respectively Calculated for an Error  $\epsilon_{-2}$  of 0.01

istic  $G$  has made possible the design of the feedback integrator used in the present MH plotter (see Section 8.41).

### 7.37 Transfer Functions of Higher Complexity

Examination of equation (7.34) readily shows that both  $\epsilon_{-1}$  and  $\epsilon_{-2}$  can be cancelled by addition of a second pole-zero pair. The doubly compensated transfer function equivalent to equation (7.39) becomes

$$T(s) = \frac{\omega_0}{s} \cdot \frac{(1 - \frac{s'_1}{s})(1 - \frac{s'_2}{s})}{(1 - \frac{s_1}{s})(1 - \frac{s_2}{s})(1 - \frac{s_3}{s})}$$

$\epsilon_{-1}$  and  $\epsilon_{-2}$  vanish if the two independent conditions

$$\sum_{1,2} s'_i = \sum_{1,2,3} s_i \quad \text{and} \quad s'_1 s'_2 = \sum_{1,2,3} s_1 s_2$$

are satisfied. If physically realizable pole positions are chosen, the condition  $\sum_{1,2} s'_i = \sum_{1,2,3} s_i$  ensures that the zeros will be also physically realizable, though normally complex. The pole positions may be optimized by minimizing  $\beta$  in the same way as before. The method clearly extends to as high an order of compensation as required.

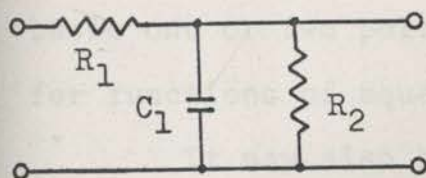
The use of such higher order transfer functions in practice requires some comment. Ideally, a circuit should provide independent adjustments of both the sum and product of the poles. Such an adjustment is given by the resistor  $R_2$  and the combination  $R_3, R_4, C_2$ , respectively, of the active network realization shown in Fig. 7.36. It is not difficult to see the extension of the present feedback integrator of Section 8.4 by the addition of a second pole zero pair (complex zeros) to give a four pole two zero compensated response. Both  $\epsilon_{-1}$  and  $\epsilon_{-2}$  can be readily adjusted to zero using a test differentiator as in Section 8.5, the latter either from the square wave response or by measuring the gain at two different frequencies.

### 7.38 Realization of the Transfer Function

#### Passive Realizations

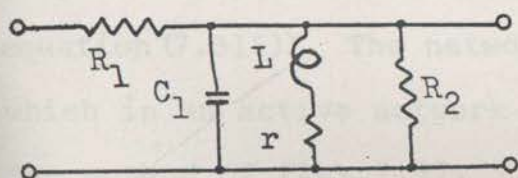
Passive network realizations of the basic single pole response of equation (7.39) and the basic two pole response of equation (7.311) are given in Fig. 7.35. Other realizations are possible, for example the dual of the networks given. If both poles are real, the two pole response can be produced by cascaded C-R sections and the use of an inductor avoided. Fig. 7.35 also shows a network giving a phase compensating





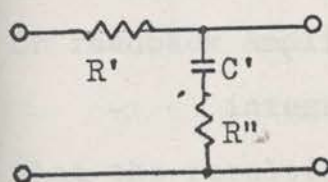
$$A(s) = \frac{1}{sC_1R_1} \cdot \frac{1}{1 + \frac{1}{s}\left(\frac{1}{C_1R_1} + \frac{1}{C_2R_2}\right)} \quad (7.327)$$

Single Pole Response



$$A(s) = \frac{1}{sC_1R_1} \cdot \frac{1 + \frac{r}{sL}}{1 + \frac{1}{s}\left(\frac{1}{C_1R_1} + \frac{1}{C_1R_2} + \frac{r}{L}\right) + \frac{1}{s^2}\left(\frac{1}{C_1L} + \frac{r}{C_1LR_1} + \frac{r}{C_1LR_2}\right)} \quad (7.328)$$

Two Pole Response



$$A(s) = \frac{R''}{R' + R''} \cdot \frac{1 + \frac{1}{sC'R''}}{1 + \frac{1}{sC'(R' + R'')}} \quad (7.329)$$

Phase Compensating Pole Zero Pair

Fig. 7.35 Passive Integration Networks

pole-zero pair, which may be connected in cascade\* with the basic one or two pole networks to give the compensated transfer functions of equations (7.313) and (7.314).

It may also be noted that Oguey<sup>01</sup> gives a simple three element network (and dual) which may be shown to combine the basic one pole response and the compensating pole-zero pair. The necessary price for this simplicity is that the poles are complex with a predetermined damping of  $\xi = 0.5$  (see equation (7.315)). The network involves, however, an induction which in an active network realization cannot be avoided by the method of Fig. 7.37.

#### Active Network Realizations

The advantages of integration by means of operational or feedback amplifiers are well known

- integration and amplification are combined such that the resulting output is independent of the amplifier gain

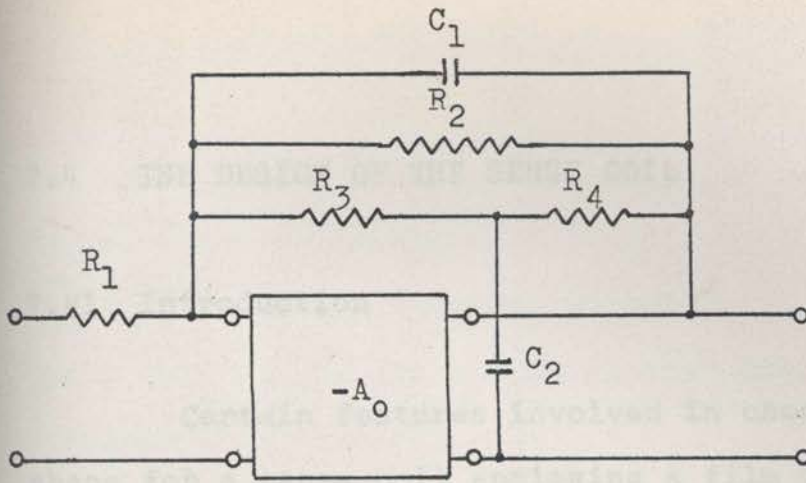
---

\* It is assumed that each section is isolated so that one does not load the other. If this is not so the formulae given in Fig. 7.35 for the pole positions will be modified.

---

- amplifier noise is not added to the signal after a large attenuation as occurs with a passive integrating network. If, as in the present application, the input waveform is a train of pulses of peak amplitude many times their mean value, then high amplification cannot be used before integration. In particular with transistor circuits, where the dynamic range is limited, the use of an operational amplifier becomes essential.

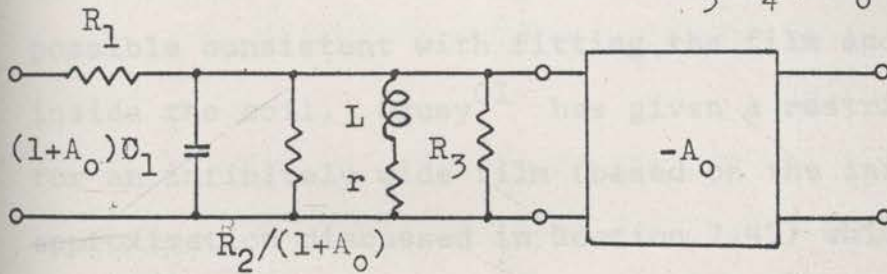
Suitable circuits realizing the basic one pole and the basic two pole transfer functions of equations (7.39) and (7.311) are shown in Figs. 7.36 and 7.37, together with expressions for the resulting transfer functions  $A(s)$ . The expressions for  $A(s)$  have been derived by a mesh analysis of the circuit and contain no approximations. It has been assumed only that the amplifier gain  $A_0$  is independent of frequency and that the amplifier has infinite input impedance and zero output impedance. Figs. 7.36 and 7.37 also give equivalent circuit representations in which the effects of feedback are represented by shunt impedances across the amplifier input. These circuits should be compared with the passive networks of Fig. 7.35 and the expressions for  $A(s)$  may alternatively be derived from the equivalent circuit element values and equations (7.327) and (7.328) of Fig. 7.35.



Equivalent circuit

$$L = C_2 R_3 R_4 / (A_0 - R_4 / R_3)$$

$$r = (R_3 + R_4) / (A_0 - R_4 / R_3)$$



$$T(s) = \frac{A_0}{s(1+A_0)C_1 R_1} \frac{1 + \frac{1}{sC_2 R_3 || R_4}}{D} \tag{7.311}$$

where

$$D = 1 + \frac{1}{s} \left[ \frac{1}{(1+A_0)C_1} \left( \frac{1}{R_1} + \frac{1}{R_3} \right) + \frac{1}{C_1 R_2} + \frac{1}{C_2 R_3 || R_4} \right]$$

$$+ \frac{1}{s^2 (1+A_0)C_1} \left[ \frac{1+A_0}{C_2 R_3 R_4} + \left( \frac{1}{R_1} + \frac{1+A_0}{R_2} \right) \frac{1}{C_2 R_3 || R_4} \right]$$

Fig. 7.37 An Active Integrating Network realizing the Basic Two Pole Transfer Function of equation (7.311). The circuit and the basic one pole transfer function of equation (7.39) follow by putting  $R_3 = R_4 = \infty$

## 7.4 THE DESIGN OF THE SENSE COIL

### 7.41 Introduction

Certain features involved in choosing the optimum shape for a sense coil enclosing a film sample may be intuitively established<sup>B3</sup>. The coil should closely surround the film and the mean length of turn should be as small as possible consistent with fitting the film and film holder inside the coil. Oguey<sup>01</sup> has given a restricted analysis for an infinitely wide film (based on the infinite pole line approximation discussed in Section 7.47) which, combined with experimental measurements of the field configuration for a finite film, provides a satisfactory description of the "enclosing type" sense coil (ETSC). This approach is inadequate for the type of sense coil used in the present instrument, where the coil is located on one side of the film only. The following analysis has thus been developed to cover this case and considers critically the effects of finite sample size and coil end effects.

Section 7.42 discusses relative advantages of different types of sense coils. Sections 7.43, 7.44, 7.45 and 7.46 develop the general analysis referred to above. Section 7.47 discusses the infinite pole line approximation

and the use of a practical rectangular coil cross section rather than the irregular optimum section given by Oguey. Finally, Section 7.43 gives experimental measurements of the sense coil of the present MH plotter confirming the theory presented.

#### 7.42 Basic Types of Sensing Coils and General Considerations

Two different types of sensing coils may be distinguished

- the sense coil may enclose the film as in Fig. 7.44
- the sense coil may be on one side only of the film as in Fig. 7.45.

The advantages and disadvantages of each type are briefly:

- The sensitivity of the "enclosing" type sense coil (ETSC) is higher than that of the single sided sense coil (SSSC). For the ETSC the fraction  $\bar{\psi}$  of the film flux effectively linking the coil is typically of the order of 0.65 while for the SSSC,  $\bar{\psi}$  is typically 0.13. A more detailed analysis of sensitivity is given in Section 7.43.
- The calibration, that is the constancy of  $\bar{\psi}$ , of the SSSC is more dependent on the relative dimensions and

position of the film sample and sense coil than that of the ETSC.\* For the present instrument using a SSSC, experimental measurements of the variation of  $\bar{\psi}$  with spacing  $d$  between the film and coil are shown in Fig. 7.41. Nevertheless, the film may be positioned with sufficient accuracy so that the repeatability in measurement of the saturation flux for any given film is better than 1 per cent.\*\*

- The SSSC leaves one side of the film completely open. This may be necessary for measurements during evaporation, or for simultaneous investigation of the film surface by, for example, the Kerr magneto-optic effect. These features have been discussed with reference to single turn coils by Oguey<sup>01</sup>.

- The SSSC very much simplifies the mechanical design of the film holder. The film holder of the present instrument is shown in Fig. 6.32. The angular accuracy in positioning the film is higher than can be expected for a holder rotated inside an ETSC by a gear<sup>B3</sup> or cord drive<sup>02</sup>. The design of other fixtures, for example, a bending jig for magneto-elastic measurements, is likewise simplified.

---

\* A long flat ETSC having an almost constant calibration factor has been discussed by Oguey<sup>01</sup>.

\*\* Over a series of 20 independent measurements, the film being removed from and replaced in the MH plotter between each measurement.

---

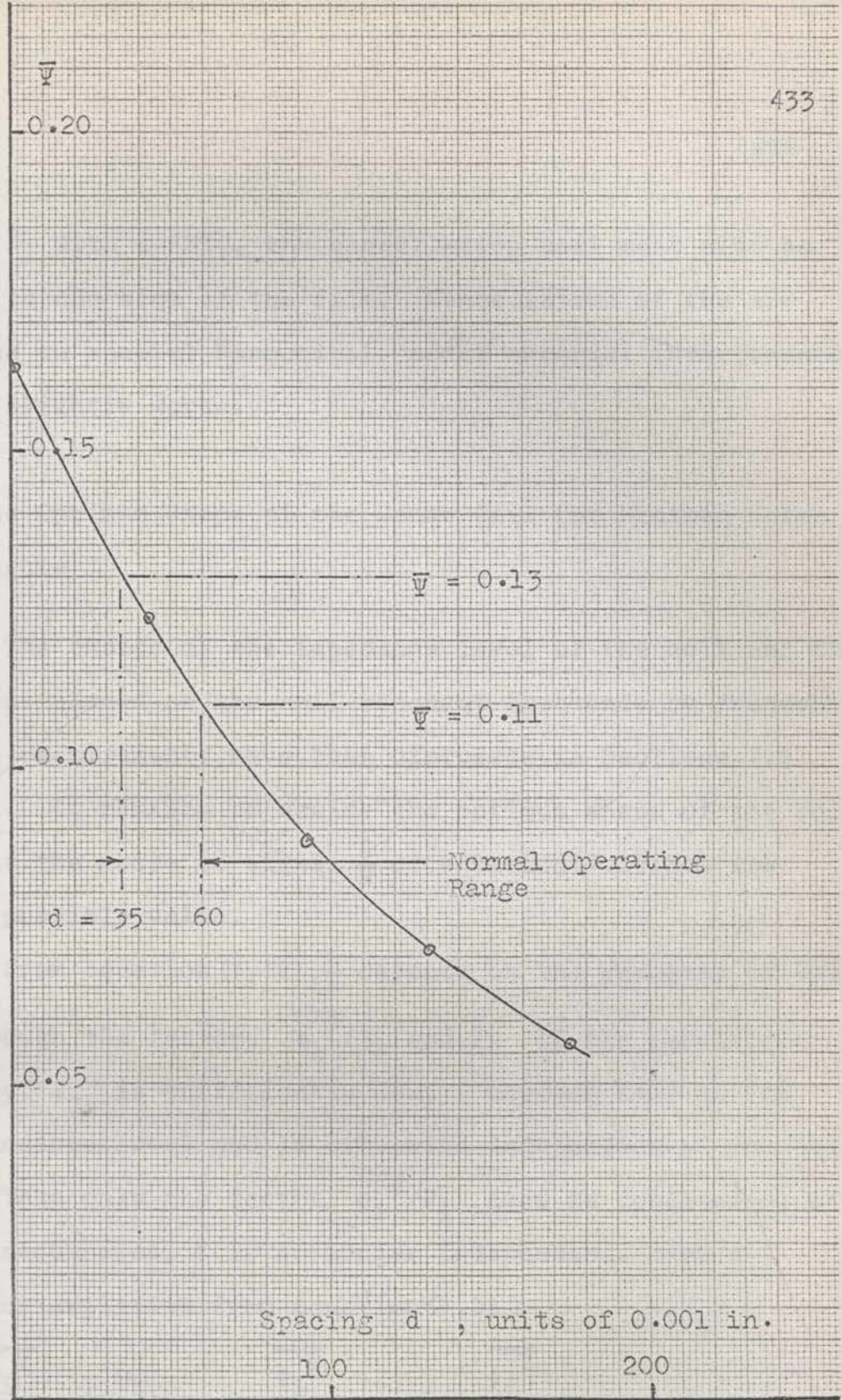


Fig. 7.41 The Variation of the Fractional Flux Linkage with the Distance  $d$  between the 1 cm Diameter Film Sample and the Sense Coil.



- With a SSSC, the cancellation coil must also be located to one side of the film. Cancellation of the air flux (due to spacial harmonics) and of external interference will be slightly worse.

### 7.43 The Optimum Shape of the Sense Coil for Minimum Noise Figure

The choice of the impedance level of the coil and the conditions placed on the coil resonant frequency by frequency response requirements have been discussed in Sections 7.2 and 6.72. It remains to decide the optimum shape of the coil such that the noise to signal  $\frac{S}{N}$  of equation (7.12) has the maximum possible value.

From equation (7.12),  $\frac{S}{N}$  depends on the geometry of the coil through the factors  $\overline{\phi_i^2}/R_i$  and  $F$ . If the repetition frequency  $\omega_0$  is sufficiently low,  $F$  depends only on the coil impedance level and is otherwise independent of the coil shape. Thus only the factor  $\overline{\phi_i^2}/R_i$  need be considered. At higher frequencies,  $F$  is no longer independent. For a transistor amplifier from equation (7.25)

$$\frac{\overline{\phi_i^2}}{R_i} \cdot \frac{1}{2} \left( \frac{\omega_0}{F} \right)_{\max} \propto \frac{\overline{\phi_i^2}}{R_i} \cdot \omega_{LR} \propto \frac{\overline{\phi_i^2}}{L_i}$$

The present instrument is intended to operate at variable frequencies  $\omega_0$ . Since the highest sensitivity, that is the maximum  $\frac{S}{N}$  ratio, is needed at the lower frequencies, we shall consider here only the low frequency case and determine the optimum coil shape by maximizing  $\overline{\phi_i^2}/R_i$ .

Now

$$\frac{\overline{\phi_i^2}}{R_i} = \frac{n^2 \overline{\phi^2} \overline{\psi^2}}{\frac{\rho_W l_W n^2}{\lambda_W A_W}} \quad (7.41)$$

where

$\overline{\phi^2}$  is the mean squared saturation flux of the film,  
 $\overline{\psi}$  is the fraction of the film flux effective in linking the sense coil, averaged over all turns in the coil cross section,

$n$  is the total number of turns of the coil,

$l_W$  is the mean length of a turn,

$A_W$  is the coil cross sectional area,

$\rho_W$  is the resistivity of the winding material (copper),

$\lambda_W$  is the space factor of the winding.

If  $l_W$  and  $A_W$  are normalized in terms of a suitable characteristic unit of length  $2L$  (for example  $2L$  may be the length of a side of a square film or the diameter of a circular film), then

$$\frac{\overline{\phi_i^2}}{R_i} = \frac{2L\lambda_W \overline{\phi^2}}{\rho_W} \cdot \frac{\alpha \overline{\psi^2}}{\nu} \quad (7.42)$$

where

$\nu = l_W/2L$  is the normalized mean length of turn, and

$\alpha = A_W/(2L)^2$  is the normalized cross sectional area.

$\alpha \overline{\psi^2}/\nu$  is a dimensionless parameter depending only on the geometry of the sense coil and film samples. The optimum shape of the coil follows by maximizing  $\alpha \overline{\psi^2}/\nu$ . The formal maximization of  $\alpha \overline{\psi^2}/\nu$  in the general case is prohibitively difficult. However, there exist two special cases for which an analytic solution may be obtained,

- the idealized rectangular coil discussed in Section 7.44 below, and
- the infinitely long sense coil discussed in Section 7.47.

We shall now consider these two cases.

#### 7.44 An Analytic Solution for a Uniformly Magnetized Rectangular Film Sheet and an Idealized "Rectangular" Shaped Sense Coil

Fig. 7.42 shows a sense coil enclosing a rectangular magnetic thin film of dimensions  $2X_p$  by  $2Z_p$ , uniformly

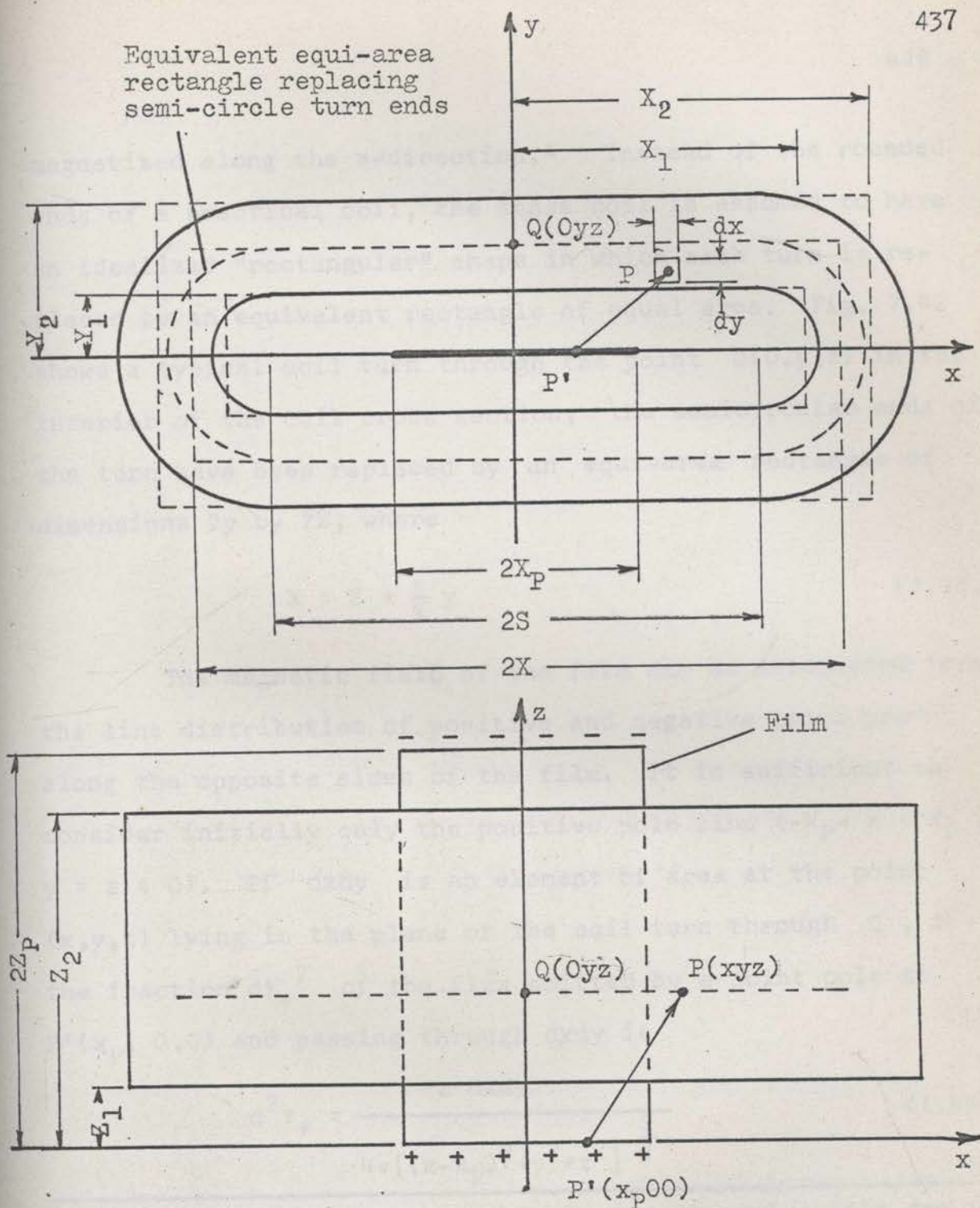


Fig. 7.42 Diagram for the Calculation of the Fractional Flux Linkage  $\bar{\psi}$  for an Idealized Rectangular Shaped Sense Coil.

magnetized along the z-direction.\* Instead of the rounded ends of a practical coil, the sense coil is assumed to have an idealized "rectangular" shape in which each turn is replaced by an equivalent rectangle of equal area. Fig. 7.42 shows a typical coil turn through the point  $Q(0,y,z)$  in the interior of the coil cross section; the semicircular ends of the turn have been replaced by an equi-area rectangle of dimensions  $2y$  by  $2X$ , where

$$X = S + \frac{\pi}{4} y \quad (7.43)$$

The magnetic field of the film can be calculated from the line distribution of positive and negative poles produced along the opposite sides of the film. It is sufficient to consider initially only the positive pole line ( $-X_P < x < X_P$ ,  $y = z = 0$ ). If  $dx dy$  is an element of area at the point  $(x,y,z)$  lying in the plane of the coil turn through  $Q$ , then the fraction  $d^2\psi_+$  of the flux emitted by a point pole at  $P'(x_P, 0, 0)$  and passing through  $dx dy$  is

$$d^2\psi_+ = \frac{z \, dx dy}{4\pi \{(x-x_P)^2 + y^2 + z^2\}^{\frac{3}{2}}} \quad (7.44)$$

---

\* For a circular film, an equivalent rectangular film can be defined having the same total flux and the same dipole and quadripole moments.

---

$d^2\psi_+$  for a uniform line distribution of poles ( $-X_P < x < X_P$ ,  $y = z = 0$ ) follows by averaging equation (7.44) as

$$d^2\psi_+ = \frac{1}{2X_P} \int_{X_P}^{-X_P} \frac{z \, dx dy dx_P}{4\pi((x-x_P)^2 + y^2 + z^2)^{\frac{3}{2}}}$$

$$= \frac{z}{4\pi(y^2 + z^2)} \cdot \frac{\frac{x_P - x}{((x-x_P)^2 + y^2 + z^2)^{\frac{1}{2}}}}{2X_P} \Bigg|_{x_P = X_P}^{x_P = -X_P} \quad (7.45)$$

The fraction  $\psi_+$  of the flux linking the upper half of the coil turn through  $Q$  is found by integrating equation (7.45) with respect to  $x$  and  $y$  over the region ( $-X < x < X$ ,  $0 < y$ ).

For  $X', X'' \neq 0$ ,\*

$$\psi_+ = \frac{X}{2X_P} f(x, y, z) \Bigg|_{x = X'}^{x = X''} \quad (7.46)$$

\* For the case  $X' = 0$

$$\frac{X'}{2X_P} \cdot f(X', y, z) = \frac{z}{2X_P} \cdot \frac{1}{2\pi} \tanh^{-1} \frac{y}{(y^2 + z^2)^{\frac{1}{2}}}$$

where equation (7.47) may be considered as constant, being replaced by a mean value of, refer to Fig. 7.44,

$$f(x,y,z) = \frac{1}{2\pi} \left( \tan^{-1} \frac{xy}{z(x^2+y^2+z^2)^{\frac{1}{2}}} + \frac{z}{x} \tanh^{-1} \frac{y}{(x^2+y^2+z^2)^{\frac{1}{2}}} \right)$$

and

$$X'' = |X + X_p|$$

$$X' = |X - X_p|$$

Equation (7.46) may be used to determine the linkage for single loop sense coils of the type used with an input transformer<sup>01</sup>. To calculate the fractional flux linkage  $\bar{\psi}_+$  for a coil of finite dimensions, then  $\psi_+$  must be averaged over the cross sectional area  $A$  of the coil

$$\bar{\psi}_+ = \frac{\int \int_A \psi_+ dydz}{\int \int_A dydz} \quad (7.47)$$

In a practical coil, the dimension  $X$  occurring in equations (7.46) and (7.47) will depend upon the particular coil turn, that is, as in equation (7.43), upon  $y$ . Now a sense coil of satisfactory design is necessarily elongated as in Fig. 7.44 so that the flux per unit area in the region of the coil ends may be taken as approximately constant. This assumption is the basis of replacing each turn of a coil with curved ends by an equivalent equi-area rectangle. It further follows that

$X$  in equation (7.47) may be considered as constant, being replaced by a mean value of, referring to Fig. 7.42,

$$\bar{X} = \frac{\int_{Y_1}^{Y_2} X(y)y \, dy}{\int_{Y_1}^{Y_2} y \, dy}$$

that is

$$\bar{X} - S = \frac{4}{3} \cdot \frac{Y_2^2 + Y_2 Y_1 + Y_1^2}{(Y_2 + Y_1)^2} \cdot \left( \frac{X_1 + X_2}{2} - S \right) \quad (7.48)$$

This assumption becomes increasingly accurate as the range of  $X$ ,  $X_1 < X < X_2$ , decreases. Thus with this approximation

$$\bar{\psi}_+ = \frac{x}{2X_P} \cdot \frac{\int \int_A f(x,y,z) \, dy \, dz}{\int \int_A dy \, dz} \quad \left. \begin{array}{l} x = X'' \\ \\ x = X' \end{array} \right\} \quad (7.49)$$

where now

$$X'' = |\bar{X} + X_P|$$

and

$$X' = |\bar{X} - X_P|$$

For  $X'$ ,  $X'' \neq 0$ , this equation may be normalized in terms of



$\zeta = y/x$  ,  $\eta = z/x$  such that

$$\bar{\psi}_+ = \frac{x}{2X_P} \cdot \frac{\int_A \int f(\zeta, \eta) d\zeta d\eta}{\int_A \int d\zeta d\eta} \left| \begin{array}{l} x = X'' \\ x = X' \end{array} \right. \quad (7.410)$$

where

$$f(x, y, z) = f(\zeta, \eta)$$

$$= \frac{1}{2\pi} \left( \tan^{-1} \frac{\zeta}{\eta(1+\zeta^2+\eta^2)^{\frac{1}{2}}} + \eta \tanh^{-1} \frac{\zeta}{(1+\zeta^2+\eta^2)^{\frac{1}{2}}} \right)$$

If the coil has a rectangular cross section ( $Y_1 < y < Y_2$  ;  $Z_1 < z < Z_2$ ), then equation (7.410) is readily integrable to give

$$\bar{\psi}_+(Y_1, Y_2; Z_1, Z_2) = \frac{yz \bar{\psi}_+(y, z)}{(Y_2 - Y_1)(Z_2 - Z_1)} \left| \begin{array}{l} y = Y_2, z = Z_2 \\ y = Y_1, z = Z_1 \end{array} \right. \quad (7.411)$$

where

$$\bar{\psi}_+(y, z) = \frac{x}{2X_P} F(\zeta, \eta) \left| \begin{array}{l} x = X'' \\ x = X' \end{array} \right.$$

and

$$F(\zeta, \eta) =$$

$$\zeta \eta \tan \frac{\zeta}{\zeta(1+\zeta^2+\eta^2)}$$

$$+ \frac{1}{2}(\eta^2 - \zeta^2) \tanh^{-1} \frac{1}{(1+\zeta^2+\eta^2)^{\frac{1}{2}}}$$

$$+ \frac{1}{2}\zeta(\eta^2 - 1) \tanh^{-1} \frac{\zeta}{(1+\zeta^2+\eta^2)^{\frac{1}{2}}}$$

$$+ \frac{1}{6}(1+\zeta^2-2\eta^2)(1+\zeta^2+\eta^2)^{\frac{1}{2}}$$

 $\zeta, \eta$ 
 $\zeta = 0, \eta = 0$ 

---


$$2\pi\zeta\eta$$

$\bar{\psi}_+$  as calculated above is the fractional flux linkage with the positive pole line only. The total fractional flux linkage  $\bar{\psi}_t$  is given by adding the flux  $\bar{\psi}_-$  of the negative pole line and the flux 0.5 passing through the upper half section  $y > 0$  of the magnetic film itself

$$\bar{\psi}_t = 0.5 - \bar{\psi}_+ - \bar{\psi}_- \quad (7.412)$$

For a coil symmetrically placed with respect to the film,  $\bar{\psi}_+ = \bar{\psi}_-$  and it follows from equations 7.411 and 7.412 that

for  $X' , X'' \neq 0$ ,\*

$$\bar{\psi}_t(Y_1, Y_2; Z_1, Z_2) = \frac{YZ\bar{\psi}_t(y, z)}{(Y_2 - Y_1)(Z_2 - Z_1)} \left| \begin{array}{l} y = Y_2, z = Z_2 \\ y = Y_1, z = Z_1 \end{array} \right. \quad (7.413)$$

where

$$\bar{\psi}_t(y, z) = \frac{x}{2X_p} F_t(\zeta, \eta) \left| \begin{array}{l} x = X'' \\ x = X' \end{array} \right.$$

and

$$F_t(\zeta, \eta) = 0.5 - 2F(\zeta, \eta) =$$

\* For the case  $X' = 0$

$$\frac{X''}{2X_p} F_t(\zeta = \frac{y}{X''}, \eta = \frac{z}{X''}) =$$

$$\frac{-\frac{1}{2} yz^2 \tanh^{-1} \frac{y}{(y^2+z^2)^{\frac{1}{2}}} \left| \begin{array}{l} y, z \\ y=0, z=0 \end{array} \right.}{2X_p \cdot \pi yz}$$

$$\begin{array}{l}
 \zeta \eta \tan^{-1} \frac{\eta(1+\zeta^2+\eta^2)^{\frac{1}{2}}}{\zeta} \\
 - \frac{1}{2}(\eta^2-\zeta^2) \tanh^{-1} \frac{1}{(1+\zeta^2+\eta^2)^{\frac{1}{2}}} \\
 - \frac{1}{2} \zeta(\eta^2-1) \tanh^{-1} \frac{\zeta}{(1+\zeta^2+\eta^2)^{\frac{1}{2}}} \\
 - \frac{1}{6}(1+\zeta^2-2\eta^2)(1+\zeta^2+\eta^2)^{\frac{1}{2}}
 \end{array}
 \left| \begin{array}{l}
 \zeta, \eta \\
 \zeta=0, \eta=0
 \end{array} \right.$$

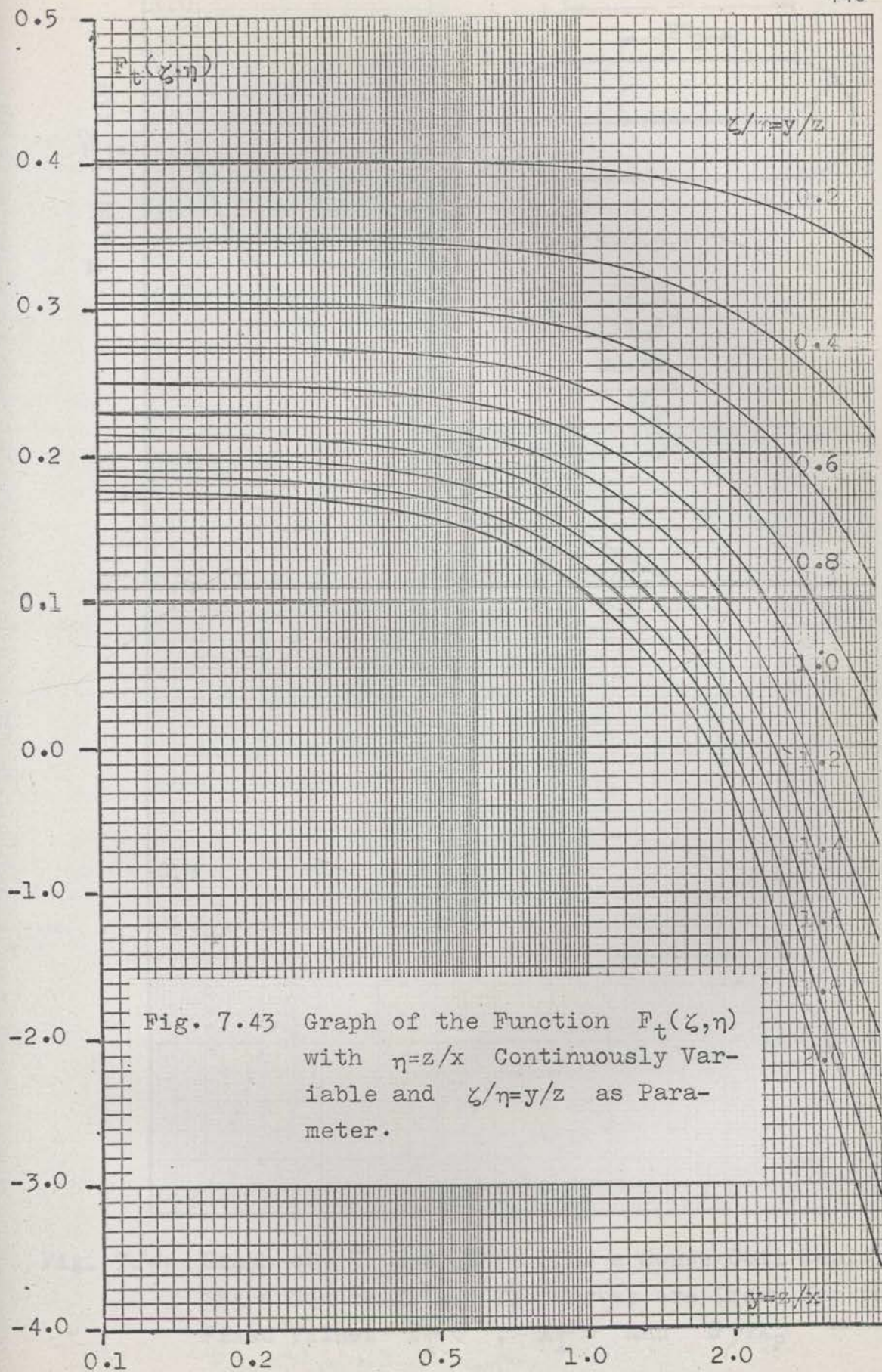

---


$$\pi \zeta \eta$$

$\bar{\psi}_t$  may be readily calculated from equation 7.413 using the values of  $F_t(\zeta, \eta)$  given in Fig. 7.43, where  $F_t(\zeta, \eta)$  is plotted as a function of  $\eta$  with  $\zeta/\eta$  as parameter.

#### 7.45 The Optimum Shape For a Sense Coil Enclosing the Film

The value of  $\bar{\psi}$  for a coil enclosing the film sample may be found by adding the values of  $\bar{\psi}$  calculated separately, from equation 7.413, for the upper and lower sides of the coil (see Fig. 7.44). Fig. 7.44 shows curves of  $\bar{\psi}$  and  $\alpha \bar{\psi}^2/v$  for such a sense coil enclosing a square film sample.  $\alpha \bar{\psi}^2/v$  is normalized in terms of the dimensions  $2X_p = 2Z_p$  of the film. Curves are given for variable values of  $Y_2$  and  $S$ , with fixed values  $Y_1 = 0$ ,  $Z_1 = 0$ , and  $Z_2 = 2Z_p$ . From



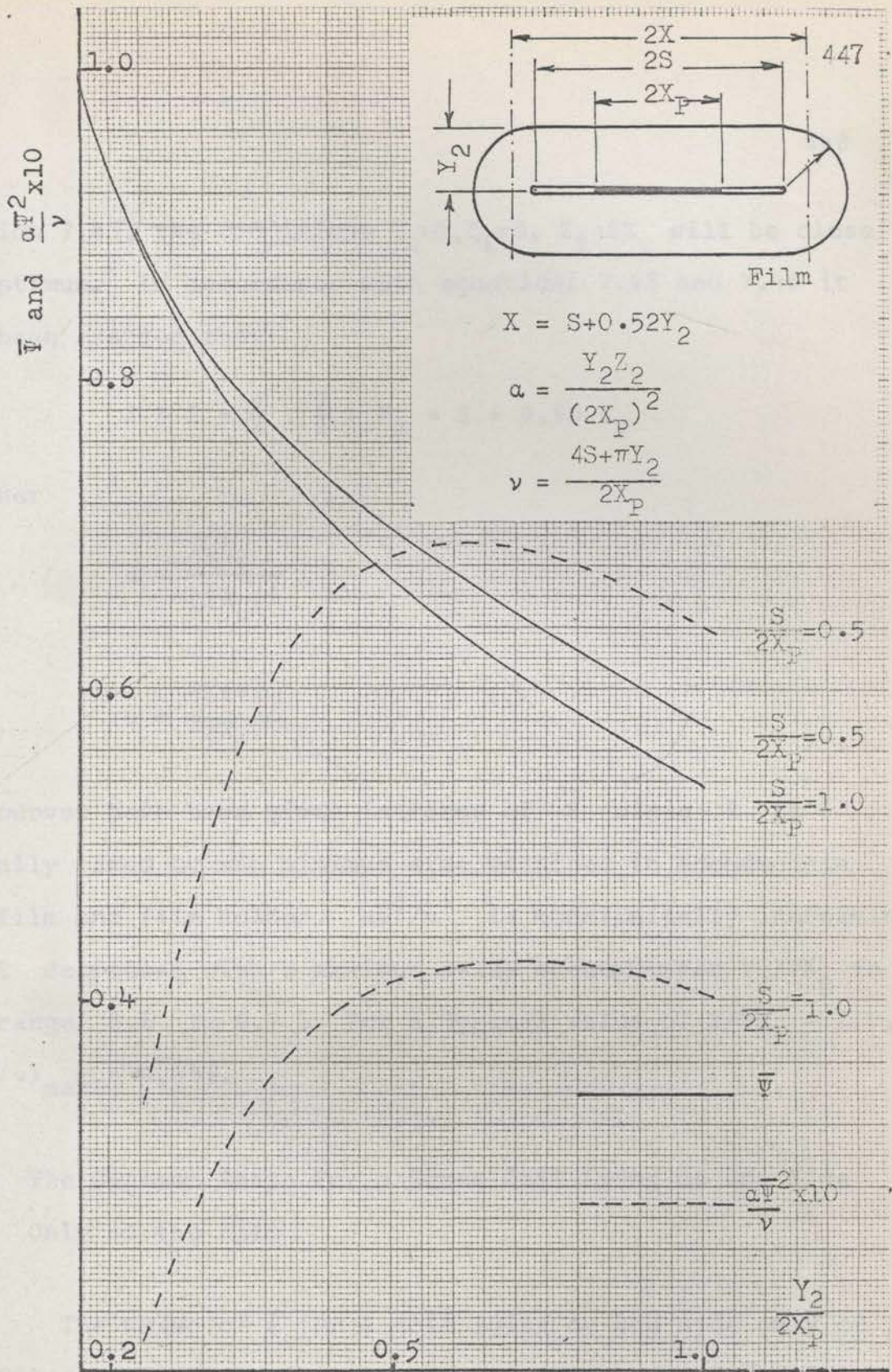


Fig. 7.44 Graph of  $\bar{v}$  and  $\frac{a\bar{v}^2}{\nu}$  for a Sense Coil Enclosing a Square Film. The Curves are Drawn for the Fixed Values  $Y_1=0$ ,  $X_1=0$  and  $S/2X_p$

Section 7.47, the conditions  $Y_1=0, Z_1=0, Z_2=2Z_p$  will be close to optimum. In accordance with equations 7.43 and 7.48 it has been assumed that

$$X = S + \frac{\pi}{4} \cdot \frac{2}{3} \cdot Y_2 = S + 0.52 Y_2$$

Further

$$\alpha = \frac{Y_2 Z_2}{(2X_p)^2}$$

$$v = \frac{4S + \pi y_2}{2X_p}$$

The curves have been given in terms of  $S$  since  $S$  is normally fixed by the minimum size required to accommodate the film and film holder.  $\alpha \bar{\psi}^2 / v$  is monotonically increasing as  $S$  decreases with a maximum value occurring for  $Y_2 / 2X_p$  in the range 0.5 to 0.7. For a typical value of  $S / 2X_p = 1.0$ ,  $(\alpha \bar{\psi}^2 / v)_{\max} = 0.042$ .

#### 7.46 The Optimum Shape For a Sense Coil Lying on One Side Only of the Film

The value of  $\bar{\psi}$  for a coil lying on one side only of the film may be found by subtracting the values of  $\bar{\psi}$  calculated separately, from equation 7.413, for the upper and

lower sides of the coil (see Fig. 7.45). Fig. 7.45 shows curves of  $\bar{\psi}$  and  $\alpha\bar{\psi}^2/\nu$  for such a sense coil and a square film sample.  $\alpha\bar{\psi}^2/\nu$  is normalized in terms of the dimensions  $2X_p = 2Z_p$  of the film. Curves are given by variable values of the dimensions  $Y, W$  and  $X$ , defined in Fig. 7.45, with fixed values of  $Z_1 = 0, Z_2 = 2Z_p$ . Again, from Section 7.47 the conditions  $Z_1 = 0, Z_2 = 2Z_p$  will be close to optimum. In accordance with equations (7.43) and (7.48) it has been assumed that

$$X = S + 0.52 \frac{\frac{3}{4}W^2 + \frac{3}{2}WY + Y^2}{W+Y} \quad (7.414)$$

Further,

$$\alpha = \frac{YZ_2}{(2X_p)^2}$$

$$\nu = \frac{4S + \pi(W+Y)}{(2X_p)^2}$$

A maximum value of  $\alpha\bar{\psi}^2/\nu$  of  $(\alpha\bar{\psi}^2/\nu)_{\max} \div 0.0024$  occurs near  $Y_2/2X_p \div 0.6, W/2X_p \div 0.6, X/2X_p \div 1.0$ .

#### 7.47 The Special Case of a Rectangular Film Sheet and an Infinitely Long Sense Coil

If the length  $2X$  of the sense coil is very much greater than its lateral dimensions  $Y_1, Y_2; Z_1, Z_2$  and the dimensions  $2X_p, 2Z_p$  of the film sample, then the total flux linking the upper half of a single coil turns through the point





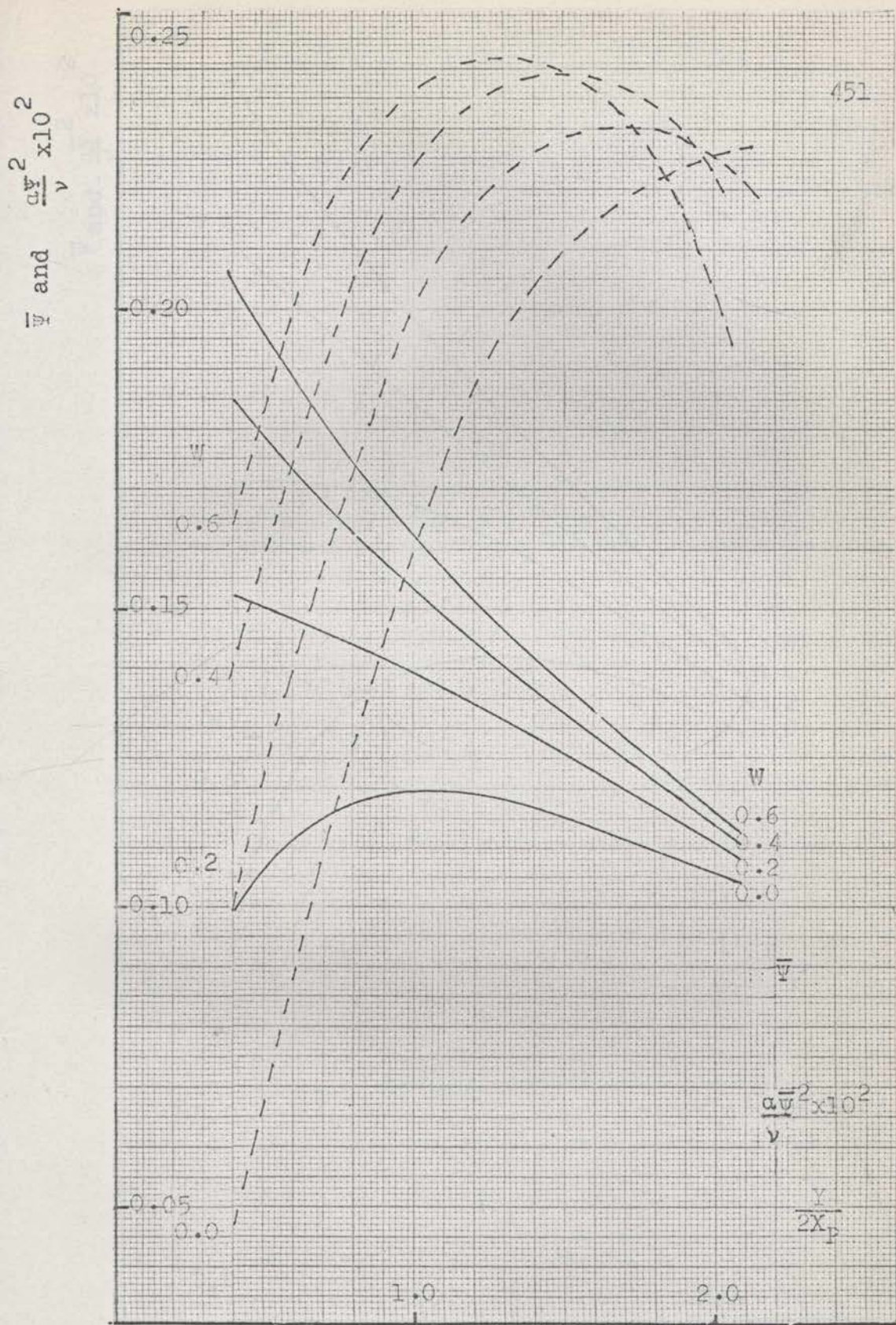


Fig. 7.45 cont. Graph of  $\bar{v}$  and  $\frac{\alpha \bar{v}^2}{\nu}$  for a Sense Coil Lying on One Side only of a Square Film. The Curves are Drawn for the Fixed Values  $Z_1 = 0$ ,  $Z_2 = 2X_p$  and  $X/2X_p = 1.0$

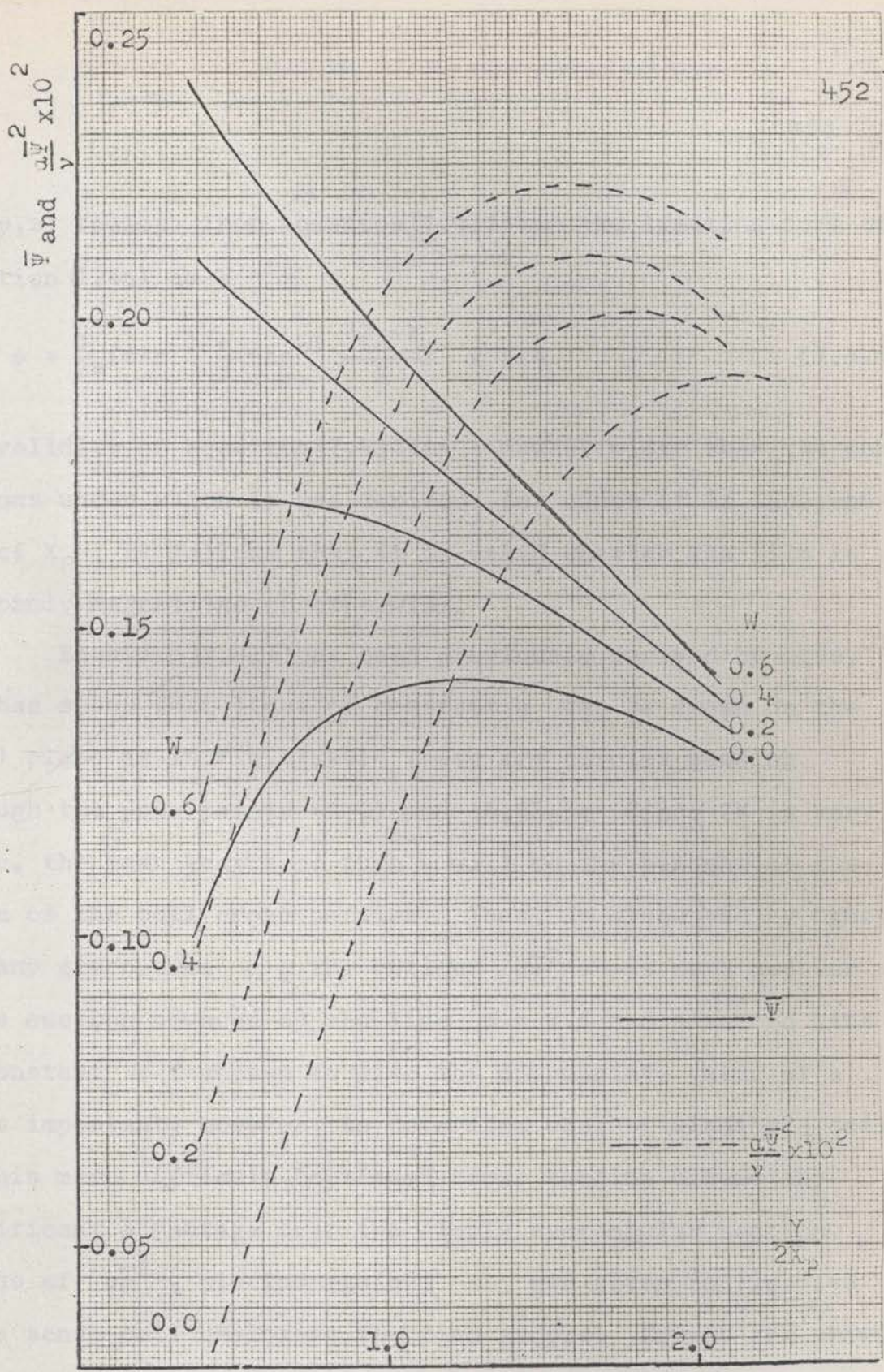


Fig. 7.45 Graph of  $\bar{V}$  and  $\frac{d\bar{V}}{dy}$  For a Sense Coil Lying on One Side only of a Square Film. The Curves are Drawn for the Fixed Values  $Z_1 = 0$  ,  $Z_2 = 2X_p$  and  $X/2X_p = 2.0$

$Q(0,y,z)$  follows from equation (7.412) and the limiting form of equation (7.46) as  $X \rightarrow \infty$  ;

$$\psi = \frac{1}{2\pi} \left( \tan^{-1} \frac{z}{y} + \tan^{-1} \frac{2Z_p - z}{y} \right) \leq 0.5 \quad (7.415)$$

The validity of equation (7.415) is somewhat wider than the conditions under which it was derived, for since it is independent of  $X_p$ , it follows that it is valid whether the film is uniformly magnetized or otherwise.

Equation (7.415) has been previously derived by Oguey<sup>01</sup> who has shown that lines of constant  $\psi$  can be drawn on the  $(y,z)$  plane as in Fig. 7.46. These are circles passing through the pole points  $(0,0)$  and  $(0,2Z_p)$ . Since  $2X$  is very large, the mean length of turn  $v$  will be independent of the shape of the coil cross section. Thus, as discussed by Oguey, for any given area  $\alpha$ , the optimum  $\alpha \bar{\psi}^2 / v$  is obtained for a cross section bounded by the line  $\psi = 0.5$  and a second line of constant  $\psi$ , chosen to give the appropriate value of  $\alpha$ . It is important, however, to determine whether winding a coil to this more difficult "optimum" cross section offers any significant advantage over the simple rectangular section. Curves of  $\alpha \bar{\psi}^2$ , plotted against  $\alpha$ , are given in Fig. 7.46 for a sense coil enclosing the film sample. Curves are shown for both the optimum cross section and a rectangular cross

Fig. 7.46. A Comparison of the Optimum Cross Section and an Approximating Rectangular Cross Section for Infinitely Long Coils.

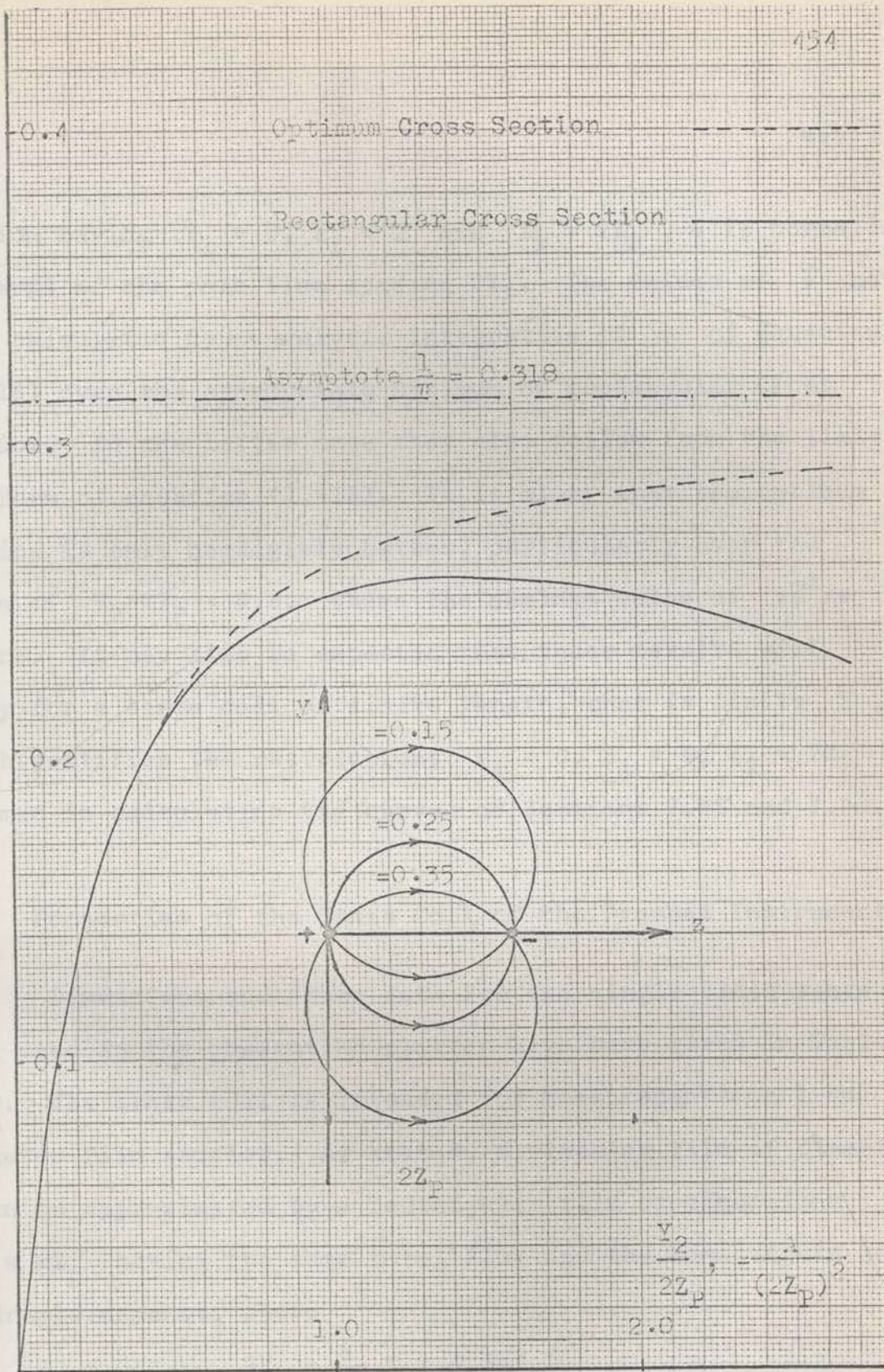


Fig. 7.46 A Comparison of  $\alpha \bar{\psi}^2$  Values between the Optimum Coil Cross Section and an Approximating Rectangular Cross Section for Infinitely Long Coils.

section having  $Y_1 = 0$ ,  $Z_1 = 0$  and  $Z_2 = 2Z_p$ ,  $\alpha$  is normalized in terms of the pole line spacing  $2Z_p$ . The values of  $\bar{\psi}$  have been calculated by an analytic integration of  $\psi$  of equation (7.415) over the appropriate optimum or rectangular cross section. In the latter case they also follow from the limiting form of equation (7.413). It is clear that the optimum section is only negligibly better, particularly over the range of  $Y_2/2Z_p < 0.8$ , where the maximum value of  $\alpha\bar{\psi}^2/v$  occurs. It may also be expected that these results will apply for a sense coil of finite length, that is finite  $X$ , which justifies the restrictions  $Y_1 = 0$ ,  $Z_1 = 0$ ,  $Z_2 = 2Z_p$  assumed in calculating the curves of Sections 7.45 and 7.46.

#### 7.48 Properties of the Sense Coil of the Present Instrument

Dimensions and other data for the single-sided sense coil used in the present MH plotter have been given in Table 6.62. The sense coil is intended for measurements on 1 cm diameter film samples. As stated, a circular film of diameter  $D$  can be approximated by a rectangular film of dimensions  $2X_p \times 2Z_p$  having the same total flux and the same dipole and quadruple moments, where

$$\begin{aligned} 2X_p &= \frac{8}{3\pi} D = 0.849 D \\ 2Z_p &= \frac{\pi}{4} D = 0.785 D \end{aligned} \tag{7.416}$$

For our present purposes we shall make the further approximation of a square film of dimensions  $2X_p = 2Z_p = 0.82 D = 0.82 \text{ cm.}$

In terms of this square film the normalized dimensions of the sense coil are  $Z_1/2X_p = 0$ ,  $Z_2/2X_p = 1.0$ ,  $Y/2X_p = 0.6$ ,  $W/2X_p = 0.4$ ,  $S/2X_p = 0.73$ ,  $X/2X_p = 1.17$ . The experimental value of  $\bar{\psi}$  has been found by measuring the saturation flux of a number of permalloy films ( $4\pi M_s = 10^4$  cgs units) of known thickness in the range  $1000 \text{ \AA}$  to  $3500 \text{ \AA}$ . Thicknesses were determined with an estimated error of  $\pm 10$  per cent using a Taylor-Hobson Talysurf Model 2. The experimental value  $\bar{\psi} = 0.165$  agrees to within 10 per cent with the theoretical value  $\bar{\psi} = 0.156$  obtained from the curves of Fig. 7.45. The small error may be accounted for in part by the error in the thickness measurement, and possibly in the assumptions made in regard to coil end effects and the "equivalent" rectangular film. In operation of the MH plotter, it is necessary for mechanical reasons to maintain some clearance between the film and the sense coil. A clearance of 0.03 in. to 0.06 in. has normally been used, giving  $\bar{\psi}$  values from 1.3 to 1.1 (see Fig. 7.41). The small loss in sensitivity is negligible for most purposes.

The quantity

## 7.5 LIST OF REFERENCES

$$\frac{n^2 \bar{\psi}^2}{R_i} = \left( \frac{2L\lambda_W}{\rho_W} \right) \left( \frac{\bar{\psi}^2}{v} \right) \quad (7.417)$$

is a convenient measure of the signal to noise performance of the coil which is readily found experimentally by measurement of  $n$ ,  $\bar{\psi}$  and  $R_i$ . The experimental value  $n^2 \bar{\psi}^2 / R_i = 1/2.06 \text{ m}\Omega$  is again in good agreement with the theoretical value  $1/1.93 \text{ m}\Omega$  using  $2L = 2X_P = 2Z_P = 0.82 \text{ cm}$ ,  $\rho_W = 1.7 \times 10^{-6} \Omega \text{ cm}$  (copper),  $\lambda_W = 0.45$  and  $\alpha \bar{\psi}^2 / v = 0.0024$  from Fig. 7.45.

- B1. "Low Noise Specifications of the Elektronik Type 122".  
 Rev. Sci. Instrum., 22, 872, (1951).
- B2. DeMatos, E.N., Somerville, N.J.,  
 "The Reduction of Low-Frequency Noise in Feedback Integrators",  
 Proc. Inst. Elect. Engrs., London, 8108, 531, (1950).
- B3. Tonger, W.R.,  
 "A Determination of  $\frac{1}{2}$  Noise Sources in Semiconductor Diodes and Triodes",  
 Transistor I., RCA Laboratories, Princeton, New Jersey, p.278, (1956).
- B4. Tonger, W.R.,  
 "Noise in Electron Devices",  
 Technology Press of the Massachusetts Institute of Technology and Wiley and Sons Inc., New York, p.20, (1957).
- B5. Giacoleto, L.J.,  
 "The Noise Figure of Junction Transistors",  
 Transistor I RCA Laboratories, Princeton, New Jersey, p.298, (1956).



## 7.5 LIST OF REFERENCES

- B1 Brophy, J.J.,  
"Low Noise Modifications of the Tektronix Type 122  
Preamplifier".  
Rev.Sci.Instrum., 26, 1076, (1955).
- B2 Brophy, J.J.,  
"Minimising Flicker Effect in Low Level Vacuum Tube  
Amplifiers".  
Rev.Sci.Instrum., 32, 204, (1961).
- B3 Bryzinski, T.F., Sahba, D.R.,  
"Hysteresis Curve Tracer for Magnetic Thin Films".  
IRE International Convention Record, V9, Pt.9,p.249,(1961).
- C3 Crittenden, E.C., Hudimac, A.A., Strough, R.J.,  
"Magnetisation Hysteresis Loop Tracer for Long Specimens  
of Extremely Small Cross Section".  
Rev.Sci.Instrum., 22, 872, (1951).
- D1 Dunstan, E.M., Sommerville, M.J.,  
"The Reduction of Low Frequency Noise in Feedback  
Integrators".  
Proc.Inst.Elect.Engrs., London, B105, 532, (1958).
- F1 Fonger, W.H.,  
"A Determination of  $\frac{1}{f}$  Noise Sources in Semi-conductor  
Diodes and Triodes".  
Transistors I., RCA Laboratories, Princeton, New Jersey,  
p.239, (1956).
- F2 Fonger, W.H.,  
"Noise in Electron Devices".  
Technology Press of the Massachusetts Institute of  
Technology and Wiley and Sons Inc., New York, p.365,(1959).
- G1 Giacoletto, L.J.,  
"The Noise Figure of Junction Transistors".  
Transistor I RCA Laboratories, Princeton, New Jersey,  
p.296, (1956).

- 01 Oguey, H.J.,  
 "Sensitive Flux Measurements of Thin Magnetic Films".  
 Rev.Sci.Instrum., 31, 701, (1960).
- 02 Oguey, H.J.,  
 "Measurements of Hysteresis Loops of Thin Magnetic Films".  
 Proc.Fifth International Conference on Instruments and  
 Measurements, Stockholm, Sweden, p.905, Sept.13, (1960).
- S1 Strassberg, D.D.,  
 "An Audio-Frequency Hysteresis for Thin Magnetic Films".  
 Group Report No. 51-10, Lincoln Lab., Massachusetts  
 Institute of Technology, (1959).
- T1 Terman, F.E.,  
 "Electronic and Radio Engineering".  
 McGraw Hill Inc., New York, p. 441, (1955).
- V1 Valley, G.E., Wallman, H.,  
 "Vacuum Tube Amplifiers".  
 McGraw Hill Inc., New York, Theorem 7, p. 28, (1948).
- Z1 Van der Ziel, A.,  
 "Noise".  
 Prentice Hall Inc., New Jersey, p. 224, (1954).

## CHAPTER 8

CIRCUITS FOR THE AMPLIFICATION AND INTEGRATION  
OF THE SENSE COIL VOLTAGE

## 8.1 INTRODUCTION

The following chapter describes the design of the transistorized preamplifier and feedback integrator used in the present MH plotter for the amplification and integration of the sense coil signal. The preamplifier has been designed for the minimum noise figure  $F$  as discussed in Section 7.1. The integrator realizes the "three pole one zero" phase compensated transfer function of Section 7.36 and is based on the feedback circuit of Fig. 7.37. The transfer function  $A(s)$  is independent of whether integration is performed before or after amplification. The present instrument is intended to display the voltage switching waveforms of a film in addition to the integrated hysteresis loops. Thus preamplification followed by integration has been used.

Section 8.2 below discusses certain general features of the system. Section 8.3 outlines the design of the preamplifier. Section 8.4 discusses the design of the integrator. Since an integrator of this type has wide application where-

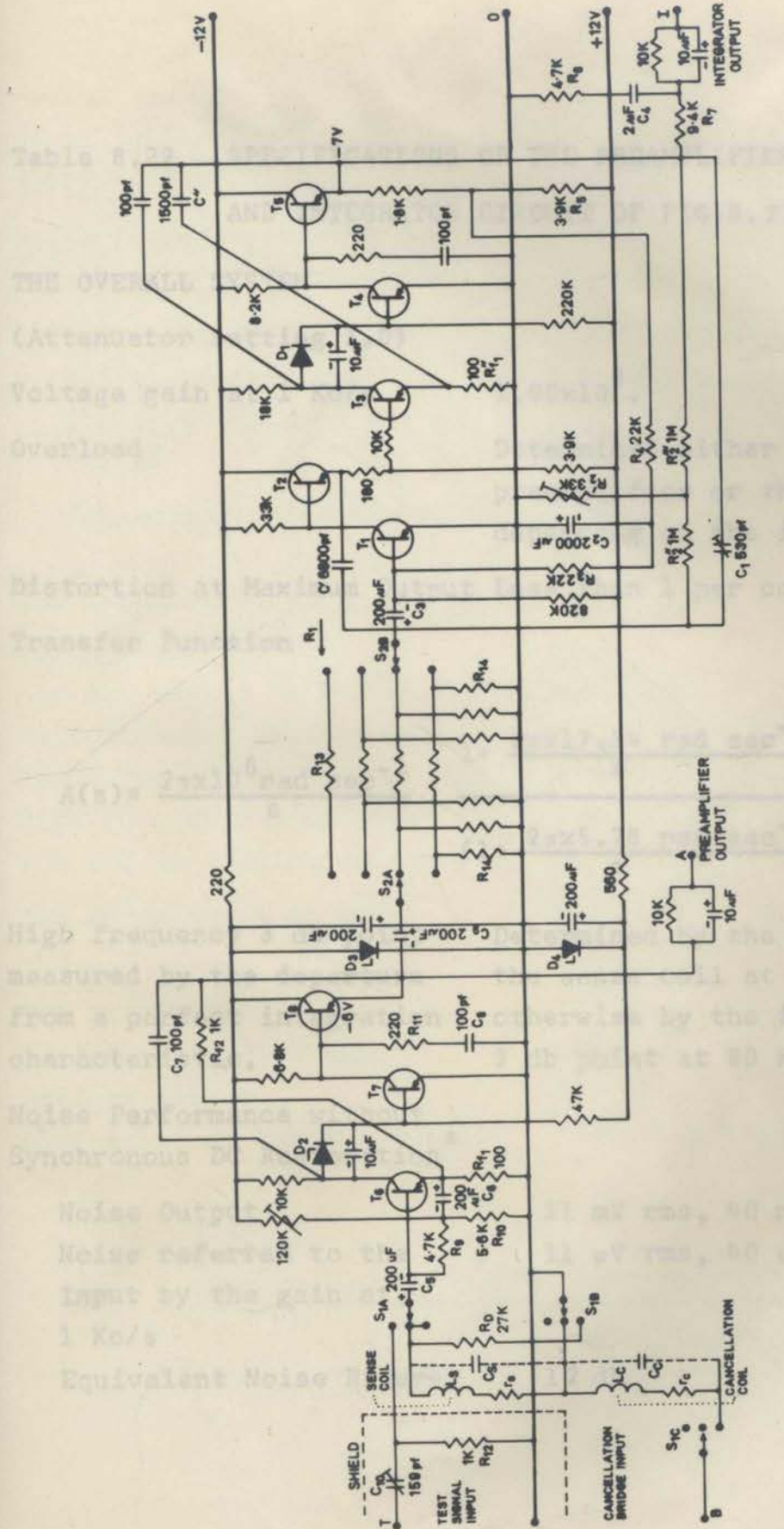
ever accurate integration and low noise are desired, the design has been described in some detail. Section 8.5 outlines briefly the method of test and adjustment of the system. This is a very necessary aspect of the design if hysteresis loop displays are to be reliably free from the effects of phase error (see Sections 6.72 and 6.73). As stated, the transfer function  $A(s)$  is independent of whether integration is performed before or after amplification. If the voltage switching waveforms are not required, prior integration has advantages in simplicity and in absence of possible preamplifier overload due to the pulsed nature of the input waveform. With MH plotters designed to date, it has been the practice to provide a high impedance across the sense coil. The minimum possible value of the integration resistor  $R_1$  (see Fig. 7.37) then occurs, if it is made equal to the resistance required for critical damping of the sense coil resonance. The equivalent input noise figure is substantially increased by this added series resistance. Prior integration has thus been avoided in high sensitivity application<sup>01</sup>. Integrator circuits can, however, be designed for which no resistance is added and no increase in noise figure occurs. Possible circuits of this type are outlined in Section 8.6. With such circuits the impedance across the sense coil approaches a short circuit. Improved high frequency response is

possible while, with correct design, the effects of induced currents in the sense coil and their associated fields are negligible in the measurement of films of  $\leq 1000 \text{ \AA}$  in thickness. Finally, Section 8.7 discusses the reduction of noise by hum synchronization and synchronous DC restoration. A circuit and performance details are given of a transistorized synchronous restorer suitable for this purpose.

## 8.2 GENERAL CONSIDERATIONS

A circuit diagram of the preamplifier and integrator is shown in Fig. 8.21. Performance specifications are given in Table 8.22. The circuit requires a  $-12 \text{ V}$  and a  $+12 \text{ V}$  regulated DC supply and a suitable circuit developed for this purpose is given in Appendix B.

The 1.0 to 0.1 times attenuator between the preamplifier and integrator allows the maximum range of film thickness to be measured. For a repetition frequency of  $f_0 = 1 \text{ Kc/s}$  and an attenuator setting of 0.1, an upper limit of  $3000 \text{ \AA}$  is then set by overload of the preamplifier rather than the integrator\*. The attenuator is of the " $\pi$ " type, having constant input and output impedances of  $1 \text{ k } \Omega$  to avoid changes in the low frequency response via the capacitors  $C_3$ ,  $C_9$  and the effective feedback integrator capacitor



T <sub>1</sub> - T <sub>8</sub>	OC 64	R <sub>13</sub>	R <sub>14</sub>
D <sub>1</sub>	OA 200	1.0K	∞
D <sub>2</sub> D <sub>4</sub>	0AZ 207	0.75K	3.00K
D <sub>3</sub>	0AZ 200	X 0.2	2.40K
		X 0.1	4.95K
			1.22K

FIG. 8-21 CIRCUIT DIAGRAM OF THE SENSE COIL VOLTAGE PREAMPLIFIER AND INTEGRATOR.

Table 8.22 SPECIFICATIONS OF THE PREAMPLIFIER  
AND INTEGRATOR CIRCUIT OF FIG.8.21

THE OVERALL SYSTEM

(Attenuator setting 1.0)

Voltage gain at 1 Kc/s	$1.00 \times 10^3$ .
Overload	Determined either by the preamplifier or the integrator depending on the input waveform.
Distortion at Maximum Output	Less than 1 per cent.

Transfer Function

$$A(s) = \frac{2\pi \times 10^6 \text{ rad sec}^{-1}}{s} \cdot \frac{1 + \frac{2\pi \times 17.34 \text{ rad sec}^{-1}}{s}}{(1 + \frac{2\pi \times 5.78 \text{ rad sec}^{-1}}{s})^3}$$

High frequency 3 db point measured by the departure from a perfect integration characteristic.	Determined by the resonance of the sense coil at 63 Kc/s, otherwise by the integrator 3 db point at 80 Kc/s.
--	--

Noise Performance without Synchronous DC Restoration \*

Noise Output	11 mV rms, 40 mV pp
Noise referred to the Input by the gain at 1 Kc/s	11 $\mu$ V rms, 40 $\mu$ V pp
Equivalent Noise Figure	12 db

Table 8.22 cont.

Noise Performance with  
Synchronous DC Restoration \*

Noise Output	0.8 mV rms, 3.0 mV pp
Noise referred to the input by the gain at 1 Kc/s	0.8 $\mu$ V rms, 3.0 $\mu$ V pp
Equivalent Noise Figure	7 db

## THE PREAMPLIFIER

Voltage Gain	10.0
Maximum Output at 80 Kc/s	4.0 V pp
Distortion at Maximum Output	Less than 1 per cent
Input Impedance	2 M $\Omega$    18 pF
High Frequency 3 db point for a 1 K $\Omega$ resistive source	1 Mc/s
Low Frequency 3 db point	0.15 c/s

## THE INTEGRATOR

Voltage Gain at 1 Kc/s	100
Maximum Output	2 V pp
Distortion at Maximum Output	Less than 1 per cent
Transfer Function	

$$A(s) = \frac{2\pi \times 10^5 \text{ rad sec}^{-1}}{s} \cdot \frac{1 + \frac{2\pi \times 17.34 \text{ rad sec}^{-1}}{s}}{\left(1 + \frac{2\pi \times 5.78 \text{ rad sec}^{-1}}{s}\right)^3}$$



Table 8.22 cont.

High frequency 3 db point 80 Kc/s  
determined by the departure  
from a perfect integration  
characteristic.

Noise Performance without  
Synchronous DC Restoration\*

Noise Output	1.7 mV rms, 60 mV pp
Noise referred to the Input by the Gain at 1 Kc/s	17 $\mu$ V rms, 60 $\mu$ V pp

Equivalent Noise Figure 16 db

Noise Performance with  
Synchronous DC Restoration\*

Noise Output	0.11 mV rms, 0.4 mV pp
Noise referred to the Input by the Gain at 1 Kc/s	1.1 $\mu$ V rms, 4 $\mu$ V pp

Equivalent Noise Figure 9 db

---

\* The equivalent or averaged noise figure  $F$  is defined in equation 7.12. Peak to peak noise voltages were estimated from an oscilloscope and are more representative of the effects on a hysteresis loop display than rms values. By measurements on a number of OC44 transistors at higher frequencies, where both peak to peak and rms values could be obtained, it has been found the ratio of the peak to peak to the rms value is approximately constant at 3.5. The rms values quoted and the noise figure  $F$  have hence been calculated assuming this value of 3.5. The preamplifier input transistor is the best of a batch of 10 units tested for low  $\frac{1}{F}$  noise. Values of  $F$  up to 24 db were obtained for particularly noisy units with the average being 16 db.

---

\* In considering the overload behaviour of the circuit, the input pulse train at the repetition frequency  $f_0$  must be considered as having both a peak pulse height and an "integrated" amplitude defined as the amplitude of the signal obtained after integration by an integrator of unity gain at  $f_0$ . With the present instrument at  $\bar{\psi} = 0.13$ , a  $1000 \text{ \AA}$ , 1 cm diameter permalloy ( $4\pi M_s = 10^4$  cgs units) film measured at  $f_0 = 1 \text{ Kc/s}$ , gives a sense coil signal having a peak pulse height of approximately 20 mV pp. and an integrated amplitude of 6.3 mV pp. From the values of gain and overload level of the preamplifier and integrator given in Table 8.22, for attenuator settings of 1.0 and 0.1, the maximum film thicknesses measurable at  $f_0 = 1 \text{ Kc/s}$  are  $300 \text{ \AA}$  and  $3000 \text{ \AA}$  set by overload of the integrator and by simultaneous overload of the integrator and preamplifier, respectively. Since the peak pulse height will depend upon the squareness of the hysteresis loop, the results quoted above apply for a typical permalloy film measured in the easy axis direction (see Fig. 4. 21). For an ideally square loop, the pulse height will be set by the damping factor  $\xi$  and the resonant frequency  $f_0$  of the sense coil, and for the present instrument, taking  $\xi = 1$  and  $f_r = 63 \text{ Kc/s}$ , will be then 300 mV pp. for a  $1000 \text{ \AA}$  film.

$$\frac{1}{(1+A_0)C_1} \quad (\text{see equation 8.44}).$$

The small preamplifier gain of 10 gives the maximum input range while being sufficient to prevent the integrator contributing to the equivalent input noise at the 1.0 attenuator setting. The 1 k  $\Omega$  impedance level of the attenuator and the low noise design of the integrator have been made for this reason. Films of greater thickness can be measured either at a lower repetition frequency  $f_0$ , or by increasing the physical spacing between the sense coil and the film. An input attenuator has not been used as it is impossible to present both a high impedance to the sense coil and a low impedance to the base of transistor  $T_6$  (for low noise) unless the minimum attenuation exceeds the ratio of the two impedances. Further the high frequency response of the system is determined by the resistance and capacitance across the sense coil, requiring a compensated attenuator to avoid variations with the gain settings.

### 8.3 THE PREAMPLIFIER

The circuit diagram of the preamplifier has been given in Fig. 8.21 and performance specifications collected

in Table 8.22.

The circuit consists of two amplifying stages  $T_6$  and  $T_7$  with an emitter follower output stage  $T_8$ . The gain is set at  $10.0 \pm 0.2$  by feedback via the resistors  $R_{f1}$  and  $R_{f2}$ . Since this feedback extends to DC, low frequency time constants are avoided and a high thermal stability obtained, the output drift being  $-1.0$  V for a temperature rise of approximately  $20^\circ$  C to  $45^\circ$  C. The open loop gain of  $4 \times 10^3$  (measured for a  $1$  k $\Omega$  source impedance) ensures linear amplification independent of transistor properties. The emitter follower stage  $T_8$  provides an output of  $4.5$  V pp. at  $1$  Kc/s and  $4.0$  V pp. at  $100$  Kc/s (distortion less than  $1$  per cent) across the  $1$  k $\Omega$  resistance  $R_{f2}$  and the  $1$  k $\Omega$  AC input impedance of the attenuator. Capacitor  $C_7$  and the capacitor and resistor  $C_8$  and  $R_{11}$  stabilize the feedback loop at high frequencies. No oscillation or low frequency squegging occurs on overload by any frequency up to  $1$  Mc/s.

The input impedance of the preamplifier is raised by feedback across  $R_{f1}$  to  $2$  M $\Omega$  in parallel with  $18$  pF, being then entirely due to the conductance and capacitance of the collector to base diode of transistor  $T_6^*$ . Loading of the

---

\* This could be improved by a more suitable type of transistor or possibly by returning the emitter of  $T_7$  to the emitter of  $T_6$ .

---

#### 8.4 THE INTEGRATOR

input by the bias resistor  $R_9$  is eliminated by returning  $R_9$  to the emitter of  $T_6$  via the capacitor  $C_6$ .  $R_9$  now appears as an inductive reactance of value  $sC_6R_9R_{10} \div 60 \text{ M}\Omega$  at 1 Kc/s. The input network  $C_5, C_6, R_9$  and  $R_{10}$  solely determines the low frequency 3 db point of  $1/2\pi C_5C_6R_9R_{10} = 0.15 \text{ c/s}$ , the circuit being otherwise DC coupled. The high frequency 3 db point is at 1 Mc/s for a 1 k $\Omega$  resistive source.

The input stage is optimized for low noise with respect to source impedance and operating current ( $I_{ec}$  for  $T_6 = 0.25 \text{ mA}$ ) as outlined in Section 7.22.  $R_{f1}$  is made low, since it is effectively added in series with the extrinsic base resistance  $r_{bb}$  of  $T_6$  in determining the input noise figure<sup>Z1</sup>. The OC44 type transistor used has been found to have a significantly lower  $\frac{1}{F}$  noise level than types OC71, OC171 and 2N501 also tested. Experimental measurements of the noise are quoted in Table 8.22, and a graph of the variation of noise figure with frequency has been given in Fig. 7.23. At the 1.0 attenuator setting, the noise level of the preamplifier determines the noise level of the overall system, additional noise from the integration being negligible.

## 8.4 THE INTEGRATOR

The circuit diagram of the integrator has been given in Fig. 8.21 and performance specification collected in Table 8.22.

Briefly, the gain is  $10^2$  at  $f_0 = 1$  Kc/s with an integration error of 0.01 per cent at  $f_0 = 1$  Kc/s increasing to 1 per cent at  $f_0 = 100$  c/s. The maximum output signal of 2 V pp. without overload and the thermal output noise level of 6 mV pp. determines the maximum  $\frac{S}{N}$  ratio of 50 db with which a hysteresis loop may be displayed. With synchronous restoration this is increased to 75 db. The low noise design of the input stage  $T_1$  assists in this regard and also in keeping the required preamplifier gain as small as possible. Typical hysteresis loops are shown in Fig. 6.74.

### 8.4.1 The Integrator Transfer Function and Low Frequency Stability

The transfer function is, in the terminology of Section 7.3, of the three pole one zero phase compensated type

$$A(s) = \frac{2\pi \times 10^5 \text{ rad sec}^{-1}}{s} \cdot \frac{1 + \frac{2\pi \times 17.34 \text{ rad sec}^{-1}}{s}}{\left(1 + \frac{2\pi \times 5.78 \text{ rad sec}^{-1}}{s}\right)^3} \quad (8.41)$$

The approximation problem in the derivation of the above transfer function and the calculation of the pole position from the 1 per cent accuracy required at  $f_0 = 100$  c/s have been fully discussed in Section 7.3. The integrator proper, based on the feedback circuit of Fig. 7.37 provides the basic two pole transfer function

$$A'(s) = \frac{2\pi \times 3 \times 10^5 \text{ rad sec}^{-1}}{s} \cdot \frac{1}{\left(1 + \frac{2\pi \times 5.78 \text{ rad sec}^{-1}}{s}\right)^2} \quad (8.42)$$

and is followed by a phase compensating section  $R_7$ ,  $R_8$  and  $C_4$  (see Fig. 7.35) giving the additional pole zero pair

$$A''(s) = \frac{1}{3} \cdot \frac{1 + \frac{2\pi \times 17.34 \text{ rad sec}^{-1}}{s}}{1 + \frac{2\pi \times 5.78 \text{ rad sec}^{-1}}{s}} \quad (8.43)$$

In high gain transistor integrator circuits, where integration extends to low frequencies, the amplifier may be either AC or DC coupled. In the former case it is almost impossible to avoid low frequency instabilities, while in the

latter case serious thermal drift of the output stage may occur. The present circuit consists of three amplifying stages  $T_1$ ,  $T_3$ ,  $T_4$  and two emitter followers  $T_2$  and  $T_5$  directly coupled throughout. High overall stability is nevertheless achieved by almost unity DC feedback via the network  $R_3$ ,  $R_4$  and  $C_2$ . Further the pole produced is controlled and forms part of the desired transfer function so that  $C_2$  has the minimum possible value.

The design of the feedback network follows a simple step by step procedure based on equation 7.331 of Fig. 7.37

- the frequency  $1/C_1R_1$  is determined by the required gain  $|A(j\omega_0)| = 1/\omega_0C_1R_1 = 3 \times 10^2$  at the frequency  $\omega_0 = 2\pi \times 10^3$  rad sec<sup>-1</sup>. The resistance  $R_1$  is the 1 k $\Omega$  output impedance of the attenuator giving  $C_1 = 530$  pF.

- the frequency  $1/C_1R_2$  is determined by the sum of the poles  $S = 2\pi \times 11.56$  rad sec<sup>-1</sup>. From equation 7.331

$$S = \frac{1}{(1+A_0)C_1} \left[ \frac{1}{R_1} + \frac{1}{R_3} \right] + \frac{1}{C_1R_2} + \frac{1}{C_2(R_3 || R_4)}$$

$$\div \frac{1}{(1+A_0)C_1R_1} + \frac{1}{C_1R_2} \quad (8.44)$$

The large amplifier gain of  $A_0 \div 4 \times 10^5$  reduces the term  $1/(1+A_0)C_1R_1$  to  $< 2\pi \times 0.8$  rad sec<sup>-1</sup>.  $S$  depends only on  $1/C_1R_2$  giving phase compensation free from drift due to



amplifier gain changes\*. It follows also that  $S$  is independent of  $R_1$  and thus of the attenuator gain settings. In the final circuit  $R_2$  of Fig. 7.37 has been replaced by an equivalent "T" network  $R_2'$ ,  $R_2''$  and  $R_2'''$  to allow more convenient component values.

- the frequency  $1/C_1 C_2 R_3 R_4$  is determined by the product of the poles  $P = (2\pi \times 5.78)^2 \text{ rad}^2 \text{ sec}^{-2}$ . From equation 7.331

$$P = \frac{1}{C_1 C_2 R_3 R_4} + \left[ \frac{1}{(1+A_0) C_1 R_1} + \frac{1}{C_1 R_2} \right] \cdot \frac{1}{C_2 (R_3 || R_4)}$$

$$\dagger \frac{1}{C_1 C_2 R_3 R_4} \quad (8.45)$$

The transfer function  $A(s)$  of equation 7.331 contains an unwanted zero whose frequency  $1/C_2 (R_3 || R_4)$  should be as low as possible to obtain full attenuation of low frequency noise\*\*. For a constant value of  $1/C_1 C_2 R_3 R_4$ ,  $1/C_2 (R_3 || R_4)$  is

\* In general it follows that if  $A_0$  is considered as having possible variations by a factor of 2, then for a given integration accuracy, the minimum value of  $A_0$  will be the same whether a phase compensated or uncompensated response is used.

\*\*  $1/C_2 (R_3 || R_4)$  is just the frequency  $r/L$  of the inductance  $L$  in the equivalent circuit of Fig. 7.37.

a minimum when  $R_3 = R_4$  and when  $R_3, R_4$  are small and  $C_2$  large. The value  $R_3 = R_4 = 22 \text{ k}\Omega$  in the present design is a compromise between increasing thermal drift (see below) on one hand, and an increasing input noise figure and value of  $C_2$  on the other. The frequency  $1/C_2(R_3 || R_4) = 2\pi \times 0.010 \text{ rad sec}^{-1}$  is negligibly small, justifying the assumptions made in equation 8.44 and 8.45.

The large value of  $C_2$  requires an electrolytic capacitor which is subject to change of value. Since the sum of the poles (equation 8.44) is independent of  $C_2$ , variations in  $C_2$  will not effect the phase compensation (see equation 7.34). The effect of  $C_2$  on the product of the poles and consequently on the error  $\epsilon_{-2} \propto 1/C_2$  and the noise bandwidth  $\beta \propto \sqrt{C_2}$  is unimportant. Finally, a divider network  $R_5$  and  $R_6$  has been used in the emitter of  $T_5$  to reduce the voltage rating of  $C_2$ . The value of  $C_2$  is modified by the voltage division ratio to give the final value of  $C_2 = 2000 \text{ }\mu\text{F}$ .

- The drift of the emitter voltage of  $T_5$  is given by

$$V \div \frac{R_5 + R_6}{R_5} \cdot \left\{ (R_3 + R_4) I_b + \frac{R_1' + R_3 + R_4}{R_1'} \cdot V_{eb} \right\} \quad (8.46)$$

where  $I_b$ ,  $V_{eb}$  are changes in the base current and the emitter base voltage, respectively, of the input stage  $T_1$  due to temperature effects or variability between different transistor units, and  $R_1'$  is the DC resistance across the base of  $T_1$ , excluding  $R_3$  and  $R_4$ .

The capacitor  $C_3$  decouples the low  $1\text{ k}\Omega$  output impedance of the attenuator from the base of  $T_1$ .  $R_1'$  then becoming just the input impedance  $h_{ie} \doteq 8\text{ k}\Omega$  of  $T_1$ . The measured output drift is  $+0.9\text{ V}$  for a temperature rise of approximately  $20^\circ\text{C}$  to  $45^\circ\text{C}$ .

An exact mesh analysis of the circuit with the capacitor  $C_3$  added has been made. The expressions are long, but the nett effect of  $C_3$  is to add an additional real pole to the transfer function  $A(s)$  of equation 7.331. If the added pole lies well below the normal poles of  $A(s)$ , then its frequency is approximately  $1/R_1 C_3\text{ rad sec}^{-1}$ . Variations in  $C_3$ , as with variations in  $C_9$ , will directly effect the phase compensation. The value  $C_3 (= C_9) = 200\text{ }\mu\text{F}$  removes the pole to a sufficiently low frequency of  $2\pi \times 0.8\text{ rad sec}^{-1}$ .

#### 8.42 High Frequency Stability

It is extremely difficult in a multi-stage transistor feedback integrator, in which essentially at high frequencies

the output is connected directly to the input by the integrator capacitor  $C_1$ , to prevent high frequency oscillation. This is especially so if the high frequency 3 db point required exceeds the  $\beta$  cut off frequency of the transistors available. However, it is possible to obtain almost any desired gain at low frequencies (in the present case  $A_0 > 4 \times 10^5$ ) while completely avoiding all high frequency instability problems by a method which may be described as a "cascade connected of separate integrators inside an overall feedback loop". In view of its general application, the theory of this method is given in some detail below.

Referring to Fig. 8.41a, if the amplifier  $A$  is assumed to have infinite input impedance and zero output impedance, then the overall gain with feedback  $A'$  is given by

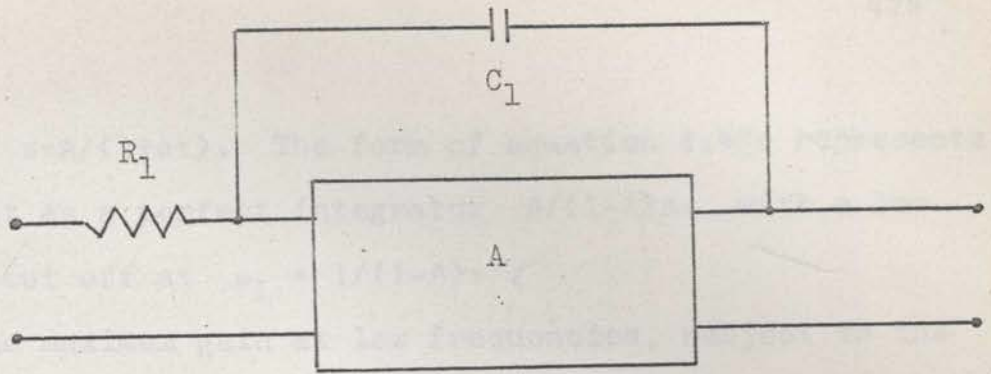
$$\frac{v_0}{v_i} = A' = \frac{A}{1+(1-A)\tau s} \quad (8.47a)$$

$$= \frac{A}{1+s\tau} \cdot \frac{1}{1-\frac{s\tau A}{1+s\tau}} \quad (8.47b)$$

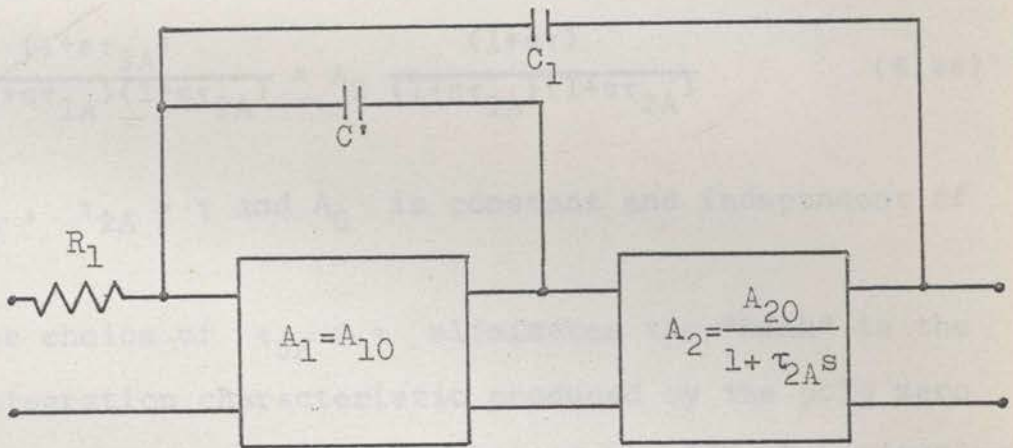
$$= \frac{A}{(1-A)s\tau} \cdot \frac{1}{1+\frac{1}{(1-A)\tau s}} \quad (8.47c)$$

where  $\tau = R_1 C_1$ .

The form of equation 8.47b places in evidence the feedback



Circuit A



Circuit B

Fig. 8.41 The High Frequency Stability of Feedback Integrators.

loop gain  $s\tau A/(1+s\tau)$ . The form of equation 8.47c represents the circuit as a perfect integrator  $A/(1-A)s\tau$  with a low frequency cut off at  $\omega_L = 1/(1-A)\tau$ .

The maximum gain at low frequencies, subject to the minimum gain at high frequencies (for reasons of high frequency stability), is obtained if the loop gain  $s\tau A/(1+s\tau)$  decreases continuously with frequency. A rate of 6 db per octave avoids critical adjustments of the circuit. This implies that A should be of the form

$$A = A_0 \cdot \frac{(1+s\tau_{3A})}{(1+s\tau_{1A})(1+s\tau_{2A})} = A_0 \frac{(1+s\tau)}{(1+s\tau_{1A})(1+s\tau_{2A})} \quad (8.48)$$

where  $\tau_{1A}, \tau_{2A} > \tau$  and  $A_0$  is constant and independent of frequency.

The choice of  $\tau_{3A} \equiv \tau$  eliminates the "kink" in the overall integration characteristic produced by the pole zero pair  $(1+s\tau_{3A})/(1+s\tau)$  otherwise contained by  $A'$ . Substituting equation 8.48 into equation 8.47,

$$A' = \frac{A_0}{1+s(\tau_{1A}+\tau_{2A}-A_0\tau)+s^2\tau_{1A}\tau_{2A}} \quad (8.49a)$$

$$= \frac{A_0}{(1+s\tau_{1A})(1+s\tau_{2A})} \cdot \frac{1}{1-\frac{s\tau A_0}{(1+s\tau_{1A})(1+s\tau_{2A})}} \quad (8.49b)$$

$$\div \frac{A_0}{s(\tau_{1A} + \tau_{2A} - A_0\tau)} \cdot \frac{1}{\left\{1 + \frac{1}{s(\tau_{1A} + \tau_{2A} - A_0\tau)}\right\}} \cdot \frac{1}{\left\{1 + \frac{s\tau_{1A}\tau_{2A}}{\tau_{1A} + \tau_{2A} - A_0\tau}\right\}}$$

(8.49c)

Equation 8.49c now represents  $A'$  as a perfect integrator with an added high frequency 3 db point at

$$\omega_H = \frac{\tau_{1A} + \tau_{2A} - A_0\tau}{\tau_{1A}\tau_{2A}} \div \frac{|\Lambda_0|\tau}{\tau_{1A}\tau_{2A}} \quad (8.410)$$

From equation 8.49b this is also the frequency at which the loop gain

$$\frac{s\tau A_0}{(1 + s\tau_{1A})(1 + s\tau_{2A})} \div \frac{A_0\tau}{s\tau_{1A}\tau_{2A}} \quad \text{for } s \gg \frac{1}{\tau_{1A}}, \frac{1}{\tau_{2A}}$$

has decreased to unity so that stability problems at higher frequencies do not exist.

The required form of  $A$  given in equation 8.48 with  $\tau_{3A} \equiv \tau$  can be automatically ensured by a cascade connection of two "integrators" as in Fig. 8.41b, where the gain of amplifier  $A_1 = A_{10}$  is independent of frequency and amplifier  $A_2$  has the transfer function  $A_2 = A_{20}/(1 + s\tau_{2A})$ . Under the assumptions of infinite amplifier input impedance and zero output impedance,  $A'$  is given by

$$A' = \frac{A_1 A_2}{1 + s(\tau' + \tau - A_1 \tau' - A_1 A_2 \tau)} \quad (8.411)$$

where

$$\tau' = R_1 C'$$

and

$$\tau = R_1 C_1$$

Substituting  $A_1 = A_{10}$  and  $A_2 = A_{20}/(1 + \tau_{2A})$ , then  $A'$  reduces exactly to the form of equation 8.49, where now

$$A_0 = A_{10} A_{20}$$

and

$$\tau_{1A} = \tau + \tau' - A_{10} \tau'$$

$\tau_{1A}$  is just the time constant of the integrator formed by  $R_1$ ,  $C'$  and the amplifier  $A_1$  (to be exact with  $C_1$  shunted across the input of  $A_1$ ). The overall integration time constant  $\tau_{1A} + \tau_{2A} - A_0 \tau \div |A_0| \tau$  is equal to that for a normal integrator of total amplifier gain  $A_0 = A_{10} A_{20}$  if the latter could be made stable. The method clearly extends to the cascade of any number of separate integrator units.

Referring to the circuit diagram of the present integrator Fig. 8.21, the amplifier stage  $T_1$  and the emitter follower  $T_2$  form the amplifier  $A_1$  with the feedback capacitor  $C' = 6800$  pF. It may be noted that the value of



$C'$  is limited by increase of the input noise figure at high frequencies<sup>Z1</sup>. Transistors  $T_3$ ,  $T_4$  and  $T_5$  form the integrator  $A_2 = A_{20}/(1+s\tau_{A2})$ . The circuit is identical to that used for the preamplifier with the feedback resistor  $R_{f2}$  replaced by the capacitor  $C'' = 2200$  pF to give an integration type characteristic. As given by equation 8.410, both the high frequency 3 db point and the point of unity loop gain occurs at

$$\omega_H \div \frac{|A_0|\tau}{\tau_{A1}\tau_{A2}} \div \frac{\tau}{\tau'} \left( \frac{A_{20}}{\tau_{A2}} \right) = \frac{C}{C'} \left( \frac{A_{20}}{\tau_{A2}} \right)$$

Since the transfer function  $A_{20}/(1+s\tau_{A2})$  is also produced by feedback

$$\frac{A_{20}}{\tau_{A2}} = \frac{1}{R_{f1}C''} = 2\pi \times 1050 \times 10^3 \text{ rad sec}^{-1}$$

giving

$$\omega_H = \frac{1}{C' C'' R_{f1}} = 2\pi \times 83 \times 10^3 \text{ rad sec}^{-1}$$

which is independent of  $A_{10}$  or  $A_{20}$ . The stability of the circuit is thus almost independent of the properties of the transistors and no adjustments of any kind are needed. The circuit shows no tendency to oscillation even on overload by signals up to 1 Mc/s in frequency. Tests of the integrator

using a differential square wave input give rise and fall times of  $4\mu\text{secs}$  for the output square wave, in agreement with the value of  $f_H = 83 \text{ Kc/s}$  calculated above.

### 8.5 TEST AND ADJUSTMENT OF THE AMPLIFIER AND INTEGRATION SYSTEM

The following section considers the accurate adjustment of gain and the cancellation of phase errors in the amplifier and integration system. This is of vital importance if the operation of the MH plotter is to be free from the peculiarities caused by phase errors (see Sections 6.72 and 6.73).

Gain and phase adjustments must be made for the overall system (indeed, it is troublesome to do otherwise). If synchronous restoration is used (see Section 8.7), then the restorer has an additional pole at approximately  $1.8 \text{ c/s}$  determined by the input impedance of the oscilloscope. The total phase shift of the preamplifier, integrator and restorer (and of the oscilloscope, if a DC coupled instrument is not available) must be set to zero with the oscilloscope connected. Cancellation of the overall phase error does not imply zero phase shift in the preamplifier output (and consequently in a switching voltage display), and this has been separately

ensured by the "DC coupled" design of the preamplifier in which the only low frequency pole occurs at 0.15 c/s.

Gain is most easily adjusted by trimming the integrator capacitor  $C_1$ . From equation 7.34, the first order phase error  $\epsilon_{-1} \approx P_{-1}$  is cancelled, if the sum of all zeros of the transfer function minus the sum of all poles is zero. The principle poles are the low frequency poles of the integrator, the sum of which (see equation 8.44) is determined by the network  $R_2'$ ,  $R_2''$  and  $R_3''$ , and the integration capacitor  $C_1$ . A potentiometer across  $R_2'$  thus provides a convenient phase adjustment with no interaction on the gain. Since only total phase errors can be measured, it is impossible to distinguish at any one frequency between first and higher order error terms ( $\epsilon_{-1}$ ,  $\epsilon_{-3}$ ,  $\epsilon_{-5}$  ..... of equation 7.36). The most accurate cancellation of low frequency phase errors is thus obtained if the adjustment is made at the lowest frequency at which these higher order terms are below the order of accuracy desired. In the present case 100 c/s is suitable giving  $\epsilon_{-3} \div 10^{-3}$ .

In the present instrument an accurate differentiating network  $C_{10}$  and  $R_{12}$  (Fig. 8.21) is used to apply a test signal to the input of the preamplifier.  $C_{10}$  and  $R_{12}$  can be considered as a perfect differentiator of transfer

identical resistors. The overall gain is unity and the phase

function  $sC_{10}R_{12}$  with a high frequency pole at  $1/C_{10}(R_{12}+R_o)$  where  $R_o$  is the output impedance of the signal generator proceeding the test signal. This pole lies at 1 Mc/s for  $R_o = 0$  and may be neglected.  $C_{10}$  and  $R_{12}$  have been accurately adjusted to give a gain of  $1.0 \times 10^{-3} \pm 0.1$  per cent at  $f_0 = 1$  Kc/s. Since the gain of the amplifier and integrator is also  $10^3$ , then using the differentiator as a reference, gain and phase adjustments can be made by direct comparison of the integrated output and the input signal to the differentiator. This comparison may be made in numerous ways. We shall briefly mention two

- the phase can be adjusted by applying the integrator output to the vertical plates of the oscilloscope as in normal use and the input signal of the differentiator to the horizontal plates. The resulting ellipse may be closed by  $R'_2$  and the coincidence of the two sides determined to within  $\pm 0.02$  of a cm division. For a 10 cm vertical deflection the phase error is  $< \pm 4 \times 10^{-3}$ .

- in normal use accurate phase cancellation is all that is needed. However, if accurate adjustment of both amplitude and phase is required, then the bridge method illustrated in Fig. 8.51 may be used.  $R'_B$  and  $R''_B$  are two identical resistors. The overall gain is unity and the phase

Differentiating  
Network

To Oscilloscope

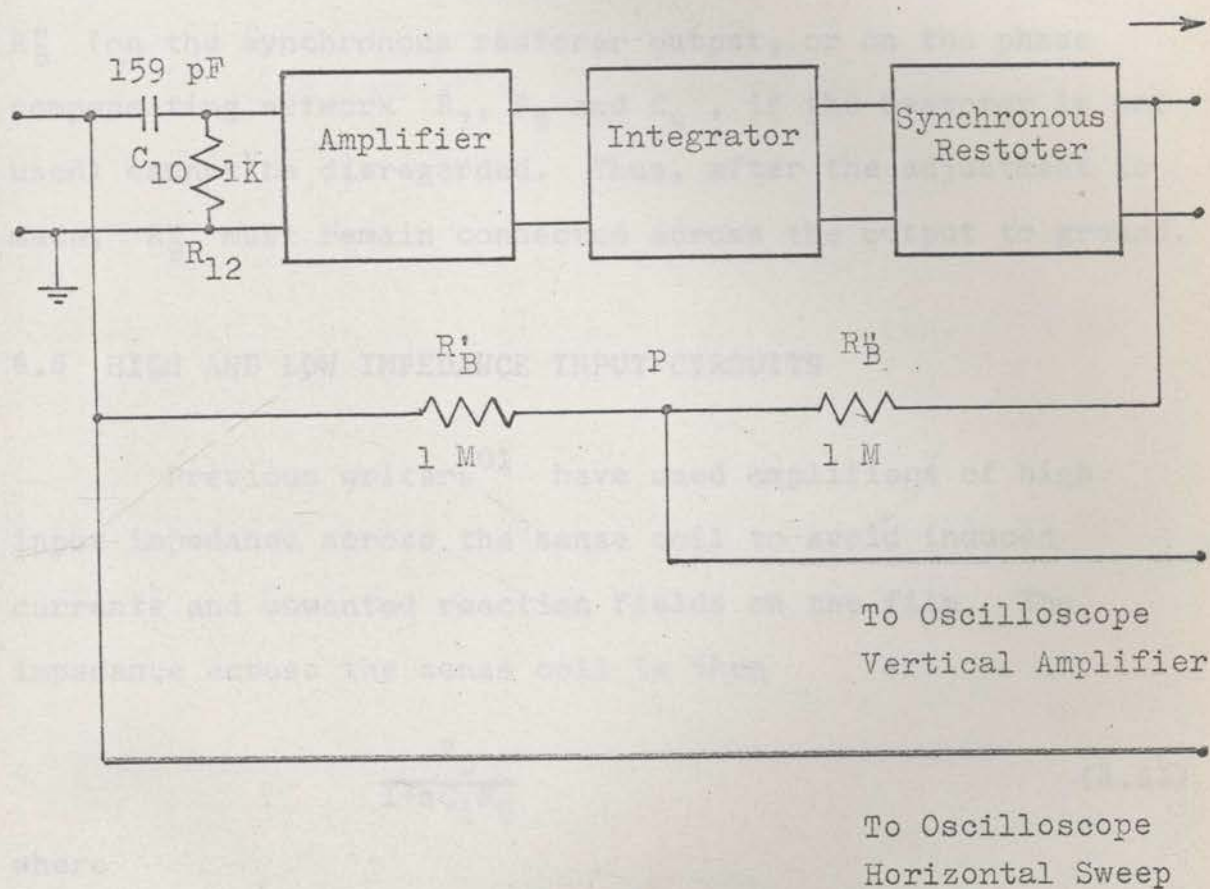


Fig. 8.51 A Bridge Method for Adjusting the Gain and Phase of the Sense Coil Voltage Preamplifier and Integrator

error zero when a null voltage occurs at the point P. Amplitude and phase errors can be distinguished from the nature of the oscilloscope display. The loading effect of  $R_B''$  (on the synchronous restorer output, or on the phase compensating network  $R_7$ ,  $R_8$  and  $C_4$ , if the restorer is not used) cannot be disregarded. Thus, after the adjustment is made,  $R_B''$  must remain connected across the output to ground.

#### 8.6 HIGH AND LOW IMPEDANCE INPUT CIRCUITS

Previous writers<sup>01</sup> have used amplifiers of high input impedance across the sense coil to avoid induced currents and unwanted reaction fields on the film. The impedance across the sense coil is then

$$\frac{R_D}{1+sC_iR_D} \quad (8.61)$$

where

$C_i$  is the self-capacitance of the coil,

$R_D$  is a resistance, normally adjusted for critical damping of the coil resonance and including the input impedance of the amplifier.

Amplifiers of low input impedance for which the resistance  $R_D$  is effectively a short circuit across the

the coil, can have certain advantages when

- the effect of capacity  $C_i$  on the high frequency response must be eliminated, or
- if it is desired to integrate the coil signal without prior amplification.

It is thus important to consider the effects of coil loading more closely. Reaction fields will arise from two causes.

#### 8.61 The Reaction Field Due to the Voltage Induced by the Air Flux

If the drive field is of magnitude  $H$  at frequency  $\omega_0$ , the reaction field  $H'$  will be

$$H' = H \frac{\omega_0 L_i}{R_i + j\omega_0 L_i + \frac{R_D}{1 + j\omega_0 C_i R_D}} \quad (8.62)$$

If, however,  $R_D$  is placed across the sense coil, cancellation coil and cancellation bridge as in Fig. 6.22, then no voltage will appear across  $R_D$  when the air flux cancellation is correctly adjusted. In this case the value of  $R_D$  can have no effect and  $H'$  becomes

$$H' \div H = \frac{\omega_0 L_i}{\left| R_i + j\omega_0 L_i + \frac{1}{j\omega_0 C_i} \right|} \quad (8.63)$$

$$\div H = \frac{\omega_0^2}{\omega_r^2} \quad \text{if} \quad \omega_r = \frac{1}{\sqrt{L_i C_i}} > \omega_0$$

For the present instrument at  $f_0 = 1 \text{ Kc/s}$ ,  $H'/H = 1$  part in  $4 \times 10^3$ , a negligible value.

### 8.62 The Reaction Field Due to the Voltage Induced by the Film Itself

In Laplace Transform notation the reaction field  $H'$  will be

$$H' = \frac{s\phi_i(s)\gamma}{R_i + sL_i + \frac{R_D}{1 + sC_i R_i}} \quad (8.64)$$

where

- $\phi_i(s)$  is the film flux linking the total coil turns,
- $\gamma$  is the field produced at the film by unit current flowing through the coil.



From equation 8.64 ,  $H'$  depends on the thickness of the film and the shape of the coil, but is independent of the number of turns. Two cases arise:

- If  $\phi_i(s)$  approximates to a sine wave of amplitude  $\phi_i$  and frequency  $\omega_0$  , then the peak amplitude of  $H'$  will be

$$H'_{\max} = 2 \left( \frac{\omega_0}{\omega_r} \right) \gamma \frac{\phi_i}{L_i}$$

for a critically damped coil having  $R_D = \frac{1}{2} \omega_r L_i > \omega_0 L_i$  (neglecting  $R_i$  ). For a short circuited coil,

$$H'_{\max} = \frac{\omega_0 \phi_i \gamma}{|R_i + j \omega_0 L_i|} < \gamma \frac{\phi_i}{L_i}$$

While  $H'$  is greatest for the short circuited case, it is nevertheless negligible for thin films, where the flux  $\phi_i$  is small. This is distinct from the situation encountered in an MH plotter designed for bulk samples. For the present instrument  $H'$  may be calculated from the measured parameters of the sense coil to give  $\gamma = 3.2 \text{ oe mA}^{-1}$  and  $H' = 22 \times 10^{-3} \text{ oe}$  for a 1000 A 1 cm diameter permalloy film ( $4\pi M_s = 10^4 \text{ cgs units}$ )

- If  $\phi_i(s)$  approximates to a square wave of zero rise time and amplitude  $\phi_i$ , then it may be shown that the

peak value of  $H'$  is again

$$H'_{\max} = \gamma \frac{\phi_i}{L}$$

and is independent of whether the coil is critically damped or short circuited. In this case the critically damped coil can thus offer no advantage. The values of  $H'$  is as before negligible for films  $\leq 1000 \text{ \AA}$ .

It is thus clear that low input impedance circuits are entirely satisfactory in this application.

### 8.63 A Low Input Impedance Feedback Preamplifier

Fig. 8.61a gives a schematic diagram of a low input impedance feedback preamplifier. In the standard manner,  $R' + sL'$  can be replaced by an impedance  $(R'+sL')/(1+A)$  across the input terminals of the amplifier. As the shunting impedance is a feedback impedance rather than a passive component, the increase in the noise figure  $F$  can be made negligible<sup>Z1</sup>. The effects of coil inductance can be cancelled and the gain  $v_o/v_i$  made independent of frequency if  $R'/R_i = L'/L_i$ . This condition can be accurately set by a bridge technique similar to that outlined in Section 8.5. For large  $A$  then

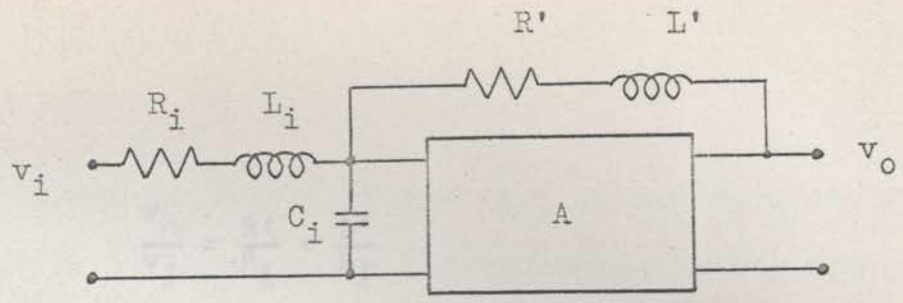


Fig. 8.61a A Low Impedance Input Feedback Preamplifier.

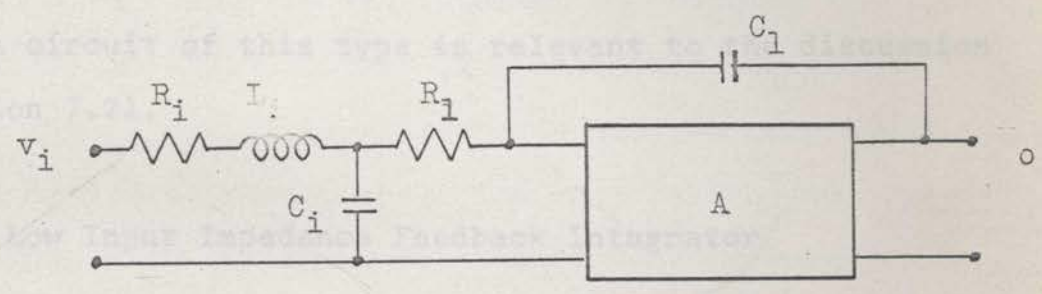


Fig. 8.61b A High Input Impedance Feedback Integrator.

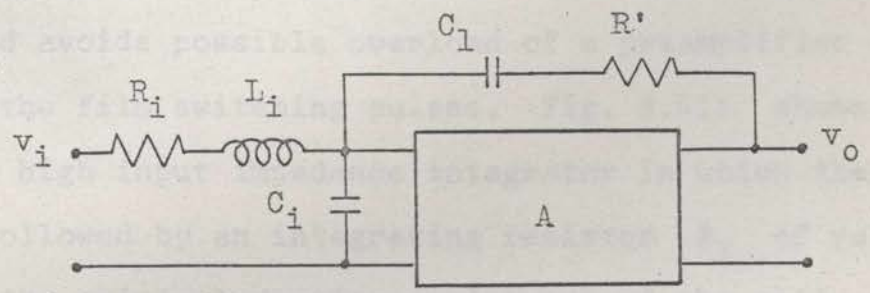


Fig. 8.61c A Low Input Impedance Feedback Integrator.

$$\frac{v_o}{v_i} = \frac{R'}{R_i} = \frac{L'}{L_i}$$

C now shunts an effective impedance of  $R_i + sL_i$  in parallel with  $(R'+sL')/(1+A)$  and the input resonance frequency can be increased by making  $(R'+sL')/(1+A)$  sufficiently low. A limit is set by the self-resonant frequency of the coil  $L'$ . The use of a circuit of this type is relevant to the discussion of Section 7.21.

#### 8.64 A Low Input Impedance Feedback Integrator

If only the integrated hysteresis loop of a film is required and not the voltage switching waveforms, no pre-amplifier is needed and the sense coil can be followed directly by an integrating network. This arrangement is simple and avoids possible overload of a preamplifier on the peaks of the film switching pulses. Fig. 8.61b shows a conventional high input impedance integrator in which the sense coil is followed by an integrating resistor  $R_1$  of value equal to the critical damping resistance of the coil. The coil damping and the overall gain cannot be independently adjusted. More important, the noise figure  $F$  of the input

stage must now be evaluated for  $R_1$  in series with  $R_i$ . For voltage amplifiers, where the equivalent noise resistance in series with the input grid may be large due to  $\frac{1}{f}$  components, this may not be serious. However, for transistor amplifiers, having an optimum source impedance for low noise, a large increase in  $F$  occurs. In Fig. 8.61b the effective integrating capacitor is the feedback capacitance  $C_1/(1+A)$ .  $F$  is increased still further if a passive capacitor is used.

Fig. 8.61c gives a schematic diagram of a low impedance feedback integrator, where the coil resistance itself is the integrator resistor. In the standard manner,  $1/sC_1 + R'$  can be replaced by an impedance  $(1/sC_1 + R')/(1+A)$  across the input terminals of the amplifier. The effect of coil inductance is cancelled if  $1/R_i C_1 = R'/L_i$ , and again this condition can be accurately set by a bridge technique similar to that outlined in Section 8.5. For large  $A$  then

$$\frac{v_o}{v_i} = \frac{1}{sC_1 R_i} = \frac{R'}{sL_i}$$

At high frequencies,  $C_i$  effectively shunts a resistance  $R'/(1+A)$ , and its effect is negligible for  $R'/(1+A)$  sufficiently low.

## 8.7 REDUCTION OF NOISE BY SYNCHRONOUS DC RESTORATION

### 8.71 Introduction

In theory, no limit exists for the sensitivity of an MH plotter. If the cancellation of air flux and other drive frequency voltages is perfect, then, since the signal from the film is periodic, random noise can be reduced to any level by correlation techniques. In practice, two methods have been found useful,

- since often the largest noise component is due to noise frequency hum, the apparent jitter of an oscilloscope display can be reduced by "hum synchronization" in which the display is unblanked for a fraction only of each hum cycle chosen at the instant when the first derivative of the hum voltage is zero. In the present instrument the hum level is negligible as discussed in Section 6.66, and hum synchronization has not been found necessary.

- low frequency noise variations may also be very successfully reduced by DC restoration synchronous with the repetition frequency  $f_0$  in which the display is ideally instantaneously reset to a fixed reference voltage once every display period  $T_0 = 1/f_0$ . The effect of restoration on

noise variations is illustrated in Fig. 8.71, where the sinusoidal voltage  $V \sin(\omega t + \phi)$  is converted to a modulated sawtooth wave  $V'$  by restoration commencing at time  $t = 0$  and occurring thereafter at times  $t = T_0, = 2T_0, \dots$  where  $T_0$  is the repetition period of the display. The peak heights of the sawtooth at times  $t = 0, T_0, 2T_0, \dots$  are given by

$$\begin{aligned} V'(\phi_0) &= V \sin \phi_0 \\ V'(\phi_1) &= V(\sin \phi_1 - \sin \phi_0) \\ &\dots \dots \dots \\ V'(\phi_n) &= V(\sin \phi_n - \sin \phi_{n-1}), \text{ where } \phi_n = n\omega T_0 + \phi_0 \end{aligned} \quad (8.71)$$

For  $\omega T_0 \ll 1$ ,

$$V'(\phi_n) \doteq \omega T_0 V \cos \phi_{n-1} - \frac{1}{2}$$

The r.m.s. value of the noise voltage is thus reduced by the factor

$$\frac{V'_{\text{rms}}}{V_{\text{rms}}} = \sqrt{\frac{2}{3}} \omega T_0 = 0.816 \omega T_0 = 5.05 \frac{\omega}{\omega_0} \quad (\text{for } \omega_0 \gg \omega) \quad (8.72)$$

As far as random noise is concerned, the action of the restorer is thus approximately equivalent to inserting an additional low frequency pole  $1/(1 + \omega_0/5.05s)$  in the amplifier

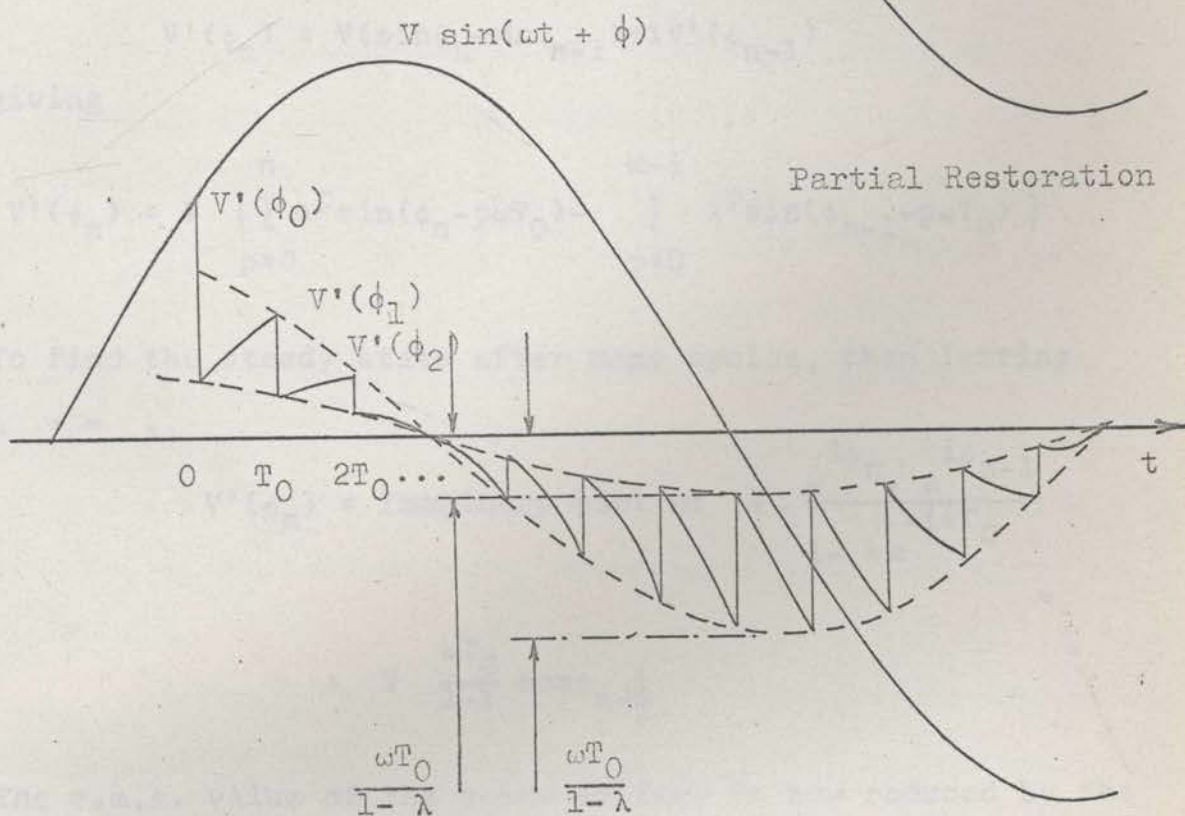
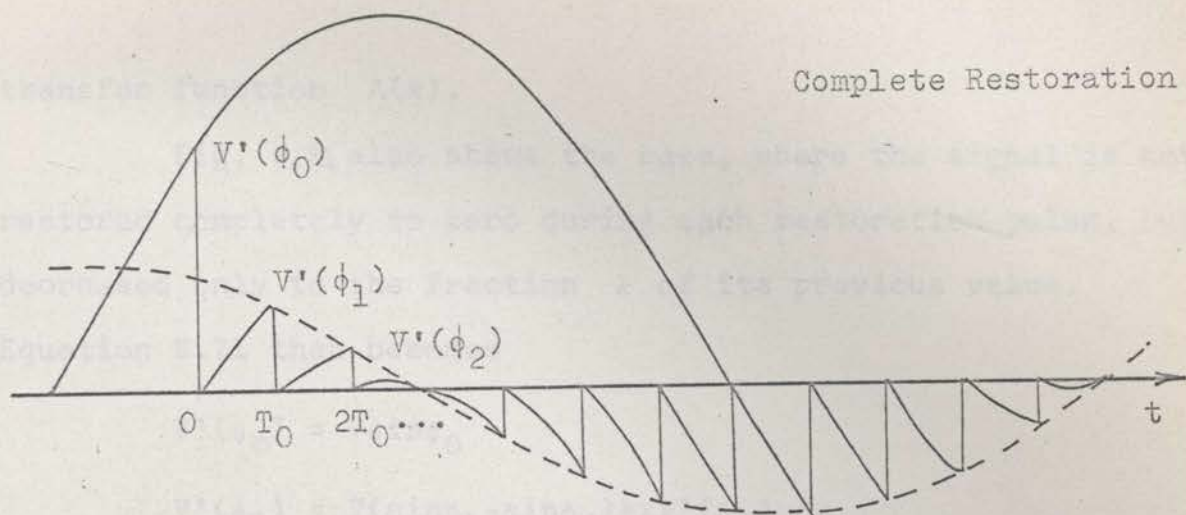


Fig. 8.71 Waveforms Showing the Reduction of a Sinoidal Noise Voltage by Synchronous DC Restoration.



transfer function  $A(s)$ .

Fig. 8.71 also shows the case, where the signal is not restored completely to zero during each restoration pulse, but decreased only to the fraction  $\lambda$  of its previous value.

Equation 8.71 then becomes

$$V'(\phi_0) = V \sin \phi_0$$

$$V'(\phi_1) = V(\sin \phi_1 - \sin \phi_0) + \lambda V'(\phi_0)$$

$$\dots \dots \dots$$

$$V'(\phi_n) = V(\sin \phi_n - \sin \phi_{n-1}) + \lambda V'(\phi_{n-1})$$

giving

$$V'(\phi_n) = V \left\{ \sum_{p=0}^n \lambda^p \sin(\phi_n - p\omega T_0) - \sum_{p=0}^{n-1} \lambda^p \sin(\phi_{n-1} - p\omega T_0) \right\}$$

To find the steady state after many cycles, then letting

$n \rightarrow \infty$ ,

$$V'(\phi_n) = \text{Imaginary part of } V \cdot \frac{e^{i\phi_n} - e^{i\phi_{n-1}}}{1 - \lambda e^{-i\omega T_0}}$$

$$\doteq V \frac{\omega T_0}{1 - \lambda} \cos \phi_{n-1/2}$$

The r.m.s. value of the noise voltage is now reduced by the factor

$$\frac{V'_{\text{rms}}}{V_{\text{rms}}} = \left( \frac{2}{3} + \frac{\lambda^2}{(1-\lambda)^2} \right)^{\frac{1}{2}} \omega T_0 = 2\pi \left( \frac{2}{3} + \frac{\lambda^2}{(1-\lambda)^2} \right)^{\frac{1}{2}} \frac{\omega}{\omega_0} \quad (8.73)$$

The ratio  $(V'_{\text{rms}}/V_{\text{rms}})/(V'_{\text{rms}}/V_{\text{rms}})_{\lambda=0}$  is plotted against  $\lambda$  in Fig. 8.72.

### 8.72 A Circuit for a Transistorized Synchronous DC Restorer

The circuit diagram of a DC synchronous restorer designed and constructed for use with the present MH plotter is shown in Fig. 8.73. The restorer operates over a range of frequencies from 0.1 to 1.0 Kc/s. Experimental measurements of the reduction of applied sinoidal "noise" signals agree closely with equation 8.72. A photograph showing the reduction by synchronous restoration of low frequency noise in the flux detecting system of the MH plotter has been shown in Fig. 6.610. Noise figure measurements for the MH plotter with and without synchronous restoration have been given in Table 8.22.

Referring to Fig. 8.73, a sine wave synchronizing signal derived from the field display is fed via the emitter follower  $T_5$  to a DC comparator formed by  $T_6$ ,  $T_7$ , and  $T_8$ . The sine wave is there clipped to produce a square

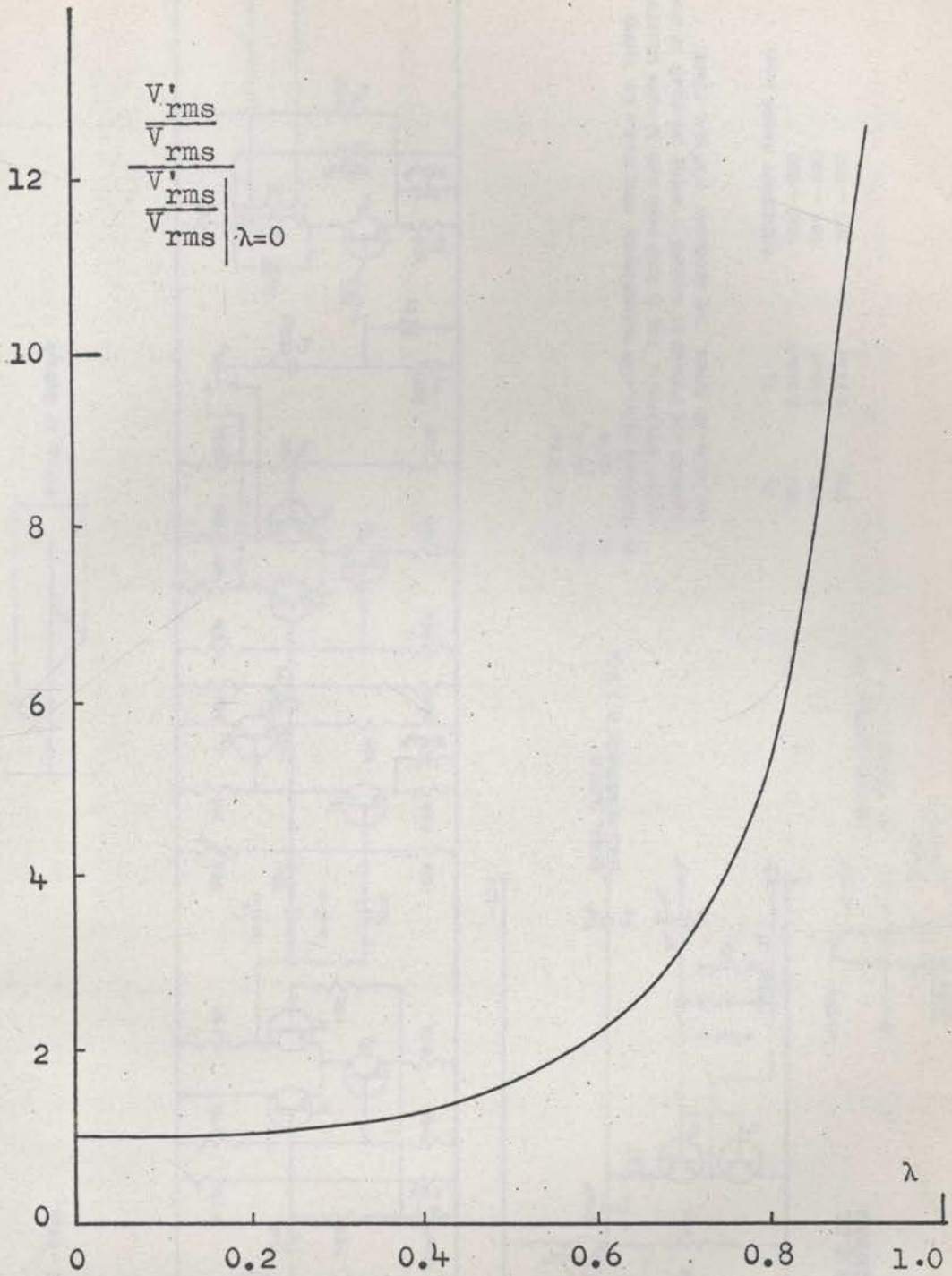
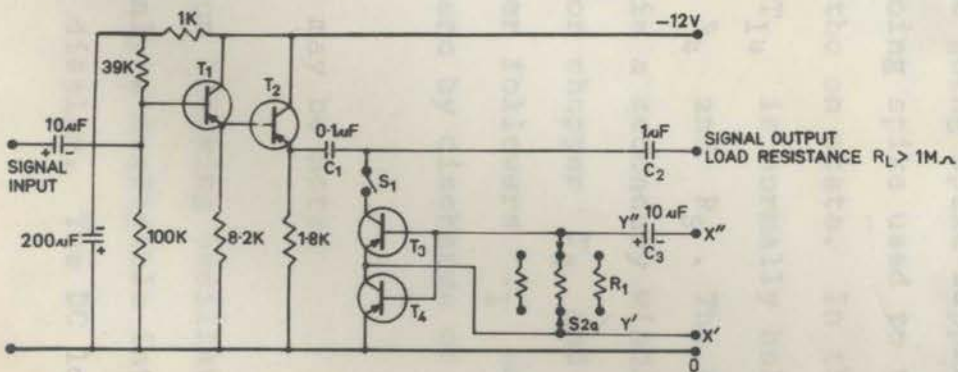
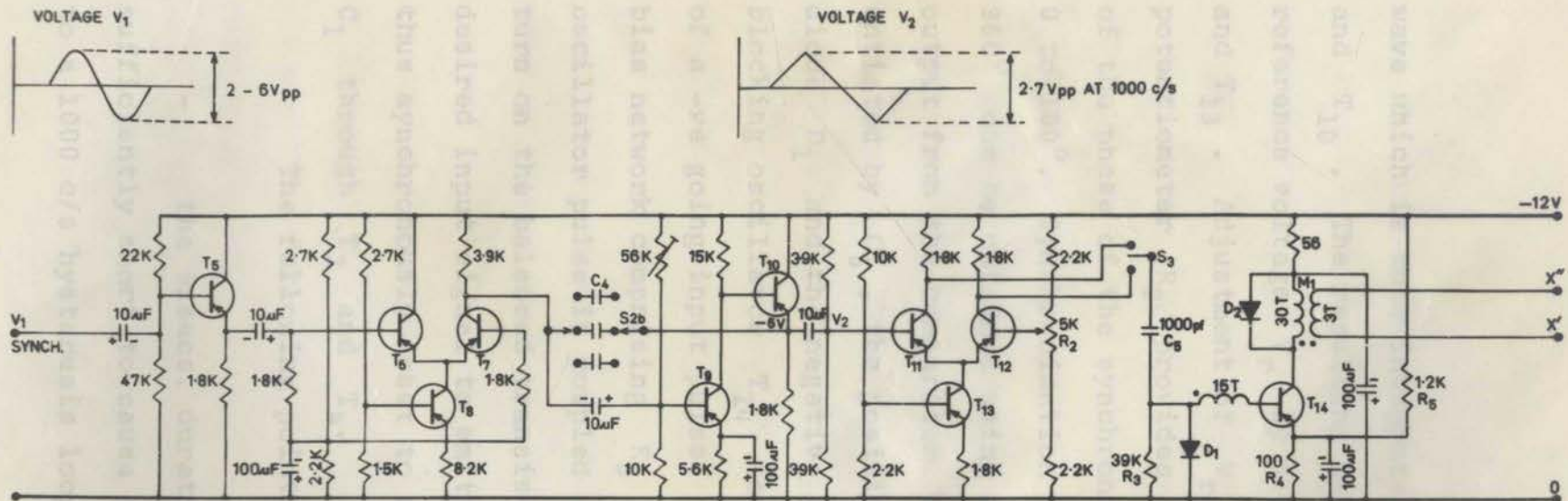


Fig. 8.72 The Variation of the rms Noise Reduction with the Fractional Restoration Efficiency  $\lambda$ .

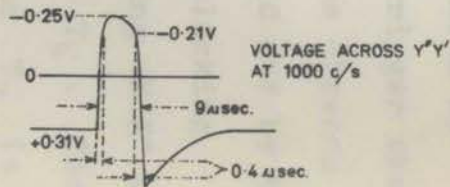


T<sub>1</sub> - T<sub>14</sub> OC 44  
 D<sub>1</sub> OA 73  
 D<sub>2</sub> OA 70

M<sub>1</sub> BLOCKING OSCILLATOR TRANSFORMER. CORE 0.45 in O.D. TOROID DUCON FERRAMIC H. THE 15 TURN BASE AND 30 TURN COLLECTOR WINDINGS ARE FORMED BY WINDING 3 WIRES TRI-FILAR TO GIVE THE TOTAL 45 TURNS. THE SECONDARY X'X'' IS 3 TURNS.

R <sub>1</sub>	C <sub>4</sub>	FREQUENCY RANGE (cps)
18 K	0.047μF	1000 - 500
39K	0.10 μF	500 - 200
82K	0.22 μF	200 - 100

FIG. 8-73 CIRCUIT DIAGRAM OF D.C. SYNCHRONOUS RESTORER



wave which is then integrated by the Miller integration  $T_9$  and  $T_{10}$ . The resulting triangular wave is compared with a reference voltage  $V_r$  by a second DC comparator  $T_{11}$ ,  $T_{12}$  and  $T_{13}$ . Adjustment of  $V_r$  by means of the front panel potentiometer  $R_2$  provides a continuous linear variation of the phase of the synchronization pulse over a range from  $0$  to  $180^\circ$ . Synchronization on the other half cycle  $180^\circ$  to  $360^\circ$  can be obtained using the switch  $S_3$ . The square wave output from the comparator  $T_{11}$ ,  $T_{12}$  and  $T_{13}$  is differentiated by  $C_5$ , the positive going spike suppressed by diode  $D_1$  and the negative going spike used to trigger the blocking oscillator  $T_{14}$  to the on state. In the absence of a -ve going input pulse,  $T_{14}$  is normally held off by the bias network comprising  $R_3$ ,  $R_4$  and  $R_5$ . The blocking oscillator pulse is coupled via a secondary winding "X'X" to turn on the balanced transistor chopper  $T_3$  and  $T_4$ . The desired input signal to emitter followers  $T_1$  and  $T_2$  is thus synchronously reset to zero by discharge of capacitor  $C_1$  through  $T_3$  and  $T_4$ .

The following points may be noted

- the  $9\mu\text{secs.}$  duration blocking oscillator pulse is sufficiently short to cause only a negligible interruption to a 1000 c/s hysteresis loop display. The DC load resist-

ance  $R_L$  across the signal output of the restorer must be not less than  $1\text{ M}\Omega$ , producing with the effective series capacitance  $C_1 C_2 / (C_1 + C_2) = 0.09\ \mu\text{F}$  a single low frequency pole at  $f \leq 1.8\text{ c/s}$ . The restorer must thus be included in the circuit when the overall phase shift of the amplifier and integration system is set to zero by the procedure outlined in Section 8.5. Switch  $S_1$  allows restoration to be used or not used as desired while leaving the frequency response unchanged. If the capacitor  $C_2$  is not used,  $R_L$  will cause an "undirectional" sag of the unclamped side of a waveform as illustrated in Fig. 8.74. Low frequency phase shift and undirectional sag will also be caused by the open circuit impedance of the chopper. The effect is difficult to analyse as the circuit is non-linear and the open circuit impedance increases rapidly with signal level. For the balance circuit used with the transistors in the "inverted" connection  $B1, C1$ , then the calculated open circuit impedance at  $25^\circ\text{ C}$  for ideal transistors obeying the equation of Ebers and Moll<sup>E1</sup> varies from  $0.5\text{ M}\Omega$  for signals  $< 25\text{ mV}$  to  $> 5\text{ M}\Omega$  for signals  $> 250\text{ mV}$ . For a practical transistor surface leakage effects across the collector to base junction will also contribute in the latter case. For the OC44 transistors used, measured saturated leakage currents

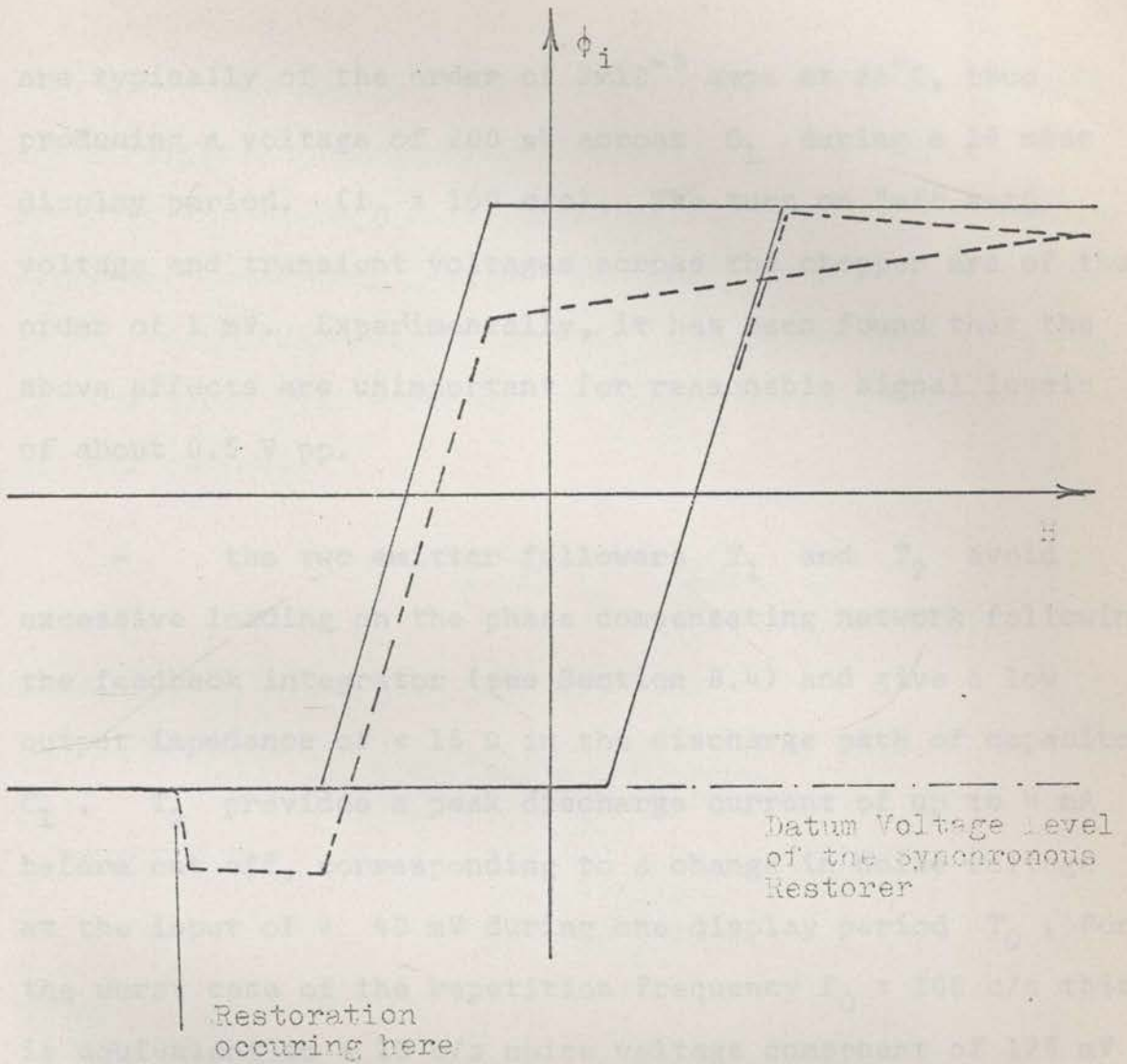


Fig. 8.74 Error in the Display of a Hysteresis Loop due to Unidirectional Sag occurring with Synchronous DC Restoration.

The dotted curve shows the error from the true response (represented by the solid line)

are typically of the order of  $2 \times 10^{-9}$  amps at  $25^\circ\text{C}$ , thus producing a voltage of  $200 \mu\text{V}$  across  $C_1$  during a 10 msec display period. ( $f_0 = 100 \text{ c/s}$ ). The turn on "off set" voltage and transient voltages across the chopper are of the order of 1 mV. Experimentally, it has been found that the above effects are unimportant for reasonable signal levels of about 0.5 V pp.

- the two emitter followers  $T_1$  and  $T_2$  avoid excessive loading on the phase compensating network following the feedback integrator (see Section 8.4) and give a low output impedance of  $< 15 \Omega$  in the discharge path of capacitor  $C_1$ .  $T_2$  provides a peak discharge current of up to 4 mA before cut off, corresponding to a change in noise voltage at the input of  $> 40 \text{ mV}$  during one display period  $T_0$ . For the worst case of the repetition frequency  $f_0 = 100 \text{ c/s}$  this is equivalent to a 10 c/s noise voltage component of 125 mV pp. The closed impedance of the chopper  $T_3$  and  $T_4$  is  $< 10 \Omega$  at all frequencies  $f_0$  giving with the  $15 \Omega$  output impedance of  $T_2$  and the  $0.1 \mu\text{F}$  capacitor  $C_1$  a time constant of  $\tau < 2.5 \mu\text{secs}$ . The discharge factor  $\lambda$  of Section 8.71 is thus  $\exp(-T_P/\tau) < 0.03$  for the  $T_P = 9 \mu\text{secs}$  duration discharge pulse used.



- the widely different on to off times of the blocking oscillator output requires the coupling network  $R_1, C_3$  by which the emitter base diodes of  $T_3$  and  $T_4$  themselves clamp the -ve going peak of the pulse to the correct DC level. Since the average current through the capacitor  $C_3$  must be zero, then equating the charge passing during the on and off periods,

$$T_F I_F = \frac{V_F - V_{be}}{r_{bb'}} T_F = \frac{V_R T_R}{R_1} = \frac{V - V_F}{R_1} T_R$$

giving

$$I_F = (V - V_{BE}) \frac{T_R}{T_R r_{bb'} + T_F R_1}$$

$$V_R = (V - V_{BE}) \frac{T_F R_1}{T_R r_{bb'} + T_F R_1} \quad (8.74)$$

where

$T_F, T_R$  are the on and off time, respectively,

$V_F, V_R$  are the on or forward voltage and the off or reverse voltage, respectively, applied across the external emitter to base terminals of transistors  $T_3$  and  $T_4$ .

$V$  is the total height of the pulse applied across X'X",

$I_F$  is the base current in the forward direction for both transistors,

$V_{EB'}$  is the voltage drop across the internal base emitter diode at the current  $I_F$ ,  $r_{bb'}$  being considered as part of the external circuit,

$r_{bb'}$  is the extrinsic base resistance of transistors  $T_3$  and  $T_4$  considered together.

The circuit has been designed with  $V_{BE} < V$  and  $T_R r_{bb'} < T_F R_1$ , so that the forward current  $I_F$  is almost independent of transistor properties and varies inversely as the resistance  $R_1$ .  $R_1$  is switched to give an approximately constant  $I_F$  of 1.3 mA per transistor over the operating frequency range 0.1 to 1.0 Kc/s.

- Care has been taken with the pulse circuitry to ensure a stable synchronization pulse with less than 0.6  $\mu$ secs. jitter and 0.5  $\mu$ secs. drift per hour at 1000 c/s under normal room conditions. Excessive jitter can introduce more apparent noise into an oscilloscope display than without restoration at all. The constant current DC comparators used have been found to give a particularly stable pick off point. The triangular waveform of  $V_2$  gives a constant stability over the full range 0 to 180° of the phase of the synchronizing pulse. The pulse waveforms in the various parts of the

circuit have been made as large as possible to ensure accurate comparison and reliable triggering of the blocking oscillator. Capacitor  $C_4$  is switched so that  $V_2$  is approximately of maximum amplitude at all operating frequencies. The amplitude of the input synchronizing signal effects only the operation of the comparator  $T_6$ ,  $T_7$  and  $T_8$ . Signals from 2 to 6 V pp. are most suitable, although the circuit will operate down to 0.4 V pp.

## 8.8 LIST OF REFERENCES

- E1 Ebers, J.J., Moll, J.L.,  
"Large Signal Behaviour of Junction Transistors".  
Proc.Inst.Radio Engrs., 42, 1761, (1954).
- O1 Oguey, H.J.,  
"Sensitive Flux Measurement of Thin Magnetic Films".  
Rev.Sci.Instrum., 31, 701, (1960).
- Z1 Van der Ziel, A.,  
"Noise".  
Prentice-Hall Inc., New York, p. 262, (1954).
- experimental set up is outlined in Section 9.2. In particular, Section 9.22 describes the electron bombardment evaporation source and gives results on the feedback stabilization of the deposition rate. Section 9.3 contains circuits for a film thickness and deposition rate monitor based on measurement of the film conductivity. An excellent review of the critical variation of film properties with the conditions of deposition has been given by Behrmd<sup>24</sup> who has discussed the effects of the substrate surface, substrate temperature, deposition rate, and impurities from the residual atmosphere and the evaporation source.

## 9.2 THE EXPERIMENTAL SETUP

The films were evaporated in a standard metal- $I$  in- $oil$  diffusion pump system (Apixion 5) by electron bombardment of the molten tip of an 81 per cent Ni, 19 per cent Fe

## CHAPTER 9

## THE VACUUM EVAPORATION OF THE FILM SAMPLES

## 9.1 INTRODUCTION

The present chapter describes the vacuum evaporation of the film samples used in this thesis and certain of the equipment constructed for this purpose. The general experimental set up is outlined in Section 9.2. In particular, Section 9.22 describes the electron bombardment evaporation source and gives results on the feedback stabilization of the deposition rate. Section 9.3 contains circuits for a film thickness and deposition rate monitor based on measurement of the film conductivity. An excellent review of the critical variation of film properties with the conditions of deposition has been given by Behrndt<sup>B4</sup> who has discussed the effects of the substrate surface, substrate temperature, deposition rate, and impurities from the residual atmosphere and the evaporation source.

## 9.2 THE EXPERIMENTAL SETUP

The films were evaporated in a standard metal 2 in. oil diffusion pump system (Apiezon B) by electron bombardment of the molten tip of an 81 per cent Ni, 19 per cent Fe

alloy rod.\* Photographs are given of the vacuum system and associated control equipment in Fig. 9.21 with details of the evaporation unit inside the bell jar in Fig. 9.22. The system has no liquid nitrogen trap, the limiting pressure being  $10^{-5}$  mm Hg rising to  $10^{-4}$  mm Hg at the end of an evaporation. Deposition rates up to  $5 \text{ \AA sec}^{-1}$  could be obtained, being held constant by the feedback control described in Section 9.22. The large Helmholtz coils surrounding the bell jar apply an orientating field of 75 oe during evaporation, uniform to 1 per cent over the substrate area. A curved metal shutter, seen just below the substrate holder at the top of Fig. 9.22, covers film bit positions 1 to 6 and 13 to 18 (the classification system is given in the following section). The shutter is magnetically operated via a soft iron plunger inside a thin walled metal tube sealed through the base plate. The actuating solenoid is wound around this tube and is outside the vacuum system.

---

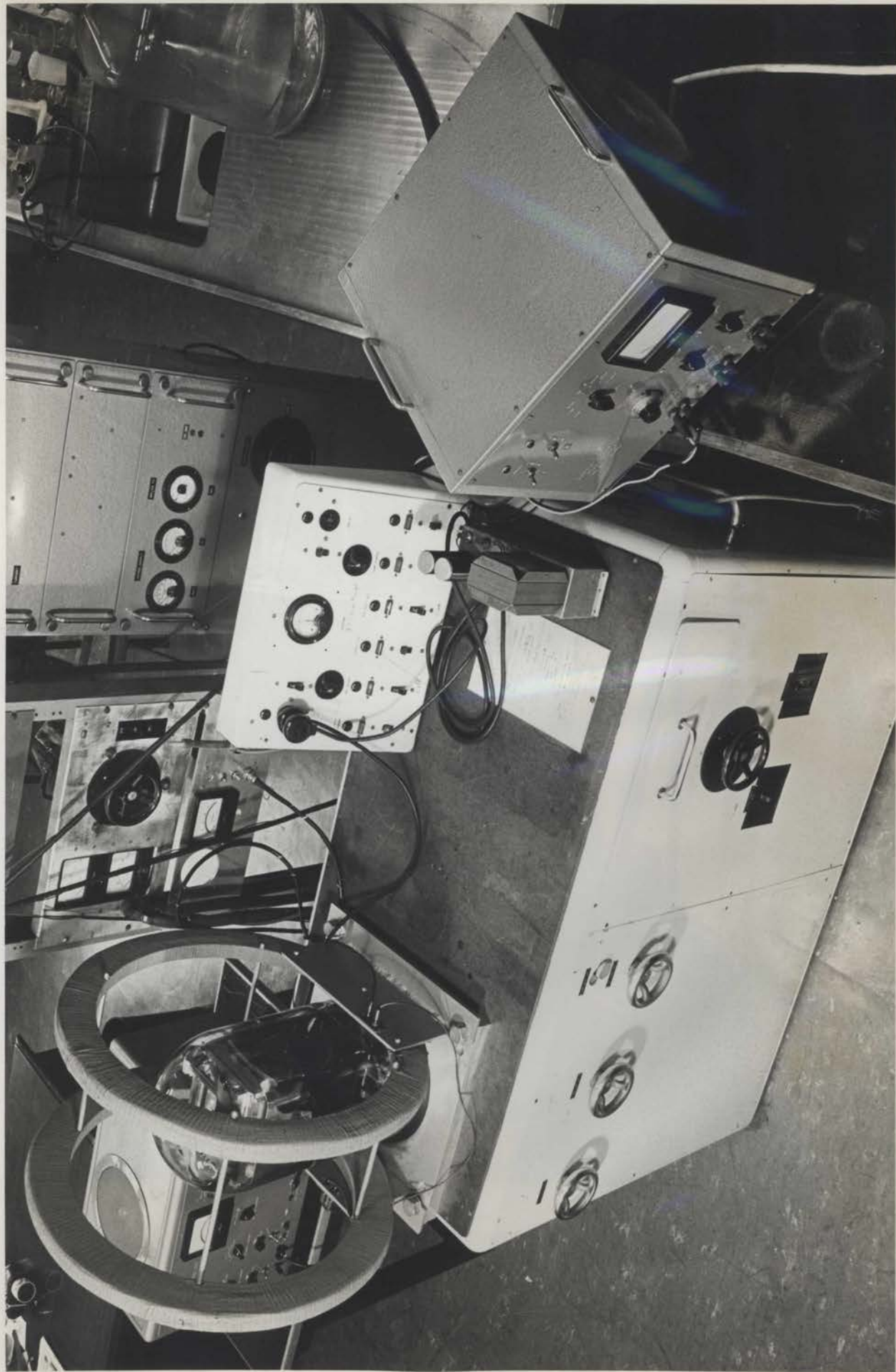
\* Supplied by H. Wiggins and Co. (England), percentage impurities C<0.01, Si<0.01 and S<0.001.

---

Photographs are given of the vacuum system and associated control equipment in Fig. 9.21 with details of the evaporation unit inside the bell jar in Fig. 9.22. The system has no liquid nitrogen trap, the limiting pressure being  $10^{-2}$  mm Hg rising to  $10^{-4}$  mm Hg at the end of an evaporation. Deposition rates up to  $5 \text{ \AA sec}^{-1}$  could be obtained being held constant by the feedback control described in Section 9.22. The large Helmholtz coils surrounding the bell jar apply an orientating field of 75 oe during evaporation, uniform to 1 per cent over the substrate area. A curved metal shutter, seen just below the substrate holder at the top of Fig. 9.22, covers film slit positions 1 to 5 and is to fit classification system is given in the following section. The shutter is magnetically operated via a soft iron plunger inside a thin walled metal tube sealed through the base plate. The actuating solenoid is wound around this tube and is outside the vacuum system.

Supplied by H. Wiggin and Co. (England), percentage  
 0.01, 0.01 and 0.001.

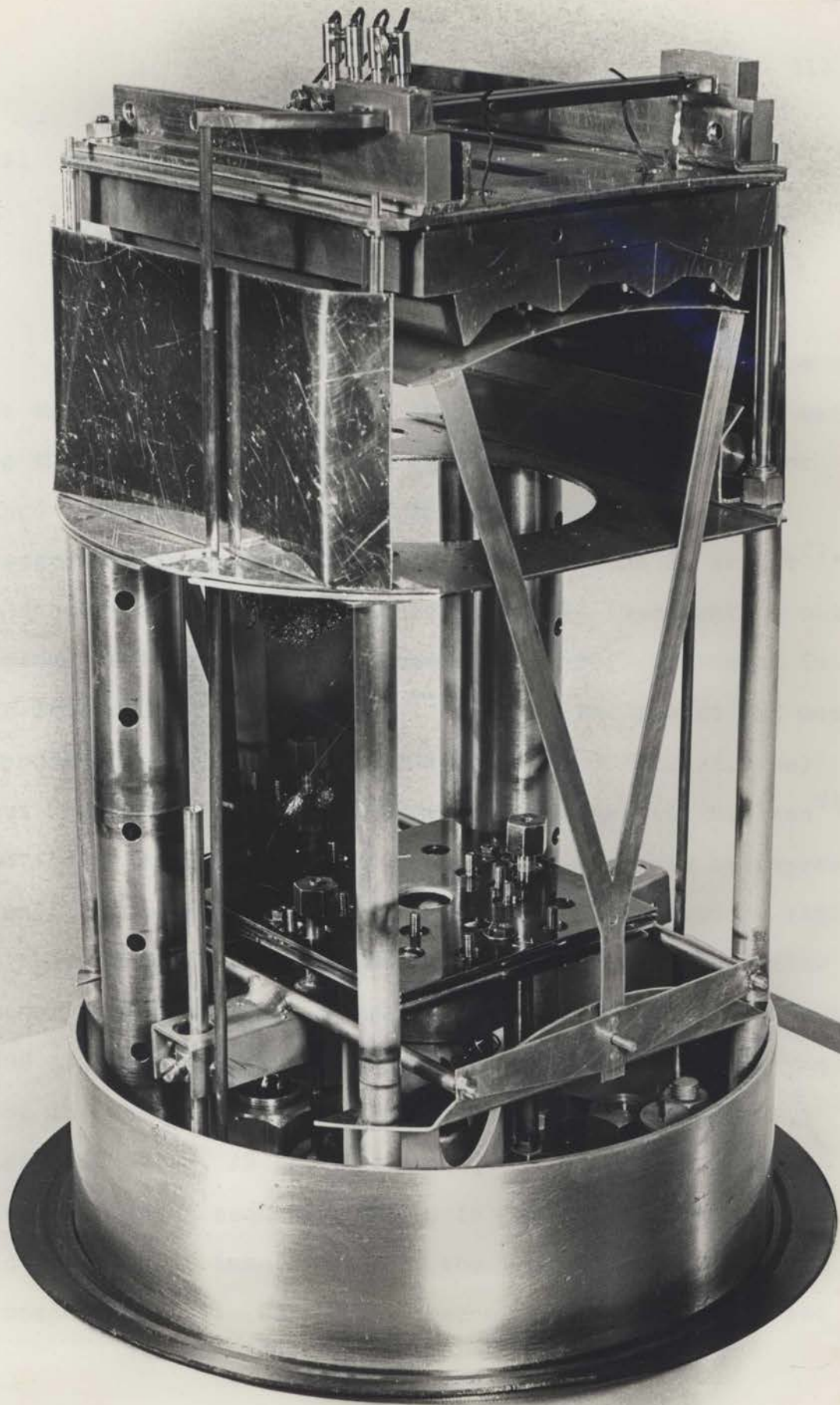
Fig. 9.21 The Vacuum System and Associated Control Equipment.





511

Fig. 9.22 Details of the Evaporation Unit inside the Bell Jar.



## 9.21 The Substrate


## Classification of Bit Positions and Bit to Bit

## Variations in Anisotropy and Thickness

3 in x 1 in soft glass microscope slides were used as the substrate. These have a thermal expansion closely matching that of permalloy with a very smooth surface. Short range roughness is less than  $10 \text{ \AA}$  <sup>W1, W2</sup> with occasional irregularities up to  $1000 \text{ \AA}$  and a few microns in extent <sup>C2, S5</sup>. As discussed by Behrndt <sup>B2</sup> it is extremely important to obtain a clean surface. Cleaning procedures for glass abound in the literature <sup>S1, H1, M2, B2, P1, N1, L1, B6</sup>. The lowest and most reproducible values of  $H_K$  (2-3 oe) and  $H_C$  (1.5-2.0 oe) have been given by the vacuum melting process of Nielsen <sup>N1</sup> and it is probable that his results can scarcely be improved upon. In the present work a simple washing procedure similar to that of Metzger <sup>M2</sup> was adopted and found to give satisfactory results ( $H_K$ , 2.5-4.0 oe,  $H_C$ , 2-3 oe for films near  $1000 \text{ \AA}$ ). The slides were scrubbed using tongs and cotton wool in a boiling filtered detergent solution (Teepol), distilled water, AR grade acetone, distilled water and distilled water sequence, dried in a radiant heating oven and transferred immediately to the vacuum system to avoid atmospheric dust. Glow discharge cleaning was also tried

but gave no discernable improvement and was thereafter discontinued.

The resistance heated substrate holder may be seen at the top of Fig. 9.22. The slides were clamped inside the holder under spring pressure, at a source to substrate distance of 9 ins. They were normally held at  $300^{\circ}\text{C} \pm 5^{\circ}\text{C}$  during deposition, as measured by a Degussa platinum resistance thermometer inside the substrate holder block. Fifteen film bits of 1 cm diameter circles were deposited simultaneously through 0.015 in thick metal masks pressed against the substrate surface, the edges of the holes being taped at  $30^{\circ}$ . Only the areas of the slides showing through these holes were exposed to an environment other than at the temperature of the substrate holder, so that it may be expected that the surface temperature will not differ greatly from that of the holder. Measurements using a Taylor-Hobson Talysurf Model 2 indicate sharp edges rising to 95 per cent of the full thickness in approximately 0.0005 in. The method of classifying bit positions (corresponding to the numbering of the film samples in Section 4) is shown in Fig. 9.23, together with angles of incidence of the depositing vapour and experimental data on the typical  $H_K$  and thickness variation found from bit to bit. The thickness distribution results from the

$H_{ki}$  Thickness  $\lambda^\circ$   $\uparrow$  Aligning Field.  
 $H_C$   Easy Axis Skew

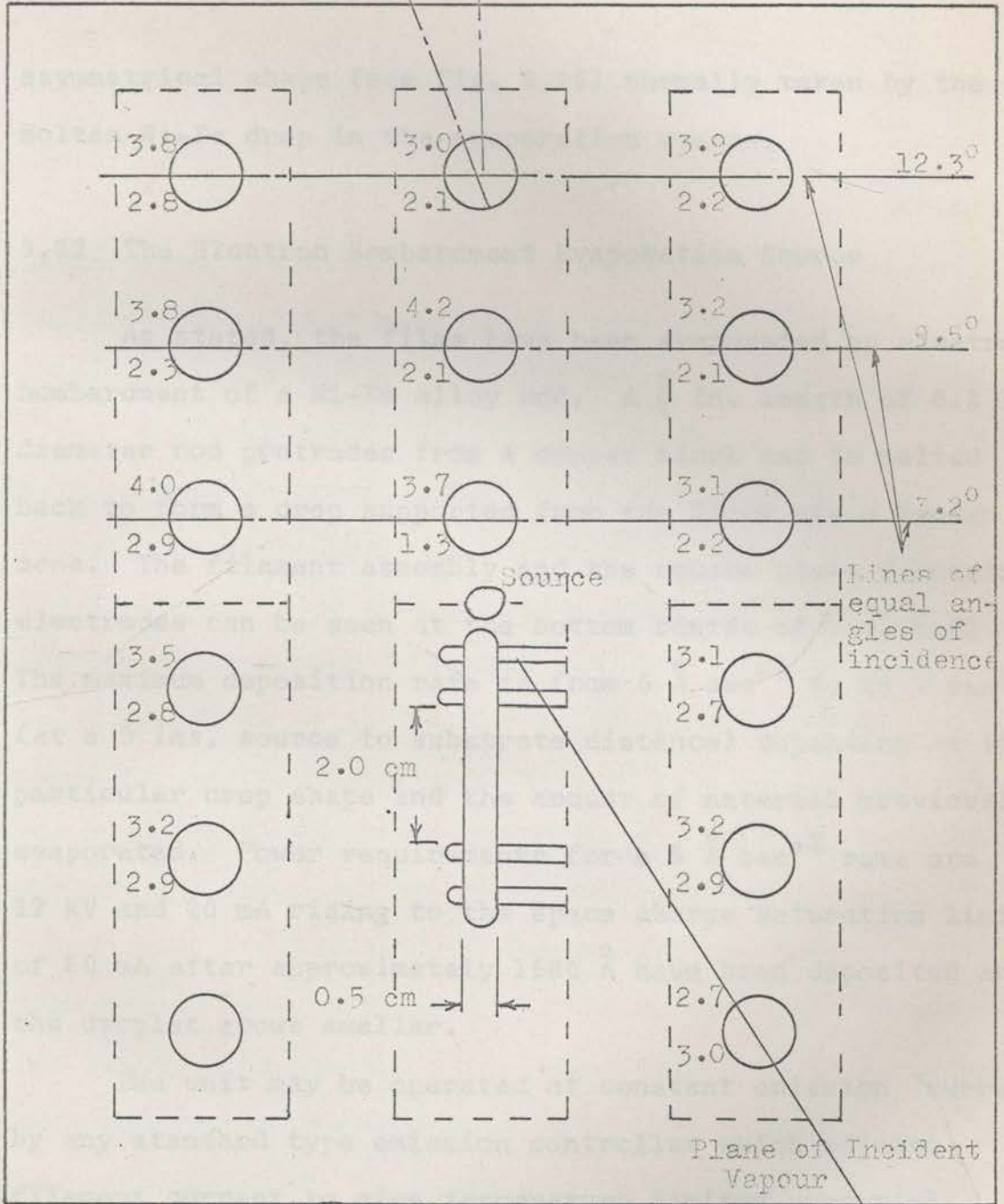


Fig. 9.23 The Positions and Method of Classifying Bit Positions.

Typical Experimental Variations of  $H_{ki}$ ,  $H_C$ , Thickness and Easy Axis Skew from Bit to Bit.

asymmetrical shape (see Fig. 9.25) normally taken by the molten Ni-Fe drop in the evaporation source.

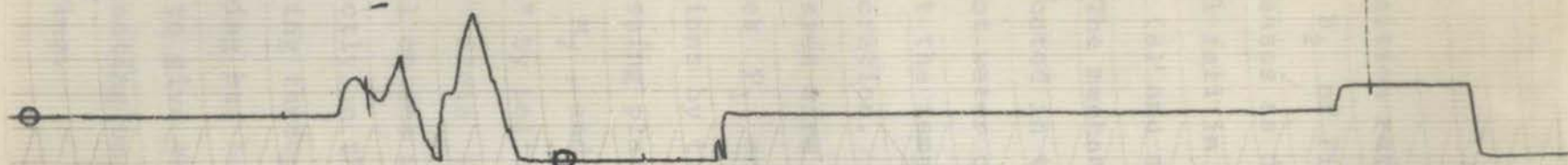
### 9.22 The Electron Bombardment Evaporation Source

As stated, the films have been evaporated by electron bombardment of a Ni-Fe alloy rod. A  $\frac{3}{4}$  in. length of 0.1 in. diameter rod protrudes from a copper block and is melted back to form a drop supported from the block via a frozen zone. The filament assembly and the square plate focussing electrodes can be seen at the bottom centre of Fig. 9.22. The maximum deposition rate is from  $5 \text{ \AA sec}^{-1}$  to  $10 \text{ \AA sec}^{-1}$  (at a 9 ins. source to substrate distance) depending on the particular drop shape and the amount of material previously evaporated. Power requirements for a  $5 \text{ \AA sec}^{-1}$  rate are 12 kV and 20 mA rising to the space charge saturation limit of 60 mA after approximately  $1500 \text{ \AA}$  have been deposited and the droplet grows smaller.

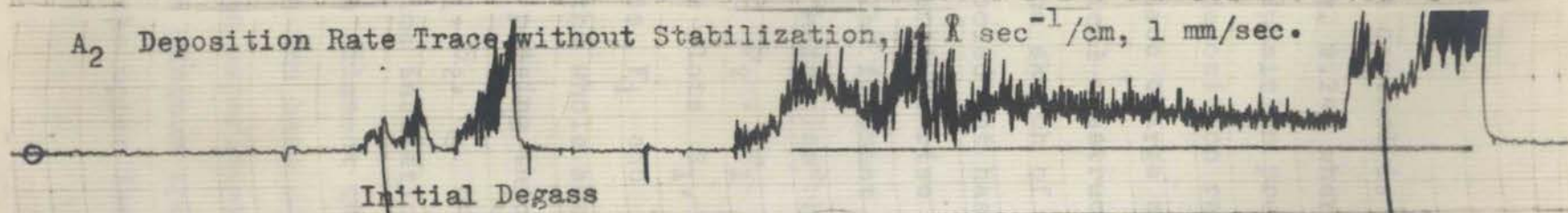
The unit may be operated at constant emission current by any standard type emission controller which adjusts filament current to give temperature limited operation (filament requirements, 8A, 10V). A transistorized emission controller was constructed for this purpose during the present work and may be seen at the far left of Fig. 9.21).

With constant emission current, appreciable variations in the evaporation rate occur. Typical fluctuations are shown in the recorder trace  $A_2$  of Fig. 9.24. As deposition rate is an important parameter in determining film properties, it is desirable that it should be held constant. Section 9.3 describes a deposition rate monitor based on measurement of the film electrical conductivity. Stabilization of the deposition rate is readily accomplished by feeding back the monitor voltage in series with the reference voltage (in this case a 1.3 V mercury cell) of the emission controller. A double loop feedback system is formed similar to the type discussed in Appendix B. The outer feedback loop through the rate monitor contains time constants due to the closed loop response of the emission controller ( $<0.02$  secs, 3 db point 8 c/s), the rate monitor itself ( $<0.02$  secs, 3 db point 8 c/s) and the thermal time constant of the evaporation source (0.4 secs, 3 db point 0.4 c/s). Any open loop transfer function attenuated at 6 db per octave to give unity loop gain near 3 c/s provides an adequate phase margin of  $45^\circ$ . In the present system the simplest course has been adopted; no other time constants have been introduced and the open loop gain from DC to 0.4 c/s made equal to 8. Clearly, as discussed in Appendix B, this may be increased at frequencies  $f < 0.4$  c/s to the value  $3/f$  if desired. The effect of the

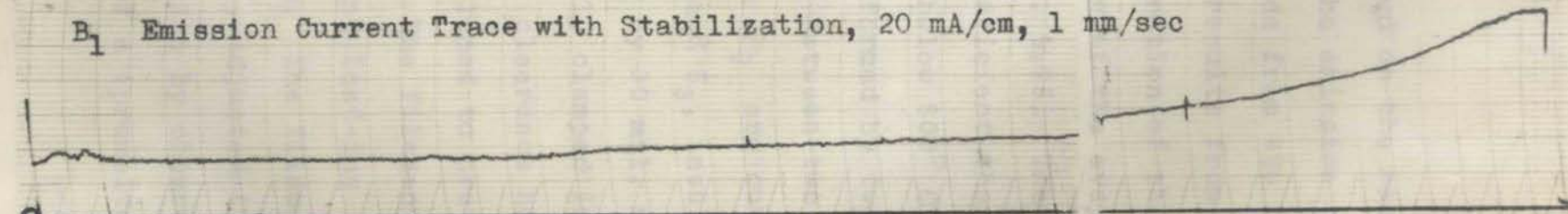
A<sub>1</sub> Emission Current Trace, 20 mA/cm, 1 mm/sec.



A<sub>2</sub> Deposition Rate Trace without Stabilization, 4 Å sec<sup>-1</sup>/cm, 1 mm/sec.



B<sub>1</sub> Emission Current Trace with Stabilization, 20 mA/cm, 1 mm/sec



B<sub>2</sub> Deposition Rate Trace with Stabilization, 4 Å sec<sup>-1</sup>/cm, 1 mm/sec.

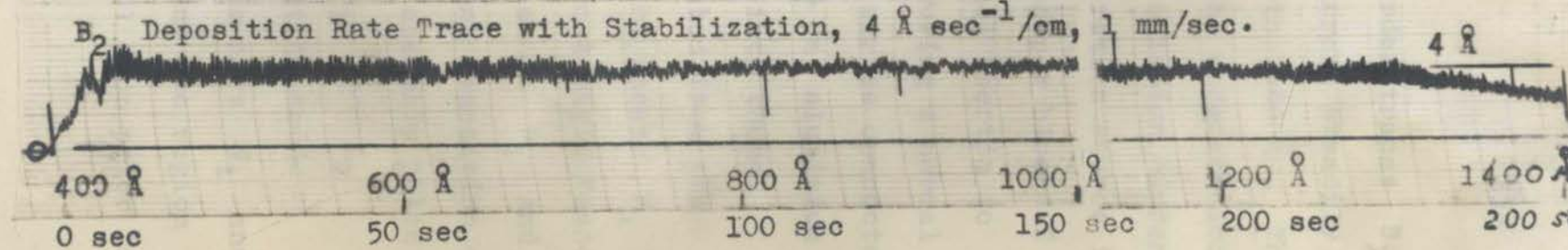


Fig 9.24 RECORDER TRACES SHOWING THE FEEDBACK STABILIZATION OF THE DEPOSITION RATE



deposition rate control is shown on the recorder traces  $B_1$  and  $B_2$  of Fig. 9.24, where the emission current steadily increases as deposition proceeds from 400 Å to 1400 Å. The final fall in deposition rate results from the moderate loop gain (8) and space charge saturation of the emission current.

The mechanical construction of the evaporation source is indicated in the sketch of Fig. 9.25. The copper block C is not water cooled but has sufficient thermal inertia to limit the temperature rise to below 500° C during a normal evaporation. The filament is formed by two series connected tungsten wire "hair pins" held between two  $\frac{1}{8}$  in. aluminium plates  $P_1$  and  $P_2$ .  $P_1$  and  $P_2$  are cut into three sections by the slots  $S_1$ ,  $S_2$  and  $S_3$ , insulated from the focussing plates  $F_1$  and  $F_2$  by 30 mil. mica sheets  $M_1$  and  $M_2$ , and the whole assembly clamped into a rigid "sandwich" by bolts passing through clearance holes in  $P_1$  and  $P_2$ . Slots  $S_1$ ,  $S_2$ ,  $S_3$  are sloped to prevent deposition of metal on the mica insulation. The filament assembly bolts directly on the filament current lead-ins  $L_1$  and  $L_2$  passing through the base plate. The filament to anode spacing has been experimentally adjusted (via nuts  $N_1$  and  $N_2$ ) to give the minimum spot size by observing the region of heating on the upper face of a (premelted) drop prior to melting.

We may add a few general comments on evaporation sources. The relative merits of different types, the tungsten filament, the induction heated crucible and others have been discussed by Thun<sup>T1</sup> and by Prutton<sup>P2</sup>. Melting by electron bombardment approaches the requirements of an ideal source. The electron beam can be focussed on a small spot on the surface of the evaporant, giving minimum heating and outgassing of the system. Filament or crucible contamination<sup>A1</sup> can be avoided by supporting the molten zone on its own surrounding solid material. This may be done by melting a pool in a large solid piece, as a pendant drop from the end of a rod<sup>H8,K1</sup>, or, as in the present case, via a frozen zone from a cooled copper tip or hearth<sup>M1,H3,H4,H5,H7</sup>. In the present work it has been found that a pendant drop melts back along the rod at deposition rates greater than about  $1 \text{ \AA sec}^{-1}$ , requiring the supporting copper block for higher values. Higher rates could be obtained in an arrangement in which the drop hangs vertically downwards, however, then there is difficulty with accumulating dust and dirt falling on the substrate. Similar results have been reported by Holland and Laurenson<sup>H4</sup>. In recent years small electron bombardment evaporations of varying degrees of complexity (water cooled anode, self-focussing guns) suitable for laboratory use have been described by a large number of

workers<sup>S3,U1,T2,C3,H10,E1,M4,V1</sup>. The present unit represents a very simple design. Electron beams have extended rapidly into industry and are used for large scale melting<sup>G2</sup>, welding<sup>M5</sup> and other operations<sup>B5</sup>. A useful review of this aspect has been given by Candidus et al<sup>C1</sup>.

### 9.23 The Operating Procedure

For each evaporation the following operating procedure has been adopted. The system is initially allowed to pump down for 12 hrs with the shutter closed (covering bits 1-6, 13-18 but not 7-9 or the thickness monitoring slide) and the substrate heater at 350°C.

The sample rod and the copper block require careful outgassing. The rod is outgassed progressively for 5 minutes at 12 kV, 1 mA, 2 mA and 3 mA. At a little above 3 mA the rod bends over and melts into a drop on the top of the rod. The current is gradually increased over a 5 minute interval to 20 mA and the drop melted down to sit on the copper block. The block is outgassed by lowering the current to 10 mA for 15 minutes. The power is insufficient to cause appreciable evaporation, but over a 15 minute period raises the block to a dull red heat. Outgassing is completed by raising the current in short bursts to 30 or 40 mA. Part of such an

initial degas is shown in the recorder trace  $A_2$  of Fig. 9.24. About 400 Å of film have evaporated at this stage. The evaporation source is allowed to cool for 1 hour during which the substrate heater is lowered to the temperature required during evaporation (normally 300°C).

The final evaporation may now be carried out. The required evaporation rate may be set either manually or automatically as described in Section 9.22. The shutter is opened when the rate has been obtained and closed again after the required film thickness is deposited. Again, this may be done manually by observing the thickness monitor, or automatically by the control described in Section 9.3 which opens and closes the shutter at two preset film thicknesses.

### 9.3 A FEEDBACK FILM THICKNESS AND DEPOSITION RATE CONTROL

Methods of determining film thickness and deposition rate may be divided into

- methods measuring the total film thickness at any moment. This may be done by measuring electrical conductivity, total magnetization, optical reflectivity or transmission<sup>S4,W3</sup>, or by mass determinations using microbalances<sup>V1,H9</sup>, or the resonant frequency shift of a quartz

crystal<sup>B3,L2</sup>.

- rate measuring methods. This may be done by measuring the momentum of the vapour impinging on a microbalance<sup>H9</sup>, or by placing an ionization gauge in the vapour stream<sup>M2,G1,S2</sup>.

With the former group the evaporation rate is obtained by differentiation, in the latter the total film thickness is obtained by integration.

In the present work the total thickness has been monitored by a four terminal measurement of the electrical conductivity. The measurement was made by evaporating a strip of film over silver tabs fired on a microscope slide in the pattern shown in Fig. 9.23, the slide being held in the substrate holder (normally at 300°C). The conductivity of Ni-Fe films may be expected to be accurately proportional to thickness after the first few hundred Å<sup>H6</sup>. The moderate temperature and compositional variations of conductivity (0.3 per cent per °C and -3 per cent per per cent Ni, in the range near 300°C and 81 per cent Ni, 19 per cent Fe) make this an acceptable measure of thickness under fixed deposition conditions.

A suitable circuit for the conductivity measurement is given in Fig. 9.31. Transistors  $T_1$  to  $T_6$  form a



THE INTER-UNIVERSITY COUNCIL  
FOR HIGHER EDUCATION OVERSEAS

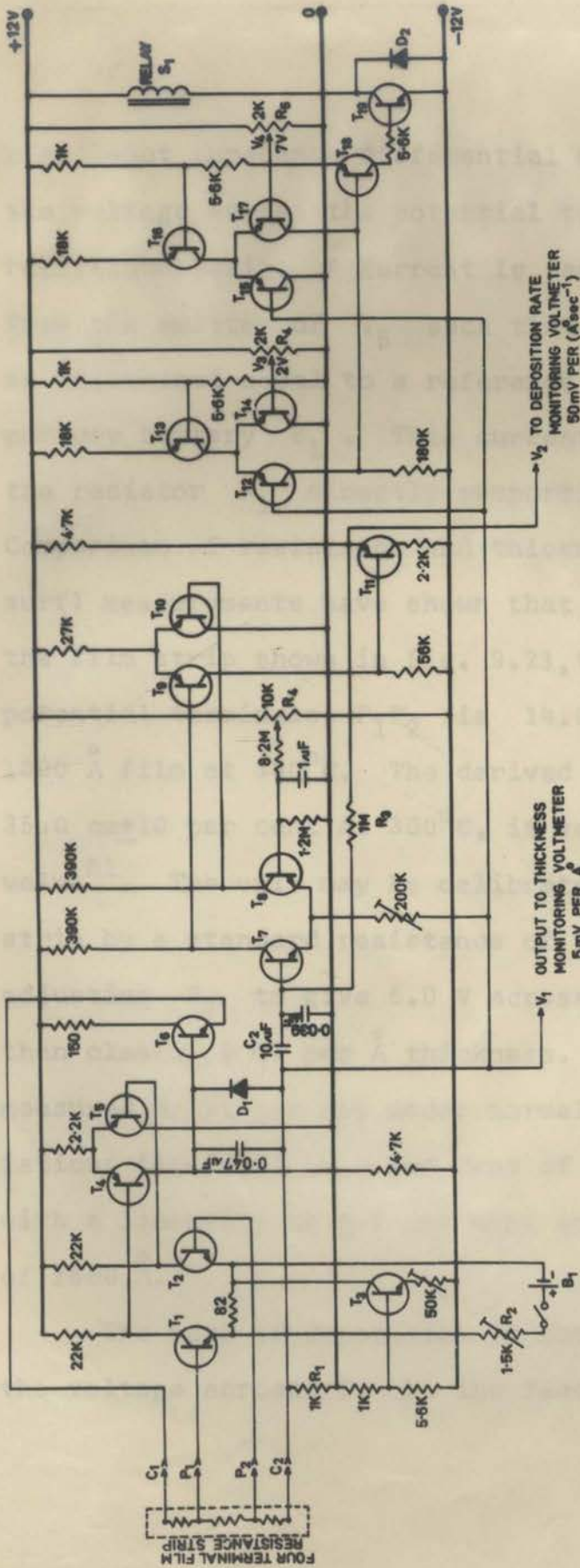
29 Woburn Square, London, W.C.1

Telephone: MUSEUM 8916

Telegrams: Interuniv London W.C.1

*[Faint handwritten notes in the top left margin, including numbers and illegible text.]*

*[Extensive handwritten notes covering the bottom half of the page, including names, dates, and various annotations.]*



- T<sub>1,2,7,8</sub> - STC TK 254 A
- T<sub>4,5,9,10,11</sub> - OC 44
- T<sub>3,19</sub> - 2N647
- D<sub>1,2</sub> - OA 200
- S<sub>1</sub> RELAY OPERATE 35mA, 24V; NON OPERATE 5mA.
- B<sub>1</sub> MERCURY CELL 1.35V

FIG. 9-31 A FILM THICKNESS AND DEPOSITION RATE CONTROL



high input impedance differential DC amplifier which measures the voltage across the potential terminals  $P_1P_2$  of the film resistance strip. A current is passed through the strip from the emitter of  $T_6$  such that the voltage across  $P_1P_2$  is maintained equal to a reference voltage derived from the mercury battery  $B_1$ . This current produces a voltage across the resistor  $R_1$  directly proportional to the film thickness. Comparison of resistance and thickness (Taylor-Hobson Taly-surf) measurements have shown that, for the proportions of the film strip shown in Fig. 9.23, the resistance between the potential terminals  $P_1P_2$  is  $14.0\Omega \pm 10$  per cent for a  $1000 \text{ \AA}$  film at  $300^\circ\text{C}$ . The derived value of resistivity,  $35\mu\Omega \text{ cm} \pm 10$  per cent at  $300^\circ\text{C}$ , is very close to the bulk value<sup>B1</sup>. The unit may be calibrated by replacing the film strip by a standard resistance of  $14.0\Omega$  across  $P_1P_2$  and adjusting  $R_2$  to give  $5.0 \text{ V}$  across  $R_1$ . The sensitivity is then clearly  $5 \text{ mV}$  per  $\text{\AA}$  thickness. With these settings the measured drift per day under normal room temperature variations ( $10\text{-}15^\circ\text{C}$ ) is 2 per cent of the thickness reading with a linearity of  $\pm 2$  per cent up to a maximum thickness of  $1600 \text{ \AA}$ .

The rate of deposition is obtained by differentiating the voltage across  $R_1$  by the feedback differentiating

circuit  $T_7$  to  $T_{11}$ . A balanced input stage using silicon planar transistors reduces drift and the output voltage is set to zero by the potentiometer  $R_4$ . The high frequency departure from perfect differentiation, caused by the time constant of  $C_1$  with  $R_1$  and the feedback input impedance of the differentiator, occurs at 9 c/s. The time constant  $C_1 R_3 = 10$  secs. gives an output sensitivity of 50 mV per  $\text{\AA} \text{ sec}^{-1}$ . Short time fluctuations over 1 minute intervals are less than  $\pm 0.02 \text{\AA} \text{ sec}^{-1}$  with a drift per day under normal room temperature variations of  $\pm 0.5 \text{\AA} \text{ sec}^{-1}$ .

Transistors  $T_{12}$  to  $T_{19}$  form an automatic control to open and close the shutter at any two preset film thicknesses. The voltage  $V_1$  is fed to the two DC comparators  $T_{12}$ ,  $T_{13}$ ,  $T_{14}$  and  $T_{15}$ ,  $T_{16}$ ,  $T_{17}$ . The reference voltages  $V_3$  and  $V_4$  are normally set, by the potentiometers  $R_4$  and  $R_5$ , at 2 V and 7 V corresponding to thicknesses of 400  $\text{\AA}$  and 1400  $\text{\AA}$ . For  $V_1 < V_3 < V_4$ ,  $T_{12}$  is on,  $T_{17}$  is off; for  $V_3 < V_1 < V_4$ , both  $T_{12}$  and  $T_{17}$  are off; for  $V_3 < V_4 < V_1$ ,  $T_{14}$  is on,  $T_{15}$  is off. If both  $T_{12}$  and  $T_{17}$  are off, then  $T_{18}$  is on, otherwise  $T_{18}$  is always off. The relay  $S_1$ , used to operate the shutter solenoid (see Section 9.2), is thus energized only during the period  $V_3 < V_1 < V_4$  when the shutter is to be held open. The circuit operates with a dead

band less than  $3 \text{ \AA}$  independent of the characteristics of the relay  $S_1$ . The drift per day under normal room temperature variations is  $< \pm 3 \text{ \AA}$ .

Suitable + and - 12 V regulated supplies for the above circuitry are given in Appendix B.

82. ~~Barrett, R.H.,~~  
 "Influence of Substrate Temperature on the Surface Properties and Reproducibility of Evaporated Nickel Iron Films",  
 J. Appl. Phys. (Suppl.), 30, 2759, (1959).
83. ~~Barrett, R.H., Tapp, E.W.,~~  
 "Control of Deposition Rate and Film Thickness with the Crystal Oscillator",  
 Trans. Seventh Vacuum Symposium, American Vacuum Soc., p. 97, (1960).
84. ~~Barrett, R.H.,~~  
 "The Influence of the Deposition Parameters on the Properties of Evaporated Thin Ferromagnetic Films",  
 Trans. Eighth Vacuum Symposium, American Vacuum Soc., p. 317, (1960).
85. ~~Day, L.B., Crandall, G., Lerch, H.,~~  
 "Contribution to the Problem of Electron Beam Design for Melting, Welding, Evaporation and Drilling Processes",  
 Trans. Ninth Vacuum Symposium, American Vacuum Soc., p. 217, (1961).
86. ~~Bartelme, R.,~~  
 "Effect of Substrate Temperature on the Properties of Evaporated Nickel Iron Films",  
 J. Appl. Phys., 33, 2476, (1962).
87. ~~Candlish, E.F., Holliman, M.H., Hoehner, E.,~~  
 "Electron Beams in Vacuum Processes",  
 Trans. Sixth Vacuum Symposium, American Vacuum Soc., p. 186, (1959).

## 9.4 LIST OF REFERENCES

- A1 Astwood, P., Prutton, M.,  
"The Influence of Crucible Material upon the Magnetic Anisotropy of Evaporated Permalloy Films".  
Brit.J.Appl.Phys., 14, 48, (1963).
- B1 Bozorth, R.M.,  
"Ferromagnetism",  
D. Van Nostrand Company Inc., New York, p. 107, (1951).
- B2 Behrndt, K.H., Maddocks, F.S.,  
"Influence of Substrate Processing on the Magnetic Properties and Reproducibility of Evaporated Nickel Iron Films".  
J.Appl.Phys.( Suppl.), 30, 276S, (1959).
- B3 Behrndt, K.H., Tone, R.W.,  
"Control of Deposition Rate and Film Thickness with the Crystal Oscillator".  
Trans. Seventh Vacuum Symposium, American Vacuum Soc., p.87, (1960).
- B4 Behrndt, K.H.,  
"The Influence of the Deposition Parameters on the Properties of Evaporated Thin Ferromagnetic Films".  
Trans. Eighth Vacuum Symposium, American Vacuum Soc., p. 912, (1960).
- B5 Bas, E.B., Cremosnik, G., Lerch, H.,  
"Contribution to the Problem of Electron Beam Design for Melting, Welding, Evaporation and Drilling Processes".  
Trans. Eighth Vacuum Symposium, American Vacuum Soc., p. 817, (1961).
- B6 Bertelsen, B.I.,  
"Silicon Monoxide Undercoating for Improvement of Magnetic Film Memory Characteristics".  
J.Appl.Phys., 33, 2026, (1962).
- C1 Candidus, E.S., Hablanian, M.H., Steinherz, H.A.,  
"Electron Beams in Vacuum Processes".  
Trans. Sixth Vacuum Symposium, American Vacuum Soc., p. 185, (1959).

- C2 Calbrich, C.J.,  
"Electron Microscopy of Glass and Quartz Substrate  
Surface for Thin Films".  
Trans. Eighth Vacuum Symposium, American Vacuum Soc.,  
p. 1013, (1961).
- C3 Chornik, B., Grunbaum, E.,  
"Electron Bombardment Apparatus for a High Vacuum Evap-  
oration Plant".  
J.Sci.Instrum. 39, 574, (1962).
- E1 Erskine, J.R., Gemmel, O.S.,  
"The Evaporation of Self Supporting Boron Films".  
Nuclear Instrum. and Methods, 24, 397, (1963).
- G1 Giedd, G.R., Perkins, M.H.,  
"Evaporation Rate Monitor".  
Rev.Sci.Instrum., 31, 773, (1960).
- G2 Gruber, H., Stephan, H., Dietrich, W., Lesser, R.,  
"Electron Beam Melting with Multiple Guns".  
Trans. Eighth Vacuum Symposium, American Vacuum Soc.,  
p. 722, (1961).
- H1 Holland, L.,  
"Surface Cleaning".  
Chapman and Hall Ltd., London, p. 70, (1956).
- H2 Holland, L.,  
"Electron Bombardment Heating".  
Chapman and Hall Ltd., London, p. 135, (1956).
- H3 Holland, L., Laurenson, L., Holden, J.T.,  
"A New Type of Titanium Getter Pump".  
Nature 182, 851, (1958).
- H4 Holland, L., Laurensen, L.,  
"Proc. Symposium on Electron Bombardment Floating Zone  
Melting and Applied Electron Bombardment Techniques".  
Research Report, Services, Electronics Research Lab-  
oratory, Baldock, Herts., England, No. M.80, p.59, (1959).
- H5 Hart, D.M.,  
"A Demountable Glass Vacuum System using Electron Bom-  
bardment in the Vacuum Deposition of Ferromagnetic Films".  
Trans. Fifth Vacuum Symposium, American Vacuum Soc.,  
p. 230, (1958).

- H6 Humphrey, F.B., Reynolds, F.W., Stilwell, G.R.,  
"Introduction to Magnetic Thin Films".  
Trans. Sixth Vacuum Symposium, American Vacuum Soc.,  
p. 204, (1959).
- H7 Holland, L., Laurensen, L.,  
"Pumping Characteristics of a Titanium Droplet Getter  
Ion Pump".  
Brit.J.Appl.Phys., 11, 401, (1960).
- H8 Heavens, O.S.,  
"Evaporation of Metals by Electron Bombardment".  
J.Sci.Instrum. 36, 95, (1960).
- H9 Hayes, R.E., Roberts, A.R.V.,  
"A Control System for the Evaporation of Silicon  
Monoxide Insulating Film".  
J.Sci.Instrum., 39, 428, (1962).
- H10 Heritage, R.J., Young, A.S., Bott, I.B.,  
"Composite Studies of Evaporated Ni-Fe Layers".  
Brit.J.Appl.Phys., 14, 439, (1963).
- K1 Kelly, J.C.,  
"Electron Bombardment Apparatus for Vacuum  
Evaporation".  
J.Sci.Instrum., 36, 89, (1960).
- L1 Lemke, J.S.,  
"Effect of Substrate Cleanness on Permalloy Thin Films".  
J.Appl.Phys.(Suppl.), 33, 1097, (1962).
- L2 Lins, S.D., Oberg, P.E.,  
"Automatic Deposition Control".  
Electronics 36, 33, (March, 1963).
- M1 Milleron, N.,  
"Continuous Evaporation of Refractory Metals by Electron  
Bombardment without using Support Materials".  
Trans.Fourth Vacuum Symposium, American Vacuum Soc.,  
p. 148, (1957).
- M2 Metzger, D.D.,  
"Process Control for Thin Film Vacuum Deposition".  
Sci.M.Thesis, Massachusetts Institute of Technology,  
(1958).

- M3 Moore, D.W.,  
"Research and Production Potentialities of Electron Bombardment Evaporator".  
Trans. Sixth Vacuum Symposium, American Vacuum Soc.,  
p. 181, (1959).
- M4 Muggleton, A.H.F., Howe, F.A.,  
"The Preparation of Thin Self Supporting Boron Films".  
Nuclear Instrum. and Methods, 13, 211, (1961).
- M5 Meier, J.W.,  
"High-Power-Density Electron Beam Welding of Several Materials".  
Trans. Eighth Vacuum Symposium, American Vacuum Soc.,  
p. 670, (1961).
- N1 Nielson, S.,  
"Clean Glass Substrates for Permalloy Films".  
Trans. Seventh Vacuum Symposium, American Vacuum Soc.,  
p. 293, (1960).
- P1 Putner, T.,  
"Method of Cleaning Glass by Vapour Degreasing and Ultrasonically Agitated Solvents".  
Brit. J. Appl. Phys., 10, 332, (1959).
- P2 Prutton, M.,  
"Structure and Anisotropy in Magnetic Films".  
Trans. Ninth Vacuum Symposium, American Vacuum Soc.,  
p. 59, (1961).
- S1 Strong, J.,  
"Modern Physical Laboratory Practice".  
Blackie & Son Limited, London and Glasgow, p.152, (1940).
- S2 Schwartz, H.,  
"Method of Measuring and Controlling Evaporation Rates during the Production of Thin Films in Vacuum".  
Rev. Sci. Instrum., 32, 194, (1961).
- S3 Suddall, G., Probyn, B.A.,  
"A Continuously-Fed Electron Bombardment Source for the Evaporation of Alloys Containing Nickel, Iron or Cobalt".  
Rev. Sci. Instrum., 33, 217, (1962).

- S4 Steckelmecher, W., English, J.,  
"Instrument for the Controlled Deposition of Optical  
Film Systems".  
Trans. Eighth Vacuum Symposium, American Vacuum Soc.,  
p. 852, (1961).
- S5 Schwartz, N., Brown, R.,  
"A Stylus Method for Evaluating the Thickness of Thin  
Films and Substrate Surface Roughness".  
Trans. Eighth Vacuum Symposium, American Vacuum Soc.,  
p. 836, (1961).
- T1 Thun, R., Rambey, J.B.,  
"A New Electron Gun for the Vacuum Evaporation of  
Metals and Dielectrics".  
Trans. Sixth Vacuum Symposium, American Vacuum Soc.,  
p. 192, (1959).
- T2 Turner, J.A., Pickard, R.M., Hoffman, G.R.,  
"Ultra-high Vacuum Systems".  
J.Sci.Instrum., 39, 26, (1962).
- U1 Unvala, B.A.,  
"Epitaxial Growth of Silicon by Vacuum Evaporation".  
Nature, 194, 4832, (June 9, 1962).
- V1 Andenhove, J.Van, Eschbach, H.L., Moret, H.,  
"Deposition by Electron Bombardment and Weighing  
under Vacuum of Thin High Purity Boron Layers".  
Nuclear Instrum. and Methods, 24, 465, (1963).
- W1 Williams, R.G., Wyckoff, W.G.,  
"Electron Shadow Micrography of the Tobacco Mosaic  
Virus Protein".  
Science, 101, 594, (1945).
- W2 William, R.C., Backus, R.C.,  
"The Electron-Micrographic Structure of Shadow-Cast  
Films and Surfaces".  
J.Appl.Phys., 20, 98, (1949).
- W3 Wilson, R.,  
"The Fundamental Limit of Sensitivity of Photometers".  
Rev.Sci.Instrum., 23, 217, (1952).



## APPENDIX A

STATISTICAL RESULTS PERTAINING TO THE EFFECT OF DISPERSION  
ON ANISOTROPY FIELD MEASUREMENTS

A1. Evaluation of  $\lambda_K = \frac{1}{H_K \cdot \left(\frac{1}{H_K}\right)}$  for a Normal Distribution of  $H_K$ .

If  $H_K$  has the normal distribution function

$$p(x) = \frac{1}{\sqrt{2\pi}} e^{-\frac{1}{2}x^2} \quad (A1)$$

then

$$\lambda_K = \frac{1}{\frac{1}{\sqrt{2\pi}} \int_{-\infty}^{\infty} \frac{e^{-\frac{1}{2}x^2}}{1+\sigma_K x} \cdot dx} \quad (A2)$$

$$= \frac{1}{\frac{1}{\sqrt{2\pi}} \int_{-\infty}^{\infty} \frac{e^{-\frac{1}{2}x^2}}{1-\sigma_K^2 x^2} \cdot dx}$$

where

$$x = \frac{H_K - \overline{H_K}}{H_K \sigma}$$

and

$\sigma_K = \frac{H_K \sigma}{H_K}$  is the normalized standard deviation of the distribution.

The integral of equation (A2) cannot be evaluated directly as the integrand is infinite at  $\sigma_K x = 1$ . If we neglect all regions with  $|x| > X$ , where  $\sigma_K X > 1$ , then the infinite integral may be replaced by an integral over the finite range  $-X < x < X$ . The integral can then be evaluated by expanding as an absolutely convergent power series in  $\sigma_K^2$ ;

$$\left| \frac{1}{\sqrt{2\pi}} \int_{-X}^X \frac{e^{-\frac{1}{2}x^2}}{1 - \sigma_K^2 x^2} dx - \sum_{n=0}^N \sigma_K^{2n} I_{2n} \right| = \frac{\sigma_K^{2(N+1)} I_{2(N+1)}}{1 - \sigma_K^2 X^2}$$

$$< \frac{(\sigma_K X)^{2(N+1)}}{1 - \sigma_K^2 X^2}$$

$$\rightarrow 0 \text{ as } N \rightarrow \infty \quad (\text{A3})$$

$I_{2n}$  is the integral  $\frac{1}{\sqrt{2\pi}} \int_{-X}^X x^{2n} e^{-\frac{1}{2}x^2} dx$  and satisfies the recurrence relationship;

$$I_{2n} = (2n-1) I_{2(n-1)} - \sqrt{\frac{2}{\pi}} X^{(2n-1)} e^{-\frac{1}{2}X^2} \quad \text{for } n \geq 1$$

where  $I_0 = \frac{1}{\sqrt{2\pi}} \int_{-X}^X e^{-\frac{1}{2}x^2} dx$  is the normal probability integral. Equation (A3) has been used for the calculation of Fig. 5.62.

A2. Evaluation of  $\lambda_\beta = \frac{1}{\overline{\cos 2\beta} \cdot \overline{\cos^2 \beta}}$  for a Normal Distribution in  $\beta$ .

If  $\beta$  has the normal distribution function

$$p(x) = \frac{1}{\sqrt{2\pi}} e^{-\frac{1}{2}x^2}$$

$$\overline{\cos n\beta} = \frac{1}{\sqrt{2\pi}} \int_{-\infty}^{\infty} e^{-\frac{1}{2}x^2} \cos(n\sigma_\beta x) dx \quad (A4)$$

$$= e^{-\frac{1}{2}n^2 \sigma_\beta^2}$$

where  $\sigma_\beta$  is the normalized standard deviation of the distribution. Noting that

$$\overline{\cos^2 \beta} = \frac{1}{2} (1 + \overline{\cos 2\beta})$$

then

$$\lambda_\beta = \frac{2}{e^{-2\sigma_\beta^2} (1 + e^{-2\sigma_\beta^2})} \quad (A5)$$

# A general purpose precision magnet supply

P. H. COLF and E. VAIRIBAT

School of Electrical Engineering, University of Sydney, Australia  
MS. received 24th February 1962, in revised form 17th May 1962

## A GENERAL PURPOSE PRECISION MAGNET SUPPLY

The supply is a precision current source, controlled by a single phase AC supply. The output of the feedback system permits use of the supply with impedances of any magnitude and with large inductance (500 H or more). Short-circuit current is limited to 10 A, less than 100 mA per ampere per hour and more in the 0.1 A range than 1 mA per ampere.

### 1. Introduction

This paper describes a 1 kW precision current supply for electromagnets. A block diagram of the system is given in figure 1. The unregulated DC supply (0.30 V dc, 0.1 A rms ripple) is obtained from a 200 V rms AC transformer. Regulation is achieved by series power transistors controlled in a feedback loop by a precision amplifier circuit. The output across the series transistors is manually adjusted to be within the operating range (0.1 V) by a variable autotransformer in the feedback supply. Voltage dependent resistors across the series transistors prevent damage if the autotransformer is wrongly made. The output current is regulated by a thermally controlled resistor and a constant current source provided by a regulated power source and a current reference battery.

In a laboratory containing a number of magnets of different types, it is desirable that a supply can be connected simply to any magnet without readjustment of the feedback loop of the regulator. In addition, for certain thermomagnetic experiments it is necessary to combine a constant precision with the facility for manual readjustment. (Specifications from small users up to 700 V rms, 1000 W rms have been reported at various places. Previous similar designs (Johnson and Sager 1959, Garwin, Hindsman, Farnum and Shapiro 1959, King and Millard 1959, Palmer 1961 unpublished, Miller 1961, Carter and Fellows 1959, Ryle and Stoddard 1962) do not provide all these features. The present regulator has therefore been developed at least to the above requirements, principally by the use of a method of feedback from the reference current source.

### 2. General description of the system of feedback

Any feedback loop containing components whose phase characteristics cannot usually be represented above a limiting upper frequency by their impedance in the loop. To prevent instability, it is therefore necessary to reduce the loop gain at very high frequencies before the feedback is reached. It is essential to maintain a satisfactory stability margin below this frequency, so the loop gain can be increased at lower frequencies with a fixed maximum rate. The contribution from gain at any frequency is hence determined.

In a single loop regulator, using a voltage amplifier, the amplifier stability requirements frequently limit the impedance of the feedback loop. A large gain that is independent of frequency is necessary to allow the amplifier to maintain its stability. In addition, if stability is to be maintained at high frequencies, the impedance should increase

at no more than 20 dB per decade below the amplifier frequency. Even with amplifier frequencies of up to 10 MHz it is possible to achieve an impedance of 1000  $\Omega$  and an effective gain for impedances of several ohms and the transformer.

A double loop system can be used to give stability to give all frequencies. Such a double loop system employs a slowly mounted amplifier in an internal loop (loop 1) and a shunt amplifier in an external loop (loop 2) as shown in figure 1. It is found in a practical system as in figure 1.

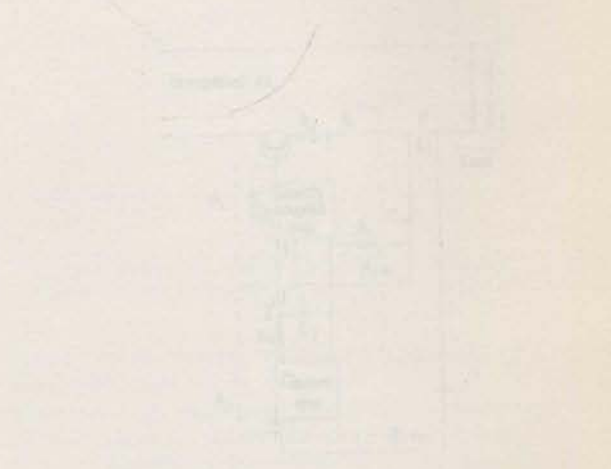


Figure 1. Block diagram of the regulator.

that feedback in loop 1 is limited by the frequency response of the series transistors and can be large. Feedback loop 2 is an active network in the shunt amplifier. It can be made much more effective than loop 1 by the presence of the current reference of figure 1, so that the overall loop gain is not limited by the shunt amplifier. It is essential to have a large gain at low frequencies, so that the overall loop gain is not limited by the shunt amplifier.

It is important to note that the precision current source is independent of the particular type of active device derived from the output current. As a result, the feedback loop can be taken from across the reference current source or across the output of the current source (see Johnson and Sager 1959, Garwin, Hindsman, Farnum and Shapiro 1959). It is important if the stability of the system is to be maintained that the output impedance is not too low. The output impedance is not too low if the output current is not too high.

# A general purpose precision magnet supply

P. H. COLE and R. VAUGHAN

School of Electrical Engineering, University of Sydney, Australia

MS. received 23rd January 1963, in revised form 17th May 1963

Complete details are given of a 1 kw precision magnet current supply. Series transistors are used as the regulating element, controlled by a solid state chopper amplifier. The nature of the feedback system permits use of the supply with magnets of any impedance and with large amplitude (500 v r.m.s. 50 c/s) external magnet modulation. D.C. drift is less than 10 parts per million per hour and noise in the 0.1-1 c/s band less than 1 part per million.

## 1. Introduction

This paper describes a 1 kw precision current supply for electromagnets. A block diagram of the system is given in figure 1. An unregulated d.c. supply (0-200 v d.c., 0.5 v r.m.s. ripple) is obtained from a single phase rectifier. Regulation is achieved by series power transistors controlled in a feedback loop by a semiconductor chopper amplifier. The voltage across the series transistors is manually adjusted to be within the operating range (2-15 v) by a variable autotransformer in the rectifier mains supply. Voltage dependent resistors across the series transistors prevent damage if this adjustment is improperly made. The output current is sampled by a thermostatically controlled resistor and compared with a reference potential provided by a multiterm potentiometer and a mercury reference battery.

In a laboratory containing a number of magnets of different types, it is desirable that a supply can be connected directly to any magnet without readjustment of the feedback loops of the regulator. In addition, for certain ferromagnetic resonance experiments it is necessary to combine d.c. current precision with the facility for external modulation. (Modulation from small values up to 500 v r.m.s. 50 c/s has been required at various times.) Previous supplies described (Johnson and Singer 1958, Garwin, Hutchinson, Penman and Shapiro 1959, Brog and Milford 1960, Patlock 1960 unpublished, Mobley 1961, Bailey and Fellows 1959, Ryley and Gambling 1962) do not possess all these features. The present regulator has therefore been developed to meet all the above requirements, principally by the use of a method of feedback from the reference resistor alone.

## 2. General discussion of the method of feedback

Any feedback loop contains components whose phase characteristics cannot usefully be compensated above a limiting upper frequency (by other elements in the loop). To preserve stability, it is therefore necessary to reduce the loop gain to unity before this frequency is reached. In addition, to maintain a satisfactory stability margin below this frequency, the loop gain can be increased at lower frequencies only at a fixed maximum rate. The maximum loop gain at any frequency is hence determined.

In a single loop regulator, using a chopper amplifier, the chopper amplifier represents a frequency limiting component of the above type. Loop gain must be reduced to below unity before approximately half the chopper frequency is reached. In addition, if stability at lower frequencies is required without adjustments of the circuit, the loop gain should increase

at no more than 6 db per octave below the chopper frequency. Even with chopper frequencies of up to 10 kc/s it is not possible to achieve, at frequencies of 1 c/s and above, sufficient gain for suppression of rectifier ripple and mains transients.

A double loop system can be used to give adequate loop gain at all frequencies. Such a double loop system, employing a directly coupled amplifier in an internal loop (loop 1) with a chopper amplifier in an overall loop (loop 2), is shown in figure 1. It is found in a practical system as in figure 1

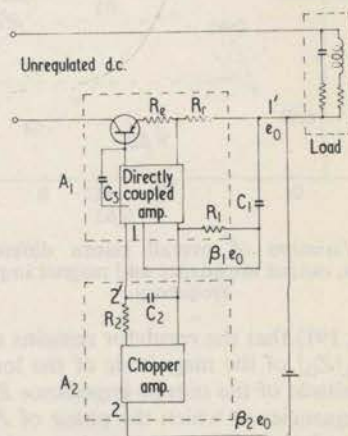


Figure 1. Block diagram of the regulator.

that feedback in loop 1 is limited by the frequency characteristics of the series transistors and driver stage. Feedback in loop 2 is as before limited by the chopper amplifier. However, the overall return difference (Bode 1945, p. 47), being the product of the return differences of loops 1 and 2, can be made greater than unity at half the chopper frequency. In addition for only 6 db per octave slope in each loop, the overall return difference may increase at 12 db per octave below half the chopper frequency.

It is important to note that the maximum possible loop gain is independent of the particular way in which feedback is derived from the output current. As a specific example, feedback may be taken from across the reference resistor alone or some fraction of the magnet voltage also included (Garwin, Hutchinson, Penman and Shapiro 1959). In the latter case, if the modification of the loop response produced by the magnet inductance is suitably compensated, the maximum possible loop gain remains determined as before

by the other frequency limiting components of the loop. In the present design, feedback is taken from the reference resistor alone.

### 3. Regulator stability for magnets of arbitrary impedance

The stability of the regulator for an arbitrary load can be established from a consideration of the regulator output impedance and the load impedance, provided the regulator is stable for a short-circuited load. The short-circuit stability and the output impedance  $Z_O$  of the regulator are derived in § 4.  $Z_O$  is plotted as curve C of figure 2. It may be shown

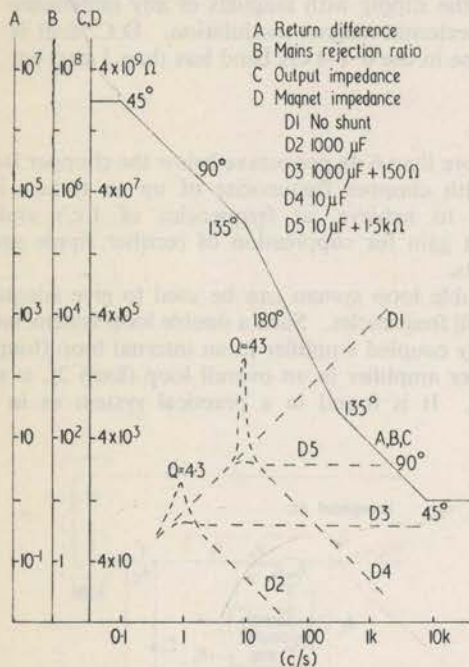


Figure 2. Variation of overall return difference, mains rejection ratio, output impedance and magnet impedance with frequency.

(Bode 1945, p. 191) that the regulator remains stable on load if the ratio  $|Z_L/Z_O|$  of the magnitude of the load impedance  $Z_L$  to the magnitude of the output impedance  $Z_O$  is less than unity at all frequencies at which the phase of  $Z_L/Z_O$  exceeds  $180^\circ$ . The impedance of the magnet alone, plotted as curve D1 of figure 2, violates this condition and the system is unstable (magnetic inductance 40 H.)

To achieve stability, the load impedance may be reduced by by-passing the magnet with a capacitor or capacitor resistor combination. Various suitable load impedances are plotted as curves D2 to D5 (figure 2). For curve D4 the phase of  $Z_L/Z_O$  exceeds  $180^\circ$  (at 10 c/s), but the magnitude  $|Z_L/Z_O|$  is at most 0.006 giving a gain margin of 44 db. For curve D5 the ratio  $|Z_L/Z_O|$  exceeds unity (at 2 kc/s), but here the phase margin is  $90^\circ$ . All these combinations have proved stable in practice.

If the filtering effect of the magnet inductance and shunt capacitor is not considered, the mains rejection ratio is given by

$$\frac{\Delta V_{\text{mains}}}{V_{\text{mains}}} \frac{\Delta i_m}{i_m} = \frac{|Z_O|}{R_m}$$

where  $i_m$  is the magnet current,  $R_m$  is the magnet resistance, and  $Z_O$  is the regulator output impedance. For the particular design of this paper the mains rejection ratio (curve B, for

a magnet resistance of  $40 \Omega$ ) has been plotted against frequency in figure 2.

While only a small capacitor is required for stability, a resonance will be produced by the magnet capacitor combination. Mains rejection will be decreased and noise increased at the resonant frequency by the  $Q$ . The resonance can, however, be effectively damped by a small resistor in series with the capacitor (curves D3 and D5) if it is found necessary.

Feedback from the reference resistor alone hence allows the regulator to be used with magnets of any impedance, the only requirement being that a shunt capacitor of sufficient size is used. No networks depending upon the magnet parameters need be inserted inside the feedback loops to maintain stability (Garwin, Hutchinson, Penman and Shapiro 1959).

The facility for external modulation results from two factors. Since no feedback is taken from the magnet voltage, no modulation voltage is injected into the input of the feedback amplifier. In addition the by-pass capacitors provide a return loop for the modulating current and reduce the modulating voltage appearing across the series transistors to a low value (for example, 500 v r.m.s. 50 c/s with a 40 H magnet and 1000  $\mu\text{F}$  by-pass capacitor produces 0.1 v r.m.s. across the series transistors).

### 4. The detailed circuit design

The solid-state chopper amplifier (figure 3), sampling at 3 kc/s, provides a d.c. gain of 3000 into a 1 k $\Omega$  load. The input is transformer coupled and hence, being completely isolated from ground, can be connected to the potential terminals of the reference resistor. To avoid inducing unwanted signals in the a.c. amplifier, the square wave oscillator is shielded, the two turn secondaries being wound with coaxial cable. The gain is stabilized so that no changes in the regulator stability can arise from component tolerances or ageing. Of extreme importance is the large chopper dynamic range of 1 mv at the input, principally determining the ability of the system to reject fast mains transients and other interference without overload. This has been achieved by using only sufficient chopper gain to prevent the directly coupled amplifier contributing to the input noise and drift. For this reason the directly coupled amplifier has a differential input stage, and the d.c. impedance in the base circuits of the input transistors T9, T10 has been made low (1 k $\Omega$ ). The directly coupled amplifier has a gain of 500 from input to the base of the series transistor T15-22 and can supply up to 0.3 A to the base of T15-22. The high frequency performance of the directly coupled amplifier is relevant to the consideration of stability upon closure of loop 1. At frequencies above 10 c/s capacitor C3, by feedback, shapes the response, stabilizes the gain (previously directly dependent on the  $\beta$  of transistor T11), and lowers the impedance presented to the bases of transistors T15-22. The low impedance seen by the bases and degeneration across the emitter resistors raise the effective collector impedance of T15-22 to approximately the back impedance of the collector base diodes. In addition, the high frequency 3 db point is raised to 80 kc/s, using normal power transistors of  $f_\beta = 10$  kc/s.

The stability on short circuit is best analysed by considering successive closure of loops 1 and 2. In figure 1,  $A_1$  and  $A_2$  are the gains from 1 to 1' and 2 to 2' respectively, calculated with the load short circuited.  $\beta_1$  and  $\beta_2$  are the fractions of the reference resistor voltage at 1' fed back to

## A GENERAL PURPOSE PRECISION MAGNET SUPPLY

1 and 2 respectively. In loop 1 around the directly coupled amplifier, the open loop gain  $\beta_1 A_1$  is reduced at 6 dB per octave by capacitor C3 to give unity loop gain at 10 kc/s. An adequate margin is hence provided against additional open loop poles occurring about 80 kc/s. The closed loop

## 5. Drift and noise performance of the regulator

For daily ambient temperature variations of 15° c, the drift in the magnetic field results principally from change in the magnet permeability and dimensions. After the initial

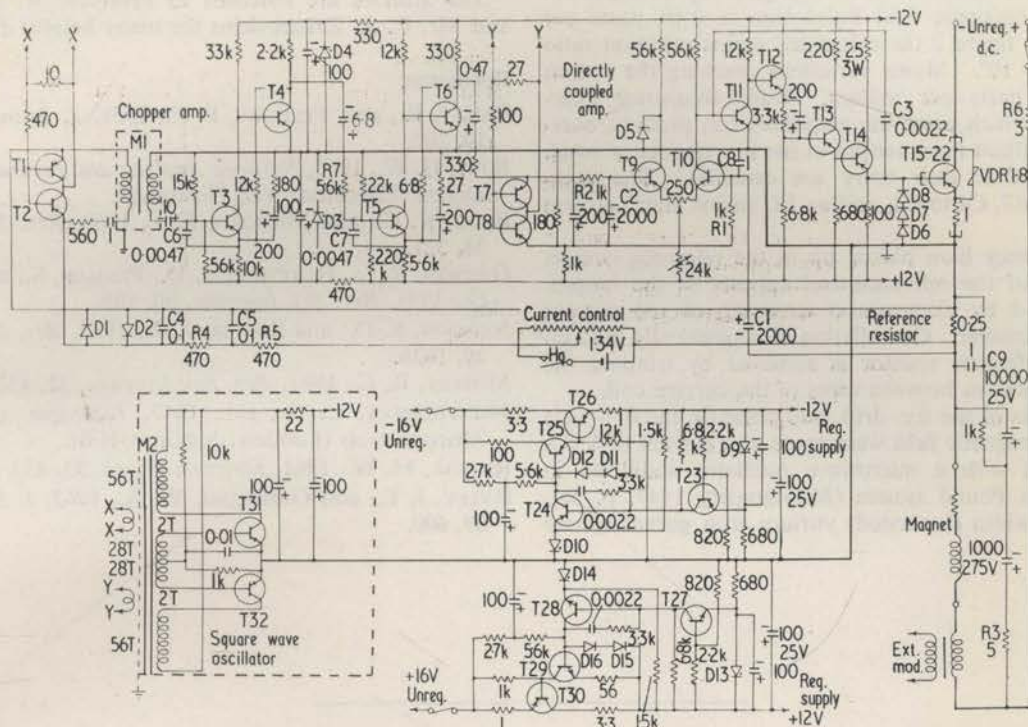


Figure 3. Regulator circuit diagram.

D1-D2	OA200	M1	Transformer Fortiphone	T13	OC74
D3-D4	OAZ207			T14-T22	ASZ16
D5	OA200	M2	Transformer Permalloy core S.T.C. WP3312 6-filar winding	T23-T24	OC44
D6-D8	OA210			T25	OC74
D9-D10	OAZ207			T26	ASZ16
D11-D12	OA200	T1-T5	OC44	T27-T29	2N647
D13-D14	OAZ207	T6	OC74	T30	ASZ16
D15-D16	OA200	T7-T12	OC44	T31-T32	OC74

response  $A_1/(1 + \beta_1 A_1)$  is unity at medium frequencies (at which  $\beta_1$  as determined by C1; R1 is unity), falling by 3 dB at 10 kc/s. In loop 2 around the entire amplifier, the open loop gain  $\beta_2 A_2 A_1 / (1 + \beta_1 A_1)$  is reduced at 6 dB per octave, by the chopper ripple filter C2, R2 to give unity loop gain at 300 c/s. An adequate margin is hence provided against additional open loop poles occurring at the 3 kc/s chopper frequency and at 10 kc/s, due to the closed loop response  $A_1/(1 + \beta_1 A_1)$  of the directly coupled amplifier. Feedback around loop 1 is blocked at d.c. by C1-R1 to prevent unwanted currents flowing in the reference resistor. The slope of  $\beta_2 A_2 A_1 / (1 + \beta_1 A_1)$  does not increase above 6 dB per octave at low frequencies provided only that  $C1R1 \geq C2R2$ .

The overall return difference is the product of the return difference of loops 1 and 2 closed successively. That is

$$1 + \beta_1 A_1 + \beta_2 A_2 A_1 = (1 + \beta_1 A_1) \left( 1 + \frac{\beta_2 A_2 A_1}{1 + \beta_1 A_1} \right).$$

This function is plotted as curve A in figure 2.

The output impedance  $Z_O$  is given by the product of the overall return difference and the effective collector impedance of the series transistors.  $Z_O$  has been plotted as curve C in figure 2.

warm up the long thermal time constant of the magnet (8 h) reduces this drift to 20 parts per million per hour. Next in importance is the temperature change of the reference cell (Mallory RM-3) which has a temperature coefficient of 17 parts per million per degc and an ageing drift of -3 parts per million per hour at its operating current of 0.7 mA. The cell is set in a metal block and insulated by expanded polystyrene foam to provide a 20 h time constant. The expected drift from this source is reduced to 6 parts per million per hour.

The drift of the chopper amplifier has been measured on open loop over a period of one week. The drift is  $0.4 \mu\text{V h}^{-1}$  referred to the input and results from ambient temperature variations. It contributes a drift of 0.4 parts per million per hour to the full load magnet current of 4 A. To reduce drift due to change of temperature of the reference resistor (alloy ISA 50, Isabellen-Hütte, W. Germany) whose coefficient is 15 parts per million per degc, it is wound on an aluminium former. A transistor regulator (Rignal 1961) maintains the former at  $50 \pm 0.1^\circ\text{C}$ . Selected aluminium electrolytic capacitors C1 and C9 produce a magnet current error of approximately their leakage current which has been measured as  $2 \mu\text{A}$  at  $25^\circ\text{C}$  after 15 minutes operation.

Tantalum electrolytic capacitors could be used for greater reliability.

The noise of the chopper amplifier in the band 0.1–1 c/s is  $10^{-8}$  v r.m.s. It arises in the 1.5 k $\Omega$  effective source resistance and 6 db measured noise figure of the a.c. amplifier. Open loop tests have shown that the noise from the chopper transistors and reference cell is negligible by comparison. The resulting magnetic field fluctuation is 0.01 parts per million. From figure 2 the calculated mains rejection ratio in this band is  $10^6$ . Mains variations reaching the output will be 0.05 parts per million. Radio-frequency interference pulses which enter the amplifiers can produce overload and a resultant noise output in the low frequency band. Precautions against their entry are essential. The components R3 to R7, C4 to C8, and an LC mains filter perform this function.

Mains frequency hum picked up in the reference circuits becomes part of the reference and appears at the output. It is minimized by electrostatic screening of the current control potentiometer. Cancellation of magnetically induced hum in the reference resistor is achieved by winding the potential connections between wires of the current coil.

Measurements of the d.c. drift, and noise (in the 0.1–1 c/s band), of the magnetic field were made at a current of 1.3 A by comparison with a microwave oscillator stabilized in frequency by a Pound system (Montgomery 1947, p. 58). A narrow linewidth (1 oersted) yttrium iron garnet sphere

was used as a magnetic field to frequency transducer. Both the drift and noise were less than the limits of reading of 10 parts per million per hour (d.c. drift) and 1 part per million (0.1–1 c/s noise).

#### Acknowledgments

The authors are indebted to Professor R. E. Aitchison and Mr. R. A. Zakarevicius for many helpful discussions.

#### References

- BAILEY, R., and FELLOWS, E. E., 1959, *J. Instn Rad. Engrs*, **19**, 309.  
 BODE, H. W., 1945, *Network Analysis and Feedback Amplifier Design* (Princeton: Van Nostrand).  
 BROG, K. C., and MILFORD, F. J., 1960, *Rev. Sci. Instrum.*, **31**, 321.  
 GARWIN, R. L., HUTCHINSON, D., PENMAN, S., and SHAPIRO, G., 1959, *Rev. Sci. Instrum.*, **30**, 105.  
 JOHNSON, S. D., and SINGER, J. R., 1958, *Rev. Sci. Instrum.*, **29**, 1026.  
 MOBLEY, R. C., 1961, *Rev. Sci. Instrum.*, **32**, 432.  
 MONTGOMERY, C. G., Ed., 1947, *Technique of Microwave Measurements* (London: McGraw-Hill).  
 RIGNAL, M. W., 1961, *Electron. Engng*, **33**, 452.  
 RYLEY, J. E., and GAMBLING, W. A., 1962, *J. Sci. Instrum.*, **39**, 600.



ACKNOWLEDGMENT

The author is indebted to Associate Professor R. E. Aitchison for his kind advice and encouragement during the course of this work. The author has had an agreeable and stimulating association with Messrs. P. H. Cole, P. J. Khan, R. Michael, R. A. Zakarevicius, and wishes to acknowledge their assistance in the checking and printing of the manuscript.

Particular thanks are due to Miss M. Winkelhag for her excellent typing.

## LIST OF PRINCIPAL SYMBOLS

Certain symbols have been listed in pairs, for example  $H$ ,  $h$  and  $M$ ,  $m$ . In such cases, the small  $h$  denotes fields normalized with respect to the anisotropy field  $H_K$ ; the small  $m$  denotes magnetisation normalized with respect to the saturation magnetisation  $M_s$ .

A	exchange constant
A	amplifier gain
A(s)	integrator transfer function
$A_W$	winding cross sectional area
$\alpha = A_W / 2L$	normalized winding cross sectional area
$\alpha_1, \alpha_2, \alpha_3$	directional cosines of the magnetisation relative to the crystallographic. (100) axis
B	detector bandwidth
$B_1, B_2$	magnetoelastic coupling coefficients
$\beta$	normalized noise bandwidth
$\beta$	angular position of the easy axis
$\beta_0$	angular position of the mean easy axis
$L\beta$	angular dispersion of the easy axis about the mean easy axis direction
$\beta_{1/2}, \beta_{1/2}, \beta_{1/2}, \beta_{1/2}$	angular dispersion as measured by Crowther's first and second
$\beta$ demag	angular dispersion due to demagnetising fields
$\beta_t$	common emitter current gain
C	capacitance
$C_s$	self capacitance of the sense coil
$C_c$	self capacitance of the cancellation coil
$C_A$	input capacitance of the sense amplifier
$C_{11}, C_{12}, C_{14}$	elastic constants
$C_1, C_2$	proportions of binary alloy, atomic percent

C	impurity concentration, atomic percent
$\gamma$	angle of the applied field H to the easy axis
$\gamma_c$	critical angle of the applied field for reversal by domain wall motion
$\gamma_1, \gamma_2$	field per unit current through the field coils of the MH plotter
d	diameter of film
$\Delta$	increment or difference in
E	energy
$e_{xx}, e_{yy}, e_{yz},$ $e_{xz}, e_{xy}$	strain components
$\epsilon$	anisotropy energy function
$\epsilon_0$	mean anisotropy energy function
$\epsilon'$	dispersion of the anisotropy energy function from the mean value
$\epsilon^{i^2}(\mathbf{k})$	power density function of $\epsilon^i$ in $\mathbf{k}$ space
$\epsilon_u$	anisotropy energy function due to non-rotatable anisotropy
$\epsilon_{-1}, \epsilon_{-2}, \dots$	fractional integration errors
F	noise figure
$F_t$	noise figure, non-reactive source
$\Delta F_{Wt}$	noise figure increment, white noise and non-reactive source
$\Delta F_{Lt}(\omega_0)$	noise figure increment, $\frac{1}{f}$ noise and non-reactive source

$F(\omega)$	spot noise figure
$\Delta F_W(\omega)$	spot noise figure increment, white noise
$\Delta F_L(\omega)$	spot noise figure increment, $\frac{1}{f}$ noise
$\Delta F_{Lt}(\omega)$	spot noise figure increment, $\frac{1}{f}$ noise and non-reactive source
$F_t(\zeta, \eta)$	function relating to the coupling between the film and sense coil
$f$	frequency
$f_0$	repetition frequency
$f_r$	frequency of sense coil resonance
$f_{LR} = L_i / 2\pi R_i$	frequency characterising the sense coil
$f_n, f'_n$	frequency characterising the noise figure of the sense coil used with a voltage amplifier
$\zeta$	angle of tilt of the depositing vapour stream
$\zeta = y/x$	normalized parameter
$H, h$	applied field
$H_p$	peak value of applied field
$H_L, h_L$	applied field component along the easy axis
$H_T, h_T$	applied field component along the hard axis
$H_i$	applied field component perpendi- cular to the film plane
$H_t, h_t$	total field
$H_i, h_i$	demagnetising field of film

$H_i^f, h_i^f$	variation of the demagnetising field of the film from the mean value
$H^f$	reaction field of the field or sense coils
$H_K$	anisotropy field
$H_{Ks}$	saturated anisotropy field
$H_{Ki}$	anisotropy field from extrapolation of hard axis initial susceptibility
$H_{K_{\text{torq}}}$	anisotropy field from torque curve data
$H_{Cr}, h_{Cr}$	coherent rotational switching threshold
$H_r, h_r$	hard axis reversibility limit
$H_C, h_C$	easy axis coercive force
$H_C^f, h_C^f$	hard axis coercive force
$\Delta H$	field interval for reversal
$\Delta H_C$	instrumentational error in coercive force measurement
$H_n$	nucleation field for reverse domains
$H_{sw}$	threshold field for expansion of a nucleated domain
$H_{Ow}$	threshold field for domain wall motion
$H_1, H_2, H_3, \dots$	threshold fields for reversal processes 1, 2, 3, . . .
$H_P$	threshold field for partial rotation
$H_n^f, h_n^f$	"null" field for torque curve measurement

$\theta$	domain wall damping parameter
$I$	current
$I_{ec}$	emitter to collector current
$I_{bc}$	base to collector current
$I_b$	base current
$I_{ecWt}$	emitter to collector current for minimum noise figure, white noise and non-reactive source
$i$	instantaneous current
$i_F$	field coil current
$\underline{i}_x, \underline{i}_y, \underline{i}_z$	orthogonal set of unit vectors attached to $\underline{M}$
$K$	anisotropy constant
$K_0$	mean anisotropy constant
$\Delta K$	dispersion of the anisotropy constant about the mean value
$K'(r), K''(r)$	components of the "vector" aniso- tropy
$K'^2(k), K''^2(k)$	power density functions of $K'(r),$ $K''(r)$ in $k$ space
$K_r$	psuedo-rotatable anisotropy constant
$K_u$	non-rotatable anisotropy constant
$K_{up}$	component of $K_u$ not rotatable by low temperature anneal
$K_{ud}$	component of $K_u$ rotatable by low temperature anneal
$K_1, K_2$	crystalline anisotropy constants
$K_{-1}, K_1, K_2, K_3, K_4$	constants characterising the shape of the integrator transfer function

$k$	Boltzmann's constant
$k$	wave propagation constant
$k_0$	propagation constant characterizing the scale of anisotropy dispersion
$k_A$	exchange cut-off propagation constant
$k_M$	magnetostatic cut-off propagation constant
$L$	inductance
$L$	characteristic length
$L_s$	inductance of the sense coil
$L_c$	inductance of the cancellation coil
$l_W$	mean length of turn
$l_W$	effective domain wall length
$\lambda$	wavelength
$\lambda_A$	exchange cut-off wavelength
$\lambda_M$	magnetostatic cut-off wavelength
$\lambda, \lambda_{111}, \lambda_{100}$	magnetostrictive coefficients
$\lambda_K, \lambda_\beta$	constants relating the initial and saturated anisotropy fields
$\lambda_W$	winding space factor
$M$	magnetisation
$M$	mutual inductance
$M_s$	saturation magnetisation
$M_L, m_L$	magnetisation component along the easy axis
$M_T, m_T$	magnetisation component along the hard axis
$M_r, m_r$	easy axis remanent magnetisation
$M_r', m_r'$	hard axis remanent magnetisation



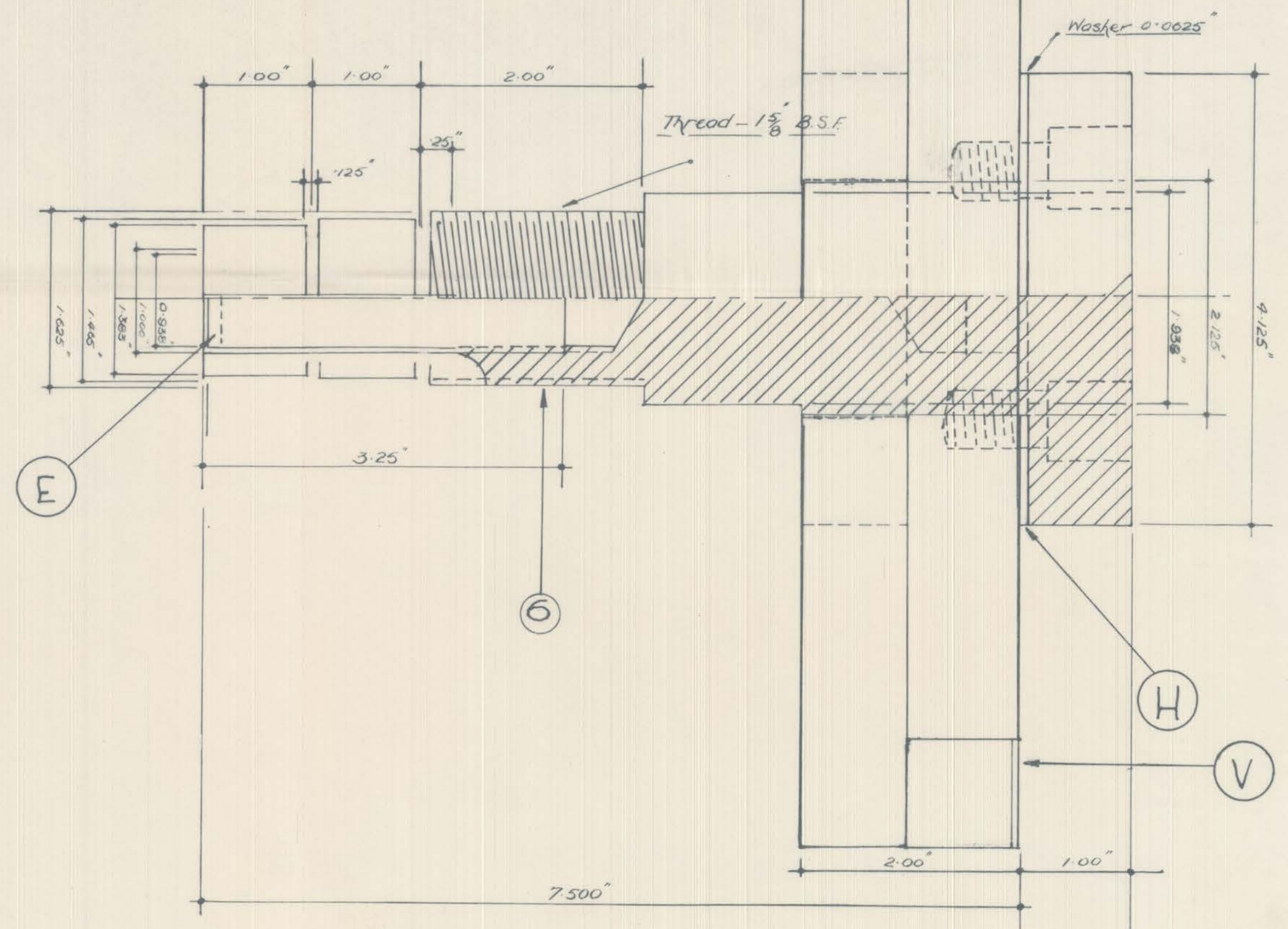
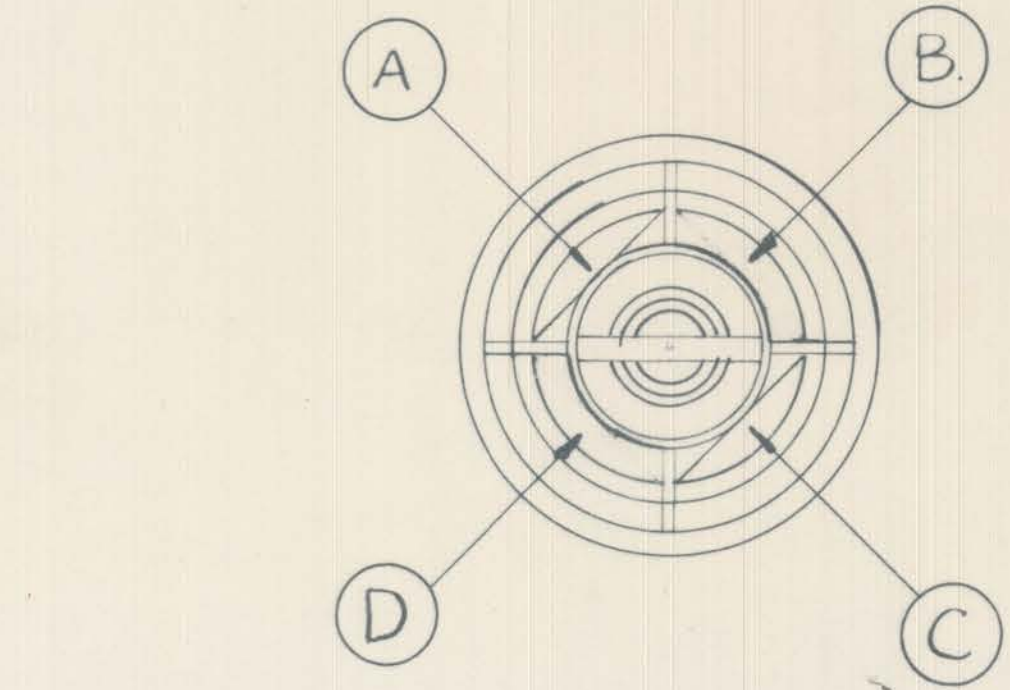
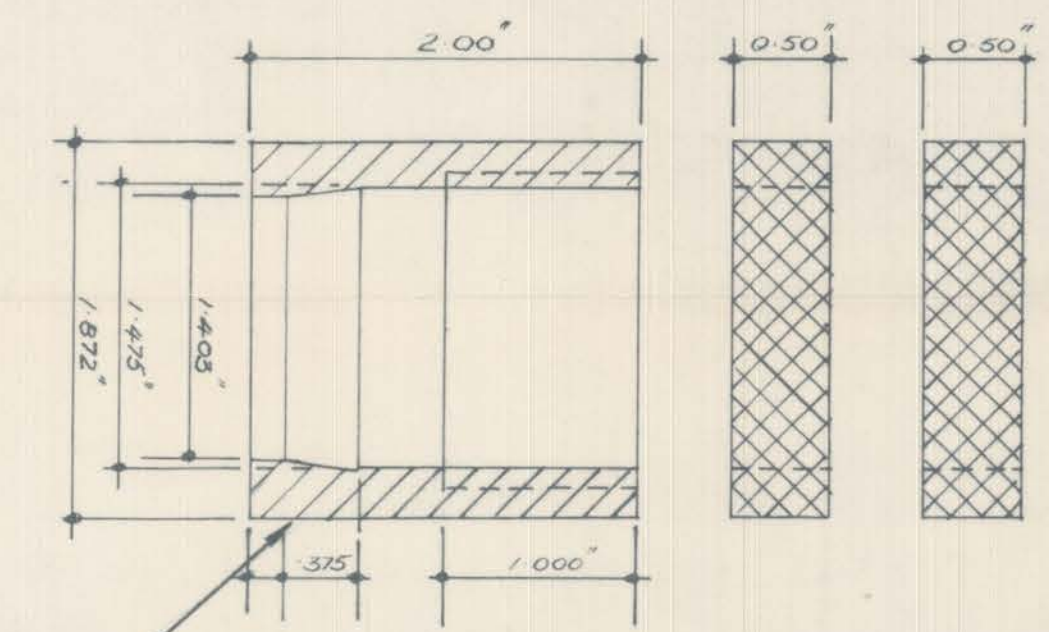
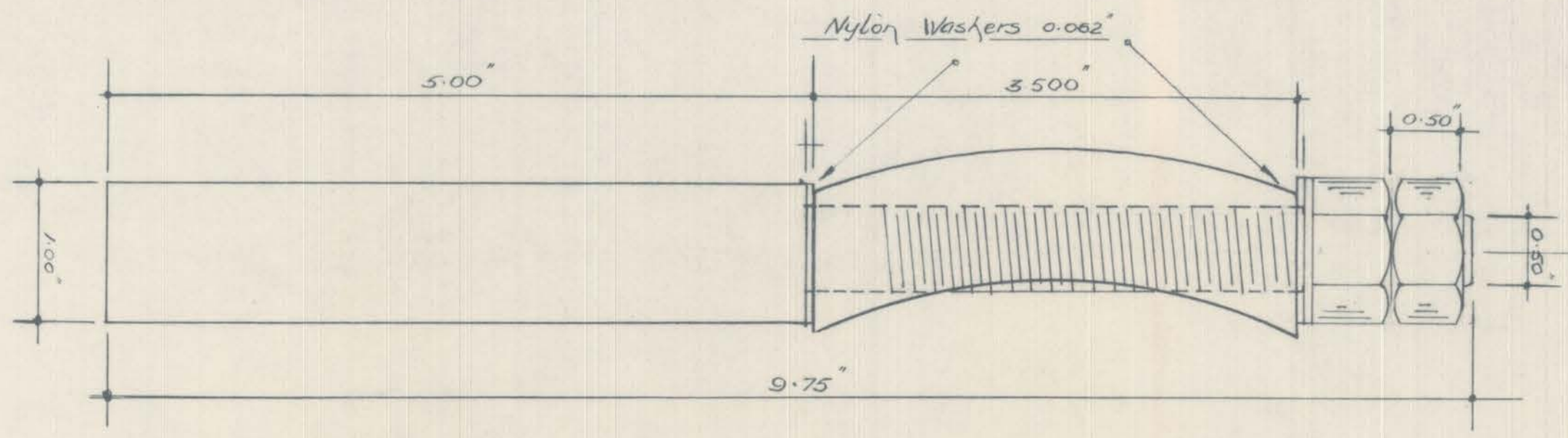
N	demagnetising factor out of the plane of the film
$N_L$	longitudinal demagnetising factor
$N_T$	transverse demagnetising factor
n	number of turns
n	number of atoms per unit volume
$\Delta n$	number of aligned pairs per unit volume
$\eta$	angle of tilt of the crystalline texture axis
$\eta = z/u$	normalised parameter
$\nu$	unit vector in the direction of the magnetisation
$\nu$	normalised mean length of turn
$\xi$	hole damping coefficient
P	sum of the products of the poles taken two at a time
$p(H_K, \beta)$	probability distribution function of anisotropy regions
Q	sum of the products of the poles taken three at a time
Q	null sensitivity factor
Q	coil quality factor
q	electronic charge
R	resistance
$R_i$	equivalent resistance of the sense coil
$R_s$	resistance of the sense coil
$R_c$	resistance of the cancellation coil

$R_D$	resonance damping resistor
$R_{it}$	source resistance for minimum noise figure, non-reactive source
$R_{iWt}$	source resistance for minimum noise figure, white noise and non-reactive source
$R_n, R_{n1}, R_{n2} / \omega$	total, white and $\frac{1}{f}$ noise resistances
$\underline{x}$	position vector
$r_0$	ohmsien characterising the scale of anisotropy dispersion
$r_{bb}$	extrinsic base resistance
$\rho$	resistivity
$\rho_W$	resistivity of winding material
$S$	sum of the poles
$S$	switching coefficient
$\frac{S}{N}$	signal to noise ratio
$s$	complex frequency
$s_n$	poles of integrator or transfer function
$s_m^*$	zeros of integrator transfer function
$\sigma$	stress
$\sigma_x, \sigma_y$	stress components in the film plane
$\sigma_K, \sigma_\beta$	normalised standard deviations in the anisotropy magnitude and direction
$T$	torque
$T$	absolute temperature
$T_A$	anneal temperature
$T(s)$	transfer function of $\overline{M}$ H plotter

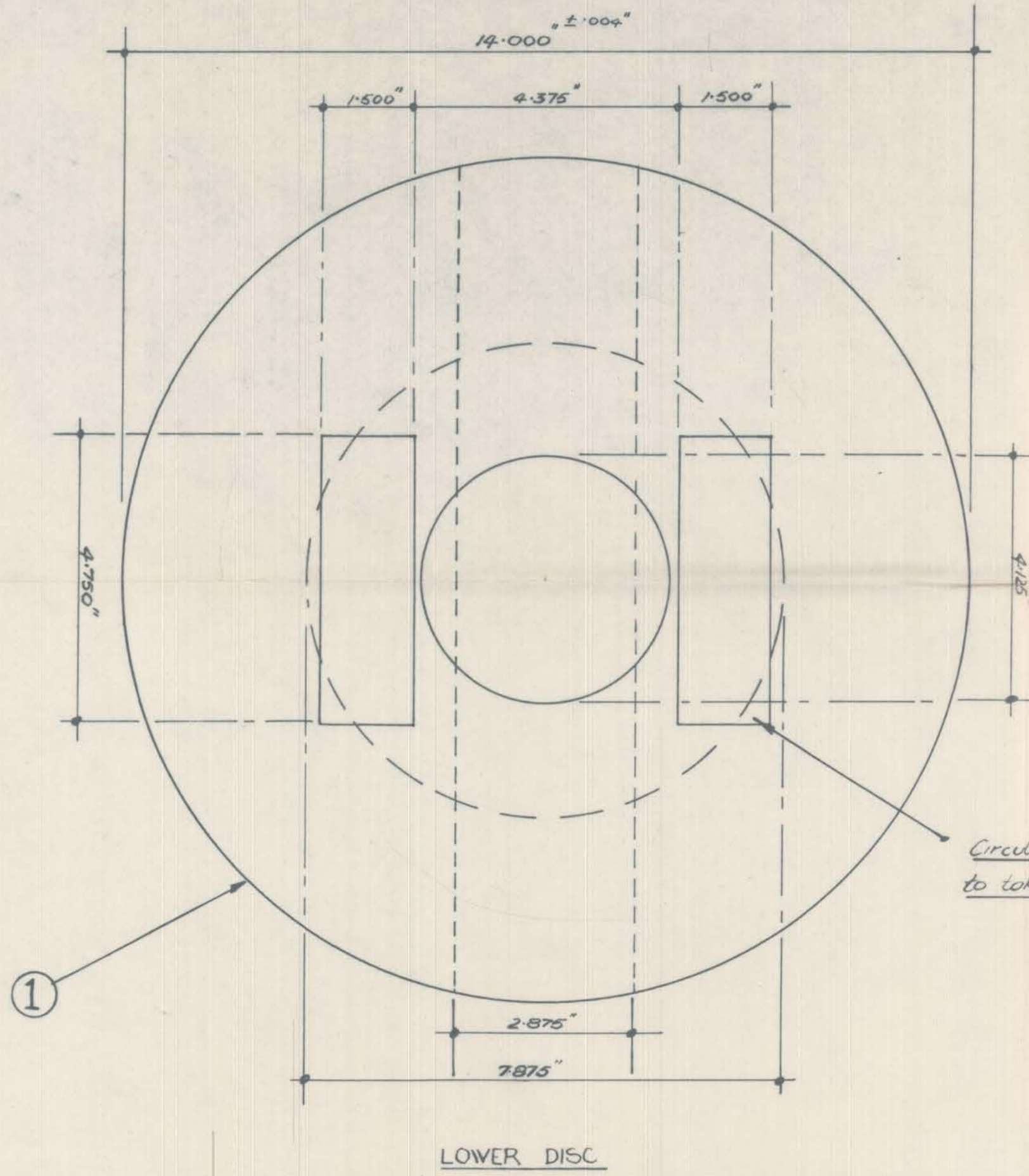
$T_0$	repetition period
$t$	film thickness
$t$	time
$\Delta t$	time interval for reversal
$\tau$	time constant
$\tau_A$	time constant for pair diffusion at the anneal temperature
$\tau_0 = 1/\omega_0$	time constant associated with the repetition frequency
$\tau_r = 1/\omega_r$	time constant associated with the sense coil resonance
$\Delta \tau_D$	instrumental delay time
$\Delta \tau_{\frac{1}{2}}$	instrumental delay time to 50 percent response
$\Delta \tau$	instrumental rise time, 10 to 90 percent response
$V$	voltage
$V$	volume of film
$v$	instantaneous voltage
$v_s$	sense coil voltage
$v_c$	cancellation coil voltage
$v_i$	input voltage
$v_o$	output voltage
$v_{-1}, v_{-2}, \dots$	integrator error voltages
$\bar{\phi}$	saturation flux of film
$\phi$	angle of the magnetisation to the easy axis
$\phi_0$	angle of the mean magnetisation to the easy axis
$\phi^*$	dispersion of the magnetisation direction about the mean direction
$\phi^{*2}(\underline{k})$	power density function of $\phi^*$ in $\underline{k}$ space

$\phi_s$	angle of the magnetisation at the matching threshold
$\phi_i$	film flux linking the sense coil
$\phi_t$	thermal equilibrium potential
$W$	dimension relating to the sense coil
$W_r, w_r$	rotational hysteresis loss
$w$	width of partial rotation band or labyrinth domain
$w(T)$	pair ordering energy at temperature $T_A$ .
$X, X_1, X_2, X; \bar{X}, \bar{X}$	dimensions relating to the sense coil
$X_p$	semi-width of rectangular film
$\chi$	angle between partial rotation band or labyrinth domain and the easy axis
$Y, Y_1, Y_2$	dimensions relating to the sense coil
$Y(T)$	Young's modulus at temperature $T$
$\psi$	angle of the magnetisation out of the film plane
$\bar{\psi}$	fraction of the saturated film flux linking the sense coil
$\psi^+, \psi^-$	fractional flux linkages for the positive and negative pole lines of a film
$Z$	impedance
$Z_{0i}$	impedance of the sense coil at resonance

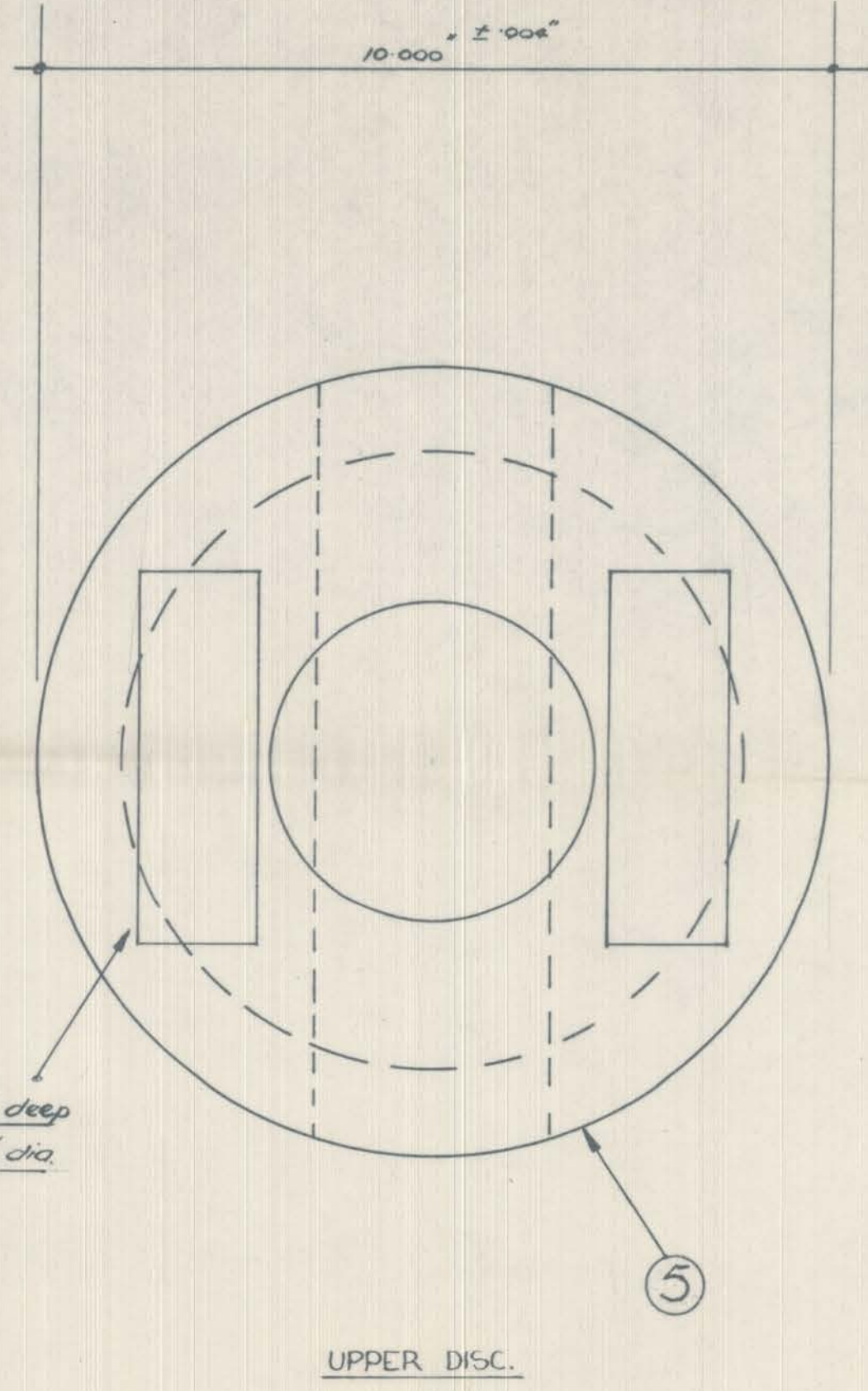
$Z, Z_1, Z_2$	dimensions relating to the sense coil
$Z_P$	semi-length of rectangular film
$\omega$	angular frequency
$\omega_0$	angular repetition frequency
$\omega_R$	angular frequency of the sense coil resonance
$\omega_H$	angular frequency of high frequency 3db point
$\omega_L$	angular frequency of low frequency 3db point
$\omega_{LR} = L_i / R_i$	frequency characterising the sense coil
$\omega_n, \omega_n^1$	frequency characterising the noise figure of the sense coil used with a valve amplifier

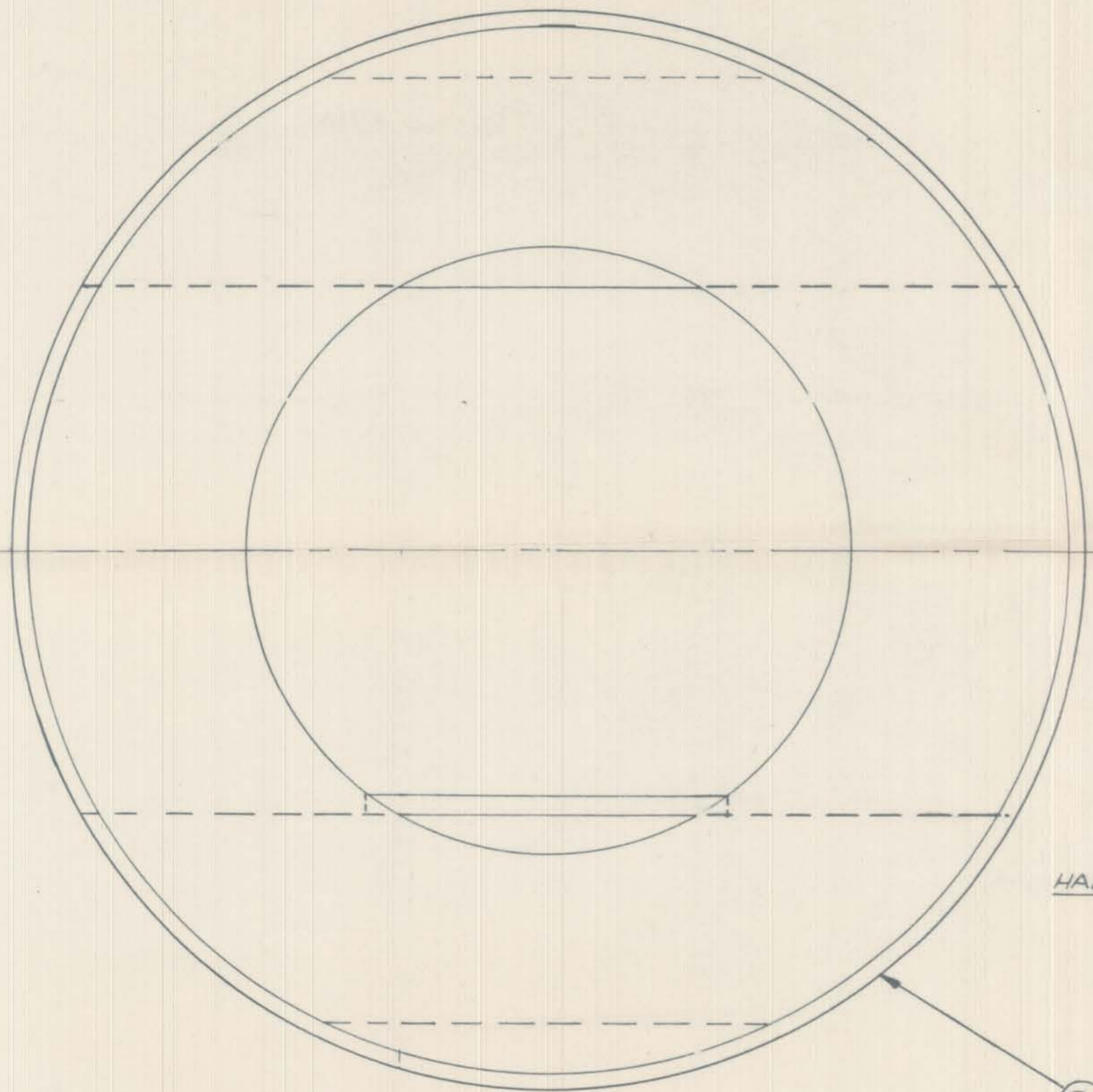


SAMPLE HOLDER AND VERNIER



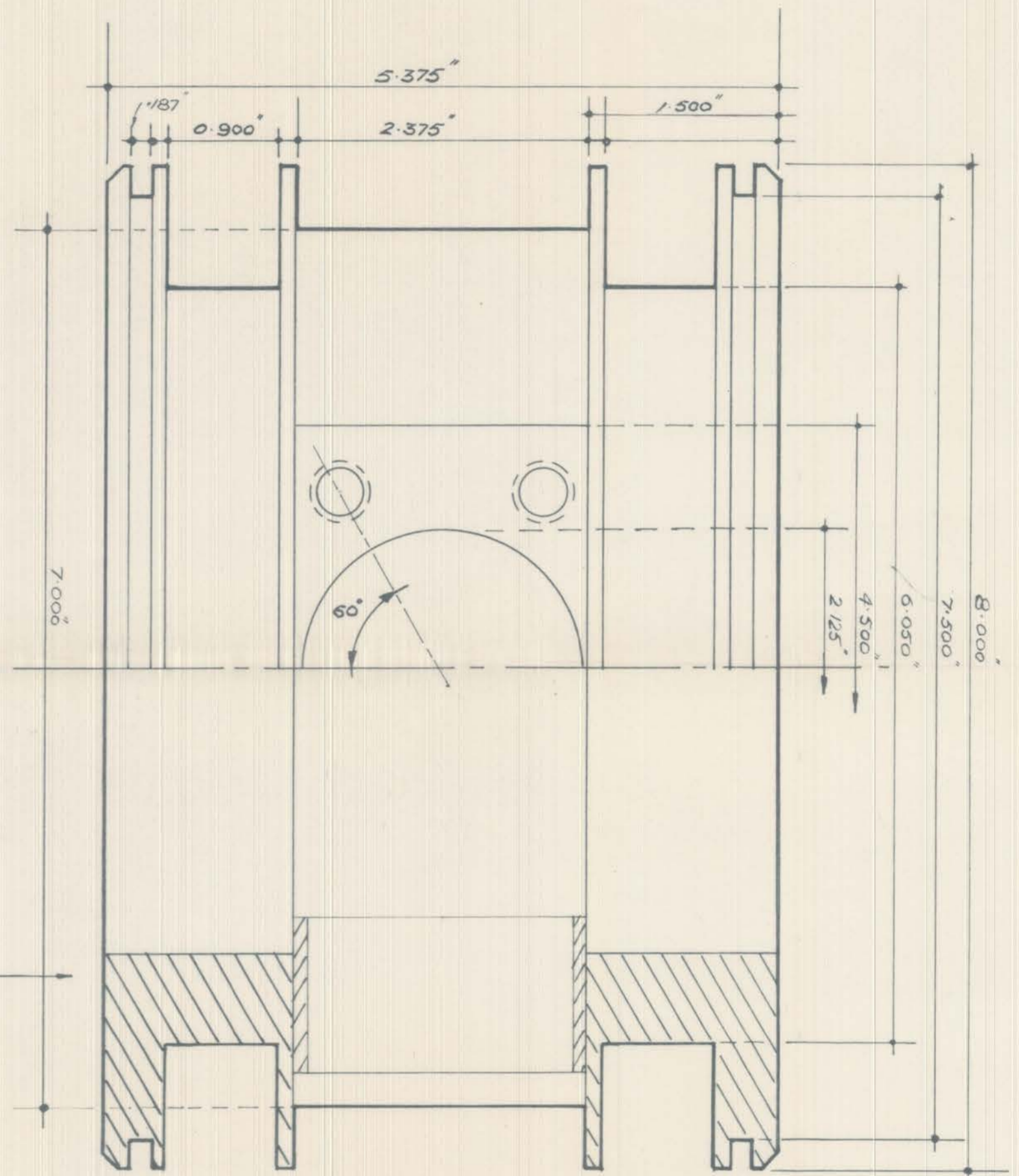
*Circular recess cut 0.500" deep  
to take section of 12.000" dia.  
coil former —*



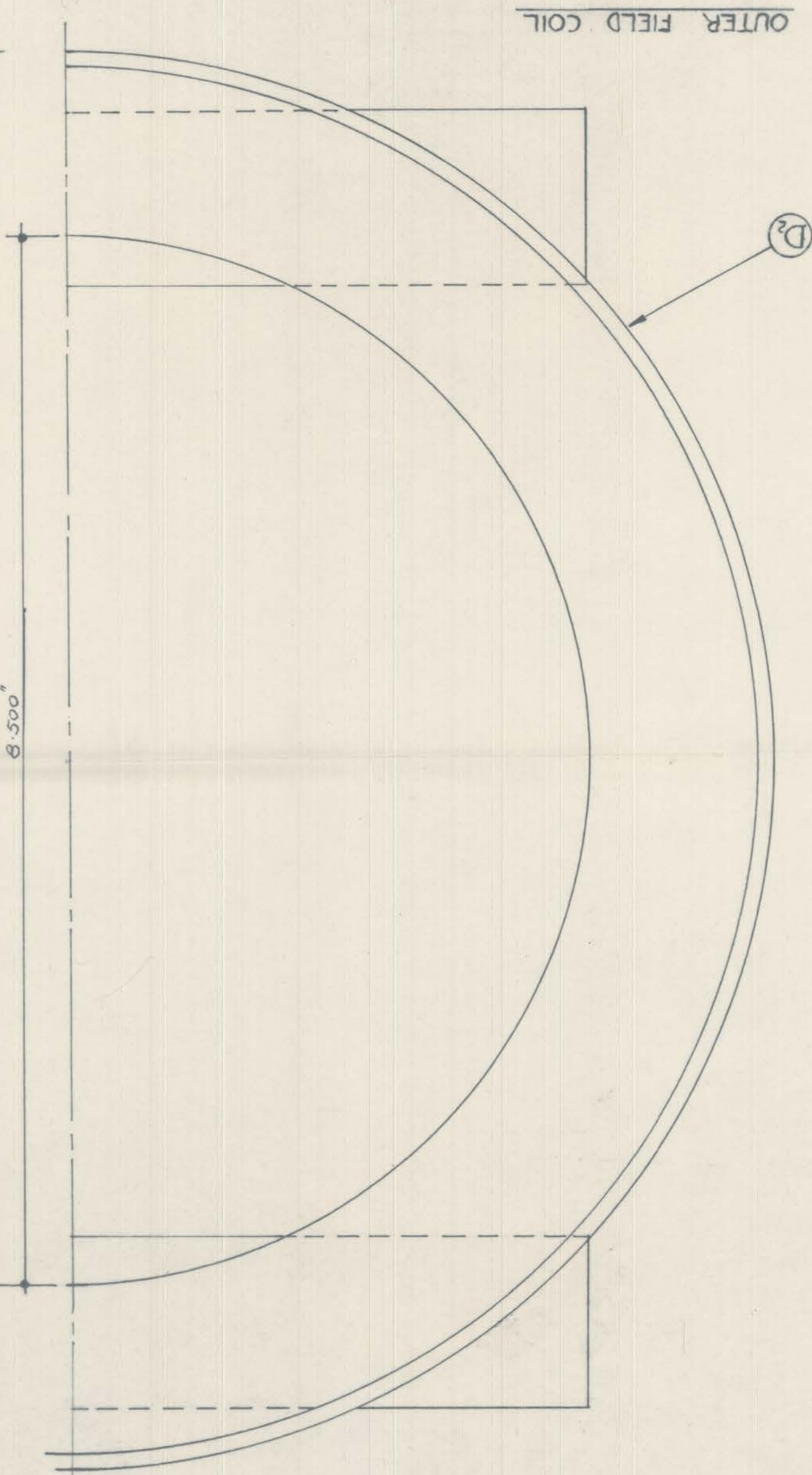
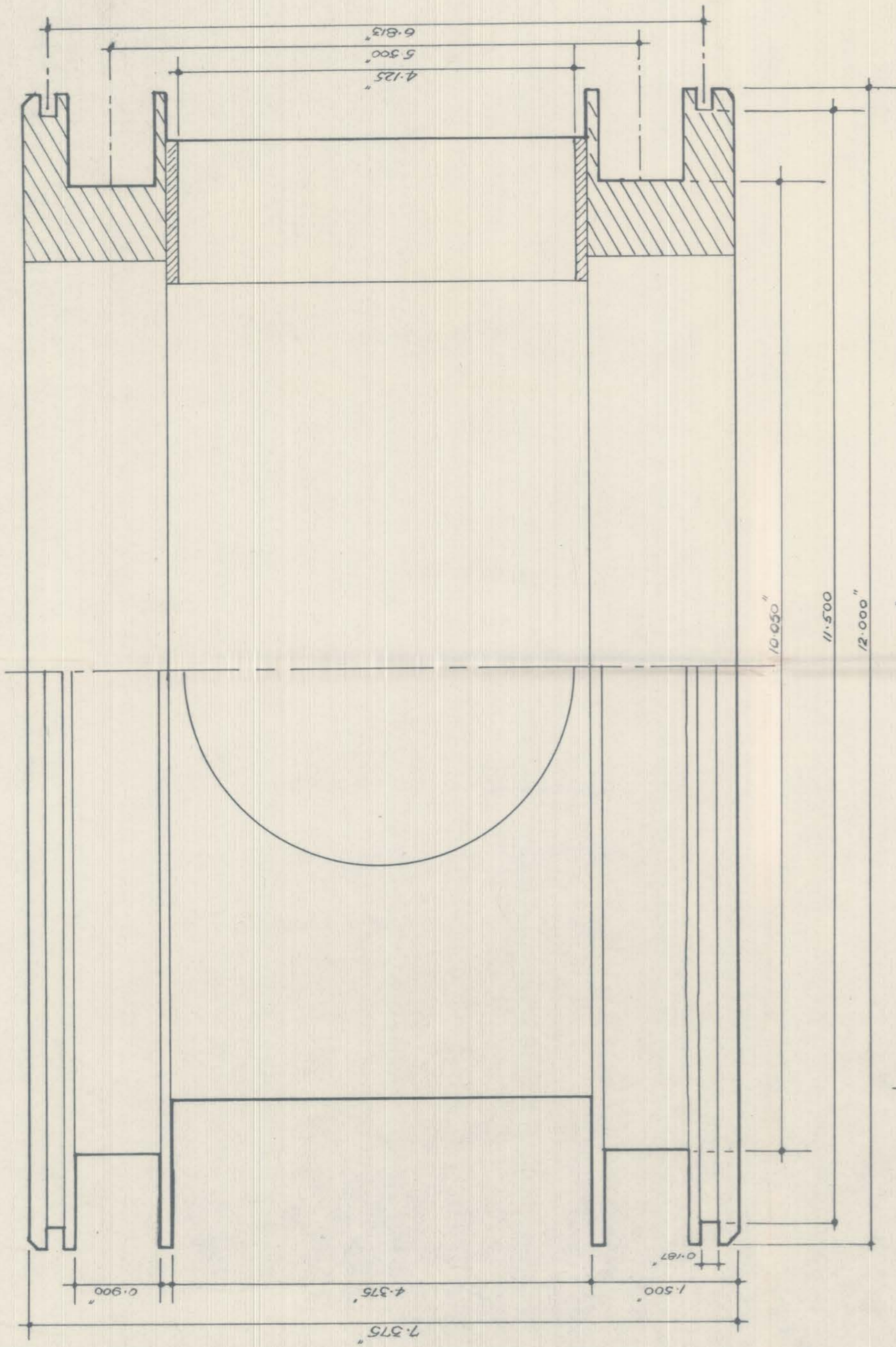


INNER FIELD COIL

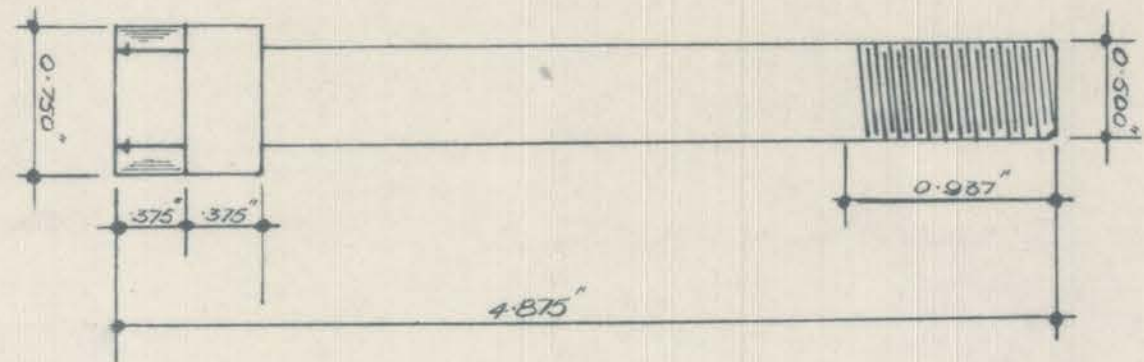
HALF SECTION.



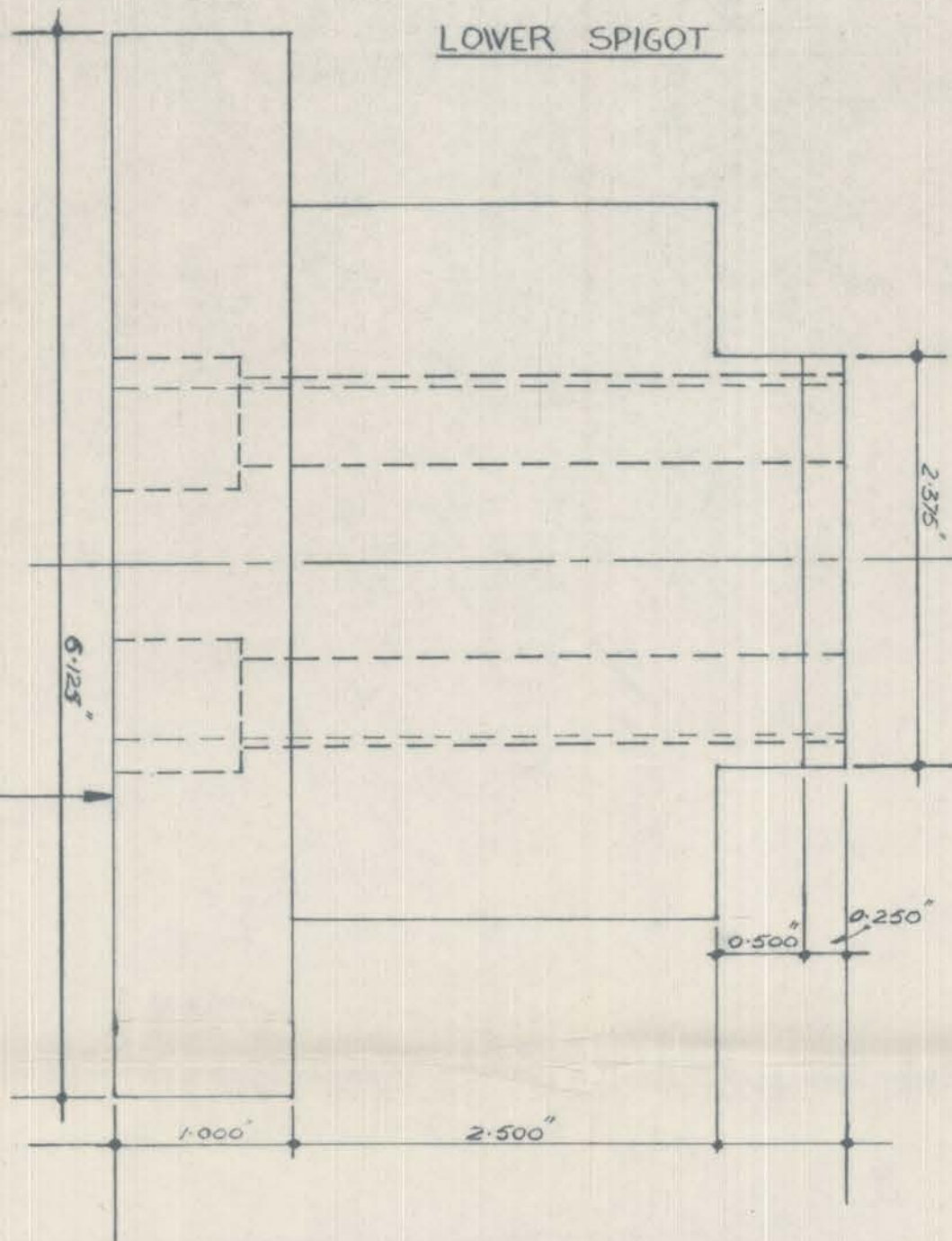




OUTER FIELD COIL

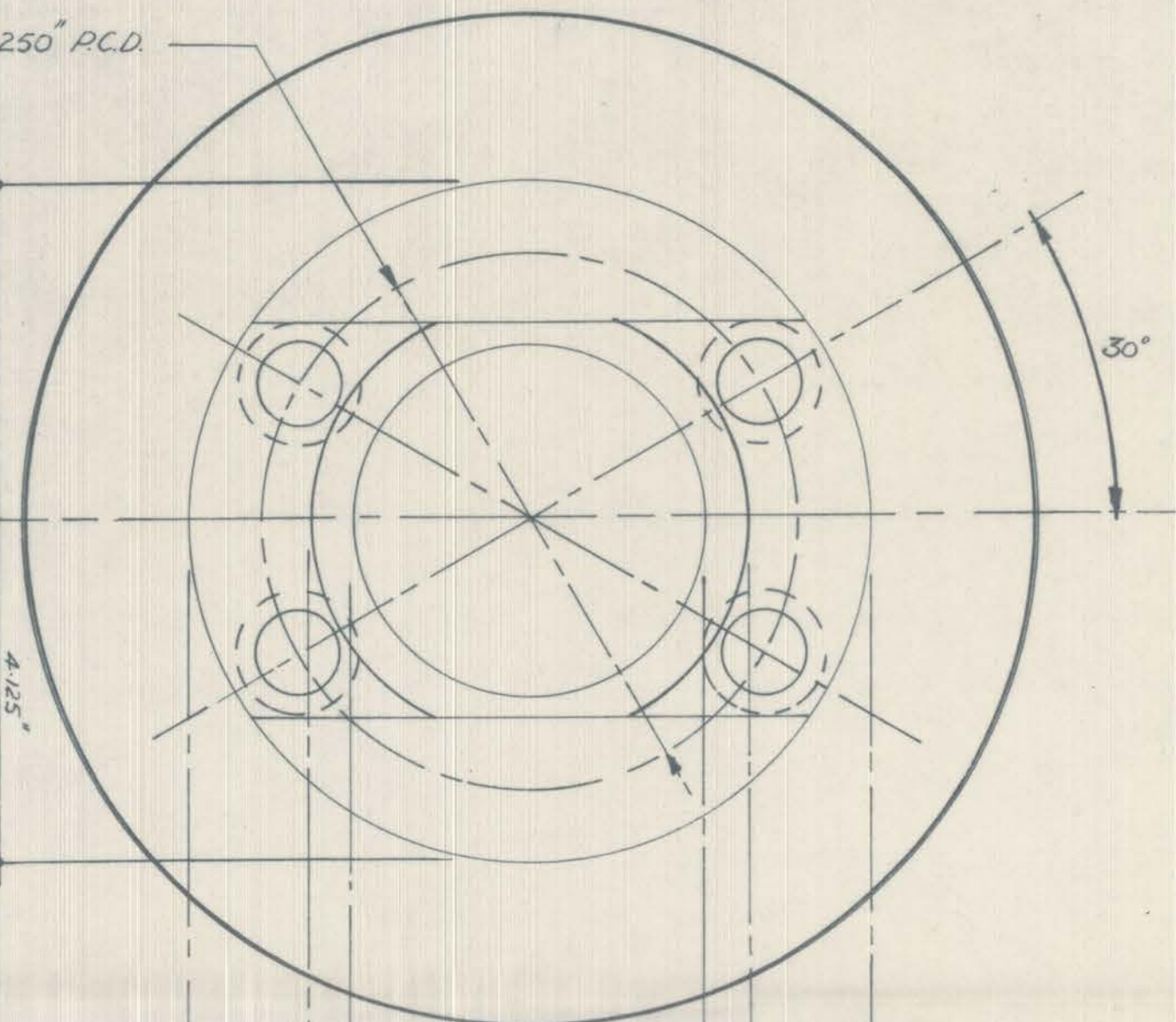


②

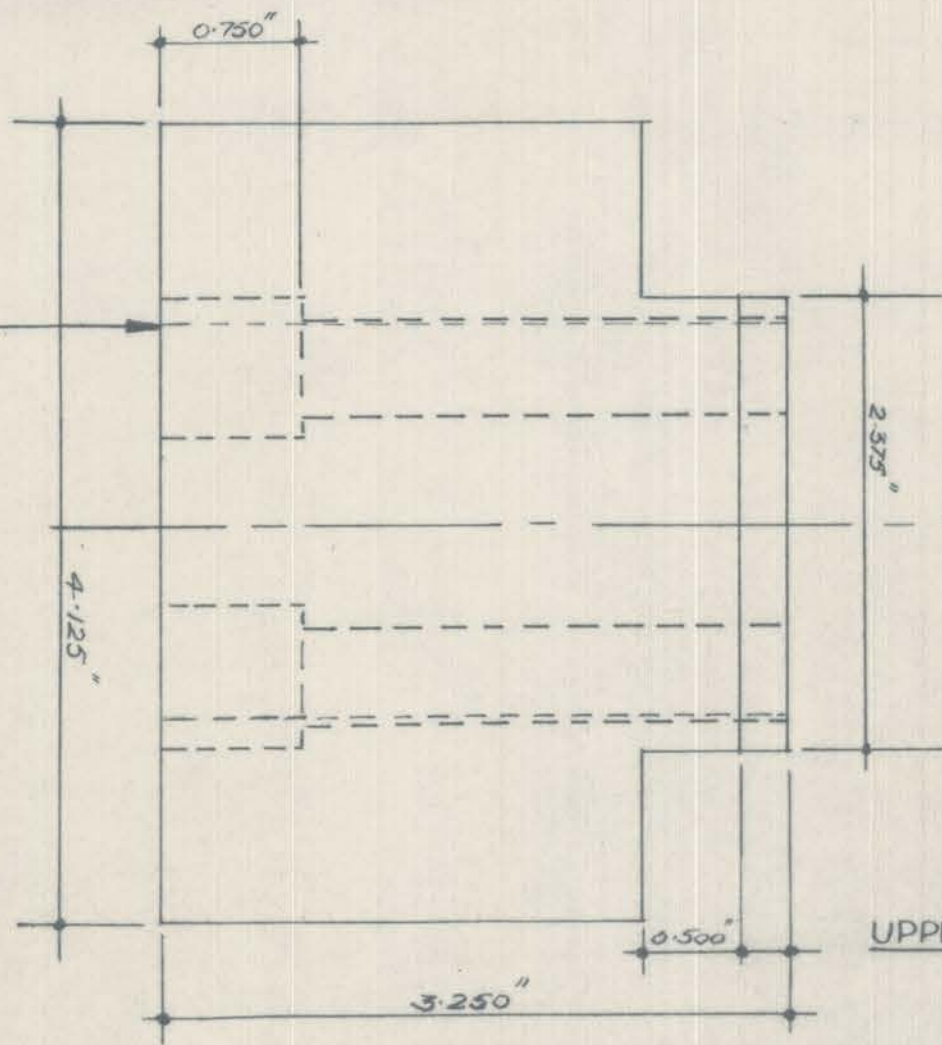


LOWER SPIGOT

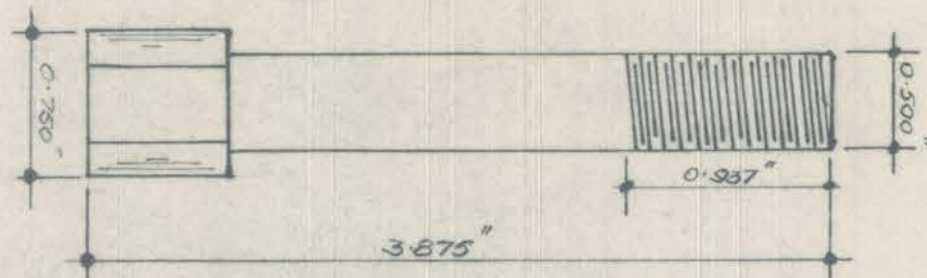
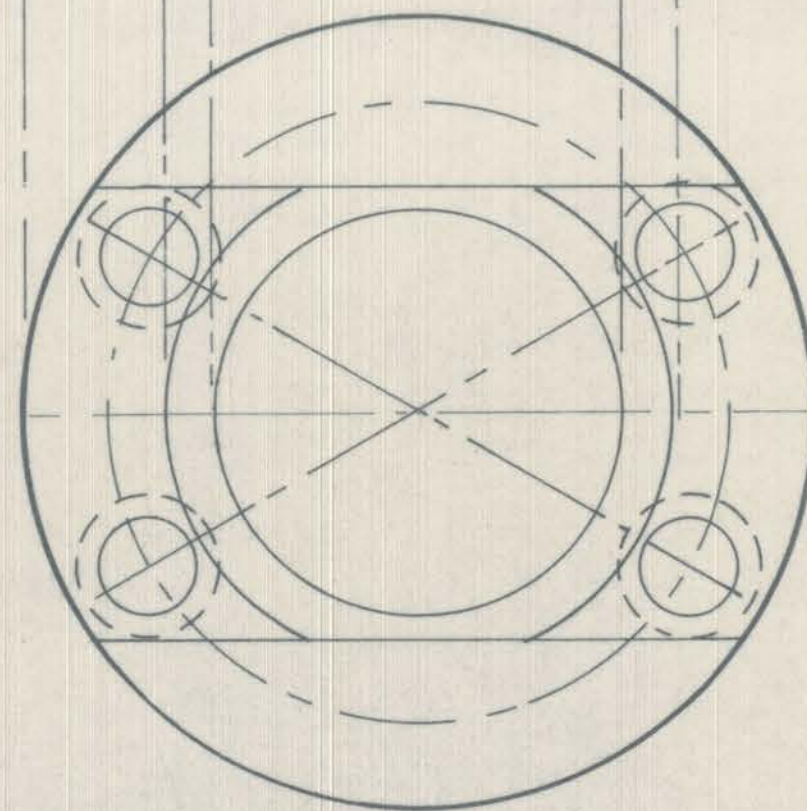
3.250" P.C.D.

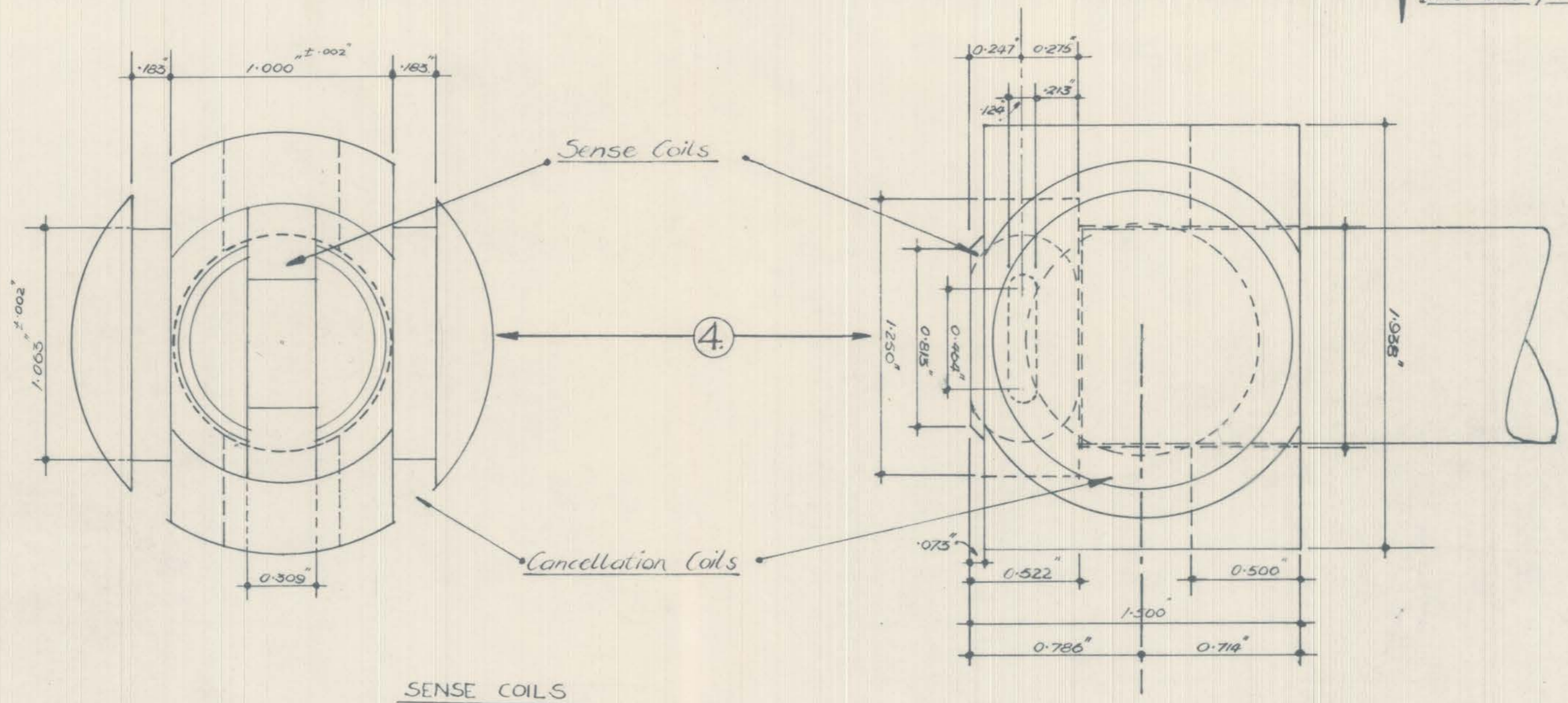
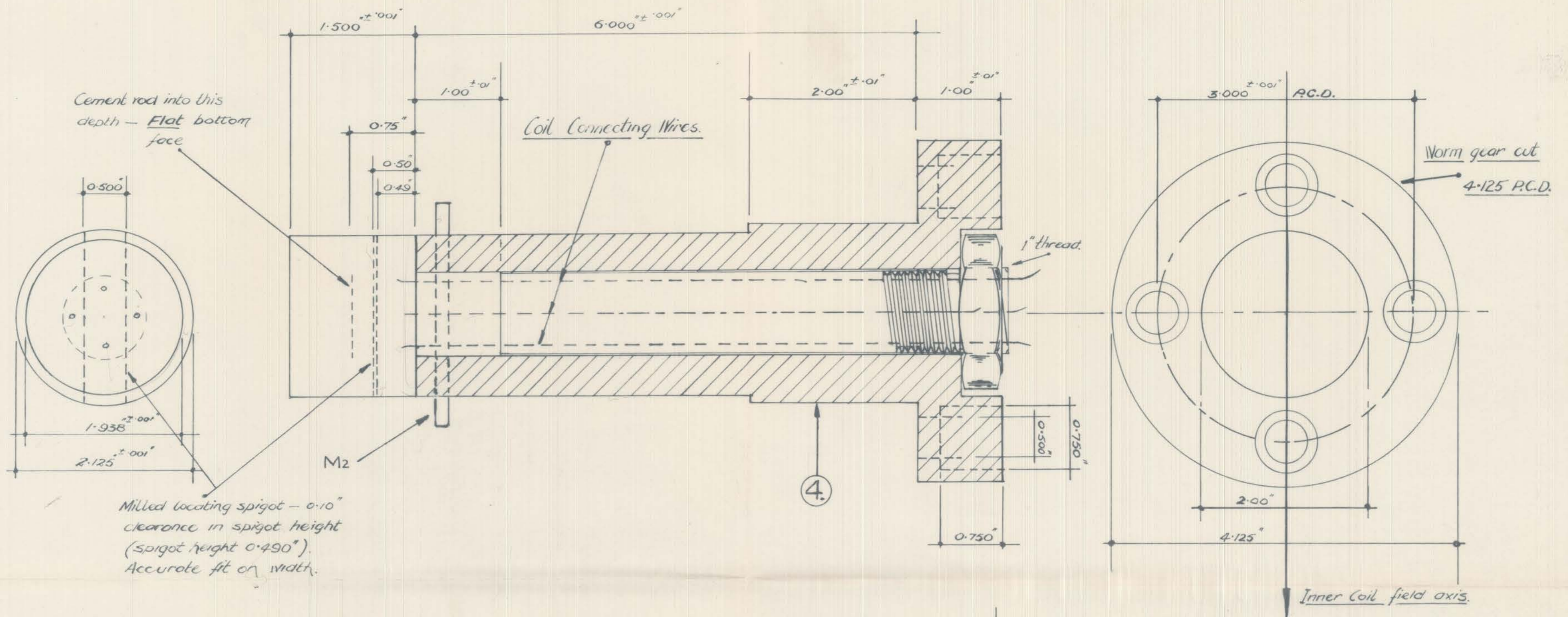


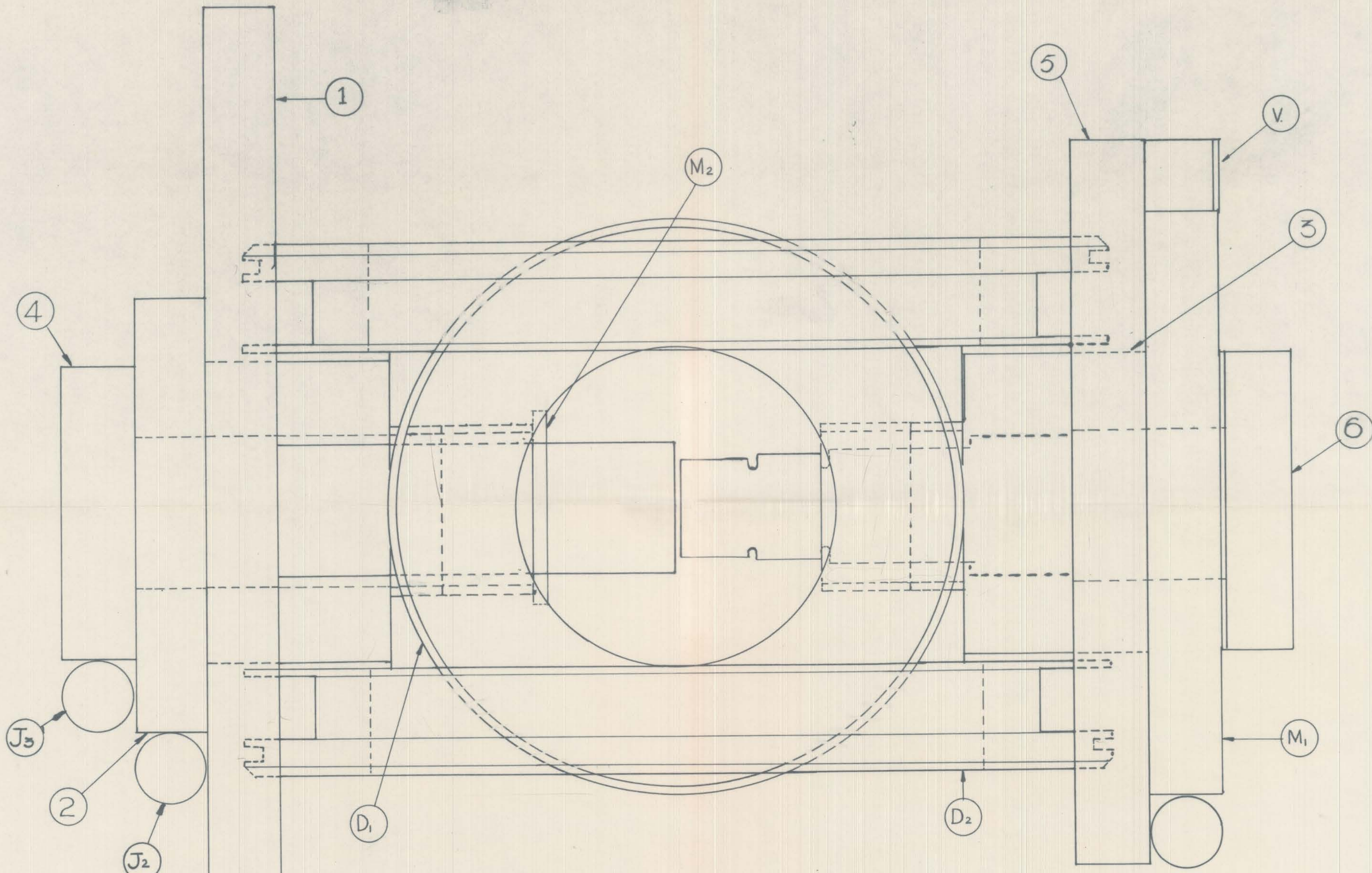
③



UPPER SPIGOT







MECHANICAL DETAILS OF M-H CURVE PLOTTER